

**CPUC-1002**

**Blade Supplemental Report (Vol. 2: SS-25 Well Failure Causes)**

**I.19-06-016**

**ALJs: Hecht/Poirier**

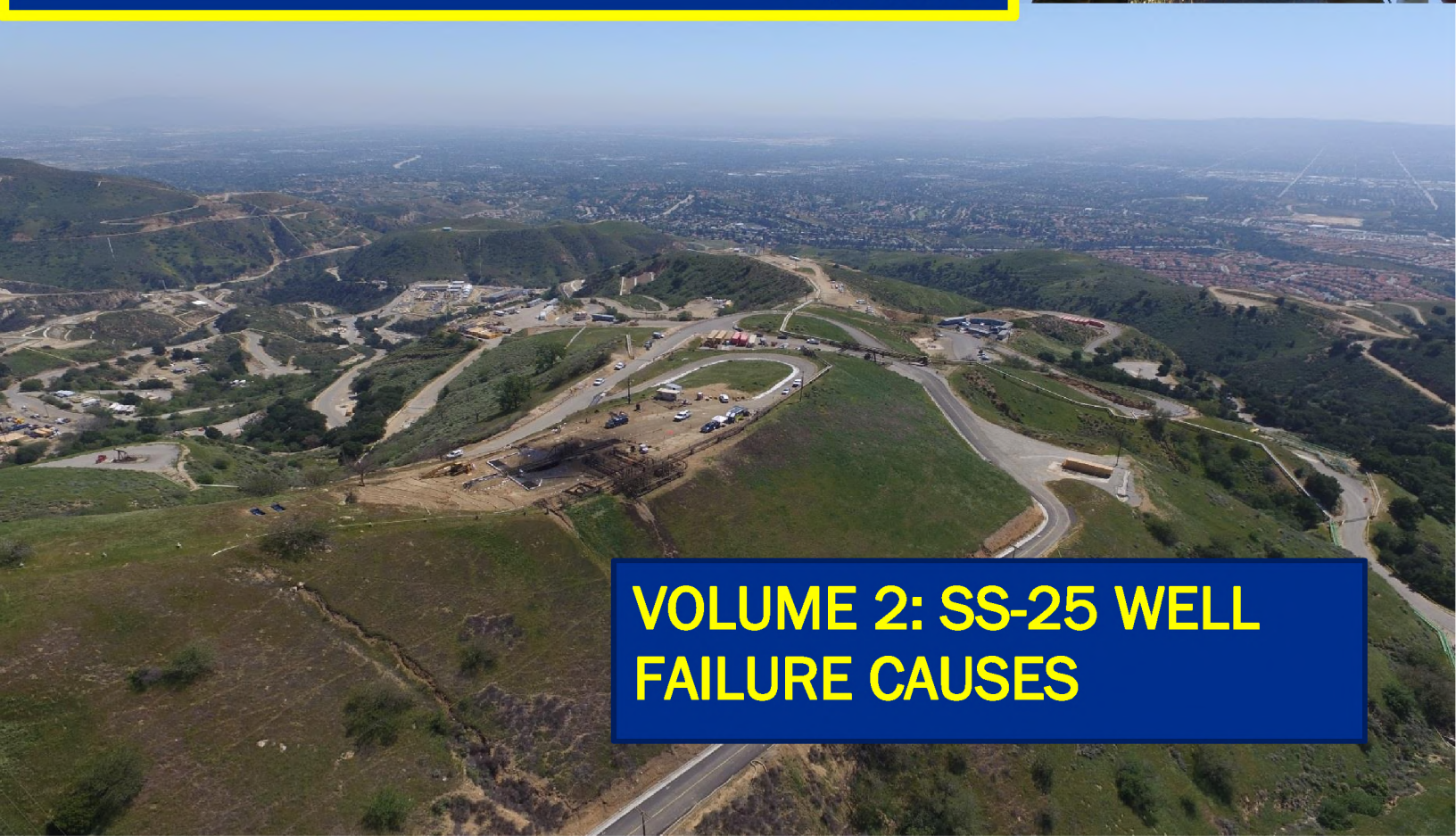
**Date Admitted: 3/24/2021**



# Root Cause Analysis of the Uncontrolled Hydrocarbon Release from Aliso Canyon SS-25

**SUPPLEMENTARY REPORTS**

May 31, 2019



**VOLUME 2: SS-25 WELL  
FAILURE CAUSES**

## Volume 2: SS-25 Well Failure Causes

This RCA work necessitated a substantial amount of testing, analyses, and modeling. The integrated work is reflected in the overall RCA report. Additionally, all the technical details and discussions are provided in supplementary reports—the source documents for the RCA report—in four volumes. This is Volume 2.

# MAIN REPORT

Root Cause Analysis of the Uncontrolled Hydrocarbon Release from Aliso Canyon SS-25

## SUPPLEMENTARY REPORTS

### Volume 1: Approach

### Volume 2: SS-25 Well Failure Causes

SS-25 Casing Failure Analysis

SS-25 7 in. Speedtite Connection Testing and 11 3/4 in. STC Assessment

SS-25 Analysis of Microbial Organisms on 7 in. Production Casing

SS-25 7 in. Casing Internal Corrosion Assessment

SS-25 Inspection Log Analyses

SS-25 Temperature, Pressure, and Noise Log Analysis

Aliso Canyon Field: Hydrology

SS-25 Geology Summary

SS-25 7 in. Casing Load Analysis

SS-25 Tubulars NDE Analyses

SS-25 Annular Flow Safety System Review

### Volume 3: Post-SS-25 Leak Events

### Volume 4: Aliso Canyon Casing Integrity

# SS-25 RCA Supplementary Report

# SS-25 Casing Failure Analysis



2600 Network Boulevard, Suite 550  
Frisco, Texas 75034

+1 972-712-8407 (phone)  
+1 972-712-8408 (fax)

16285 Park Ten Place, Suite 600  
Houston, Texas 77084

1-800-319-2940 (toll free)  
+1 281-206-2000 (phone)  
+1 281-206-2005 (fax)

[www.blade-energy.com](http://www.blade-energy.com)

## **Purpose:**

Report on the analyses and results of the SS-25 7 in. casing failure.

## **Date:**

May 31, 2019

Blade Energy Partners Limited, and its affiliates ('Blade') provide our services subject to our General Terms and Conditions ('GTC') in effect at time of service, unless a GTC provision is expressly superseded in a separate agreement made with Blade. Blade's work product is based on information sources which we believe to be reliable, including information that was publicly available and that was provided by our client; but Blade does not guarantee the accuracy or completeness of the information provided. All statements are the opinions of Blade based on generally-accepted and reasonable practices in the industry. Our clients remain fully responsible for all clients' decisions, actions and omissions, whether based upon Blade's work product or not; and Blade's liability solely extends to the cost of its work product.

## Abstract

The gas storage well Standard Sesnon 25 (SS-25) in the Aliso Canyon Gas Storage Field located in Los Angeles County, California, started leaking gas in October 2015. A relief well was drilled, and SS-25 was brought under control. The leak stopped in February 2016.

In January 2016, as part of their investigation of the leak, the California Public Utilities Commission (CPUC) and the Division of Oil, Gas, and Geothermal Resources (DOGGR) selected and gave provisional authority to Blade Energy Partners (Blade) to perform an independent RCA. The Blade Team and parties under Blade's direction were responsible for directing the work of subcontractors who performed the extraction of the SS-25's wellhead, tubing, and casings and the preservation and protection of associated evidence. Blade's RCA Reports, including this report, document and describe the key activities undertaken in support of the RCA effort.

The objective of this report was to determine the cause of the SS-25's 7 in. casing failure. An interdisciplinary approach was used for the investigation, including metallurgical, mechanical, chemical, and biological analyses. The key findings are summarized as follows:

- An axial rupture and circumferential parting occurred in the 7 in. casing at 892 ft (joint 22). The axial rupture originated from an 85% metal loss due to corrosion, which was characterized by striated grooves with V-shaped tips. Metallurgical, chemical, and biological evidence showed that the corrosion was most likely influenced by microbes. The release of cold gas from the opening formed by the axial rupture resulted in rapid cooling of the adjacent casing material. The rapid cooling resulted in the circumferential parting.
- The failure temperature for the circumferential parting was estimated to be between  $-60^{\circ}\text{C}$  and  $-39^{\circ}\text{C}$ , which is consistent with an independent thermal model that estimated a failure temperature of  $-34^{\circ}\text{C}$ .
- The finite element analysis (FEA) and fracture mechanics analyses supported the metallurgical findings.

In conclusion, the axial rupture occurred in the 7 in. casing due to an 85% deep corrosion on the outside diameter (OD) surface, most likely influenced by microbes. Rapid cooling due to the release of cold gas from the axial rupture led to the circumferential parting.

## Table of Contents

<b>1</b>	<b>Introduction.....</b>	<b>13</b>
1.1	Abbreviations and Acronyms .....	14
<b>2</b>	<b>Background.....</b>	<b>17</b>
2.1	SS-25 Failure Overview.....	18
2.2	Field Operations and Investigation Summary .....	25
<b>3</b>	<b>7 in. Casing Failure Events and Sequence .....</b>	<b>71</b>
3.1	Overview.....	71
3.2	Axial Rupture Analysis .....	78
3.3	Initiation and Propagation of the Circumferential Parting.....	132
3.4	Summary.....	148
<b>4</b>	<b>7 in. Casing Failure Validation.....</b>	<b>150</b>
4.1	Axial Rupture Failure Pressure .....	150
4.2	Axial Rupture Tearing Instability .....	160
4.3	Circumferential Parting Critical Crack Size and Failure Temperature .....	164
4.4	Circumferential Parting Final Overload .....	169
4.5	Summary.....	171
<b>5</b>	<b>Corrosion Feature and Mechanism Related to the 7 in. Casing Failure.....</b>	<b>173</b>
5.1	Corrosion Distribution .....	173
5.2	Type I Corrosion Characterization .....	178
5.3	Scale Analysis.....	195
5.4	Biological Analysis .....	202
5.5	Integration of Evidence .....	206
5.6	Corrosion Rate.....	209
5.7	Summary.....	209
<b>6</b>	<b>Additional Features.....</b>	<b>211</b>
6.1	Other Types of Corrosion .....	211
6.2	7 in. Casing Linear Indication.....	222
<b>7</b>	<b>Material Testing.....</b>	<b>228</b>
7.1	7 in. Casing Testing.....	229
7.1	2 7/8 in. Tubing Testing .....	262
7.2	11 3/4 in. Casing Testing.....	269

<b>8</b>	<b>Conclusions.....</b>	<b>273</b>
<b>9</b>	<b>References.....</b>	<b>275</b>
Appendix A	<b>2 7/8 in. Tubing Samples .....</b>	<b>A-1</b>
Appendix B	<b>7 in. Casing Samples .....</b>	<b>B-1</b>
Appendix C	<b>X-Ray Diffraction Results for C025 Scale Samples .....</b>	<b>C-1</b>

## List of Figures

Figure 1:	2D Map Showing the SS-25 Site and Surrounding Wells.....	18
Figure 2:	Root Cause Analysis Site Map.....	19
Figure 3:	SS-25 Well Schematic.....	20
Figure 4:	Example of 2 7/8 in. Connection.....	21
Figure 5:	Super EU (Speedtite) Connection Configuration.....	22
Figure 6:	November 08, 2015, Temperature Survey (During Blowout).....	25
Figure 7:	(a) Outer and (b) Inner CPUC Incident Site Boundaries.....	27
Figure 8:	Phase 1 Search Zones and Grids.....	28
Figure 9:	SS-25 Site Condition on February 25, 2016.....	28
Figure 10:	SS-25 Site Top Aerial View Post-Blowout on April 01, 2016.....	29
Figure 11:	SS-25 Site West Aerial View Post-Blowout on April 01, 2016.....	29
Figure 12:	Missing 11 3/4 in. Casing Valve Taken on February 25, 2016.....	30
Figure 13:	Versa-Line HPT Log Data.....	31
Figure 14:	MID Results Showing 38% Metal Loss at Approximately 890 ft.....	32
Figure 15:	Microvertilog Results at 890 ft.....	33
Figure 16:	Wellhead Schematic.....	34
Figure 17:	SS-25 Wellhead in January 2015.....	34
Figure 18:	SS-25 Wellhead in February 2016.....	34
Figure 19:	Scaffolding for Wellhead Examination.....	35
Figure 20:	Wellhead Magnetic Particle Inspection.....	36
Figure 21:	SS-25 Tree Removal and Blowout Preventer Installation.....	36
Figure 22:	Crating of Wellhead Component W001A.....	38
Figure 23:	T155–T156 Connection Before and After Breakout.....	39
Figure 24:	Torque Distribution of 2 7/8 in. Tubing Breakout.....	39
Figure 25:	Minor Mechanical Damage on Box of Joints 185 and 207.....	40
Figure 26:	Moving Procedure of Tubing from the Rig Floor to the Pipe Racks.....	40
Figure 27:	Tubing Joints on the SS-25 Pipe Rack.....	41
Figure 28:	Permanent Identification Mark for Joint 1.....	41
Figure 29:	Sample Taken from Joint 32 at the SS-25 Pipe Rack.....	42
Figure 30:	Unloading of Tubing at the PS-20 Site.....	43
Figure 31:	Swabbing the 2 7/8 in. Tubing ID at PS-20.....	43
Figure 32:	Examples of Minor Metal Loss.....	44
Figure 33:	Examples of Mechanical Damage.....	44
Figure 34:	Examples of Manufacturer Stamps.....	44
Figure 35:	Bolstered Tubing on Trailer.....	45
Figure 36:	(a) Side and (b) Downhole Cameras on the EV Camera Logging Tool.....	46
Figure 37:	EV Lower Camera Snapshots from August 31, 2017, Showing the Parted 7 in. Casing.....	47

Figure 38: EV Side Camera Snapshots from August 31, 2017, Showing Upper Fracture Surface ..... 48

Figure 39: EV Side Camera Snapshots from August 31, 2017, Showing Lower Fracture Surface ..... 49

Figure 40: (a) HRVRT and (b) UCI Results Between 939 ft and 1,000 ft Showing External Corrosion ..... 50

Figure 41: Joint Sequence Number Versus Joint Number Example ..... 52

Figure 42: Wellhead Components (a) Before, (b) During, and (c) After Crating ..... 53

Figure 43: Ensign 540 Rig ..... 54

Figure 44: (a) Casing Running Tool on Rig Floor and (b) Stabbing 7 in. Casing ..... 55

Figure 45: (a) Cleaned Pipe Section for NDE, (b) Ultrasonic Transducer, and (c) MPI Linear Indication ..... 55

Figure 46: 7 in. Cutting Operation ..... 56

Figure 47: Casing Pipe Handler ..... 56

Figure 48: Corrosion Features on C018 (a) Pipe Body and (b) Connection ..... 57

Figure 49: C022 Extraction ..... 57

Figure 50: Parted Casing (C022) on the SS-25 Pipe Rack ..... 57

Figure 51: Diagram Showing Typical Cut to Remove Connection ..... 58

Figure 52: (a) C004, (b) C005, and (c) C012 Linear Indication Identified by MPI ..... 59

Figure 53: Shallow Metal Loss on Connection C014 ..... 59

Figure 54: Connection Corrosion on (a) C019 and (b) C020 ..... 59

Figure 55: Pipe Body Corrosion on (a) C016, (b) C017, and (c) C018 ..... 60

Figure 56: Examples of Corrosion with Striated Grooves from (a) C018 and (b) C022 ..... 60

Figure 57: Pipe Body Corrosion on C020 ..... 60

Figure 58: C022 Cut Locations ..... 61

Figure 59: Fracture Surface During (a) Extraction from C022 and After (b) Cleaning with Sentinel 909 ..... 61

Figure 60: Corrosion with Striated Grooves Adjacent to Fracture Surface ..... 62

Figure 61: (a) Circumferential Fracture Surface Showing (b) Erosion and (c) Chevron Marks ..... 62

Figure 62: Lower Fracture Surface (a) In and (b) Out of the Pawl Tool ..... 63

Figure 63: Axial Rupture and Circumferential Parting at PS-20 (C023A) ..... 63

Figure 64: Circumferential Parting Fracture Surface (a) Features and (b) Chevron Marks ..... 64

Figure 65: C023 and C024 Cut Diagrams ..... 64

Figure 66: Holes in 11 3/4 in. Surface Casing ..... 66

Figure 67: Baker Hughes Caliper Results for 11 3/4 in. Casing Joints 4–8 November 07, 2017 ..... 67

Figure 68: Versa-Line (a) MID-2 and (b) MID-3 Logs for 11 3/4 in. Casing ..... 67

Figure 69: Caliper and HRVRT Logs for 700–990 ft ..... 68

Figure 70: EV Camera Snapshot of ID Corrosion on 11 3/4 in. Casing ..... 68

Figure 71: UCI Log of 11 3/4 in. Longitudinal Feature in 11 3/4 in. Casing Resembling 7 in. Rupture ..... 69

Figure 72: Caliper Log of 11 3/4 in. Casing Joint 23 (888–898 ft) ..... 69

Figure 73: 11 3/4 in. Casing Extraction ..... 70

Figure 74: SS-25 7 in. Casing String Schematic ..... 72

Figure 75: Schematic and Photo of the Axial Rupture and Circumferential Parting ..... 73

Figure 76: Images of Axial Rupture Showing (a) Bulging, (b) Corrosion, and (c) Chevron Marks ..... 74

Figure 77: (a) Field Photo and (b) Laser Scan Indicating the (c) Lower Turning Point and (d) Lower Arrest Point; and (e) Upper Turning Point and (f) Upper Arrest Point ..... 75

Figure 78: (a) Laser Scan and (b) Circumferential Parting ..... 76

Figure 79: Stitched Images of the Lower Circumferential Parting Fracture Surface ..... 76

Figure 80: 7 in. Casing Failure Sequence Schematic ..... 77

Figure 81: (a) Front and (b) Top Views of Fracture Surface B Identifying Zones 1 and 2 ..... 79

Figure 82: Close-up of Zone 1 and Zone 2 of the Axial Rupture ..... 79

Figure 83: Remaining Wall Thickness Measurements of Axial Rupture ..... 80



Figure 84: Zone 2 Featureless Area on Upper Side of the Origin .....	80
Figure 85: Plot of Fracture Surface Mouth Opening Versus Axial Position .....	81
Figure 86: Macro Image of the Two Upper Turning Points and Single Arrest Point .....	81
Figure 87: Macro Images of the Lower Turning and Arrest Points.....	82
Figure 88: (a) Schematic and (b) Image of the Cut Locations for the Axial Fracture Surfaces .....	83
Figure 89: (a) Dry Saw Cut Example and (b) Fracture Surfaces After Cuts 1 and 2 .....	83
Figure 90: Five Specimens Cut from C023A1B2 for Fractographic Study.....	84
Figure 91: Cleaning Procedure Tests on Charpy V-Notch Specimen .....	85
Figure 92: SEM Images of Specimen C023A1B2C (a) Before and (b) After Cleaning.....	85
Figure 93: (a) Macro and (b) 25× Stereo Image of J-R Specimen L4-000.....	86
Figure 94: SEM Images of J-R Specimen L4-000 Taken at (a) 100×, (b) 1,000×, and (c) 5,000× .....	86
Figure 95: Joint 22 Corroded OD Specimen C022A1A1C3D (a) Before and (a) After Cleaning .....	87
Figure 96: C022A1A1C3D SEM Images Showing Pearlite Features (a) Before and (b) After Cleaning.....	87
Figure 97: Pearlite and Ferrite (Pitting) Corrosion at (a) 100×, (b) 1,000×, (c) 2,500×, and (d) 5,000× .....	88
Figure 98: SEM Examination of Cleaned Fracture Surfaces of C023A1B2C and C023A1B2D.....	89
Figure 99: SEM Images Comparing Fracture Surfaces from (a) J-R Tearing, (b) CVN, and (c) C023A1B2C ...	90
Figure 100: SEM Images of Area 3 Taken at (a) 30×, (b) 100×, (c) 500×, and (d) 1,000× .....	90
Figure 101: SEM Images of Area 4 Taken at (a) 30×, (b) 100×, (c) 500×, and (d) 1,000× .....	91
Figure 102: SEM Images of Area 8 Taken at (a) 30×, (b) 100×, (c) 500×, and (d) 1,000× .....	91
Figure 103: SEM Images of Area 10 Taken at (a) 30×, (b) 100×, (c) 500×, and (d) 1,000× .....	92
Figure 104: SEM Images of Area 17 Taken at (a) 30×, (b) 100×, (c) 500×, and (d) 1,000× .....	92
Figure 105: SEM Images of Area 19 Taken at (a) 30×, (b) 100×, (c) 500×, and (d) 1,000× .....	93
Figure 106: SEM images of Area 20 Taken at (a) 30×, (b) 100×, (c) 500×, and (d) 1,000× .....	93
Figure 107: C023A1B2D SEM Images of A30 Showing a Mixed Mode Morphology .....	94
Figure 108: C023A1B2D SEM Images of A37 Showing Woody-Type Morphology and Deformation Marks without Cleavage Facets.....	95
Figure 109: Origin Measurements Based on Micro Definition for C023A1B2C and C023A1B2D.....	96
Figure 110: (a) Macro Image and (b) Micrograph of C023A1B2C2 Showing the Remaining Wall .....	97
Figure 111: (a) C023B2C3 Section Layout and (b) Resulting C023B2C3B Mount .....	97
Figure 112: Micrographs of Equiaxed Grain Shape at Thinnest Area Taken at 200× .....	98
Figure 113: C023A1B2C3B Micrographs of Equiaxed Grain Shape Taken at 200×.....	98
Figure 114: Specimen C023A1B2D Lower Zone 2 SEM Investigation Areas.....	99
Figure 115: SEM Images from Locations A30 and A31 Showing Mixed Fracture Mode .....	101
Figure 116: SEM Images from Locations A28 and A29 Showing Mixed Fracture Mode .....	102
Figure 117: SEM Images from Locations A16 and A26 Showing Mixed Fracture Mode .....	103
Figure 118: Specimen C023A1B2B Upper Zone 2 SEM Investigation Areas.....	104
Figure 119: SEM Images for Areas A6, A7, and A8 Taken at 100×, 500×, and 1,000× .....	105
Figure 120: SEM Images for Areas A15, A16, and A17 Taken at 100×, 500×, and 1,000× .....	106
Figure 121: Specimen C023A1B2A5B1 Extraction Location and SEM Investigation Areas .....	107
Figure 122: Specimen C023A1B2A5B1 SEM Images from ID to OD .....	108
Figure 123: Overview of Upper Featureless Zone .....	109
Figure 124: Fracture Surface A Featureless Region of Upper Zone 2.....	109
Figure 125: Representative SEM Images of Erosion Marks (White Arrows) Taken at 800×.....	110
Figure 126: Erosion Mark Width Distribution.....	110
Figure 127: Specimen C023A1A1B1C (a) Before and (b) After Cleaning .....	111
Figure 128: SEM Images of A1 Erosion Marks Taken at (a) 30×, (b) 100×, (c) 500×, and (d) 1,100× .....	111
Figure 129: SEM Images of A2 Erosion Marks Taken at (a) 30×, (b) 100×, (c) 500×, and (d) 1,000× .....	112

Figure 130: SEM Images of A3 Erosion Marks Taken at (a) 30×, (b) 100×, (c) 500×, and (d) 1,000× ..... 112

Figure 131: SEM Images of A4 Erosion Marks Taken at (a) 30×, (b) 100×, (c) 500×, and (d) 1,000× ..... 113

Figure 132: Specimen C023A1B2E2A Extracted from C023A1B2E ..... 114

Figure 133: SEM Images of C023A1B2E2A (a) Before and (b) After Cleaning ..... 114

Figure 134: SEM Images of C023A1B2E2A A2 Taken at (a) 30×, (b) 100×, (c) 500×, and (d) 1,000× ..... 115

Figure 135: SEM Images of C023A1B2E2A A3 Taken at (a) 30×, (b) 100×, (c) 500×, and (d) 1,000× ..... 116

Figure 136: SEM Images of C023A1B2E2A A1 Taken at (a) 30×, (b) 100×, (c) 500×, and (d) 1,000× ..... 116

Figure 137: SEM Images of C023A1B2E2A A18 Taken at (a) 30×, (b) 100×, (c) 500×, and (d) 1,000× ..... 117

Figure 138: SEM Images of C023A1B2E2A A19 Taken at (a) 30×, (b) 100×, (c) 500×, and (d) 1,000× ..... 118

Figure 139: SEM Images of C023A1B2E2A A20 Taken at (a) 30×, (b) 100×, (c) 500×, and (d) 1,000× ..... 118

Figure 140: SEM Images of C023A1B2E2A A14 Taken at (a) 30×, (b) 100×, (c) 500×, and (d) 1,000× ..... 119

Figure 141: SEM Images of C023A1B2E2A A13 Taken at (a) 30×, (b) 100×, (c) 500×, and (d) 1,000× ..... 120

Figure 142: Specimen C023A1A1B4 Extraction ..... 121

Figure 143: Specimen C023A1A1B4 Showing SEM Locations Near Upper Arrest Region ..... 121

Figure 144: Specimen C023A1A1B4 A4 Showing OD, MW, and ID at 100× and 500× ..... 122

Figure 145: Specimen C023A1A1B4 A2 Showing OD, MW, and ID at 100× and 500× ..... 123

Figure 146: Specimen C023A1A1B4 A3 Showing OD, MW, and ID at 100× and 500× ..... 124

Figure 147: Specimen C023A1A1B4 Showing SEM Locations at the Second Upper Turning Point ..... 125

Figure 148: SEM Images of C023A1A1B4 A7 OD Taken at (a) 30×, (b) 100×, (c) 500×, and (d) 1,000× ... 126

Figure 149: SEM Images of C023A1A1B4 A7 MW Taken at (a) 30×, (b) 100×, (c) 500×, and (d) 1,000× . 126

Figure 150: SEM Images of C023A1A1B4 A7 ID Taken at (a) 30×, (b) 100×, (c) 500×, and (d) 1,000× ..... 127

Figure 151: SEM Images of C023A1A1B4 A9 OD Taken at (a) 30×, (b) 100×, (c) 500×, and (d) 1,000× ... 128

Figure 152: SEM Images of C023A1A1B4 A9 OD-2 Taken at (a) 30×, (b) 100×, (c) 500×, and (d) 1,000× ..... 128

Figure 153: SEM Images of C023A1A1B4 A9 MW Taken at (a) 30×, (b) 100×, (c) 500×, and (d) 1,000× . 129

Figure 154: SEM Images of C023A1A1B4 A9 MW-2 Taken at (a) 30×, (b) 100×, (c) 500×, and (d) 1,000× ..... 129

Figure 155: SEM Images of C023A1A1B4 A9 ID Taken at (a) 30×, (b) 100×, (c) 500×, and (d) 1,000× ..... 130

Figure 156: SEM Images of C023A1A1B4 A10 OD Taken at (a) 30×, (b) 100×, (c) 500×, and (d) 1,000× . 131

Figure 157: SEM Images of C023A1A1B4 A10 MW Taken at (a) 30×, (b) 100×, (c) 500×, and (d) 1,000× ..... 131

Figure 158: SEM Images of C023A1A1B4 A10 ID Taken at (a) 30×, (b) 100×, (c) 500×, and (d) 1,000× ... 132

Figure 159: (a) Circumferential Parting and (b) Upper and (c) Lower Fracture Surfaces ..... 133

Figure 160: (a) Stereo Images and (b) Schematic of Three Failure Zones and (c) Zone 3 Image ..... 134

Figure 161: Circumferential Parting (a) Origin and Critical Crack Candidates (b) 1 and (c) 2 ..... 135

Figure 162: Zone 2 Chevron Marks and Crack Propagation Direction ..... 135

Figure 163: Schematic of the Axial and Circumferential Failure Crack Path ..... 136

Figure 164: Photos of the (a) Caliper and (b) Thickness Probe Used for Wall Thickness Measurement .... 137

Figure 165: The Measured Wall Thickness Data for Specimen C023A1A2 ..... 137

Figure 166: The Measured Wall Thickness Data for Specimens C023A1A1 and C023A1A2A ..... 138

Figure 167: Cut Locations and Specimen Identification for Circumferential Parting ..... 139

Figure 168: Specimen C023A1A1A (a) Stereo and (b) SEM Images of Zone 1 (Origin) Investigation Areas ..... 140

Figure 169: SEM Images of Pre-existing Flaws at (a) 1A, (b) 2A, and (d) 4A Taken at 500×, and (c) 3A Taken at 250× ..... 141

Figure 170: EDS Results for Pre-Existing Flaws ..... 141

Figure 171: SEM Images of C023A1A1A Areas (a) 1A, (b) 2A, (c) 3A, and (d) 4A Taken at 500× ..... 142

Figure 172: SEM Images of C023A1A1A Areas (a) 1B, (b) 2B, (c) 3B, and (d) 4B Taken at 500× ..... 142

Figure 173: C023A1A1A ID Fracture Surface Morphology Taken at (a) 100× and (b) 250× ..... 143

Figure 174: Specimen C023A1A1A2A Showing Fine Chevron Marks and Representative SEM Location ... 144

Figure 175: SEM Images of A9 OD at (a) 30×, (b) 100×, (c) 500×, and (d) 1,000× ..... 144

Figure 176: SEM Images of A9 MW at (a) 30×, (b) 100×, (c) 500×, and (d) 1,000× ..... 145

Figure 177: SEM Images of A9 ID at (a) 30×, (b) 100×, (c) 500×, and (d) 1,000× ..... 145

Figure 178: (a) Schematic and (b) (c) Image of Zone 3 (Final Overload Failure) ..... 146

Figure 179: Fracture Surface Morphologies near the ID, MW, and OD Taken at 100× ..... 147

Figure 180: Fracture Surface Morphologies near the ID, MW, and OD Taken at 1,000× ..... 148

Figure 181: Corrosion Feature Dimensions at the Rupture Location (892 ft) ..... 151

Figure 182: Corrosion Feature Geometry ..... 152

Figure 183: Model 2 Schematic and Mesh for Corrosion Feature and 2.13 in. Notch ..... 153

Figure 184: Model 3 Schematic and Mesh for Corrosion Feature and 4.8 in. Notch ..... 153

Figure 185: FE Model Mesh Elements ..... 154

Figure 186: Engineering and True Stress-Strain Responses of the Grade J55 Casing Material ..... 155

Figure 187: DFDI Evolution with Differential Pressure for Models 1, 2, and 3 ..... 157

Figure 188: Model 1 (a) Von Mises and (b) DFDI Plots ..... 158

Figure 189: Model 2 (a) Von Mises and (b) DFDI Plots ..... 158

Figure 190: Model 3 (a) von Mises and (b) DFDI Plots ..... 159

Figure 191: Pipe Bulge at the Center of the Corrosion Feature ..... 159

Figure 192: Model 3 Bulge at the Center of the Corrosion Feature ..... 160

Figure 193: Schematic of 3D Quarter Symmetric Casing Segment with Crack ..... 161

Figure 194: Average Half-Size Charpy Impact Energy Versus Temperature for C-L Orientation ..... 162

Figure 195: Symmetric Boundary Conditions ..... 163

Figure 196: Stress Intensity Factor Evolution with Applied Internal Pressure ..... 164

Figure 197:  $K_Q$  Versus Test Temperature ..... 167

Figure 198: Average Half-Size Charpy Impact Energy Versus Temperature for L-C Orientation ..... 168

Figure 199: Final Overload Schematic and Dimensions ..... 170

Figure 200: Geometry and FEA Results of the Final Overload Failure ..... 171

Figure 201: 7 in. Casing OD Corrosion Distribution for Joints 1 to 25 ..... 174

Figure 202: 7 in. Casing OD Corrosion Distribution for Joints 15 to 25 ..... 175

Figure 203: Types I, II, and III Corrosion Features ..... 176

Figure 204: (a) Joint 22 Axial Rupture and (b) Type I Feature Showing V-Shaped Tips ..... 178

Figure 205: (a) Specimen C022B1 from Circumferential Parting Showing (b) Regions 1 and 2 ..... 179

Figure 206: ImageJ Thresholding for Specimen C022B1 ..... 179

Figure 207: Striated Groove Orientation for Specimen C022B1 ..... 180

Figure 208: (a) Specimen from Joint 21 and (b) Type I Corrosion Feature ..... 181

Figure 209: (a) Specimen C021A3C Cross Section and (b) (c) Striated Groove Profile ..... 181

Figure 210: (a) Top and (b) Tilted View of C021A3C2 and (c) Cross Section Showing Tips 1 and 2 ..... 182

Figure 211: Stereo Microscope Image of (a) Tip 1 and (b) Tip 2 ..... 183

Figure 212: Microstructure Adjacent to (a) Tip 1 and (b) Tip 2 Tunnels ..... 183

Figure 213: SEM Images of the Largest Tip 1 Tunnel ..... 184

Figure 214: (a) Backscatter and (b) SEM Images of Tip 2 Tunnels ..... 184

Figure 215: EDS Analysis of Largest Tip 1 Tunnel (C021A3C2) ..... 184

Figure 216: Specimen C021A3C2 after Second Polish ..... 185

Figure 217: Raman Spectra Showing Organic Matter, Modified Hematite, and Magnetite [38] ..... 185

Figure 218: Specimen C021A3C3 (a) V-pointed Groove Tips and (b) Cross Section Location ..... 186

Figure 219: Stereo Images of Specimen C021A3C3A Cross Section Taken at (a) 15× and (b) 20× ..... 186

Figure 220: C023A1B2A5 Groove Tunnel Adjacent to Axial Rupture Fracture Surface ..... 187

Figure 221: Specimen C023A1B2A5B2's (a) SEM Image and (b) Metallographic Section Showing Tunnel ..... 187

Figure 222: (a) FIB Sectioning Schematic and SEM Image of Cut with a (b) 0° and (c) 52° Tilt ..... 188

Figure 223: FIB Cross Section of the Groove Wall in C023A1B2A5B2 at (a) 100× and (b) 5,000× ..... 189

Figure 224: FIB Cross Section of the Groove Tip Viewed at (a) 100× and (b) 3,000× ..... 189

Figure 225: EDS Mapping of the Corrosion Deposit Inside the Tunnel ..... 190

Figure 226: (a) Small Tunnel and (b) Extra-Cellular-Like Material..... 190

Figure 227: (a) Metallographic Cross Section of C023A1B2A5B2A and (b) High Magnification Image of Corrosion Deposit Inside the Tunnel ..... 191

Figure 228: (a) Second Metallographic Cross Section of C023A1B2A5B2A and (b) High Magnification Image of Corrosion Deposit..... 191

Figure 229: Metallographic Images of C023A1B2C2 ..... 192

Figure 230: (a) SEM Image of Tunnel with Acicular Deposit and EDS Color Maps for (b) S and (c) Mn..... 192

Figure 231: Specimen C022B2A5..... 193

Figure 232: (a) Top View of Groove Tip and (b) High Magnification Image of Globule Cluster ..... 193

Figure 233: FIB Cross Section of Globules ..... 193

Figure 234: Specimen C025A3B Sample (a) Layout and (b) Areas of Investigation ..... 194

Figure 235: (a) White Deposit on the Surface of C025A3B3 Area 1; (a) Globules on C025A3B3 Area 4..... 194

Figure 236: XRD Weight Percentages Before Adjustment..... 197

Figure 237: XRD Weight Percentages After Adjustment ..... 198

Figure 238: Weight Percentages of Iron Oxides Present in Scale Samples from C001–C025 ..... 199

Figure 239: Recalculated Percentages of Iron Hydroxides, Iron Oxides, Carbonates, and Formation..... 200

Figure 240: Ferrous/Ferric Hydroxide Stability Domains in the Presence of Carbonate (Condition 1)..... 201

Figure 241: Ferrous/Ferric Hydroxide Stability Domains in the Presence of Carbonate (Condition 2)..... 202

Figure 242: Culturable Bacteria per Gram of Sample ..... 203

Figure 243: Specimens with Type II Feature Extracted from Joint 22 ..... 211

Figure 244: Stereoscopic Image of Specimen C022B2A5B5 Type II Corrosion Feature ..... 212

Figure 245: Backscatter Image of (a) Globules and (b) Acicular Features ..... 212

Figure 246: (a) EDS Spectrum and (b) Dot Map Overlay for Corrosion Deposit on Specimen C022A5B5 .. 213

Figure 247: (a) SEM Image and (b) EDS Dot Map Overlay for the Deposit on Specimen C022A5B6 ..... 213

Figure 248: Backscatter Images of C022A5B7 Taken at (a) 500× and (b) 5,000× ..... 214

Figure 249: (a) Specimen C022A5B5B Cut Layout (b) C022A5B5B1 Polished Cross Section..... 214

Figure 250: (a) SEM Image of Corrosion Pit and (b) FIB Cross Section of Small Hole..... 215

Figure 251: Schematic of Small Hole Generated by Metallographic Cross Section ..... 215

Figure 252: (a) Type III Corrosion Feature on 7 in. Casing Connection and (b) Pipe Body ..... 216

Figure 253: (a) Connection C024B and (b) Type III Corrosion Specimen C024B1B ..... 216

Figure 254: Stereoscopic Images of C024B1B (a) Area 1 and (b) Area 5 ..... 217

Figure 255: Backscatter Images of Specimen C024B1B A1 Taken at (a) 150× and (b) 1,000× ..... 217

Figure 256: (a) EDS Spectrum and (b) Dot Map Overlay for Type III Small Acicular Features..... 217

Figure 257: (a) FIB Cut and (b) Cross Section View of Specimen C024B1B Corrosion Deposit ..... 218

Figure 258: (a) C024B1B Cut Layout and (b) C024B1B1A Corrosion Profile..... 218

Figure 259: SEM Image of Small Holes Under the Metal Surface of C024B1B1A..... 219

Figure 260: Laser Scan Data Overlaid with HRVRT Log Data ..... 221

Figure 261: Schematic of 7 in. and 11 3/4 in. Casing Contact ..... 221

Figure 262: Field and As-Received Images of the C004C Linear Indication..... 222

Figure 263: Black and White MPI Results for C004C .....	222
Figure 264: Eddy Current 2D Depth Color Map [79] .....	223
Figure 265: Cut Locations for Metallographic Sections A and B.....	223
Figure 266: Micrographs of Cross Section B (a) Polished and (b) Etched with 1% Nital .....	224
Figure 267: Micrographs of Cross Section B (a) Polished (15×) and (b) Etched with 1% Nital (1,000×)....	224
Figure 268: Metallographic Cross Section A Etched with 1% Nital and Taken at 200× .....	225
Figure 269: C004C1C After Opening at Liquid Nitrogen Temperature .....	225
Figure 270: C004C1C Fracture Surface After Opening at Liquid Nitrogen Temperature .....	226
Figure 271: SEM Images of C004C1C Taken at (a) 100×, (b) 500×, (c) 1,000×, and (d) 2,000× .....	226
Figure 272: EDS Spectra for C004C1C Area 1 .....	227
Figure 273: Typical Material Testing Specimen Layout .....	230
Figure 274: Joint 22 Material Testing Specimen Layout.....	230
Figure 275: As-Received Condition for Specimen C006A2 .....	231
Figure 276: Post-Cleaning Condition for Specimen C006A2.....	231
Figure 277: Post Abrasive Blasting for Specimen C006A2 .....	232
Figure 278: Joint 24 Features Identified After Abrasive Blasting .....	232
Figure 279: Field and Permanent Orientation Mark.....	233
Figure 280: Circumferential Orientation of Specimens .....	234
Figure 281: Material Testing Layout for Specimen C006A2 .....	234
Figure 282: Joint 22 Grain Size 7.0 at 100× 4% Picral .....	236
Figure 283: ASTM Grain Size Histogram .....	237
Figure 284: Polished Micrograph for Joints (a) 10 and (b) 15 Showing Inclusions at 100× .....	239
Figure 285: Micrographs of Joints 21, 22, and 23 Microstructure at 200× and 500×.....	240
Figure 286: ASTM A370 Specimen No. 4 [84] .....	241
Figure 287: Curved Grip Tensile Specimens .....	241
Figure 288: Final Cross-Sectional Area for Specimen 862 from Joint 20.....	243
Figure 289: Tensile Property Frequency Plots .....	244
Figure 290: Sub-Size Tensile Specimens .....	245
Figure 291: Silhouette Image of Tensile Specimen from Blade Vision System .....	246
Figure 292: Blade Critical Strain Test Setup.....	246
Figure 293: Transverse Tensile Specimen Schematic and Approximate Weld Locations .....	247
Figure 294: Hardness Ring with Three Indentations at the OD, MW, and ID in Four Quadrants.....	248
Figure 295: Hardness Rockwell B Value Distribution.....	250
Figure 296: CVN Testing Apparatus .....	250
Figure 297: ASTM E23 CVN Specimen Dimensions [86] .....	251
Figure 298: (a) ASTM E1823 Crack Plane Orientation [89] and (b) API 5CT CVN Orientations [90].....	252
Figure 299: Full, Three-Quarter, and Half-Size CVN Specimen Layout.....	252
Figure 300: Ductile-to-Brittle Transition Curve .....	253
Figure 301: CVN Fracture Surface Image.....	254
Figure 302: DBTT Curves for Joints 2 and 20 .....	255
Figure 303: Average CVN Properties Plotted Against Temperature.....	256
Figure 304: Impact Energy and Percent Shear DBTT Histograms.....	256
Figure 305: Vintage J55 Microstructure in the Longitudinal Direction (Joint 23) .....	261
Figure 306: New J55 Microstructure in the Longitudinal Direction .....	262
Figure 307: (a) 2 7/8 in. Layout, (b) Schematic, and (c)(d) T021B MPI Features.....	263
Figure 308: Grain Size Micrographs for (a) T005B, (b) T124B, and (c) T196B Taken at 100× .....	265
Figure 309: Microcleanliness Micrographs for (a) T005B, (b) T124B, and (c) T196B Taken at 100×.....	266

Figure 310: Microstructural Micrographs for (a) T005B, (b) T124B, and (c) T196B Taken at 500× ..... 266  
 Figure 311: Hardness Rockwell B Distribution for J55 Joints ..... 268  
 Figure 312: 11 3/4 in. Casing Grain Size Micrographs Taken at 100× ..... 270  
 Figure 313: 11 3/4 in. Casing Micrographs from Three Locations Taken at 100× ..... 270  
 Figure 314: 11 3/4 in. Casing Microstructural Micrographs Etched and Taken at 200× and 500× ..... 271  
 Figure 315: X-Ray Diffraction Spectra Used to Determine the Compounds Present in C025 ..... C-1

## List of Tables

Table 1: Nominal Dimensions for 7 in. Casing ..... 21  
 Table 2: Nominal Strength Properties for 7 in. Casing ..... 21  
 Table 3: Fracture Surface A and B Length Measurements ..... 81  
 Table 4: FEA Material Property Summary ..... 155  
 Table 5: Gas Injection Conditions and the Relevant Load Summary at a Depth of 892 ft ..... 156  
 Table 6: Differential Pressure ( $\Delta P$ ) Summary ..... 158  
 Table 7: Average C-L CVN Results and Estimated  $K_{mat}$  Values for 7 in. Casing ..... 163  
 Table 8:  $K_{IC}$  for Two Crack Candidates for the Circumferential Parting ..... 166  
 Table 9: Average L-C CVN Results and Estimated  $K_{mat}$  Values for 7 in. Casing ..... 168  
 Table 10: Estimated Failure Temperature for Circumferential Parting ..... 168  
 Table 11: Dominant Corrosion Features in 7 in. Casing ..... 176  
 Table 12: OLI Software Inputs ..... 200  
 Table 13: Average Abundance and Number of Species of Each Trait ..... 204  
 Table 14: GRI Scoring Sheet for MIC [35] ..... 207  
 Table 15: Electrochemical Test Results Summary for Simulated Groundwater Testing [65] ..... 220  
 Table 16: Electrochemical Test Results Summary for Synthetic Seawater Testing ..... 220  
 Table 17: EDS Results for Areas 1–4 of C004C1C Showing C, O, Fe, and Mn ..... 227  
 Table 18: API 5A 18<sup>th</sup> Edition Chemical Requirements for Seamless Pipe [80] ..... 228  
 Table 19: Typical Analyses for API Casing and Tubing [81] ..... 228  
 Table 20: API 5A 18<sup>th</sup> Edition Tensile Requirements for Casing and Tubing [80] ..... 229  
 Table 21: 7 in. Casing Optical Emission Spectroscopy Results ..... 235  
 Table 22: Inclusion Width and Diameter Parameters (ASTM E45 Methods A and D) [83] ..... 237  
 Table 23: Minimum Values for Severity Level Numbers [83] ..... 238  
 Table 24: Microcleanliness Results for Joints 1–25 ..... 238  
 Table 25: 7 in. Casing A370 Flat Grip Tensile Results ..... 242  
 Table 26: ASTM A370 Flat Grips Versus Curved Inserts Results ..... 244  
 Table 27: ASTM E8 Sub-Size Tensile Specimen Results for Joint 22 ..... 245  
 Table 28: Critical Strain Tensile Test Results ..... 248  
 Table 29: 7 in. Casing Hardness Rockwell B Results ..... 249  
 Table 30: Anderson Fracture Toughness Results Summary ..... 258  
 Table 31: Metcut Fracture Toughness Results Summary ..... 258  
 Table 32: Vintage and New J55 Phosphorous and Sulfur Comparison ..... 260  
 Table 33: Vintage and New Grade J55 Charpy V-Notch Comparison ..... 262  
 Table 34: 2 7/8 in. Tubing Optical Emission Spectroscopy Results (wt%) ..... 264  
 Table 35: 2 7/8 in. Tubing Grain Size Results ..... 264  
 Table 36: 2 7/8 in. Tubing Microcleanliness Results ..... 265  
 Table 37: 2 7/8 in. Tubing Flat Grip Tensile Results ..... 267  
 Table 38: 2 7/8 in. Tubing Vickers Hardness Results ..... 267

**SS-25 Casing Failure Analysis**

---

Table 39: 2 7/8 in. Tubing Hardness Rockwell B Results .....	268
Table 40: 2 7/8 in. Charpy V-Notch Results .....	268
Table 41: 11 3/4 in. Casing Optical Emission Spectroscopy Results (wt%).....	269
Table 42: 11 3/4 in. Casing Microcleanliness Results .....	270
Table 43: 11 3/4 in. Tensile Results .....	271
Table 44: 11 3/4 in. Hardness Rockwell B Results .....	272
Table 45: 11 3/4 in. Charpy V-Notch Results .....	272
Table 46: Field Samples Collected from 2 7/8 in. Tubing .....	A-1
Table 47: Field Samples Collected from 7 in. Casing .....	B-1
Table 48: X-Ray Diffraction Data from C025 Scale Analysis.....	C-1

# 1 Introduction

---

In October 2015, Southern California Gas's (SoCalGas) well SS-25 experienced a blowout. Blade was contracted to perform an RCA. Logs identified that the 7 in. casing had potentially parted at 892 ft. A downhole camera inspection confirmed that joint 22 had parted. An axial rupture and a circumferential parting were observed after the extraction of the failed 7 in. casing joints.

The extracted failed 7 in. casing segments, 7 in. casing joints, 2 7/8 in. tubing joints, wellhead components, and samples collected in the field were transported to Houston, TX, for a metallurgical investigation.

The objective of this report was to determine the cause of the SS-25 7 in. casing failure by using an interdisciplinary approach: metallurgical, mechanical, chemical, and biological analyses. This report summarizes the activities and results of the investigation and is organized in seven sections:

- Section 2 gives backgrounds of the failure and of the field investigation. The failure background provides details of the well construction, well history, and blowout timeline and events. The field investigation background includes details about the logging, extraction, and inspection of the tubulars at Aliso Canyon.
- Section 3 provides a detailed macro- and micro-fractographic analysis of the axial rupture and circumferential parting. It also discusses the events and sequence for the 7 in. casing failure.
- Section 4 presents the results from the mechanical analyses. The axial rupture and circumferential parting were validated using finite element analysis (FEA) and fracture mechanics approaches based on observations from Section 3.
- Section 5 presents the results from the 7 in. casing OD corrosion analysis. It includes the distribution and characterization of the corrosion and the results from the chemical and biological analysis of the 7 in. casing OD surface deposits. The findings were integrated to determine possible corrosion mechanisms.
- Section 6 presents the results from additional features identified on the OD surface of the 7 in. casing, including corrosion features not associated with the axial rupture and linear indications identified in the field.
- Section 7 presents the material testing results for the 7 in. casing, 2 7/8 in. tubing, and 11 3/4 in. casing. The results were used to confirm the structure and properties of the materials and support analyses in other sections.
- Section 8 discusses and integrates all the relevant findings regarding the cause of the 7 in. casing failure. The key findings and conclusions are also presented in this section.



## 1.1 Abbreviations and Acronyms

Term	Definition
ADR	Automated Drill Rig
Aliso Canyon	Aliso Canyon Gas Storage Field
AOI	Area of Investigation
APB	Acid-Producing Bacteria
API	American Petroleum Institute
ASTM	American Society for Testing and Materials
AWT	Actual Wall Thickness
BCC	Body-Centered Cubic
Blade	Blade Energy Partners
BOP	Blowout Preventer (equipment)
BS	British Standard
CCL	Casing Collar Locator
COC	Chain of Custody
CPET	Corrosion Protection Evaluation Tool
CPUC	California Public Utilities Commission
CRA	Corrosion-Resistant Alloy
CRT	Casing Running Tool
CVN	Charpy V-Notch
DBTT	Ductile-to-Brittle Transition Temperature
DCPD	Direct Current Potential Drop
DE	Diatomaceous Earth
DFDI	Ductile Failure Damage Indicator
DOGGR	Division of Oil, Gas, and Geothermal Resources
DSA	Double Studded Adapter
EBW	Electron Beam Weld
EDS	Energy Dispersive Spectroscopy
EMI	Electromagnetic Inspection
EOT	End of Tubing
EUE	External Upset End
EUL	Extension Under Load
FE	Finite Element
FEA	Finite Element Analysis
FIB	Focused Ion Beam
FLUT	Full-Length Ultrasonic Testing
FMI	Formation Microimager

Term	Definition
GHB	General Heterotrophic Bacteria
GR	Gamma Ray
GRI	Gas Research Institute
GR-JB	Gauge Ring Junk Basket
HAZ	Heat-Affected Zone
HPT	High Precision Temperature
HRB	Hardness Rockwell B
HRVRT	High-Resolution Vertilog Service
IBC	Isolation Scanner
ICAL	Imaging Caliper
ID	Internal Diameter
INTeX	Integrity eXplorer Cement Evaluation Service
IRB	Iron-Reducing Bacteria
ISO	International Organization for Standardization
JSN	Joint Sequence Number
LCM	Lost Circulation Material
LIDAR	Light Detection and Ranging
LVI	Laser Video Image
MIC	Microbiologically Influenced Corrosion
MID	Magnetic Imaging Defectoscope
MPC	Mechanical Pipe Cutter
MPI	Magnetic Particle Inspection
MPN	Most Probable Number
MTR	Material Test Report
MVC	Microvoid Coalescence
MVRT	MicroVertilog Tool
MW	Mid-Wall
NACE	National Association of Corrosion Engineers
NDE	Nondestructive Evaluation
NDT	Nondestructive Testing
NOAA	National Oceanic and Atmospheric Administration
NOV	National Oilwell Varco
NRB	Nitrate-Reducing Bacteria
NTU	Nephelometric Turbidity Units
NWT	Nominal Wall Thickness
OCP	Open Circuit Potential
OCTG	Oil Country Tubular Goods

Term	Definition
OD	Outside Diameter
OES	Optical Emission Spectrometer
P	Porter
PS	Porter Sesnon
RBP	Retrievable Bridge Plug
RCA	Root Cause Analysis
RFTEF	Rig Floor Tubulars Extraction Form
RIA	Reduction in Area
RRUFF	Raman Spectra Database
SCCM	Standard Cubic Centimeters per Minute
SEA	Special End Area
SEM	Scanning Electron Microscope
SLM	Standard Liter Per Minute
SNL	Spectral Noise Log
SoCalGas	Southern California Gas Company
SRB	Sulfur-Reducing Bacteria
SS	Standard Sesnon
SSCAN	Sonic Scanner
TD	Total Depth
TOL	Texas OilTech Laboratories
UCI	Ultrasonic Corrosion Imager
UT	Ultrasonic Testing
UTS	Ultimate Tensile Strength
VCI	Volatile Corrosion Inhibitor
VME	Von Mises Ellipse
WBM	Water-Based Mud
WLM	Wireline Measurement
XRD	X-Ray Diffraction
ZRA	Zero-Resistance Ammeter

## 2 Background

---

Blade was contracted to conduct an RCA of the leak in January 2016. The investigation was organized in six phases:

1. Phase 0—Data collection, collation, and analysis
2. Phase 1—Well site evidence collection and documentation
3. Phase 2—Well site restoration to rig readiness
4. Phase 3—Tubing, casing, and wellhead extraction
5. Phase 4—Metallurgical examination
6. Phase 5—Data integration and interpretation and final report

This report describes the activities, results, and conclusions completed for Phase 4. The majority of the data analyzed during this phase were collected in the field during Phases 0, 1, and 3. Activities and observations completed during subsequent phases pertaining to the metallurgical investigation are discussed in this report. An outline for the metallurgical investigation is described in the Phase 4 Protocol [1].

Phase 0 was the initial phase of the project, which began at the start of the RCA, and focused primarily on collecting current and historical data of the SS-25 well and, more generally, of the Aliso Canyon field. Access to the SS-25 site was limited during and immediately after the blowout due to operational and safety risks. Samples were collected in Phase 0 both during and after the blowout. Gas samples were taken during the blowout and sent to a third-party lab in Houston, TX, for analysis. A few items were also collected while being removed from the SS-25 site. Some of the historical and blowout data collected during Phase 0 are presented in Section 2.1.

Phase 1's objective was to collect evidence accessible from the surface prior to any well site restoration work in Phase 2 and included well site documentation and evidence collection. Soil, liquid, and solid samples were collected. The well site was also examined for evidence that might have been ejected from the well during the blowout. A detailed discussion of the Phase 1 operations and evidence collection can be found in the Phase 1 protocol [2] and summary report [3].

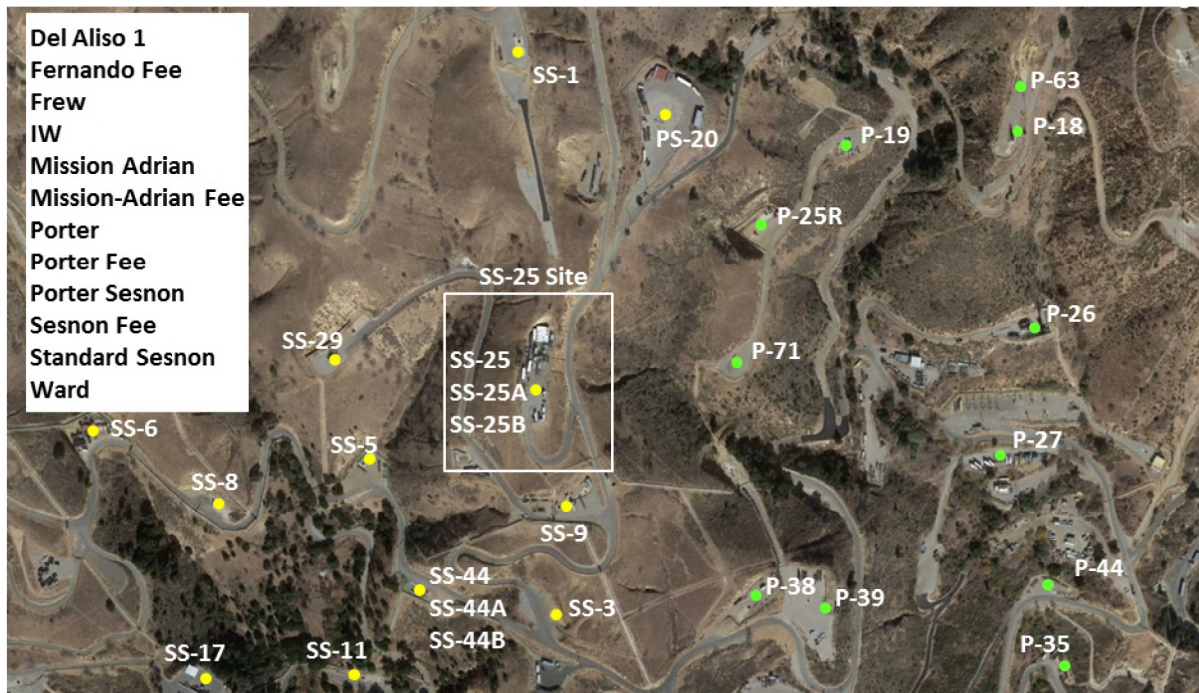
Phase 3's objective was to collect physical evidence used for the metallurgical investigation, including the tubing, casing, and wellhead components, which were extracted from the well and sent to Houston, TX, for detailed examination. The evidence collected during this phase is discussed throughout this report. A detailed discussion of the Phase 3 operations, equipment, and procedures may be found in the Phase 3 extraction protocol [4], evidence handling protocol [5], and summary report [6].

Phase 4 discusses the activities and results of the metallurgical investigation, which included the metallurgical investigation and all associated activities—reconstruction of the 7 in. casing failure, nondestructive evaluation (NDE) of the tubing and casing, laser scanning, and connection testing. Details of the additional activities are discussed in the Phase 4 protocol [1] and summary [7].

## 2.1 SS-25 Failure Overview

### 2.1.1 Well Site Description

SS-25 is a gas storage well located in the Standard Sesnon lease of the Aliso Canyon field. Aliso Canyon had approximately 114 active gas wells at the time of the blowout. Figure 1 shows a map of the SS-25 site and surrounding wells. The white box in Figure 1 identifies the SS-25 site location. The area immediately surrounding SS-25 contains wells from the Porter (P), Porter Sesnon (PS), and Standard Sesnon (SS) leases. The SS-25 site contains three wells: SS-25, SS-25A, and SS-25B. These wells are located in close proximity to one another on top of a knoll.



**Figure 1: 2D Map Showing the SS-25 Site and Surrounding Wells**

The following well sites were used throughout the RCA to assist with the investigation:

- SS-1—Located north of SS-25 on top of the north slope, it served as the initial vantage point during the blowout due to its higher elevation and proximity to SS-25. The initial photos provided to the Blade team were taken from SS-1.
- SS-9—Located south of SS-25 at the bottom of the south slope, it served as a staging area for equipment and vehicles and was the first location for the Phase 1 evidence trailers.
- PS-20—Located northeast of SS-25, it initially served as a staging area for equipment and a turnaround spot for large vehicles and later became the staging area for the metallurgical investigation. Trailers, pipe racks, sea containers, and other equipment were brought to PS-20 to assist with the Phase 3 pipe inspection. PS-20 was chosen due to its size and proximity to SS-25 and was a key site during Phase 3.

Figure 2 shows a 3D map of SS-25 and the surrounding wells. The image includes a list of the primary metallurgical roles for each site.

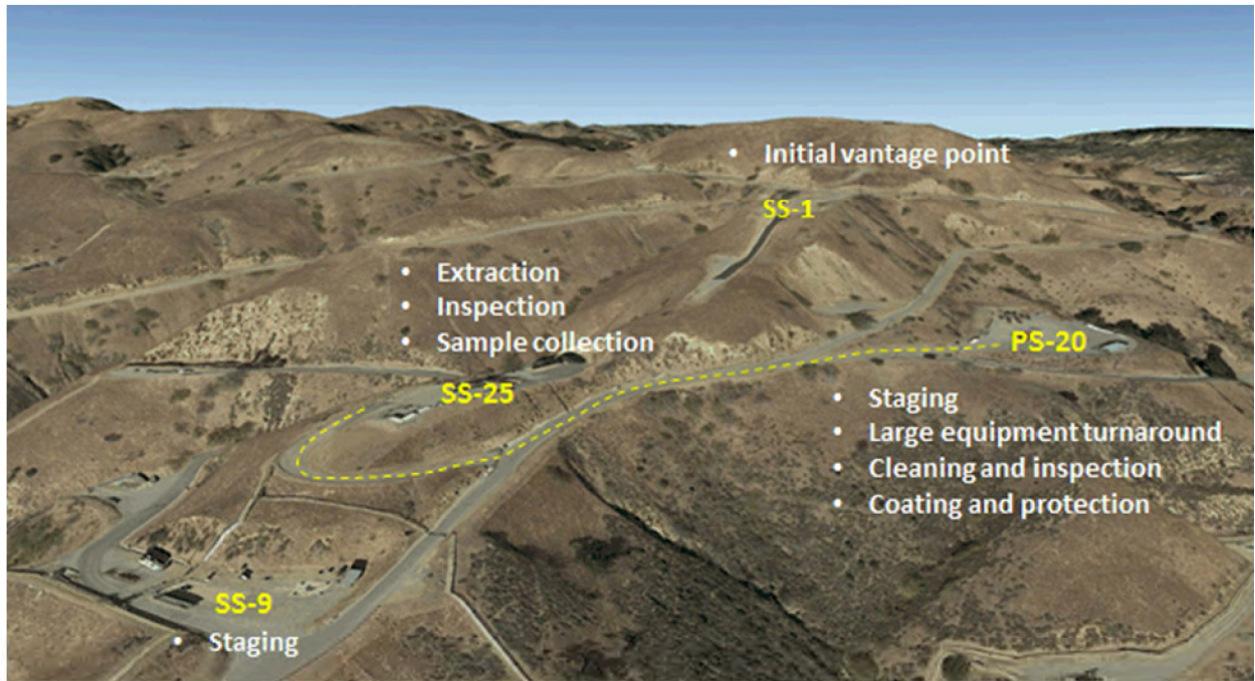


Figure 2: Root Cause Analysis Site Map

### 2.1.2 SS-25 Well History and Summary

The SS-25 drilling operations began on October 01, 1953, and ended on February 20, 1954. The well produced oil for approximately 20 years until it was converted to a gas storage well in June 1973. Converting the well from oil production to gas storage involved:

1. Pulling the existing tubing.
2. Pulling the packer.
3. Installing a new casing head on the 11 3/4 in. casing.
4. Running new 2 7/8 in. tubing.

SS-25 was worked over in July 1976 and February 1979. The purpose of the 1979 workover was to repair or replace a Camco annular flow safety system. Because the attempts to repair the system were unsuccessful, the valve and pack-off were pulled. The removal of the internal parts allowed communication between the tubing and casing above the packer, giving the well the capability to inject and produce through the tubing and casing simultaneously. Figure 3 shows SS-25's schematic. The well comprised the following four strings:

- 2 7/8 in. tubing
- 7 in. casing
- 11 3/4 in. casing
- 20 in. conductor

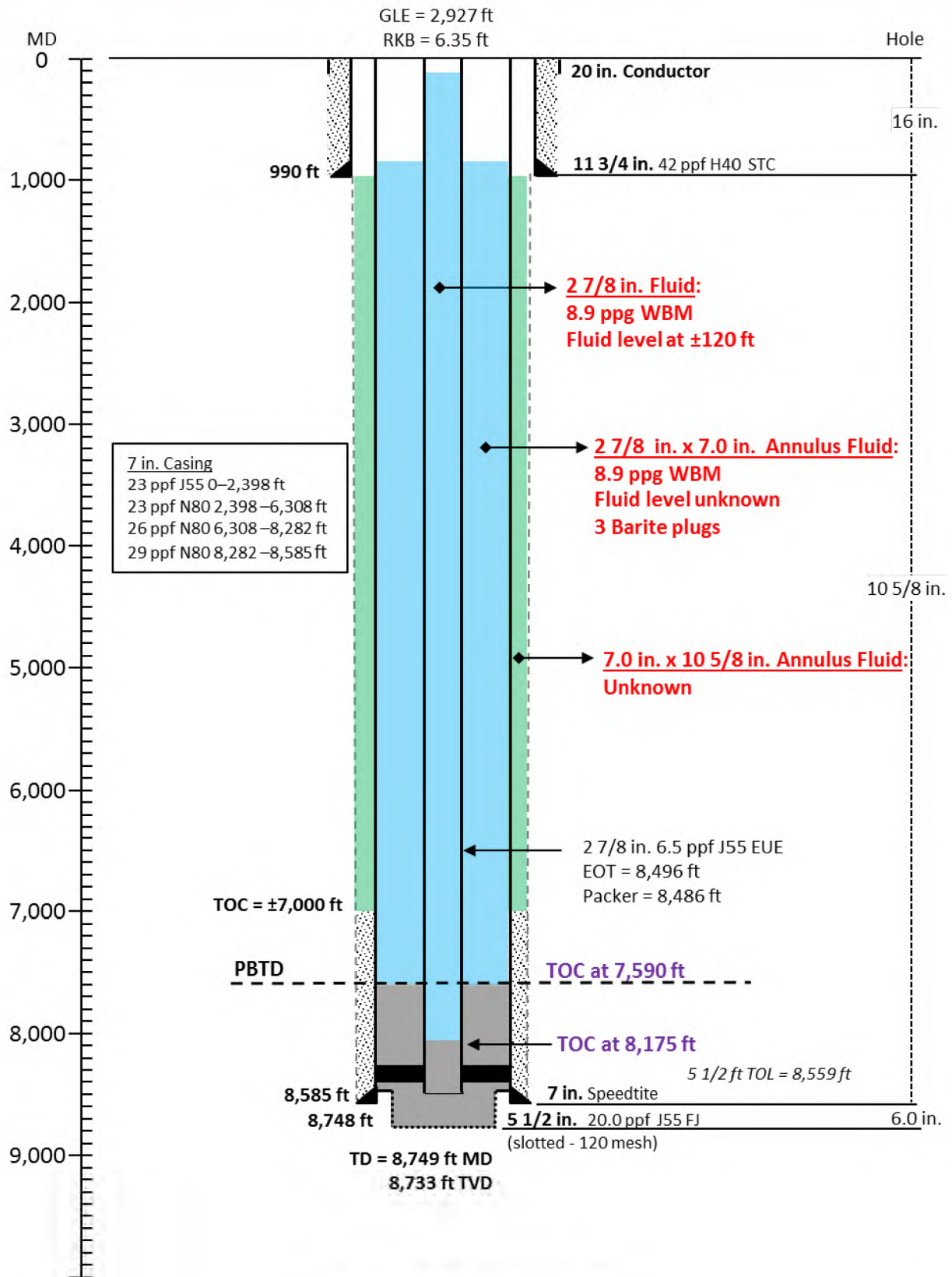


Figure 3: SS-25 Well Schematic

The 2 7/8 in. tubing string comprised grades J55 and N80 material. The tubing string consisted of six grade N80 joints and 265 grade J55 joints, from the hangar to 8,393 ft. The remainder of the string consisted of various completion equipment.

The connections for the 2 7/8 in. string were API 8 round external upset end (EUE), a type of tubing connection in which the external diameter of the tubing end connections are larger than the pipe body. The internal tubing surface is flush to enable good fluid-flow characteristics. Figure 4 shows an example of the 2 7/8 in. connection. The image shows how the external diameter of the pipe body increases at the upset.

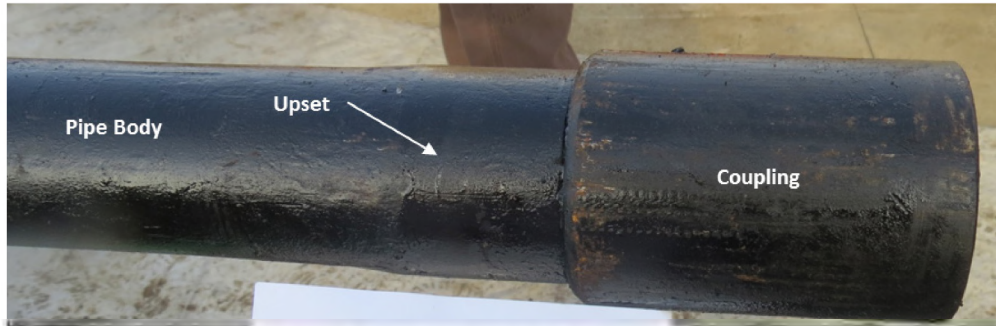


Figure 4: Example of 2 7/8 in. Connection

The 7 in. casing comprised four different material and weight combinations. Table 1 shows the top, bottom, and lengths of the sections and the nominal dimensional properties. Table 2 shows the nominal strength properties for the 7 in. casing pipe body. The majority of the string contained 23.00 ppf grades J55 and N80 joints. The remaining joints were located at the bottom of the string and consisted of heavier 26.00 and 29.00 ppf grade N80 joints.

Table 1: Nominal Dimensions for 7 in. Casing

Grade	Weight (ppf)	Top (ft)	Bottom (ft)	Length (ft)	Pipe Body	
					Wall Thickness (in.)	ID (in.)
J55	23.00	0	2,398	2,398	0.317	6.366
N80	23.00	2,398	6,308	3,910	0.317	6.366
N80	26.00	6,308	8,282	1,974	0.362	6.276
N80	29.00	8,282	8,585	303	0.408	6.184

Table 2: Nominal Strength Properties for 7 in. Casing

Grade	Weight (ppf)	Pipe Body				
		Burst (psi)	Collapse (psi)	Tension (lbf)	OD (in.)	ID (in.)
J55	23.00	4,360	3,270	366,000	7.444	6.285
N80	23.00	6,340	3,830	532,000	7.444	6.285
N80	26.00	7,240	5,410	604,000	7.444	6.196
N80	29.00	8,160	7,030	676,000	7.573	6.104



The 7 in. casing had Speedtite connections, which are no longer commercially available. The available information suggests that Speedtite connections are identical to Hydril's Super EU connections, and that Youngstown Steel (the manufacturer of the 7 in. casing run in SS-25) was licensed to cut Super EU connections and market them under the name Speedtite. Super EU connections are no longer commercially available either, but there is some publicly available information regarding features and design. Figure 5 shows a schematic of the Super EU connection. Please refer to the 7 in. connection testing report [8] for a more detailed description of the Speedtite connections.

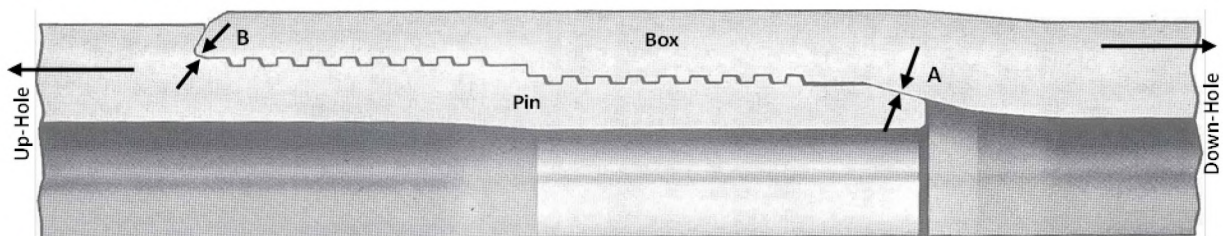


Figure 5: Super EU (Speedtite) Connection Configuration

### 2.1.3 Blowout Timeline

The sequence of events during the blowout influenced the interpretation of several aspects of the metallurgical investigation.

The smell of gas was detected around the SS-25 site on October 23, 2015. Seven kill operations were attempted from the time the leak was detected to December 22, 2015, and all were unsuccessful. A relief well (P-39A) was spudded prior to Kill Attempt #7 on December 4, 2015. The SS-25 well was eventually killed after the relief well intersected it on February 11, 2016. The following is a summary of notable events that occurred between the start and end dates of the blowout:

- October 23, 2015—Noise was heard in the wellhead, and the smell of gas was present on the lease road while SS-25 was on injection.
- October 24, 2015—Kill Attempt #1. A polymer fluid was pumped into the well. The tubing plugged, and the kill attempt was unsuccessful.
- October 28, 2015—A slickline bailer tagged up at 437 ft.
- October 29, 2015—Ice and hydrates were observed in fissures around the cellar.
- November 06, 2015—The tubing plug (ice and hydrates) was removed by using coil tubing and glycol.
- November 07, 2015—A gauge ring was run to total depth (TD) to confirm the clearance of the tubing internal diameter (ID).
- November 08, 2015—Temperature and production logs were run and recorded a minimum temperature of 18°F at approximately 364 ft.
- November 09, 2015—Western Wireline ran a temperature-noise log.
- November 12, 2015—A tubing bridge plug was set at 8,393 ft.
- November 13, 2015—Kill Attempt #2. The tubing above the bridge plug was perforated. 9.4 ppg polymer pill, 9.4 ppg CaCl<sub>2</sub>, 8.6 ppg brine water, and junk shot were pumped into the well. The kill attempt was unsuccessful. A blowout vent opened 20 ft from the wellbore shooting debris 75 ft in the air. Gas, oil, and brine were observed in the fissures at surface.

- November 15, 2015—Kill Attempt #3. 9.4 ppg CaCl<sub>2</sub> and a barite pill were pumped into the well. The kill attempt was unsuccessful. Gas rate from the fissures increased, followed by oil and brine. Flow stopped briefly and then gas began to flow.
- November 18, 2015—Kill Attempt #4. 9.4 ppg CaCl<sub>2</sub> and an 18 ppg barite pill were pumped into the well. The kill attempt was unsuccessful. Gas, oil, and brine were observed in the fissures at surface. Barite to surface was also reported.
- November 24, 2015—Kill Attempt #5. 9.4 GEO ZAN pill, fresh water, 18 ppg barite pill, and 9.4 ppg CaCl<sub>2</sub> were pumped into the well. The kill attempt was unsuccessful. Gas rate from the crater increased. 700 bbl of fluid were recovered from location.
- November 25, 2015—Kill Attempt #6. 9.4 ppg GEO ZAN lost circulation material (LCM) pill, fresh water, and 9.4 ppg CaCl<sub>2</sub> were pumped into the well. The kill attempt was unsuccessful. Gas activity and water flow increased in the crater. A flow line from the 7 in. casing and tubing head broke. The nipple on the wellhead broke. The crater around the wellhead increased and damaged several casing valves. The valve on the 11 3/4 in. × 7 in. annulus backed out.
- November 30, 2015—Western Wireline ran temperature and noise logs.
- December 04, 2015—Relief well P-39A was spudded.
- December 22, 2015—Kill Attempt #7. 15 ppg water-based mud (WBM), 15 ppg WBM with LCM, and a 9.4 ppg GEO ZAN LCM pill were pumped downhole. LCM included Diaseal (diatomaceous earth [DE]) and Nutplug (ground walnut or pecan hull). The kill attempt was unsuccessful. A mud-oil mist was observed in the crater. Liquid began to come out of the casing at the surface. High wellhead movement occurred, and mud was ejected from the crater.
- December 23, 2015—The crater enlarged due to the open 11 3/4 in. × 7 in. annulus outlet.
- January 02, 2016—Crater depth was measured at 25.6 ft on the north side.
- January 23, 2016—Temperature-pressure log was run.
- February 11, 2016—Relief well intersected the SS-25 well. The gas influx was stopped. The well was dead.

Several kill fluids were used during the kill attempts, including polymer pills, barite (BaSO<sub>4</sub>) pills, GEO ZAN pills, 10 ppg mud, 15 ppg mud, and 15 ppg mud with LCM. Junk shot was used during Kill Attempt #2 to try and bridge gaps in the casing. The details of the kill attempts are not presented in this report. A detailed review and analysis of all seven kill attempts are discussed in the transient kill simulation report [9]. The presence of these kill fluids influenced the interpretation of the metallurgical, biological, and chemical analyses described in Section 5.

Junk shot was used during the kill operations in an attempt to bridge gaps in the casing. Objects or *junk*, such as golf balls, bits of rope, and steel balls were pumped downhole with the goal of bridging gaps in the casing where losses were occurring. Junk shot was unsuccessful, and the golf balls pumped downhole returned to surface. This observation suggested that the gap or hole in the casing was large enough to allow golf ball size objects (approximately 1.68 in. diameter) to pass through.

These kill techniques are mentioned due to the risk they posed to the evidence downhole, and they were noted to assist with the assessment of fracture surfaces and other features during the metallurgical investigation. Any corrosion, fracture surfaces, or other features could have sustained damage due to some of these operations.

Pills are a special blend of drilling fluid used to perform a particular task within the well. Diaseal-M and Nutplug are examples of the LCM pills that were used to plug loss zones in the wellbore. The objective of the pills used during the SS-25 kill attempts was to slow down or stop the blowout.

Kill Attempt #1 occurred one day after gas was detected at the SS-25 site. A polymer fluid was pumped into the well during the kill attempt, and that proved unsuccessful. Slickline operations were conducted following the first kill attempt. A slickline bailer tagged what was assumed to be a hydrate or ice plug at a depth of 437 ft on October 28, 2015. Ice and hydrates were observed in fissures at the surface on the following day. Glycol was pumped through coiled tubing to remove the hydrate plug. The plug was removed on November 06, 2015. A gauge ring was run the following day to the total well depth to confirm the tubing ID was clear of obstructions.

The presence of ice or hydrates, both in the well and at the surface, were of primary interest during the kill operations and during the RCA investigation. A production log was run on November 08, 2015, after the tubing plug was removed. The logging tool included sensors for gamma radiation, pressure, temperature, induction collar locator, fluid density, fluid dielectric, and flow. Figure 6 shows temperature and pressure data collected from the log down pass and up pass. The temperature profiles appeared to have detected a temperature anomaly at an approximate depth of 890 ft. Warming was observed during the up pass, which was attributed to movement of the gas flow path away from the logging tool. The most notable observation for the metallurgical investigation is that the well cooled to a temperature of 26.9°F at the suspected leak location. The well temperature had a significant impact on the failure behavior of the tubulars. Historical pressure and temperature logs exist dating back to 1974. A comparison of pressure and temperature data before, during, and after the SS-25 blowout is discussed in the SS-25 temperature, pressure, and noise logs report [10]. Based on the report, the pressure and temperature data show no anomalies prior to October 23, 2015.

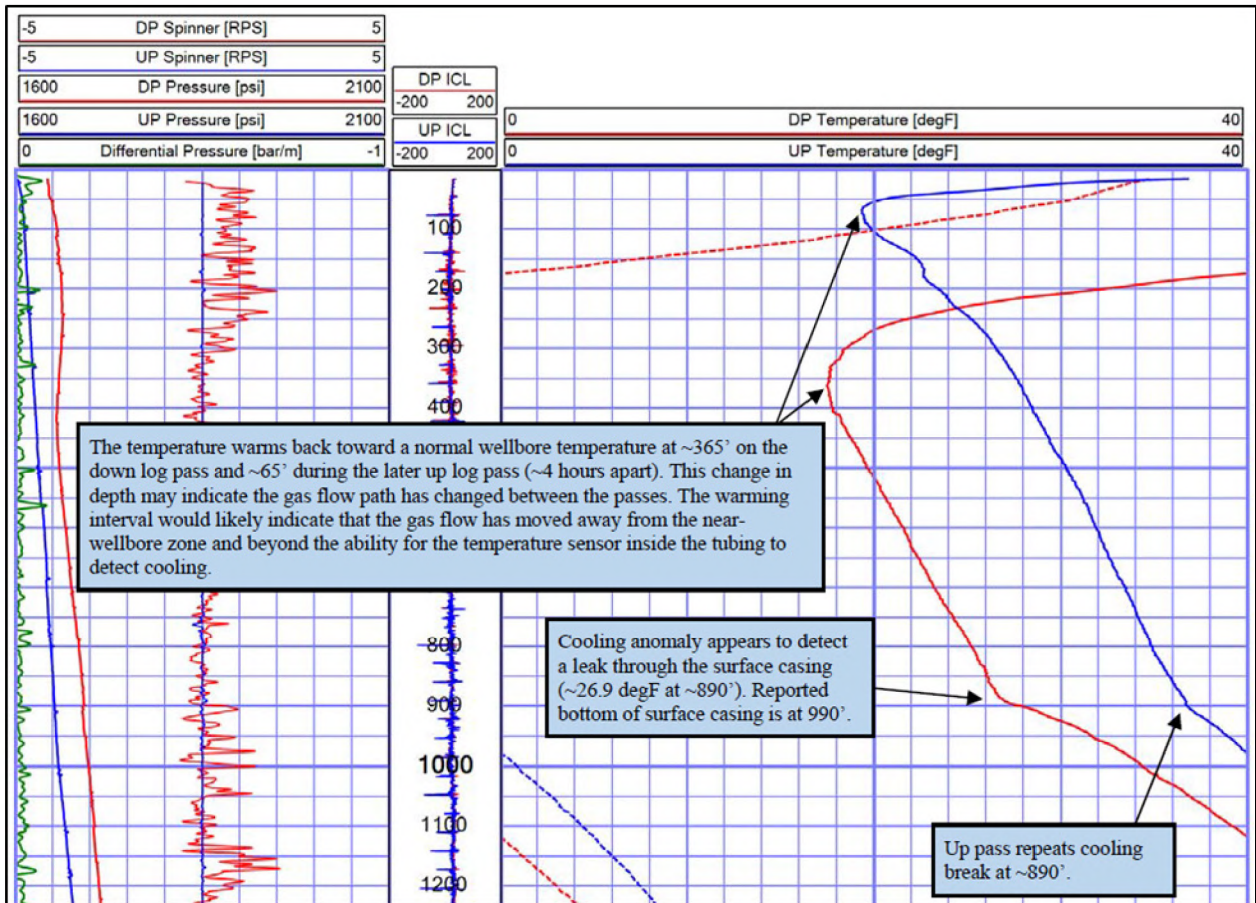


Figure 6: November 08, 2015, Temperature Survey (During Blowout)

The November 08, 2015, log was the first available data set with some indication of a leak location. The 26.9°F temperature reported by the production logs represents an upper bound to the temperature at that location. The temperature was recorded at the ID of the tubing. This suggests that the temperature of the casing at the leak location was colder than the recorded temperature of 26.9°F.

## 2.2 Field Operations and Investigation Summary

Field operations required a substantial amount of planning and effort to ensure the safe retrieval of downhole evidence. Each step was carefully considered to maximize the amount of information collected while minimizing the risk of damage to evidence. Planning considerations included extraction methodology, equipment, and sequence. The field operations are summarized into the following steps:

1. Searching, collecting and documenting the evidence
2. Logging the 2 7/8 in. tubing
3. Examining the wellhead
4. Extracting the tubing
5. Logging the 7 in. casing
6. Extracting the 7 in. casing

7. Logging the 11 3/4 in. casing
8. Extracting the 11 3/4 in. casing

The SS-25 site and well were altered as phases were completed. Data had to be collected prior to any alterations in an effort to preserve evidence. Evidence preservation was notably important during the extraction phases of the investigation. Extraction operations are inherently risky. Damage can occur during extraction or certain circumstances can arise that may prevent extraction of the pipe. The amount of data available for the investigation would have been limited if pipe extraction had been unsuccessful. Therefore, the extraction sequence played an important role when collecting downhole evidence. The primary risk was that each operation could have been the last one. This guiding principle was used to determine the extraction and logging sequence.

Logging operations preceded each extraction step with the goal of collecting as much data as possible prior to executing risky extraction operations, with the added benefit of providing additional data for decision making. The additional data assisted with mitigating risk and increased the chances of a successful extraction.

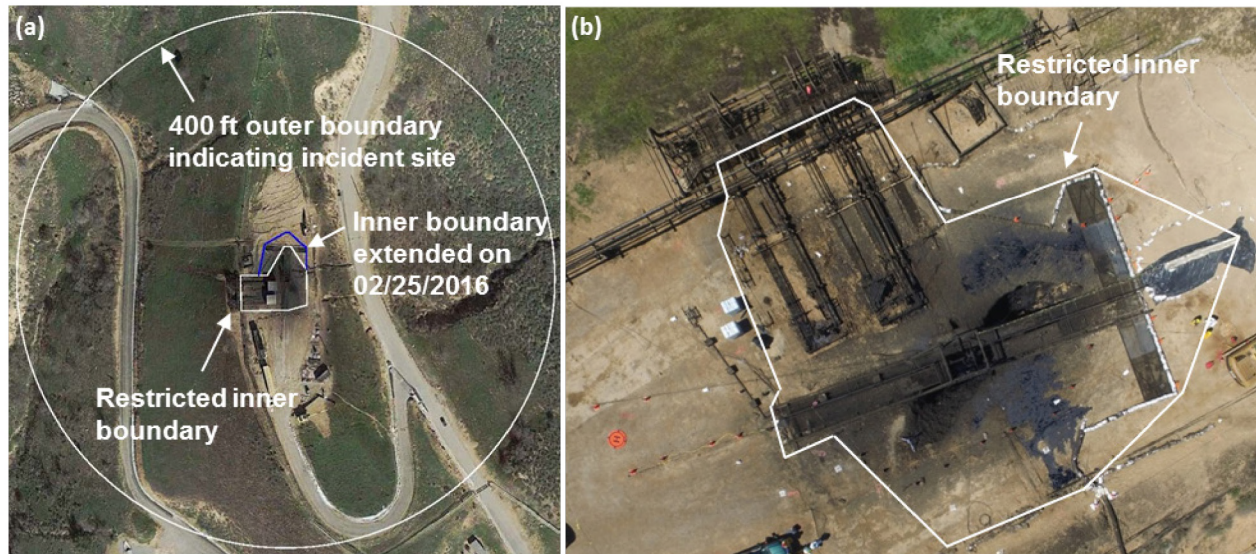
### 2.2.1 Evidence Search, Collection, and Documentation

On February 19, 2016, CPUC sealed the SS-25 site, which had been exposed to various operations prior to the seal date, including operations related to kill attempts and logging. The RCA required a thorough search of the site to identify, collect, and document any evidence associated with the failure. CPUC established a perimeter at a 400 ft radius from the SS-25 wellhead for the official incident site. A smaller perimeter was subsequently adopted as the inner boundary and declared a restricted area. Due to the proximity to the crater, entering the inner perimeter required special safety equipment and permission from Blade and CPUC. Figure 7 shows the (a) outer and (b) inner perimeters set by CPUC at the start of the investigation.

Phase 2 was the well site restoration to rig readiness. This phase required a complete transformation of the SS-25 site and included:

- Removing contaminated soil from the area and crater.
- Filling the crater.
- Grading the north slope.
- Extending the south slope.

The operations required removal and placement of dirt around the site. Since evidence present on the SS-25 site would potentially be lost, contaminated, or destroyed by the Phase 2 operations, Phase 1's main objective was to search, document, and collect evidence in preparation for Phase 2.



**Figure 7: (a) Outer and (b) Inner CPUC Incident Site Boundaries**

The incident site defined by CPUC was subdivided into search zones, which were determined based on the required search method. For example, zone 1 (light blue) was an area adjacent to the SS-25 wellhead; a grid system to search around the equipment and crater was used, and each sector of the grid was searched systematically. The grid system provided an organized way to search an area that was obstructed by equipment and debris, and it ensured that the entire surface area surrounding the wellhead was thoroughly searched. Figure 8 (a) shows the search zones labeled and color-coded.

Zone 2 (purple) included the north and south slopes—they were clear of obstacles and generally safe to walk. Specialized equipment was not required for access. This zone was walked in parallel lines by Blade personnel. Zones 3 (green) and 4 (black) were on the west slope of the SS-25 site. The slopes were steep and required harnesses for safety. These zones were walked in an arch pattern using ropes tied to anchors located at the top of the site. The search paths for zones 2, 3, and 4 are identified in Figure 8 (a) by lines. The 'No Go' (red) sections were areas where it was unsafe to physically search for evidence; they were excluded from the search.

The SS-25 site was divided into two grids for documentation purposes: the inner and the outer grid. The inner grid, Figure 8 (b), corresponded to zone 1 of the search regions and was physically divided into 20 ft sectors by using stakes and ropes. The outer grid, Figure 8 (c), was a continuation of the inner grid and extended out to the boundary of the incident site. It was a virtual grid divided into 40 ft sectors and not physically staked out. Grid sectors were recorded for evidence collected during Phase 1. The grid sectors approximated the location where evidence was collected.



Figure 8: Phase 1 Search Zones and Grids

Phase 1 was the first opportunity for the Blade team to observe and document the SS-25 site. Figure 9 shows one of the first images taken after the site was opened to the team. The image shows the SS-25 tree, crater, bridge spanning the crater, SS-25A and B heat shields, and piping for SS-25, SS-25A, and SS-25B. The majority of the non-permanent items in the image were removed throughout Phase 1 or during Phase 2, and they included the trailer, bridge, heat shields, sand bags, cones, and concrete beam.



Figure 9: SS-25 Site Condition on February 25, 2016

Formation of the crater occurred during the blowout events described in Section 2.1.3. Figure 10 and Figure 11 show aerial photographs of the crater looking down and west, respectively. The images also show the SS-25A and 25B wellheads after removal of the heat shields. The bridge and concrete beam were installed during the kill operations to provide access to the wellhead; it also provided a platform for personnel to connect lines and operate valves. The concrete beam was used to anchor a steel cable handrail.

Figure 12 shows an image of a missing 11 3/4 in. × 7 in. annulus valve. The valve backed off during the kill attempts and was not located during the Phase 1 evidence search. The valve most likely ended up at the bottom of the crater when the cellar collapsed during its formation. A portion of the concrete pad that was attached to the cellar was hanging from the south side of the crater.



Figure 10: SS-25 Site Top Aerial View Post-Blowout on April 01, 2016

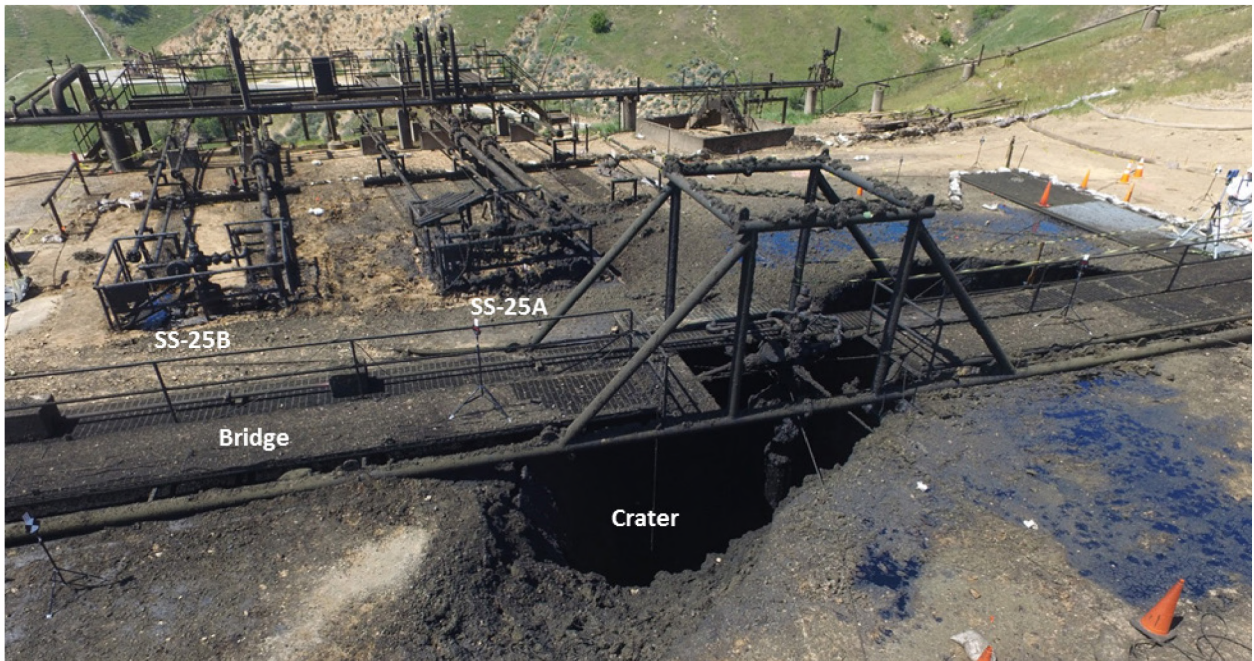


Figure 11: SS-25 Site West Aerial View Post-Blowout on April 01, 2016



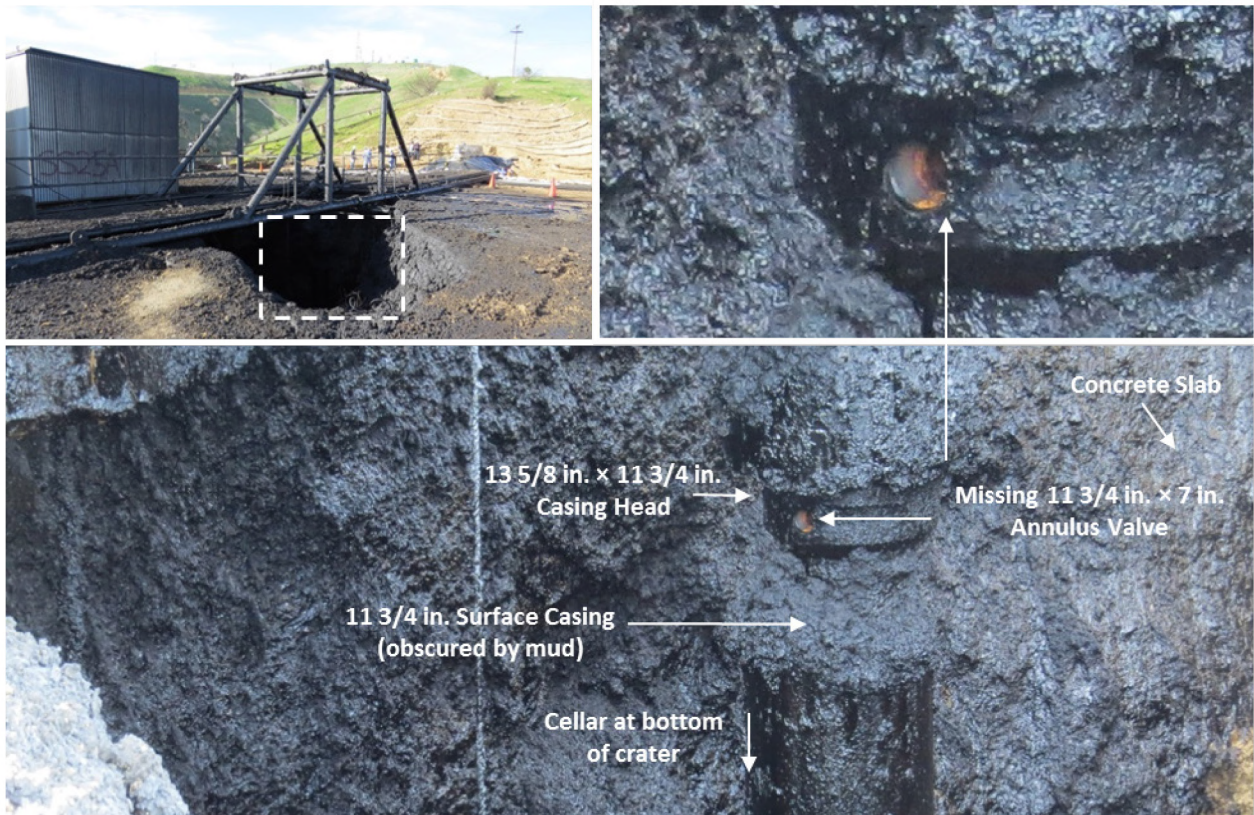


Figure 12: Missing 11 3/4 in. Casing Valve Taken on February 25, 2016

### 2.2.2 Logging of 2 7/8 in. Tubing

Logging of the 2 7/8 in. tubing occurred after completion of Phase 1's evidence search. Logging began on April 04, 2016, and was completed on April 22, 2016. The objective of the logging was to collect as much information about the well as possible prior to extraction operations. The logs included in the 2 7/8 in. logging program were as follows:

1. April 07, 2016—Baker Hughes Gamma Ray (GR)/Casing Collar Locator (CCL)/Junk Catcher-Gauge Ring
2. April 08, 2016—Baker Hughes Imaging Caliper (ICAL) 24-Arm Mechanical Caliper Log
3. April 12, 2016—Versa-Line High Precision Temperature (HPT) Log
4. April 13–18, 2016—Versa-Line Spectral Noise Log (SNL)
5. April 18–19, 2016—Versa-Line Magnetic Imaging Defectoscope-2 (MID-2) Log
6. April 20, 2016—Versa-Line Magnetic Imaging Defectoscope-3 (MID-3) Log
7. April 20–22, 2016—Baker Hughes MicroVertilog (MVRT) Log

The first run included a GR log, CCL, and gauge ring. The combination of the GR log and casing collar is commonly used for depth correlation between cased-hole logs and openhole logs. The GR log detects gamma radiation from the formation. Different formations emit different amounts and spectra of gamma radiation. The CCL tool uses a coil-and-magnet arrangement to detect collars. The CCL log serves as the primary depth correlation for cased-hole logs. The gauge ring is a precisely machined ring with a diameter

equal to the pipe drift. The ring ensures that logging tools will pass through the ID of the tubing. The data collected during the first run were used to prepare for future logging runs.

The second run was used to identify features on the ID surface of the tubing. A 24-Arm Caliper uses an array of mechanical fingers to measure the ID of the tubing at 24 circumferential locations. Calipers can identify issues, such as internal corrosion, manufacturing defects, and ovality. The caliper run did not identify significant issues with the tubing. This observation indicates that corrosion was not present on the ID of the tubing.

The third run was used to collect an accurate temperature profile of the SS-25 well. The temperature profile collected with the Versa-Line HPT was used to accurately profile the cold zone identified during the blowout (Figure 6) and compare with previous temperature logs. Figure 13 shows the temperature profiles for the up and down passes of the HPT log. The profiles show that the 26.9°F temperature recorded by the November 08, 2015, temperature log at the suspected leak location (approximate depth of 890 ft) had warmed to the geothermal gradient. The coldest location recorded by the November 08, 2015, temperature log was 18°F at an approximate depth of 365 ft. That location had an HPT-recorded temperature of 46.3°F, which was colder than the geothermal gradient at that location.

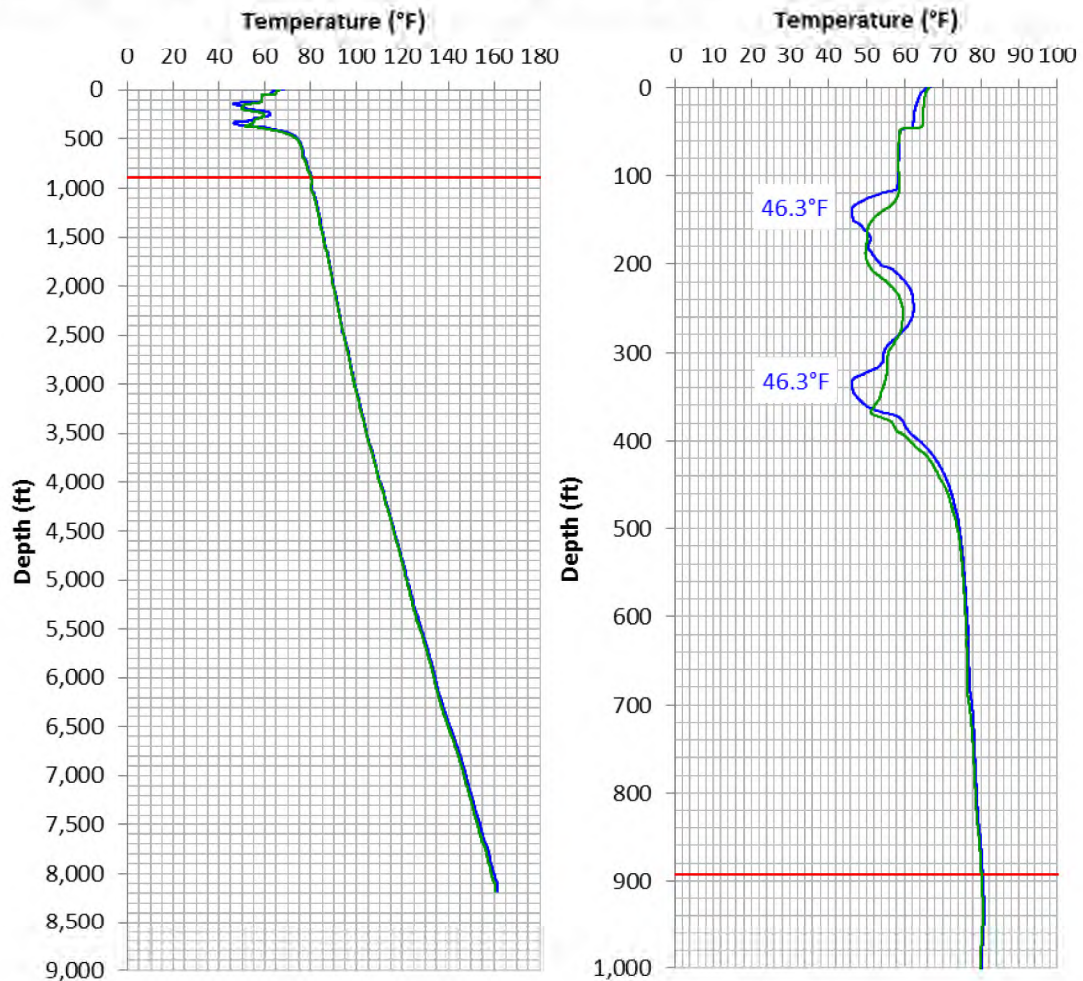


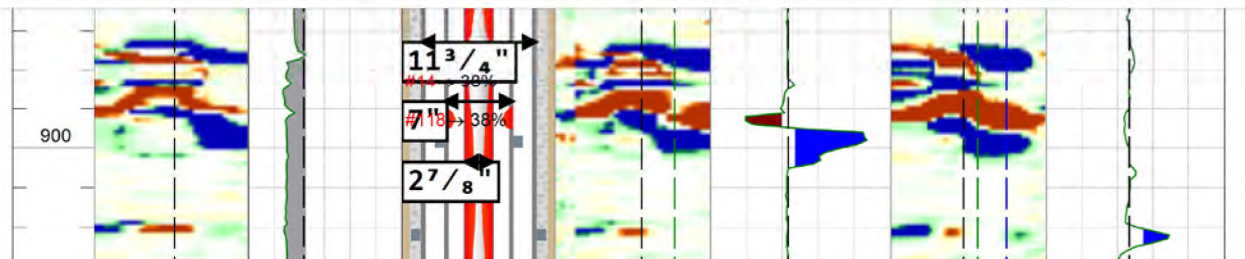
Figure 13: Versa-Line HPT Log Data

The SS-25 Temperature, Pressure, and Noise Logs Analysis [10] compared temperature data from before, during, and after the blowout. The data in [10] were used as inputs in the SS-25 thermal modeling analysis [11]. Both [10] and [11] provide discussions explaining the changing temperature profile during the blowout.

The fourth run was the SNL. The goal of the SNL was to detect fluid movement within and near the wellbore. The SNL identified a few zones with frequencies different than the background noise. A noise of 2.8 kHz was detected between 820 ft and 1,200 ft. A 3–5 kHz noise was also detected between 252 ft and 294 ft. The log data were used to assist with interpretation of the well condition and did not provide data directly relevant to the metallurgical investigation.

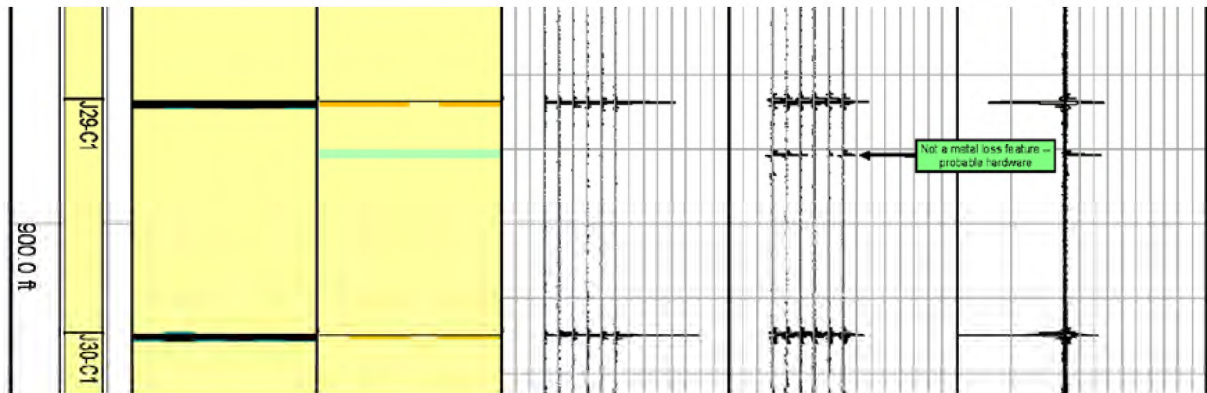
The fifth and sixth logs were run with the Magnetic Imaging Defectoscope (MID) tool, designed to record the time response to electromagnetic pulses. This technology can detect metal loss or gain in up to three barriers. The MID tools MID-2 and MID-3 were run within the 2 7/8 in. tubing (first barrier) to identify anomalies in the 7 in. casing (second barrier) and 11 3/4 in. casing (third barrier) of SS-25. Time responses from the electromagnetic pulses were compared to numerical models to determine the metal loss or gain. The MID-2 tool has two sensors that inspect for metal loss and/or gain on the first and second strings. The MID-3 tool has an additional sensor that inspects for metal loss and/or gain on the third string. The MID tools were validated at a pipe yard in Bakersfield, California. The results from the validation and a review of the MID technology are discussed in the Versa-Line MID Validation Report [12].

The MID tools detected metal loss at several locations along the length of the 7 in. casing. The most notable location was at 895 ft—Figure 14 shows the MID logs results at this depth; the three color maps represent the near delta (left), medium delta (middle), and far delta (right) responses and correspond to the tubing, 7 in. casing, and 11 3/4 in. casing, respectively. Figure 14 also shows a 38% metal-loss feature on the 7 in. casing. The significant metal-loss feature corresponded with the assumed leak based on the temperature profile from the production log run on November 08, 2015. The log suggested that the 7 in. casing had significant metal loss at that depth. This was the first indication of a significant feature at this location. These data were used to guide future extraction operations.



**Figure 14: MID Results Showing 38% Metal Loss at Approximately 895 ft**

The seventh log was the MicroVertilog (MVRT). An MVRT detects flaws in tubing by observing the flux leakage induced by a permanent magnet as the tool is pulled through the tubing string of interest. The MVRT did not identify any features on the 2 7/8 in. tubing. However, the tool did identify a metal gain at an approximate depth of 890 ft. Figure 15 shows the metal-gain feature on the MVRT log at 890 ft. The MVRT is a single barrier tool, meaning that it cannot detect beyond the string it is run in. However, metal gain can be detected if the barrier that the MVRT is run in is in contact with another barrier. The metal gain detected at 890 ft was interpreted as the 7 in. casing was making contact with the outside diameter (OD) of the 2 7/8 in. tubing. These data contributed to the theory that the 7 in. was parted at this depth and was in contact with the tubing.



**Figure 15: Microvertilog Results at 890 ft**

The tubing logs were critical to the metallurgical investigation—they influenced the decisions during the extraction operations. The HPT, MID, and MVRT logs all had an indication at an approximate depth of 890 ft. The MID and MVRT suggested that the 7 in. behind the tubing might have been parted. These assumptions were used during the planning stages of Phase 3 to minimize the risk of damaging the 7 in. casing at 890 ft when pulling the tubing.

### 2.2.3 Wellhead Examination

The wellhead examination occurred during well site restoration to rig readiness operations and are discussed in the Phase 2 summary report [13]. The wellhead examination began on July 13, 2016, and was completed on July 17, 2016. The examination was planned during Phase 1 but was not executed until Phase 2 because of limited access to the wellhead. As noted in Section 2.1.3, a crater formed during the kill operations, and a bridge was installed to span the crater and provide access to the wellhead (Figure 10 and Figure 11). The bridge had limited space, which prevented the installation of scaffolding to inspect the wellhead. Part of the wellhead was positioned below the bridge, increasing the difficulty and risk involved with inspecting the wellhead during Phase 1. The examination was postponed until the crater was partially filled and personnel could safely access the wellhead.

Figure 16 shows a schematic of the wellhead in the as-found condition. Some components were installed during the kill operations and have been identified in the schematic. The wellhead shifted during Kill Attempt #7 due to the instability caused by the growth of the crater. Wellhead stability was restored using tension cables for support. Figure 17 shows images of the SS-25 wellhead in 2015, and Figure 18 shows images just after the well was killed in 2016. The 2015 images were extracted from a data request provided by SoCalGas. The images were taken in 2015 as part of a survey to evaluate 3D laser technology for Aliso Canyon, and SS-25 was one of the well sites chosen to evaluate the technology. Several viewpoints were selected around the SS-25 site for taking images. Many of them were taken at each location and combined to form a single 360° view from the selected viewpoints. The images in Figure 17 were extracted from two different viewpoints.

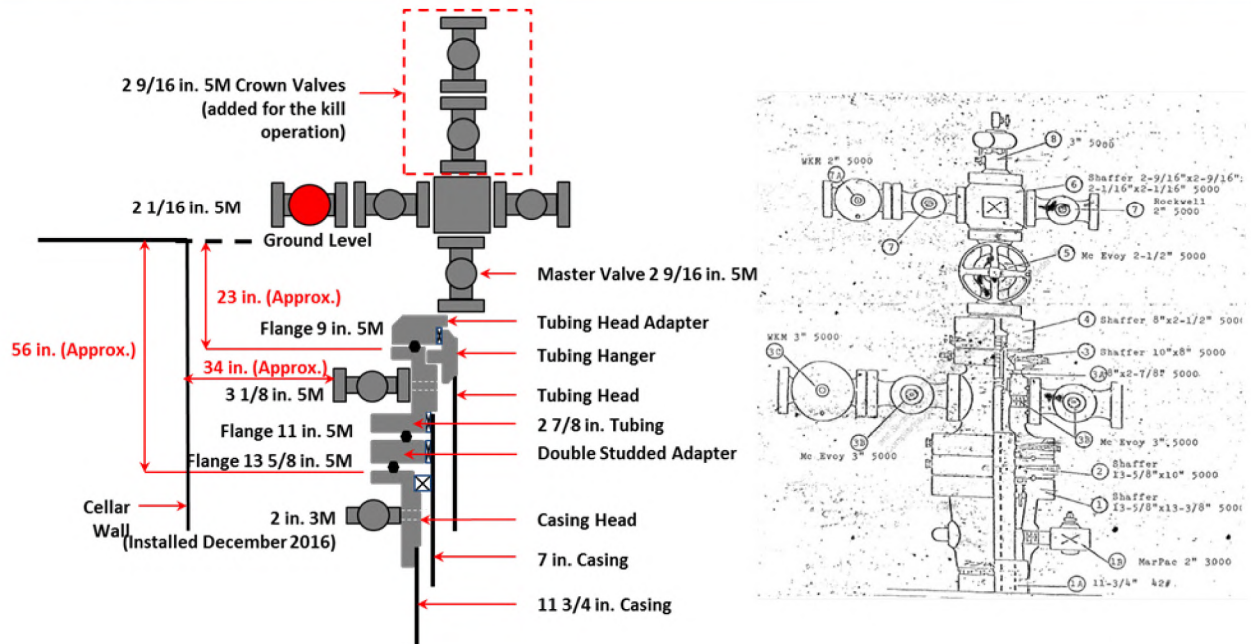


Figure 16: Wellhead Schematic

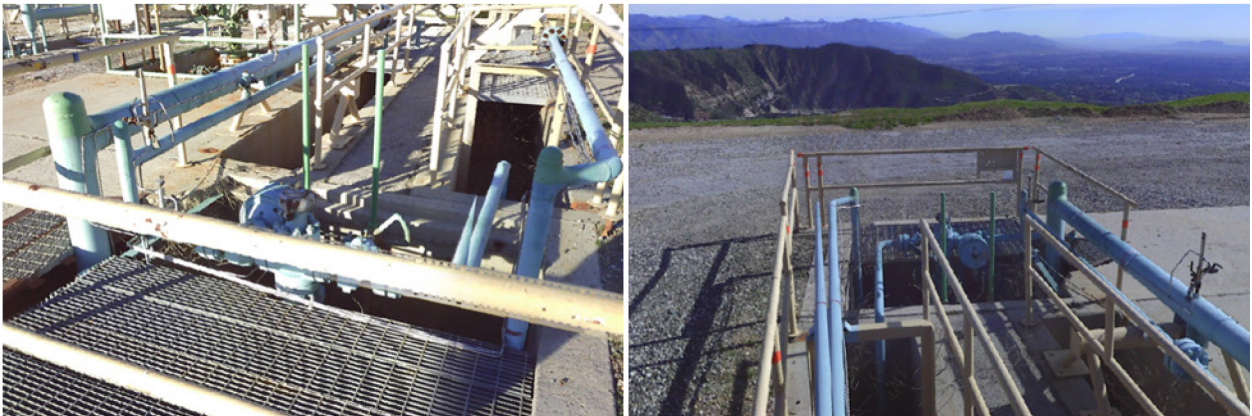


Figure 17: SS-25 Wellhead in January 2015



Figure 18: SS-25 Wellhead in February 2016

The crater was partially filled to provide a stable foundation for the scaffolding during Phase 2. The scaffolding allowed safe access to the wellhead for the examination (Figure 19). The image shows the top of the crater restoration work that acted as a foundation for the scaffolding. A combination of mechanical removal, chemical stripping agents, and abrasive blasting was used to prepare the wellhead for NDE.

Tests were conducted on similar components prior to cleaning the SS-25 wellhead. The tests were designed to quantify the aggressiveness of various cleaning methods. Application of chemical stripping agents and pressure washing were performed on discs made from a material similar to the SS-25 wellhead. The discs were then examined for damage. The goal was to select a cleaning method that would effectively clean the wellhead while minimizing damage. The Phase 1 report [3] provides a detailed discussion of the testing.

The NDE work began once a satisfactory surface condition was achieved. The goal of the examination was to identify any indications and determine if they were associated with the blowout. Figure 20 shows the condition of the wellhead during the NDE work—the white contrast paint is used for magnetic particle inspection (MPI). The two valves above the flow cross (no contrast paint) were not part of the SS-25 original tree and were not inspected. No indications associated with the blowout were found during the examination.

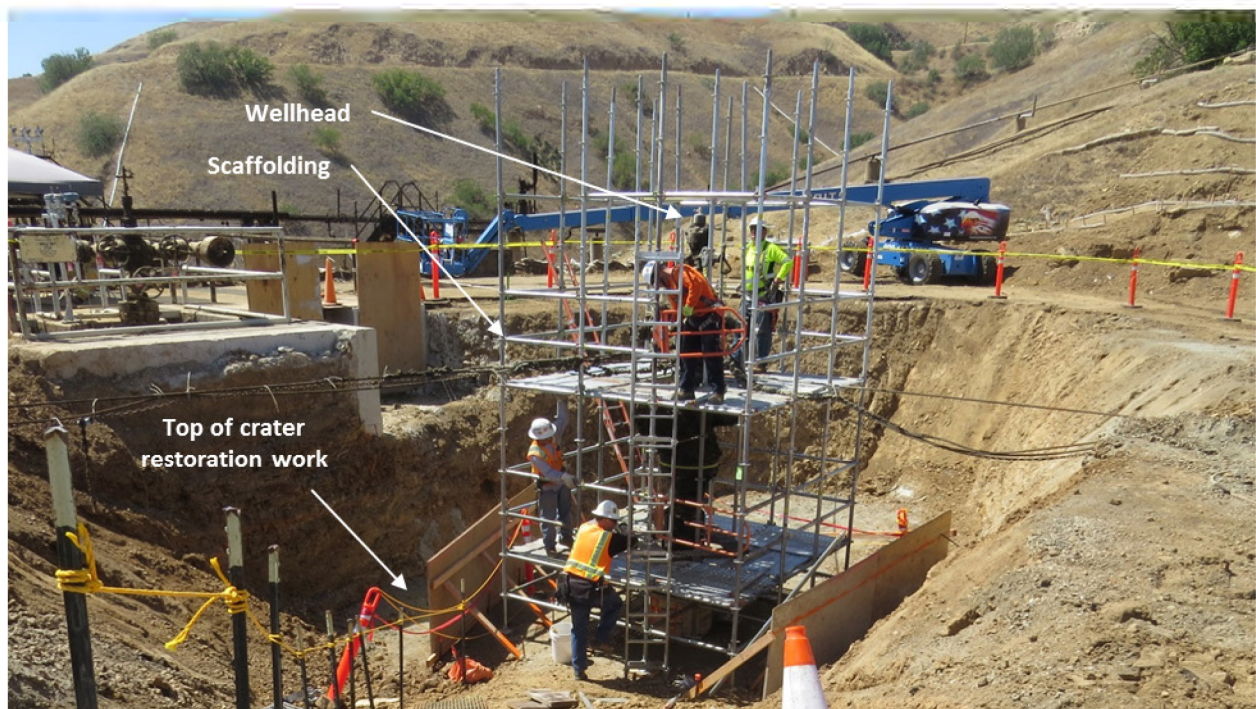


Figure 19: Scaffolding for Wellhead Examination



Figure 20: Wellhead Magnetic Particle Inspection

### 2.2.4 Tubing Extraction

The wellhead and tubing were the first components extracted from the well. Most of the wellhead components were removed and replaced with a blowout preventer (BOP), a safety device designed to maintain control of the well in the event of a blowout. The wellhead components were removed and transported to PS-20 for inspection. Figure 21 shows removal of the SS-25 tree and the installed BOP. All evidence collected during tubing extraction was handled according to the Phase 3 tubulars and wellhead handling protocol [5]. The Phase 3 extraction protocol [4] discusses all the steps of the tubing extraction.



Figure 21: SS-25 Tree Removal and Blowout Preventer Installation

All evidence extracted from SS-25 was given a joint sequence number (JSN) for identification purposes. JSNs are described in the Phase 3 tubulars handling protocol [5]. On August 19, 2017, the wellhead was separated into nine components, which were assigned the following JSNs:

- W001A—Actuated valve
- W001B—North-facing manual valve
- W001C—South-facing manual valve
- W001D—1502 adapter
- W001E—Flow cross
- W001F—Master valve
- W001G—Double studded adapter (DSA)
- W002—Cut studs
- W003—Tubing hanger

The ID of each component was inspected after disassembly. The OD was not inspected because it had been inspected previously during the wellhead inspection discussed in Section 2.2.3. No features were identified on the OD surface of the wellhead components. The following dried mud samples were taken from the ID and sent to Texas OilTech (TOL) for analysis:

- W001BS1
- W001CS1
- W001ES1
- W001ES2

Samples taken from a particular well component were also given a JSN that included the JSN of the component it was collected from. For example, W001BS1 represents a sample (S1) collected from the north-facing manual valve (W001B). The wellhead components were coated with a corrosion inhibitor (Tectyl 846) and crated for protection. A Mylar sheet and volatile corrosion inhibitor (VCI) packets were used as additional safeguards against corrosion. The Mylar sheet was placed on top of the crate bottom. The wellhead component was then placed on top of the Mylar sheet, and VCI packets were placed with the component. The Mylar sheet was then wrapped around the component and sealed with a heat sealer. A small hole was left open, and a vacuum was used to remove the air from inside the newly formed Mylar bag, which acted as a moisture barrier and simultaneously provided an effective environment for the VCI packets. Figure 22 shows the crating procedure for the wellhead component W001A.

Tubing extraction began on August 22, 2017, using the Ensign 334 rig. The rig was mobilized to the SS-25 well site and rigged up between August 10, 2017, and August 15, 2017. A Baker mechanical pipe cutter (MPC) was used to cut the 2 7/8 in. tubing at approximately 7,555 ft. The cut location was determined based on a free point analysis of the tubing. The Baker MPC was tested at the Baker shop prior to field use. The tests showed that the cutter successfully produced a clean cut and posed a minimal risk to damaging the 7 in. casing during the process.





**Figure 22: Crating of Wellhead Component W001A**

A total of 244 joints identified as T001 through T244 were extracted from the SS-25 well. The final joint was extracted on September 01, 2017. The extraction dates for each of the joints were as follows:

- August 22, 2017—T001 to T002
- August 23, 2017—T003 to T033
- August 24, 2017—T034 to T062
- August 25, 2017—T063 to T092
- August 26, 2017—T093 to T122
- August 27, 2017—T123 to T152
- August 28, 2017—T153 to T182
- August 29, 2017—T183 to T209
- August 30, 2017—T210 to T213
- August 31, 2017—T214 to T215
- September 01, 2017—T216 to T244

The primary objective of the tubing extraction was evidence collection and preservation. Information collected during the logging of the 2 7/8 in. tubing was used to refine the extraction protocol. Tubular handling procedures were developed by Blade and are presented in the Phase 3 tubulars handling protocol [5]. The steps taken in the field are repeated in this section for convenience. The main philosophy of the tubing extraction process was to inspect the pipe at each stage of the extraction process. The first opportunity to inspect the pipe was on the rig floor. Blade personnel were present on the rig floor to inspect and document each joint as it came out of the well.

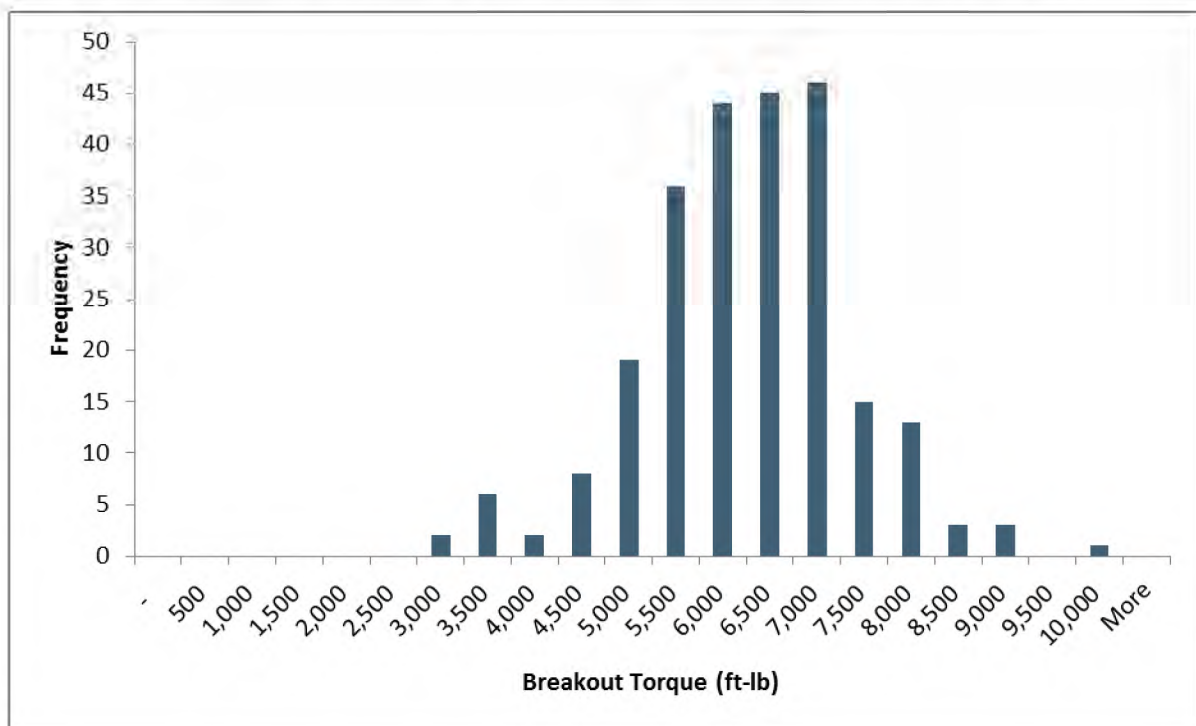
The rig floor was the only location where the made-up connections could be inspected. Each connection was inspected before and after breakout. Figure 23 shows the connection between T155 and T156 before and after breakout. The white line in Figure 23 is the orientation mark applied to the joints on the rig

floor. The orientation mark represented the west face of the string. This mark was used throughout the metallurgical investigation as a circumferential origin location.



**Figure 23: T155–T156 Connection Before and After Breakout**

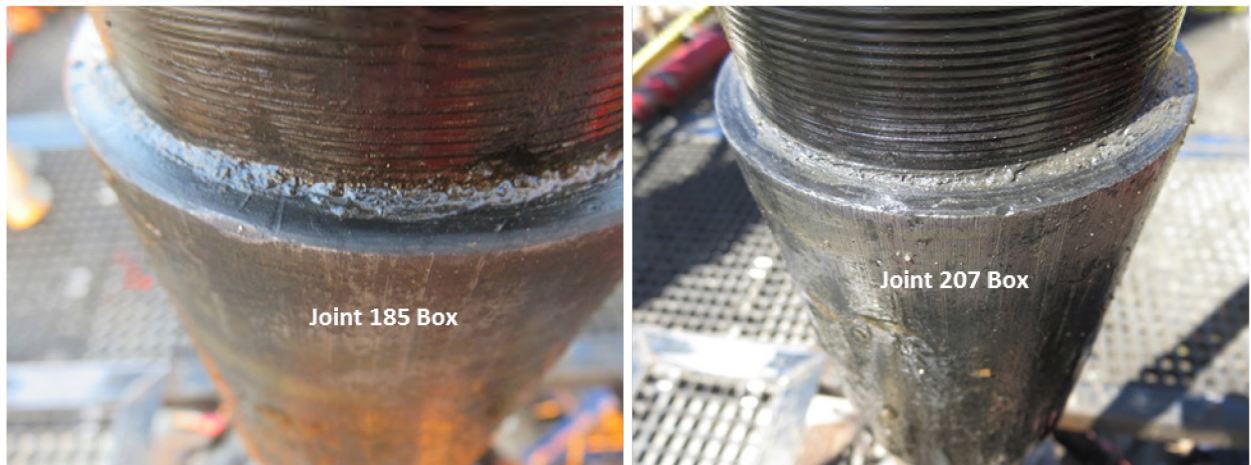
Figure 24 shows the breakout torque distribution for the 2 7/8 in. tubing connection. The minimum, maximum, and average breakout torques were 2,709, 9,894, and 5,997 ft-lb, respectively. H<sub>2</sub>S and CO<sub>2</sub> concentrations were recorded using Draeger tubes. (Draeger tubes are glass tubes filled with a reagent that reacts to a specific chemical.) A bellows pump was used to draw in an air sample. Readings were taken at joints 8, 38, 74, 105, 134, 164, and 195. All readings recorded 300 ppm for CO<sub>2</sub> and 0 ppm for H<sub>2</sub>S.



**Figure 24: Torque Distribution of 2 7/8 in. Tubing Breakout**

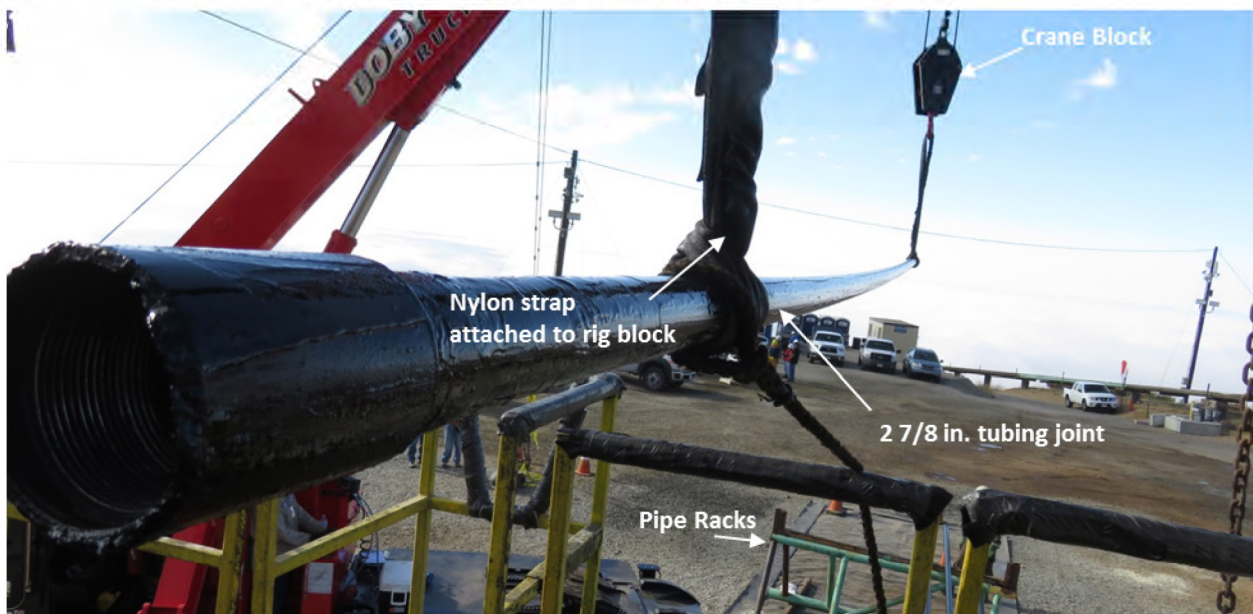
Observations of the tubing and connections at the rig floor were recorded on the Rig Floor Tubulars Extraction Form (RFTEF) [14]. The form contained entry locations for breakout time, JSN, static string weight, pick up weight, breakout torque, H<sub>2</sub>S and CO<sub>2</sub> Draeger results, and comments. Observations included whether the joint was clean or dirty, straight or bent, and any unique observations. No

significant features were identified on the rig floor. Most of the observations were of minor mechanical damage to the box. This type of feature was attributed to damage that occurred while running or pulling the tubing. Figure 25 shows examples of the damage noted on the rig floor. Several joints were identified as bent, including joints 40, 80, 112, 116, 147, 158, and 160.



**Figure 25: Minor Mechanical Damage on Box of Joints 185 and 207**

Joints were moved to pipe racks on the SS-25 site after rig inspection and breakout. Evidence handling was a major consideration when creating the tubular handling protocol [5]. The objective was to avoid damage to the tubing after its extraction from the well. When joints were moved from the rig floor to the pipe racks, with a rig block and a crane, they were supported on both ends by nylon straps. Care was taken to prevent joints from making metal-to-metal contact. For example, metal pipe racks were covered with wood during inspections. Figure 26 shows the setup and procedure for moving tubing joints from the rig floor to the pipe racks. Figure 27 shows tubing joints on the SS-25 pipe rack.



**Figure 26: Moving Procedure of Tubing from the Rig Floor to the Pipe Racks**



**Figure 27: Tubing Joints on the SS-25 Pipe Rack**

The SS-25 pipe rack was the second opportunity for the Blade team to inspect the tubing joints. The joints were inspected in the as-recovered condition. The surface condition of the pipe limited the ability to identify features. The length of the joint was recorded, and a permanent identification mark was placed on the OD surface at each end. The identification marks were placed at the same circumferential position as the temporary orientation mark shown in Figure 23. The location of the permanent identification served as the permanent orientation mark. Figure 28 shows the permanent identification mark for joint 1. The mark is located on the west face of the joint as identified by Blade personnel on the rig floor.



**Figure 28: Permanent Identification Mark for Joint 1**

The SS-25 inspection was the first opportunity to collect samples from the ID and OD surfaces. Blade personnel primarily used plastic scrapers to collect oil and scale from the pipe surface. Samples were properly identified and placed in sample bags or glass sample jars. Samples were kept in a refrigerator in

the SS-25 Blade trailer. The trailer was locked at all times to prevent unauthorized access to the samples. Samples were eventually moved to the evidence trailer located at the PS-20 site. Appendix A contains a complete list of the 2 7/8 in. tubing samples collected in the field and includes the sample JSN, sampling date, and description. Figure 29 shows a sample collection from the OD surface of joint 32. It shows the use of a scrapper and sample bag to collect oil. Scale and other samples were collected using a similar procedure.



**Figure 29: Sample Taken from Joint 32 at the SS-25 Pipe Rack**

Joints were moved from the SS-25 pipe rack to a flatbed truck. Wood was used to secure the joints in a single layer. The joints were transported to the PS-20 site for cleaning, inspection, and storage preparation. Joints were moved from the flatbed truck to the PS-20 pipe racks using a stinger crane truck, spreader bar, and nylon slings. Containment barriers, plastic, and other chemical safety materials were placed at the PS-20 site for pipe cleaning and storage preparation. Figure 30 shows unloading of the tubing from the flatbed truck to the PS-20 pipe racks. The following operations were performed on the tubing at PS-20:

1. Additional sampling
2. Cleaning
3. Post-cleaning inspection
4. Corrosion protection
5. Bolstering

The first task was to collect additional samples prior to cleaning. The majority of the samples were collected at SS-25. Sampling at PS-20 consisted primarily of swabbing the ID of the tubing: A clean cloth was attached to the end of a PVC pipe and was pushed through the ID of the pipe and collected into a large sample bag at the opposite end. Figure 31 shows images of the swabbing procedure. Swabs were taken from joints at various depths. This was done at the PS-20 site because it was operationally more convenient.



**Figure 30: Unloading of Tubing at the PS-20 Site**



**Figure 31: Swabbing the 2 7/8 in. Tubing ID at PS-20**

Argus, a third party vendor used to clean the tubulars and other wellhead components, cleaned the OD and ID surfaces of the tubing with Sentinel 909, brushes, and rags per the cleaning procedure described in the Phase 3 tubulars handling protocol [5]. Aggressive cleaning methods were prohibited during this process. The goal of the cleaning was to remove oil, loose scale, and other debris that could obscure surface features and also prepare the surface for coating with a corrosion inhibitor. Sentinel 909 was applied to the ID and OD surfaces using sprayers and soaked for approximately 30 minutes. Rags and brushes were then used to remove oil and debris. Joints were then rolled down the pipe racks for inspection by Blade personnel. The objective of the PS-20 inspection was to identify features that had been obscured during the SS-25 inspection.

Notes were taken and documented on evidence data sheets [14]. The inspection at the PS-20 site identified minor metal loss, bent joints, and minor mechanical damage. The majority of the mechanical damage appeared to be caused by tongs, slips, and other minor damage associated with running the pipe. Significant features were not identified during the tubing inspections. The box and pin were also inspected for damage. Some minor metal loss was observed on the box, and galling was identified in some of the threads. Stamps from the manufacturer were observed on many of the joints, indicating the environment was not aggressive enough to remove the marks. Figure 32 and Figure 33 shows examples of minor metal loss and mechanical damage, respectively. Figure 34 shows examples of manufacturer stamps still visible on the OD surface.

Inspected joints were rolled further down the racks to be coated with the corrosion inhibitor Tectyl 846, which was chosen based on tests conducted by Blade.

Tectyl 846 had the following ideal properties for protecting the tubulars:

- It effectively protected against corrosion.
- It was transparent when applied, allowing field marks to remain visible.
- It required non-aggressive techniques to remove the coating.



Figure 32: Examples of Minor Metal Loss



Figure 33: Examples of Mechanical Damage



Figure 34: Examples of Manufacturer Stamps

The corrosion inhibitor was allowed to cure overnight on the pipe rack prior to bolstering. VCI packets were placed inside the ends of each joint the following day. Thread protectors were used to seal the inside of the pipe and trap the internal volume for the VCI to work in. Joints were then moved from the pipe racks to bolsters on a trailer. The bolsters were the primary device used to protect the joints from transportation damage and had individual slots sized to fit the 2 7/8 in. tubing; the slots prevented the joints from contacting each other during transportation. Although the bolsters could hold up to 42 joints of tubing, their weight capacity had been limited to 8,000 lb for safety. Figure 35 shows the trailer loaded with the bolstered tubing. The wellhead components and tubing left Aliso Canyon on October 23, 2017, and were received in Houston, TX, on October 26, 2017.



Figure 35: Bolstered Tubing on Trailer

### 2.2.5 Logging of 7 in. Casing

Logging of the 7 in. casing occurred during several stages of Phase 3. The first logs were MID-2 and MID-3, which were run during logging of the tubing in April 2016. Additional logs were run during tubing extraction followed by a full logging program of the remaining 7 in. casing after tubing extraction. A 7 in. tieback casing was used to log the remaining 7 in. casing joints. The logs included in the 7 in. logging program were as follows:

- Logs run through the 2 7/8 in. tubing:
  - Versa-Line Magnetic Imaging Defectoscope-2 (MID-2) Log (Tubbing Logging April 18–19, 2016)
  - Versa-Line Magnetic Imaging Defectoscope-3 (MID-3) Log (Tubbing Logging April 20, 2016)
  - EV Camera and Caliper (Tubing Extraction August 30, 2016)
  - EV Camera (Tubing Extraction August 31, 2016)
- Log run through the original 7 in. casing string: EV Camera and Baker Hughes 56-Arm Caliper (October 10, 2016)
- Logs run through the 7 in. tieback:
  - Baker Hughes Gauge Ring/Junk Basket (November 27, 2016)
  - Baker Hughes 56-Arm Caliper and High-Resolution Vertilog (HRVRT) (December 01, 2016)
  - Versa-Line Magnetic Imaging Defectoscope-2 (MID-2) and 3 (MID-3) (December 02, 2016)
  - Schlumberger Ultrasonic Corrosion Imaging (UCI) (December 03, 2016)
  - Schlumberger Isolation Scanner (IBC) and Sonic Scanner (SSCAN) (December 04, 2016)
  - Schlumberger Corrosion Protection Evaluation Tool (CPET) (December 07, 2016)
  - EV Camera (December 10, 2016)

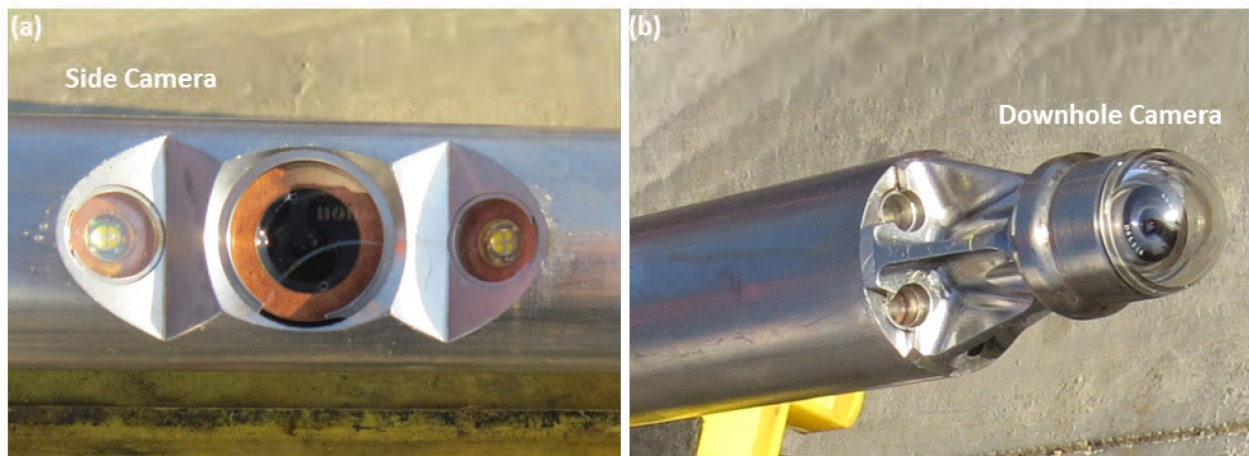
Details and results of the 7 in. casing logs are discussed in the log summary report [15]. A general discussion is provided in this section for convenience. The MID-2 and MID-3 tools had the capability to inspect the 7 in. and 11 3/4 in. casings through the tubing; these logs are discussed (with the tubing logs) in Section 2.2.3. The data suggested that the 7 in. casing was parted at approximately 890 ft.

The first opportunity to run a camera to visually confirm that the casing was parted was during tubing extraction on August 30, 2017. The tubing was extracted to approximately 1,050 ft, and a clear brine was used to displace mud to surface to increase the camera's visibility. The brine was filtered to a



nephelometric turbidity unit (NTU) reading of 10 or less. (Turbidity is a measure of a fluid's cloudiness caused by suspended solids. A high quantity of suspended solids in a fluid results in high turbidity and, consequently, low visibility.) Additional joints were extracted until the end of tubing (EOT) was at approximately 850 ft. An EV camera was run through the tubing to a depth of 890 ft. It identified the parted 7 in. casing and was able to show that the lower string was offset from the upper string. The camera lens was partially blocked by debris during the first run, and although it identified the parting, a thorough investigation was not possible on the first run. The camera was run again the following day on August 31, 2017. The second run was more successful and produced a higher quality video.

The EV tool used two cameras to capture video: a side camera and a downhole camera. Figure 36 shows the position of the (a) side and (b) downhole cameras on the tool. The tool could rotate, which allowed the side camera to see 360°. The side camera was typically used for detailed viewing of the casing fracture surfaces. The downhole camera was a fish eye camera, which distorted the image but provided a wide viewing angle. This camera was used to look at the top of the lower 7 in. string from inside the upper string.

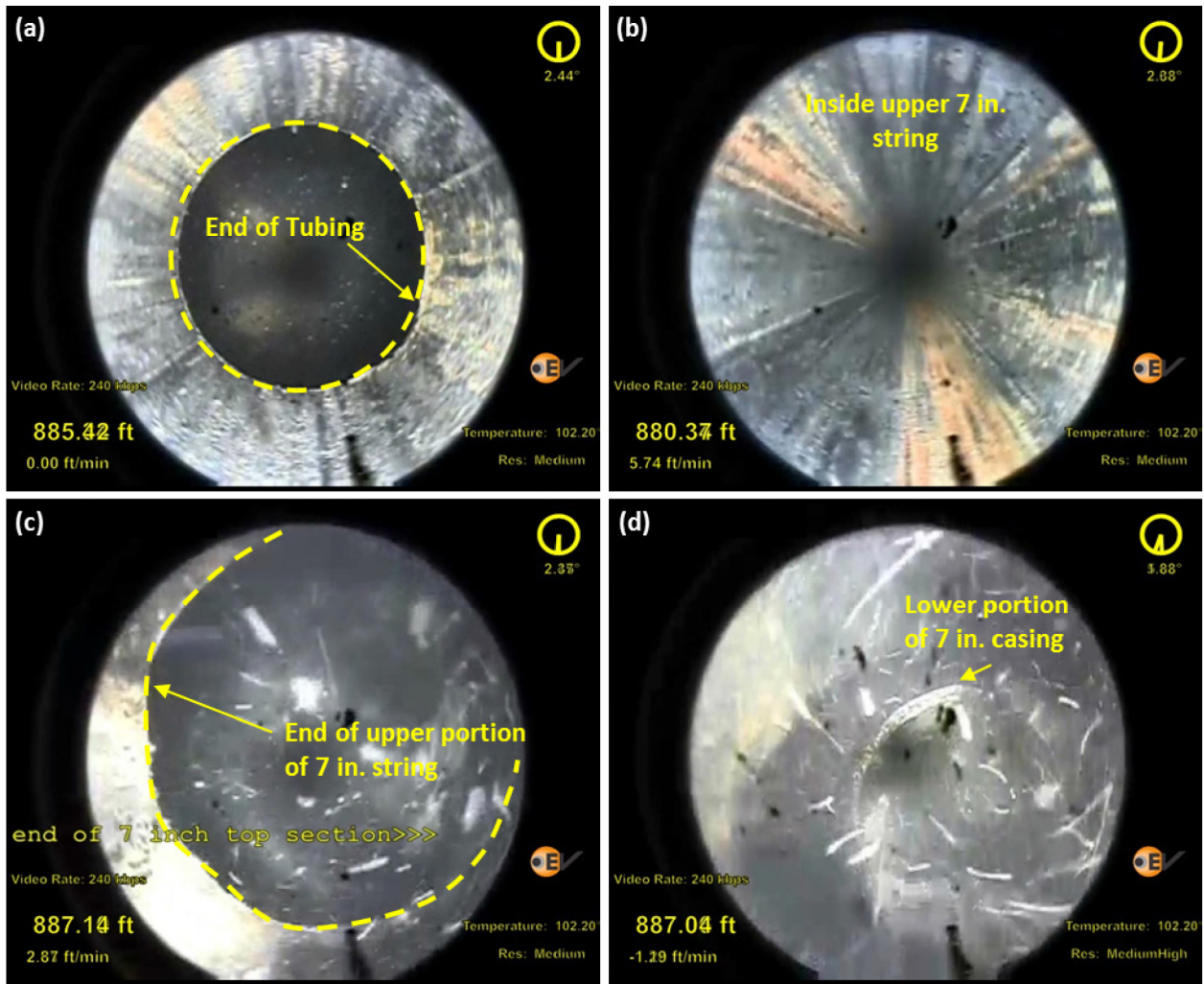


**Figure 36: (a) Side and (b) Downhole Cameras on the EV Camera Logging Tool**

Figure 37 shows four images extracted from the camera log video captured during the second run. These images show the following three distinct locations in the well:

1. EOT
2. End of upper section of 7 in. casing
3. Top of lower section of 7 in. casing

Figure 37 shows (a) the end of the tubing, which was set at approximately 885 ft; (b) the camera inside the upper 7 in. casing string after exiting the tubing; and (c) the end of the upper 7 in. casing string. This was the location of the parted 7 in. casing. The camera exited the upper string and looked down at the lower string. Figure 37 (d) shows the lower 7 in. casing string offset from the camera. The lower string was sitting at approximately 5 in. below the upper string. The camera runs confirmed that the 7 in. casing was parted and that the lower fish was offset from the upper string. Identification of the offset was significant to the fishing operations. A custom-built pawl tool was used to recover the lower fish. The pawl tool swallowed the casing, and spring-loaded pawls latched under a connection upset to pull tension while cutting. After cutting the casing, the fish was recovered in the pawl tool. A spear was not used as it could potentially contact the fracture surface several times before entering the casing.



**Figure 37: EV Lower Camera Snapshots from August 31, 2017, Showing the Parted 7 in. Casing**

The camera was lowered so that the side camera could view the upper fracture surface. The tool was rotated 360° to provide full coverage of the fracture surface. Figure 38 shows snapshots of the upper fracture surface taken from the side camera. The surface appeared to be mostly flat, although the initial observations were limited due to the quality of the video. The camera was lowered inside the lower string so that the side camera could see the lower fracture surface. Figure 39 shows snapshots of the lower fracture surface taken from the side camera. The camera was not centered inside the lower casing due to the offset, which allowed only a small section of the surface to be in focus. Most of the fracture surface was blurred due to the proximity of the camera to the casing ID. The lower fracture surface also appeared to be flat, as expected, based on the upper fracture surface observations.

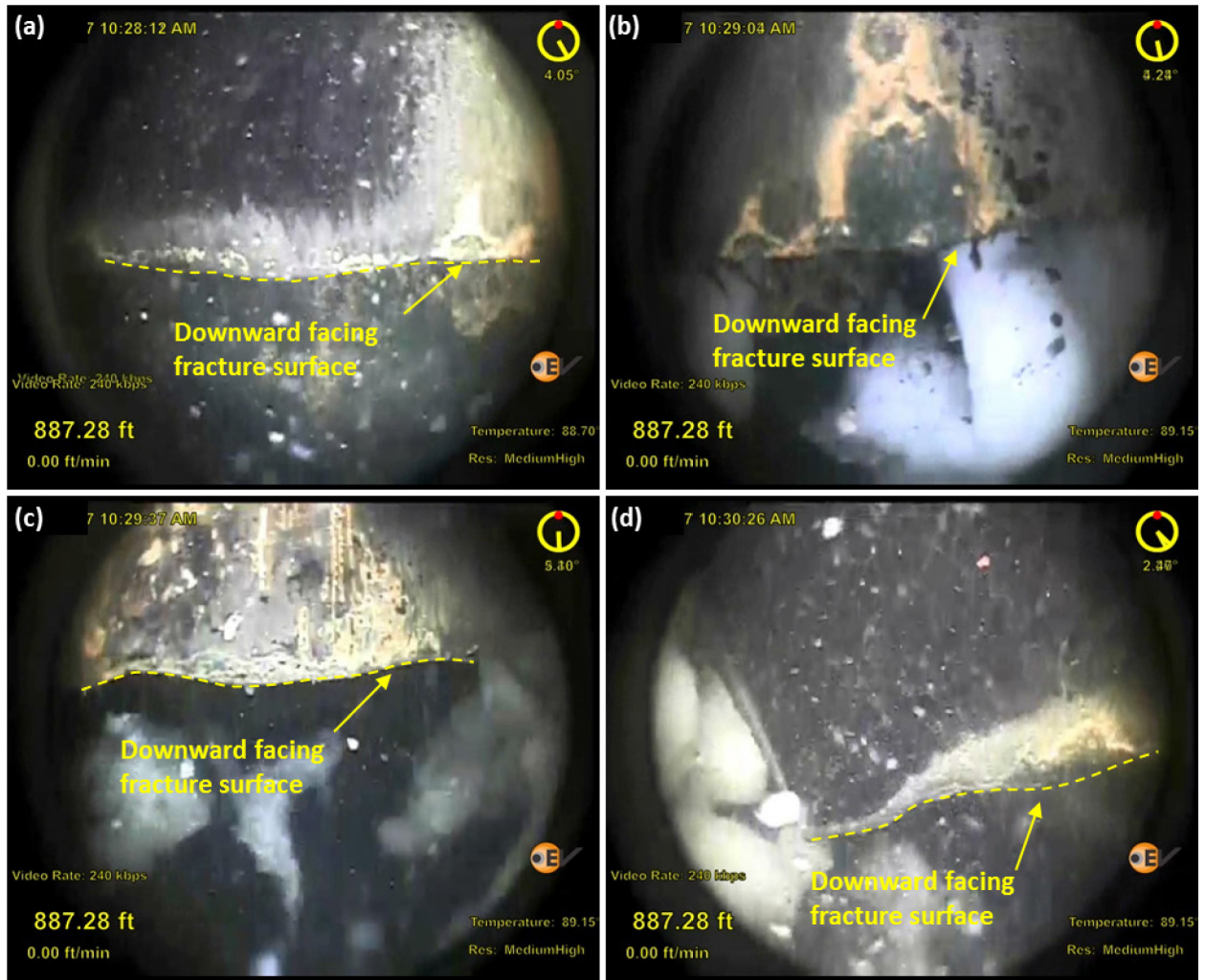
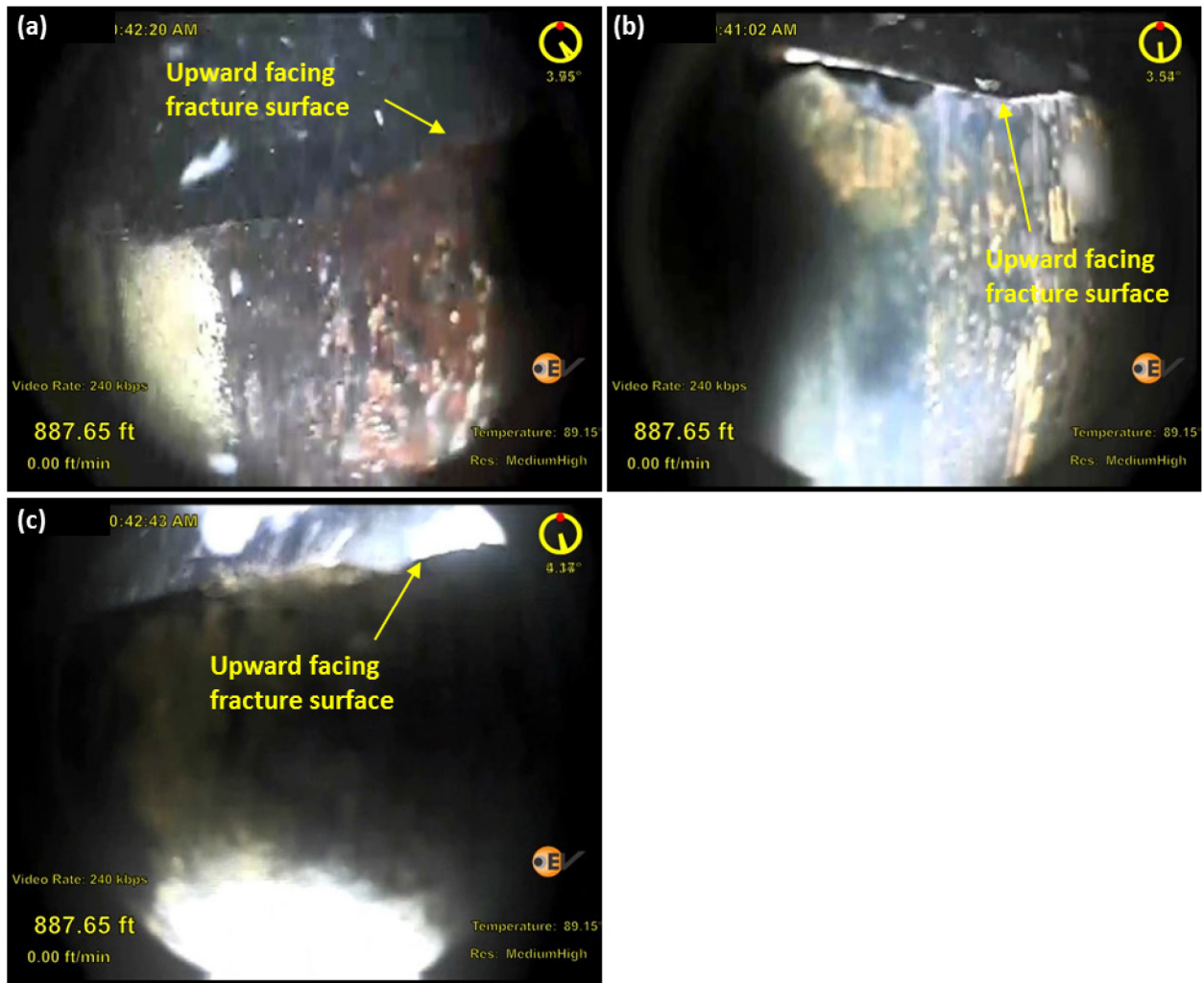


Figure 38: EV Side Camera Snapshots from August 31, 2017, Showing Upper Fracture Surface



**Figure 39: EV Side Camera Snapshots from August 31, 2017, Showing Lower Fracture Surface**

Tubing joints from the work string were used to lower the end of the tubing below the brine-mud interface. Mud was used to displace the brine to surface. The remaining tubing joints were extracted after the brine was displaced and were inspected as described in Section 2.2.4. The 7 in. casing logging continued on October 10, 2017, with another run using a camera and a 56-Arm Caliper tool. The camera was run to the top of the fluid level (322 ft) to inspect the ID of the casing. No notable features were identified. The caliper was run to 865 ft to inspect the ID of the casing.

A camera and caliper were the only tools run through the top of the original 7 in. casing string. The remaining logs began on November 27, 2017, after extraction of the 7 in. casing above the approximate cut depth of 939 ft. The remaining logs were intended to inspect the non-recovered 7 in. casing joints. A tieback was installed to provide access to the lower joints. On October 12, 2017, the casing was cut, and the first 7 in. casing joint was extracted and inspected by Blade. Inspection of the 7 in. casing is discussed in Section 2.2.5. The first joint was extracted using the Ensign 334 rig to provide a gap between the upper and lower fracture surfaces. The objective was to protect the fracture surfaces in the event the upper string slipped while in the slips. The following events occurred before logging continued on November 27, 2017:

1. Ensign 334 rig was rigged down and demobilized (October 13–14, 2017)

2. Ensign 540 rig was mobilized and rigged up at the SS-25 site (October 16–28, 2017)
3. 7 in. casing joints were extracted up to the lower fracture surface (October 29–November 07, 2017)
4. 7 in. casing was cut below the parted casing depth, and the lower fracture surface was extracted (November 08–14, 2017)
5. 11 3/4 in. casing was logged to 990 ft (November 15–16, 2017)
6. Tieback was run to existing 7 in. casing stub at 939.5 ft (November 17, 2017)

7 in. casing logging continued on November 27, 2017, with a gauge ring and junk basket to ensure logging tools could pass through the tieback and 7 in. casing. All logging tools were run to TD to inspect the non-recovered 7 in. casing joints. A 56-Arm Caliper and HRVRT were both run on December 1, 2017, to inspect the ID and OD of the casing. The caliper inspected the ID only and identified corrosion concentrated in a 200 ft zone at approximately 1,900 ft. The corrosion was most likely associated with a gas-lift mandrel that was set at 1,965 ft.

The MID-2 and MID-3 tools were run on December 2, 2017, to inspect both the 7 in. and 11 3/4 in. casings. The MID tools were capable of identifying and differentiating ID and OD corrosion. The caliper and MID tools were first used in the tubing and are discussed in detail in Section 2.2.2.

The HRVRT is designed to identify internal versus external corrosion, holes, depth of penetration, and other defects. The tool can differentiate between metal-loss (corrosion) and metal-gain (hardware) features and distinguish between general corrosion and isolated pitting. The tool uses an array of *hall effect* sensors that measure magnetic flux leakage generated by defects in the casing. The HRVRT identified extensive external corrosion between the end of the tieback—939 ft—and 1,000 ft. The remaining joints generally did not contain any external features. However, a few external features with metal loss penetrations between 15 and 25% were identified between 1,500 and 3,750 ft. The HRVRT detected ID corrosion consistent with the caliper findings.

The UCI tool is designed to identify, locate, and quantify casing corrosion. It can identify holes, weight changes, internal and external scale buildup, external metal loss, and damage caused by milling, fishing, or plastic deformation. The UCI tool has a rotating ultrasonic transducer that analyzes signal reflections to provide casing thickness, surface condition images, and small defects on both internal and external casing surfaces. The results were consistent with the HRVRT findings for both the internal and external surfaces. Figure 40 shows a comparison of the HRVRT and UCI results for the OD surface between 939 ft and 1,000 ft. The joints at these depths were eventually extracted, and the OD corrosion was confirmed.

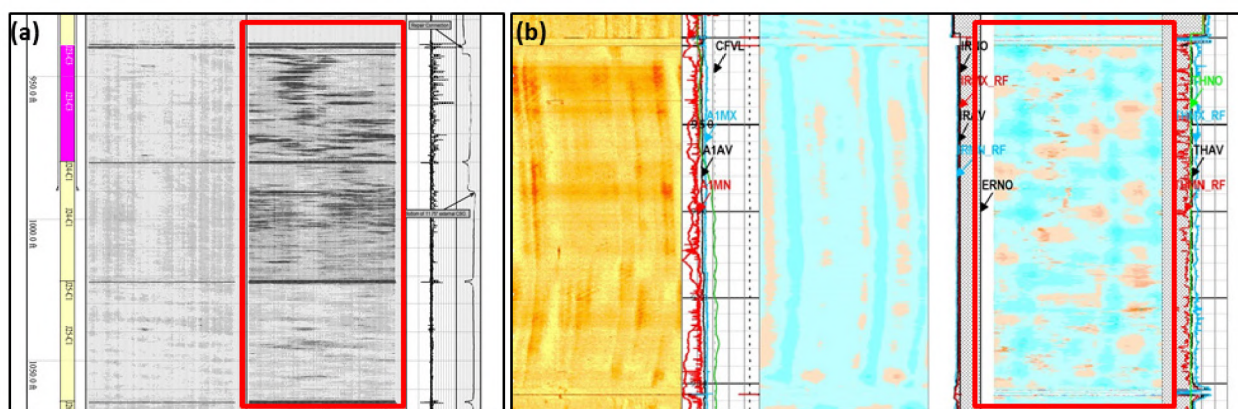


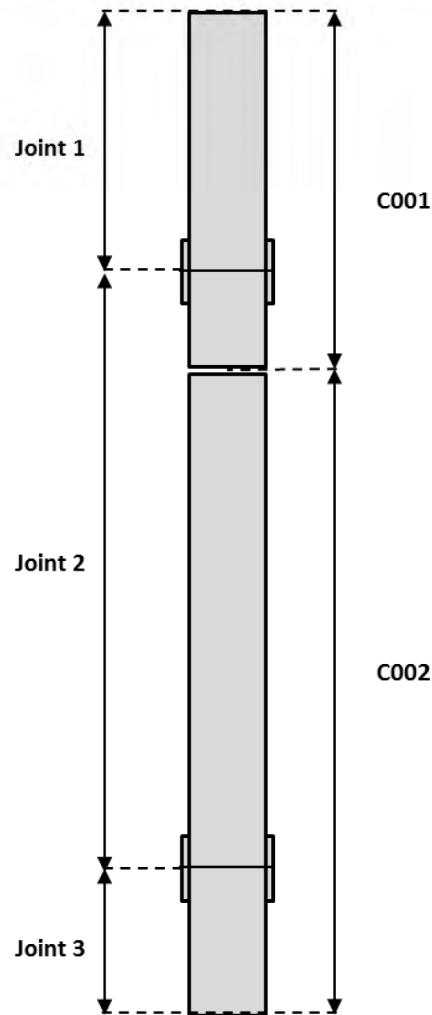
Figure 40: (a) HRVRT and (b) UCI Results Between 939 ft and 1,000 ft Showing External Corrosion

The Schlumberger IBC and SSCAN tools were used to analyze the annulus behind the casing. The IBC tool is designed to map cement placement in the annulus. It can map annulus material as solid, liquid, or gas by combining pulse-echo techniques with ultrasonic techniques to confirm zonal isolation and identify channels in the cement. The Schlumberger SSCAN tool is designed to analyze the formations surrounding the wellbore. It is typically used for geophysics, reservoir characteristics, and cement bond quality.

The last Schlumberger tool run in the casing was the Corrosion Protection Evaluation Tool (CPET), which is designed to test the effectiveness of an existing cathodic protection system or assess the need for cathodic protection. These logs were run to assist with the RCA interpretations but did not provide the data directly required for the metallurgical investigation.

### 2.2.6 7 in. Casing Extraction

Twenty-five casing joints were extracted from the SS-25 well, identified as C001 to C026. JSN refers to the individual **sections** of the casing that were cut and extracted from the string. The casing was cut below each connection, unlike the tubing, which was broken out at the connection. JSNs for the casing do not directly correspond to individual joints as was the case for tubing. Casing was cut in such a way that a joint included the connection and part of the following joint. The JSNs also deviated from the joint number when the parted casing was recovered. This occurred because the circumferential parting separated a single joint into two sections that required individual JSNs. Again, JSNs are used throughout this section to identify **sections** of pipe extracted from the well, rather than joint numbers. Figure 41 shows an example comparing the JSNs C001 and C002 with their corresponding joint numbers. C001 included joint 1, connection 1, and part of joint 2. C002 included joint 2, connection 2, and part of joint 3. The Phase 3 tubulars handling protocol [5] provides a detailed discussion of the JSNs and cutting procedure. Schematics of the casing showing the JSNs and joint numbers are provided in the Phase 4 summary [7].



**Figure 41: Joint Sequence Number Versus Joint Number Example**

The parted casing separated the casing string into upper and lower fish. The upper fish included C001 through C022 (joint 1 to part of joint 22). C001 was extracted on October 12, 2017, using the Ensign 334 rig to create a gap between the fractures surfaces downhole. The Ensign 334 rig was rigged down, demobilized, and replaced with the Ensign 540 rig to extract the remaining 24 joints. C002 through C022 were recovered as part of the upper fish. C023 and C024 (part of joint 22 to joint 24) were recovered on November 14, 2017, and November 15, 2017, after cutting below the parted casing and recovering the lower fish with the pawl tool. C025 and C026 (joint 24 to part of joint 26) were extracted on August 8, 2018, after completing several well operations. The extraction dates for each JSN were as follows:

- October 12, 2017—C001
- October 30, 2017—C002
- October 31, 2017—C003 to C005
- November 01, 2017—C006 to C008
- November 02, 2017—C009 to C011
- November 03, 2017—C0012 to C014

## SS-25 Casing Failure Analysis

- November 04, 2017—C015 to C017
- November 05, 2017—C018 to C020
- November 06, 2017—C021
- November 07, 2017—C022
- November 14, 2017—C023
- November 15, 2017—C024
- August 08, 2018—C025 to C026

Wellhead components were removed on October 11, 2017, the day before casing extraction began, and were transported to the PS-20 site for cleaning, ID inspection, and coating. Components removed from the wellhead prior to the 7 in. casing extraction included the following:

- W004A—Wing valve
- W004B—Tubing head and DSA assembly
- W004C—Wing valve
- W005—Slip assembly

The wellhead component ID surface was the only surface inspected because the OD had been inspected during the wellhead examination described in Section 2.2.3. Components were coated with the corrosion inhibitor Tectyl 846 and crated for storage. Figure 42 (a) shows the wellhead components at the PS-20 site after cleaning, inspection, and coating. Figure 42 (b) shows the components during crating, and Figure 42 (c) shows the components in storage after crating. Wellhead component crating followed the same procedures that were executed during tubing extraction (Section 2.2.4). W004BS1 was the only sample collected from the wellhead components.



**Figure 42: Wellhead Components (a) Before, (b) During, and (c) After Crating**

A retrievable bridge plug (RBP) and a full opening safety valve were installed as well control barriers after the extraction of C001. The well was shut in, and the Ensign 334 rig was rigged down and demobilized. The Ensign 540 rig was then mobilized to the SS-25 site and rigged up. The Ensign 540 is a small footprint automated drilling rig (ADR). The rig was a modular type rig designed for pad drilling, which provided added flexibility for placing the rig components on the narrow SS-25 site. The Ensign 540 was better equipped to handle the 7 in. casing and had a fully-equipped mud system and two mud pumps.

Figure 43 shows the Ensign 540 rig on the SS-25 site. Extraction resumed with C002 on October 30, 2017. All evidence collected during casing extraction was handled according to the Phase 3 tubulars and wellhead handling protocol [5].



The Phase 3 extraction protocol [4] has a complete list of steps for casing extraction. The following steps are a summary of the procedure:

1. The casing running tool (CRT) was engaged in the 7 in. casing.
2. One joint was pulled and the casing was set in the rotary so a cut could be made 24–30 in. below the top of the connection box.
3. A casing clamp was installed above the slips.
4. The casing was cut using the Cameron casing cold cutter.
5. The joint was laid down with the casing pipe handler.
6. The joint was removed from the pipe handler arm with nylon slings and a crane.
7. The joint was placed on the pipe rack for inspection and documentation.



**Figure 43: Ensign 540 Rig**

The 7 in. casing was stabbed using the CRT, and each joint was pulled above the rig floor. The casing was pulled far enough above the rig floor to make a cut approximately 24–30 in. below the top of the connection box. Figure 44 (a) shows the CRT on the rig floor and Figure 44 (b) shows the CRT stabbing the 7 in. casing. The image also shows the engaged slips and casing collar. The target cut location was cleaned using Sentinel 909 and acetone and inspected with MPI and ultrasonic testing (UT).

Figure 45 shows the (a) cleaned target cut location and the (b) ultrasonic transducer. Figure 45 (c) shows an example of a linear indication identified by MPI. NDE was performed prior to cutting to ensure the cut did not damage any casing features. Cut locations were moved for C012, C014, C016, C017, and C018 due to the linear indications identified by NDE on the rig floor. The MPI evidence data sheets [16] provide details of the linear indications identified during the rig floor inspection.

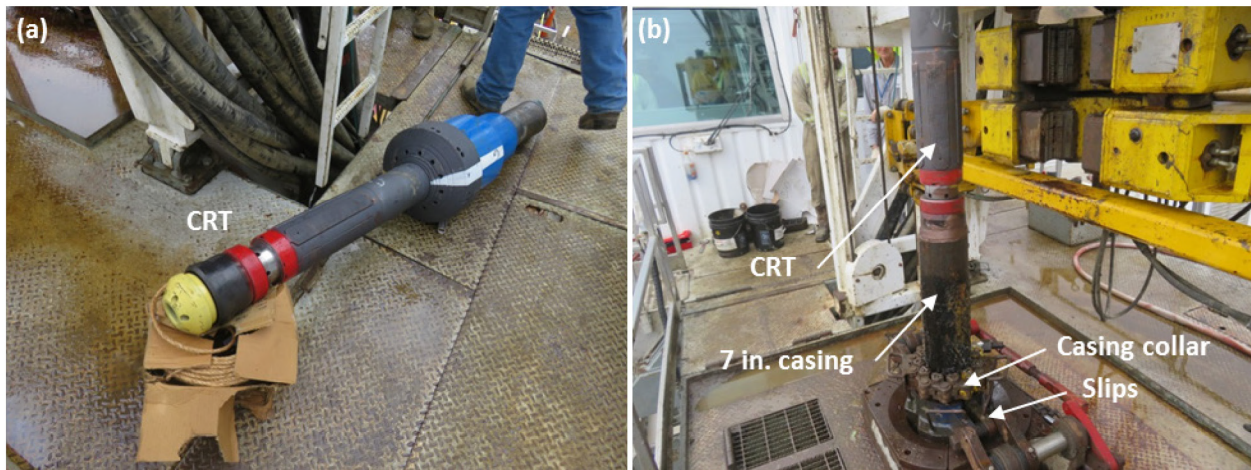


Figure 44: (a) Casing Running Tool on Rig Floor and (b) Stabbing 7 in. Casing



Figure 45: (a) Cleaned Pipe Section for NDE, (b) Ultrasonic Transducer, and (c) MPI Linear Indication

Casing was cut using a Cameron casing cold cutter after the inspection to preserve the connections. The connections were intended for leak testing at the Blade warehouse in Houston, TX. Figure 46 (a) shows the cut location for the 7 in. casing. Figure 46 (b) shows the Cameron casing cold cutter installed on the 7 in. casing, and Figure 46 (c) shows the casing after the cut. The 7 in. casing was laid down using the casing pipe handler. The pipe handler used hydraulics to grab the casing on the rig floor and bring it down to ground level. Figure 47 shows the casing pipe handler laying down casing. (The casing pipe handler simplified laying down the casing and minimized the risk of damage.) The casing was moved from the pipe handler to the pipe racks using a crane and nylon slings. The same precautions used for tubing handling were implemented for the casing.

The casing was inspected and documented in a manner similar to the tubing. The pipe was inspected on the rig floor, at the SS-25 site pipe racks, and at the PS-20 site pipe racks. When compared to the tubing inspection, the rig floor inspection was limited because the connections were left intact rather than broken out. The rig floor inspection was focused on the OD surface of the casing body and connections. Blade personnel focused primarily on monitoring the casing NDE and cut. Notes were recorded on the RFTEF [16] as it had been done with the tubing.

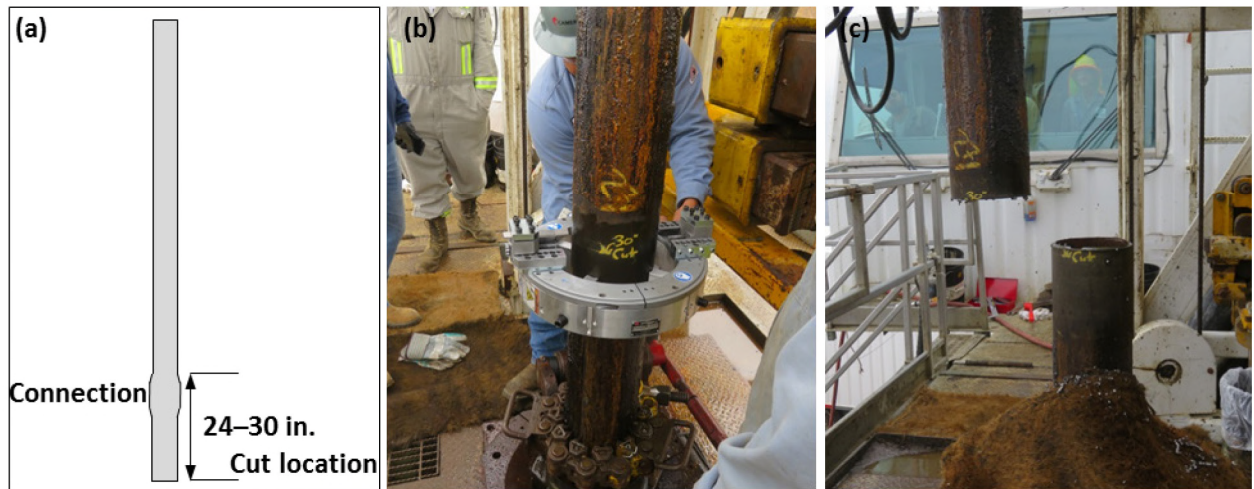


Figure 46: 7 in. Cutting Operation



Figure 47: Casing Pipe Handler

The casing was inspected in the as-recovered condition on the SS-25 site pipe racks. Samples were taken using the same procedures used for the tubing. (Appendix B contains a list of the samples collected from the 7 in. casing.) C001 through C017 were covered with a tar-like deposit that obscured the OD surface and prevented a detailed inspection; however, minor mechanical damage from extraction, slips, and tongs were noted. Corrosion features were first identified on C018. Figure 48 shows examples of corrosion features identified on the (a) body and (b) connection of C018. Corrosion features were also identified on the remaining joints (C019–C026).

C022 was extracted on November 07, 2018, and contained the circumferential parting identified during logging and visually confirmed with the downhole camera. Figure 49 (a) shows the parted casing hanging above the rig floor. Figure 49 (b) through (d) shows the fracture surface above the rig floor. The fracture surface was thoroughly examined on the rig floor and then moved to the pipe rack for further inspection.



Figure 48: Corrosion Features on C018 (a) Pipe Body and (b) Connection

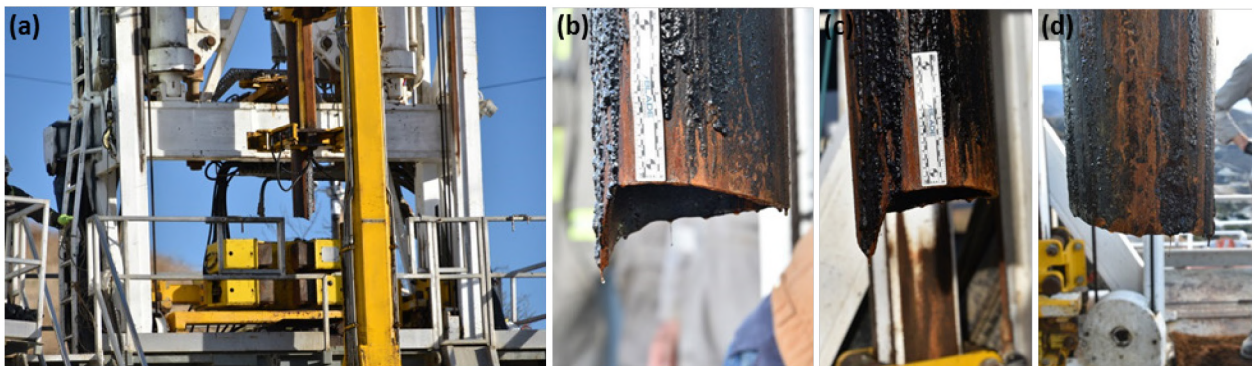


Figure 49: C022 Extraction

Figure 50 shows the parted casing on the pipe rack. The fracture surface was obscured because it was covered with oil and scale. The circumferential parting appeared to be mostly flat with a pointed section that faced the south side of the rig floor. Figure 50 shows an (a) overall and (b) close-up image of the fracture surface. Corrosion features adjacent to the fracture were identified (Figure 50 [c]).

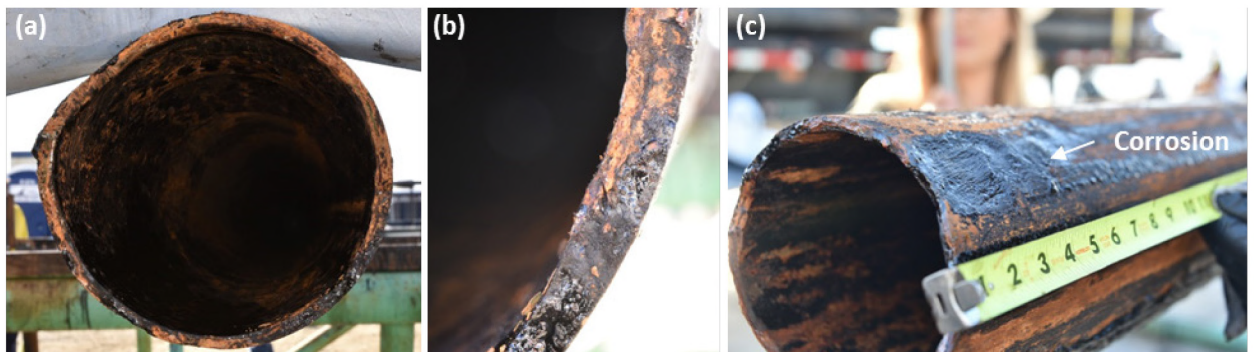
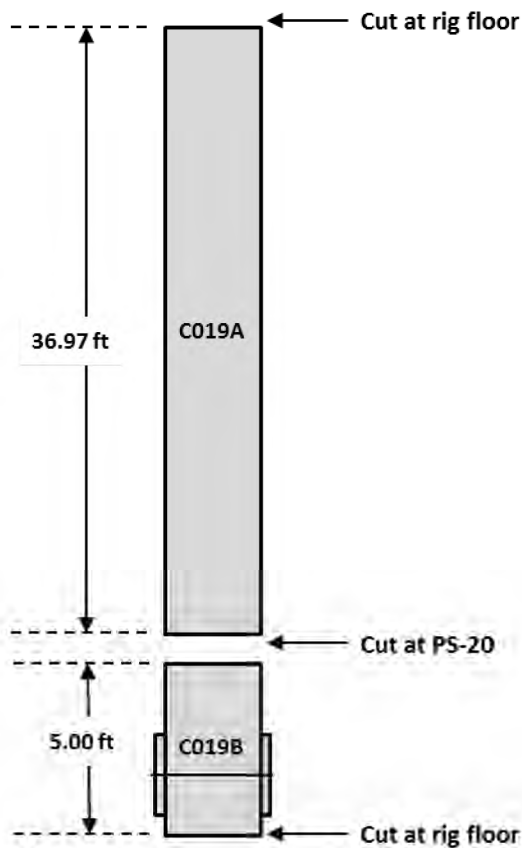


Figure 50: Parted Casing (C022) on the SS-25 Pipe Rack

The casing was moved from the SS-25 pipe rack to a flatbed truck. Joints were secured in a single layer using wood. The casing was transported to the PS-20 well site for cleaning, inspection, and storage preparation. Casing was moved from the flatbed truck to the pipe racks on the PS-20 site using a stinger crane truck, spreader bar, and nylon slings. The casing joints were cleaned by Argus using the same methods as the 2 7/8 in. tubing joints. The casing was moved down the pipe racks for inspection by Blade

personnel after being cleaned with Sentinel 909. The cleaning procedures removed the oily deposits and revealed more of the corrosion features that were obscured during the rig and SS-25 inspections. Observations were photo-documented and recorded on the PS-20 evidence data sheets [16]. The PS-20 inspection included MPI and UT inspections on sections of the casing selected by Blade. NDE sections were selected based on visual inspection findings. The PS-20 NDE evidence data sheets [16] provide details of the MPI and UT results.

Connections were removed and given a new JSN after the inspections. The connections were removed for transportation and testing purposes. Pipe sections containing connections were limited to a maximum length of 7 ft based on connection testing requirements. The short lengths also permitted individual crating of each connection for protection. Figure 51 shows a diagram of the typical cut location for removing a connection. C019 was cut above the connection at the PS-20 site, creating a section of pipe body (C019A) and a 5 ft long connection section (C019B). This was typical for most casing joints. Pipe cuts at the PS-20 site were made using the Cameron casing cold cutter.



**Figure 51: Diagram Showing Typical Cut to Remove Connection**

Casing from the upper fish (C001–C022) was examined first. Corrosion features were not noted on C001 through C013; however, minor mechanical damage and linear indications were identified. Linear indications were found on C004, C005, C009, C011, C012, and C013. Figure 52 shows linear indications from (a) C004, (b) C005, and (c) C012. The linear indications were slightly angled with respect to the pipe longitudinal axis.

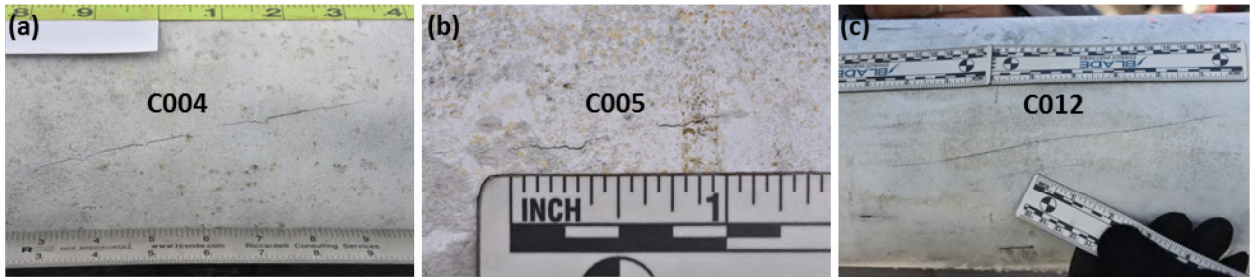


Figure 52: (a) C004, (b) C005, and (c) C012 Linear Indication Identified by MPI

Shallow metal loss was first identified on the C014 connection and was present on the remainder of the extracted casing pipe bodies and connections. Corrosion was identified on many of the connections below C014 with increasing severity. Figure 53 shows the shallow corrosion on the C014 connection. Figure 54 shows corrosion on the connections for (a) C019 and (b) C020; the corrosion is similar to C014’s but more severe.



Figure 53: Shallow Metal Loss on Connection C014

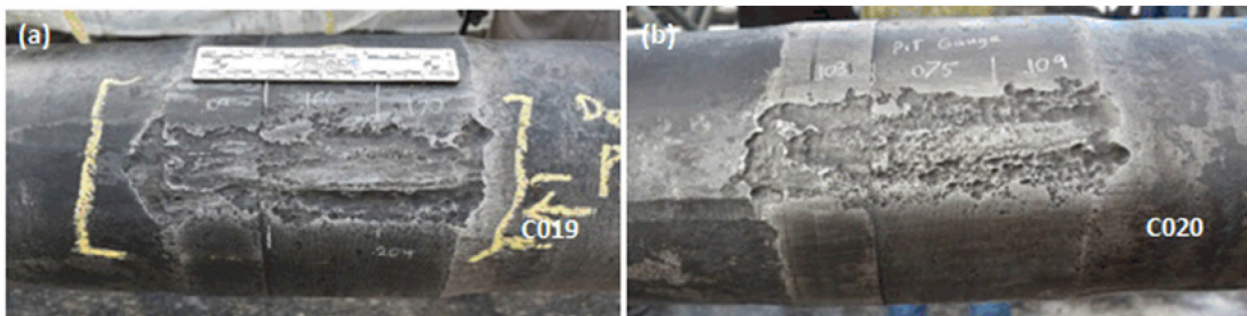


Figure 54: Connection Corrosion on (a) C019 and (b) C020

Corrosion was also identified on the pipe bodies beginning with C014. Figure 55 shows examples of pipe body corrosion from (a) C016, (b) C017, and (c) C018. Figure 55 (c) shows corrosion with striated grooves slightly angled from the longitudinal axis of the pipe. This type of feature was identified at many locations along the casing below C014. Figure 56 shows examples of corrosion with striated grooves from (a) C018

and (b) C022. Figure 57 shows the largest corrosion feature identified during the PS-20 inspection. The shape and morphology appear to be consistent with the features found on the connections (Figure 54).



Figure 55: Pipe Body Corrosion on (a) C016, (b) C017, and (c) C018

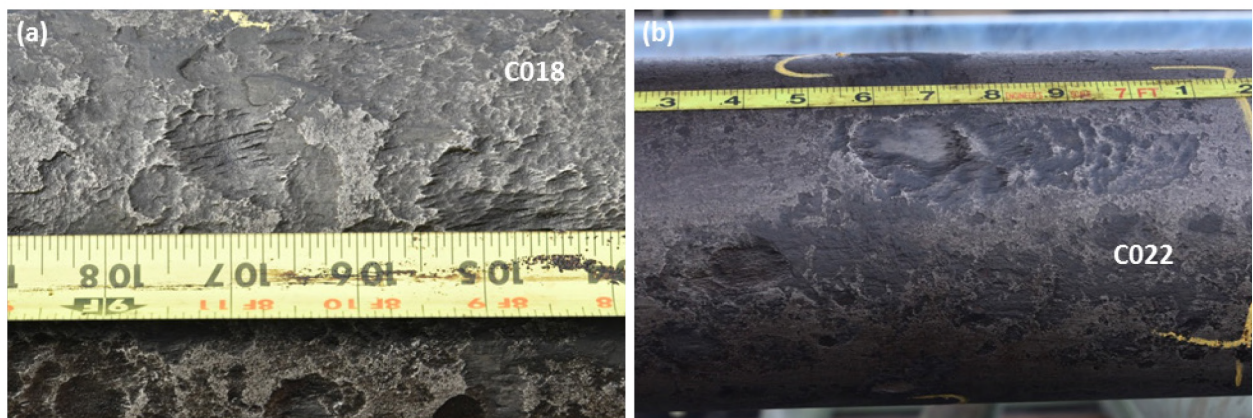


Figure 56: Examples of Corrosion with Striated Grooves from (a) C018 and (b) C022



Figure 57: Pipe Body Corrosion on C020

The fracture surface was removed from C022 prior to cleaning and inspection. A cut location approximately 1 ft from the fracture surface was selected, cleaned, and inspected with MPI and UT. An additional cut was made on C022 to remove the connection. Figure 58 shows a diagram of the C022's cut locations. The diagram shows that the section containing the fracture surface was designated C022B after the cuts were executed. Cuts were made with the Cameron casing cold cutter the same way it had been done on the rig floor. Figure 59 (a) shows the Cameron casing cold cutter installed on C022. Figure 59 (b) shows the fracture surface cleaned with Sentinel 909. Corrosion features adjacent to the fracture surface after cleaning were clearly visible. Figure 60 shows the C022B corrosion features adjacent to the fracture surface.

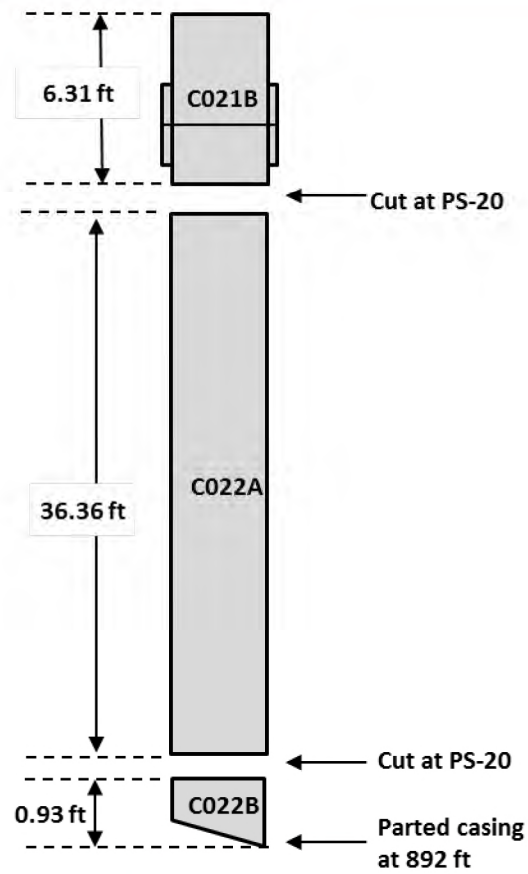
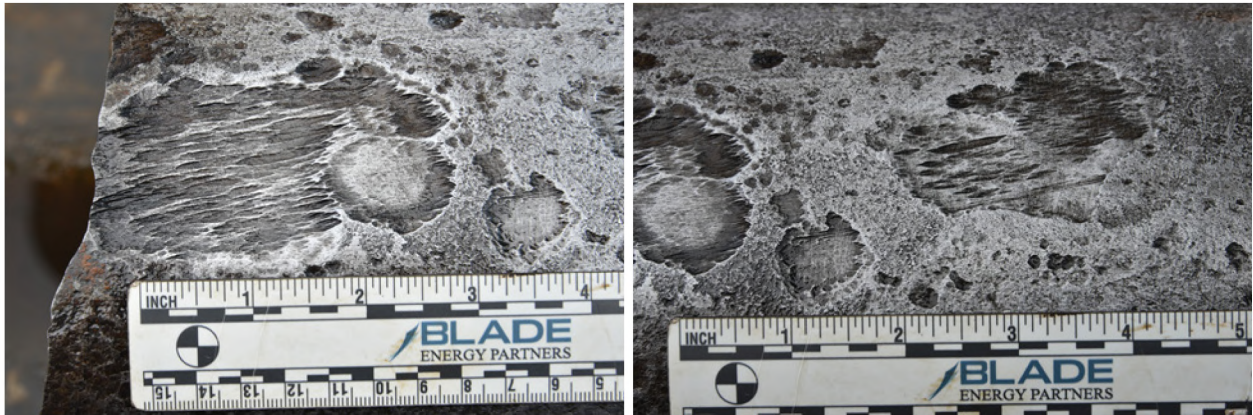


Figure 58: C022 Cut Locations



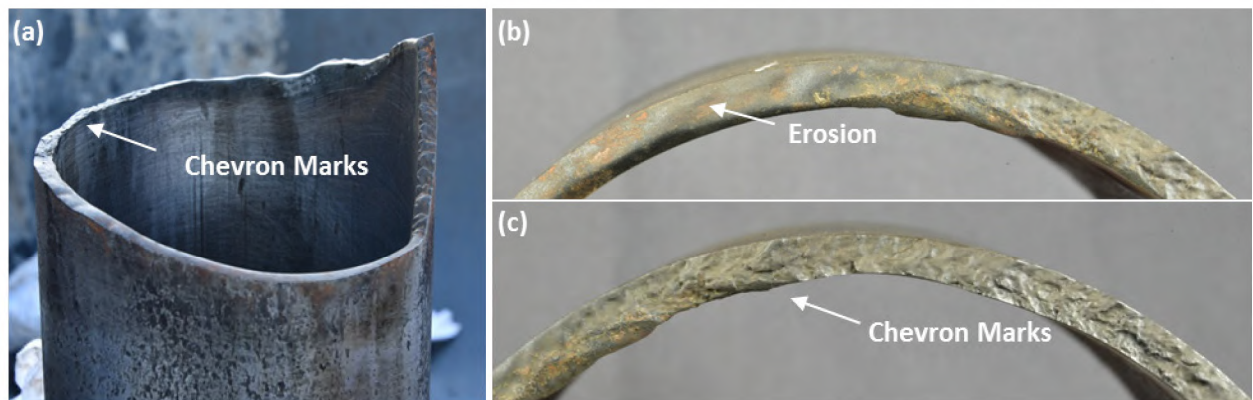
Figure 59: Fracture Surface During (a) Extraction from C022 and After (b) Cleaning with Sentinel 909





**Figure 60: Corrosion with Striated Grooves Adjacent to Fracture Surface**

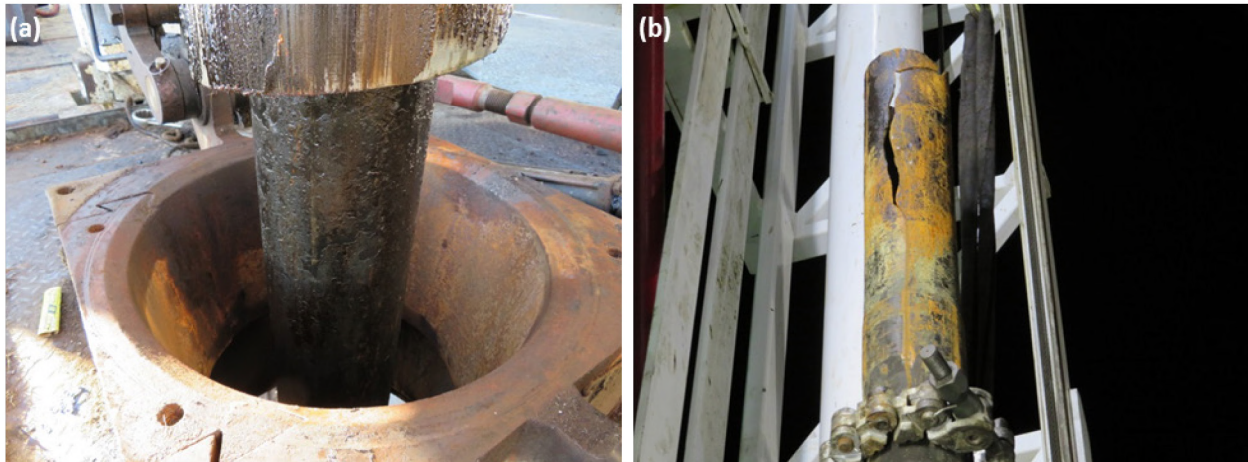
The fracture surface was examined after being cleaned with Sentinel 909. Most of the fracture surface appeared to be eroded; chevron marks were visible in some areas. The eroded fracture surface provided limited information as to the cause of the circumferential parting. Figure 61 (a) shows the circumferential fracture surface after cleaning with Sentinel 909. A field lab was constructed in the trailer at the PS-20 site to provide access to equipment that could assist the field investigation. The field lab included an ultrasonic cleaner, cleaning tools, a stereo microscope, and photography equipment. The fracture surface was cleaned with acetone in a large ultrasonic cleaner. Figure 61 (b) and (c) show close-up images of the fracture surface taken in the field lab after undergoing ultrasonic cleaning. The eroded areas appeared to be smooth and featureless. The chevron marks were visible but also appeared to be eroded.



**Figure 61: (a) Circumferential Fracture Surface Showing (b) Erosion and (c) Chevron Marks**

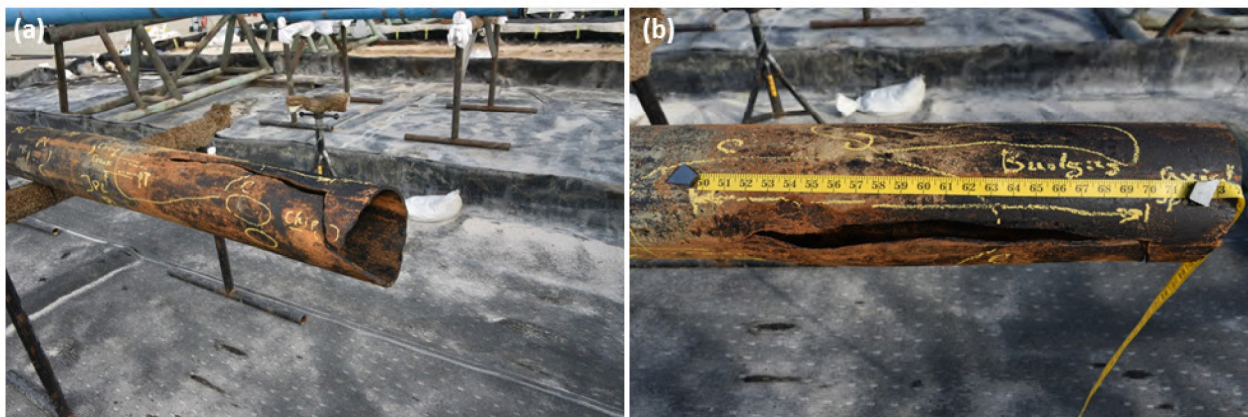
C023 was extracted on November 14, 2017, using the pawl tool and a chemical cutter. The casing was cut at approximately 939 ft with the chemical cutter, and the lower fracture surface was extracted. Figure 62 shows the lower fracture surface on the rig floor with the tool (a) over the fish and (b) removed. This was the first opportunity to visually examine the lower fracture surface. The first major observation was the presence of an axial rupture below the circumferential parting. C023 was moved from the rig floor to the pipe racks by using the crane and a nylon sling. The pipe handler was not used in an attempt to prevent damage to the axial rupture and circumferential parting. The fracture surfaces were wrapped with VCI and covered for the night. C024 was extracted on November 15, 2017. A 13 ft section (C023A) of C023 was cut on the SS-25 pipe rack using the Cameron casing cold cutter to remove the axial rupture and circumferential parting. The pipe sections (C023A, C023B, and C024) were transported to the PS-20 site for further inspection. These sections were not subjected to the same protocol at PS-20 as previous

casing. These pipe sections were inspected at the PS-20 site and preserved in the as-recovered condition for further analysis in Houston, TX.



**Figure 62: Lower Fracture Surface (a) In and (b) Out of the Pawl Tool**

Figure 63 (a) and (b) show the axial rupture and circumferential parting on the PS-20 pipe rack. The axial rupture was located below the circumferential parting and was surrounded by a corrosion feature. Wall thinning was observed near the middle of the axial rupture. Bulging (ductile deformation) was observed adjacent to the axial rupture. The top fracture surface in Figure 63 (b) appeared to be more bulged than the lower fracture surface. The axial rupture had one arrest point away from the circumferential parting, adjacent to the connection. The axial rupture appeared to run towards the connection and eventually turned and arrested. An upper arrest location was not observed. The upper portion of the axial rupture turned similar to the lower arrest point but continued on a path inclined from the pipe axis and was connected to the circumferential parting.



**Figure 63: Axial Rupture and Circumferential Parting at PS-20 (C023A)**

The fracture surface was covered with an oil deposit and scale products, but features were identifiable. Figure 64 (a) and (b) show surface features, chevron marks, and other features. C023A was preserved in the as-recovered condition and cut into smaller sections for transportation. A 5.80 ft section (C023A1) containing the axial rupture, circumferential parting, and connection was cut using the Cameron casing cold cutter. Additional cuts were made at the PS-20 site for connection testing and transportation logistics. Figure 65 shows a diagram summarizing the cuts made to C023 and C024.

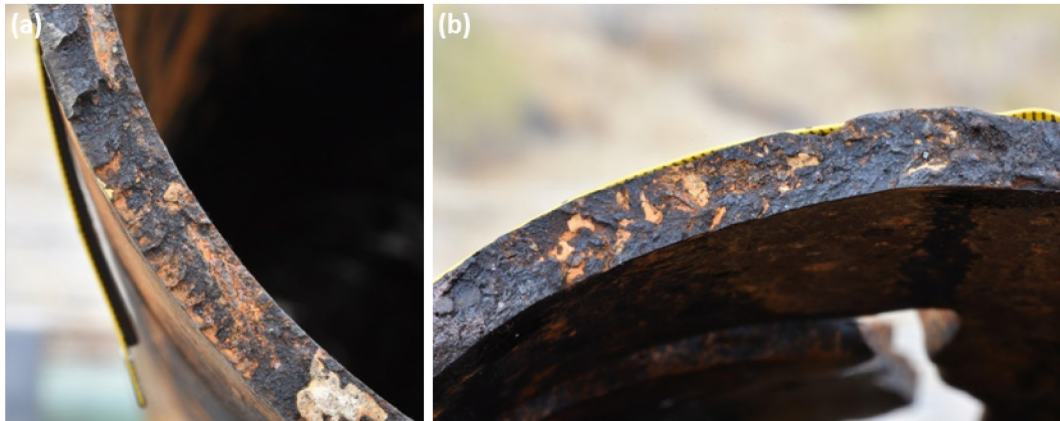


Figure 64: Circumferential Parting Fracture Surface (a) Features and (b) Chevron Marks

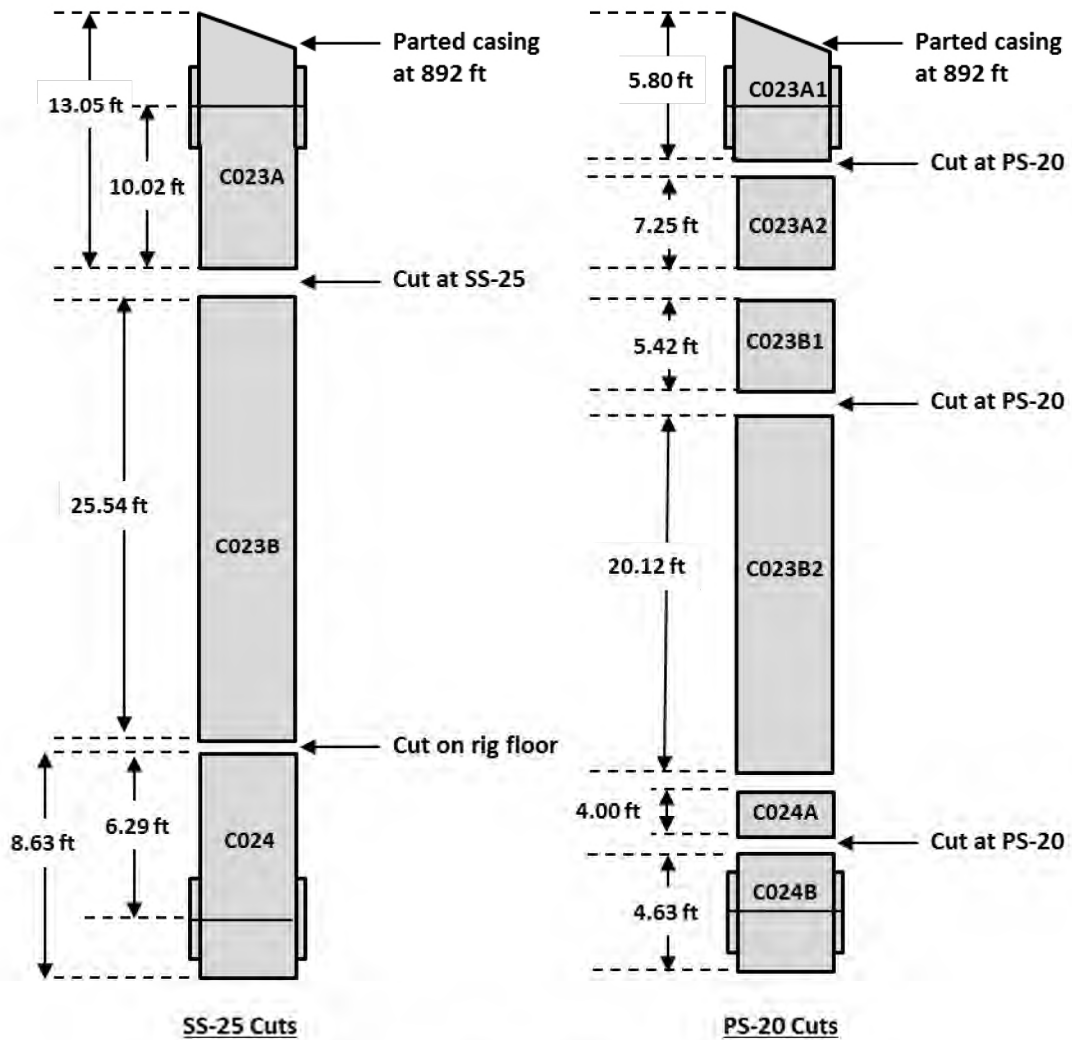


Figure 65: C023 and C024 Cut Diagrams

### 2.2.7 Logging of 11 3/4 in. Casing

The 11 3/4 in. casing logs were run during several different stages of Phase 3. Logging tools were specifically selected for each stage. Formation logging tools were also run through the surface casing. Results from the formation logging tools are not discussed in this report but were relevant to the RCA. Details for the 11 3/4 in. logging are discussed in the SS-25 logging analysis report [15]. The complete 11 3/4 in. casing logging program was as follows:

- Log run through 2 7/8 in. tubing: Versa-Line MID-3 Log (Tubbing Logging April 20, 2016)
- Logs run through 11 3/4 in. casing after 7 in. casing extraction C001–C022:
  - EV Camera and Baker Hughes 56-Arm Caliper (November 07, 2017)
  - EV Camera (November 08–09, 2017)
  - Baker Hughes 56-Arm Caliper (November 15, 2017)
  - Versa-Line MID-2 and Schlumberger Litho Scanner (November 16, 2017)
- Logs run through 7 in. tieback:
  - Versa-Line MID-2 (December 01, 2017)
  - Versa-Line MID-3 (December 02, 2017)
- Logs run through 11 3/4 in. casing after 7 in. casing extraction C023–C024:
  - Noise-Temperature and Gyro (May 20, 2018)
- Logs run through 11 3/4 in. casing after 7 in. casing extraction C025–C026:
  - Schlumberger 4-Arm Caliper and Formation Microimager (FMI) Tool (August 10, 2018)
  - Baker Hughes Noise and Temperature, GR-CCL-JB Logs, and 56-Arm Caliper (August 11, 2018)
  - Baker Hughes 56-Arm Caliper, HRVRT, and Integrity eXplorer Cement Evaluation (INTeX), and Gyro (August 12, 2018)
  - Scientific Drilling Directional Survey and Baker Hughes HRVRT (August 13, 2018)
  - Baker Hughes HRVRT and Schlumberger IBC (August 14, 2018)
  - Schlumberger UCI and SSCAN (August 15, 2018)
  - EV Camera (August 18–19, 2018)

The first 11 3/4 in. log was the Versa-Line MID-3 log that was run through the tubing in April 2016. The MID-3 tool is capable of inspecting up to three barriers, which allowed the tool to inspect the 11 3/4 in. casing through the tubing. The percent metal loss reported by the MID tools is volumetric and considers the entire pipe section when performing the metal loss calculations. The first feature was 34% at a depth of 150.9–152.5 ft, and the second feature was 36% at a depth of 191.4–193.8 ft. No other metal loss was recorded for the surface casing. This first look at the 11 3/4 in. casing was a high-level examination based on the fact that the tool was inspecting three barriers at once. The sizing from the tool on the third barrier was a rough estimate that could have been influenced by many factors, including the presence of the first two barriers. The objective of this first step was to gather data for the 11 3/4 in. casing in the event additional data could not be gathered.

Logging continued after extraction of the upper 7 in. casing fish in November 2017. The 11 3/4 in. casing was exposed from the lower 7 in. circumferential parting (approximately 892 ft) to surface. This portion of the 11 3/4 in. casing was logged with the EV camera, Baker Hughes 56-Arm Caliper, and Versa-Line MID-2. Section 2.2.2 discusses the caliper and MID-2 functionality. The Schlumberger Litho Scanner was also run to evaluate the surrounding formation. The Litho Scanner is a formation log designed to determine the concentration of elements in the formation surrounding the borehole. The Litho Scanner emits neutrons that induce GR emission from the formation. Spectra are acquired during each neutron burst. These spectra are decomposed into a linear combination of standard spectra from individual elements. Data acquired from this tool were not utilized during the metallurgical investigation but provided information for the overall RCA.

The EV camera was the first tool run in the surface casing after extraction of the upper 7 in. casing fish. Section 2.2.5 discusses the EV camera tool. Holes were identified during the camera inspection. Figure 66 shows snapshots of the holes recorded by the camera. The size of the holes was estimated by a software that used images from the camera and the camera parameters to scale the corrosion holes. Several holes were selected for sizing. The minimum and maximum areas measured with the software were 0.15 in<sup>2</sup> and 3.62 in<sup>2</sup>, respectively. The shape of the holes and the surrounding ID suggested that corrosion occurred from the OD to the ID. General corrosion and pitting were not observed on the surrounding ID surface.

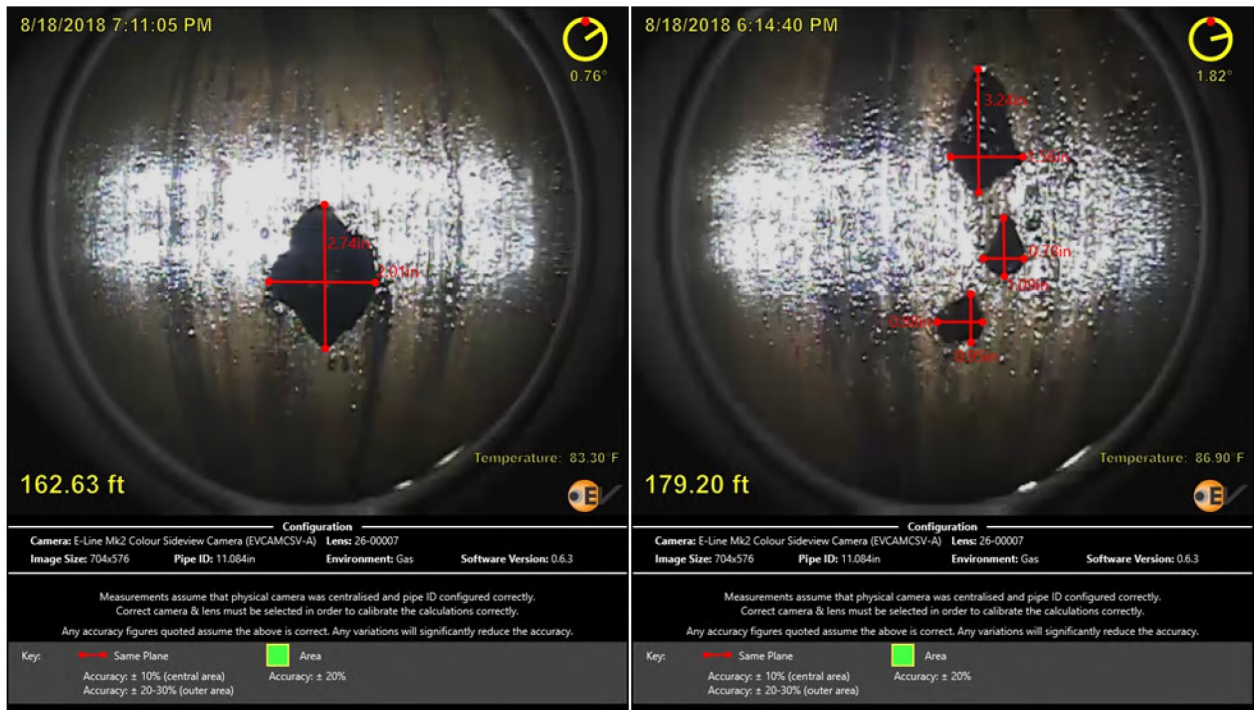


Figure 66: Holes in 11 3/4 in. Surface Casing

The Baker Hughes 56-Arm Caliper tool was run on the same day from 8.8–870.2 ft. The caliper identified several anomalies, including deformation—ovality, holes, and pitting. Holes were identified between 134 and 300 ft. These findings were consistent with the observations made with the EV camera. Figure 67 shows the caliper log and 3D view for joints 4–8. The dark red peaks in the log and 3D view indicate possible holes in the 11 3/4 in. casing. These were locations where the caliper arm penetrated completely through the casing wall.

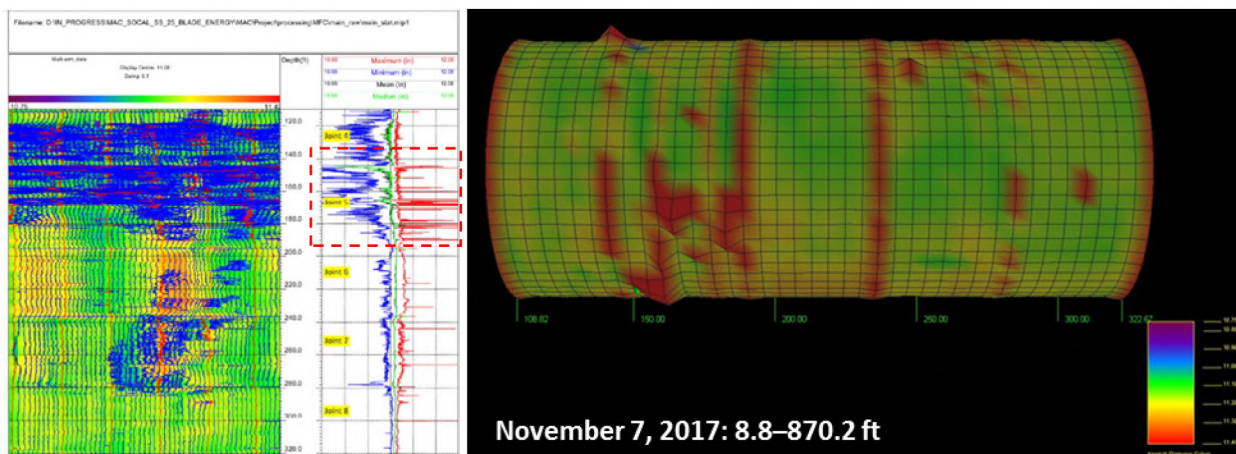


Figure 67: Baker Hughes Caliper Results for 11 3/4 in. Casing Joints 4–8 November 07, 2017

The EV camera was run on the following two days to assist with fishing operations and was used to observe the lower 7 in. casing fish entering the National Oilwell Varco (NOV) extraction tool. The data from this camera run were not used during the metallurgical investigation. The Baker 56-Arm Caliper was run a second time in the 11 3/4 in. casing. The tool was run deeper than the previous run because additional joints (C023 and C024) had been removed during the previous days. The results were the same as the November 07, 2017, caliper run. Holes were observed in several locations, with a majority of the holes located on joint 5.

The Versa-line MID-2 tool was run the following day on November 16, 2017. The MID-2 was used rather than the MID-3 because the first barrier (7 in. casing) was not present. The MID-2 and MID-3 were also run on December 01–02, 2017, after the 7 in. tieback was installed. The MID-3 was used to inspect the surface casing on the second run because the first barrier (7 in. tieback) was present. Both runs identified metal loss on joints 5–9. The most significant metal loss was 33% on joint 5. These findings correspond well with the previous logs that identified holes at these depths. Figure 68 shows the MID-2 and MID-3 results for the surface casing; the table in the figure shows the maximum metal loss detected by the MID-3 for each joint.

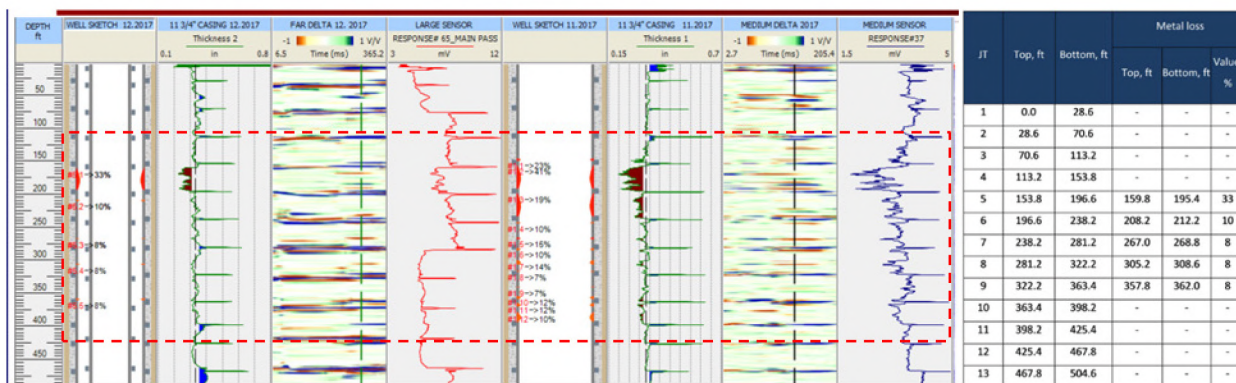


Figure 68: Versa-Line (a) MID-2 and (b) MID-3 Logs for 11 3/4 in. Casing

The caliper and HRVRT log runs in the 11 3/4 in. casing identified internal metal loss beginning at approximately 700 ft and extending to the shoe (joints 18–25). The corrosion had a scattered distribution and non-uniform depths. Figure 69 shows results from the caliper and HRVRT logs. The corrosion identified by these logs was correlated to the corrosion features identified on the OD of the 7 in. casing

pipe body (Section 5.1) and connections (Section 6.1.2). The camera run on August 18–19, 2018, visually confirmed corrosion on the ID surface of the 11 3/4 in. casing. Figure 70 shows an example of the ID corrosion observed on the 11 3/4 in. casing. The corrosion appeared to be similar to the corrosion associated with the axial rupture of the 7 in. casing.

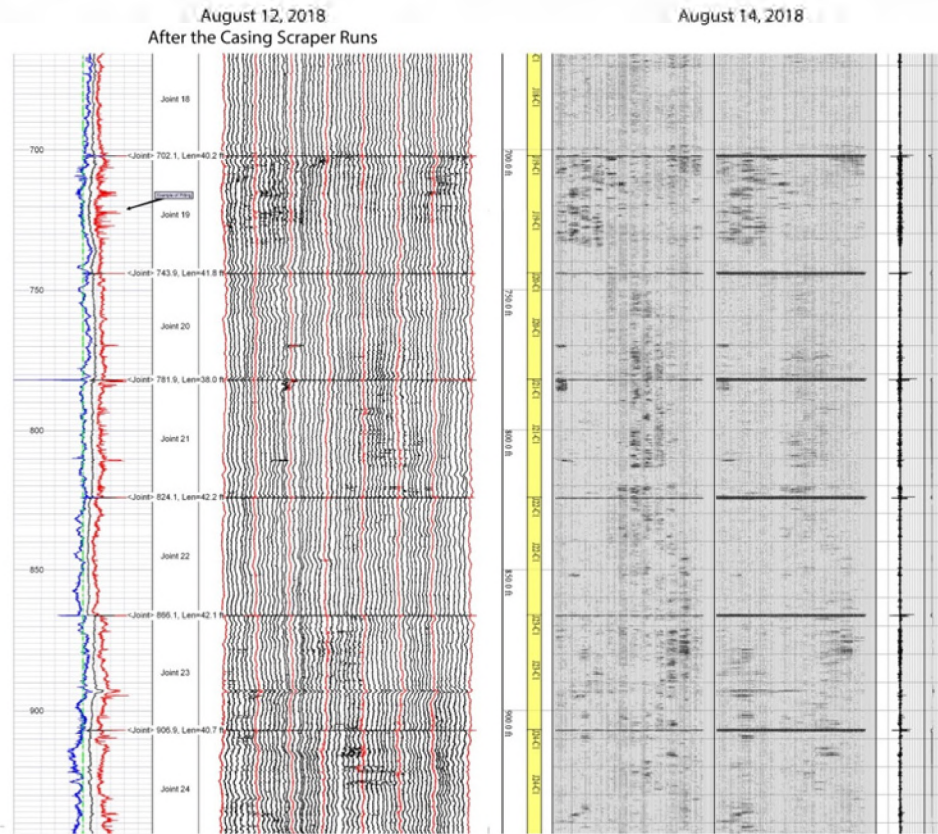


Figure 69: Caliper and HRVRT Logs for 700–990 ft



Figure 70: EV Camera Snapshot of ID Corrosion on 11 3/4 in. Casing

The caliper and UCI logs identified two features that appeared to be associated with the axial rupture and the circumferential parting. The UCI log identified a 21 in. long feature with an average width of 1.8 in. and a maximum penetration of 48% (Figure 71). The axial feature appeared at a similar depth as the axial rupture. Interpretations of the log suggest the feature was related to erosion during the blowout. The caliper log (Figure 72) identified a circumferential feature at a similar depth to the circumferential parting. This feature was also interpreted as erosion during the blowout. The erosion associated with these features is consistent with the erosion identified on the axial and circumferential fracture surfaces during the metallurgical investigation. Section 3.2.5 describes the observation and analysis associated with the axial rupture fracture surface erosion.

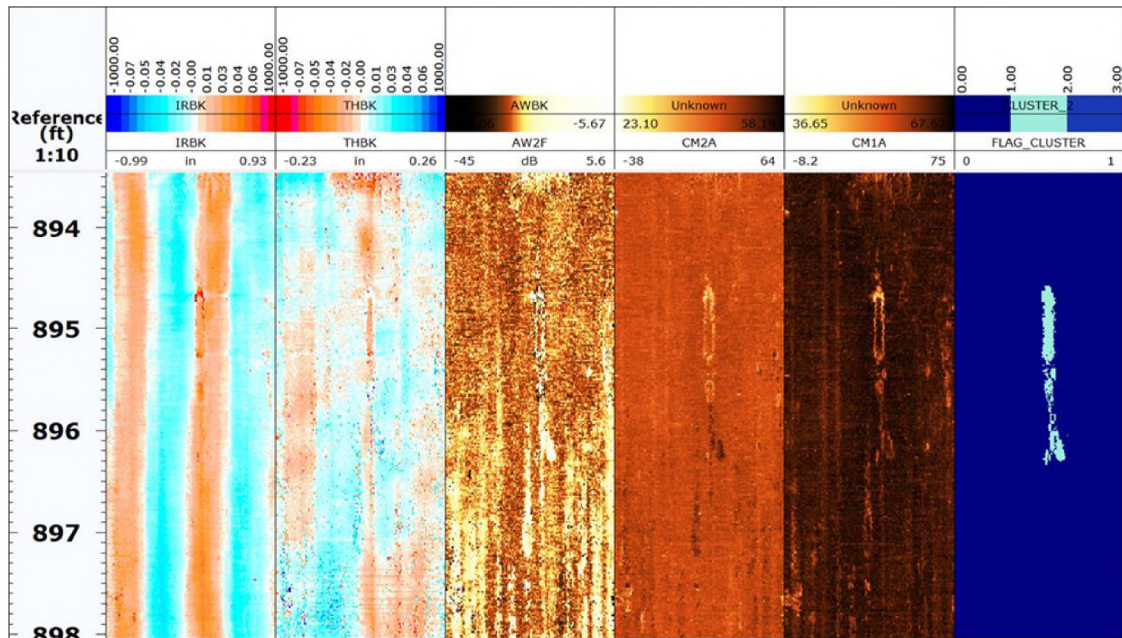


Figure 71: UCI Log of 11 3/4 in. Longitudinal Feature in 11 3/4 in. Casing Resembling 7 in. Rupture

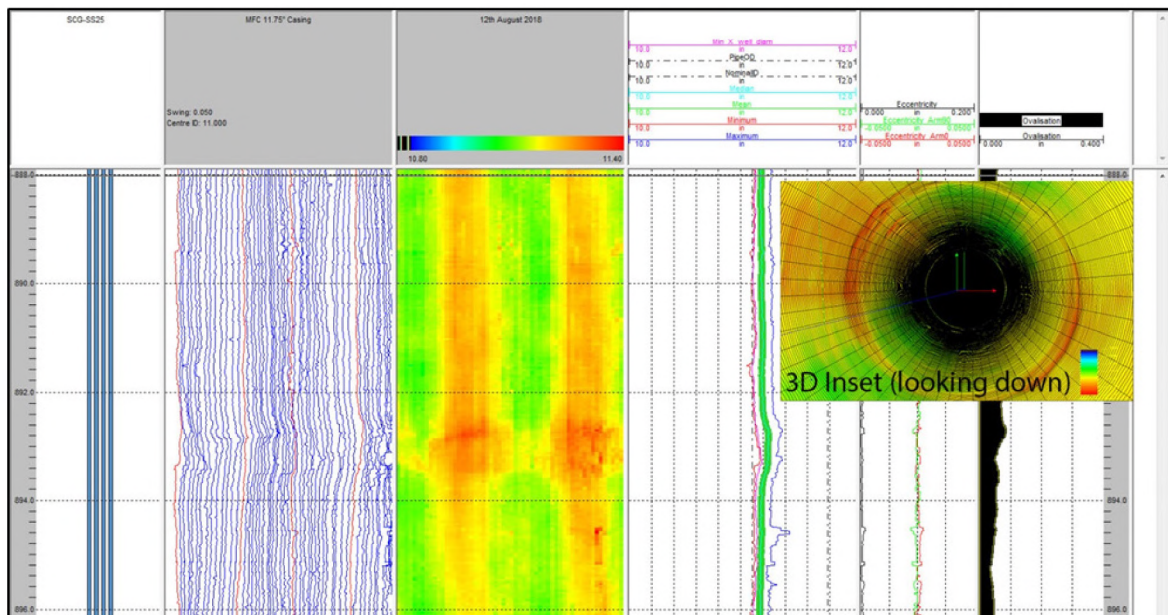


Figure 72: Caliper Log of 11 3/4 in. Casing Joint 23 (888-898 ft)



## 2.2.8 11 3/4 in. Casing Extraction

The 11 3/4 in. casing was not extracted due to operational challenges, which posed a risk to damaging the evidence. The 11 3/4 in. casing was partially cemented at the top and bottom of the string, and this would make extraction challenging. Extracting the 11 3/4 in. casing string would most likely damage most of the evidence during the extraction process. Blade determined that the evidence collected during the 11 3/4 in. logging was sufficient, given that the string did not directly contribute to the 7 in. casing failure. The casing head and approximately 3 ft of the 11 3/4 in. casing were removed from the well on September 10, 2018, and released to Blade as part of the RCA. Figure 73 shows images of the removal of the casing head and 11 3/4 in. casing material. The following steps were used to extract the casing head and 11 3/4 in. casing material:

1. The 20 in. conductor casing was circumferentially torch cut at approximately 10 ft below ground level.
2. The conductor was vertically torch cut and removed.
3. The cement around the 11 3/4 in. casing was removed.
4. The 11 3/4 in. casing was circumferentially torch cut above the conductor cut location.
5. The 11 3/4 in. casing was circumferentially torch cut above the weld that joined the casing head and the 11 3/4 in. casing.

The 11 3/4 in. casing material was identified as W006B and was shipped to Houston, TX, for the metallurgical investigation. The material was used for mechanical testing, which is discussed in Section 7.2.

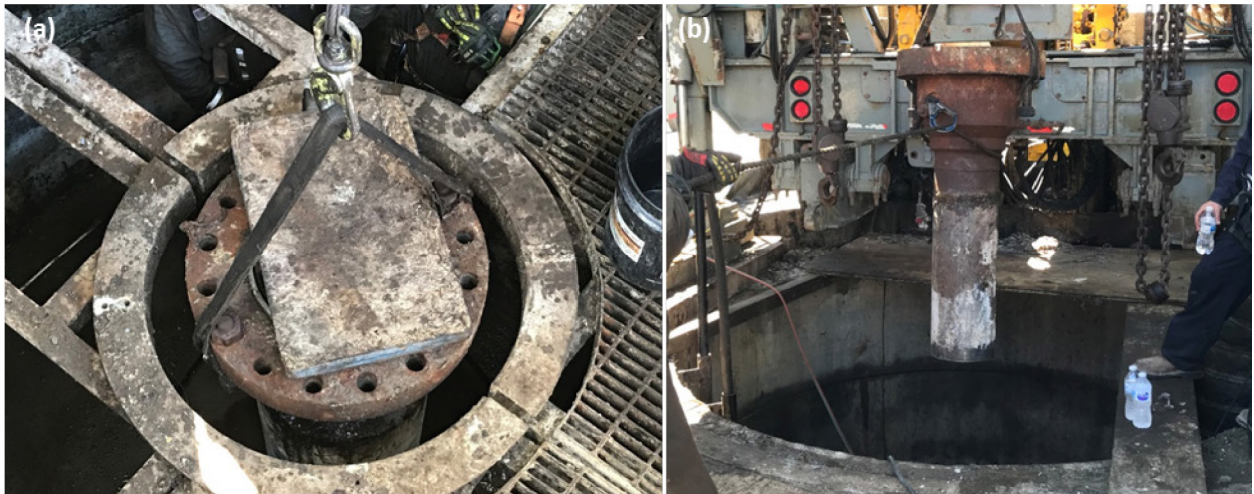


Figure 73: 11 3/4 in. Casing Extraction

## 3 7 in. Casing Failure Events and Sequence

---

### 3.1 Overview

The 7 in. casing extraction confirmed the findings of the EV downhole camera, which identified a fully parted casing at an approximate depth of 887 ft WLM. The top and bottom fracture surfaces of the parted casing (joint 22) were recovered. The lower parted casing (upward-facing fracture surface) was 2.80 ft away from connection 22. Visual examination of the lower parted casing showed a 2 ft long axial rupture that had merged with the circumferential fracture. Section 2.2.5 discusses the EV downhole camera findings. Section 2.2.6 describes the extraction and field examination of the fracture surfaces.

Figure 74 shows the 25 joints recovered from the well and indicates the location of the parted casing. It also shows the official depths used by Blade. These depths are based on consolidation and verification from downhole tools and physical measurements. The official depth for the parted casing is 892 ft as shown in the schematic. Figure 75 shows the field photographs taken during extraction with a diagram of the parted casing and axial rupture. The image shows the failed casing oriented as it was in the well, with the axial rupture below the circumferential parting.

The fracture surfaces were initially examined in the field followed by a detailed examination at the Blade warehouse. Reconstruction of the failure found that all fracture pieces were recovered from the well. Details of the reconstruction process are discussed in the Phase 4 summary [7].

SS-25 Casing Failure Analysis

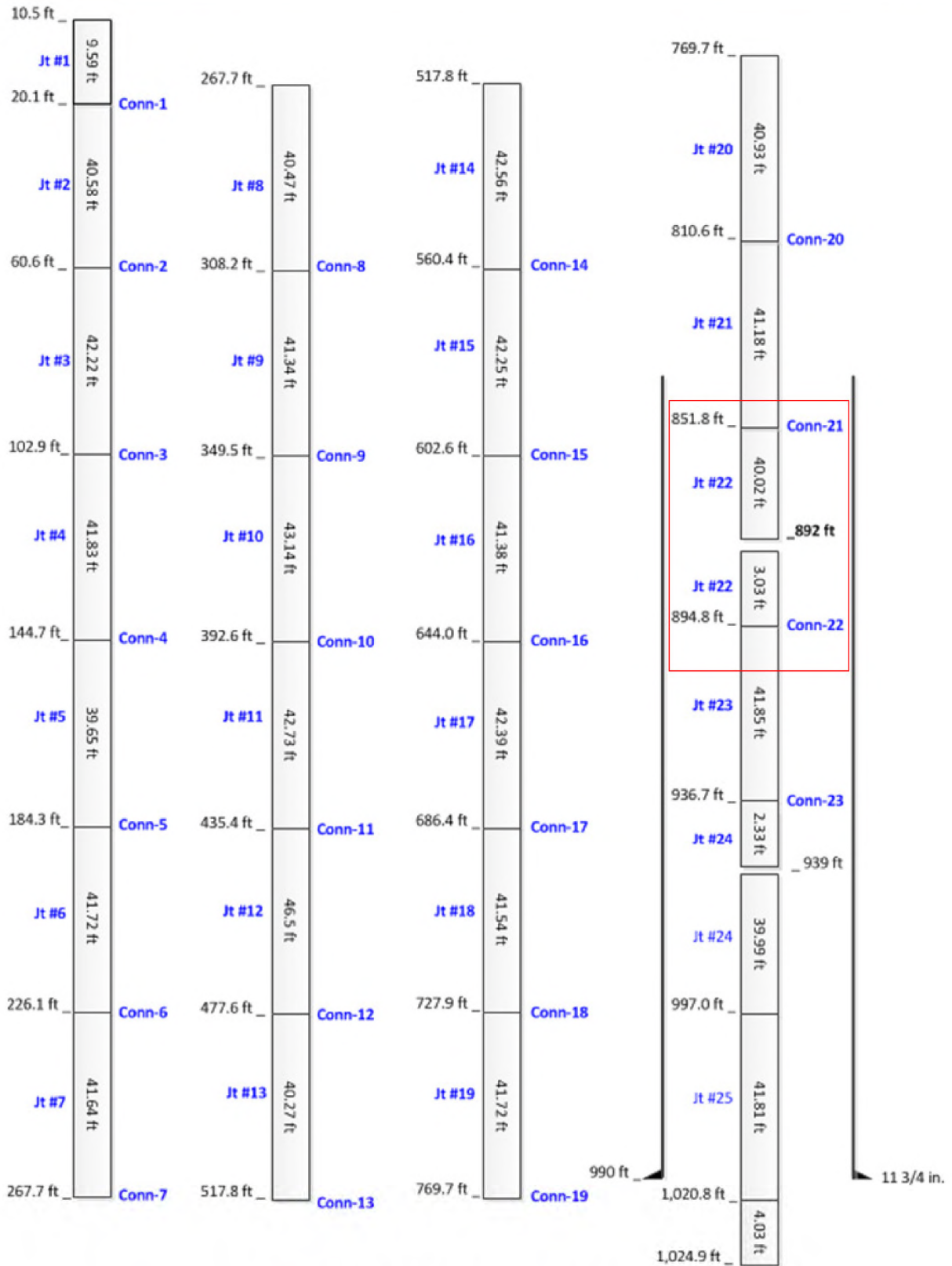
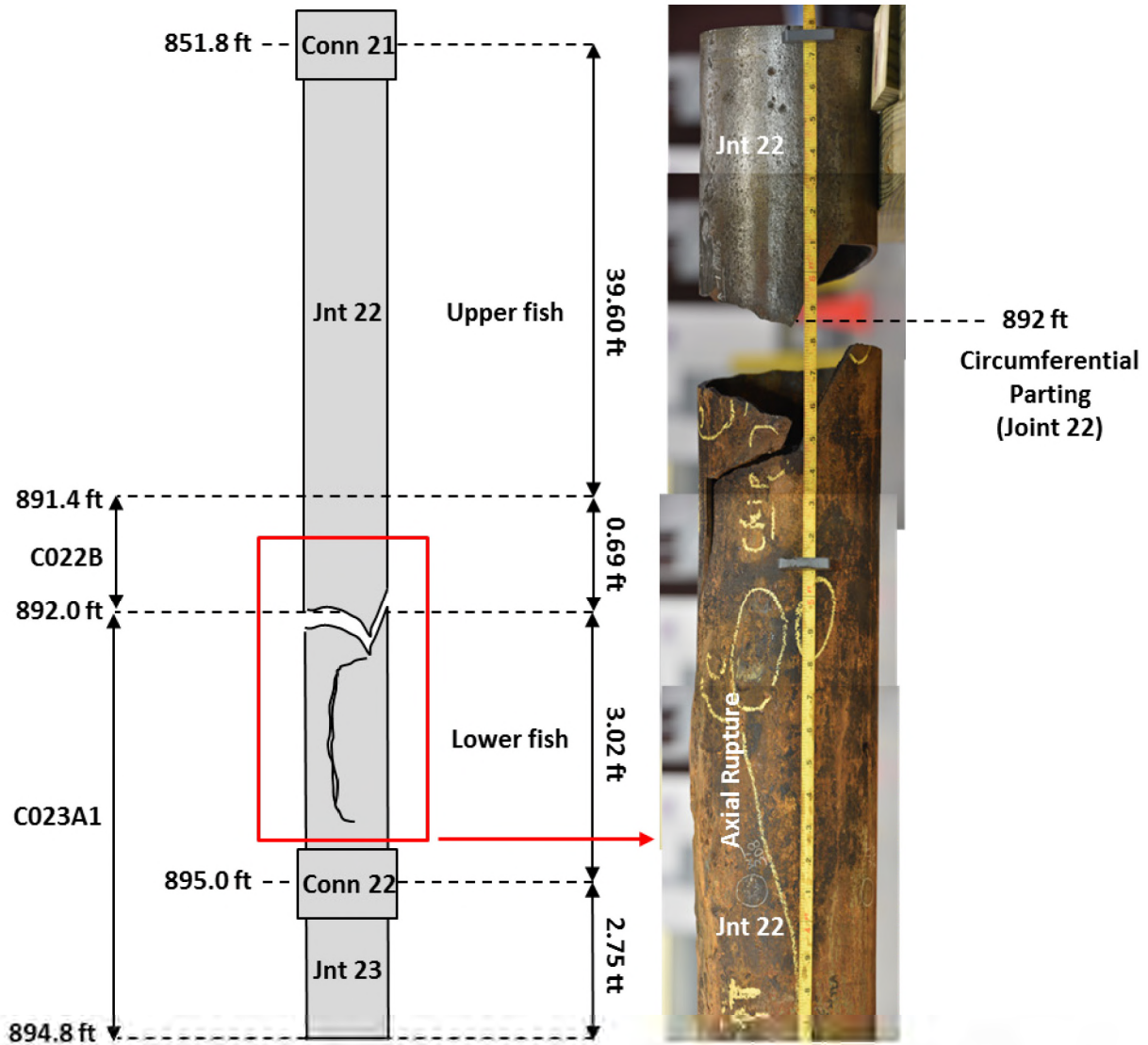


Figure 74: SS-25 7 in. Casing String Schematic



**Figure 75: Schematic and Photo of the Axial Rupture and Circumferential Parting**

The laboratory examination showed that the 7 in. casing failure originated from an 85% metal loss due to corrosion. The casing was under an internal pressure of approximately 2,700 psi. The 85% deep corrosion failed, resulting in a 2 ft long axial rupture (fracture). Figure 76 (a) and (b) show the bulging and corrosion associated with the axial rupture. Figure 76 (c) is a top view of the fracture surface showing the 85% metal loss that initiated the failure.

The visual examination showed that during the axial rupture, plastic bulging occurred first with slow ductile tearing due to the internal pressure. Tearing instability occurred once the axial flaw reached the critical size and was followed by a rapid crack propagation in the axial direction that left behind chevron marks (Figure 76 [c]). The crack changed direction (upper and lower turning points) and finally arrested due to dynamic energy consumption [17] [18] [19]. There were two turning points on the upper and lower side of the rupture. This phenomenon is not uncommon for an axial rupture.

Figure 77 (a) and (b) show a close-up and laser scan image of the axial rupture. The failure origin is indicated by the white box. The direction of the crack propagation is indicated on both sides of the origin

by white arrows. The upper and lower crack arrest points are indicated by the green circles. Figure 77 (c) through (f) show close-up images of the lower and upper arrest and turning points. Figure 77 (d) and (e) show the change in the direction of the crack propagation at the turning points caused by a dynamic change in the local maximum stress at the crack tip.

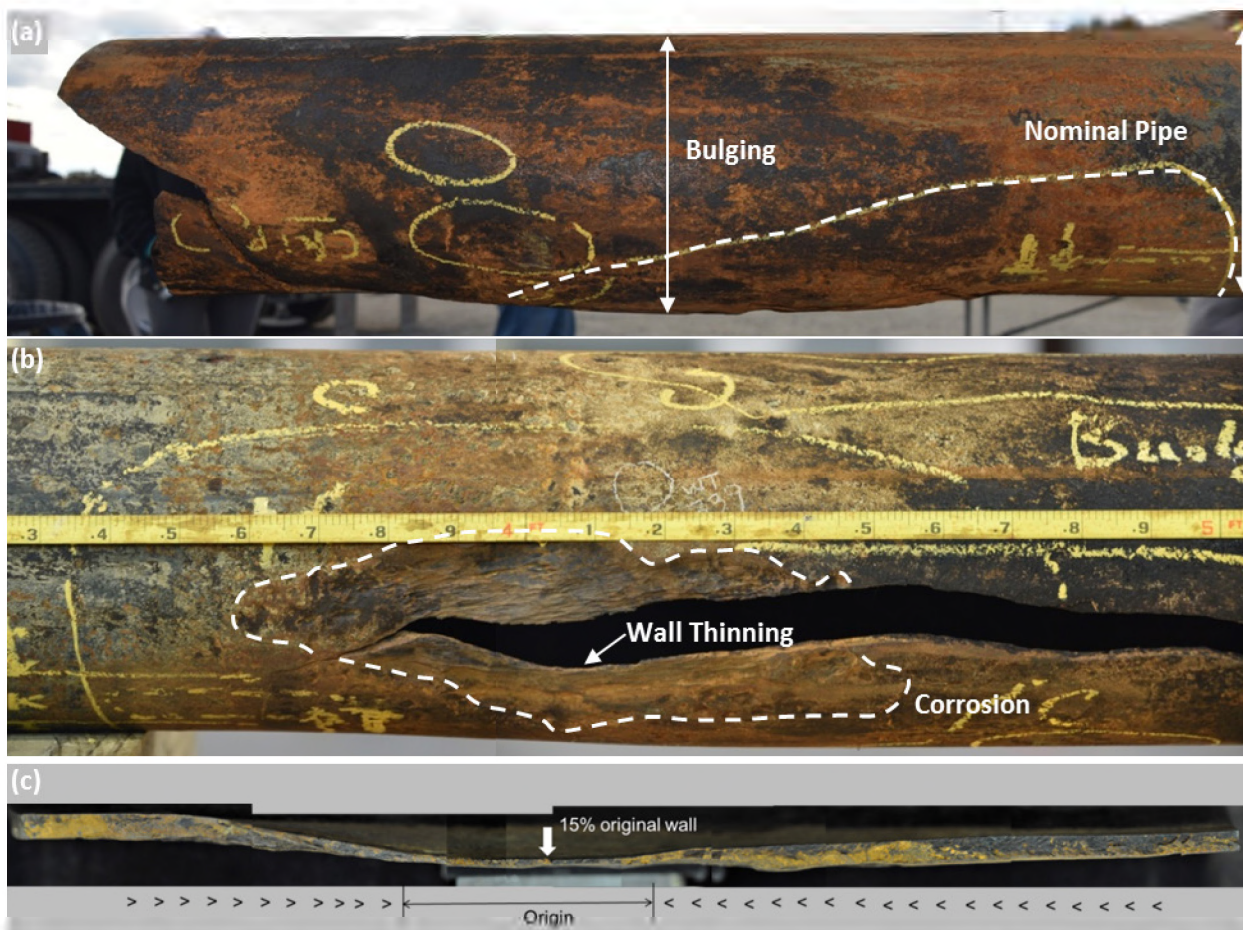
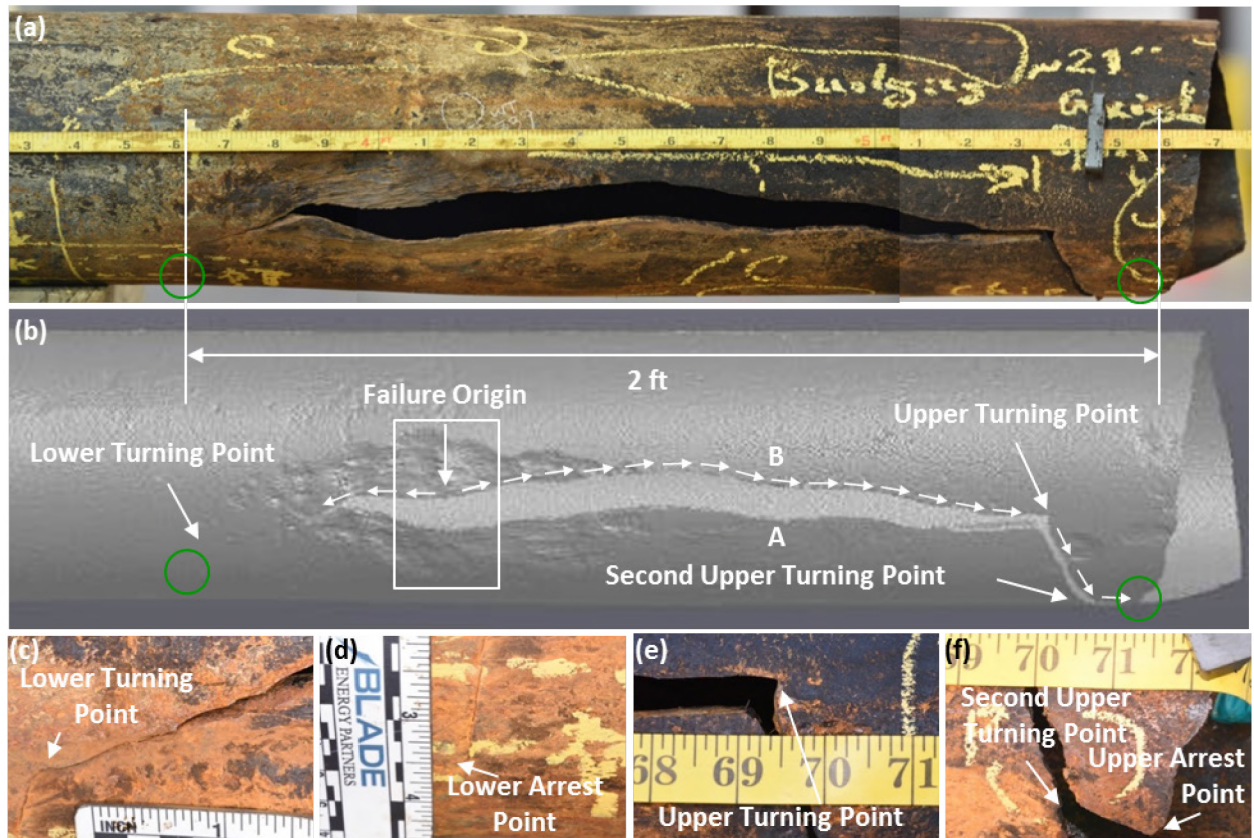


Figure 76: Images of Axial Rupture Showing (a) Bulging, (b) Corrosion, and (c) Chevron Marks



**Figure 77: (a) Field Photo and (b) Laser Scan Indicating the (c) Lower Turning Point and (d) Lower Arrest Point; and (e) Upper Turning Point and (f) Upper Arrest Point**

The axial rupture occurred at an estimated temperature of approximately 80°F. This estimate was based on the historical temperature profile data at the failure depth [10] and is consistent with the observed bulging and ductile tearing associated with the axial rupture.

Visual and stereoscopic examination of the circumferential parting showed that the failure was not a continuation of the axial rupture, but it had rather re-initiated near the corner on one side of the parted casing. The origin site was determined from the chevron marks identified on the fracture surface. Figure 78 shows a (a) laser scan and an (b) image that identify the upper arrest point, origin of the circumferential parting, and final overload failure. The stitched stereo images in Figure 79 show the chevron marks and propagation direction of the circumferential parting. These observations indicate that the axial rupture and the circumferential parting were two separate events despite their close proximity, and that they were most likely related to each other.

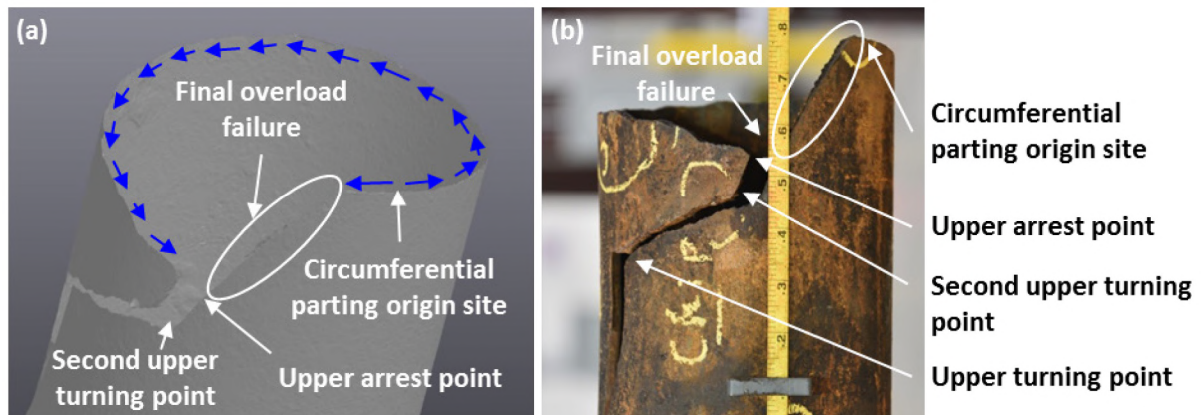


Figure 78: (a) Laser Scan and (b) Circumferential Parting

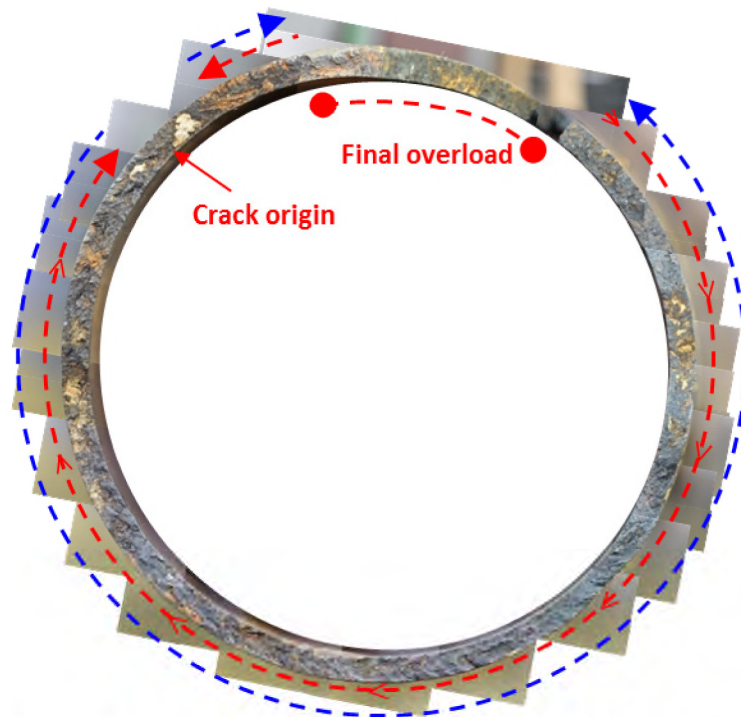


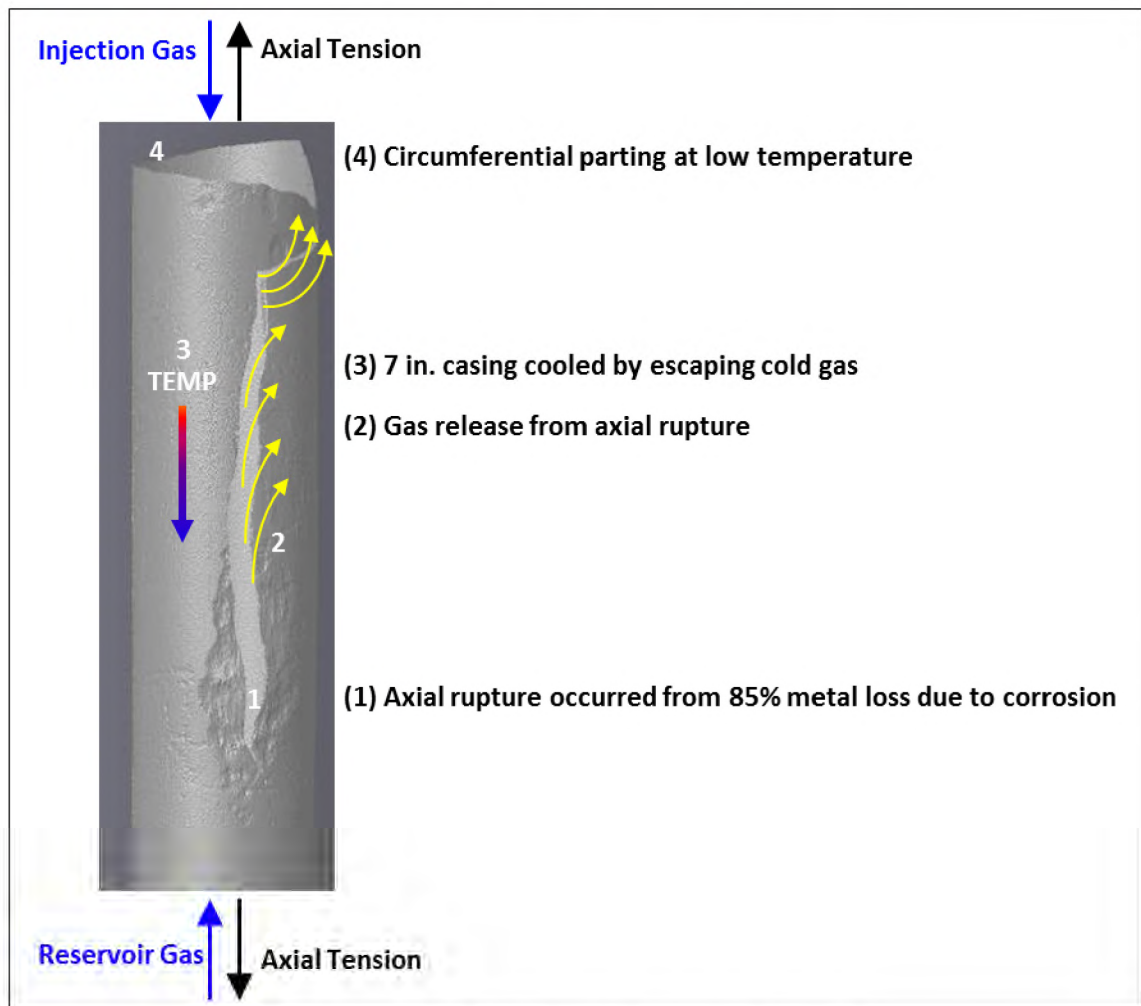
Figure 79: Stitched Images of the Lower Circumferential Parting Fracture Surface

The circumferential parting was brittle, which was different from what had been observed with the axial rupture. There was no evidence of local plastic deformation or overload necking for both of the circumferential fracture surfaces. The previously discussed evidence and the detailed metallurgical investigation presented later in this section suggest that the circumferential parting of the 7 in. casing was a consequence of the axial rupture. The suggested failure sequence for the axial rupture and circumferential parting is as follows:

1. An axial rupture occurred from an 85% metal loss due to corrosion.
2. Highly compressed natural gas was released from the opening of the newly formed axial rupture.
3. Rapid cooling occurred due to the escaping cold gas [11].

4. The steel became brittle due to the super cooling, and a crack initiated from a small flaw under the axial tensile loading, resulting in the circumferential parting.

Figure 80 shows a schematic based on the laser scan data of C023A1 and illustrates the suggested failure sequence for the axial rupture and circumferential parting. The full cleavage fracture mode was examined, and the temperature for the circumferential parting was estimated to range between  $-76^{\circ}\text{F}$  ( $-60^{\circ}\text{C}$ ) and  $-38^{\circ}\text{F}$  ( $-39^{\circ}\text{C}$ ). Section 3.3.1 discusses the details of the temperature estimation.



**Figure 80: 7 in. Casing Failure Sequence Schematic**

On October 23, 2015, the SS-25 leak was first detected by the smell of gas, which may have represented the first indication of the casing failure caused by the axial rupture and circumferential parting. A vent opened up at the surface during Kill Attempt #2 on November 13, 2015. Debris was ejected approximately 75 ft into the air when the vent was opened. Gas collecting around the well may have built up pressure, which led to the ejection of the debris. The SS-25 7 in. casing failure occurred in the following two separate but interlinked events:

1. Axial rupture
2. Circumferential parting



The axial rupture was caused by an 85% metal loss due to corrosion, while the circumferential parting occurred at a lower temperature as a consequence of the escaping cold gas [11]. The circumferential parting occurred after the axial rupture in a matter of hours rather than days. Sections 3.2 and 3.3 contain the detailed metallurgical investigations for the axial rupture and circumferential parting, respectively.

## 3.2 Axial Rupture Analysis

This sub-section presents the investigation details for the axial rupture that caused the 7 in. casing failure. Visual (macro), microscopic, and scanning electron microscope (SEM) examinations were conducted to determine the fracture surface characterization and micro mechanism for cracking.

### 3.2.1 Visual and Stereoscopic Examination

Figure 77 (b) shows a schematic based on laser scan data, and it identifies key features of the axial rupture. The axial rupture produced two mating fracture surfaces denoted as A and B. Fracture surface B appeared to have experienced more plastic deformation (bulging) than fracture surface A. The following three fracture zones were identified based on the visual and stereoscopic examinations:

- Zone 1: Axial rupture origin
- Zone 2: Crack propagation
- Zone 3: Crack arrest

Figure 81 illustrates the three zones of the axial rupture. Zone 1 is a short section of the axial rupture that was identified by severe wall thinning due to corrosion. Zone 2 extends from the lower and upper boundaries of Zone 1 to the boundary of the lower and upper arrest region. Lower and Upper Zone 2 contained chevron marks. However, Upper Zone 2 also contained a featureless segment created by erosion. Zone 3 is the lower and upper arrest regions. The arrest points in Zone 3 cannot be seen in Figure 81 (a) or (b).

Zone 1 was initially determined based on the chevron marks in Zone 2. The apexes of the chevron marks generally point towards the origin of a failure [20] [21]. The chevron marks in Zone 2 pointed towards the area with the maximum metal loss. Both observations suggested that this area was the origin of the axial rupture and was denoted as Zone 1. Figure 82 is a close-up image of fracture surface B and shows the apex of the chevron marks in Zone 2 pointing towards the origin of the axial rupture.

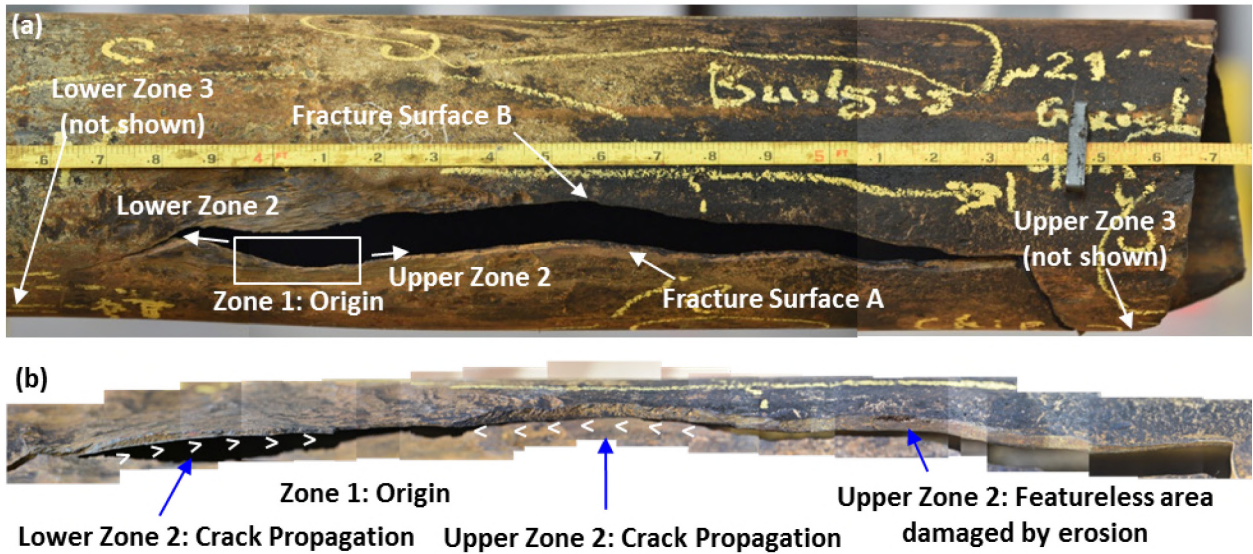


Figure 81: (a) Front and (b) Top Views of Fracture Surface B Identifying Zones 1 and 2



Figure 82: Close-up of Zone 1 and Zone 2 of the Axial Rupture

The size of the origin was originally measured with a tape measure for length and an ultrasonic thickness probe for depth. The measured length of the axial rupture origin was 4.8 in. (123 mm), based on chevron marks. The minimum remaining wall thickness measured with the thickness probe was 0.126 in. This was a rough approximation due to the limitations of the ultrasonic thickness probe. The size of the probe prevented taking measurements that were directly adjacent to the fracture surface. The probe also averaged the measurement over the probe area.

Figure 83 shows a plot of the remaining wall thickness as a function of axial position along the fracture surface. The origin for the axial position was taken as the downhole cut below connection 22. The cut face was flat, which allowed for consistent axial measurements regardless of circumferential orientation. The average wall thickness of the pipe was 0.303 in. The measured minimum remaining wall thickness was 0.126 in. The estimated maximum metal loss based on the measured remaining wall thickness and AWT was 0.177 in. (58.4% AWT).



Figure 83: Remaining Wall Thickness Measurements of Axial Rupture

Figure 81 shows that the origin was not symmetrically located at the center of the rupture. The non-symmetric location of the origin can be explained by the proximity of the origin to connection 22. The axial crack initiated in Zone 1 and propagated in opposite directions. The lower crack front propagated towards connection 22, which provided additional constraint as opposed to the pipe body. The additional constraint assisted with arresting the crack at approximately 1 ft from the connection. The upper crack was not influenced by any additional constraint allowing the crack to propagate further before arresting.

Zone 2 is characterized by chevron marks located on each side of the origin. The upper side of the origin only partially contained chevron marks. A 9 in. length of Zone 2 on the upper side of the origin had been eroded by the gas release that occurred after the axial rupture. Figure 84 shows the featureless area where the chevron marks appeared to be eroded away.

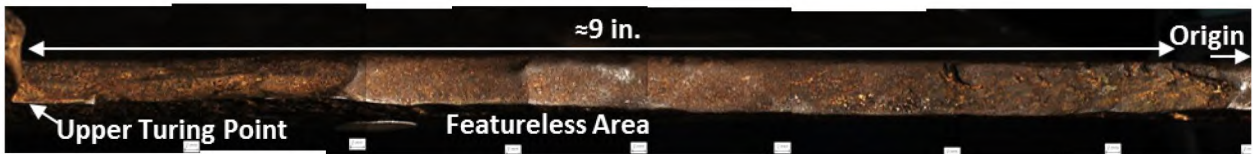


Figure 84: Zone 2 Featureless Area on Upper Side of the Origin

The lengths of fracture surfaces A and B were measured using a tape measure. The fracture surface lengths were based on the distance from the lower turning point to the upper turning point. Table 3 shows the measured fracture surface length values for A and B. The profile lengths refer to the measured distance between the turning points along the fracture surface. The axial lengths refer to the measured distance between the turning points along the longitudinal axis of the pipe. The profile lengths needed not be the same because they were influenced by deformation. The axial lengths should be approximately the same because axial length generally does not change with deformation.

The axial lengths measurements for fracture surfaces A and B were 20.7 in. and 20.58 in., respectively. The profile lengths measurements for A and B were 28.12 in. and 31.50 in. The differences in length between the profile and axial lengths for fracture surfaces A and B were 7.42 in. and 10.92 in., respectively. The length values suggest that bulging (plastic deformation) occurred during the axial rupture.

Figure 85 shows measurements of the fish mouth opening plotted versus axial position. The opening measurements were converted into an estimated opening area that is equivalent to a 4.5 in. x 4.5 in. square or a 5.1 in. diameter hole. The significant plastic deformation of the 7 in. casing material is consistent with the estimated casing temperature of 80°F.



Figure 85: Plot of Fracture Surface Mouth Opening Versus Axial Position

Table 3: Fracture Surface A and B Length Measurements

Fracture Surface A Crack Profile Length	28.12 in.
Fracture Surface B Crack Profile Length	31.50 in.
Fracture Surface A Axial Length	20.70 in.
Fracture Surface B Axial Length	20.58 in.

Zone 3 was taken as the fracture surfaces in the arrest point regions. The lower portion of the crack had a well-defined turning and arrest point. The crack terminated after changing directions twice and arrested just beyond the second lower turning point. The lower arrest point was contained within a tight crack tip. The upper portion of the crack also changed directions twice, with the second change occurring 50° from the longitudinal pipe axis. The circumferential parting connected to the upper arrest point, and the final overload failure completely parted the casing. The upper arrest point was not contained within a tight crack tip at the time of recovery. Figure 86 shows the upper turning point, second upper turning point, and arrest point. The image clearly shows Zone 3 for the upper section of the axial rupture. Figure 87 shows the lower turning and arrest points.



Figure 86: Macro Image of the Two Upper Turning Points and Single Arrest Point

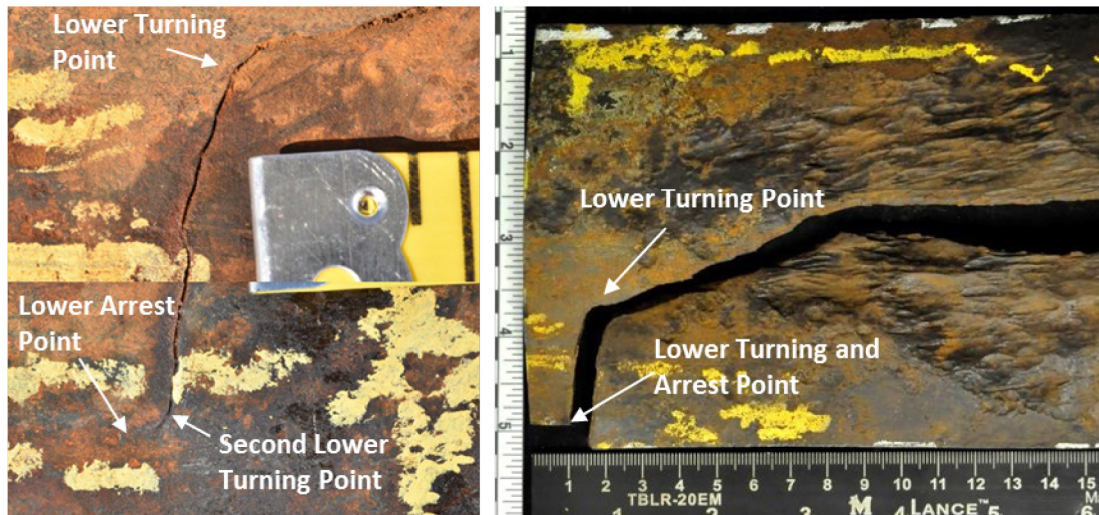


Figure 87: Macro Images of the Lower Turning and Arrest Points

### 3.2.2 Micro-Fractographic Characterization of Zone 1 (Origin)

The micro-fractographic characterization had the following objectives:

- Characterize the fracture mode for Zone 1.
- Verify visual measurements for Zone 1.
- Characterize the fracture mode for Zone 2.
- Characterize the featureless segment of Zone 2.
- Characterize the fracture mode for Zone 3.

Zone 1 was the primary focus for the micro-fractographic characterization. The fracture surfaces were originally received as part of C023A1, which was a 5.5 ft section of the 7 in. casing that contained the axial rupture, lower circumferential parting, connection 22, and part of joint 23. The fracture surfaces were extracted from C023A1 using dry saw cuts. The fracture surfaces were protected with foam padding, and the saw clamps were lined with wood to prevent metal-to-metal contact during cutting. The fracture surfaces were supported with small wood blocks to prevent them from falling when the cut was completed (Figure 88).

The length of the fracture surfaces had to be reduced for cutting and handling purposes. A 14 in. long section of the fracture surface was chosen for extraction and detailed examination. Four cuts were made to extract the 14 in. section of the fracture surfaces. Figure 88 (a) shows a schematic of C023A1 with the four cut locations identified. Figure 88 (b) shows C023A1 after the fracture surface extraction. Cut 1 was located through the featureless area in the upper portion of Zone 2 (above Zone 1). This location was chosen to minimize the amount of information lost by the cut. The area was damaged due to erosion, which means that the relevant information had already been compromised. The cut was designed to reduce the length of the axial rupture and remove the circumferential parting from the rest of C023A1.

Cut 2 was a circumferential cut designed to remove the lower part of C023A1 from the pipe section that contained the target fracture surfaces. A 14 in. long pipe section remained after completion of cuts 1 and 2. Cut 3 was longitudinal and extended from cut 1 to cut 2. Cut 3 was designed to go through the lower arrest point to separate the two fracture surfaces and release the remaining residual stress.

Cut 3 extracted fracture surface A. Cut 4 was longitudinal and extended from cut 1 to cut 2. Cut 4 extracted fracture surface B. Figure 89 (a) shows an example of the dry saw cuts with protective padding around the critical areas of C023A1 and the wooden blocks used to protect C023A1 from metal-to-metal contact.

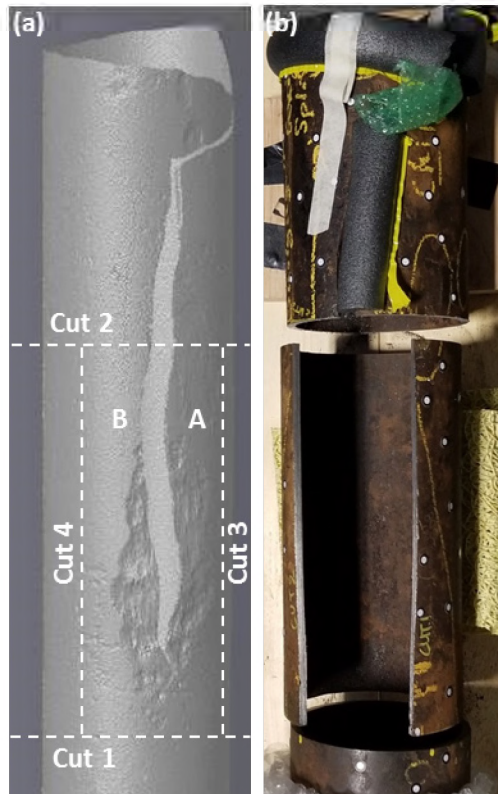


Figure 88: (a) Schematic and (b) Image of the Cut Locations for the Axial Fracture Surfaces

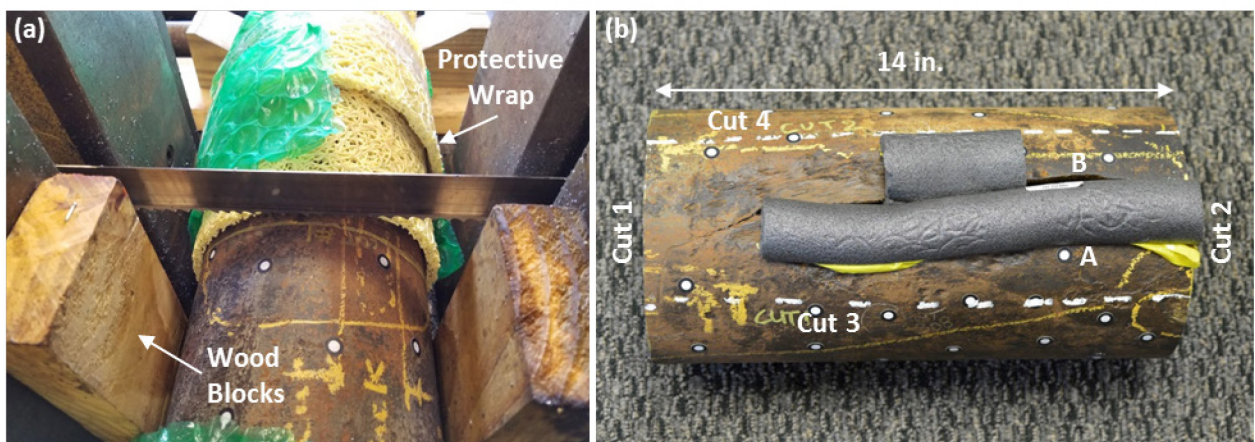
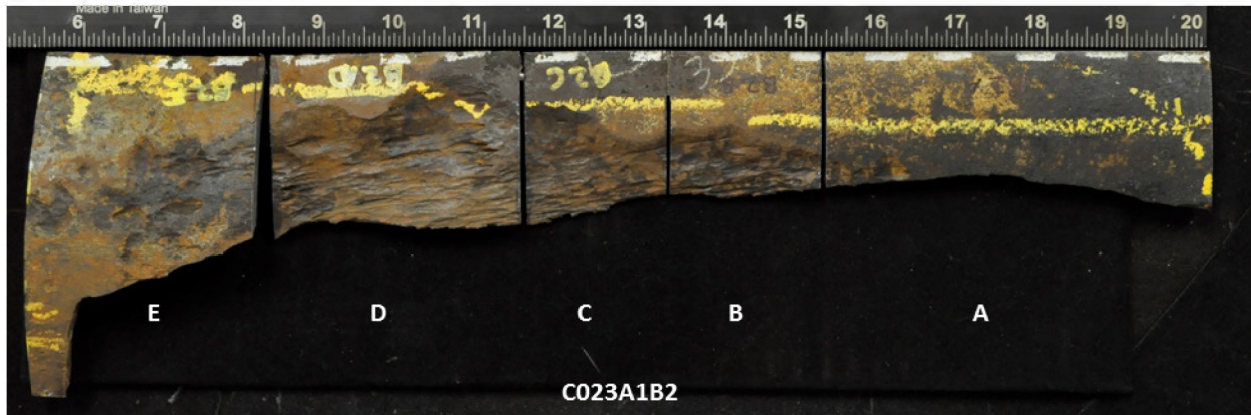


Figure 89: (a) Dry Saw Cut Example and (b) Fracture Surfaces After Cuts 1 and 2

Fracture surface B was chosen for a detailed examination and analysis. It was cut into five smaller specimens (Figure 90). The cut locations were determined based on the fracture surface features and size limitations imposed by the SEM. Specimen identification was based on JSNs as outlined in the

metallurgical protocol [1] and described in the Phase 4 summary report [7]. Fracture surface B was denoted as C023A1B2. Two specimens (C023A1B2B and C023A1B2D) were chosen for detailed examination to determine the fracture mode for Zone 1 (origin). These samples were chosen because they contained the entire origin and a small portion of Zone 2 (crack propagation). Fracture surface A was preserved.



**Figure 90: Five Specimens Cut from C023A1B2 for Fractographic Study**

The axial rupture had been exposed to fluids in the 11 3/4 in. × 7 in. annulus for more than two years prior to its extraction from the SS-25 well. The fracture surfaces were contaminated and corroded by the annulus fluids and required cleaning for the fractographic examination. Cleaning requires the removal of contaminants and corrosion deposits while preventing attack (damage) to the fracture surfaces. A cleaning procedure was developed and tested to ensure both effectiveness and safety.

The specimens were initially cleaned in an ultrasonic acetone bath for 3 to 5 minutes for degreasing and removing loose contaminants. The specimens were then ultrasonically cleaned in a 1% Citranox bath for 3 to 9 minutes. Citranox was chosen based on Blade's experience and industry common practice because it is effective at removing metal oxides, corrosion deposits, and contaminants with minimum attack to the fracture surface [19] [22] [23].

Freshly produced fractures surfaces from Charpy V-notched (CVN) specimens were used to verify the cleaning procedure. These specimens were grade J55 steel from casing material extracted from the SS-25 well. The SEM examination of the fracture surface after cleaning found no resolvable attack at magnifications up to 1,000×. Figure 91 is a comparison of the fracture surface before and after cleaning and clearly demonstrates no attack from up to 9 minutes of ultrasonic cleaning in 1% Citranox solution. The results showed that the cleaning procedure was safe to use on the fracture surface specimens.

The effectiveness of the cleaning procedure was also tested on a specimen from the origin of the axial rupture (C023A1B2C). The specimen was examined before cleaning and after 3 minutes of ultrasonic cleaning in a 1% Citranox solution. Figure 92 shows the fracture surface (a) before and (b) after cleaning at a magnification of 30×. Most of the corrosion scales, deposits, and contaminants were effectively removed from the fracture surface. The woody-type morphology was clearly seen on the cleaned surface, confirming the effectiveness of the cleaning procedure. The Charpy and fracture surface tests showed that cleaning times up to 9 minutes could be used, if required, with minimal damage to the fracture surface.

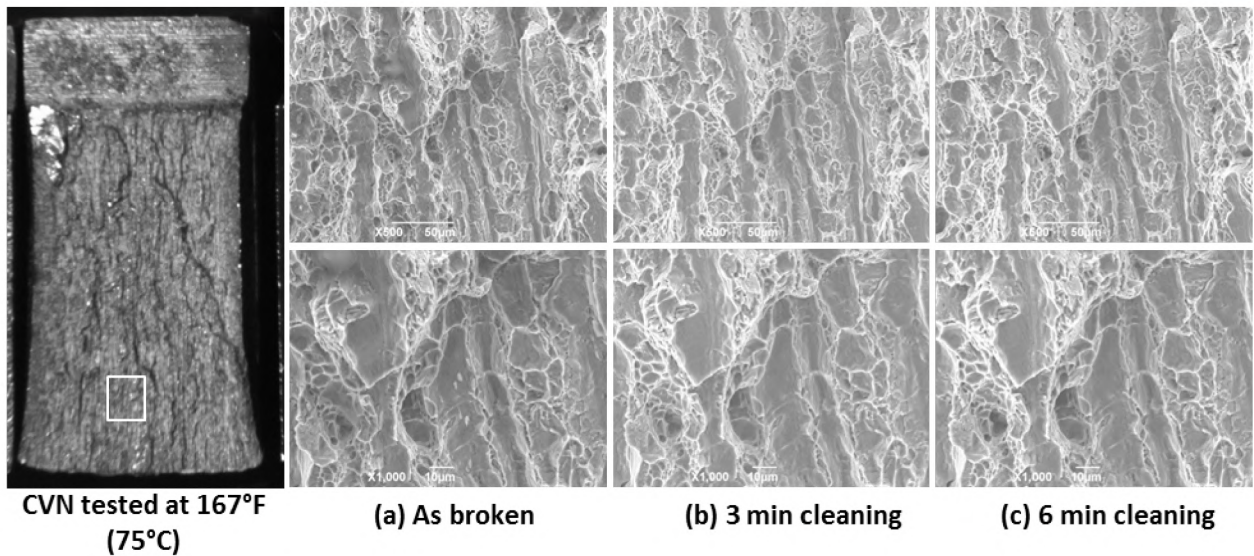


Figure 91: Cleaning Procedure Tests on Charpy V-Notch Specimen

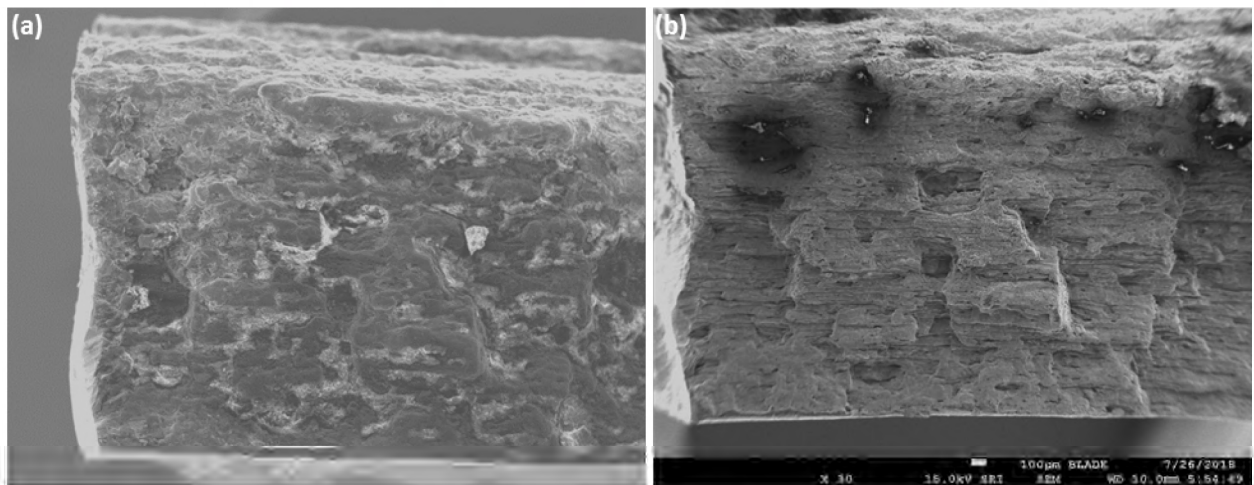
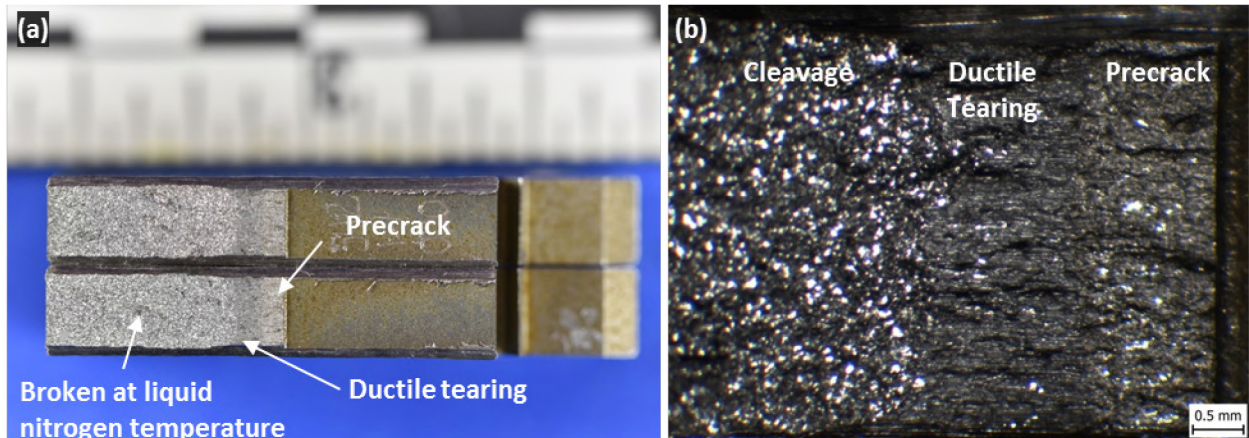


Figure 92: SEM Images of Specimen C023A1B2C (a) Before and (b) After Cleaning

The initial examination of the axial rupture suggested that its origin experienced ductile tearing based on the bulging and lack of chevron marks. A complete fractographic characterization of known ductile tearing specimens was conducted for comparison with the origin fracture surfaces. Anderson and Associates and Metcut conducted J-R fracture toughness testing as part of the material testing program for the 7 in. casing. The tests produced a ductile tearing zone. Section 7.1.9 discusses the fracture toughness testing conducted at the third-party laboratories.

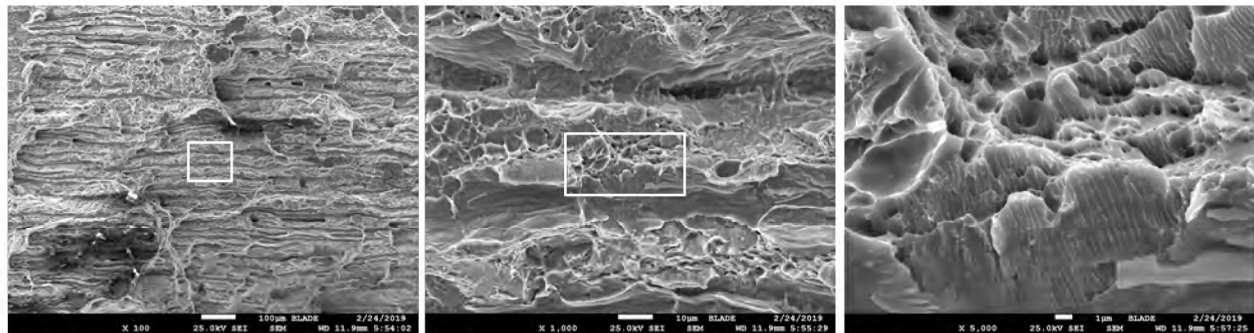
One specimen (L4-000) was selected for fractographic examination to determine ductile tearing characteristics for the grade J55 7 in. casing material. Specimen L4-000 was tested at room temperature, which was comparable to the estimated downhole temperature at the time of the axial rupture. Figure 93 shows a (a) macro image of the J-R specimen and a (b) stereo image taken at 25× showing the pre-crack, ductile tearing, and cleavage zones. The pre-crack was created prior to testing to initiate a crack in the notch. Ductile tearing occurs during the J-R testing, and cleavage occurs when the specimen is broken at liquid nitrogen temperature. The ductile tearing zone shows the same woody-type morphology shown in Figure 92. The ductile tearing zone was examined with the SEM to identify relevant characteristics.





**Figure 93: (a) Macro and (b) 25× Stereo Image of J-R Specimen L4-000**

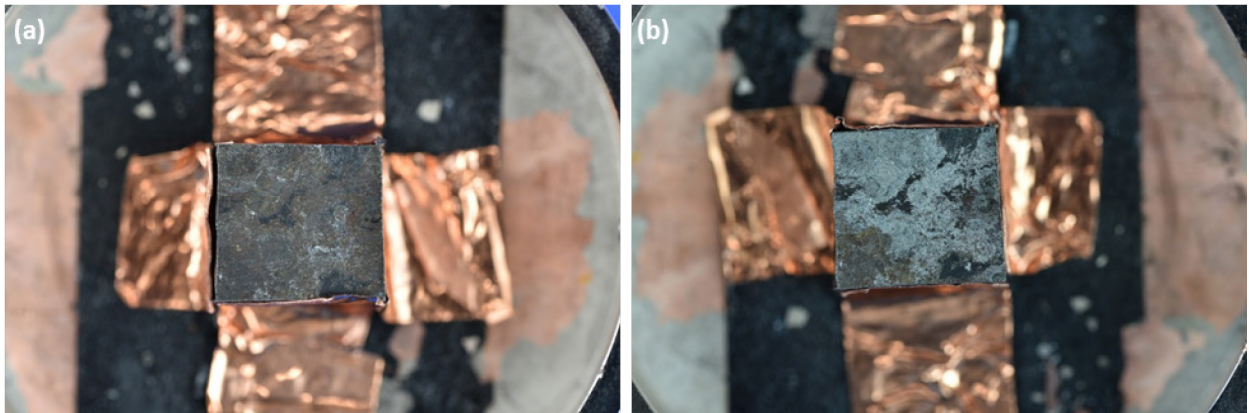
Figure 94 shows the SEM images taken at (a) 100×, (b) 1,000×, and (c) 5,000×. Figure 94 (a) shows the same woody morphology observed in the stereo image and in the SEM images of C023A1B2C. Figure 94 (b) shows dimples, deformation markings, and pearlite, which are confirmed at 5,000× in Figure 94 (c). Pearlite is a two-phased lamellar (layered) structure composed of alternating layers of ferrite (87.5 wt%) and cementite (12.5 wt%). Results from the examination show that ductile tearing can reveal pearlite. This finding is important for understanding the micro mechanism for the initiation of the axial rupture. It is apparent that the presence of pearlite on the fracture surface is one of the fractographic components of ductile tearing. The appearance of pearlite is often associated with corrosion because the ferrite is attacked, exposing the layered structure.



**(a) Woody type morphology at 100× (b) Dimples, deformation markings, and pearlite at 1,000× (c) Pearlites and dimples at 5,000×**

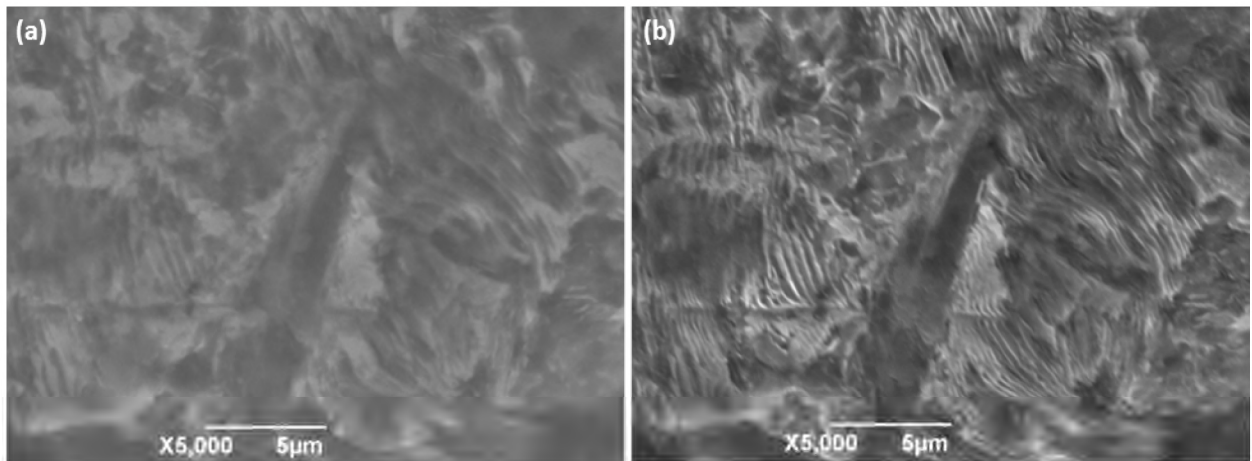
**Figure 94: SEM Images of J-R Specimen L4-000 Taken at (a) 100×, (b) 1,000×, and (c) 5,000×**

The axial rupture had been exposed to fluids in the 11 3/4 in. × 7 in. annulus for over two years before extraction. Corrosion could have played a role in exposing pearlite on the fracture surface. A corroded specimen from the OD surface of joint 22 was examined to determine the effects of the 11 3/4 in. × 7 in. annulus environment to the grade J55 material. Specimen C022A1A1C3D was examined before and after ultrasonic cleaning for 3 minutes in a 1% Citranox solution. Figure 95 shows the specimen (a) before and (b) after cleaning. The images show that the cleaning effectively removed most of the OD corrosion product.



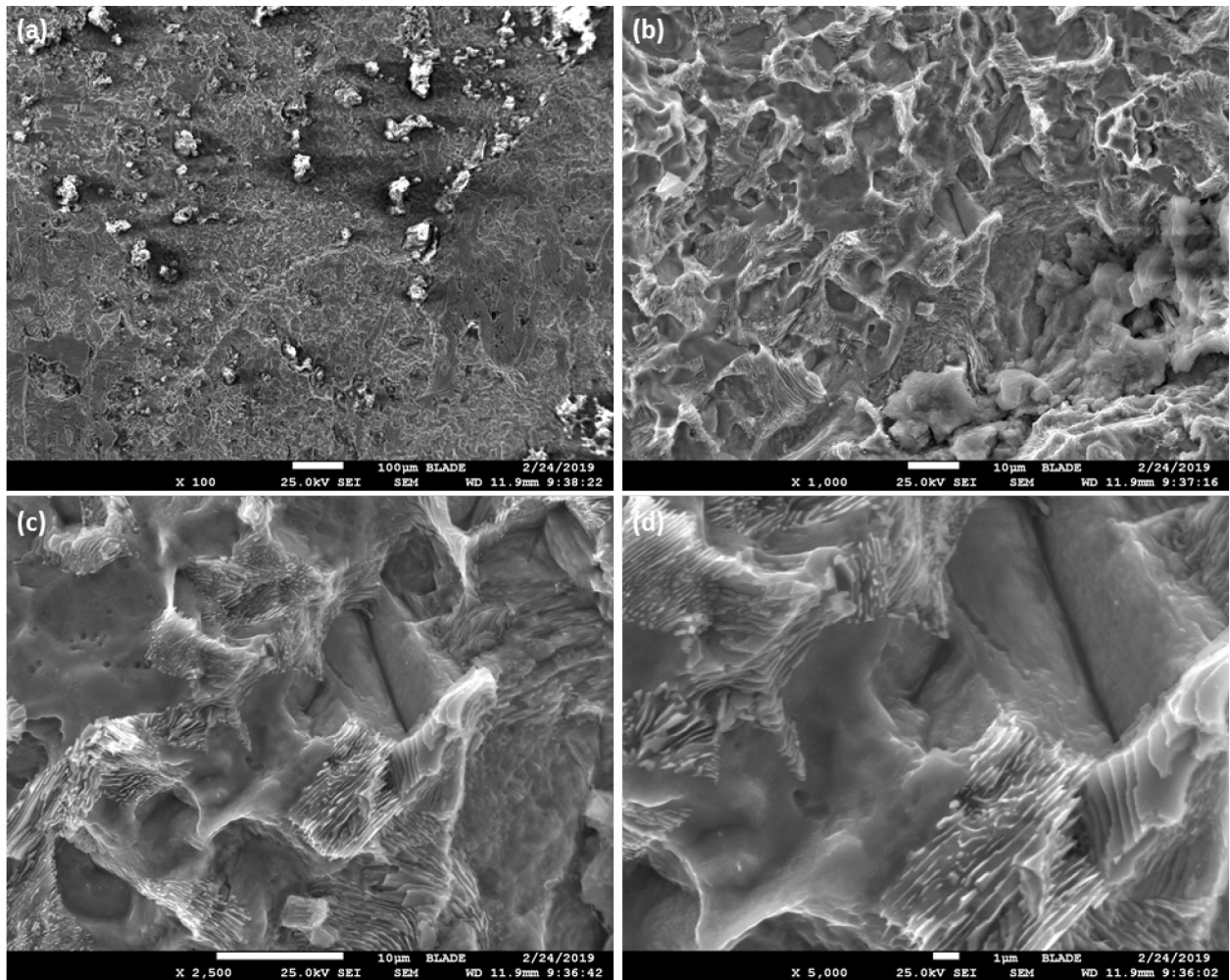
**Figure 95: Joint 22 Corroded OD Specimen C022A1A1C3D (a) Before and (a) After Cleaning**

Figure 96 shows the SEM images at 5,000 $\times$  (a) before and (b) after cleaning. The results show that the pearlite features are present before and after cleaning but appear to be more pronounced after cleaning. The results from the J-R ductile tearing examination and the OD surface corrosion testing show that the pearlite features can be revealed by ductile tearing but may have been enhanced by corrosion from exposure to fluids in the 11 3/4 in.  $\times$  7 in. annulus for over 2 years.



**Figure 96: C022A1A1C3D SEM Images Showing Pearlite Features (a) Before and (b) After Cleaning**

Pearlite can be revealed by corrosion alone because corrosion attacks ferrite; however, the detailed morphology in this scenario would have been different. Corrosion always attacks the ferrite in the pearlite structure and forms pits in the surrounding ferrite—Figure 97 shows an example of pearlite with corrosion pits in the surrounding ferrite. Care must therefore be taken when examining fracture surfaces so that it is distinguishable whether pearlite was revealed by ductile tearing or corrosion.



**Figure 97: Pearlite and Ferrite (Pitting) Corrosion at (a) 100 $\times$ , (b) 1,000 $\times$ , (c) 2,500 $\times$ , and (d) 5,000 $\times$**

Results from the initial examination, cleaning testing, and fracture surface comparison between the CVN and J-R specimens were considered during the examination of the origin specimens C023A1B2C and C023A1B2D. Both specimens were examined with the SEM at several locations and with different magnifications to identify the fracture mode of the origin (Zone 1). Figure 98 shows the areas of investigation (AOIs) that were chosen for the SEM examination. Cleavage and grain boundary facets were not observed in any of the AOIs. The woody morphology (low magnification) and deformation markings (high magnification) described in the previous discussion were typically observed.

Figure 99 shows a comparison of the woody-type morphology produced by the J-R testing at room temperature, the CVN testing at the upper shelf temperature (167°F [75°C]), and the origin of the axial rupture. J-R and CVN specimens were selected from the same orientation as the axial rupture. The woody-type morphology was the characteristic feature of ductile tearing along the longitudinal direction of the grade J55 7 in. casing steel. A woody-type morphology is caused by the presence of coarse and elongated MnS inclusions [24]. Section 7.1.5 discusses the microstructure of the 7 in. casing steel and shows the presence of the MnS inclusions.

C023A1B2C contained most of the origin and was selected for detailed examination. Twenty-seven AOIs were examined with the SEM. Figure 100 to Figure 104 shows the SEM images of five AOIs (A3, A4, A8, A10, and A17) selected to represent the typical features identified in the origin during the examination.

The images show the woody-type morphology, deformation markings, possible dimples, and pearlite-like features due to corrosion.

A transition from ductile to a ductile-brittle mix was observed beginning at C023A1B2C A19 (Figure 98). The transition showed a shift from woody-type morphology to a mix of woody-type morphology and cleavage. The number of cleavage facets appeared to have increased from location A19 to A27. The observations implied that the speed of the axial rupture was increasing through the transition zone until the crack became fully unstable. Figure 105 and Figure 106 show SEM images from A19 and A20 with the ductile-brittle mixed fracture mode. The images show areas of cleavage facets and deformation markings.

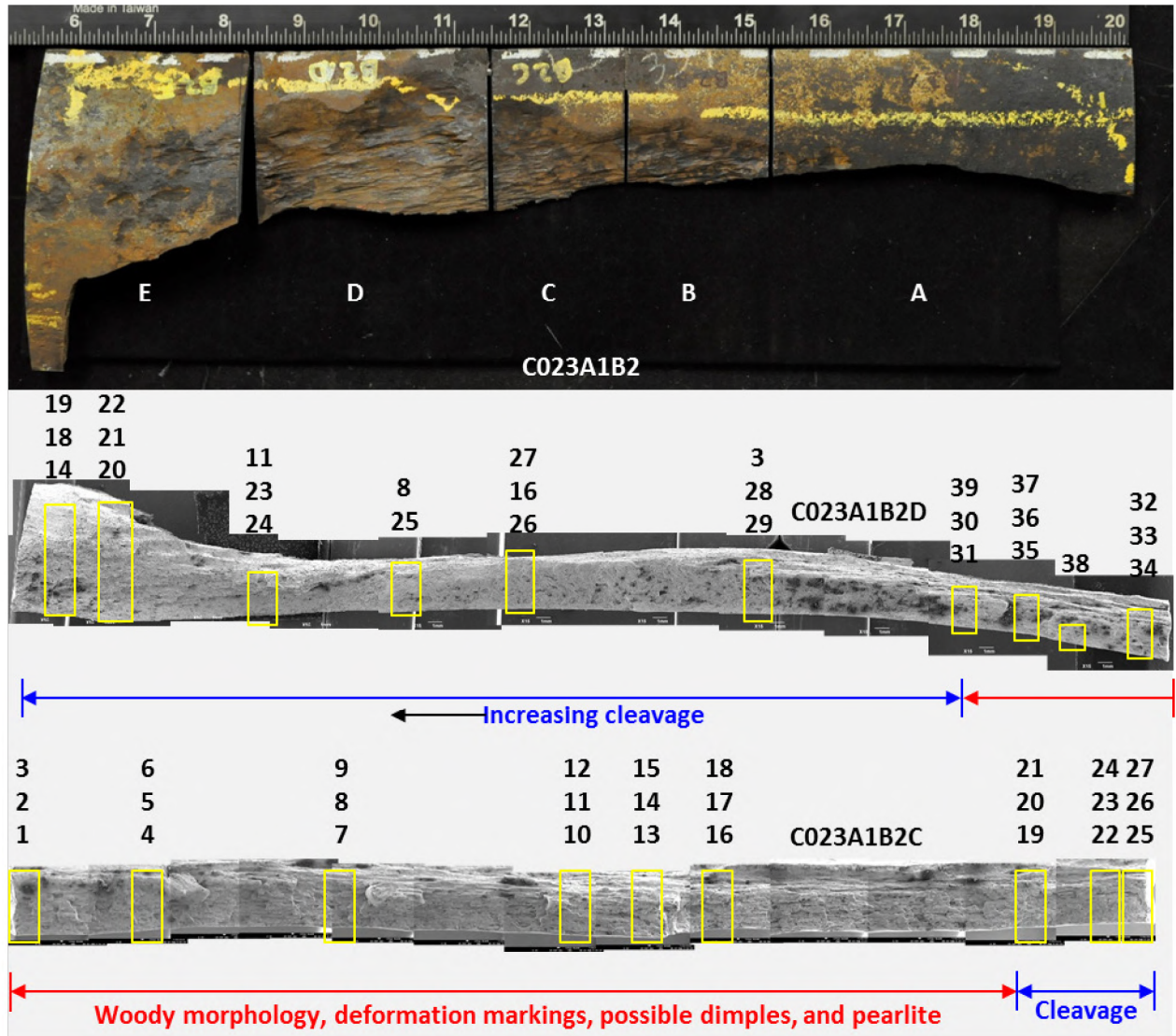


Figure 98: SEM Examination of Cleaned Fracture Surfaces of C023A1B2C and C023A1B2D

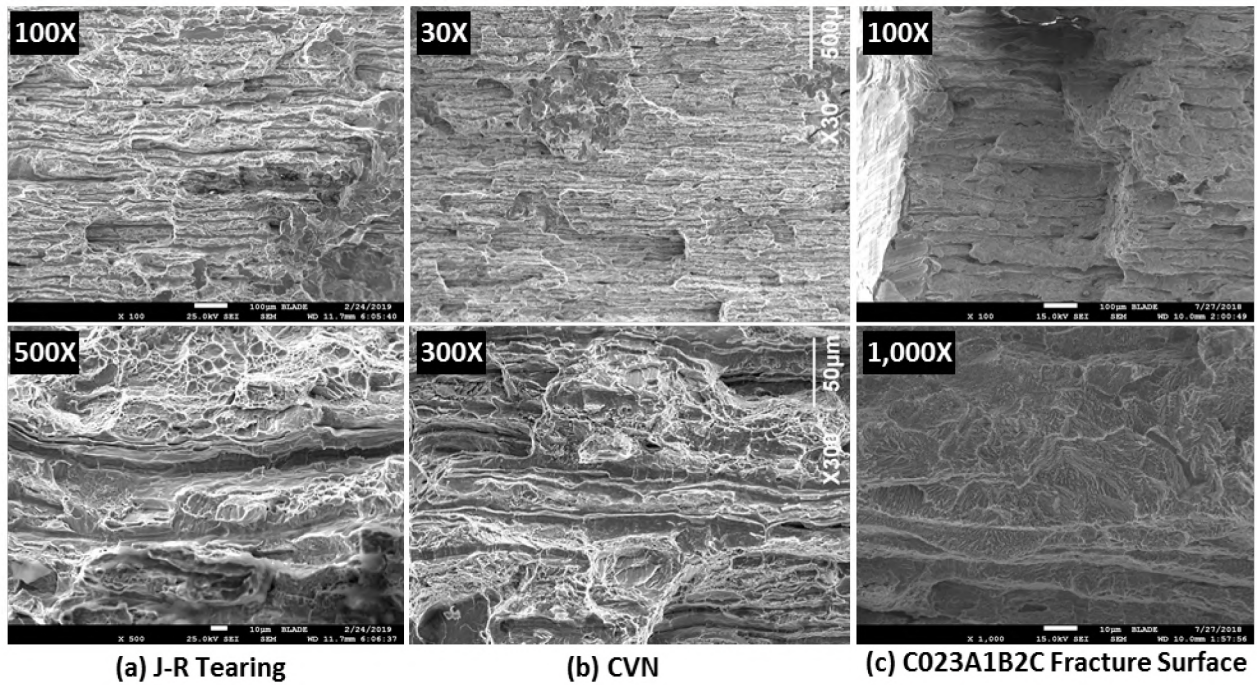


Figure 99: SEM Images Comparing Fracture Surfaces from (a) J-R Tearing, (b) CVN, and (c) C023A1B2C

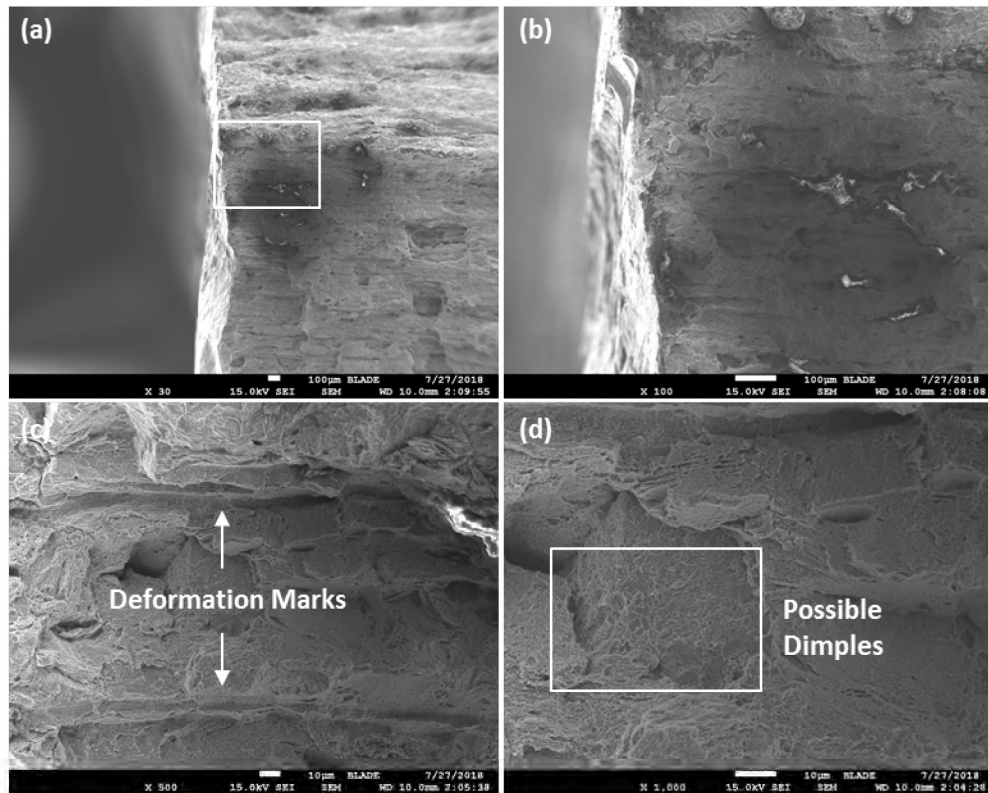


Figure 100: SEM Images of Area 3 Taken at (a) 30 $\times$ , (b) 100 $\times$ , (c) 500 $\times$ , and (d) 1,000 $\times$

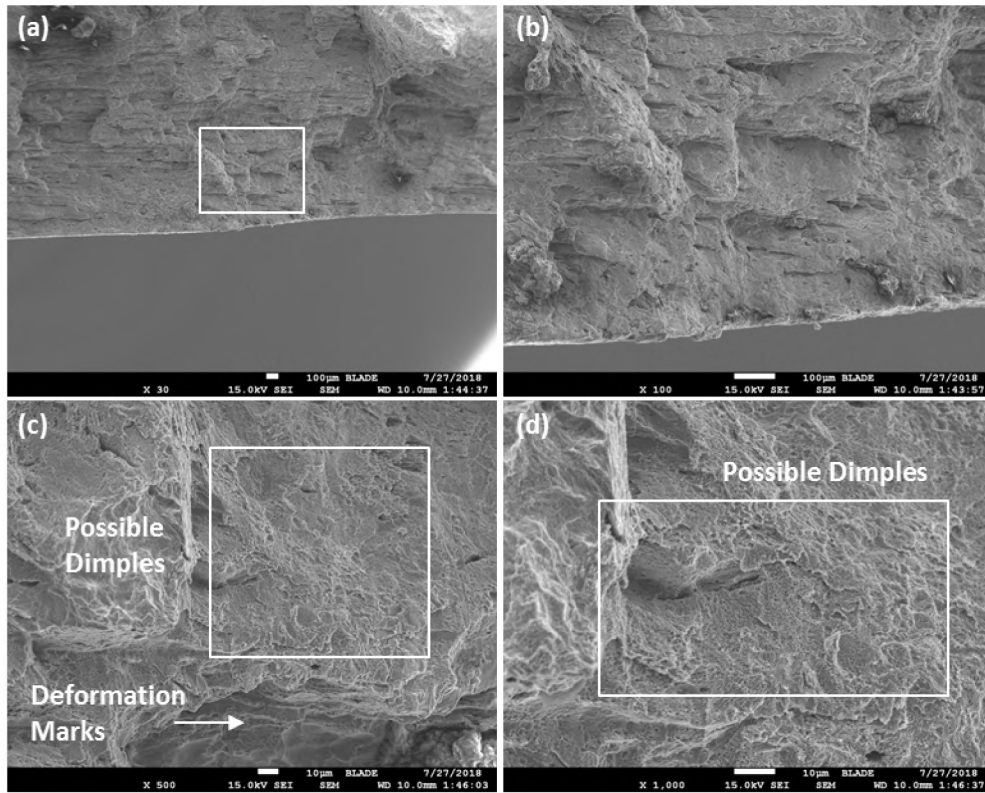


Figure 101: SEM Images of Area 4 Taken at (a) 30 $\times$ , (b) 100 $\times$ , (c) 500 $\times$ , and (d) 1,000 $\times$

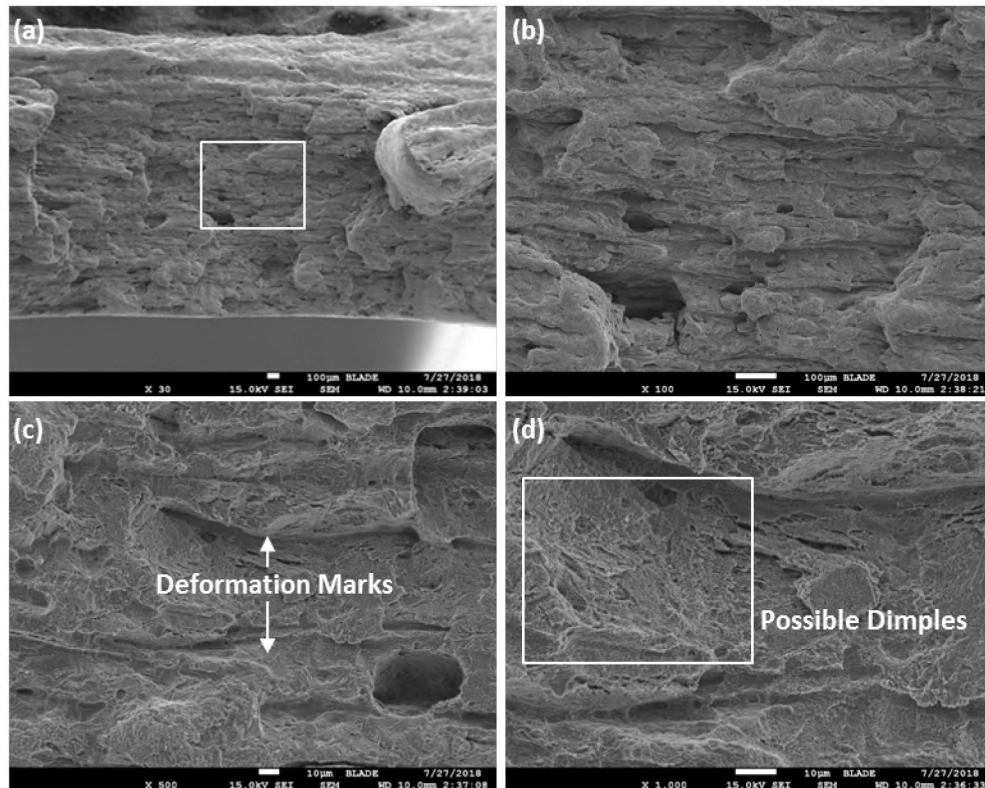


Figure 102: SEM Images of Area 8 Taken at (a) 30 $\times$ , (b) 100 $\times$ , (c) 500 $\times$ , and (d) 1,000 $\times$

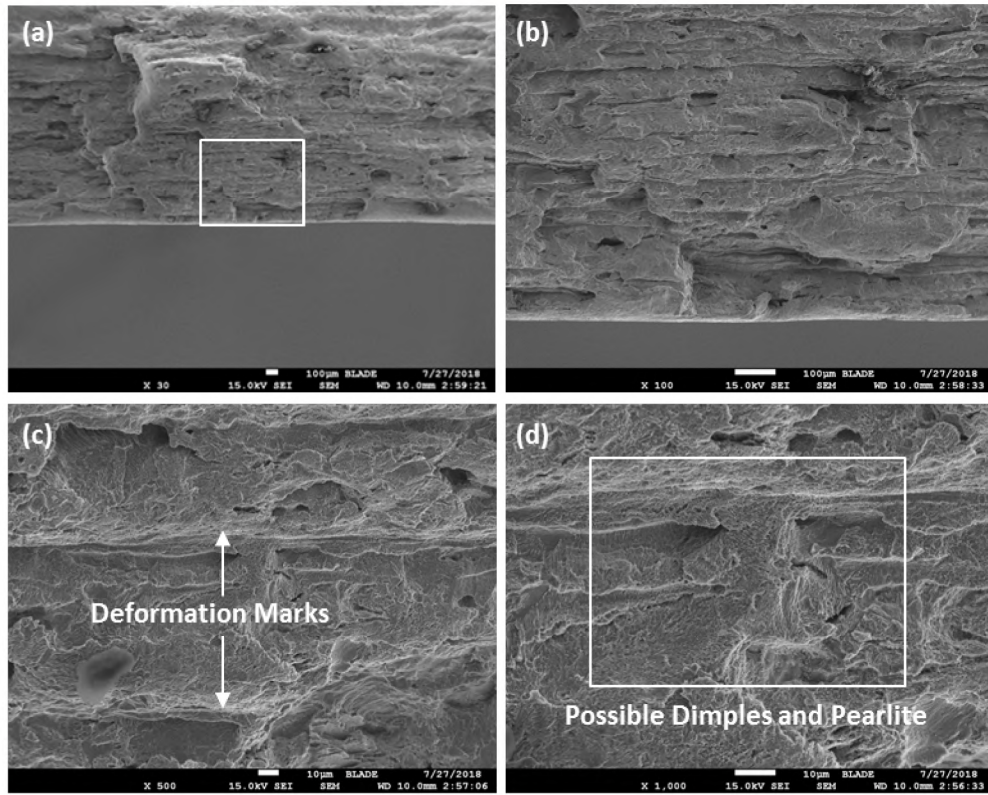


Figure 103: SEM Images of Area 10 Taken at (a) 30×, (b) 100×, (c) 500×, and (d) 1,000×

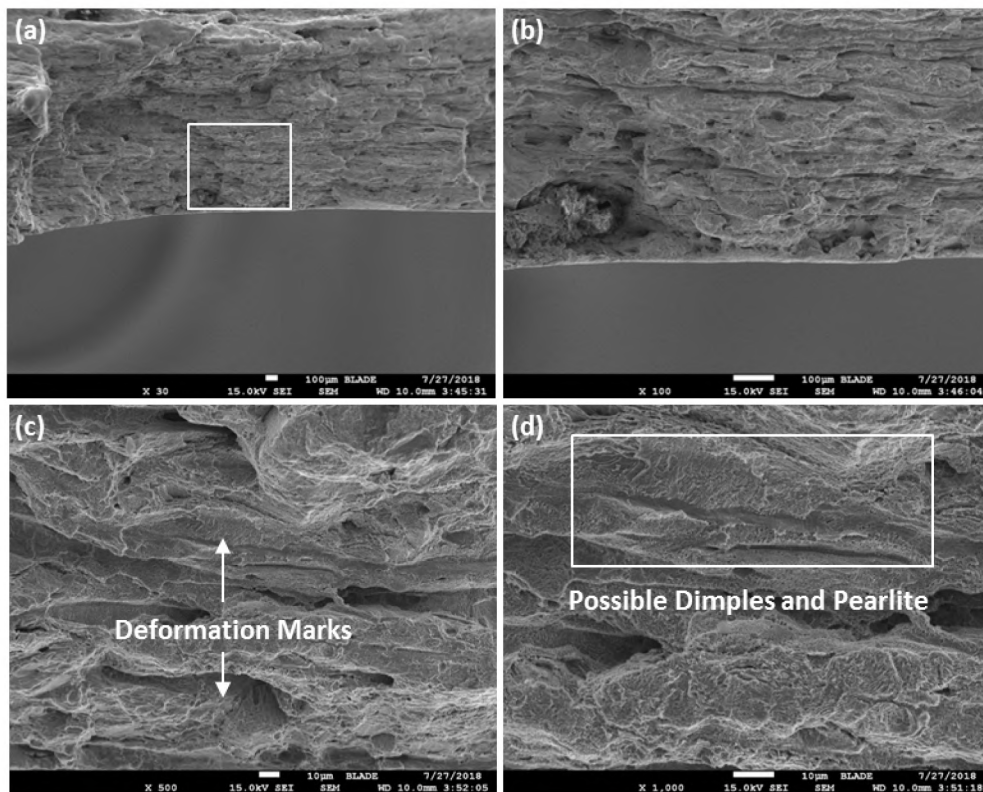


Figure 104: SEM Images of Area 17 Taken at (a) 30×, (b) 100×, (c) 500×, and (d) 1,000×

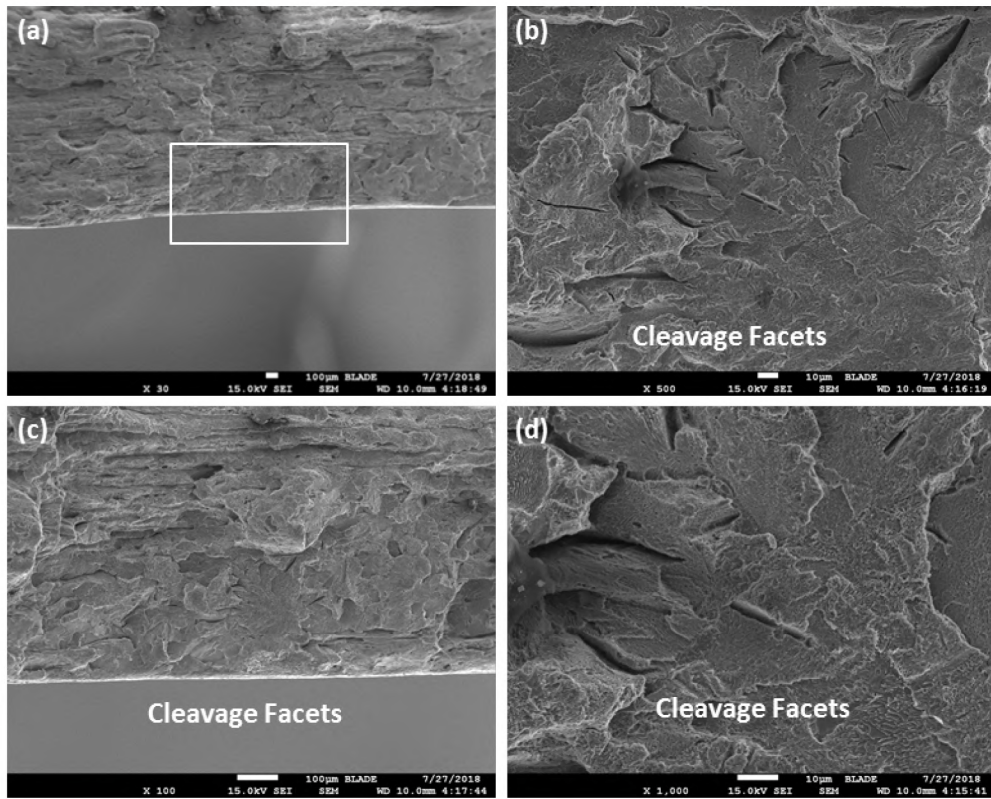


Figure 105: SEM Images of Area 19 Taken at (a) 30×, (b) 100×, (c) 500×, and (d) 1,000×

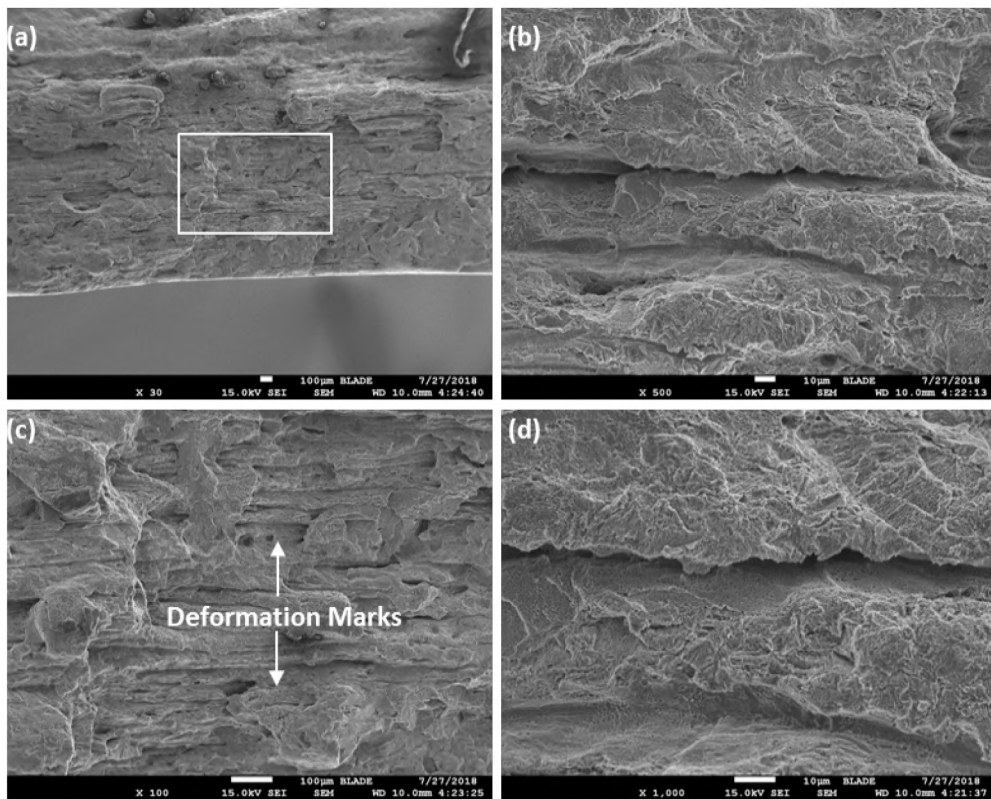


Figure 106: SEM images of Area 20 Taken at (a) 30×, (b) 100×, (c) 500×, and (d) 1,000×



Many AOIs from specimen C023A1B2D were examined with the SEM. C023A1B2D was primarily composed of Zone 2 with a small area identified as Zone 1. Ductile features were observed in locations to the right of A30 (Figure 98). Locations to the left of A30 showed a ductile-brittle fracture mode with cleavage surrounded by deformation marks. Figure 107 shows the morphology for A30. These observations suggest that the length of the origin could be refined and measured between the transition zones identified on fracture surfaces C023A1B2C and C023A1B2D. Section 3.2.3 discusses the refining of the origin based on the observations made in this section. Figure 108 shows A37 (to the right of A30), which contained deformation marks.

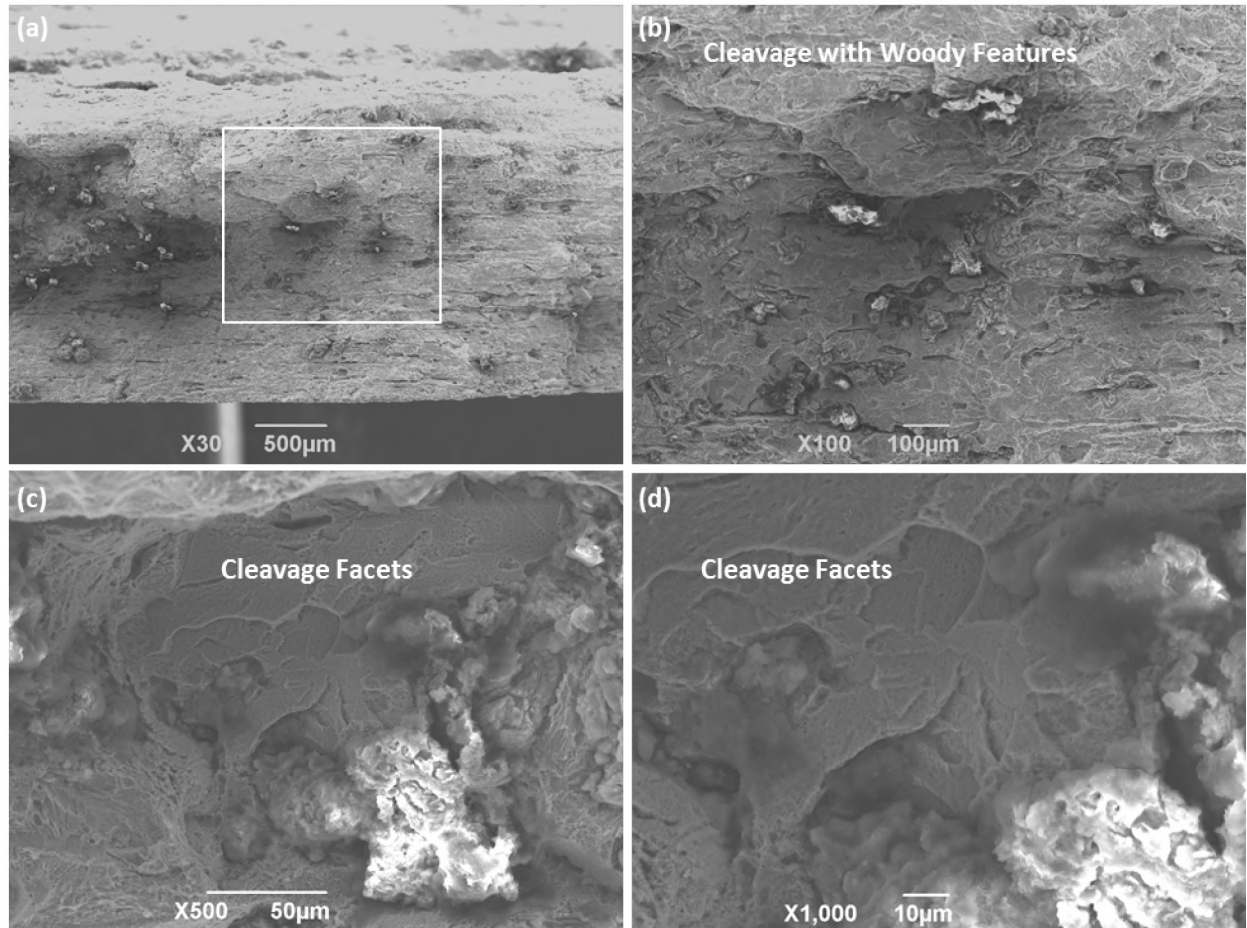
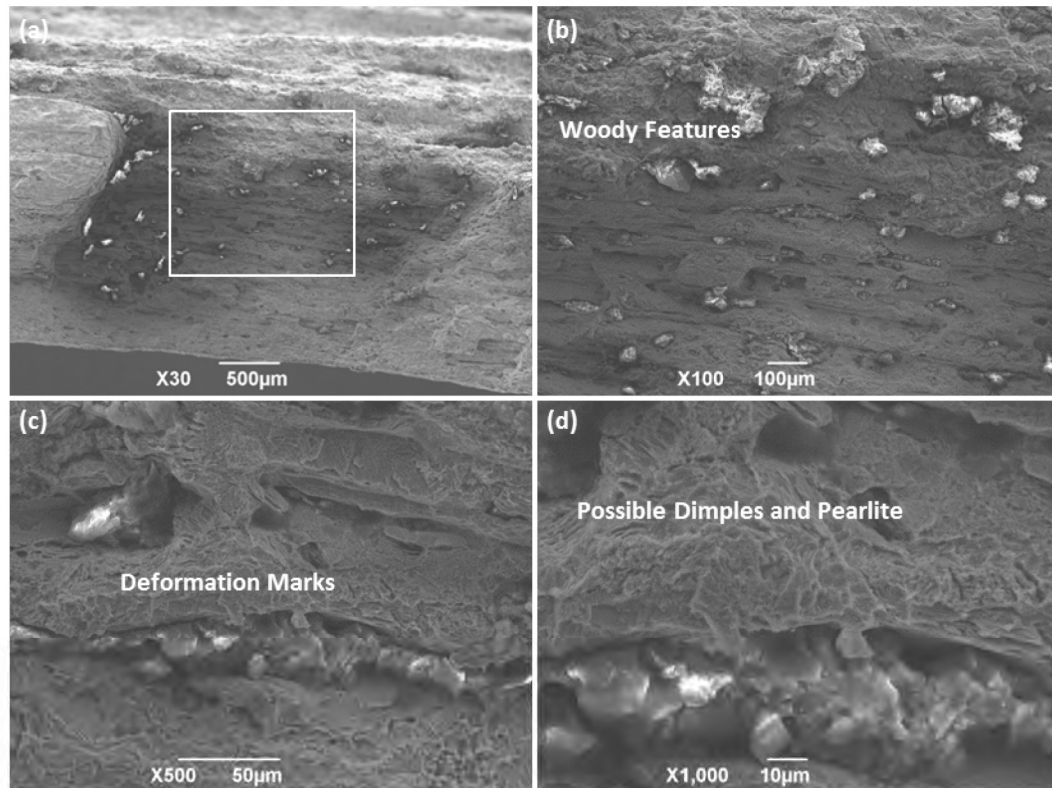


Figure 107: C023A1B2D SEM Images of A30 Showing a Mixed Mode Morphology

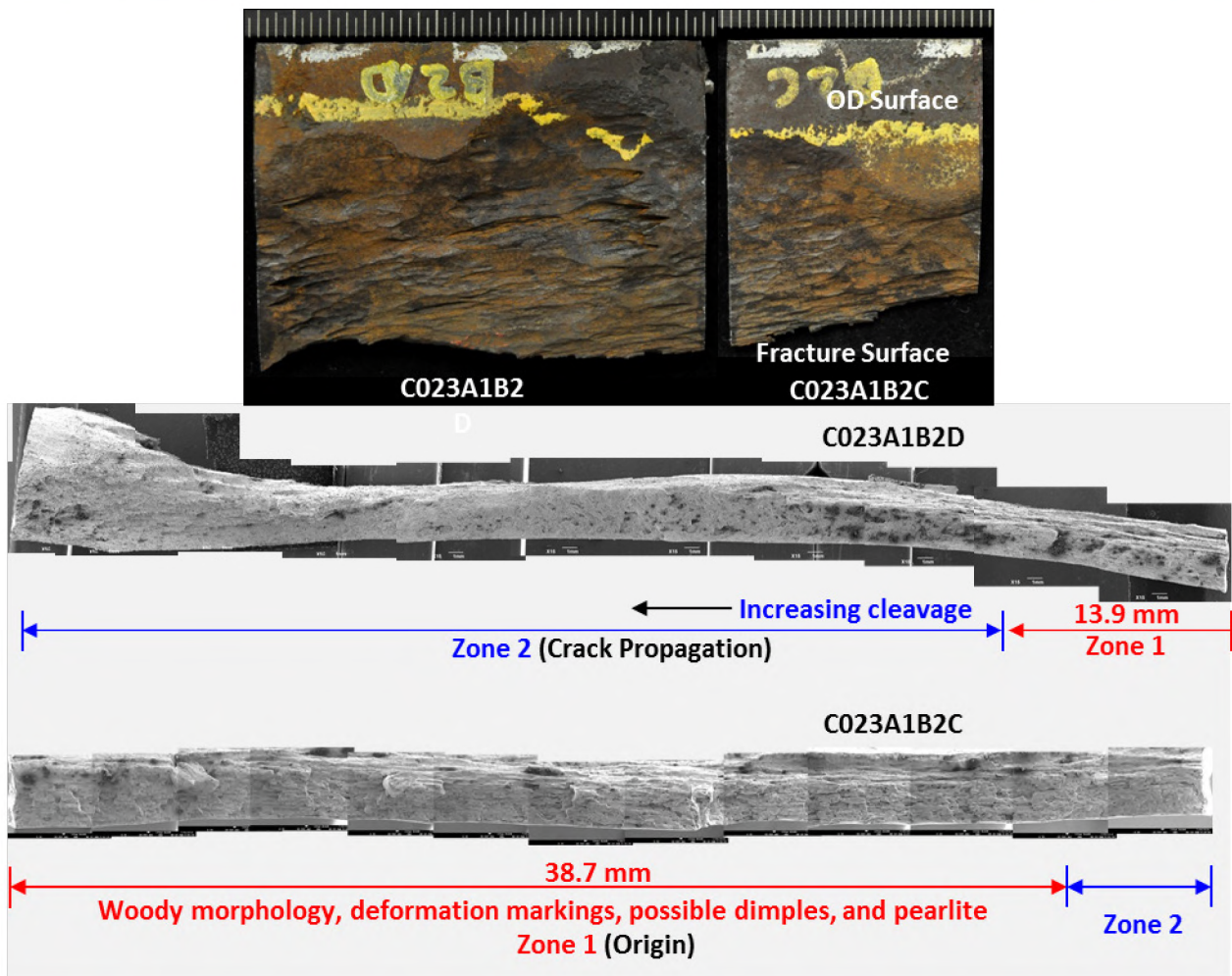


**Figure 108: C023A1B2D SEM Images of A37 Showing Woody-Type Morphology and Deformation Marks without Cleavage Facets**

### 3.2.3 Zone 1 Size Refinement

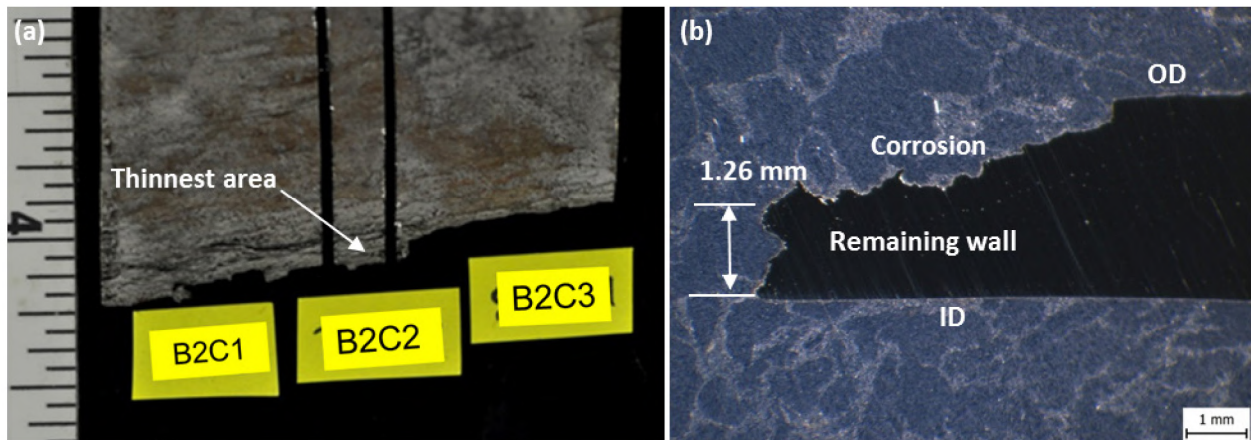
The origin was initially defined based on the metal loss measurements and chevron marks identified on the fracture surface. The origin length based on this criteria was measured at 4.8 in. (123 mm). The origin was redefined based on the micro-scale features identified on the fracture surface. The micro-scale-based measurement was defined as the length of fracture surface that exhibited fully ductile tearing without cleavage facets. The origin length based on the new micro-scale definition was 2.13 in. (54.0 mm). Figure 109 shows the Zone 1 measurements for C023A1B2C and C023A1B2D based on the new origin definition. The origin measurements for C023A1B2C and C023A1B2D were 0.55 in. (13.9 mm) and 1.52 in. (38.7 mm), respectively. The band saw cut removed approximately 0.06 in. (1.4 mm) of material. The measurements resulted in a total Zone 1 length of 2.13 in. (54.0 mm). The initial origin length was reduced by more than a factor of 2. Section 3.2.2 describes the observations from the SEM images that set the basis for redefining the origin length.

The length difference of the origin based on the micro (SEM) and macro (visual) definitions may reflect the difference in the role they played for the axial rupture. The micro definition measurement of 2.13 in. represents the initial size of the crack origin. The macro definition measurement of 4.8 in. represents the rapid propagation of the crack as indicated by the chevron marks.



**Figure 109: Origin Measurements Based on Micro Definition for C023A1B2C and C023A1B2D**

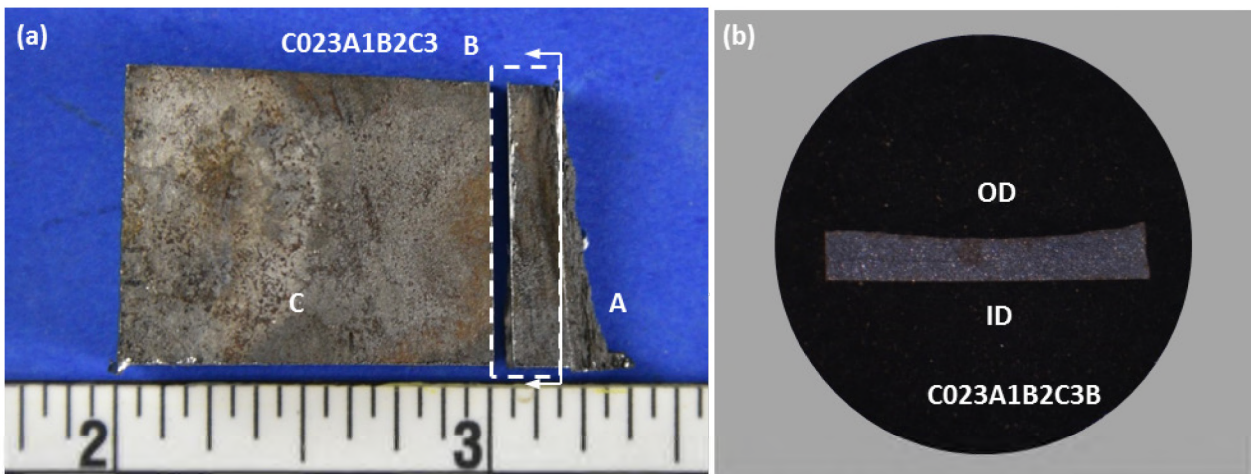
The maximum corrosion depth (metal loss) of the origin was originally measured with an ultrasonic thickness probe. Limitations with the probe prevented an accurate measurement of the maximum corrosion depth. A metallographic cross section was made to accurately measure the minimum remaining wall. The origin specimens (C023A1B2C and C023A1B2D) were visually examined to identify the thinnest area. The selected area was cross-sectioned, mounted, and polished for metallographic examination. Figure 110 shows the location of the (a) metallographic section of C023A1B2C and the (b) measured remaining wall thickness on the polished specimen. The measured remaining wall is 0.0496 in. (1.26 mm), and the measured wall thickness of the unaffected area was 0.321 in. (8.15 mm). The calculated maximum metal loss, or maximum corrosion depth, was 85% AWT. The comparison of the original measurement of 0.126 in. (3.2 mm) with the refined measurement of 0.0496 in. shows a significant error as was expected. The refined measurement of 0.0496 in. was accurate and was used as an input parameter for failure pressure calculations.



**Figure 110: (a) Macro Image and (b) Micrograph of C023A1B2C2 Showing the Remaining Wall**

Ductile tearing and bulging could have contributed to the final remaining wall by ductile deformation. The measured remaining wall would have then been a combination of the original metal loss due to corrosion and thinning caused by the axial rupture. Cross sections adjacent to the fracture surface were examined to determine if bulging and ductile tearing contributed to the remaining wall thickness measurement.

Two specimens (C023A1B2C2 and C023A1B2C3) were examined for elongated grains. C023A1B2C2 (Figure 110 [b]) was used to determine the refined remaining wall measurement. The same specimen was etched to examine the grain structure perpendicular to the axial rupture orientation. C023A1B2C3 was a specimen adjacent to C023A1B2C2 and was selected to be examined for its microstructure parallel to the axial rupture. A small specimen was extracted from C023A1B2C3 adjacently to the fracture surface. The objective was to section it as close to the fracture surface as possible. A diamond saw was used to make a precise cut with limited material loss (0.5 mm). Figure 111 shows (a) C023A1B2C3 prior to the extraction of the specimen and the (b) mount after the specimen was cut. Figure 112 and Figure 113 show the microstructure for the circumferential (C023A1B2C2) and longitudinal (C023A1B2C3B) cross sections etched with 3% nital. The grains appear equiaxed and are not elongated. The findings suggest that the measured remaining wall loss of 85% was caused by metal loss due to corrosion.



**Figure 111: (a) C023B2C3 Section Layout and (b) Resulting C023B2C3B Mount**

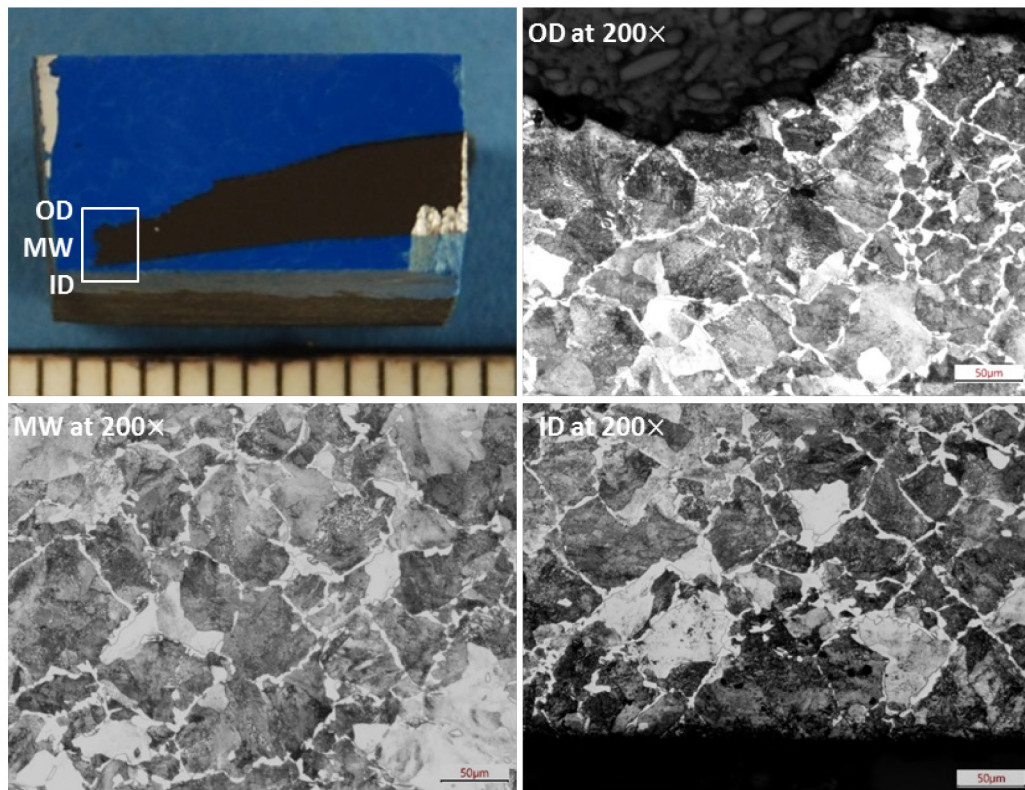


Figure 112: Micrographs of Equiaxed Grain Shape at Thinnest Area Taken at 200X

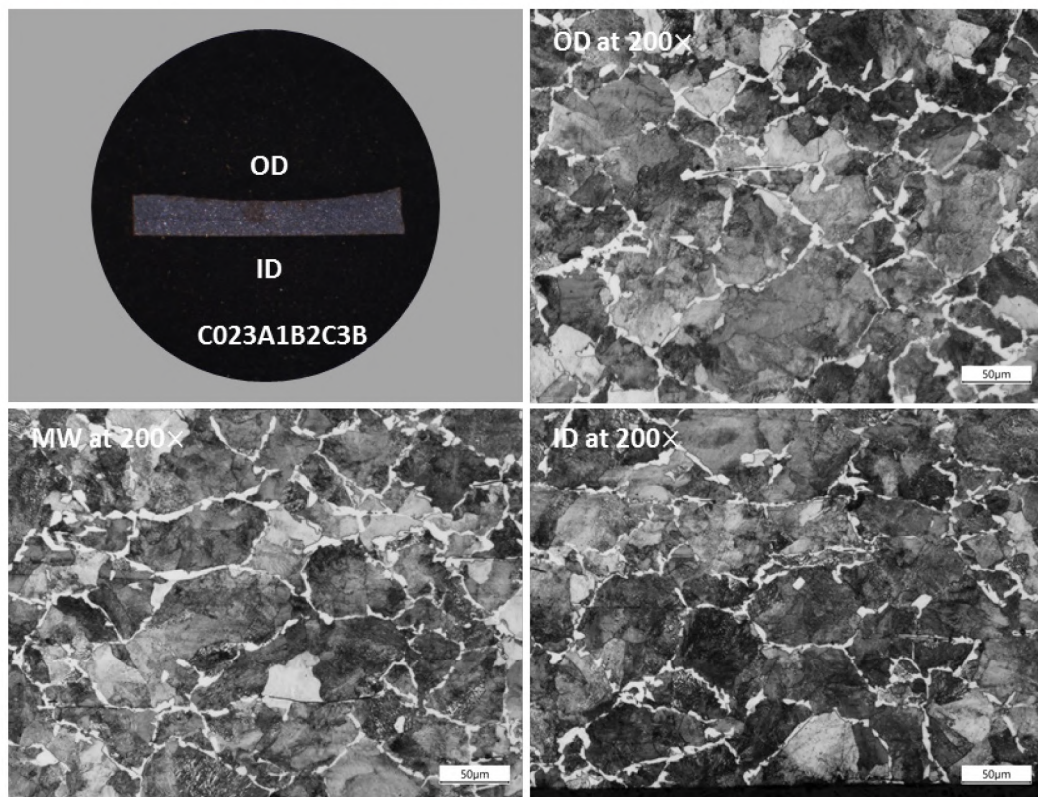


Figure 113: C023A1B2C3B Micrographs of Equiaxed Grain Shape Taken at 200X

### 3.2.4 Micro-Fractographic Characterization of Zone 2 (Crack Propagation)

Zone 2 was generally characterized by chevron marks on both sides of the origin. Chevron marks are evidence of rapid propagation of a mixed ductile-brittle fracture mode, at the micro-scale, during a rapid crack propagation [20] [21]. Chevron marks are not observed when propagation occurs in a purely brittle or ductile mode. The fracture mode of the material also determines the appearance of the chevron marks. Chevron marks in a brittle material response appear finer and more closely spaced as compared to a ductile response and can be visually identified. Also, the direction of the crack propagation is opposite to the apex of the marks. This section describes the micro mechanism for crack propagation of Zone 2.

Zone 2 was separated by Zone 1 (origin) into two segments referred to as Upper and Lower Zone 2 in reference to the zones' relative position in the SS-25 well. Figure 114 shows the separation of Lower and Upper Zone 2. Specimen C023A1B2D in Lower Zone 2 was examined first in detail. Figure 114 shows the non-cleaned (macro) and cleaned (SEM) C023A1B2D fracture surface. Both specimen conditions were examined with the SEM. Only the results from the cleaned examination are discussed in this section. Figure 114 shows the areas investigated with the SEM.

The SEM examination showed a mixed fracture mode that consisted of cleavage (brittle) and microvoid coalescence and dimples (ductile). The amount of cleavage increased with distance from the origin but decreased as the crack approached the lower turning point. Figure 115 through Figure 117 show typical SEM images taken from three locations in Lower Zone 2 (indicated by the blue boxes in Figure 114).

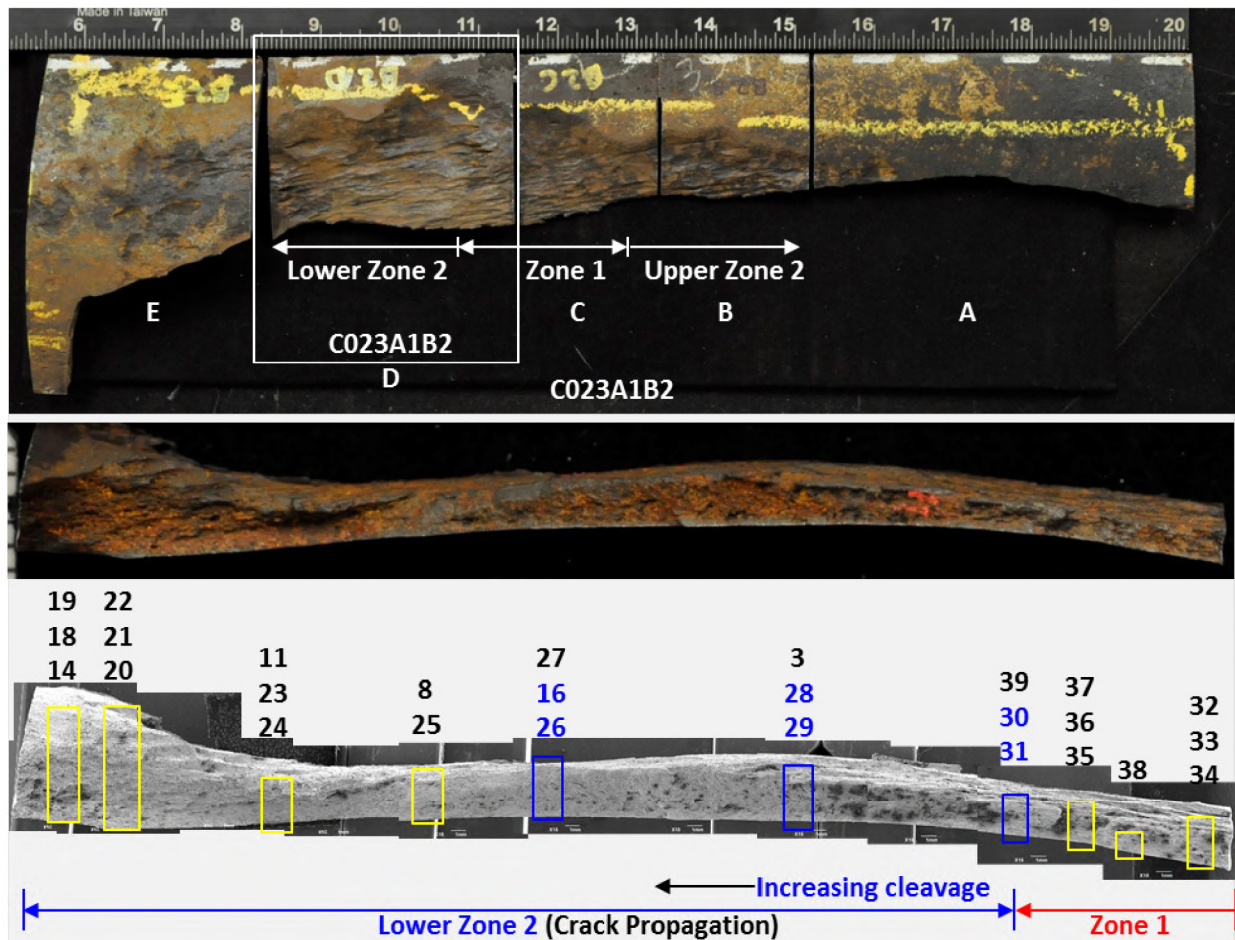


Figure 114: Specimen C023A1B2D Lower Zone 2 SEM Investigation Areas

Figure 115 shows SEM images of A30 and A31, located at the mid-wall (MW) and the ID of the fracture surface, respectively. These areas were located directly below Zone 1 (origin). Figure 115 (a) and (b) show SEM images of A30 at 30 $\times$  and 100 $\times$ . The 100 $\times$  image shows cleavage mixed with woody features. Figure 115 (c) and (d) show SEM images of a cleavage facet taken at 500 $\times$  and 1,000 $\times$ . Figure 115 (e) and (f) show SEM images of deformation marks at A31 near the ID taken at 500 $\times$  and 1,000 $\times$ . The images show a mix mode fracture in Lower Zone 2.

Figure 116 shows SEM images of A28 and A29, located at the MW and ID of the fracture surface, respectively. These areas were located below A30 and A31, which were farther from the origin towards the lower turning point. Figure 116 (a) and (b) show SEM images of A28 at 30 $\times$  and 100 $\times$ . The 100 $\times$  image shows cleavage mixed with woody features that are consistent with the observations of A30. Figure 116 (c) and (d) show SEM images of deformation marks and possible pearlite taken at 500 $\times$  and 1,000 $\times$ . Figure 116 (e) and (f) show SEM images of cleavage facets at A29 near the ID taken at 500 $\times$  and 1,000 $\times$ . The observations of A28 and A29 were consistent with the observations of A30 and A31.

Figure 117 shows SEM images of A16 and A26, located at the MW and ID of the fracture surface, respectively. These areas were located below A28 and A29, which were farther from the origin towards the lower turning point. Figure 117 (a) and (b) show SEM images of A16 at 30 $\times$  and 100 $\times$ . The 100 $\times$  image shows cleavage mixed with woody features, which are consistent with observations for A28 and A30. Figure 117 (c) and (d) show SEM images of cleavage facets taken at 500 $\times$  and 1,000 $\times$ . Figure 117 (e) and (f) show SEM images of deformation marks and dimples at A26 near the ID taken at 500 $\times$  and 1,000 $\times$ . Observations for all the selected areas were consistent.

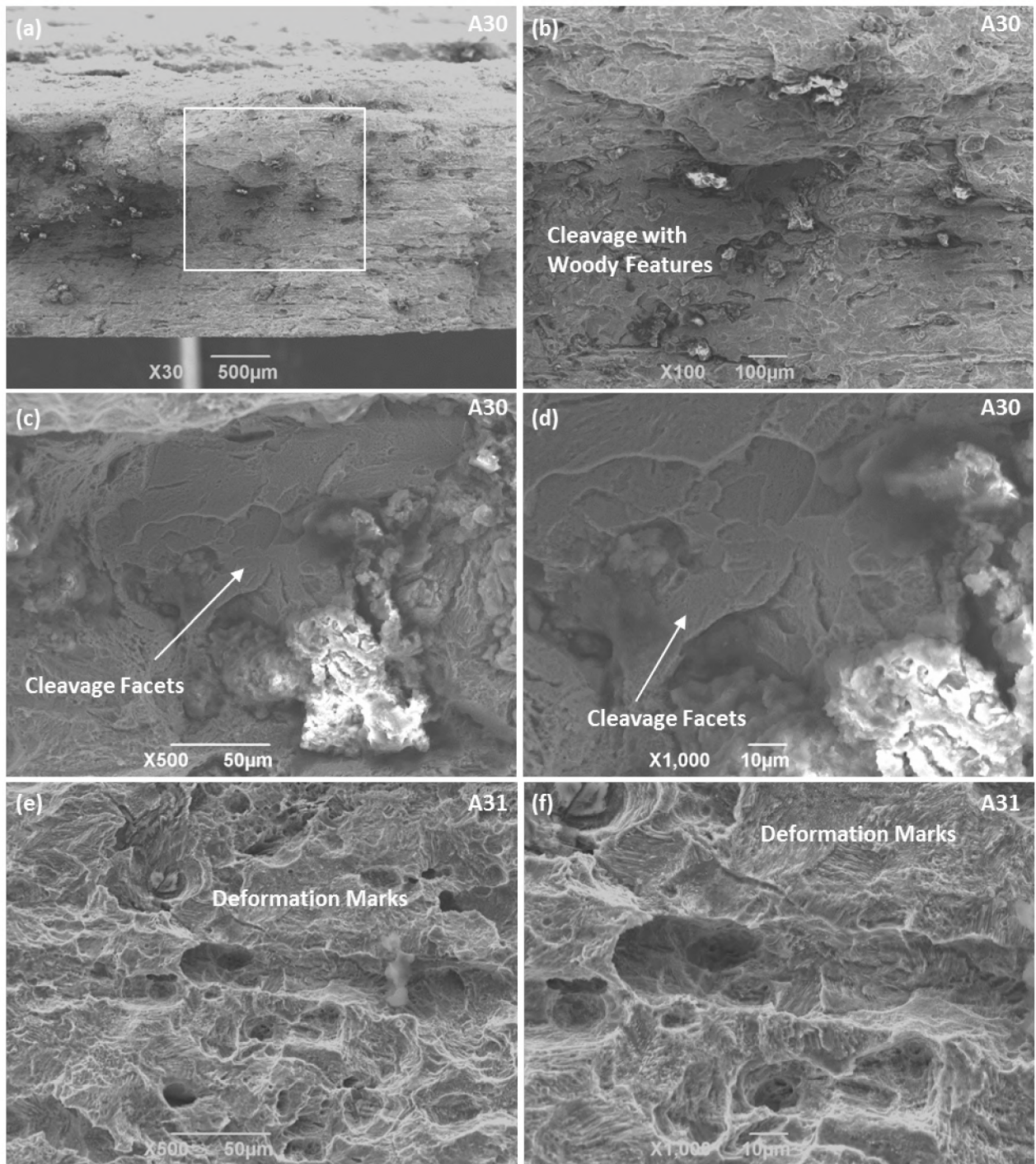


Figure 115: SEM Images from Locations A30 and A31 Showing Mixed Fracture Mode



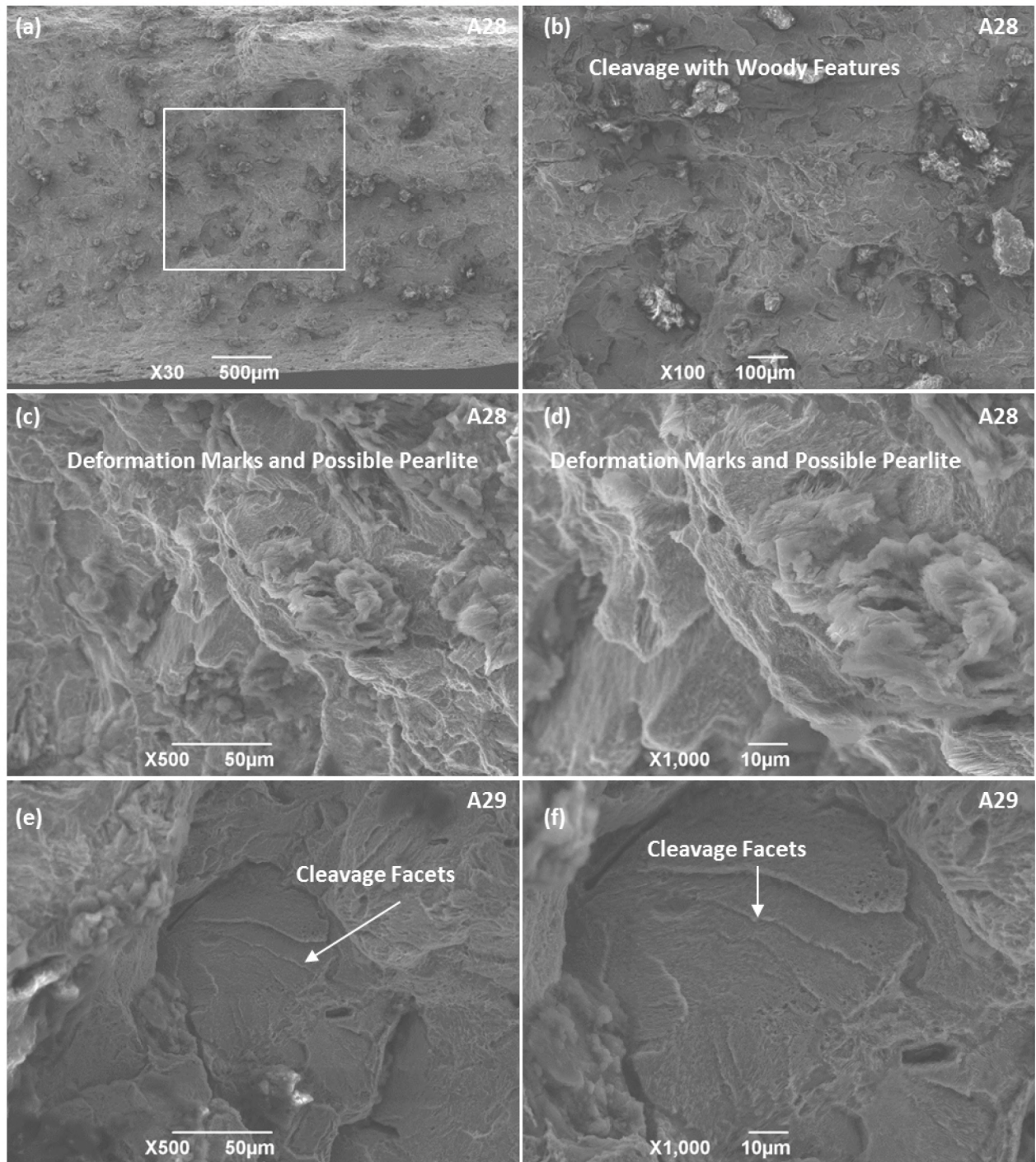
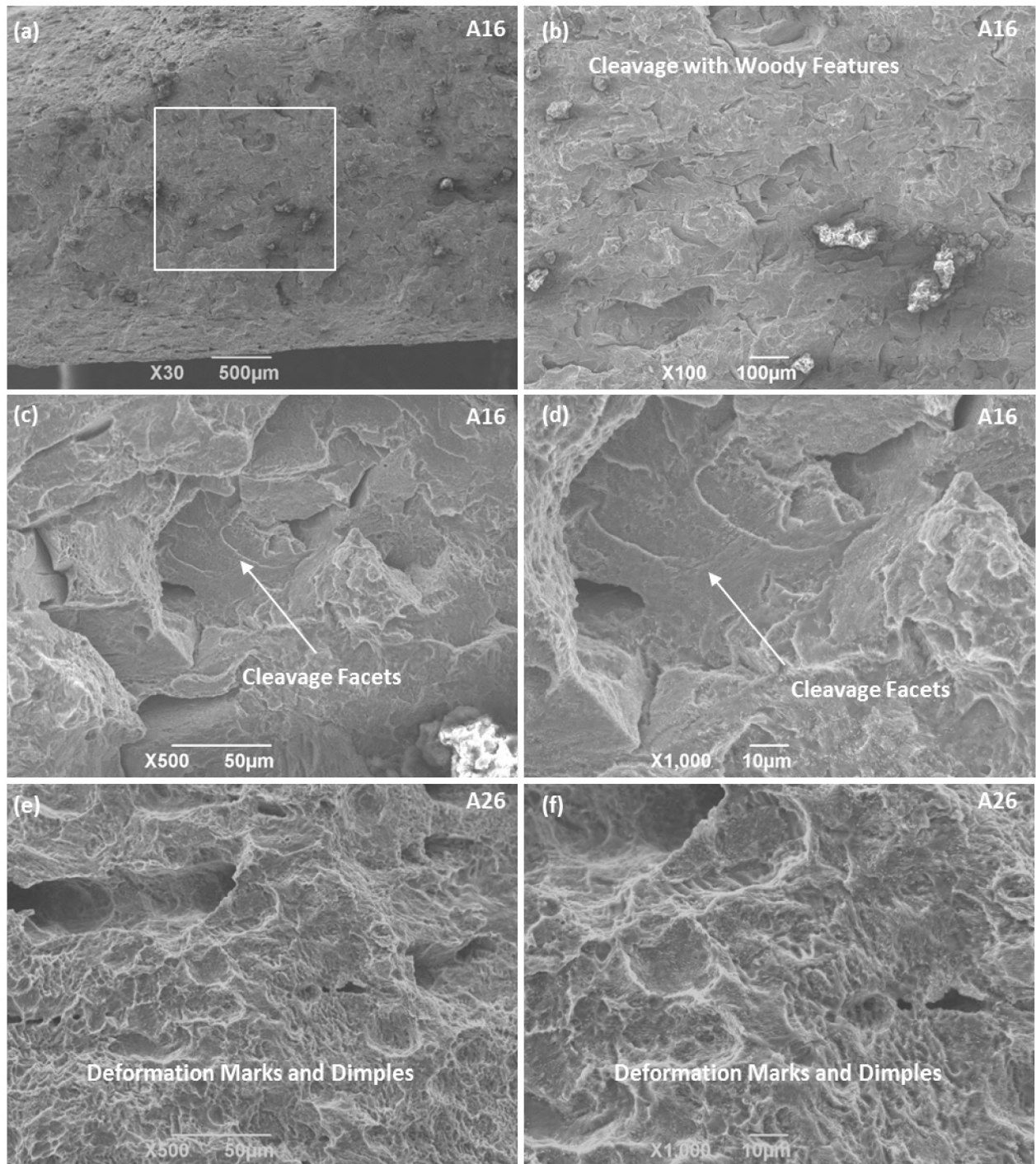


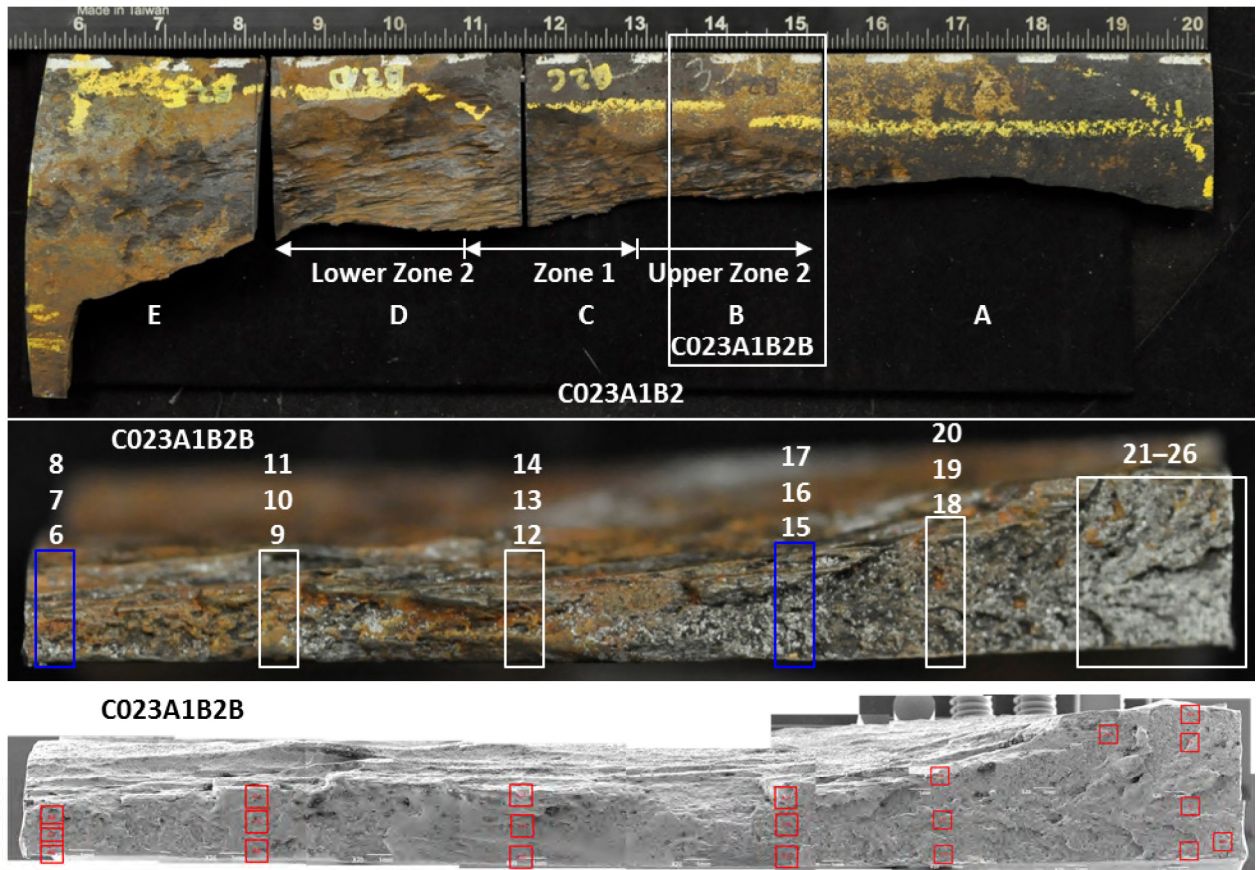
Figure 116: SEM Images from Locations A28 and A29 Showing Mixed Fracture Mode



**Figure 117: SEM Images from Locations A16 and A26 Showing Mixed Fracture Mode**

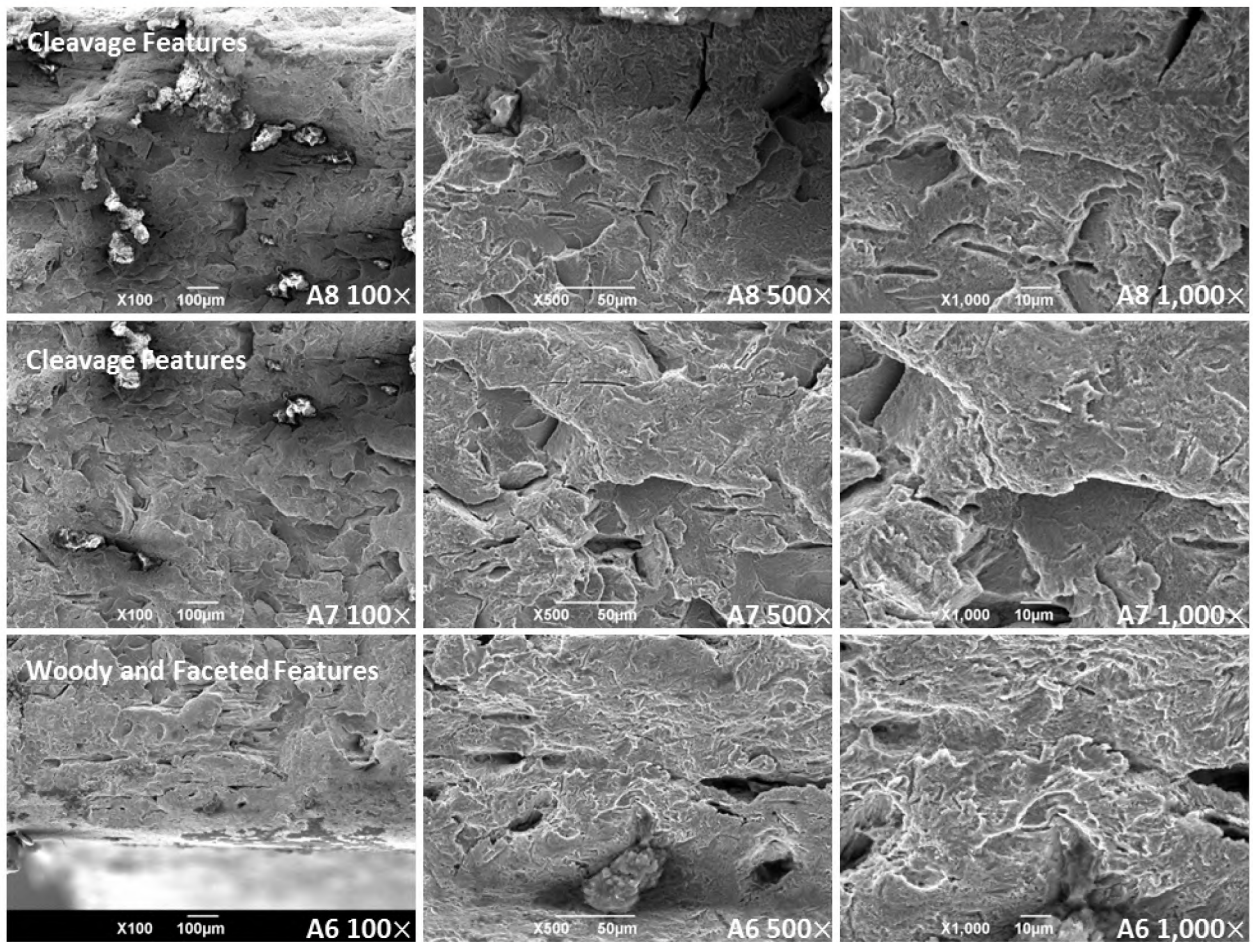
The occurrence of cleavage in Zone 2 is understandable. In body-centered cubic (BCC) metals such as mild steels, cleavage is promoted by low service temperature, high strain rate, presence of stress concentrators (stress state), specimen size, material (composition and microstructure), and certain environments [25]. The axial rupture in the 7 in. casing occurred at an approximate temperature of 80°F, which would not have caused cleavage during slow loading. Based on this observation, the main contributing factor for cleavage was related to strain rate.

Upper Zone 2 was also examined with the SEM. Specimen C023A1B2B was selected for a detailed examination of Upper Zone 2 with the SEM. Figure 118 shows the non-cleaned (macro) and cleaned (SEM) C023A1B2B fracture surface. Both specimen conditions were examined with the SEM. Only the results from the examination of the cleaned fracture surface are discussed in this section. Figure 118 also shows the areas investigated with the SEM. The observed micro mechanism for crack propagation was a mixed fracture mode consisting of cleavage and dimples. Figure 119 and Figure 120 show typical SEM images from two locations in Upper Zone 2 (indicated by the blue boxes in Figure 118). The micro structure for Upper Zone 2 appears to be similar to Lower Zone 2.



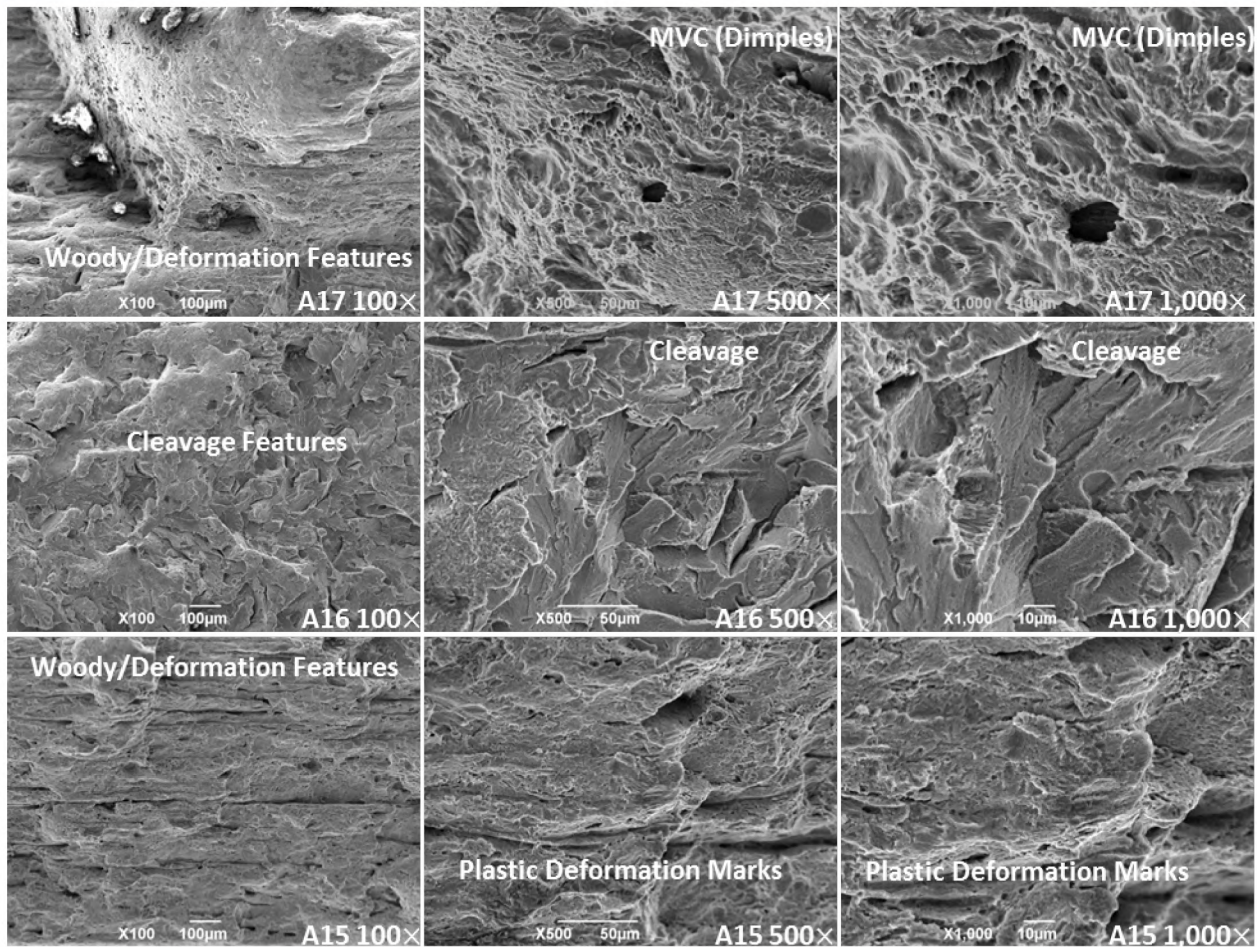
**Figure 118: Specimen C023A1B2B Upper Zone 2 SEM Investigation Areas**

Figure 119 shows SEM images of the cleaned fracture surfaces for A6, A7, and A8. These areas were located directly above Zone 1 (origin). A6 was located at the ID and was characterized by woody and faceted features. Instead of typical cleavage, faceted features were observed in some areas; this could be because the original cleavage structure had been corroded away. A7 and A8 were at the MW and OD of the fracture surface, respectively. Both areas were characterized by cleavage features.



**Figure 119: SEM Images for Areas A6, A7, and A8 Taken at 100×, 500×, and 1,000×**

Figure 120 shows SEM images of the cleaned fracture surface for A15, A16, and A17. These areas were located above A6, A7, and A8, closer to the full wall thickness and visible chevron marks. A15 was at the ID of the fracture surface and was characterized by woody deformation features and plastic deformation marks. A16 was located at the MW of the fracture surface and was characterized by cleavage. A17 was located at the OD of the fracture surface and was characterized by both cleavage and woody deformation features. The high magnification images of A17 show MVC (dimples).



**Figure 120: SEM Images for Areas A15, A16, and A17 Taken at 100×, 500×, and 1,000×**

Specimen C023A1B2A was also examined with the SEM. Specimen C023A1B2A consisted entirely of Upper Zone 2 fracture surface. The specimen was cut into several smaller specimens to accommodate the size restrictions imposed by the SEM stage. Specimen C023A1B2A5B3 was examined with the SEM in detail. Figure 121 (a) shows the extraction location for specimen C023A1B2A5B1. Figure 121 (b) shows C023A1B2A5B in the non-cleaned condition prior to extracting specimen C023A1B2A5B1 for cleaning and SEM investigation. Figure 121 (c) shows an SEM image of specimen C023A1B2A5B1 in the cleaned condition. The SEM images were taken from the ID to the OD at 1,000× and stitched together to form a complete cross section of the fracture surface. Figure 122 shows the stitched SEM images. Cleavage facets with dimples and plastic deformation marks were observed throughout the cross section. The observations confirm a mix mode fracture in Upper Zone 2 (crack propagation). These findings are consistent with Upper Zone 2’s specimen C023A1B2B and Lower Zone 2’s specimen C023A1B2D.

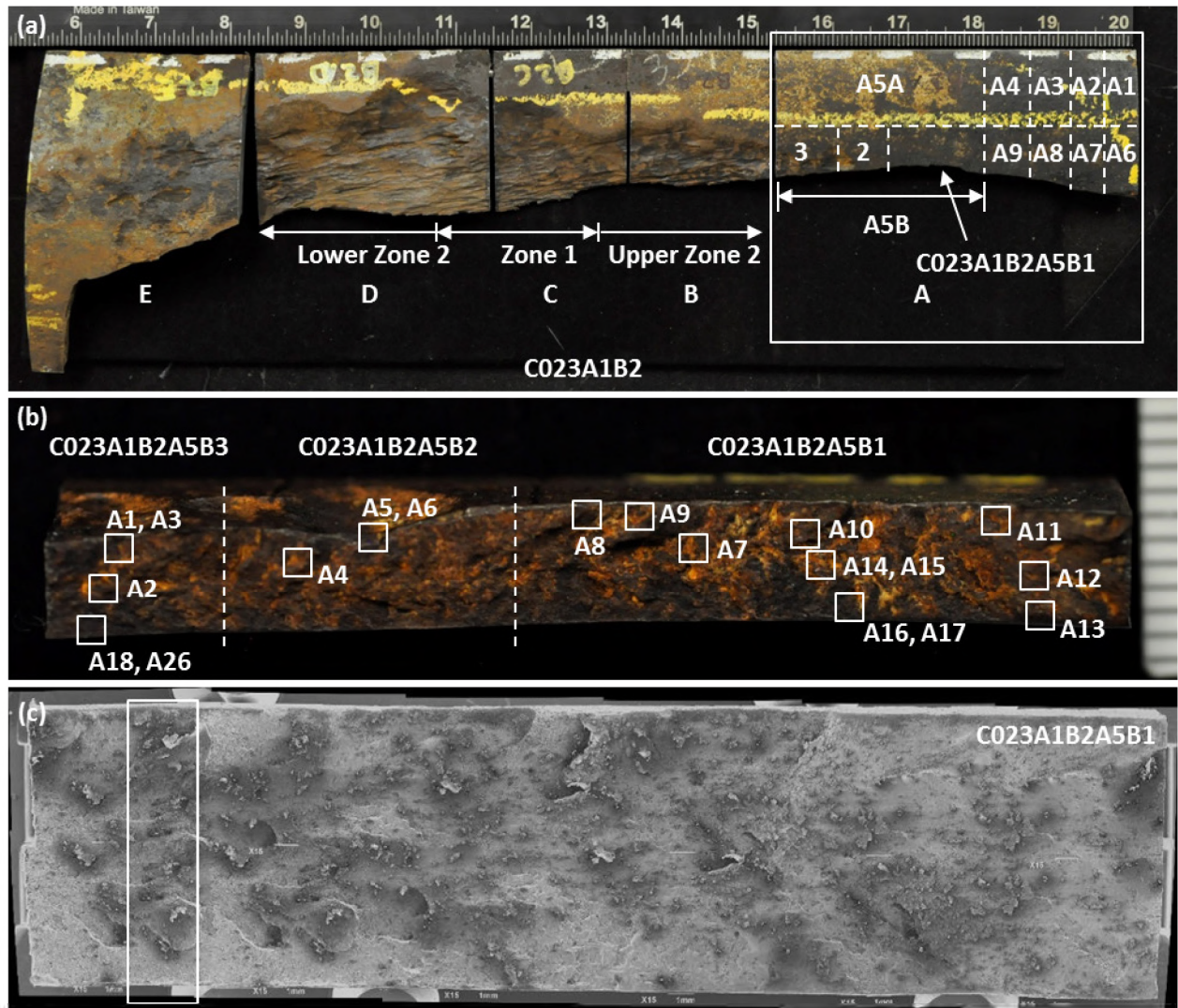


Figure 121: Specimen C023A1B2A5B1 Extraction Location and SEM Investigation Areas

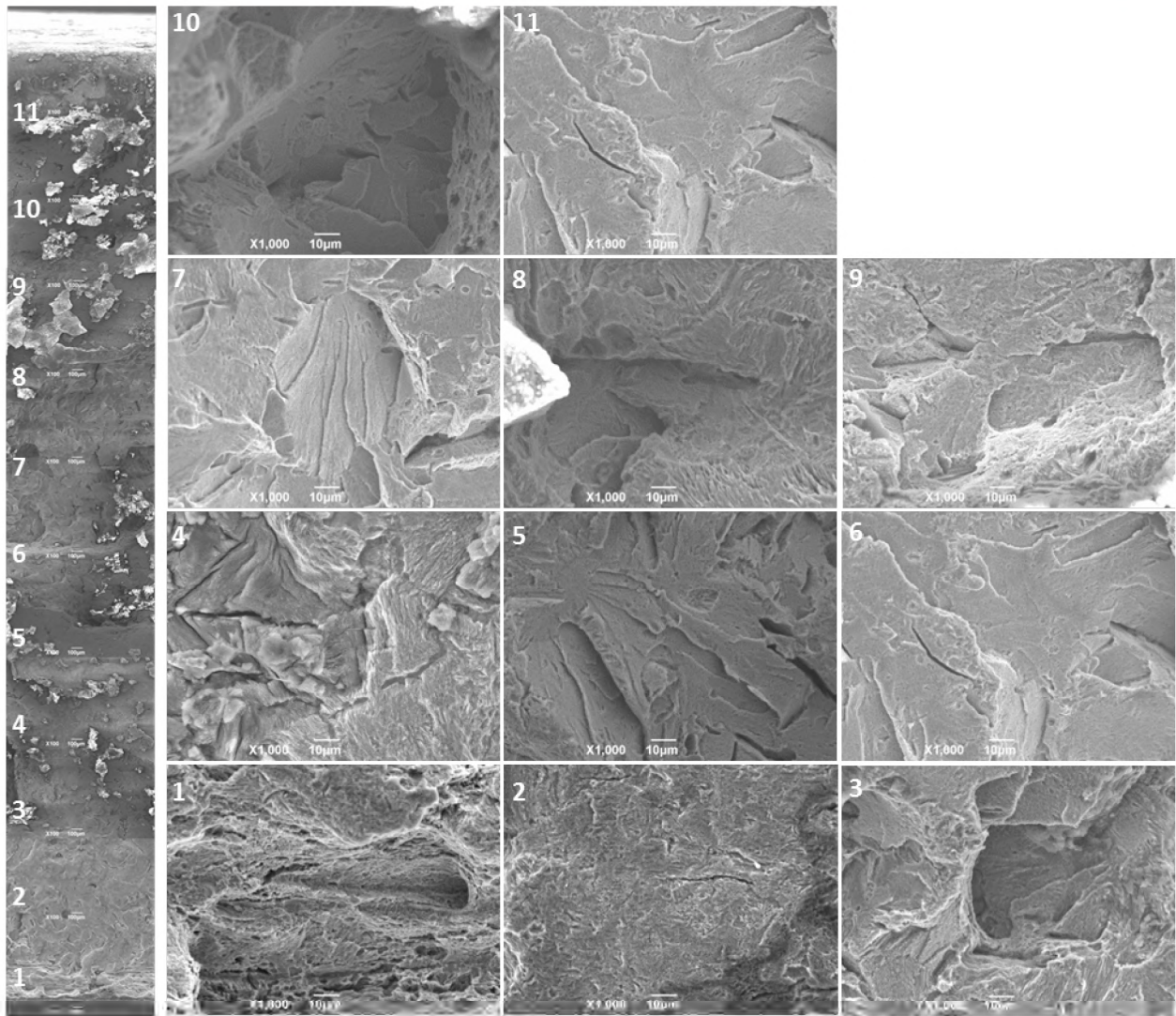


Figure 122: Specimen C023A1B2A5B1 SEM Images from ID to OD

### 3.2.5 Characterization of Featureless Segment of Upper Zone 2

Section 3.2.1 indicated that the upper portion of Zone 2 (crack propagation) contained chevron marks and a 9 in. long featureless region that was not present in Lower Zone 2. The 9 in. featureless region appeared to be relatively smooth with no visible chevron marks. Visual examination of the featureless region suggested that the fracture surface had been eroded by escaping gas caused by the axial rupture. This section discusses the detailed micro examination performed on the featureless region of the upper portion of Zone 2.

Figure 123 is an overview of the upper portion of Zone 2. Fracture surfaces A and B are the mating surfaces of the rupture that show the Zone 2 featureless segment. Fracture surface A was used in the examination, while fracture surface B was preserved.



Figure 123: Overview of Upper Featureless Zone

Two specimens were investigated to characterize the Upper Zone 2 featureless region. Figure 124 shows a schematic with the specimen locations. Specimen C023A1A1B5B contained a small section of the featureless zone and the upper turning point. Specimen C023A1A1B1C contained a portion of the featureless zone directly below specimen C023A1A1B5B. Both specimens were examined with the SEM.

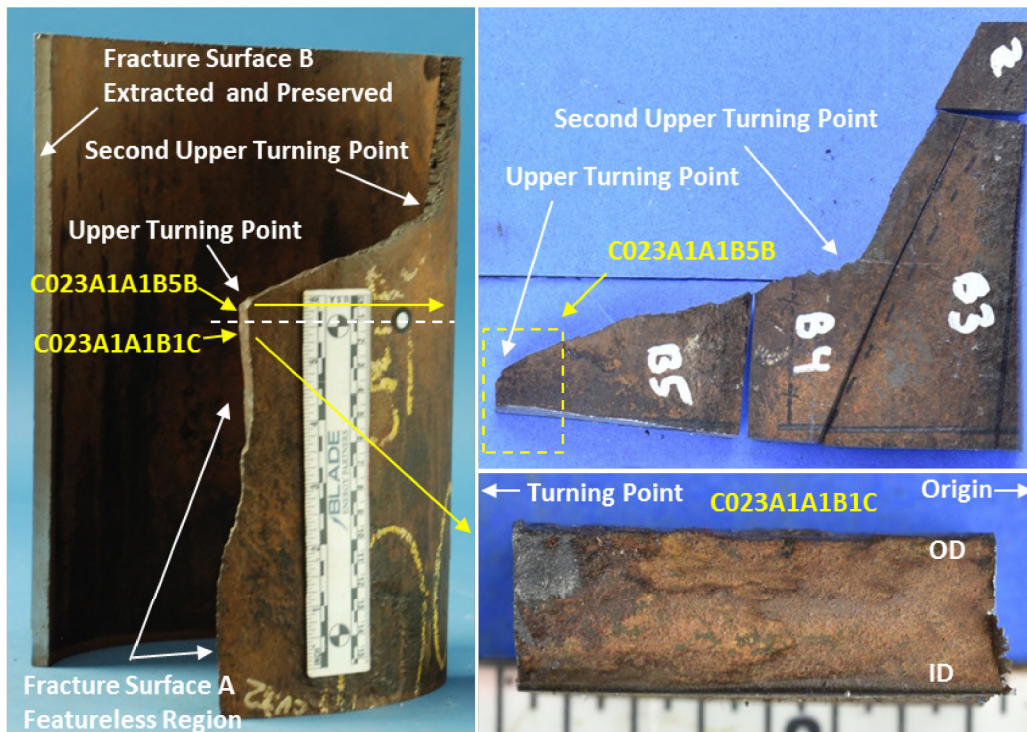


Figure 124: Fracture Surface A Featureless Region of Upper Zone 2



Specimen C023A1A1B5B was examined first; it was extracted and cleaned ultrasonically in a 1% Citranox solution for 6 minutes at room temperature. SEM observations revealed an eroded fracture surface with fine erosion marks. Figure 125 shows the representative SEM images of the eroded fracture surface. Erosion marks left on the fracture surface were readily identified at magnifications above 500 $\times$ . Thirty randomly selected erosion marks were measured to estimate the particle size of the solids in the released gas flow. Figure 126 shows the measured width distribution of the 30 randomly selected erosion marks. The results showed that the erosion marks had a maximum measured width of 8  $\mu\text{m}$ , and more than 60% of the erosion marks had measured widths within the range of 4–6  $\mu\text{m}$ .

Multiple factors may contribute to the width of erosion marks, including solid particle size, hardness, brittleness, speed, and angle of impingement. A factor of 3 was used to estimate the particle size based on the width of the erosion marks. Based on this assumption, the particles had a maximum size of 24  $\mu\text{m}$ , and more than 60% of the particle sizes were in the range of 12–18  $\mu\text{m}$ . These observations confirm that the featureless segment of Upper Zone 2 was affected by erosion.

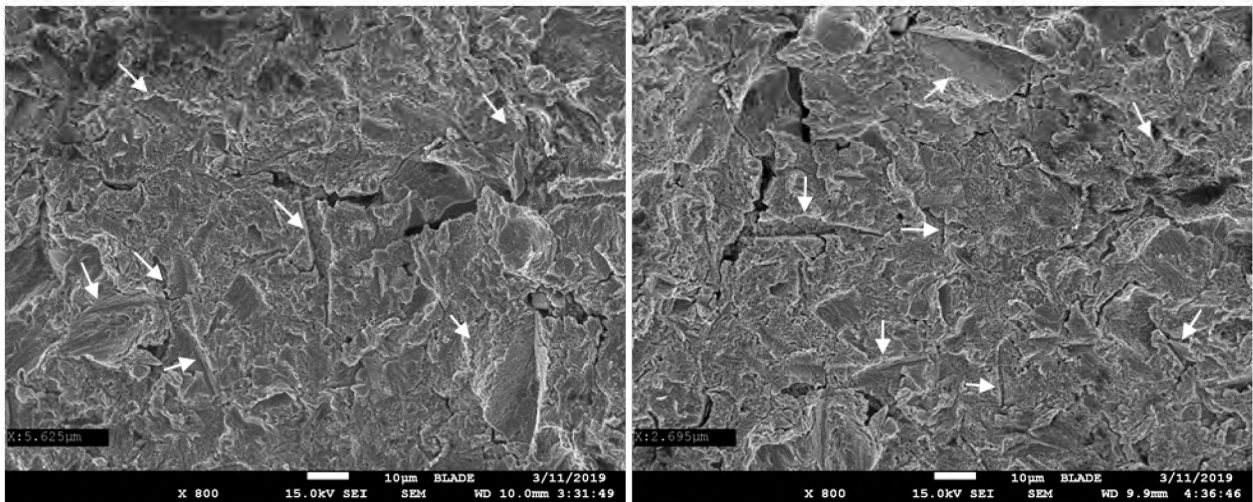


Figure 125: Representative SEM Images of Erosion Marks (White Arrows) Taken at 800 $\times$

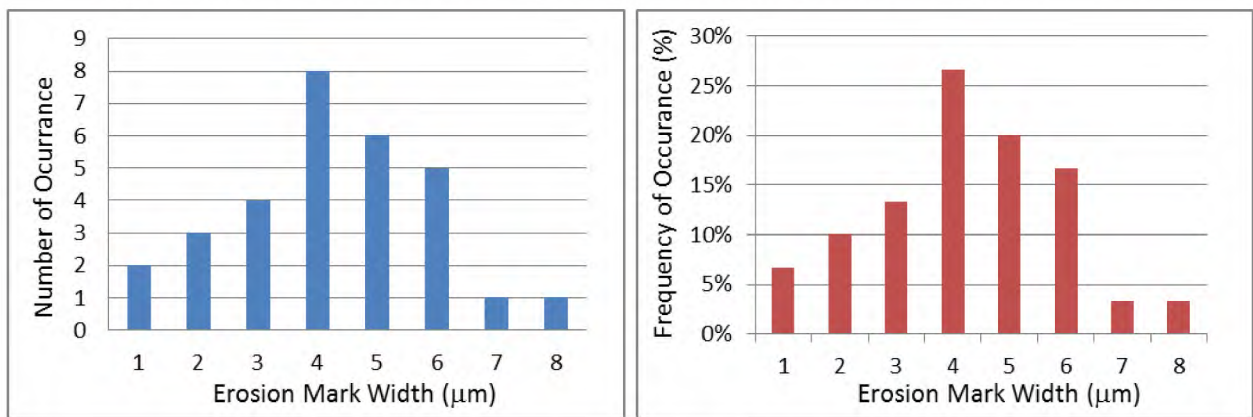


Figure 126: Erosion Mark Width Distribution

Specimen C023A1A1B1C was also located in the featureless segment of Upper Zone 2. Figure 127 shows the specimen in the (a) non-cleaned and (b) cleaned conditions. Figure 127 (b) shows the four areas examined with the SEM. A1 was the closest to the previously examined specimen C023A1A1B5B (adjacent to upper turning point). A2–A4 were progressively lower (towards visible chevron marks in Zone 2) on the

specimen. Figure 128 through Figure 131 show representative SEM images of specimen C023A1A1B1C. The SEM images show some erosion marks as was observed with the previous specimen. The fracture surface that revealed the pearlite microstructure appeared to be corroded. The marks appeared to be less defined due to the corroded surface.

These observations are consistent with the observations from the previous specimen. The observations from both specimens from the featureless segment of Upper Zone 2 confirmed that the featureless segment was a result of erosion-corrosion produced by the high-pressure gas release after the axial rupture. The erosion marks are fine, with sizes on an order of magnitude less than 8  $\mu\text{m}$ , which is not visible to the naked eye. Therefore, the surface morphology of the segment appeared to be smooth and featureless. These findings are consistent with the log interpretation in Section 2.2.7, which identified erosion features.

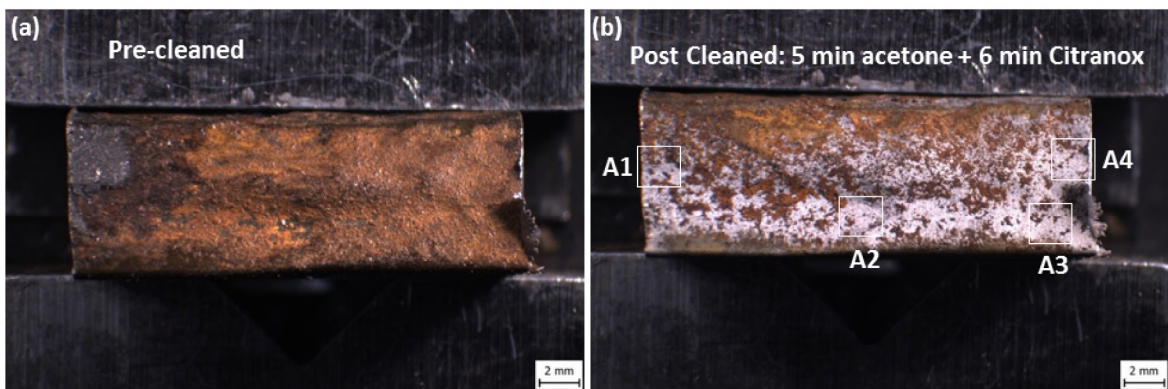


Figure 127: Specimen C023A1A1B1C (a) Before and (b) After Cleaning

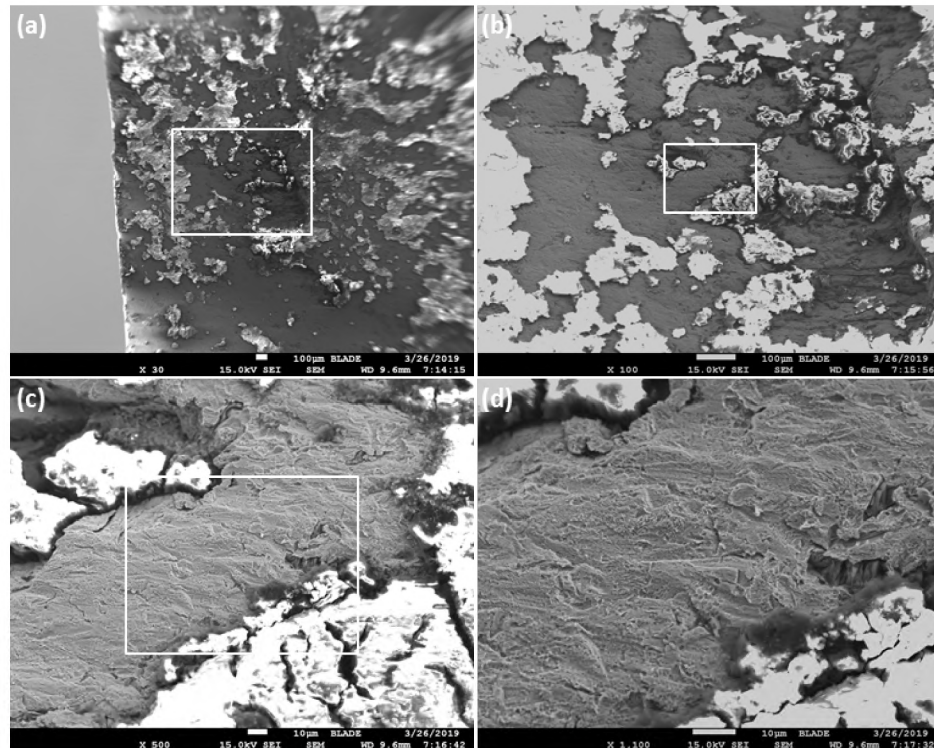


Figure 128: SEM Images of A1 Erosion Marks Taken at (a) 30 $\times$ , (b) 100 $\times$ , (c) 500 $\times$ , and (d) 1,100 $\times$

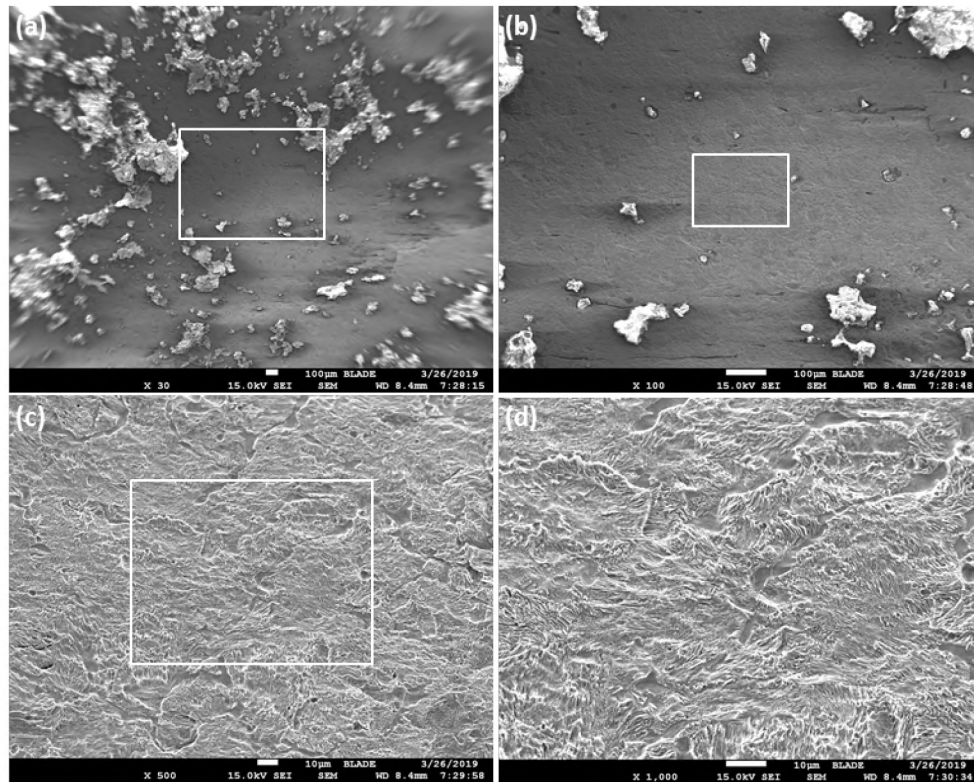


Figure 129: SEM Images of A2 Erosion Marks Taken at (a) 30×, (b) 100×, (c) 500×, and (d) 1,000×

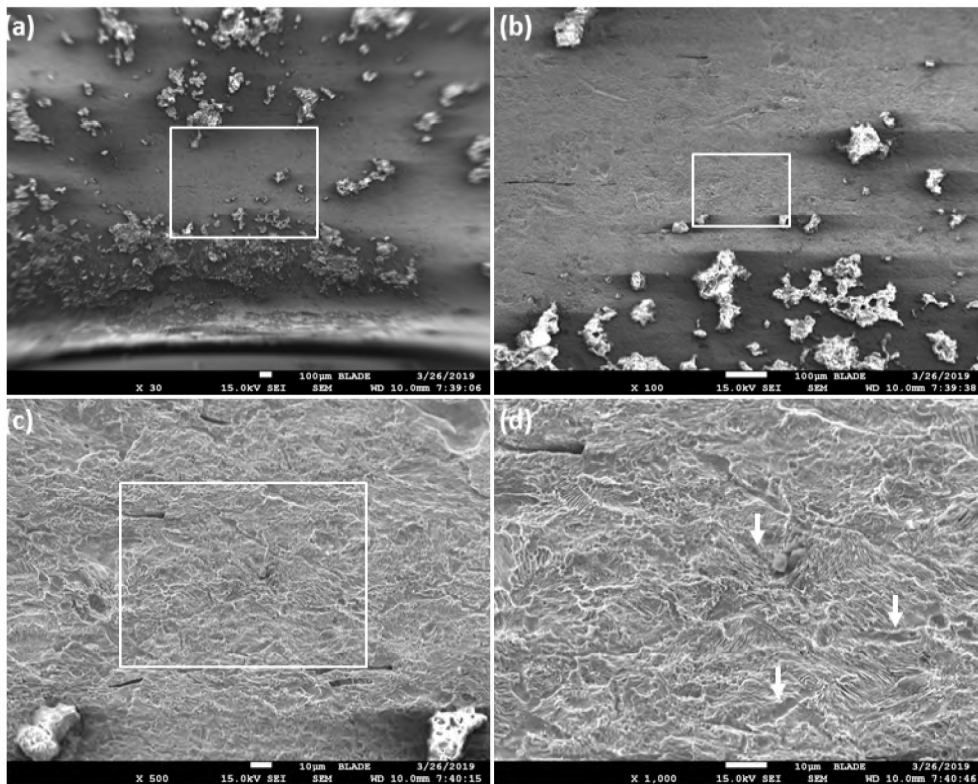


Figure 130: SEM Images of A3 Erosion Marks Taken at (a) 30×, (b) 100×, (c) 500×, and (d) 1,000×

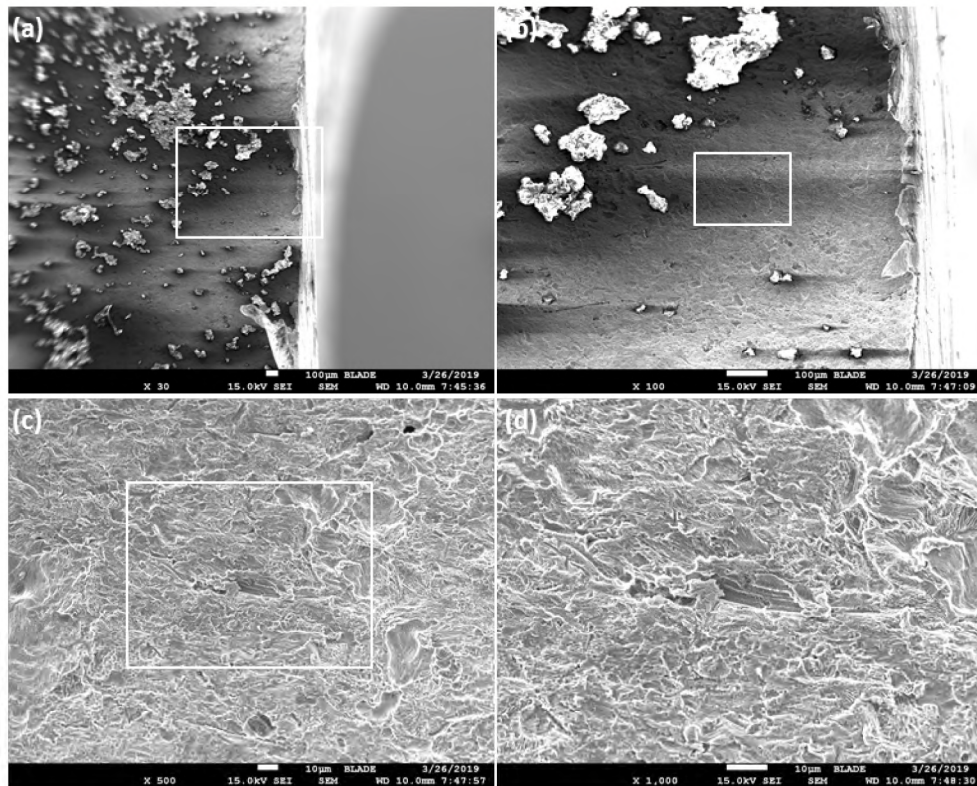


Figure 131: SEM Images of A4 Erosion Marks Taken at (a) 30 $\times$ , (b) 100 $\times$ , (c) 500 $\times$ , and (d) 1,000 $\times$

### 3.2.6 Micro-Fractographic Characterization of Zone 3 (Crack Arrest)

Zone 3 contained the upper and lower crack arrest points. Zone 3 was divided into two areas identified as Lower and Upper Zone 3, similar to what was done for Zone 2. Lower Zone 3 represents the arrest region below Zone 1 (origin) and Upper Zone 3 represents the arrest region above Zone 1. The lower arrest point occurred after the crack underwent two directional changes (first and second lower turning points) due to energy dissipation and changes in stress state. The same sequence occurred with the upper arrest point. The lower arrest point was slightly past the second turning point, whereas the upper arrest point was approximately 2 in. beyond the second upper turning point. The difference in extension can be explained by a difference in constraint between the two locations. The lower arrest point was adjacent to connection 22, which provided additional constraint. The upper arrest point was approximately 2 ft from the lower arrest point in the pipe body. The pipe body provided less constraint as compared to the area adjacent to the connection.

The lower arrest region is presented first. Characterization of Lower Zone 3 included the fracture surface from the lower turning point to the lower arrest point. Specimen C023A1B2E was selected for a detailed SEM investigation of the lower arrest region. The specimen was cut into smaller specimens due to the size limitations imposed by the SEM chamber. Figure 132 shows the cut locations for specimen C023A1B2E. Specimen C023A1B2E2A was examined with the SEM. The specimen contained the lower turning point, second lower turning point, and lower arrest point. All three areas were investigated as part of the Lower Zone 3 characterization. Figure 133 shows SEM images of C023A1B2E2A (a) before and (b) after cleaning. The specimen was ultrasonically cleaned with acetone for 6 minutes followed by a 1% Citranox solution for 6 minutes. Chevron marks were visible after cleaning, and this is consistent with the Upper Zone 3 observations.

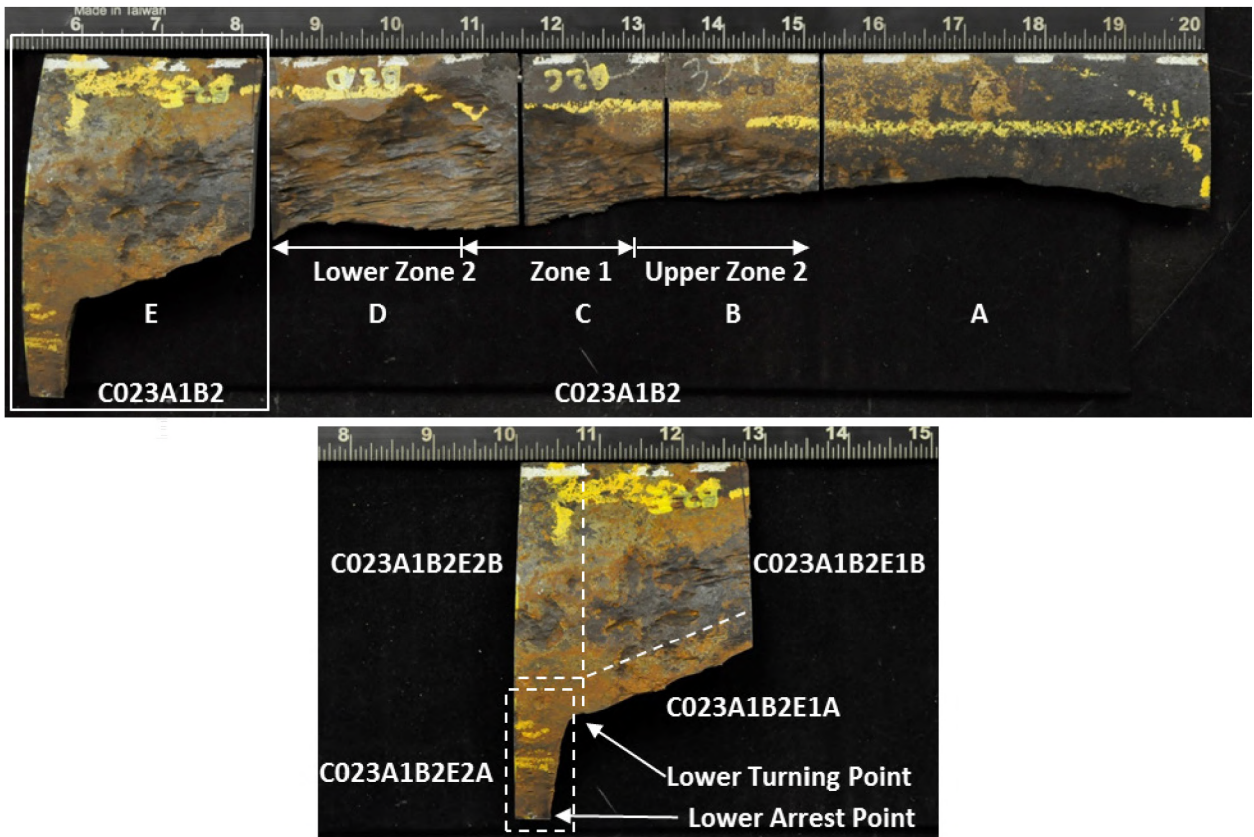


Figure 132: Specimen C023A1B2E2A Extracted from C023A1B2E

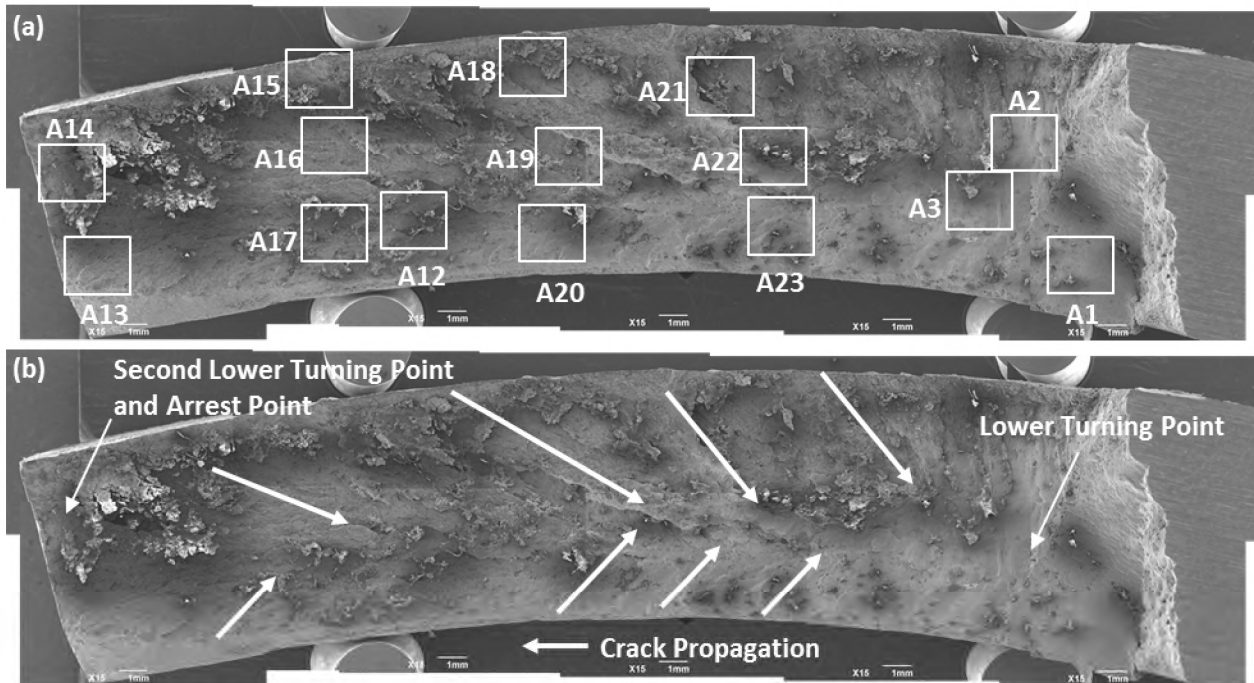


Figure 133: SEM Images of C023A1B2E2A (a) Before and (b) After Cleaning

Several areas were investigated with the SEM (Figure 133). Figure 134 through Figure 136 show SEM images of A1–A3, located at the lower turning point. The fracture surface appeared to be relatively smooth and flat at low magnifications but faceted with some deformation marks when viewed at higher magnifications. Typical cleavage facets were not observed. This observation could be due to the fact that the original cleavage structure had been corroded away.

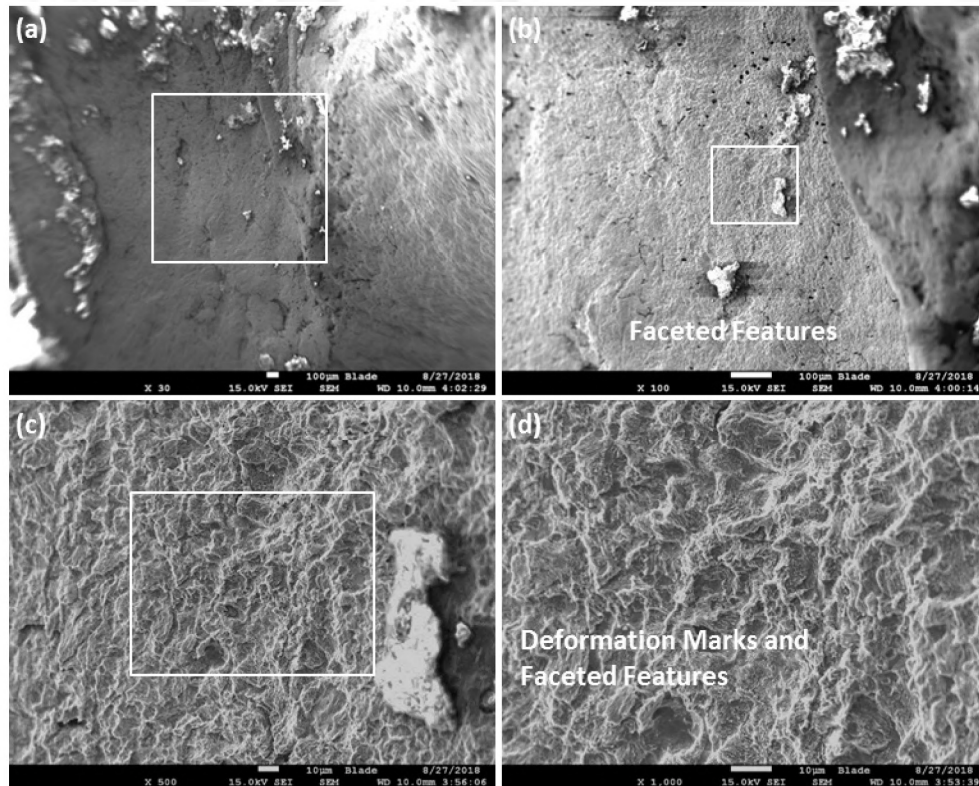


Figure 134: SEM Images of C023A1B2E2A A2 Taken at (a) 30 $\times$ , (b) 100 $\times$ , (c) 500 $\times$ , and (d) 1,000 $\times$

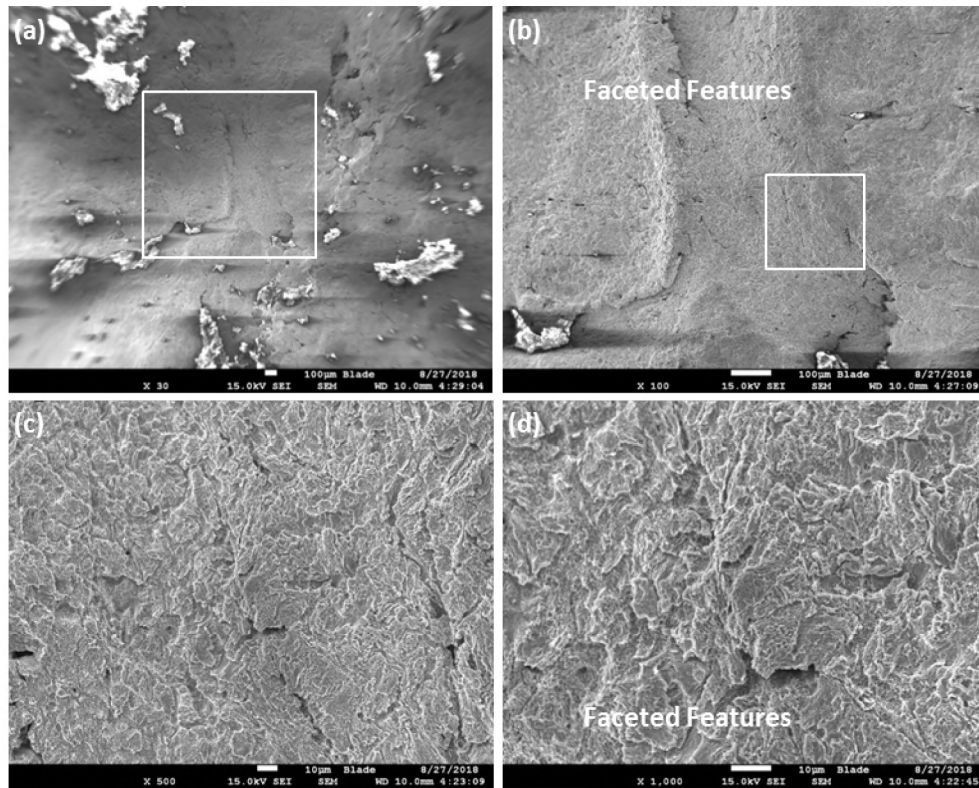


Figure 135: SEM Images of C023A1B2E2A A3 Taken at (a) 30×, (b) 100×, (c) 500×, and (d) 1,000×

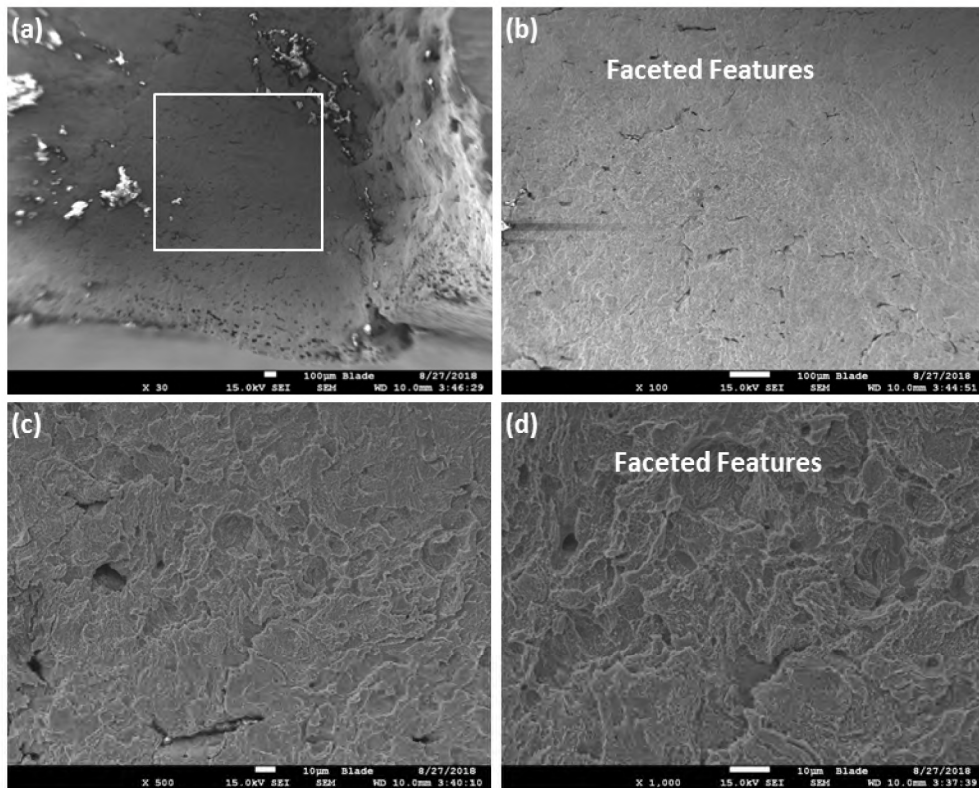


Figure 136: SEM Images of C023A1B2E2A A1 Taken at (a) 30×, (b) 100×, (c) 500×, and (d) 1,000×

Figure 137 through Figure 139 show SEM images of A18–A20, which are from the mid-section between the lower turning point and arrest area. The fracture surface appears to be relatively smooth and flat at low magnifications. The fracture surface appears to contain faceted features and small amounts of cleavage at higher magnifications. The OD side of the fracture surface contains microvoids that were associated with inclusions (and confirmed with EDS). The MW and ID fracture surfaces did not contain similar microvoids. The cause for this difference is unclear.

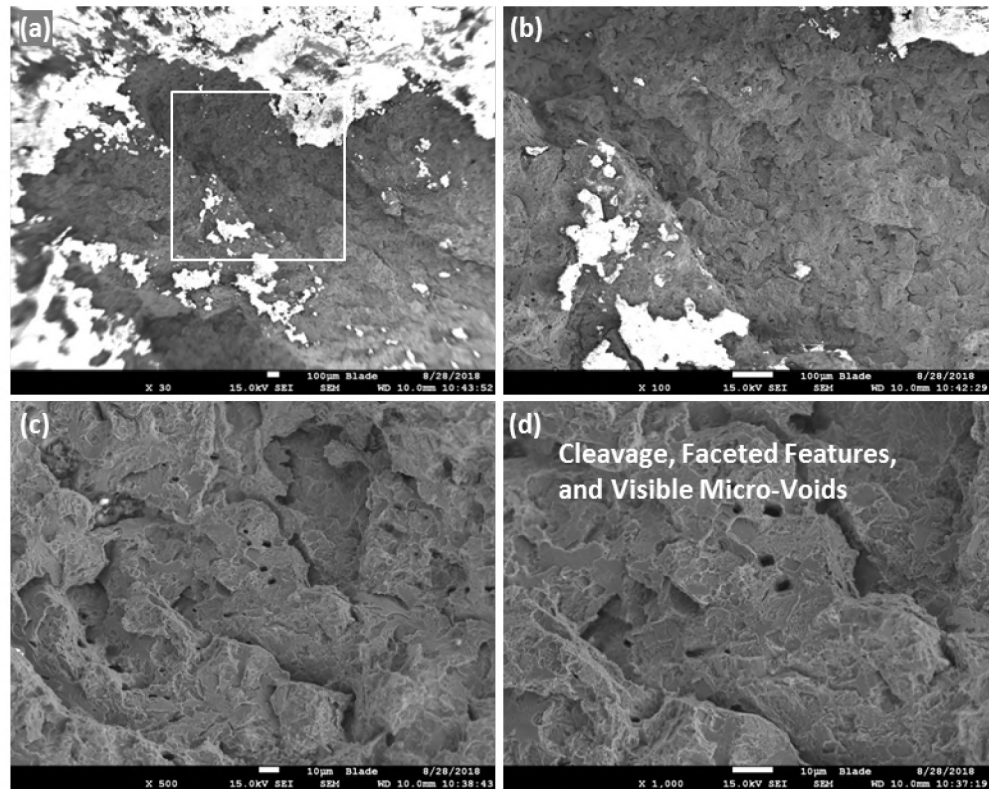


Figure 137: SEM Images of C023A1B2E2A A18 Taken at (a) 30×, (b) 100×, (c) 500×, and (d) 1,000×



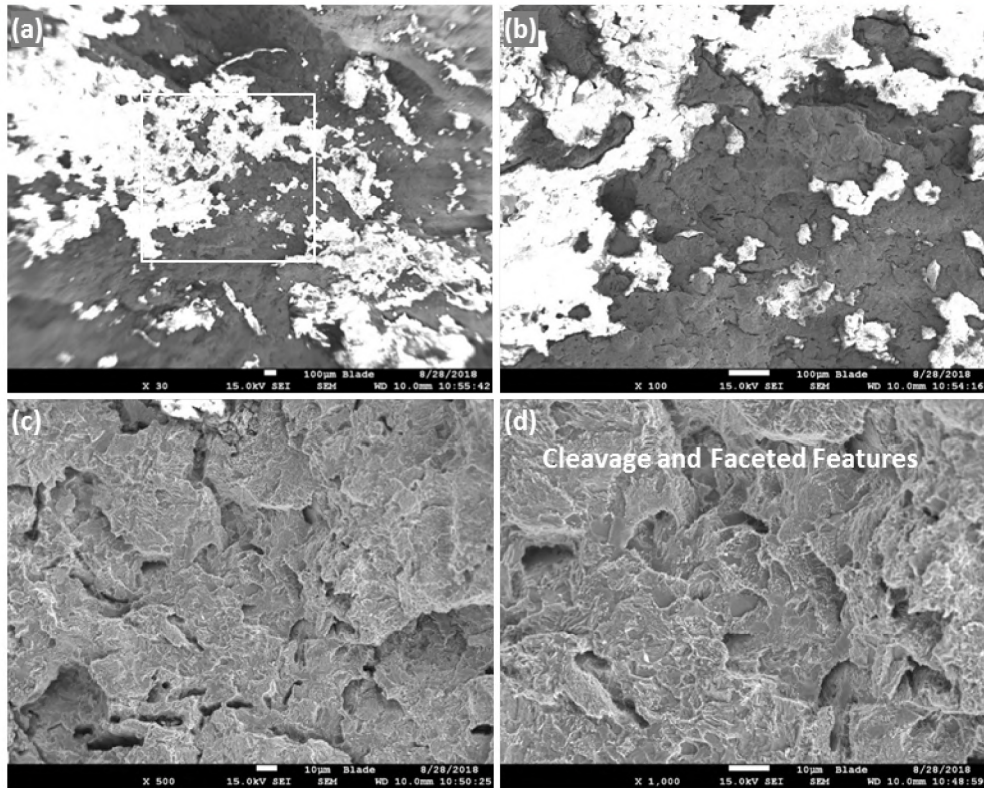


Figure 138: SEM Images of C023A1B2E2A A19 Taken at (a) 30×, (b) 100×, (c) 500×, and (d) 1,000×

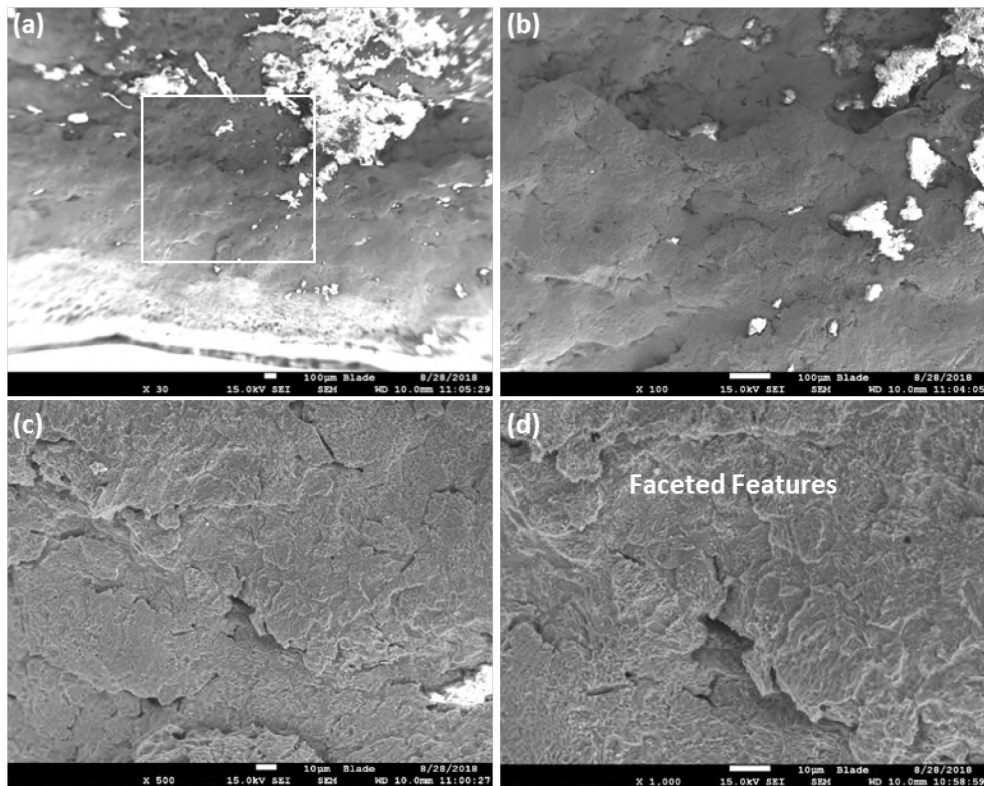


Figure 139: SEM Images of C023A1B2E2A A20 Taken at (a) 30×, (b) 100×, (c) 500×, and (d) 1,000×

Figure 140 and Figure 141 show SEM images of A13 and A14. The fracture surface also appears relatively smooth and flat at low magnifications. The fracture surface appears to contain faceted features and cleavage at higher magnifications. The OD fracture surface contains microvoids that were associated with inclusions (confirmed with EDS). The MW and ID fracture surfaces did not contain similar microvoids. The cause for this difference is unclear.

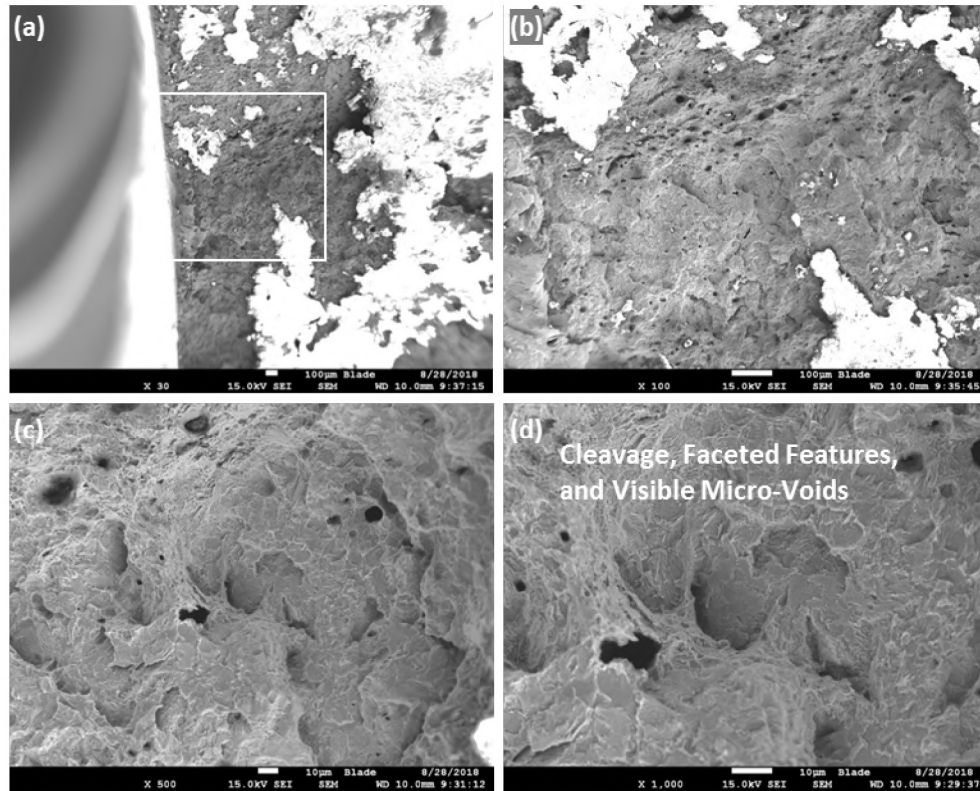
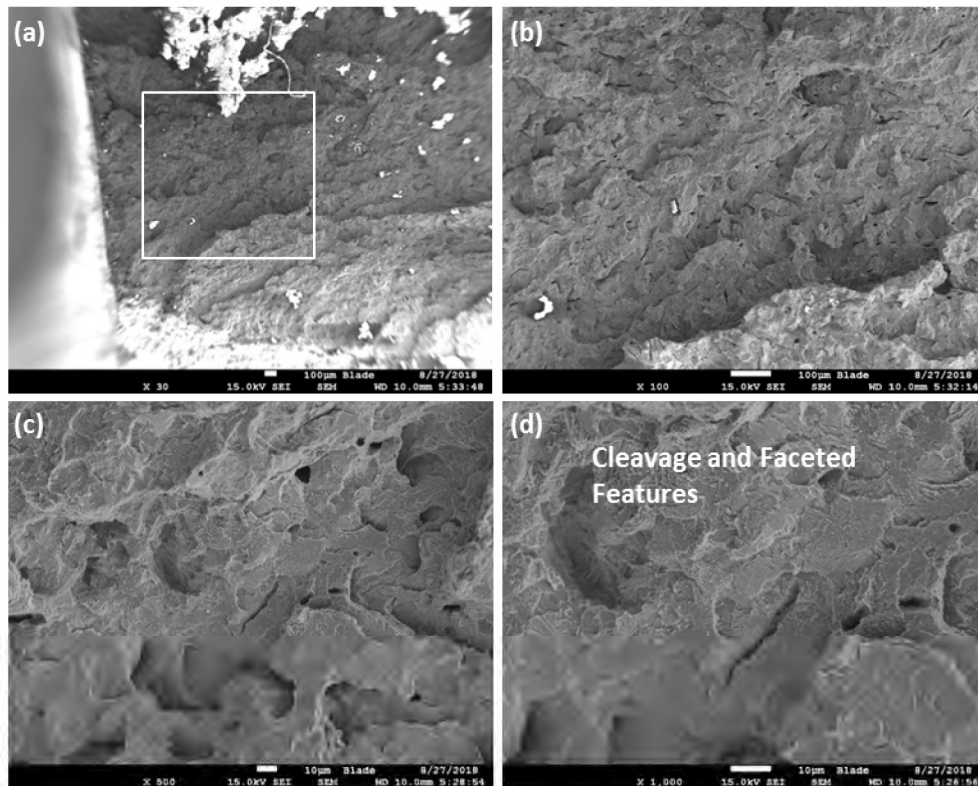


Figure 140: SEM Images of C023A1B2E2A A14 Taken at (a) 30×, (b) 100×, (c) 500×, and (d) 1,000×



**Figure 141: SEM Images of C023A1B2E2A A13 Taken at (a) 30 $\times$ , (b) 100 $\times$ , (c) 500 $\times$ , and (d) 1,000 $\times$**

The fracture surface morphology in the region between the lower turning point and the arrest point (Lower Zone 3) is different from Zone 2. The fracture surface appeared to have less cleavage separation and more faceted features and microvoids. The reason for this difference may be associated with a change in crack propagation speed.

Upper Zone 3 was also investigated with the SEM, and it contained an area between the second upper turning point and crack arrest region. Both areas were included in the Zone 3 characterization. Procedures similar to the ones used for Lower Zone 3 were used during the investigation of Upper Zone 3.

Figure 142 (a) shows the extraction location for specimen C023A1A1B4 and (b) shows specimen C023A1A1B4 after extraction. Specimen C023A1A1B4 contained the second upper turning point and upper arrest point. The upper arrest point was defined on C023A1A1B4 by a slight angle change on the inclined surface. Figure 142 (c) shows the mating surface to C023A1A1B4. The arrest location on the mating surface was clearly defined by the paths of the axial and circumferential fractures.

Specimen C023A1A1B4 was ultrasonically cleaned with acetone for 6 minutes followed by 6 minutes in 1% Citranox. Two segments of Upper Zone 3 were examined with the SEM. The first segment contained the upper arrest region. Areas were selected to examine the fracture surface above, below, and near the upper arrest region to identify any change in fracture surface characteristics. Figure 143 (a) shows specimen C023A1A1B4 and the first segment for examination (white box). Figure 143 (b) shows the areas selected for SEM examination of the first segment. The second segment contained the fracture surface between the first and second upper turning points. This segment was examined for comparison with Lower Zone 3. Figure 147 (a) shows specimen C023A1A1B4 and the second segment for examination (white box). Figure 147 (b) shows the areas selected for SEM examination of the second segment.

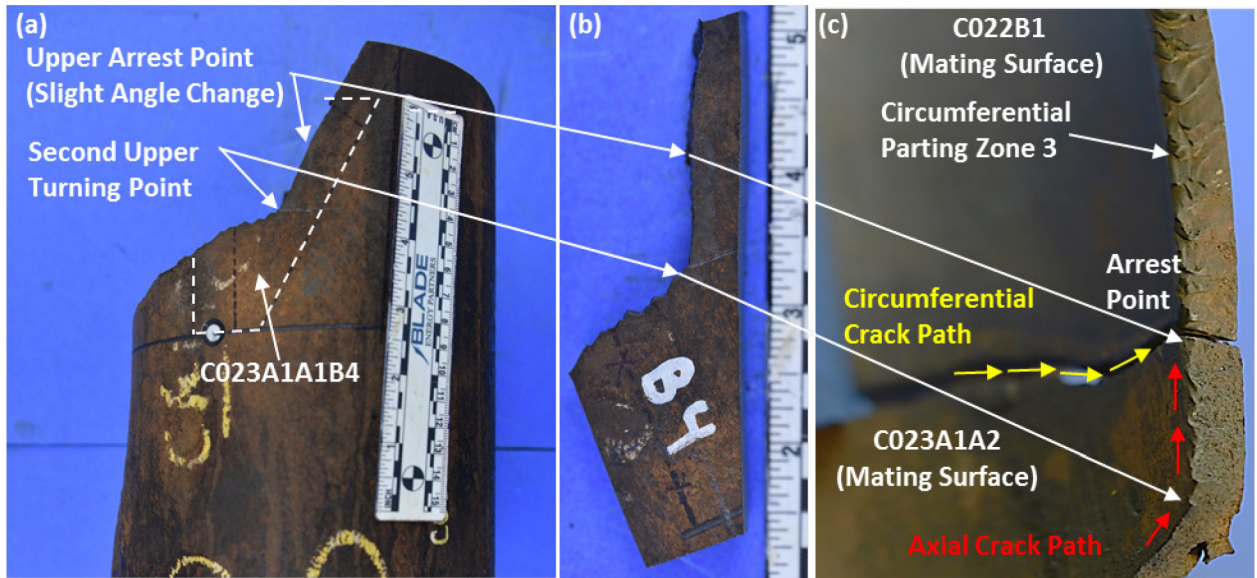


Figure 142: Specimen C023A1A1B4 Extraction

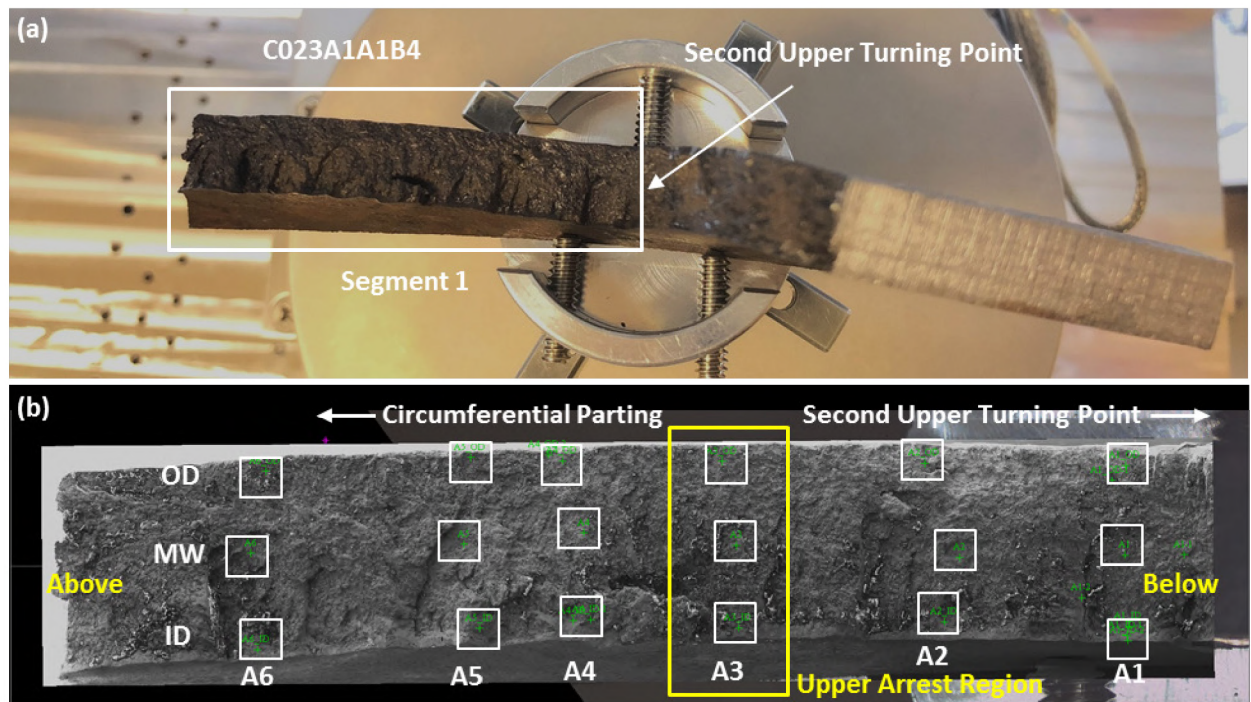


Figure 143: Specimen C023A1A1B4 Showing SEM Locations Near Upper Arrest Region

Figure 144 through Figure 146 show SEM images from areas above (A4), below (A2), and near (A3) the arrest region. The OD, MW, and ID of Area A4 (above arrest region) contained mostly cleavage features. The OD and MW of Area A2 (below arrest region) contained mostly cleavage features while the ID contained deformation marks. The OD of Area A3 (arrest region) contained some faceted features. The MW and ID appeared ductile and did not contain cleavage. The observations show a clear transition between A2 and A4, with A3 representing the arrest region, which is most likely associated with a change in crack propagation speed.

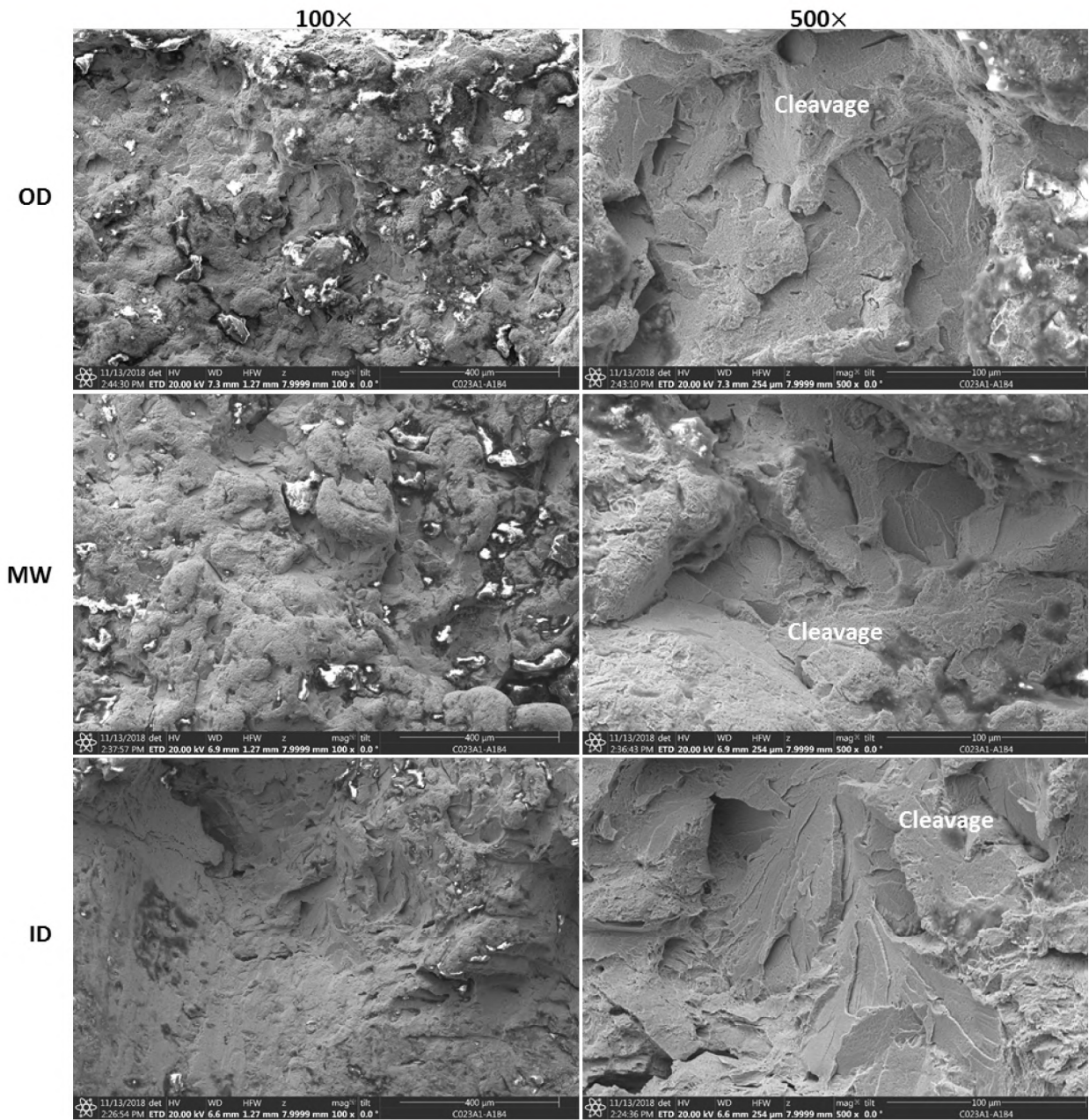


Figure 144: Specimen C023A1A1B4 A4 Showing OD, MW, and ID at 100× and 500×

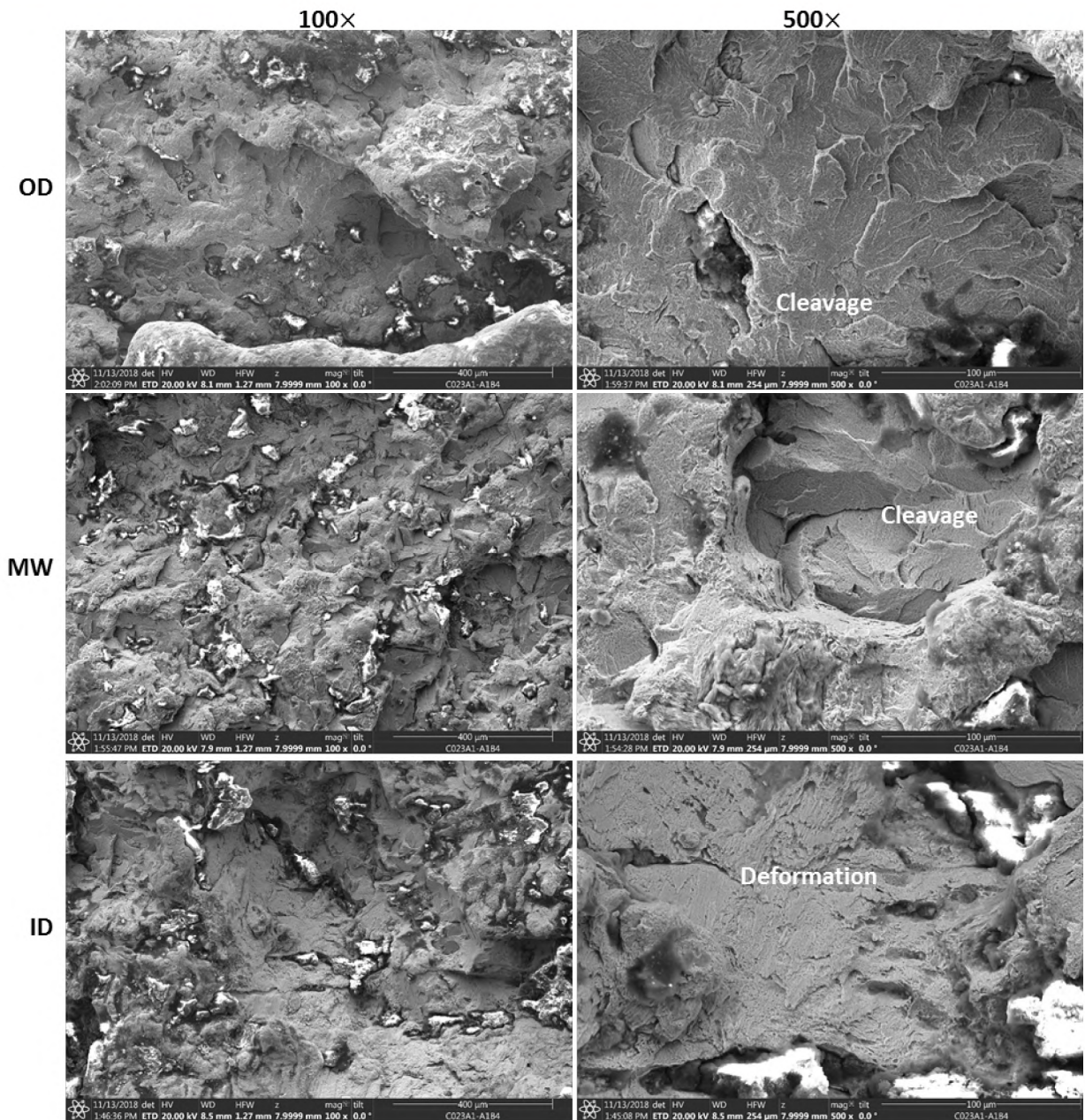


Figure 145: Specimen C023A1A1B4 A2 Showing OD, MW, and ID at 100x and 500x

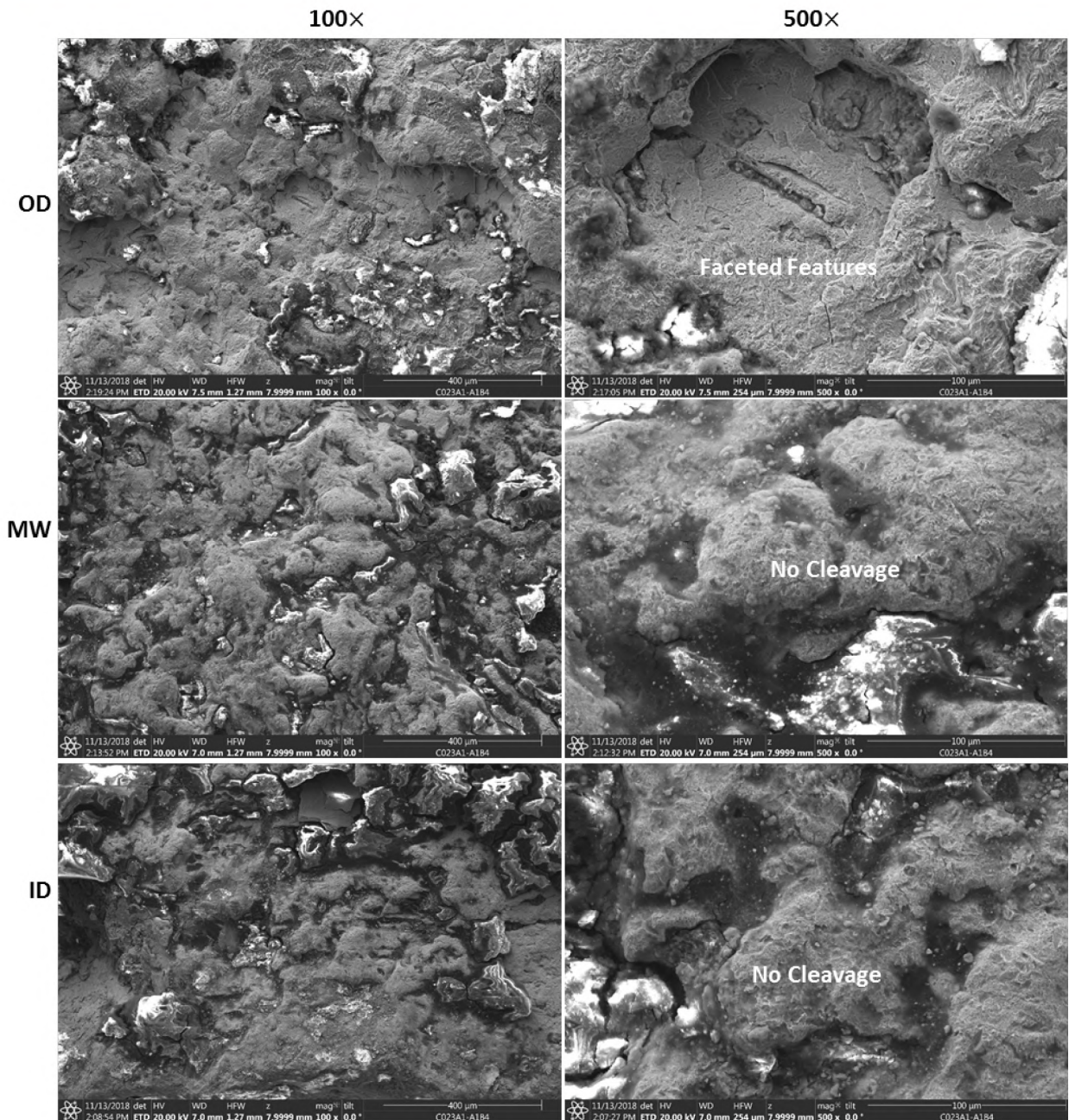
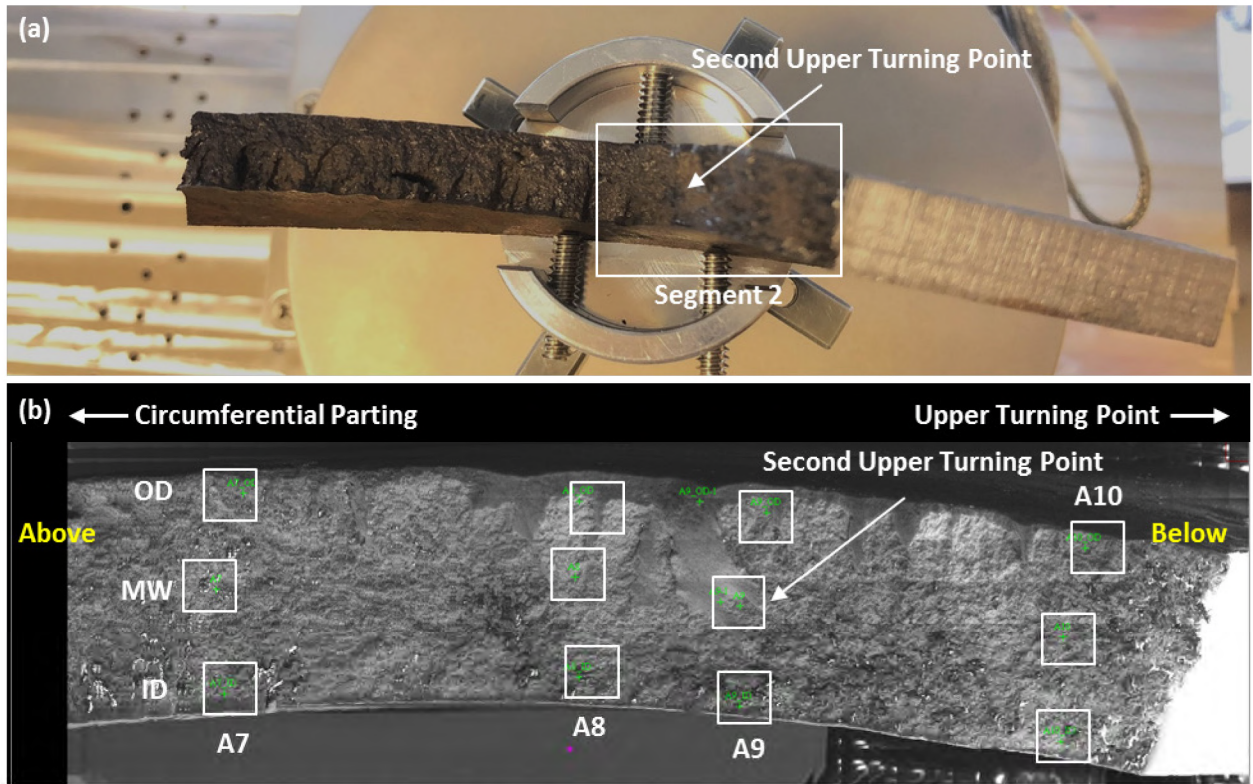


Figure 146: Specimen C023A1A1B4 A3 Showing OD, MW, and ID at 100x and 500x



**Figure 147: Specimen C023A1A1B4 Showing SEM Locations at the Second Upper Turning Point**

Figure 148 through Figure 150 show SEM images of the OD, MW, and ID for A7, respectively. Area A7 was located between the first and second upper turning points. The fracture surface appears relatively rough on the OD side as compared to the ID. The OD fracture surface was composed of mixed cleavage facets with deformation marks (Figure 148). The MW and ID fracture surfaces were predominantly cleavage separation when viewed at higher magnifications (Figure 149 and Figure 150).



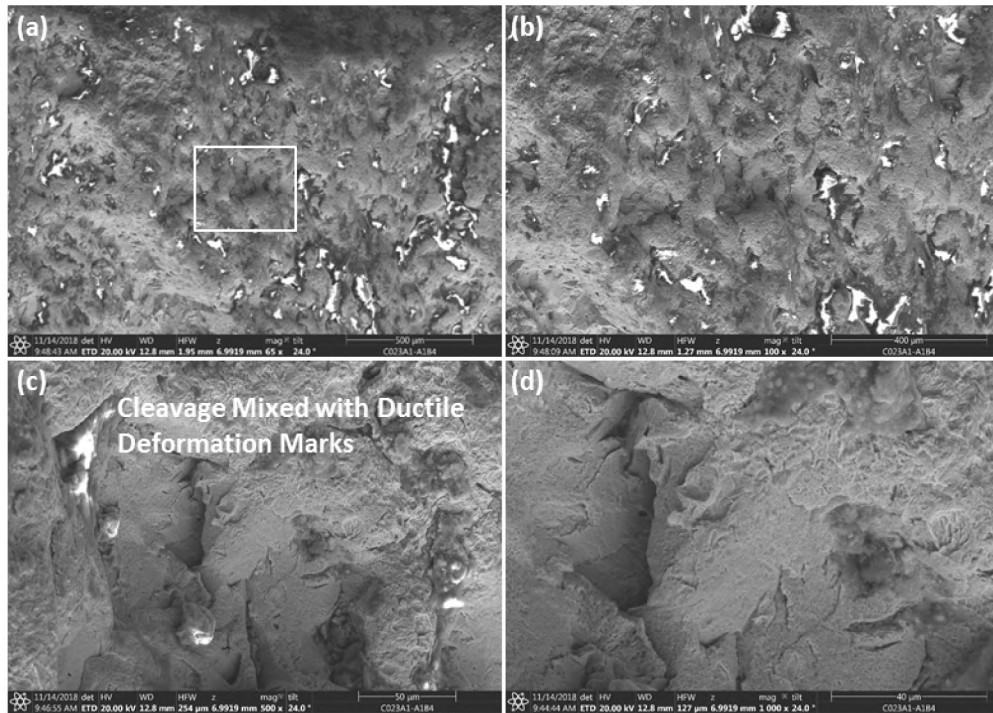


Figure 148: SEM Images of C023A1A1B4 A7 OD Taken at (a) 30 $\times$ , (b) 100 $\times$ , (c) 500 $\times$ , and (d) 1,000 $\times$

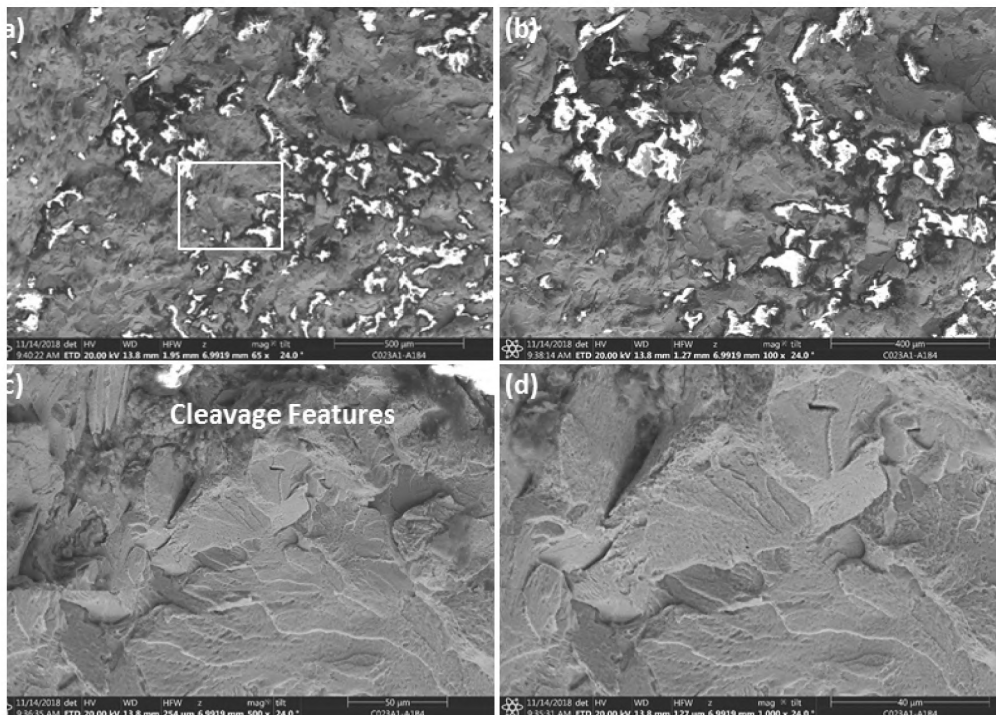
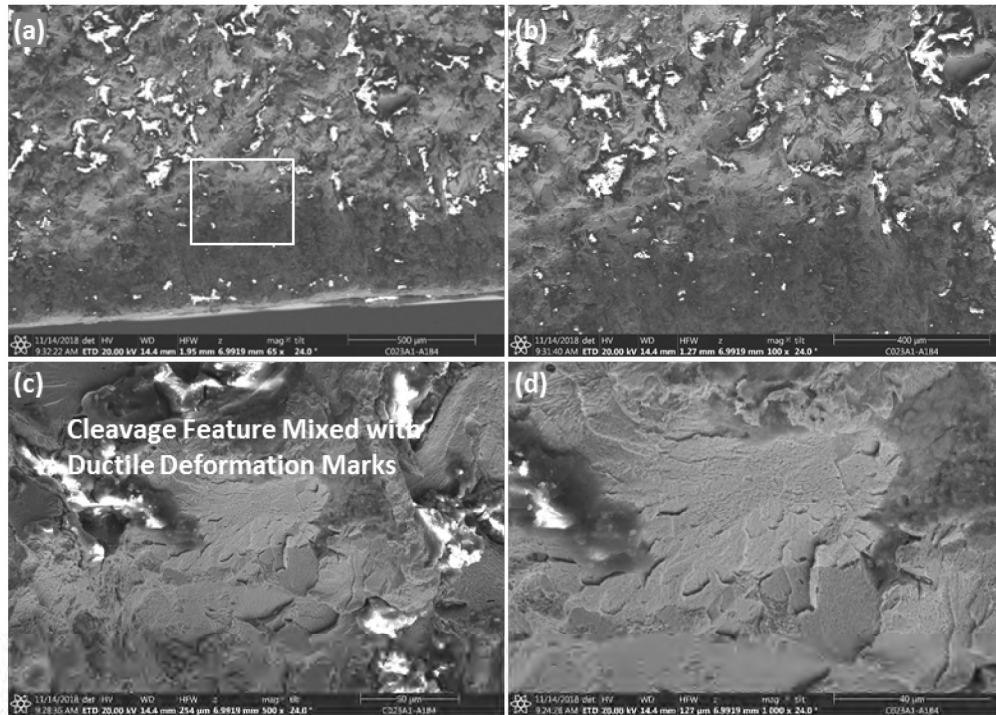


Figure 149: SEM Images of C023A1A1B4 A7 MW Taken at (a) 30 $\times$ , (b) 100 $\times$ , (c) 500 $\times$ , and (d) 1,000 $\times$



**Figure 150: SEM Images of C023A1A1B4 A7 ID Taken at (a) 30 $\times$ , (b) 100 $\times$ , (c) 500 $\times$ , and (d) 1,000 $\times$**

Figure 151 through Figure 155 show SEM images of the OD, MW, and ID of Area A9. Area A9 was located at the second upper turning point. The OD fracture surface appeared relatively rough (Figure 151 and Figure 152) and was a mix of small amounts of cleavage facets and deformation marks. Similar fracture surface morphology was observed in the MW (Figure 153); some erosion marks were also observed (Figure 154). The ID fracture surface contained more cleavage separation (Figure 155).

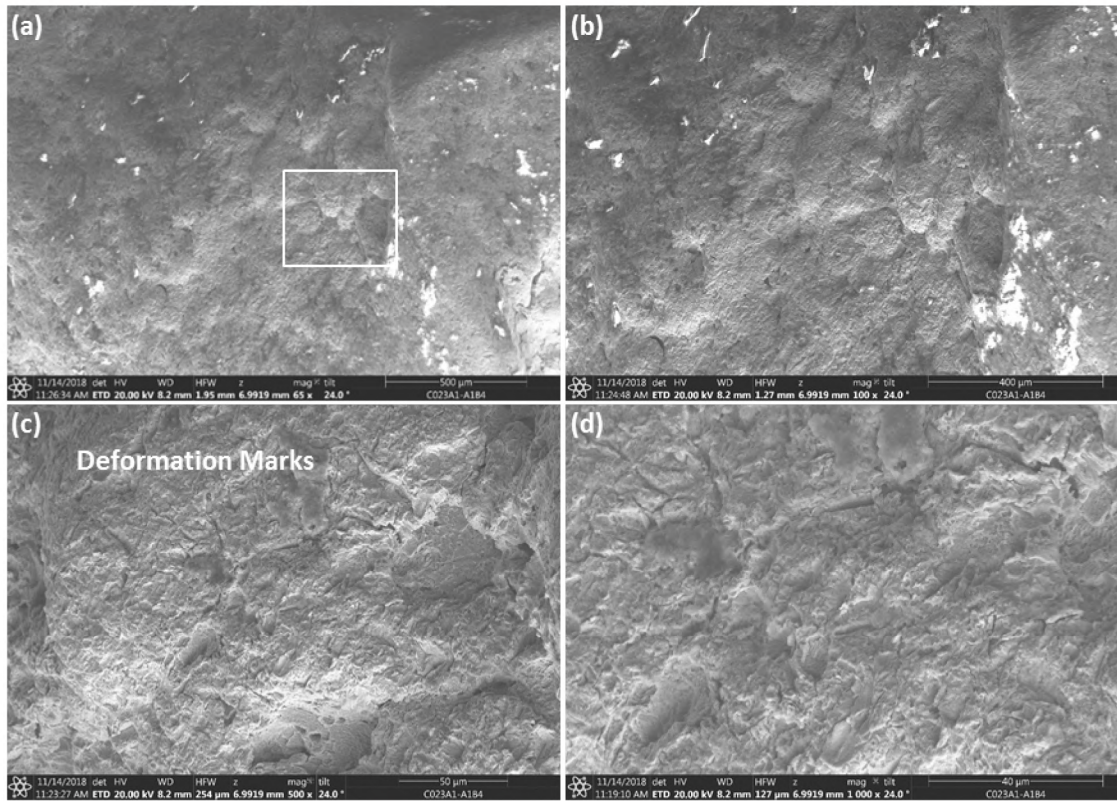


Figure 151: SEM Images of C023A1A1B4 A9 OD Taken at (a) 30×, (b) 100×, (c) 500×, and (d) 1,000×

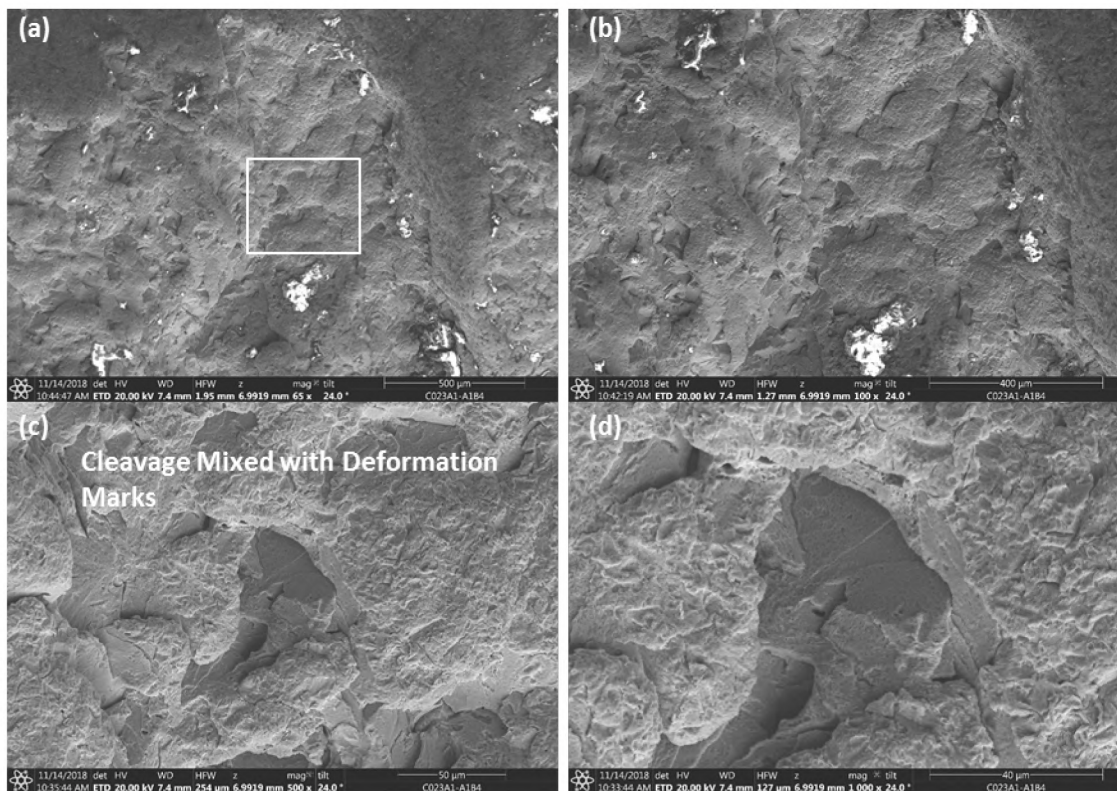


Figure 152: SEM Images of C023A1A1B4 A9 OD-2 Taken at (a) 30×, (b) 100×, (c) 500×, and (d) 1,000×

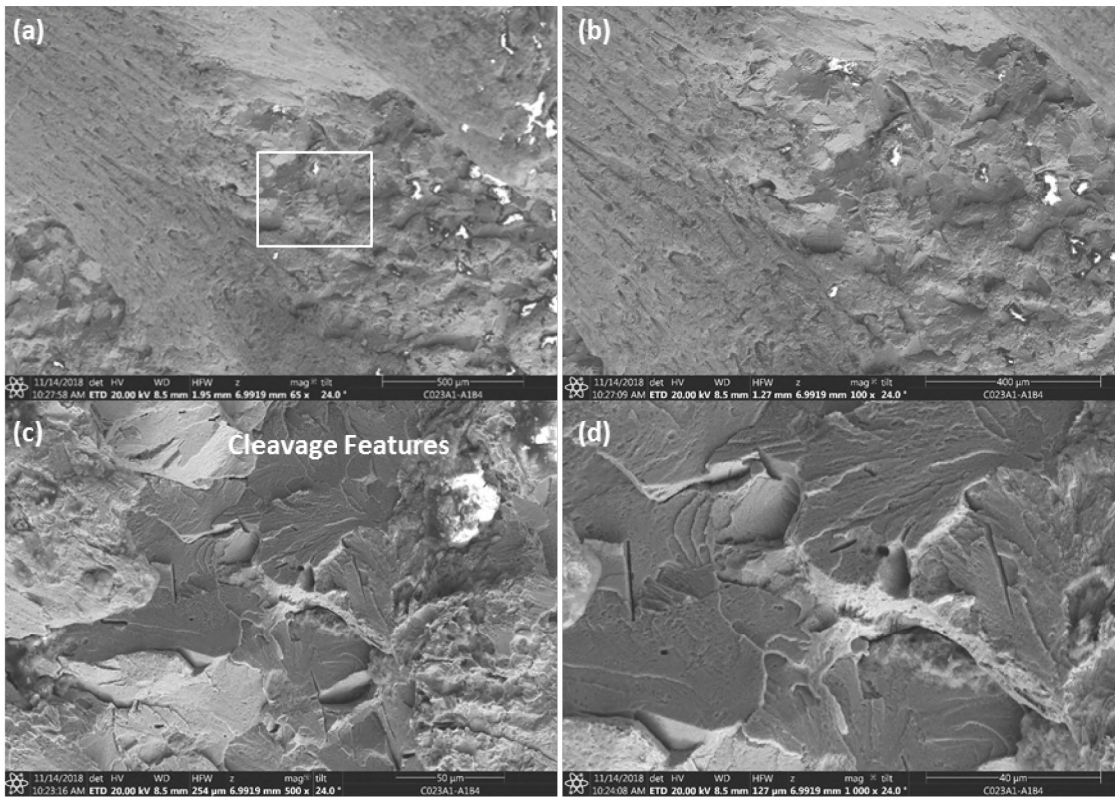


Figure 153: SEM Images of C023A1A1B4 A9 MW Taken at (a) 30×, (b) 100×, (c) 500×, and (d) 1,000×

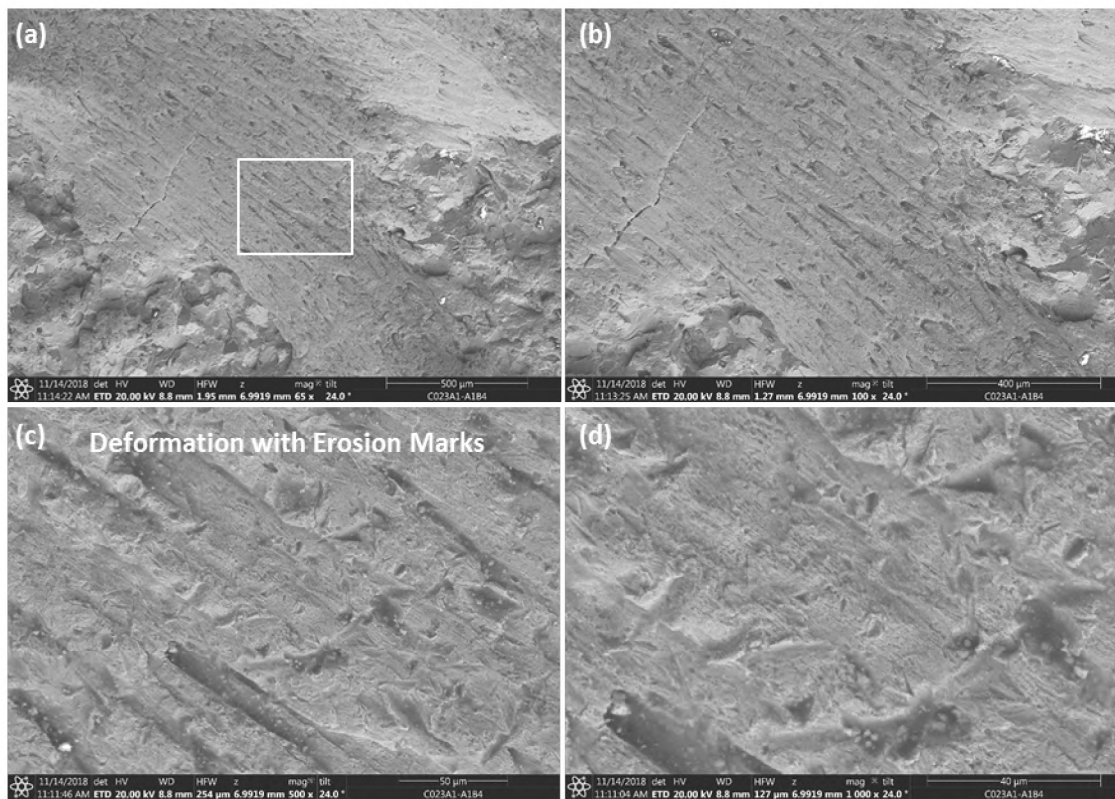
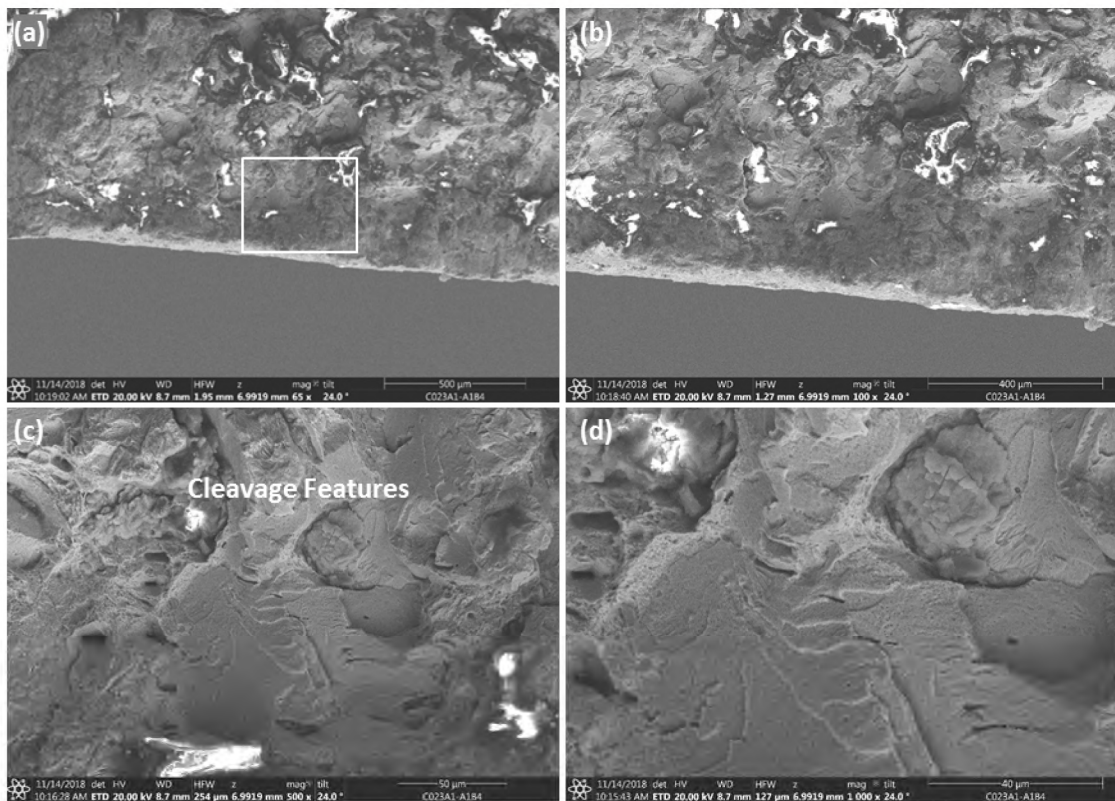


Figure 154: SEM Images of C023A1A1B4 A9 MW-2 Taken at (a) 30×, (b) 100×, (c) 500×, and (d) 1,000×



**Figure 155: SEM Images of C023A1A1B4 A9 ID Taken at (a) 30 $\times$ , (b) 100 $\times$ , (c) 500 $\times$ , and (d) 1,000 $\times$**

Figure 156 through Figure 158 show SEM images of the OD, MW, and ID of Area A10, respectively. Area A10 was located above the second upper turning point towards the upper arrest region. There was no resolvable difference in surface roughness between the OD and ID. The micro-fractographic morphology is similarly composed of mixed cleavage facets with deformation marks. More cleavage separation was observed at the MW and ID areas (Figure 157 and Figure 158).

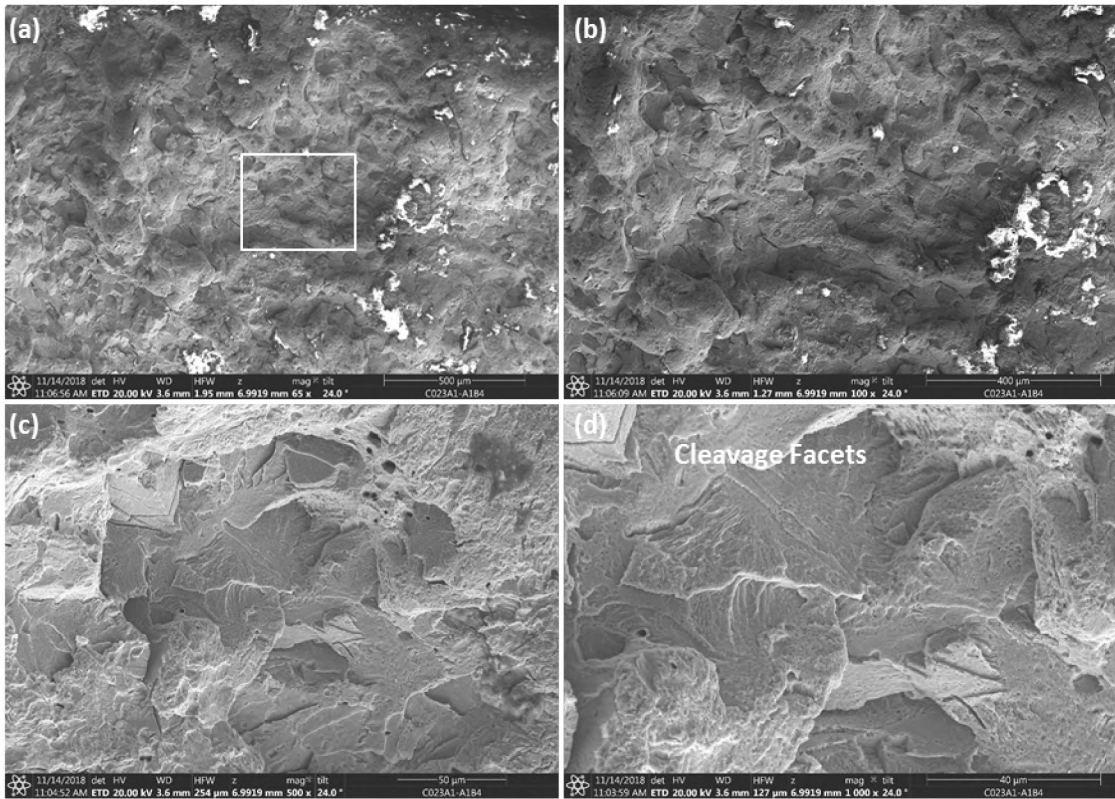


Figure 156: SEM Images of C023A1A1B4 A10 OD Taken at (a) 30×, (b) 100×, (c) 500×, and (d) 1,000×

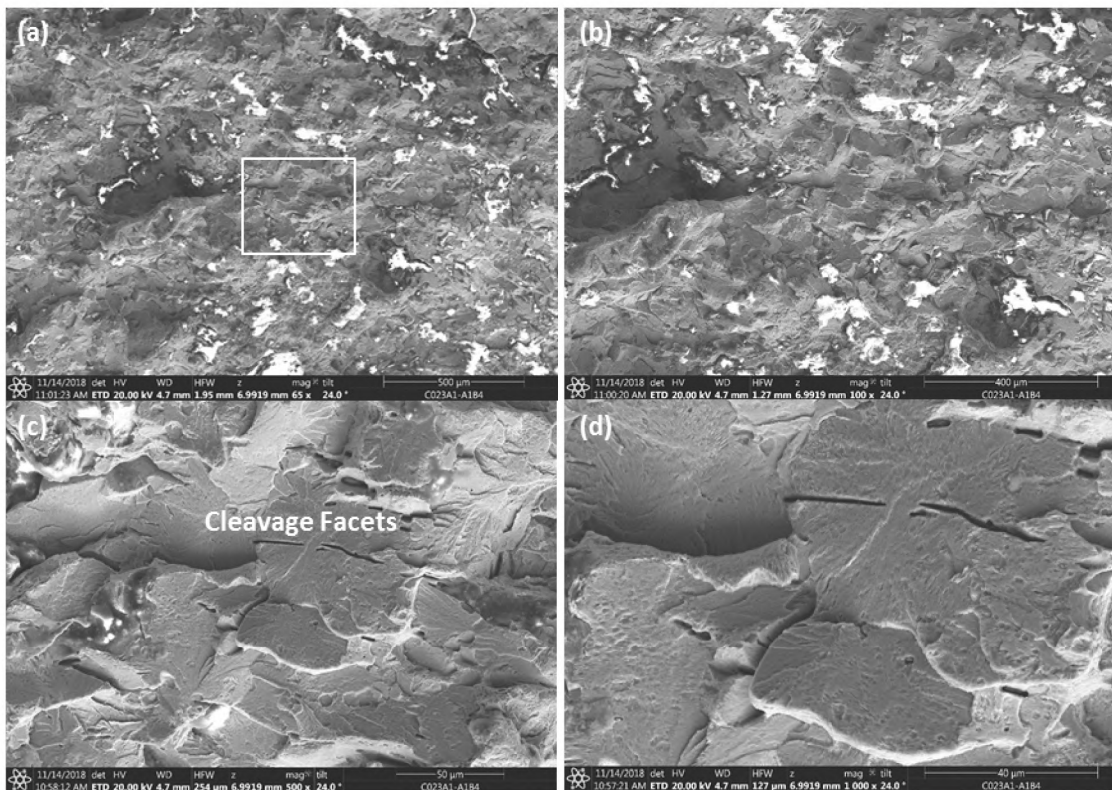


Figure 157: SEM Images of C023A1A1B4 A10 MW Taken at (a) 30×, (b) 100×, (c) 500×, and (d) 1,000×

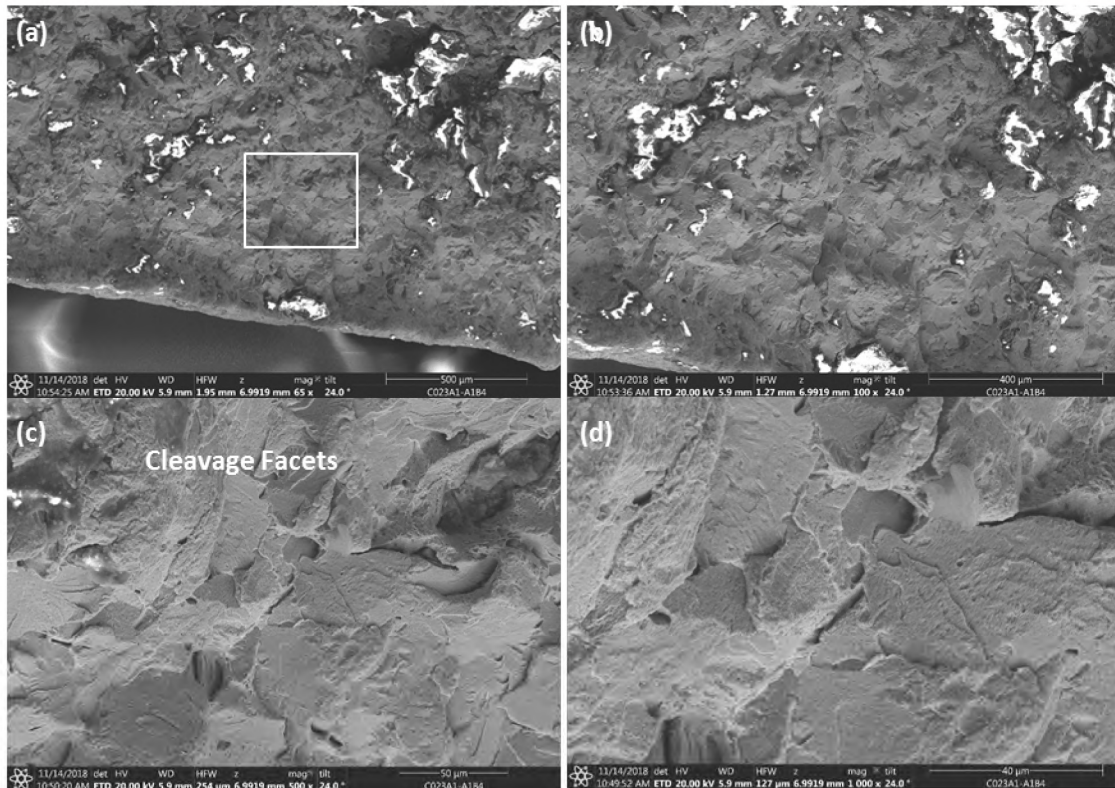


Figure 158: SEM Images of C023A1A1B4 A10 ID Taken at (a) 30 $\times$ , (b) 100 $\times$ , (c) 500 $\times$ , and (d) 1,000 $\times$

The micro-fractographic morphology observed in the area adjacent to the second upper turning point consisted of cleavage facets and deformation marks. The OD fracture surface appeared rougher than the ID side, and this is consistent with more ductile deformation. There is no clear evidence of faceted features as observed at the lower arrest area.

### 3.3 Initiation and Propagation of the Circumferential Parting

In this section, the circumferential parting is investigated in detail. The approach used for the investigation was similar to the one used for the axial rupture. It included visual (macro) and stereo microscopic examination and SEM characterization of the fracture surface and micro mechanism for cracking.

#### 3.3.1 Visual and Stereoscopic Examination

The circumferential parting produced two mated fracture surfaces identified as the lower and upper fracture surfaces. The upper circumferential parting was extracted first. A short length of the pipe was extracted from C022 and examined at the on-site lab. The extracted section was designated as C022B. The lower circumferential parting was fished out of the SS-25 well with a pawl tool. A short section containing the axial rupture, circumferential parting, and connection 22 was extracted from C023A and designated as C023A1. Section C023A1 was shipped to the warehouse for further visual examination. Section 2.2.6 discusses the extraction of the upper and lower circumferential parting.

The upper fracture surface was facing down after the parting; it had been severely eroded by the high-pressure gas that had escaped from the reservoir. The lower fracture surface was facing up during the blowout and appeared to be well preserved. Figure 159 (a) shows the lower and upper fracture

surfaces during the examination. The specimens are oriented in the same position as they were in the well. The pointed section of C022B was identified as the south-facing side of the pipe on the rig floor. Figure 159 (b) shows the erosion to the upper fracture surface. Remnants of chevron marks were visible in some areas of the fracture surface. Most of the surface appeared to be smooth and featureless. Figure 159 (c) shows the condition of the lower fracture surface during the examination. The chevron marks are more visible and well defined when compared to the upper fracture surface. The lower fracture surface had no indications of erosion. It was later confirmed by stereo and SEM examinations that erosion was not present.

The following three fracture zones were identified during the visual and stereoscopic examination of the circumferential parting:

- Zone 1: Origin (initiation site) of circumferential parting
- Zone 2: Crack propagation
- Zone 3: Final overload failure of the remaining ligament

Figure 160 illustrates the three zones of the circumferential parting. Figure 160 (a) is a close-up image of the lower circumferential parting with the three fracture zones identified. Figure 160 (b) is a schematic showing the location of the three zones and the crack propagation direction. Figure 160 (c) is a close-up image of the Zone 3 fracture surface.

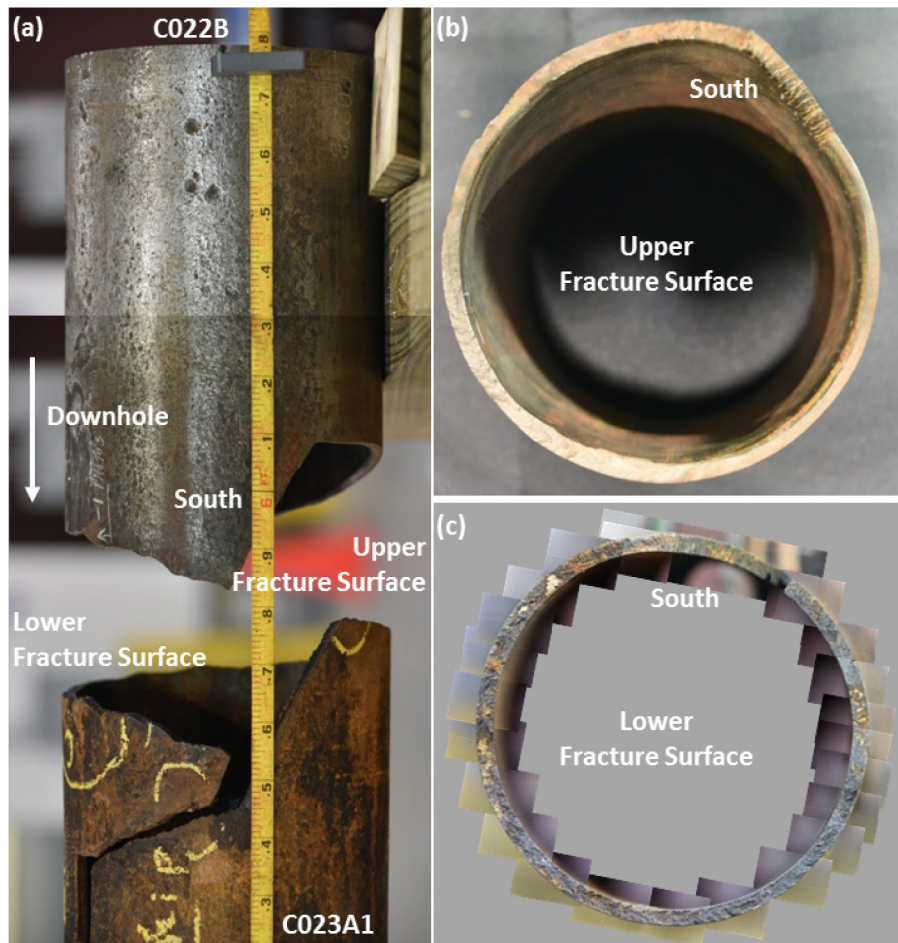
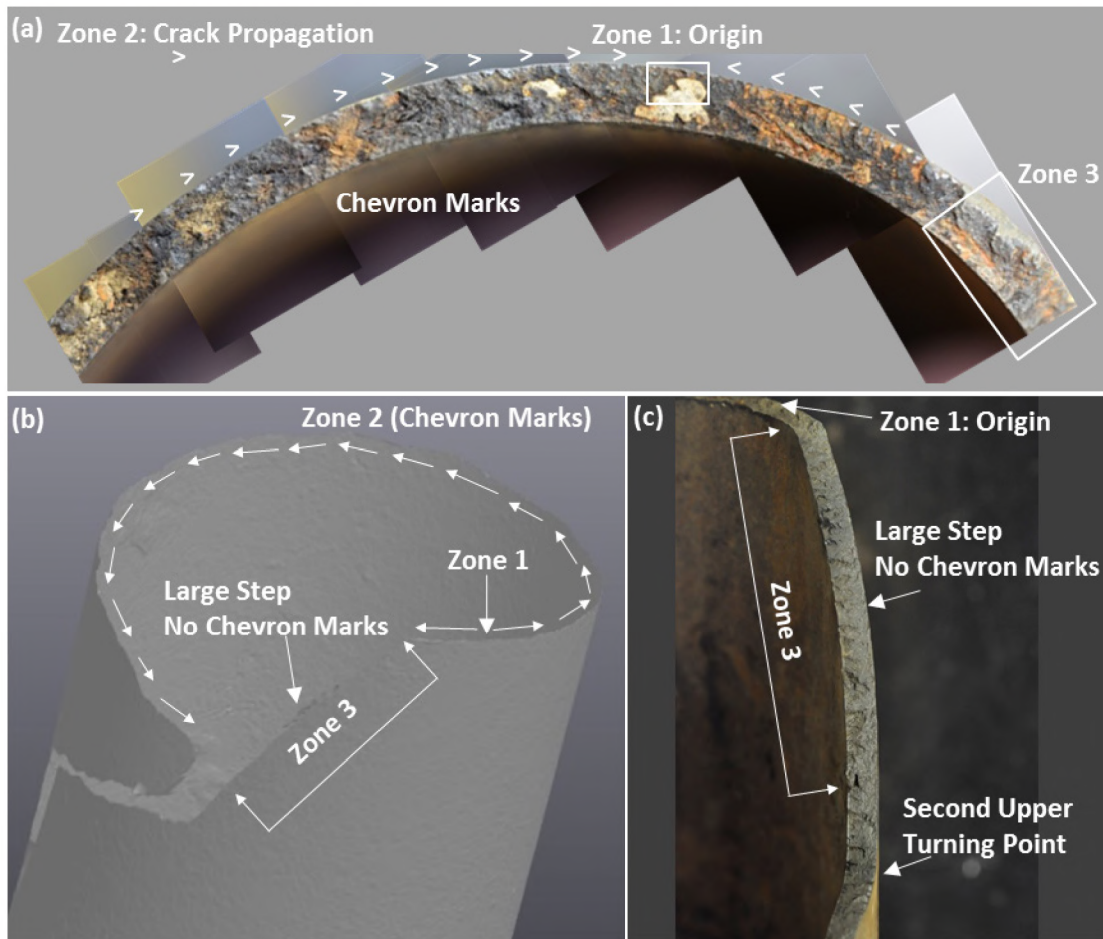


Figure 159: (a) Circumferential Parting and (b) Upper and (c) Lower Fracture Surfaces

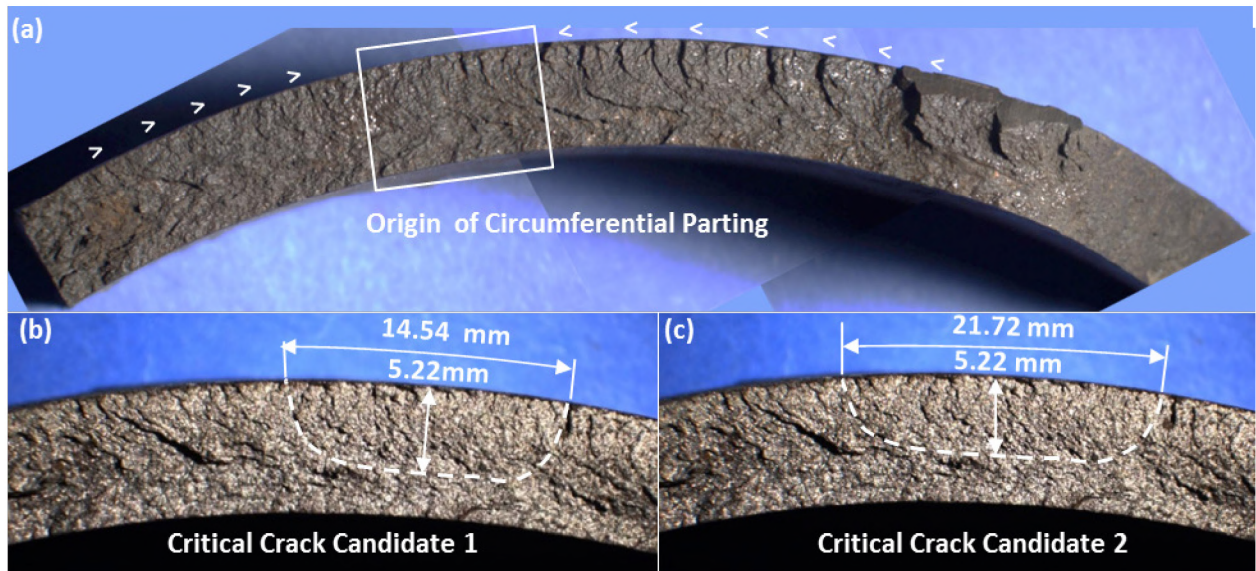




**Figure 160: (a) Stereo Images and (b) Schematic of Three Failure Zones and (c) Zone 3 Image**

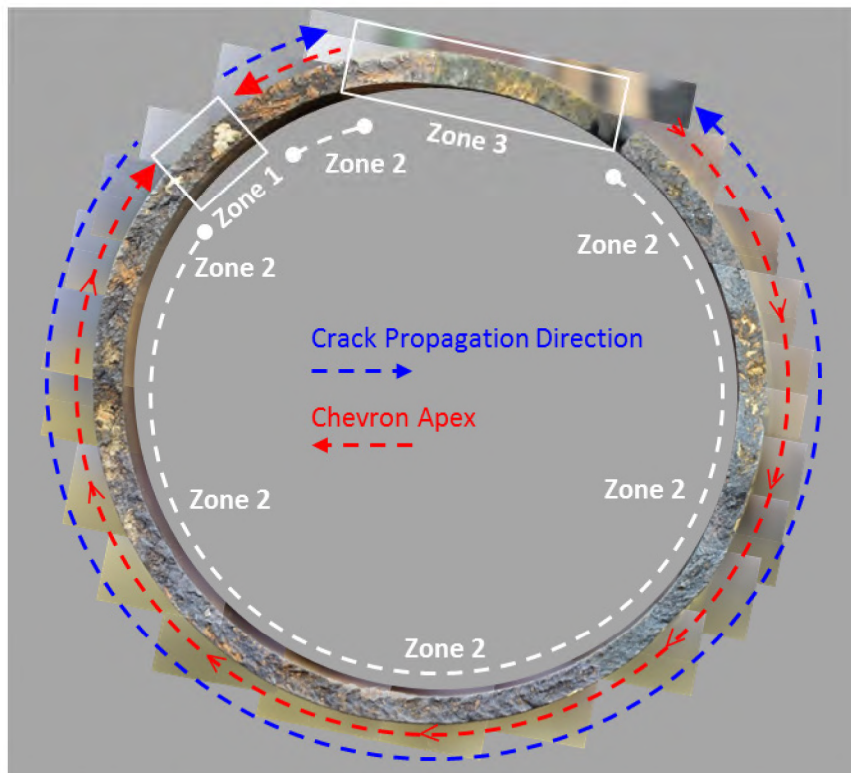
Zone 1 was identified based on the chevron marks that were observed on the fracture surface. An initial area was identified as a possible origin site based on visual and stereoscopic examinations. The proposed origin site was thoroughly examined with the stereo microscope and SEM to determine the origin size. Two semi-elliptical areas were identified as possible critical crack sizes (origin) for the circumferential parting. The first critical crack candidate was 14.55 mm long and 5.2 mm deep. There was uncertainty in identifying the fine chevron marks adjacent to the origin. A second critical crack candidate was identified, which extended just beyond the first critical crack candidate. The second critical crack candidate was 21.72 mm long and 5.22 mm deep. Figure 161 (a) shows the origin area for the circumferential parting. Figure 161 (b) and (c) show the location and sizes of the critical crack candidates.

Additional clarification and verification are required when there is uncertainty in the critical crack size. Temperature was used to verify the critical crack sizes for the circumferential parting, which is discussed in Section 4.3. The results showed that the estimated temperature at the time of the circumferential parting was between  $-60.4^{\circ}\text{C}$  and  $-56.8^{\circ}\text{C}$  for the first critical crack candidate (14.53 mm). The estimated temperature for the second critical crack candidate (21.72 mm) was between  $-40.1^{\circ}\text{C}$  and  $-39.1^{\circ}\text{C}$ . The failure temperature predicted by the thermal model [11] was  $-34^{\circ}\text{C}$ . Both candidates were consistent with the thermal model prediction; however, the second critical crack candidate resulted in a closer temperature prediction.



**Figure 161: Circumferential Parting (a) Origin and Critical Crack Candidates (b) 1 and (c) 2**

Zone 2 was characterized by chevron marks, and their apices were oriented towards Zone 1 (origin). Figure 162 shows the fracture surface in the non-cleaned condition. The chevron marks are clearly visible on the majority of the fracture surface in Zone 2, identified by the dashed white circle in Figure 162. The dashed red and blue circles represent the chevron apices and crack propagation, respectively. Zone 2 began at Zone 1 and arrested at the upper arrest point for the axial rupture. The beginning and end points for Zone 2 are indicated by the white dots at the end of the white circle.



**Figure 162: Zone 2 Chevron Marks and Crack Propagation Direction**

Zone 3 was the large, inclined step between the two circumferential crack tips produced by the spiral crack path. The fracture surface of Zone 3 was rough and did not contain chevron marks. The observations suggest that the fracture surface was not produced by a running crack but by an overload of the remaining ligament.

Additional detailed visual and stereoscopic examination showed that the circumferential parting was not an extension of the axial rupture. Chevron marks produced by the circumferential parting did not follow the chevron marks produced by the axial rupture. The initiation site and chevron marks produced by the circumferential parting were located at approximately 3.70 in. (94 mm) from the upper arrest point of the axial rupture. Figure 163 is a schematic of the crack path for the axial rupture and circumferential parting. The schematic shows how the circumferential parting initiated above the arrest point of the axial rupture. The crack propagated circumferentially until it reached the axial rupture's arrest point. The final ligament failed due to the axial force generated by the weight of the 7 in. casing string. The axial rupture and circumferential parting are thought to be two separate events due to a lack of evidence that the chevron marks from the axial rupture continued into the circumferential parting. The close proximity of the two failures suggests that they are related despite being two separate events.

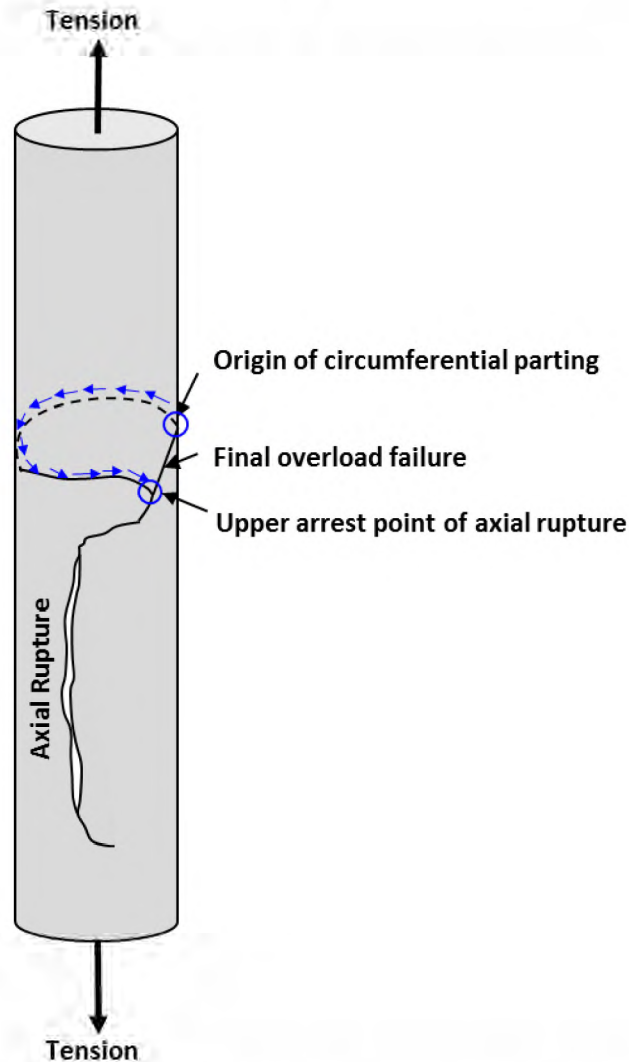


Figure 163: Schematic of the Axial and Circumferential Failure Crack Path

Observations during the visual examination identified a significant difference between the axial rupture and the circumferential parting. The circumferential parting was brittle, unlike the axial rupture, which was characterized by bulging and ductile tearing. There was no evidence of plastic deformation or necking along the circumferential parting. Measurements of the fracture surface were made to confirm this observation. The fracture surface and adjacent wall were measured using a caliper and an ultrasonic thickness probe. The difference between the fracture surface and the wall thickness measurements was compared to identify any measurable ductility. The caliper and the thickness probe were checked against a 0.3000 in. calibration block. The caliper read 0.3005 in., and the thickness probe read 0.300 in.; both measurements were deemed acceptable for this task. Figure 164 shows the calibration block check with the (a) caliper and (b) thickness probe.

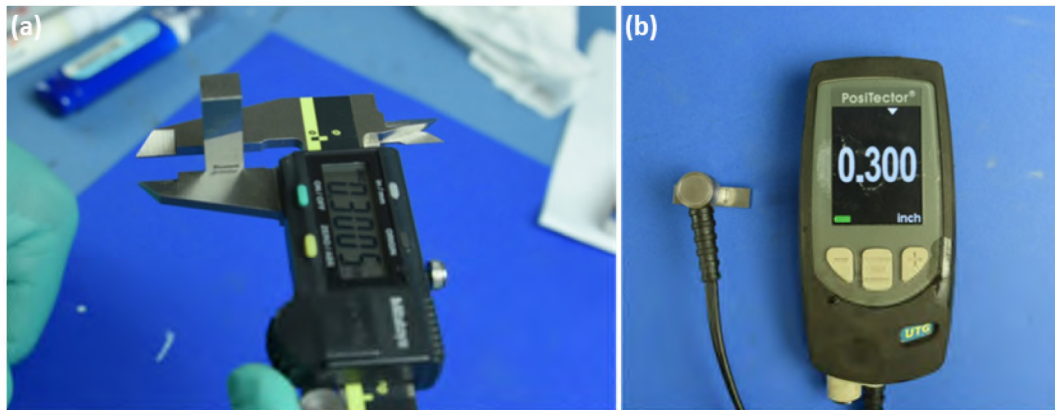


Figure 164: Photos of the (a) Caliper and (b) Thickness Probe Used for Wall Thickness Measurement

The measurements were taken after most of the SEM work had been completed. The lower fracture surface had been cut into multiple specimens. Three specimens (C023A1A2, C023A1A2A, and C023A1A1) were selected to cover most of the lower fracture surface. Figure 165 shows the results for specimen C023A1A2. Measurements of the fracture surface were taken with the caliper at nine equally spaced locations. The wall thickness was measured with the thickness probe at the nine locations directly below the fracture surface. Locations 5 and 8 were not measured due to corrosion on the OD surface. The results show that the maximum reduction in wall thickness was 0.009 in. with an average wall thickness difference of 0.000 and -0.002 in. for runs one and two, respectively.

Location	Fracture Surface Thickness		Wall Thickness (in.)	Delta 1 (in.)	Delta 2 (in.)
	Run 1 (in.)	Run 2 (in.)			
0	0.318	0.319	0.316	0.002	0.003
1	0.313	0.306	0.305	0.008	0.001
2	0.306	0.300	0.309	-0.003	-0.009
3	0.309	0.307	0.307	0.002	-0.001
4	0.313	0.305	0.308	0.005	-0.004
5	-	-	0.298	-	-
6	0.290	0.295	0.294	-0.004	0.001
7	0.305	0.302	0.308	-0.004	-0.006
8	-	-	0.314	-	-
9	0.312	0.311	0.313	-0.002	-0.002
			<b>Min</b>	<b>-0.004</b>	<b>-0.009</b>
			<b>Max</b>	<b>0.008</b>	<b>0.003</b>
			<b>Average</b>	<b>0.000</b>	<b>-0.002</b>

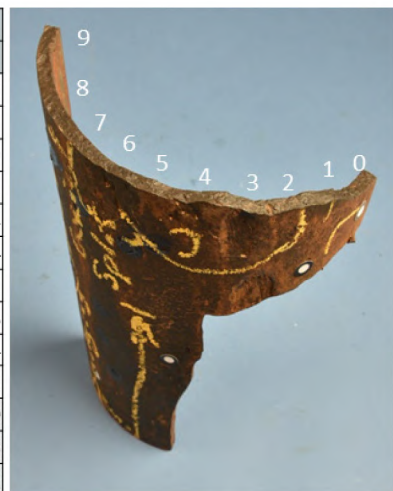


Figure 165: The Measured Wall Thickness Data for Specimen C023A1A2

Figure 166 shows the results for specimens C023A1A1 and C023A1A2A. Measurements were taken at four locations from each specimen. Wall thickness measurements were taken at the cut face of the specimen with the caliper. The results show that the maximum reduction in wall thickness was 0.007 in. with an average of -0.001 in. These values are within the error range of the measurement technique and suggest minimal to no ductility associated with the circumferential parting.



Location	Fracture Surface Thickness		Wall Thickness		Delta	
	Run 1 (in.)	Run 2 (in.)	Run 1 (in.)	Run 2 (in.)	Run 1 (in.)	Run 2 (in.)
0	0.321	0.319	0.320	0.320	0.001	-0.001
1	0.317	0.316	0.319	0.318	-0.002	-0.002
2	0.323	0.325	0.328	0.322	-0.005	0.003
3	0.333	0.332	0.336	0.334	-0.003	-0.003
4	0.319	0.321	0.328	0.323	-0.003	-0.007
5	0.324	0.324	0.320	0.317	0.001	0.004
6	0.319	0.317	0.320	0.321	0.002	-0.003
7	0.327	0.327	0.330	0.330	0.000	-0.003
<b>Minimum</b>	<b>0.317</b>	<b>0.316</b>	<b>0.319</b>	<b>0.317</b>	<b>-0.005</b>	<b>-0.007</b>
<b>Maximum</b>	<b>0.333</b>	<b>0.332</b>	<b>0.336</b>	<b>0.334</b>	<b>0.002</b>	<b>0.004</b>
<b>Average</b>	<b>0.323</b>	<b>0.322</b>	<b>0.325</b>	<b>0.323</b>	<b>-0.001</b>	<b>-0.001</b>

Figure 166: The Measured Wall Thickness Data for Specimens C023A1A1 and C023A1A2A

The distinct difference in macro fracture mode (ductile vs. brittle) between the axial rupture and the circumferential parting indicates that they occurred at two different temperature regimes. The axial rupture initiated at a temperature above the ductile-to-brittle transition temperature (DBTT) for slow loading. The circumferential parting occurred at a temperature below the DBTT. The DBTT for slow loading was approximately 50–100°C lower than the DBTT determined by the CVN (fast loading) [26]. The DBTT based on the half-size CVN testing of the material from the 25 joints of the 7 in. casing was 108.5°F (42.5°C) (Section 7.1.8). The DBTT was shifted 11.1°C, based on API 579, to account for the specimen size effect [27]. Therefore, the DBTT for slow loading, based on the adjusted and full-size CVN’s DBTT of 128.5°F (53.6°C), would have ranged between 38.5°F (3.6°C) and -51.5°F (-46.4°C). The estimated temperature for the circumferential parting most likely was within these temperature ranges.

This evidence supports the conclusion that the axial rupture and the circumferential parting were two separate events. The circumferential rupture of the 7 in. casing was most likely a consequence of the axial rupture, based on the finding that it occurred at a lower temperature. The release of cold gas [11] from the opening of the axial rupture resulted in rapid cooling of the surrounding casing material. The grade J55 steel then became brittle due to the super cooling condition.

### 3.3.2 Micro-Fractographic Characterization (SEM) of the Circumferential Parting

The micro-fractographic characterization of the circumferential rupture followed the same procedures of the axial rupture, and its objectives were to:

1. Identify the fracture modes for Zone 1.
2. Identify the fracture mode for Zone 2 (crack propagation).
3. Identify the fracture mode for Zone 3 (final overload failure).

### 3.3.3 Micro-Fractographic Characterization for Zone 1 (Origin for Failure)

Specimens were extracted from C023A1A for a detailed examination with the SEM. The parent specimen was cut longitudinally to remove the axial rupture mating surface and a section of the circumferential parting (C023A1A2). The remaining circumferential fracture surface was removed with a circumferential cut through the top portion of Zone 3. The circumferential fracture surface was cut into shorter lengths so that the specimen could fit inside the SEM chamber. Zones 1 and 2 of specimen C023A1A1A were selected for a detailed examination with the SEM. Figure 167 shows the cuts required to extract the SEM specimens. C023A1A1A is identified by the white box.

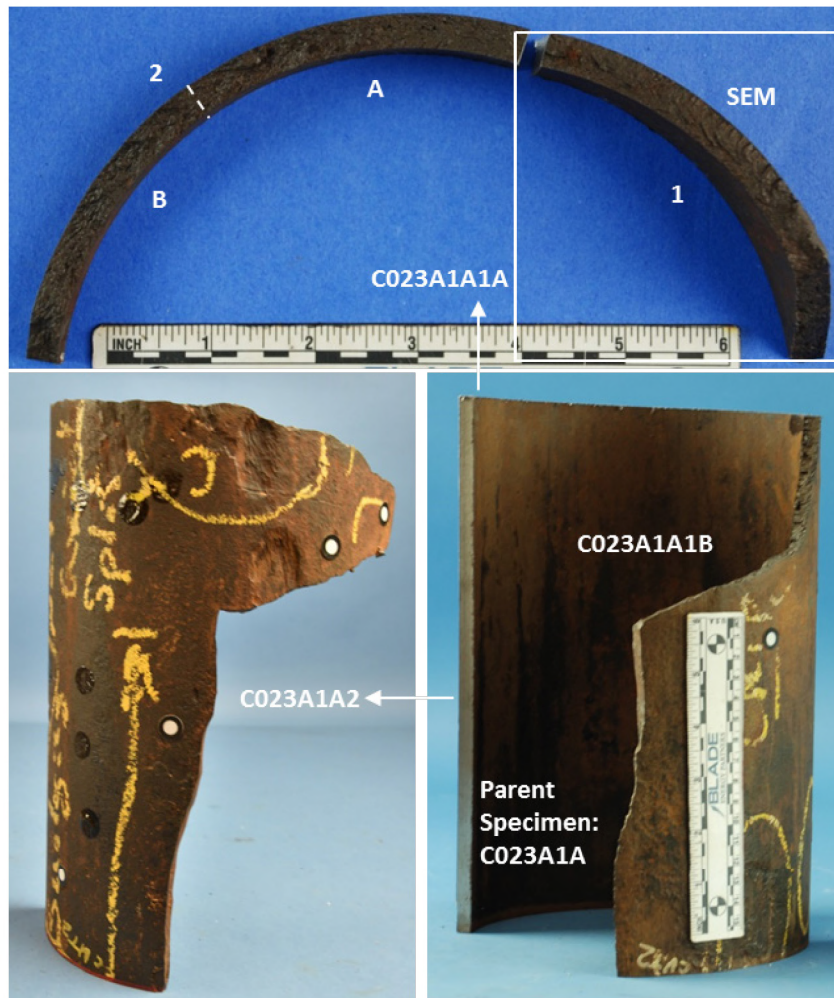
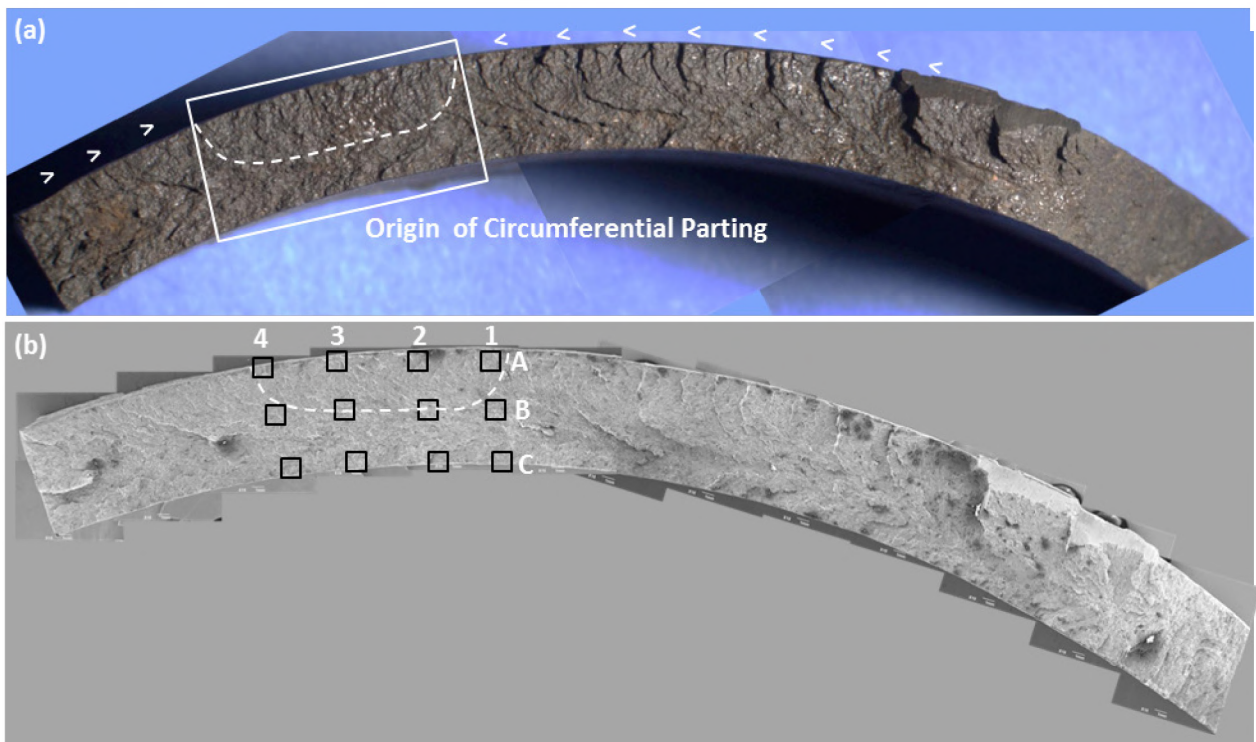


Figure 167: Cut Locations and Specimen Identification for Circumferential Parting

To prevent contamination, all cuts were made without coolant. Care was taken to protect all fracture surfaces and features during the cutting process. Specimen C023A1A1A, which contained the origin for the circumferential parting, was cleaned by using the same procedures described in Section 3.2.2. Figure 168 (a) shows stitched stereo images of the fracture surface after it was ultrasonically cleaned in a 1% Citranox solution for three minutes. Figure 168 (b) shows stitched SEM images of the same cleaned fracture surface. The black boxes show the locations for the detailed SEM examinations. Zone 1 was examined in a grid with numbers representing columns and letters representing rows. Row A was located at the OD side of the Zone 1 fracture surface. Row B and C were located at the MW and ID of Zone 1, respectively.



**Figure 168: Specimen C023A1A1A (a) Stereo and (b) SEM Images of Zone 1 (Origin) Investigation Areas**

The SEM examination of Zone 1 identified a pre-existing, crack-like flaw on the OD side of the origin. Figure 169 shows SEM images of the crack-like flaw on the OD surface. The crack-like flaw was shallow, with a measured maximum depth of 196  $\mu\text{m}$ . Figure 170 shows an EDS analysis indicating that the surface of the flaw was severely oxidized by a scale that had not been removed during cleaning. The adjacent fracture surface was easily cleaned and clearly showed cleavage facets. This observation suggests that the flaw existed prior to the circumferential parting. The OD surface flaw may have promoted brittle cracking from the origin of the circumferential parting, even though the flaw was shallow.

Further detailed SEM examination identified that the fracture mode of the origin was characterized by cleavage with a small number of microvoids (Figure 171). The small amount of microvoids is associated with inclusions in the material. Similar features were also observed along the edge of the origin (Figure 172).

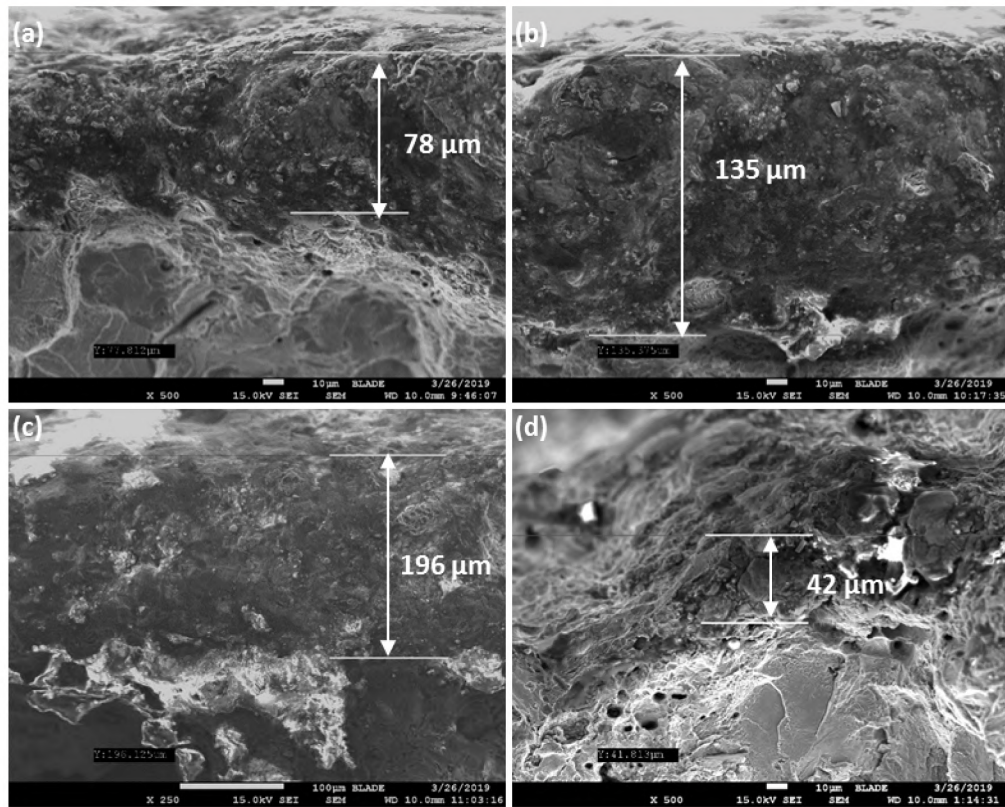
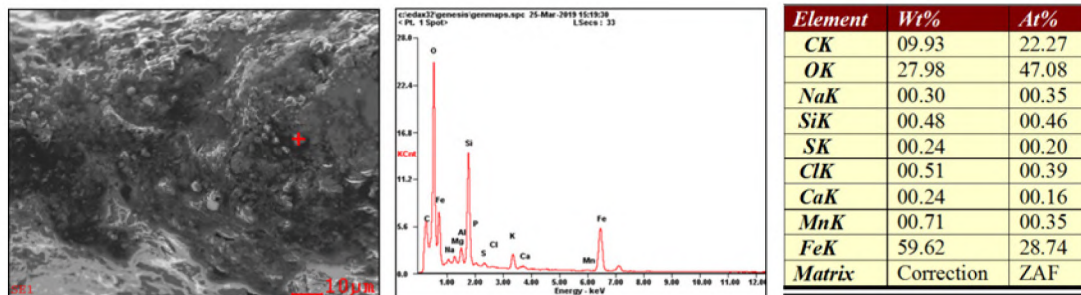


Figure 169: SEM Images of Pre-existing Flaws at (a) 1A, (b) 2A, and (d) 4A Taken at 500X, and (c) 3A Taken at 250X



(a) SEM image. The red spot is where the EDS analysis was performed

(b) EDS Spectra. A high oxygen peak is noticeable

(c) Concentration of the scale showed iron oxide

Figure 170: EDS Results for Pre-Existing Flaws



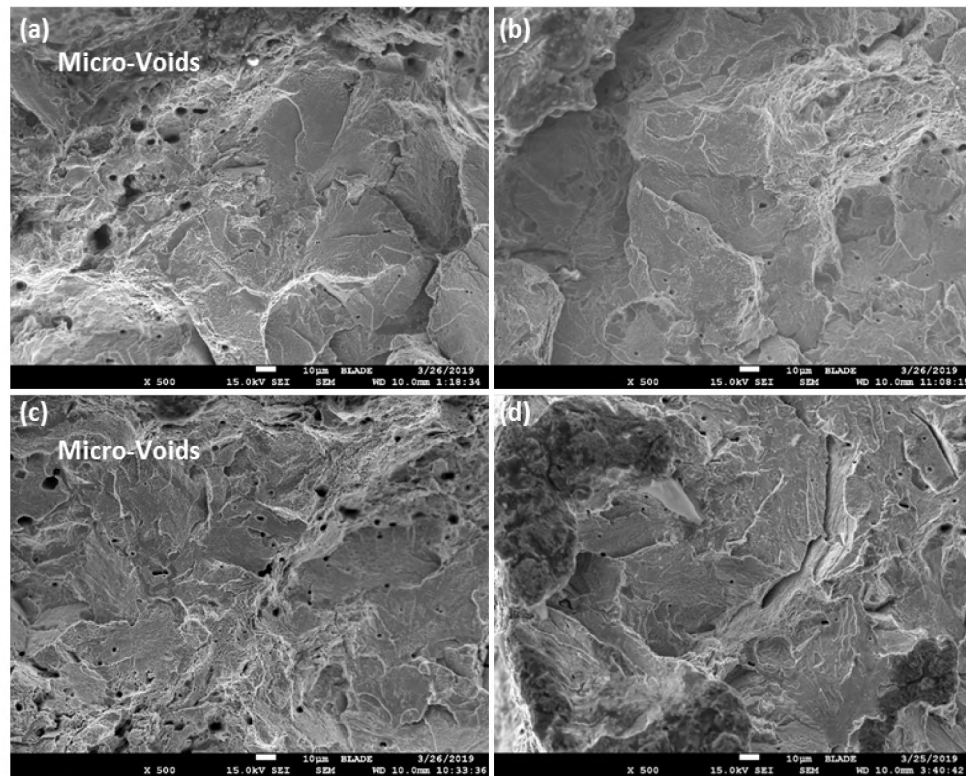


Figure 171: SEM Images of C023A1A1A Areas (a) 1A, (b) 2A, (c) 3A, and (d) 4A Taken at 500×

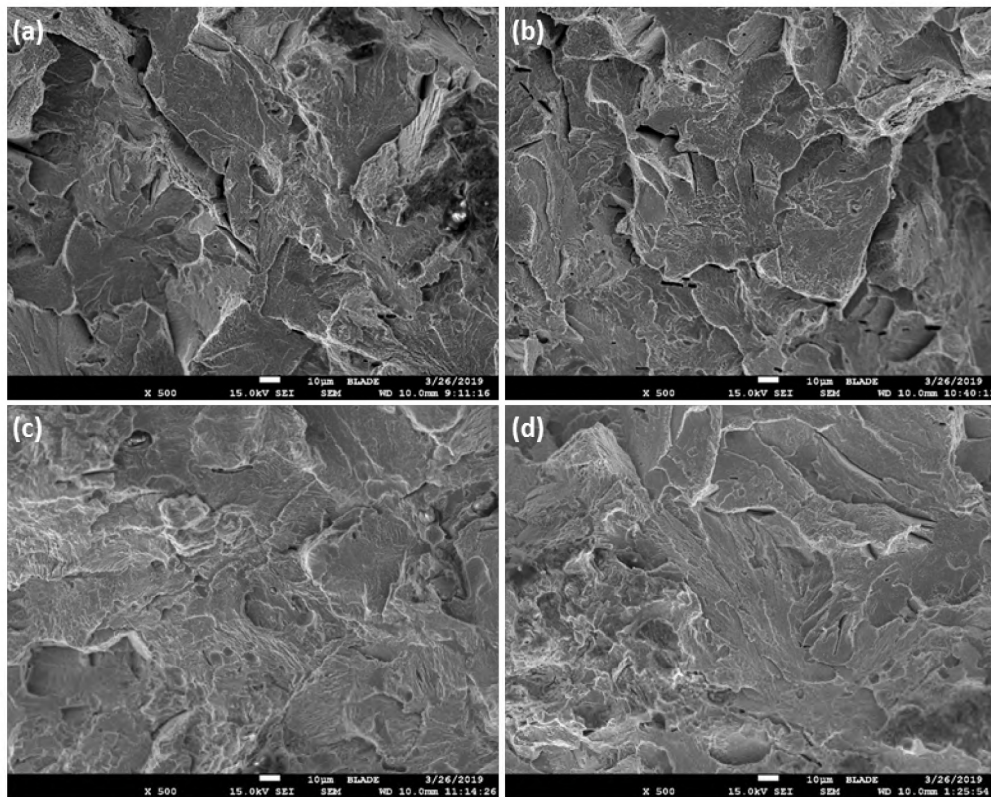
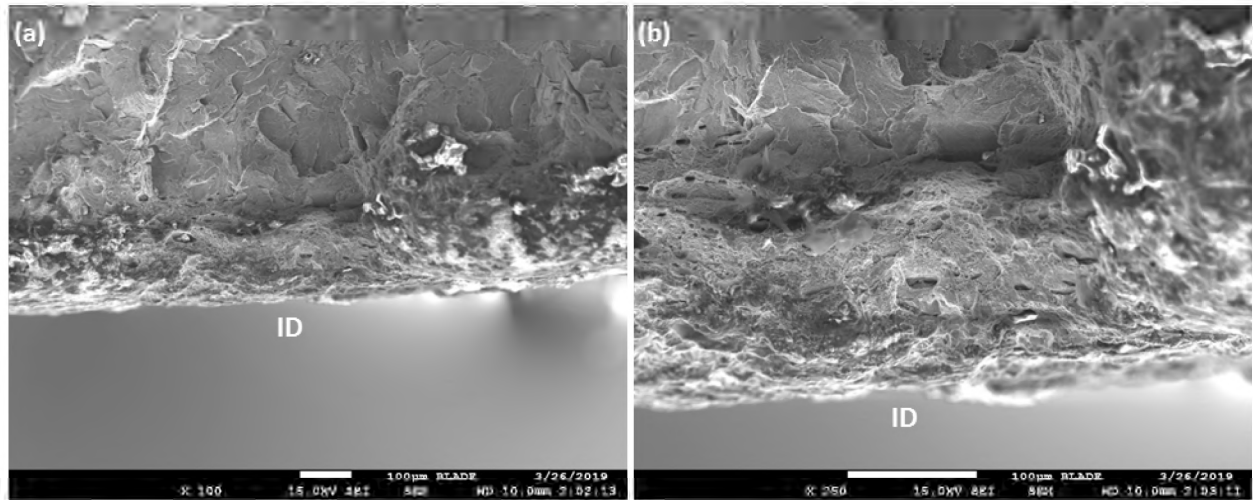


Figure 172: SEM Images of C023A1A1A Areas (a) 1B, (b) 2B, (c) 3B, and (d) 4B Taken at 500×

No noticeable changes in the fracture mode were observed outside of the origin, except for an area close to the ID. Deformation marks were observed on the fracture surface of Zone 1 near the ID. The deformation is thought to be associated with a small shear lip. Figure 173 shows the typical fracture surface morphology observed near the ID surface.



**Figure 173: C023A1A1A ID Fracture Surface Morphology Taken at (a) 100× and (b) 250×**

The circumferential parting originated from a shallow crack-like flaw on the OD surface. The micro-fracture mode of the origin was characterized by cleavage. Small quantities of microvoids were observed but appeared to be associated with inclusions within the material. The size of the origin was identified by visual and stereoscopic examination. The origin size was based on chevron marks because no noticeable change was observed in the micro-fractographic morphology between the origin and the surrounding area.

### 3.3.4 Micro-Fractographic Characterization for Zone 2 (Crack Propagation)

Cleavage separation was the predominant micro mechanism for Zone 2 (crack propagation). Most of the circumferential fracture surface was characterized by fine chevron marks. Fine chevron marks indicate that the limited micro-plastic deformation occurred in the steps between the cleavage planes. Macro-plastic deformation, such as necking, did not occur as discussed in Section 3.3.1. These observations are consistent with brittle fracture of mild steels at temperatures below the DBTT [19] [20].

Figure 174 shows stitched stereo images of C023A1A1A2A with the chevron mark orientation and the SEM examination location. Many locations were examined with the SEM, and the same micro mechanism was observed at each location, but only one set of the representative fracture morphology is shown here. Figure 175 through Figure 177 show the morphology for the OD, MW, and ID for Area A9. The SEM images show cleavage features through the thickness of the circumferential fracture surface. This was consistent with all examined locations.

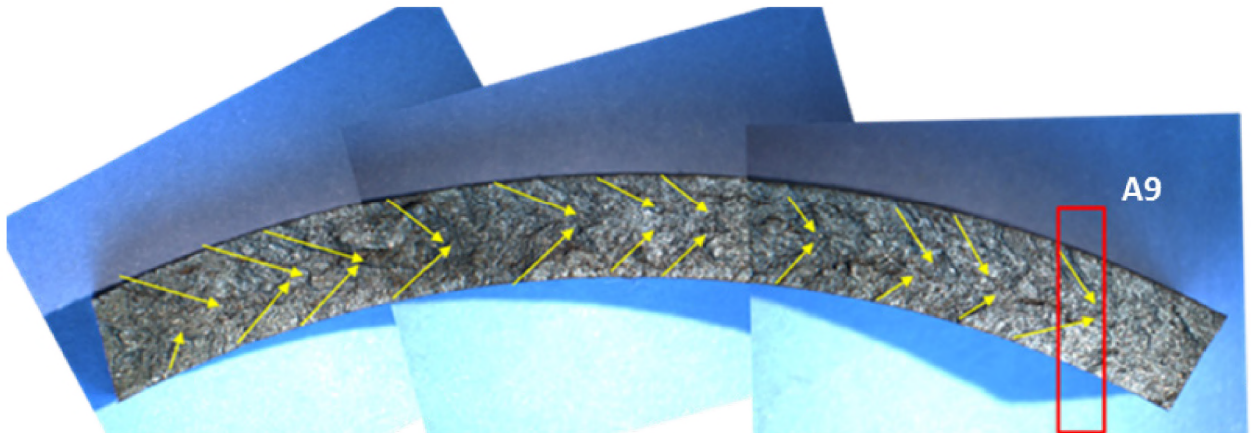


Figure 174: Specimen C023A1A1A2A Showing Fine Chevron Marks and Representative SEM Location

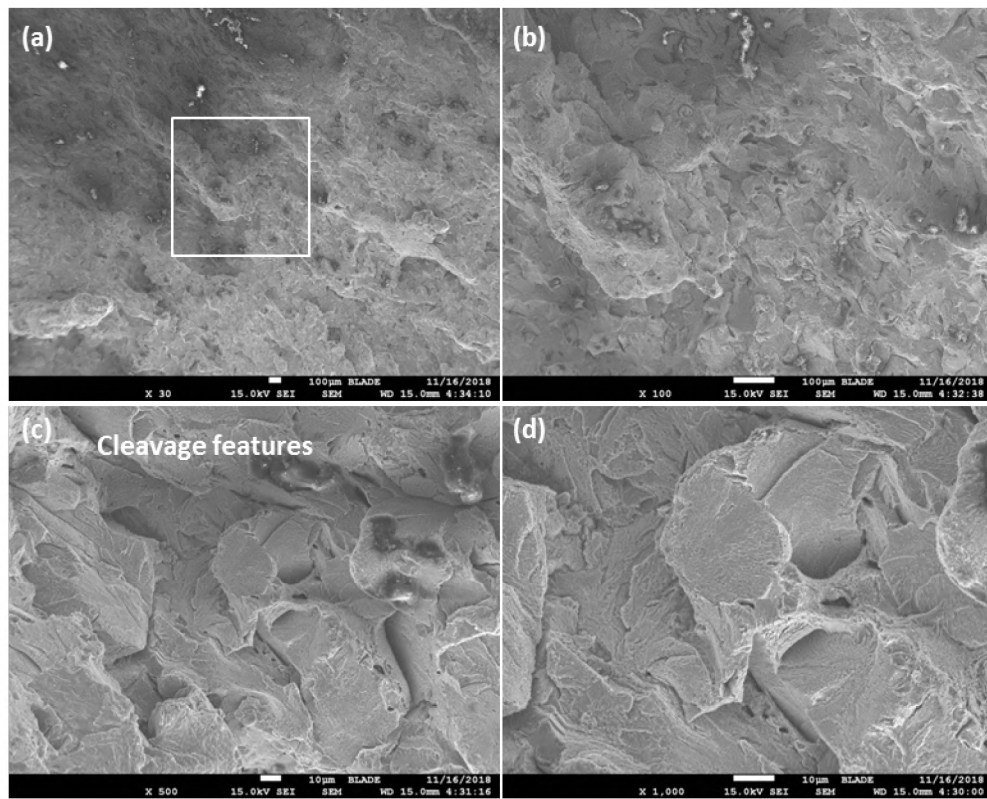


Figure 175: SEM Images of A9 OD at (a) 30 $\times$ , (b) 100 $\times$ , (c) 500 $\times$ , and (d) 1,000 $\times$

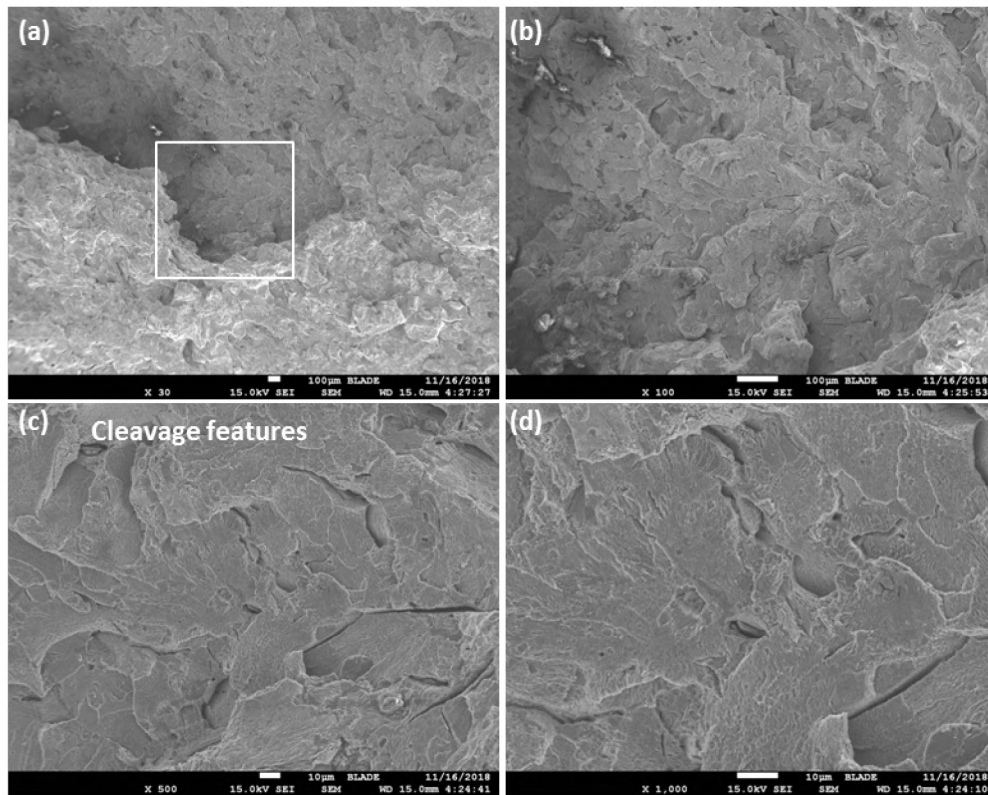


Figure 176: SEM Images of A9 MW at (a) 30 $\times$ , (b) 100 $\times$ , (c) 500 $\times$ , and (d) 1,000 $\times$

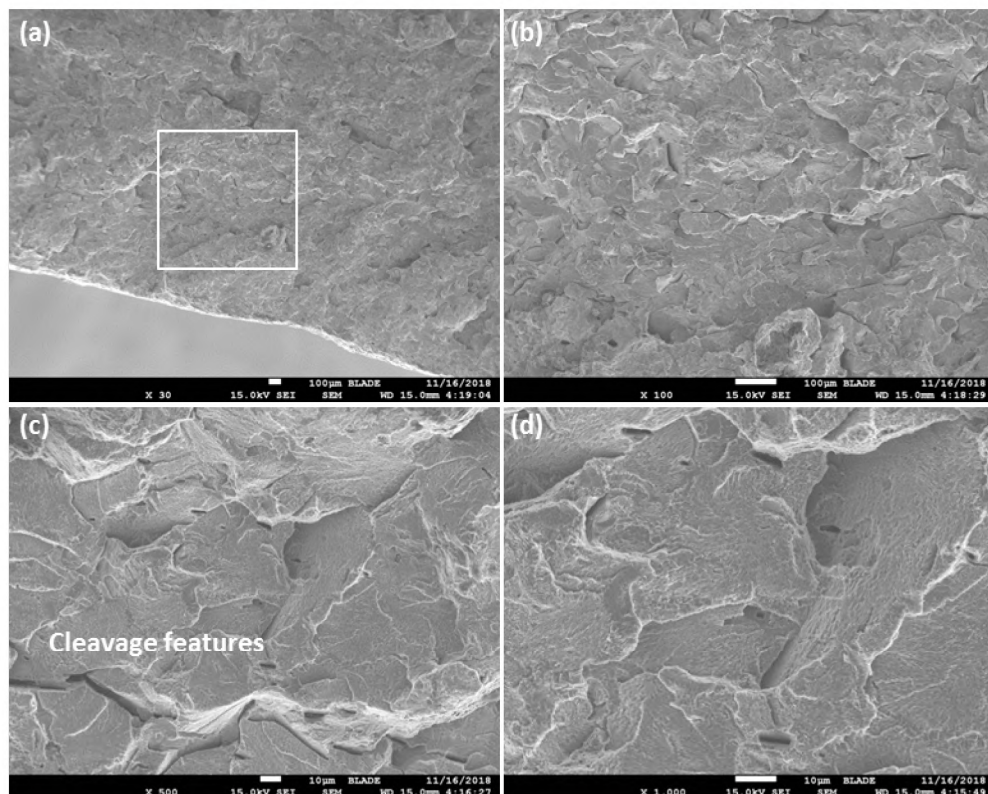


Figure 177: SEM Images of A9 ID at (a) 30 $\times$ , (b) 100 $\times$ , (c) 500 $\times$ , and (d) 1,000 $\times$

### 3.3.5 Micro-Fractographic Characterization for Zone 3 (Final Overload Failure)

Zone 3 is the final overload failure that occurred when the remaining ligament failed due to the axial force. The axial force at the time of failure was between 202,230 lbf and 236,545 lbf, based on the loads presented in Table 5. FEA of the failure showed that the remaining ligament would have failed based on the axial force at the failure depth. Section 4.4 discusses the modeling approach and results for the FEA of the final overload failure. Zone 3 was characterized by:

- Rough surface appearance (steps) near the ID side of the fracture surface.
- Absence of chevron marks.
- Brittle fracture with no visible plastic deformation.

Figure 178 (a) shows a schematic showing the location of Zone 3. Figure 178 (b) and (c) show macro and stereo images of Zone 3. The images show a step-like appearance on the ID side of the fracture surface. The OD side of the fracture surface appears to be smooth. The SEM examination showed that the fracture surface near the OD side was mostly cleavage separation, while the ID side showed a mix of cleavage facets and a woody type of plastic deformation. The fracture surface morphology at the MW was a combination of the OD and ID morphologies.

The observed mixed fracture mode near the ID was consistent with the rough surface observed on the ID side of the fracture surface (Figure 178 [c]). The ridge-like appearance is associated with multiple initiation sites at different levels during tearing. Figure 179 and Figure 180 show representative SEM micro-fractographic features of the overload failure as indicated by the white box in Figure 178 (b). The micro mechanism was predominantly cleavage separation due to failure at low temperatures. Some degree of plastic deformation was observed on the ID side of the fracture surface. The change in surface condition from the ID to the OD suggests that the final overload failed from the ID (rough) to the OD (relatively smooth).

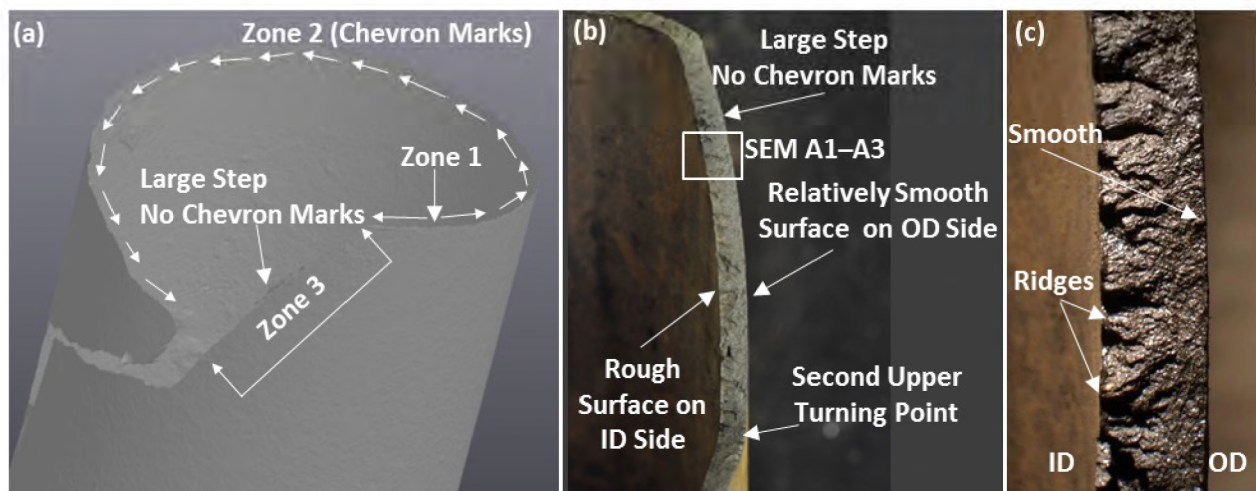


Figure 178: (a) Schematic and (b) (c) Image of Zone 3 (Final Overload Failure)

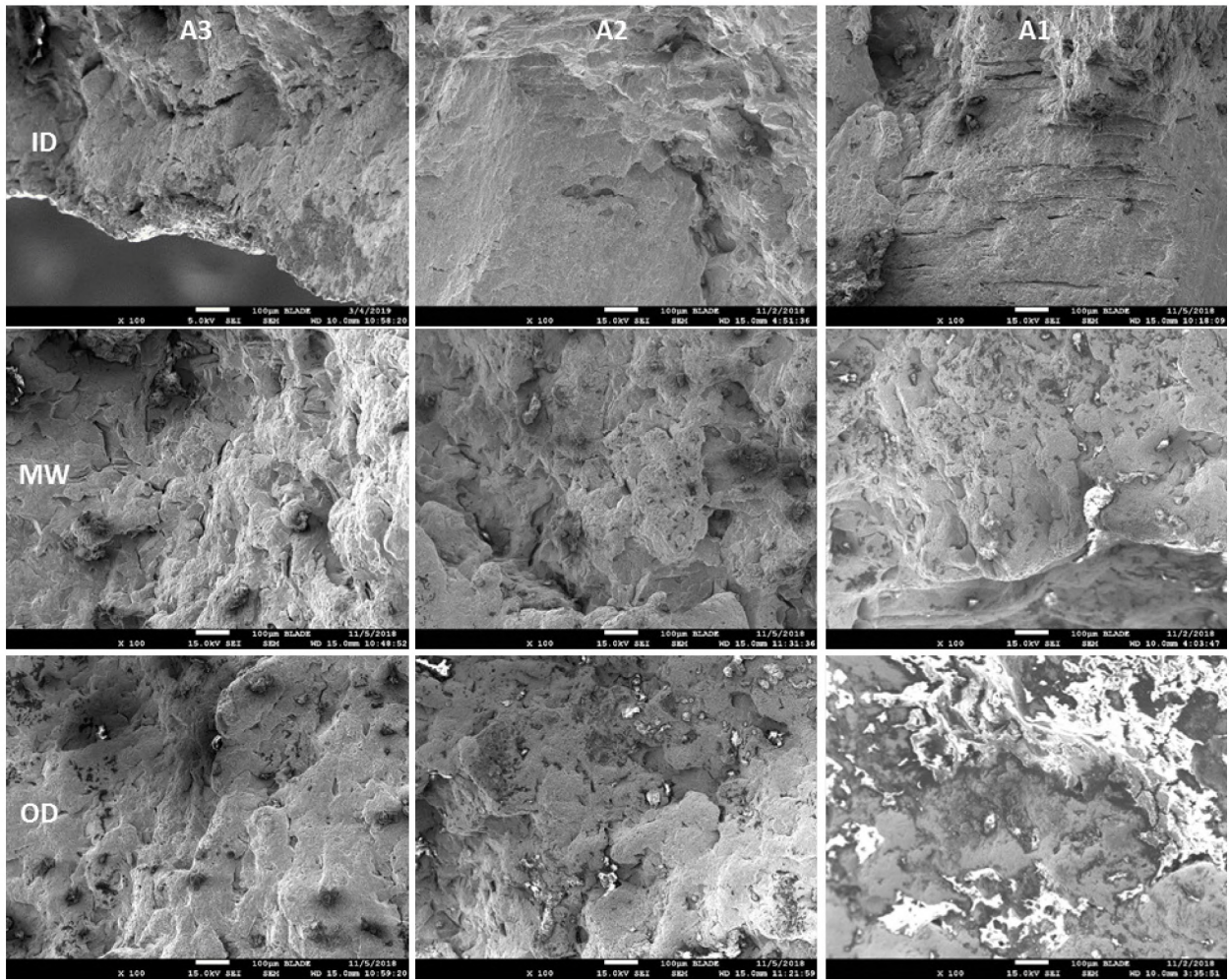


Figure 179: Fracture Surface Morphologies near the ID, MW, and OD Taken at 100×

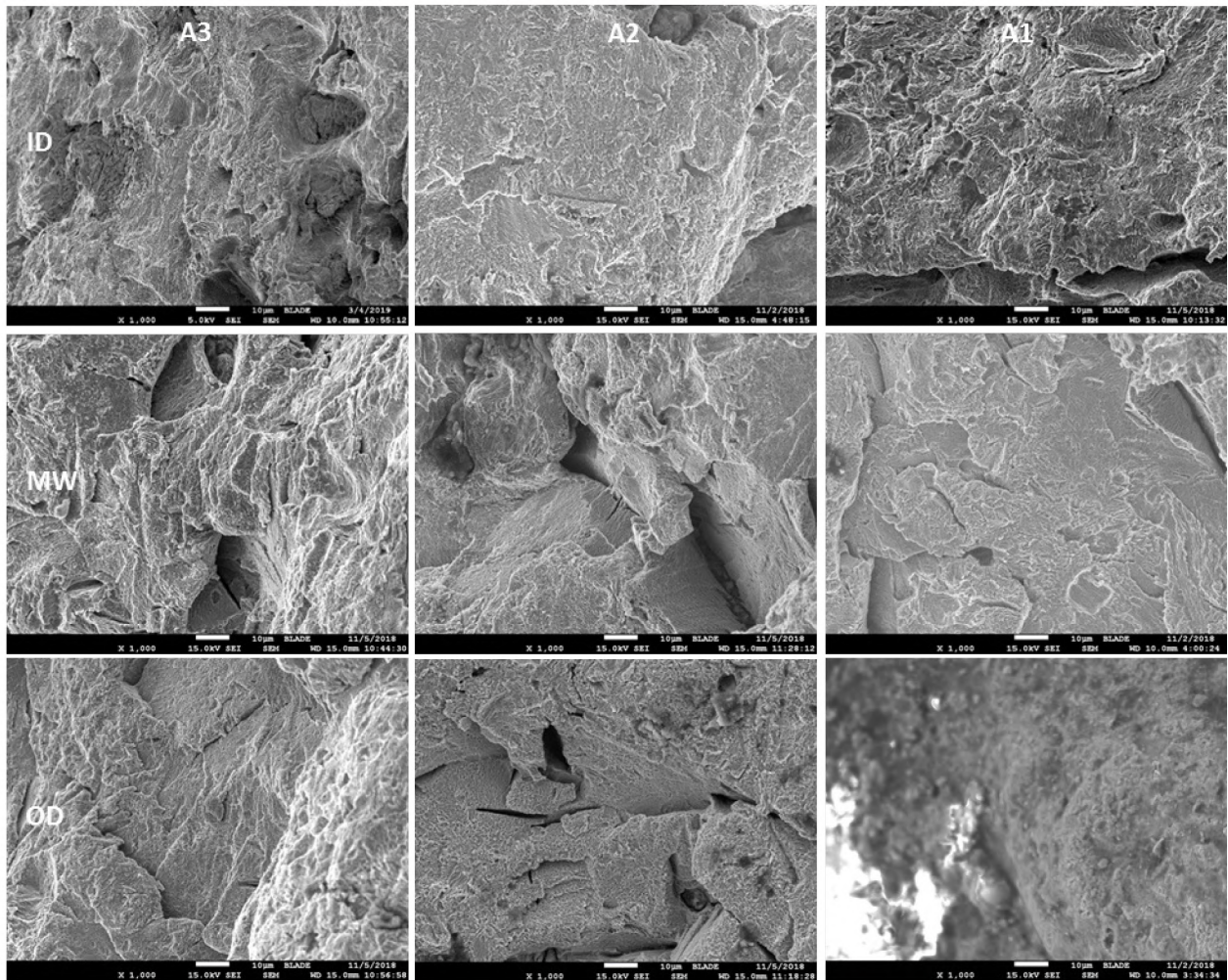


Figure 180: Fracture Surface Morphologies near the ID, MW, and OD Taken at 1,000×

### 3.4 Summary

The following conclusions can be made based on the visual (macro) and SEM (micro) investigations of the SS-25 7 in. casing failure:

- The 7 in. casing failure originated from an 85% metal loss due to corrosion, resulting in a 2 ft long axial rupture under an internal pressure of approximately 2,700 psi in the 7 in. × 2 7/8 in. annulus.
- The internal pressure caused slow ductile tearing of the thinnest region. A crack formed in the 2.13 in. origin, at which point tearing instability occurred, followed by a rapid crack propagation that left chevron marks behind. Bulging was observed around the axial rupture.
- The propagating cracks finally arrested after changing direction twice due to changes in the stress state and the energy dissipation.
- The axial rupture occurred at an estimated temperature of 80°F, based on the historical temperature profile data at the failure depth of 892 ft. This temperature is consistent with the observed bulging and ductile tearing associated with the axial rupture.

- The circumferential parting was not a continuation of the axial rupture. The axial rupture and circumferential parting were two separate events even though they were in close proximity.
- The circumferential parting was brittle. There was no evidence of local plastic deformation or overload necking based on wall thickness measurements of the fracture surface.
- The circumferential parting was a consequence of the axial rupture. The release of cold gas [11] from the opening formed by the axial rupture resulted in rapid cooling of the adjacent casing material.
- The grade J55 steel casing became brittle due to the cooling condition. The circumferential parting initiated from a semi-elliptical flaw, as estimated from the chevron marks.
- Two critical crack candidates were identified during the visual and stereoscopic examinations. The first critical crack candidate was 14.5 mm long and 5.2 mm deep. The second critical crack candidate had the same depth but was slightly longer—21.7 mm.
- The estimated temperature for the circumferential parting from the two possible critical crack sizes ranged between  $-60.4^{\circ}\text{C}$  and  $-56.8^{\circ}\text{C}$  for the first critical crack size (14.5 mm long) and  $-40.1^{\circ}\text{C}$  and  $-39.1^{\circ}\text{C}$  for the second critical crack size (21.7 mm).
- An independent thermal analysis predicted that  $-34^{\circ}\text{C}$  was the lowest temperature that could have been achieved by the release of gas from the axial rupture. The second critical crack candidate (21.72 mm  $\times$  5.22 mm) was closer and was most likely the critical crack size for the circumferential parting.



## 4 7 in. Casing Failure Validation

---

This section uses FEA and fracture mechanics models to verify the failure sequence presented in Section 3. The failure sequence was described by the following three events:

1. Axial rupture
2. Circumferential cracking
3. Final overload failure of the remaining ligament

FEA was used to model the axial rupture and estimate the failure pressure. Actual grade J55 material properties from the failed joint (joint 22) were used to accurately capture the material behavior. The corrosion feature and striated groove geometry associated with the axial rupture were included in the finite element (FE) models. The axial rupture led to the circumferential parting, which occurred at a lower temperature due to the escaping cold gas [11]. Fracture mechanics models and material fracture properties were used to investigate crack initiation sizes and failure temperatures for the circumferential parting. A ligament remained after the axial rupture and circumferential cracking had occurred. An FE model was used to investigate the stress state of the remaining ligament to determine if the tensile load was high enough to cause the final overload failure.

### 4.1 Axial Rupture Failure Pressure

Section 3 described how the axial rupture occurred from wall thinning due to corrosion. The corrosion feature contained striated grooves. FEA was used to model the corrosion feature and estimate the failure pressure of the axial rupture. Three models were created to represent the corrosion feature with and without striated grooves. The models were as follows:

- Model 1: Corrosion feature without a notch
- Model 2: Corrosion feature with a 2.13 in. notch
- Model 3: Corrosion feature with a 4.8 in. notch

ABAQUS, a commercially available FE package, was used to model and analyze the axial rupture. A 100 in. long casing segment near the failure location (892 ft) was modeled with 3D elements. Analyses were conducted by applying internal pressure and a tensile force on the casing model. Actual casing material properties were used to model the constitutive behavior of the grade J55 7 in. casing material. Local stresses and strains in the corrosion feature were obtained from the models and analyzed to derive the failure condition. The corrosion severity was assessed using stress, strain, and the ductile failure damage indicator (DFDI). Local stresses and strains were incorporated into the DFDI parameter to quantify the damage evolution at the corrosion feature. A DFDI value of 1.0 was used to determine the differential pressure at which a crack would initiate within the corrosion feature.

#### 4.1.1 Corrosion Feature Geometry and Finite Element Modeling

The first task for constructing the FEA was to model the 7 in. casing segment and corrosion feature. The corrosion feature size was approximated from scaled images. Figure 181 shows the corrosion feature and estimated axial and circumferential dimensions. The feature had a length of 9.25 in. (23.5 cm) and a width of 3.72 in. (9.4 cm). The measurement of the wall thickness of the pipe body was 0.321 in., and it was measured by using a UT wall thickness probe at locations away from the corrosion feature. The yellow

dotted line in Figure 181 represents the corrosion feature boundary where the wall thickness returned to the measured pipe body value of 0.321 in.

The casing pipe body was modeled as a 7 in. 3D cylinder with a wall thickness of 0.321 in. The corrosion feature was modeled as a semi-elliptical bowl with a major and minor axis of 9.25 in. and 3.72 in., respectively. The bottom of the semi-elliptical bowl was first modeled as a flat circular region representing the ductile tearing region of the axial rupture.

The diameter of the flat circular region was 2.13 in. (53.9 mm), which corresponds to the origin length of the axial rupture. Section 3.2.3 defined the origin of the axial rupture based on a micro-scale definition. The micro-scale definition defined the origin length as being the length of fracture surface that exhibited full ductile tearing without cleavage facets. The boundaries of the origin were identified and measured with the SEM.

The minimum remaining wall thickness was measured from a cross section through the thinnest area of the corrosion feature. Figure 110 (b) shows the metallographic section and the thinnest remaining wall measurement of 0.0496 in. (1.26 mm). This value was used for the thickness of the inner circle region (origin). Figure 182 shows the model of the corrosion feature with the origin identified. The image shows the corrosion feature positioned within the pipe such that the remaining wall matched the minimum value measured from the metallographic cross section. The remaining wall thickness gradually increased from the inner circle (0.0496 in. remaining wall) to the outer boundary of the corrosion feature (0.321 in. remaining wall) based on the semi-elliptical bowl profile. The semi-elliptical bowl with the inner circle (corrosion feature) was modeled as a solid object and was subtracted from the pipe body to obtain the geometry shown in Figure 182. This model is referred to in this section as Model 1 (corrosion feature without a notch).

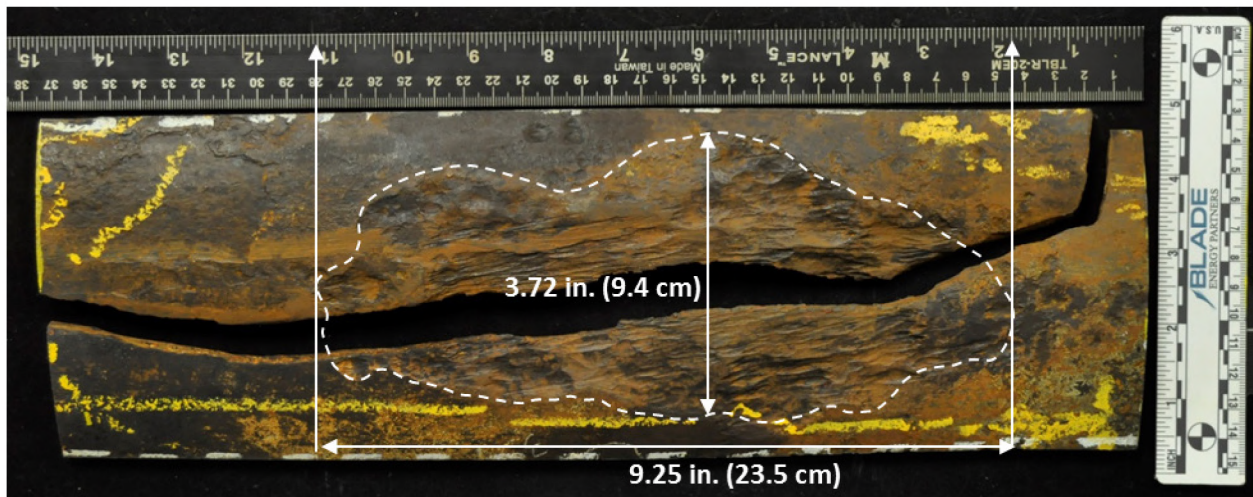
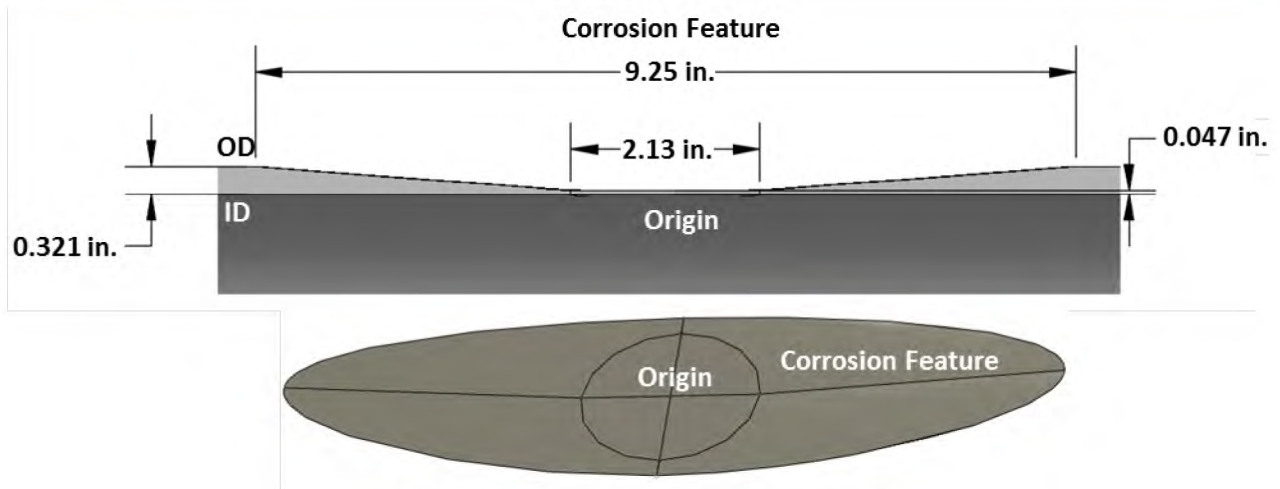


Figure 181: Corrosion Feature Dimensions at the Rupture Location (892 ft)

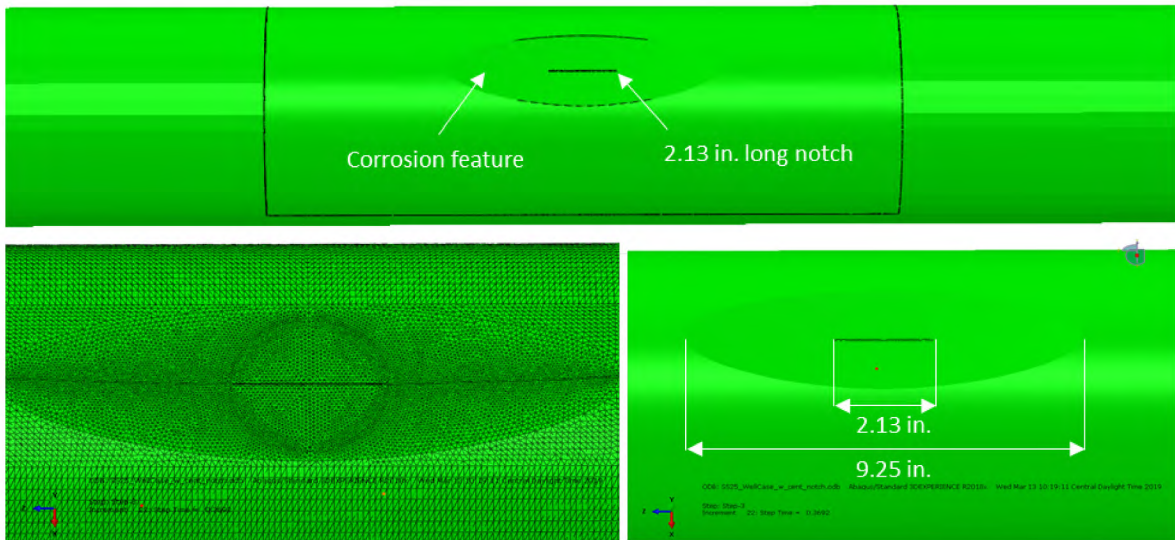


**Figure 182: Corrosion Feature Geometry**

Model 1 was a simplified model that investigated the effects of the wall thinning without the presence of the striated grooves. Models 2 and 3 attempted to model the effects of the grooves on the failure pressure. Striated grooves were modeled as a single groove, which was estimated from the observed grooves in the corrosion feature. Individual grooves could not be modeled due to their small size and distribution complexity. The single notch was designed to approximate a collective effect of the striated grooves.

Notch geometry was estimated from the grooves shown in the metallurgical cross section of the thinnest region (Figure 110 [b]). The measured radius of the notch was approximately 0.2 mm in diameter. This radius was beyond the capabilities of an FEA due to the global meshing requirements. A notch radius of 1.0 mm was chosen to simplify the mesh and to approximately capture the notch effect. The notch was placed in the central circular region of the semi-elliptical corrosion feature. The bottom of the notch was placed at a depth such that the remaining wall was equal to 1.26 mm, which is the same remaining wall as Model 1. The entire corrosion feature was raised by 1.0 mm to ensure the bottom of the notch coincided with the minimum remaining wall for Model 1. The length of the notch was sized to match the length of the origin 2.13 in. (origin length). This model is referred to in this section as Model 2. Figure 183 shows the 3D schematic and mesh for the Model 2 corrosion feature with the 2.13 in. notch. The modeling assumptions for Model 2 were made to satisfy the following two objectives:

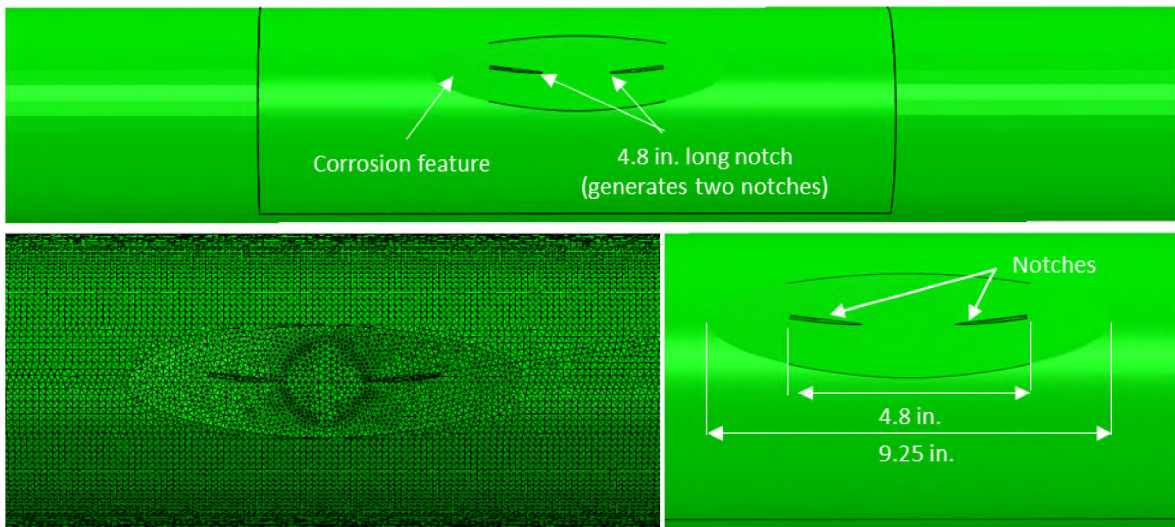
- Illustrate the combined effect of the striated grooves and corrosion feature.
- Model the remaining wall thickness (85% wall loss) with the presence of a notch (grooves).



**Figure 183: Model 2 Schematic and Mesh for Corrosion Feature and 2.13 in. Notch**

Figure 183 shows the raised corrosion feature, which had the effect of reducing the total volumetric metal loss. The presence of the notch introduced a stress concentration in the thinnest section of the corrosion feature, which had the effect of reducing the estimated failure pressure. However, the reduced volumetric metal loss would have had an opposing effect of increasing the estimated failure pressure.

A third model was designed to introduce the notch effect while maintaining the wall thinning within the ductile tearing region (2.13 in. circular region). The semi-elliptical bowl was modeled in the same way as Model 1. Unlike Model 2, the minimum wall thickness of 1.26 mm was maintained within the ductile tearing zone. A notch was introduced with its length increased to the macro definition of the origin (4.8 in.). Section 3.2.3 defines the macro definition of the origin as the length of the fracture surface between the chevron marks. The notch was positioned so that the deepest point was tangent to the circular ductile tearing region. Placement of the 4.8 in. long notch had the effect of creating two notches adjacent to the ductile tearing region. This model is referred to in this section as Model 3. Figure 184 shows the Model 3 notch geometry and position relative to the corrosion feature.



**Figure 184: Model 3 Schematic and Mesh for Corrosion Feature and 4.8 in. Notch**

These three models were developed to capture the complex effects of the corrosion feature geometry on the failure pressure. All models were meshed using 10-noded quadratic tetrahedron elements at the corrosion feature. The pipe geometry away from the corrosion feature was meshed with 8-noded linear brick elements (C3D8). An element size of approximately 0.1 to 0.05 in. was assumed at the corrosion feature. An element size of roughly 0.5 in. was used in regions away from the corrosion feature. This element size was established by running several models with varying element sizes to achieve a stress state independent of element size. Figure 185 represents the mesh of the 3D model used in the analyses. The FE models used a detailed meshing approach near the corrosion feature and a coarser mesh away from the feature to obtain the stresses and strains.

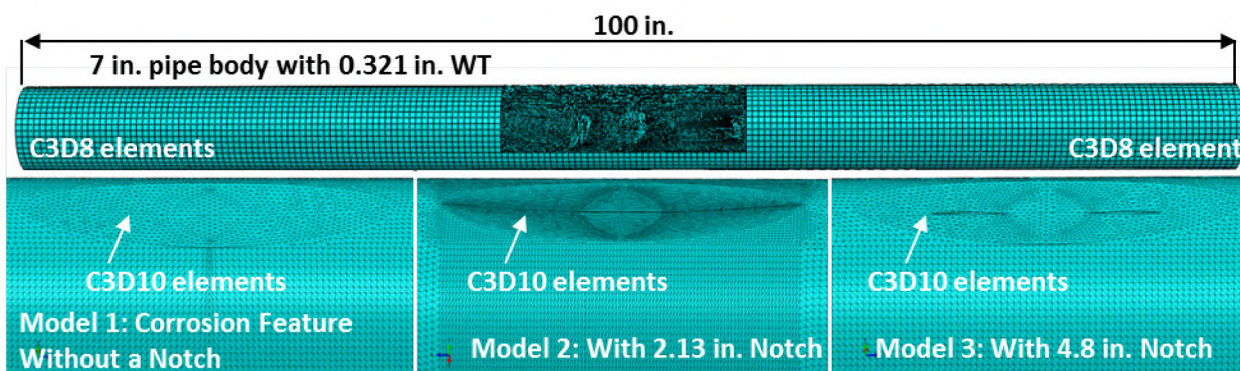
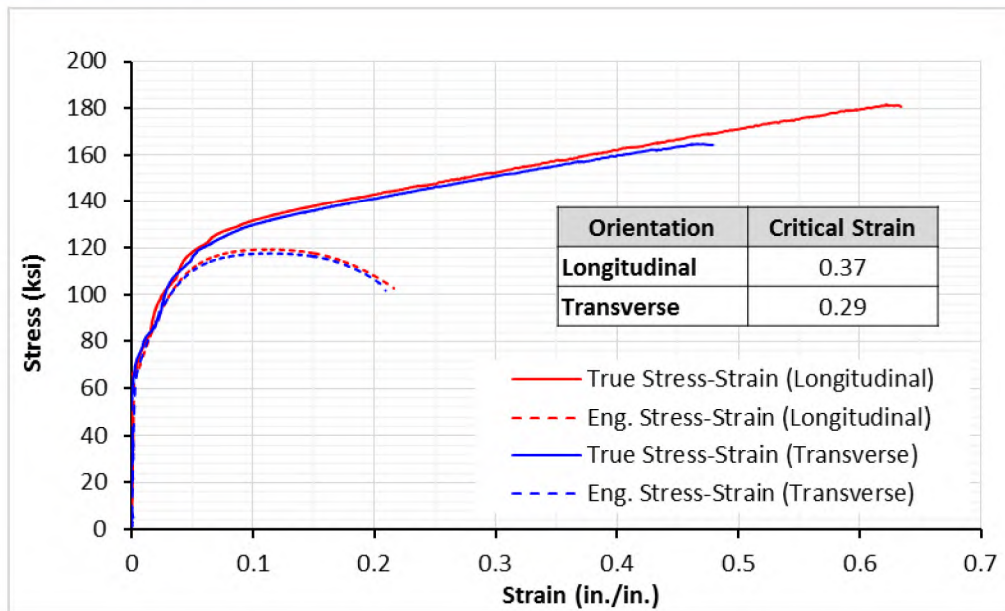


Figure 185: FE Model Mesh Elements

#### 4.1.2 Material Parameters

Blade conducted tensile tests on material extracted from joint 22 (failed joint) to capture the true stress-strain behavior of the grade J55 casing material and determine the critical strain, which is an important parameter used to determine strain-based failure conditions. The true stress-strain curves define the constitutive properties for an FEA. Section 7.1.6 discusses the specimen geometry, test method, and results for the critical strain testing. Figure 186 illustrates the representative true stress-strain curves and engineering stress-strain responses of the material in the transverse and longitudinal directions. Figure 186 also shows a table with the average longitudinal and transverse critical strain values taken from Table 28.



**Figure 186: Engineering and True Stress-Strain Responses of the Grade J55 Casing Material**

The average critical strain in the longitudinal and transverse orientations was 37% and 29%, respectively. The FE models used the average transverse critical strain of 29% for the strain-based failure prediction. Table 4 lists the grade J55 material properties used for the FE modeling. Typical Young’s modulus of 30,000 ksi and Poisson’s ratio of 0.3 were used in the analyses. The FE analyses used a yield strength of 55 ksi and the measured transverse stress-strain behavior in Figure 186 to compute the characteristic stiffness. The analyses used these constitutive properties to obtain the displacements, stresses, and strains at all elements and nodes of the model.

**Table 4: FEA Material Property Summary**

<b>Modulus of Elasticity (ksi)</b>	30,000
<b>Poisson’s Ratio</b>	0.3
<b>Critical Strain</b>	0.29
<b>Yield Strength (ksi)</b>	55

Casing and tubulars with notches or areas with metal loss develop higher stresses and strains when compared to a regular pipe section. The stress triaxiality would be higher and the induced stress state would be beyond the yield and ultimate tensile strength (UTS) at the localized notch and corrosion feature regions. Such local areas near the corrosion feature would develop large strains from the applied pressure and axial forces. A local linear indication or notch-like feature could further increase the stress triaxiality. Initiation, growth, and coalescence of microvoids to form cracks, known as “ductile plastic damage”, occur at the local regions, resulting in initiation of a crack by ductile tearing. Strain-based damage models were used to determine the onset of cracking due to local plasticity. Failure strain limit is a damage parameter that integrates local stress and strain states. The failure strain is a function of stress triaxiality, von Mises’s stress, and material mechanical properties.

Hancock [28] and Rice [29] et al. proposed a reference failure strain,  $\epsilon_f$ , i.e., a strain limit for ductile failure as:

$$\epsilon_f = 1.65\epsilon_0 \exp\left(-\frac{3\sigma_m}{2\sigma_{eq}}\right) \tag{1}$$

Where,

$$\sigma_m = \frac{1}{3}(\sigma_1 + \sigma_2 + \sigma_3) \tag{2}$$

$$\sigma_{eq} = \frac{1}{\sqrt{2}}\sqrt{(\sigma_1 - \sigma_2)^2 + (\sigma_2 - \sigma_3)^2 + (\sigma_3 - \sigma_1)^2} \tag{3}$$

The strain-based damage indicator,  $D_i$ , is computed based on incremental plastic strain, stress triaxiality, and the failure strain given by Eq. 4.

$$D_i = \int_0^{\epsilon_{eq}} \frac{d\epsilon_{eq}}{\epsilon_f} \tag{4}$$

$$D_i = DFDI = \frac{1}{1.65\epsilon_0} \int_0^{\epsilon_{eq}} \exp\left(\frac{3\sigma_m}{2\sigma_{eq}}\right) d\epsilon_{eq} \tag{5}$$

Where,

$\epsilon_{eq}$  = equivalent strain

$\epsilon_f$  = reference strain

$\epsilon_0$  = critical strain

$\sigma_m$  = mean stress

$\sigma_{eq}$  = equivalent stress

$\sigma_1, \sigma_2,$  and  $\sigma_3$  = principal stresses

### 4.1.3 Loads and Boundary Conditions

The 3D pipe models were modeled, meshed, and analyzed using the FE procedure. They were constrained at one end to restrict movement along the longitudinal and transverse directions. An internal pressure varying from 0 to 4,000 psi was applied to the interior surface of the pipe geometry to generate hoop stress. Axial force, external pressure, and internal pressure were inferred from the gas injection load summary, as listed in Table 5. A maximum axial tensile force of 236.5 klf was applied at one end of the 3D pipe model. Internal pressure was varied to 4,000 psi to determine the point of crack initiation (i.e., internal pressure at which DFDI=1.0).

**Table 5: Gas Injection Conditions and the Relevant Load Summary at a Depth of 892 ft**

Surface Gas Inj. Temp. (°F)	Gas Inj. Rate (MMscf/D)	Inj. Period	Internal Pressure (psi)	External Pressure (psi)	Dog Leg Severity (Deg/100°)	Axial Force (lbf)	Temp. (°F)
70	6	12 hr	2,791	386	1.79	218,187	77
70	6	9 mo	2,791	386	1.79	227,607	75
70	30	12 hr	2,791	386	1.79	230,983	74
70	30	9 mo	2,791	386	1.79	236,545	74

The loads at 892 ft were estimated by setting up the wellbore configuration in the tubular mechanics and wellbore heat transfer analysis program StrinGnosis. The wellbore heat transfer model simulates the heat

transfer of fluids based on a range of gas rates, injection temperatures, and injection periods. The model estimates the temperature profile of the wellbore and casing vs. depth. The reported surface pressures and fluids in the wellbore and the temperature and directional profile were used in the tubular mechanics model to calculate the internal and external pressures and axial force vs. depth at the depth of interest of 892 ft. The gas injection temperature at the wellhead was not recorded in the field. A surface injection temperature of 70°F is a reasonable injection temperature for the gas of October 23, 2015. The reported historical National Oceanic and Atmospheric Administration (NOAA) temperatures at the Van Nuys, California, airport for October 23, 2015, were 90°F maximum and 58°F minimum. The axial force does vary somewhat with temperature, but the change is small over the range of injection rates and period of injection.

### 4.1.4 Results and Findings

Models 1, 2, and 3 were analyzed with the loads and boundary conditions described in Section 4.1.3. Differential pressure was applied to the interior surface of the pipe geometry, and the stress and strain states of the models were analyzed. DFDI was computed at all elements and nodes and was compared to the failure criteria of DFDI = 1.0. Figure 187 shows the DFDI evolution with differential pressure at the edge of the notch, supposedly the most critical location of the pipe model. The DFDI evolution was exponential, which means that the DFDI increased from 1.0 to 1.4 with a small increase in pressure, which suggests that a crack could initiate and grow by ductile tearing.

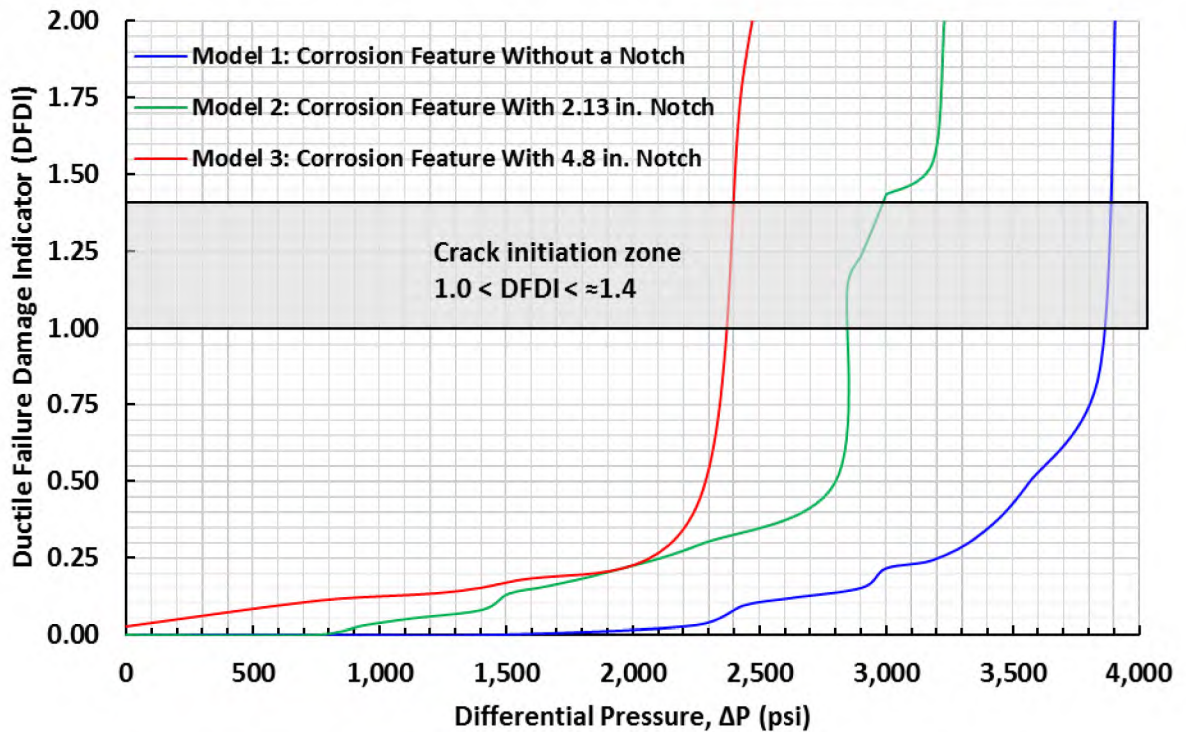


Figure 187: DFDI Evolution with Differential Pressure for Models 1, 2, and 3

The stress state for Model 1 was the least severe of the three models. The point of crack initiation occurred at an approximate pressure of 3,850 psi. The corrosion feature (i.e., semi-elliptical bowl) was raised for Model 2 by 1.0 mm, which reduced the volumetric metal loss due to corrosion. The point of crack initiation for Model 2 was approximately 2,836 psi. Model 3 increased the length of the notch to 4.8 in. and maintained the corrosion feature geometry from Model 1. Introduction of the notch geometry

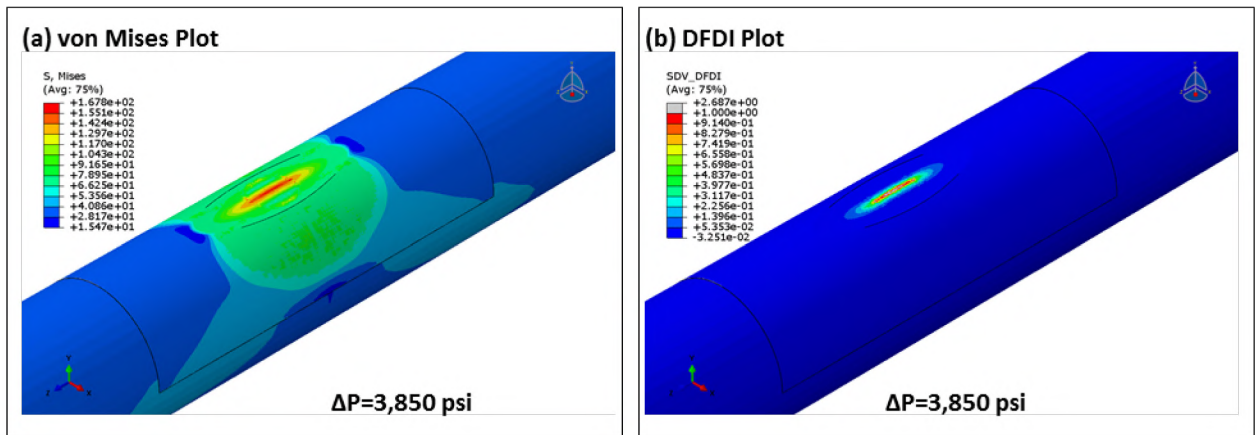


into the corrosion feature created two notches on each side of the origin region. Results for Model 3 showed that a crack would initiate at a differential pressure of approximately 2,327 psi. The modeling assumptions and results suggest that the actual differential pressure for the corrosion feature and linear indications would have been between 2,327 psi (Model 3) and 2,836 psi (Model 2). Table 6 lists the differential pressures for crack initiation on the three models.

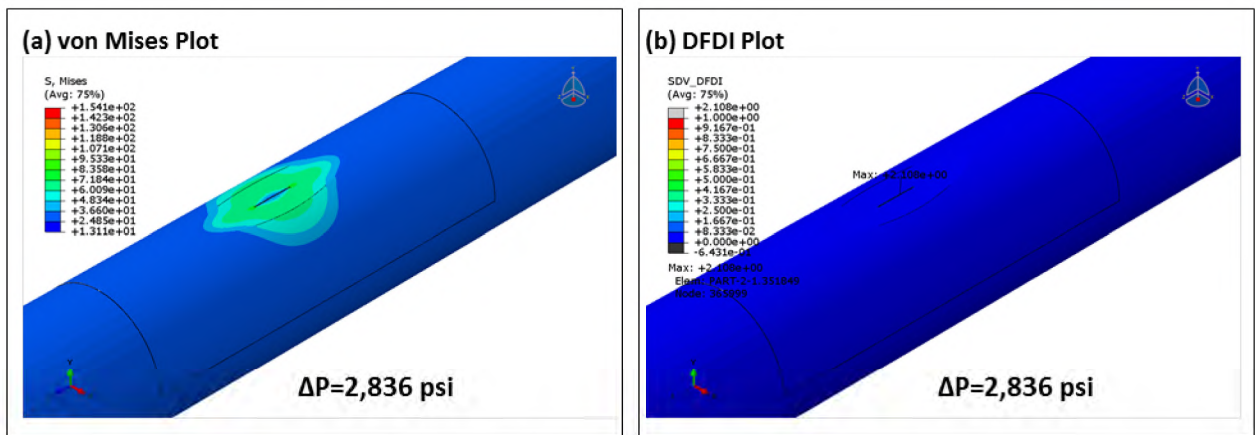
**Table 6: Differential Pressure ( $\Delta P$ ) Summary**

Model	Differential Pressure (psi)
<b>Model 1:</b> Corrosion feature without a notch	3,850
<b>Model 2:</b> Corrosion feature with a 2.13 in. notch	2,836
<b>Model 3:</b> Corrosion feature with a 4.8 in. notch	2,327

The von Mises and DFDI plots for Models 1, 2, and 3 are shown in Figure 188, Figure 189, and Figure 190, respectively. The figures illustrate that the ductile tearing region has a high stress state and a localized region with a DFDI > 1.0.



**Figure 188: Model 1 (a) Von Mises and (b) DFDI Plots**



**Figure 189: Model 2 (a) Von Mises and (b) DFDI Plots**

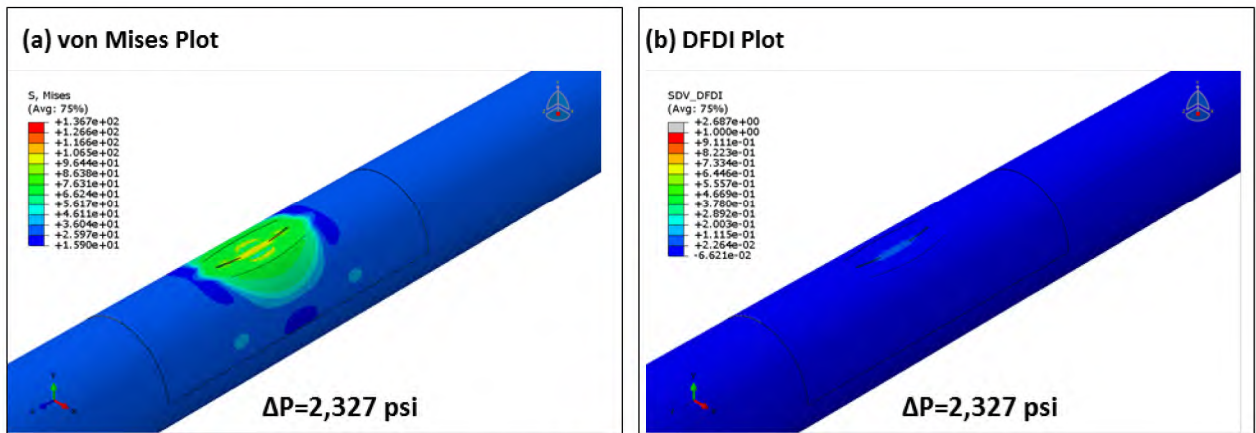


Figure 190: Model 3 (a) von Mises and (b) DFDI Plots

3D pipe models cause radial expansion with increased internal pressure. Localized regions near the corrosion feature have a significantly lower wall thickness and bulge considerably with the increasing pressure. Figure 191 illustrates the maximum bulge at the center of the corrosion feature for Models 1 and 3. Model 3 showed a bulge of approximately 0.17 in., as shown in the displacement contour (Figure 192). The bulge in Model 3 (4.8 in. notch) is higher than in Model 1 (no notch). Model 2 (2.13 in. notch) showed bulging below Models 1 and 3 due to the increase in remaining wall. Model 2 was not included in the plot. The plots in Figure 191 show that the bulge increased exponentially once the crack initiation stage (DFDI >1.0) was reached. These results further support that the ductile tearing occurred after the crack had initiated.

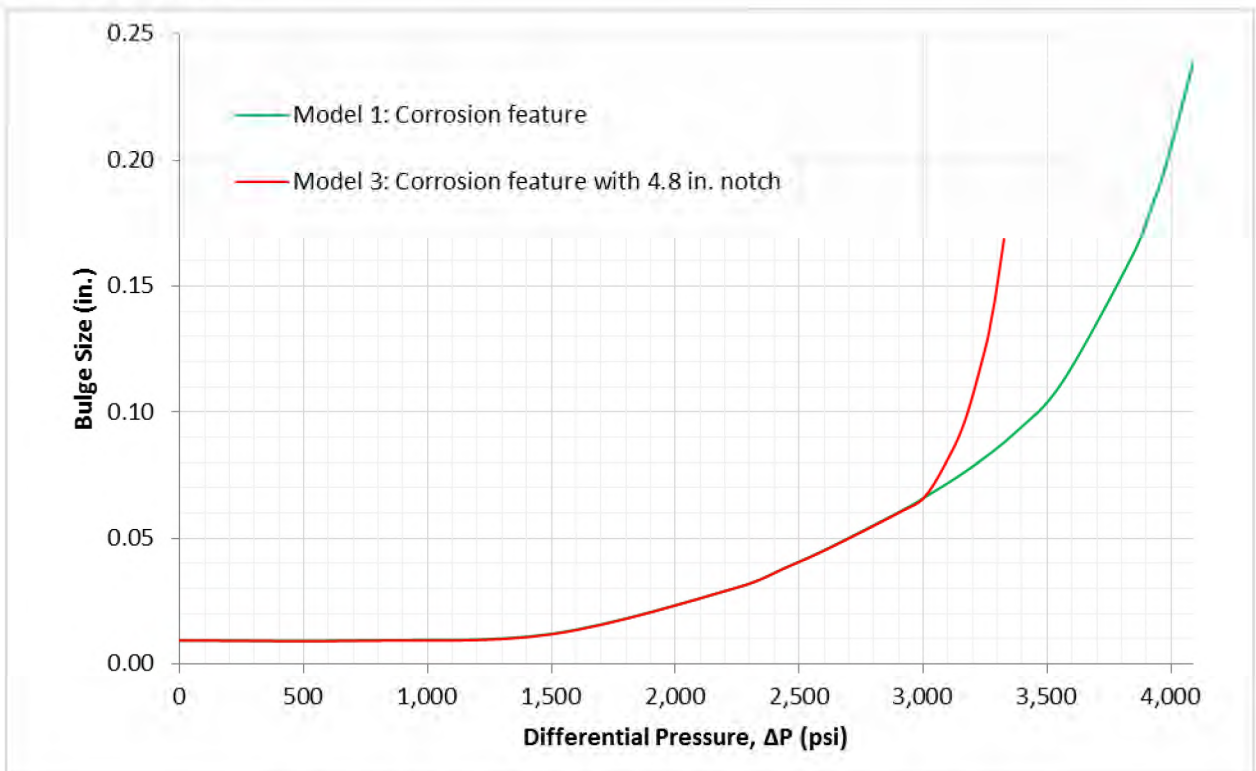


Figure 191: Pipe Bulge at the Center of the Corrosion Feature

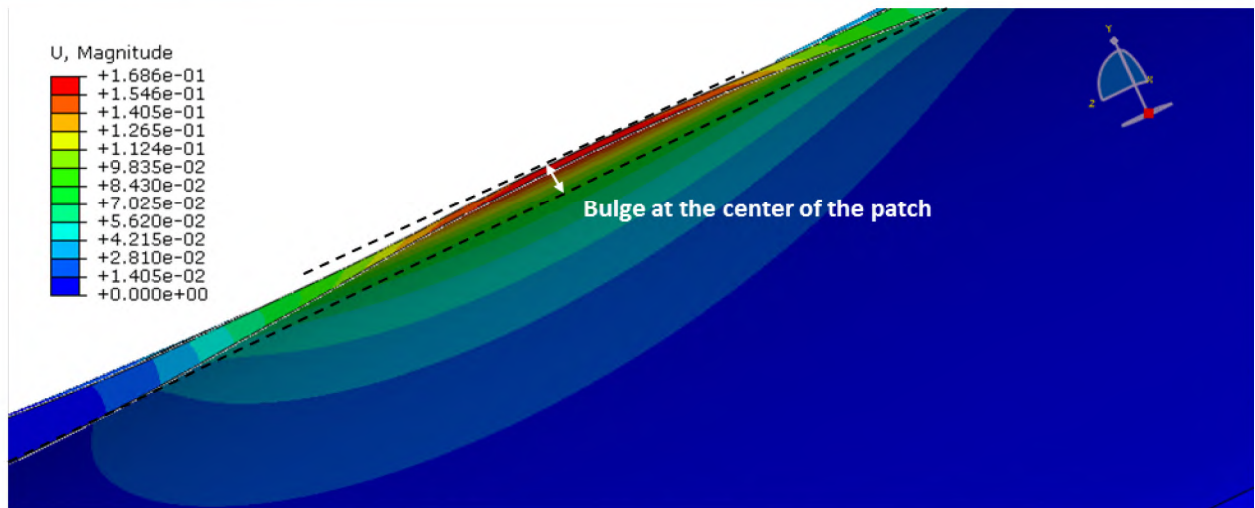


Figure 192: Model 3 Bulge at the Center of the Corrosion Feature

## 4.2 Axial Rupture Tearing Instability

The FEA and DFDI showed that a 2.13 in. long and an 85% deep crack could form at a differential pressure of 2,327–2,836 psi in the 2.13 in. ductile tearing region. An FE crack model was used to determine if a 2.13 in. long and an 85% deep crack would be unstable. A fracture toughness-based failure criterion was used to assess the instability of the crack.

A 3D quarter symmetric cylindrical geometry was used to analyze the crack in the 7 in. casing with a wall thickness of 0.321 in. The casing segment had a length of 35 in. (i.e., Length = 5 × OD). Figure 193 shows the pipe and crack geometry. The model was sufficiently refined with an element size of 0.002 in. near the crack tip. Strains are singular at the crack tip and generate very high stresses. Wedge elements were used at the crack front to capture the strain singularity and effectively obtain the contour integrals and stress intensity factors. Figure 193 shows the location of the wedge elements.

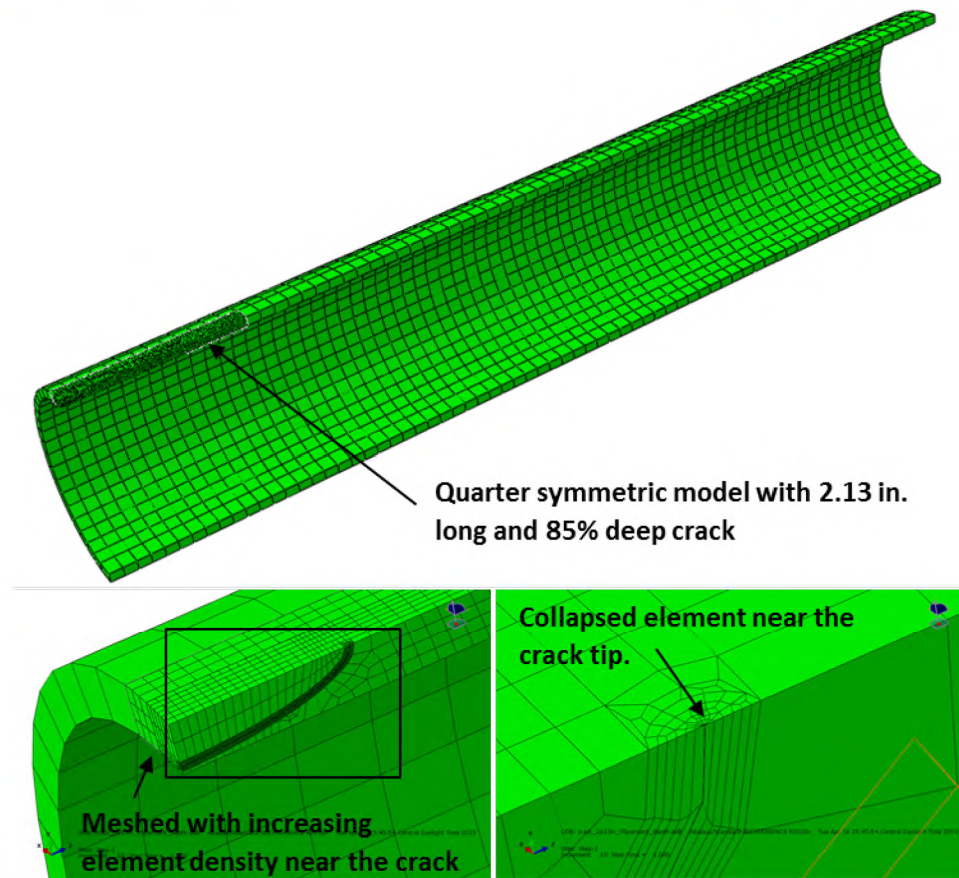


Figure 193: Schematic of 3D Quarter Symmetric Casing Segment with Crack

#### 4.2.1 Material Charpy V-Notch to Fracture Toughness ( $K_{mat}$ ) Conversion

Charpy impact energy is an indirect measure of material toughness and serves as a tool to study DBTT. It is widely applied to demonstrate the relative toughness of materials. Section 7.1.8 discusses the specimens, methodology, and results of the Charpy V-notch testing for the 7 in. casing material. The specimens were tested at various temperatures, and ductile-brittle transition curves were established for each extracted joint. Fracture toughness testing is a quantitative method for evaluating the fracture toughness of a material. Section 7.1.9 discusses the fracture toughness testing of the specimens, methodology, and results for the 7 in. casing material. The results from the testing were not valid and could not be reliably used for this analysis due to the specimens' size and material behavior.

For the Charpy impact energy to be used quantitatively for the analysis, it had to be converted to fracture toughness. Empirical and semi-empirical correlations exist in literature for conversion from CVN impact energy to fracture toughness. The British Standard (BS) 7910 presents the following three correlations for CVN impact energy and fracture toughness:

- Lower bound relations for lower shelf and transitional behavior
- Lower bound relations for upper shelf behavior
- Master curve approach for lower shelf and transitional behavior

The lower bound relations for lower shelf and transitional behavior were chosen to convert the CVN impact energies into fracture toughness. Figure 198 shows a plot of the average half-size impact energy vs. the temperature for the specimens from all the 25 extracted casing joints. The lower bound relations for lower shelf and transitional behavior provide a conversion for a wide range of steels on the lower shelf and in the transition region. The lower bound, lower shelf conversion gives the fracture toughness values given by Eq. 6 [30].

$$K_{mat} = \left[ (12\sqrt{C_v} - 20) \left( \frac{25}{B} \right)^{0.25} \right] + 20 \tag{6}$$

Where,

$K_{mat}$  = fracture toughness estimate (MPa√m)

$B$  = thickness of the material for which an estimate of  $K_{mat}$  is required (mm)

$C_v$  = lower bound Charpy V – Notch impact energy at the service temperature (J)

Table 7 shows the half-size impact energies, converted full-size impact energies, and estimated  $K_{mat}$  values for the points within the box in Figure 194. Half-size Charpy impact energies were converted to full-size by multiplying them by a factor of 2 [27]. The goal of the conversion was to estimate the fracture toughness of the grade J55 material based on the orientation and temperature of the axial rupture. This corresponds to the C-L orientation and a temperature of 80°F (26.7°C). The closest test temperature was 25°C, which gave an estimated  $K_{mat}$  value of 48.3 ksi-in<sup>1/2</sup>.

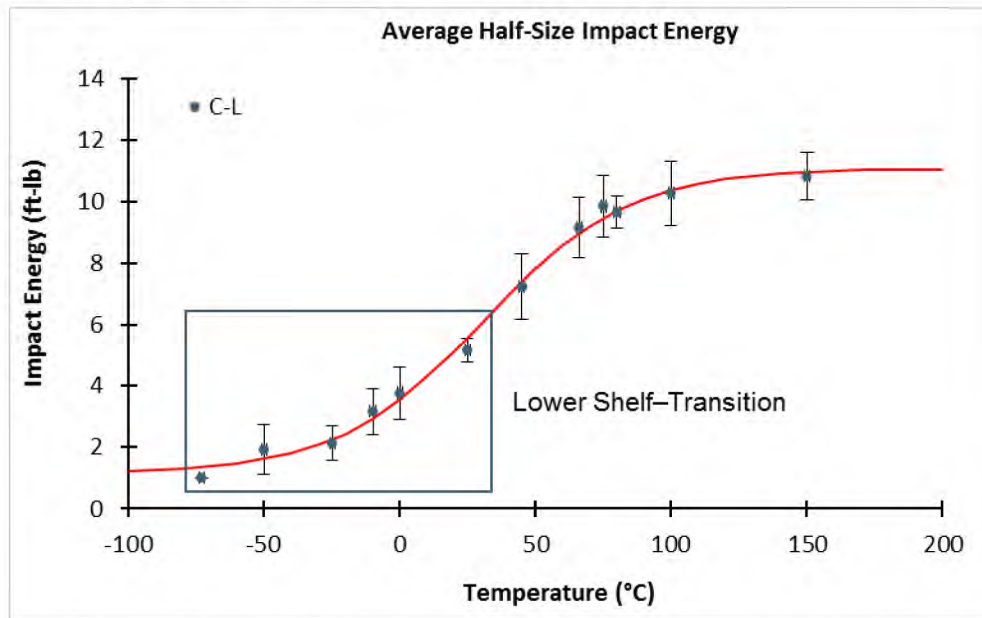
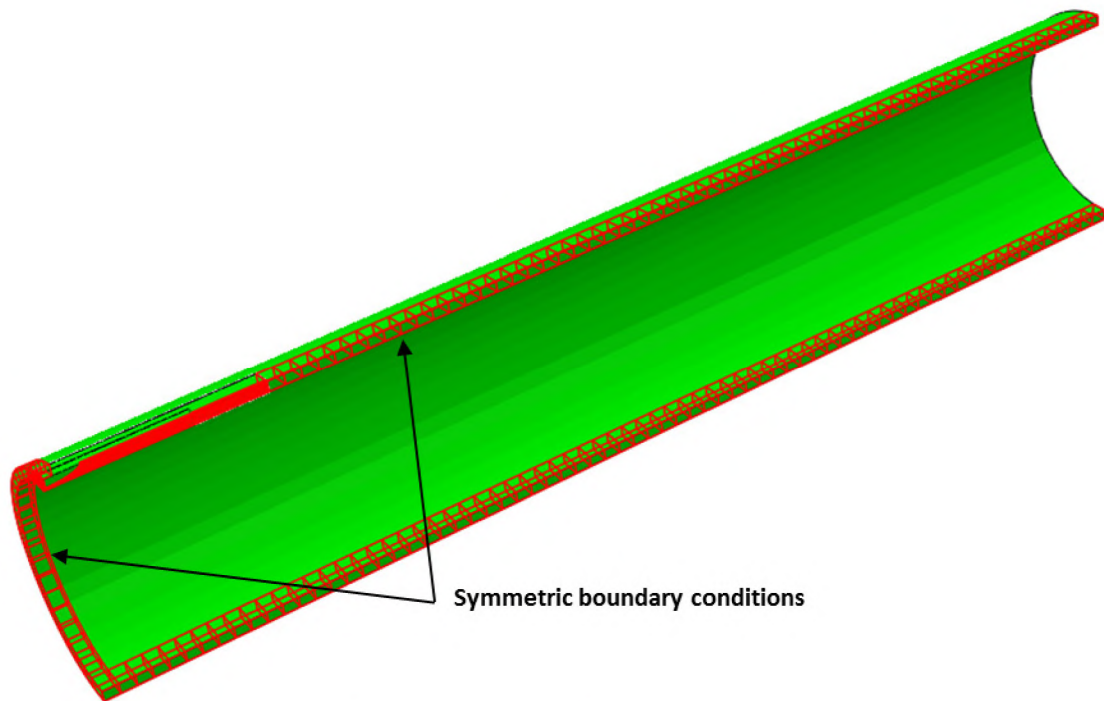


Figure 194: Average Half-Size Charpy Impact Energy Versus Temperature for C-L Orientation

**Table 7: Average C-L CVN Results and Estimated  $K_{mat}$  Values for 7 in. Casing**

Temperature (°C)	Orientation	Average Half-Size Impact Energy (ft-lb)	Average Full-Size Impact Energy (J)	Estimated $K_{mat}$ (ksi-in <sup>1/2</sup> )
25	C-L	5.17	14.0	48.3
0	C-L	3.77	10.2	40.4
-10	C-L	3.17	8.6	36.5
-25	C-L	2.13	5.8	28.9
-50	C-L	1.92	5.2	27.1
-73	C-L	1.00	2.7	17.9

The mesh at the crack front was used to accurately obtain the stresses and strains surrounding the crack tip. Symmetric boundary conditions were used to simplify the model. The boundaries were applied on symmetric surfaces and corresponded to the pipe axes. Figure 195 shows the boundary conditions for the model. Stress intensity factors were computed at the crack front using the surrounding nodes. Values from the third or fourth contours were considered appropriate and are plotted at various pressures in Figure 196.



**Figure 195: Symmetric Boundary Conditions**

The stress intensity factor for the crack model reached a value of 48.3 ksi-in<sup>1/2</sup> when the internal pressure was approximately 1,950 psi. Figure 196 illustrates that the crack was unstable beyond an internal pressure of 1,950 psi. The results show that a 2.13 in. long and an 85% deep crack would have propagated at differential pressures  $\geq 1,950$  psi. The estimated strain-based failure pressure (2,327–2,836 psi) was above the fracture toughness-based instability pressure (1,950 psi). This shows that as soon as the 2.13 in. crack formed by ductile tearing, it became unstable.

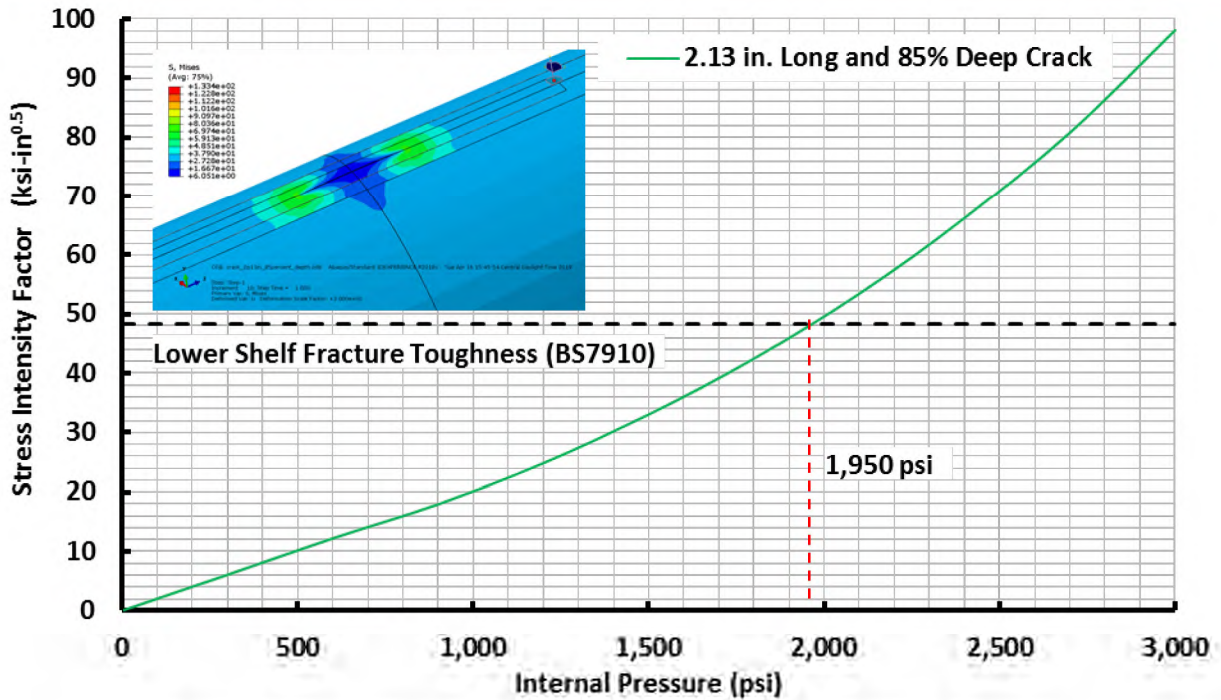


Figure 196: Stress Intensity Factor Evolution with Applied Internal Pressure

### 4.3 Circumferential Parting Critical Crack Size and Failure Temperature

Section 3.3.1 discusses how the circumferential parting originated from one of two possible critical crack candidates. The first crack candidate had a length of 14.54 mm and a depth of 5.22 mm. The other candidate had a length of 21.72 mm and a depth of 5.22 mm. Figure 161 shows macro images of the critical crack candidates. The sizes of the crack candidates were based on visual and stereoscopic observation of the chevron marks. In this section, the sizes of the critical crack candidates were validated by estimating the material conditions at the time of the circumferential parting. The following were the methods used for the investigation:

1. Fracture mechanics calculations were performed to determine  $K_I$  for the two critical crack candidates.
2. The fracture-based failure criterion  $K_I=K_{IC}$  to determine  $K_{IC}$  was used.
3. The temperature of the material was estimated at the time of the circumferential parting based on the estimated  $K_{IC}$  values.
4. The estimated temperature was compared with the thermal model prediction [11] to validate the critical crack size and the failure temperature.

#### 4.3.1 Fracture Toughness of the Circumferential Parting

The circumferential parting of the SS-25 7 in. casing was characterized by cleavage without measurable macro-plastic deformation. A linear elastic fracture mechanics analysis was applicable because of the brittle nature of the circumferential parting. The failure condition was then defined by Eq. 7.

$$K_I \geq K_{IC} \quad (7)$$

$K_I$  is the stress intensity factor for a given crack and represents the driving force for the failure.  $K_{IC}$  is the plane strain fracture toughness of the material and represents the fracture resistance of the material. According to Eq. 7, the point at which the material fails can be determined by calculating a driving force ( $K_I$ ) that is equivalent to the fracture resistance of the material ( $K_{IC}$ ).

The following two industry-standard fracture mechanics methods were used to calculate  $K_I$  for a given crack geometry and size, casing dimensions, and loading conditions:

- API 579/ASME FFS-1 2016 Part 9—Assessment of Crack-Like Flaws [27]
- BS 7910 Guide to Methods for Assessing the Acceptability of Flaws in Metallic Structures [30]

In the current work, we have estimated the Mode I stress intensity factor ( $K_I$ ) by using the equations stated in API 579 and BS 7910. According to API 579, the Mode I stress intensity factor for a cylinder with an external semi-elliptical surface crack in the circumferential orientation under axial stress (no internal pressure) is given by Eq. 8 (Annex 9B.5.13.1 of API 579).

$$K_I = \left[ G_0 \left( \frac{pR_i^2}{R_0^2 - R_i^2} + \frac{F}{\pi(R_0^2 - R_i^2)} \right) + G_5\sigma_5 + G_6\sigma_6 \right] \sqrt{\frac{\pi a}{Q}} \quad (8)$$

Where,

$$Q = \begin{cases} 1.0 + 1.465 \left( \frac{a}{c} \right)^{1.65} & \text{for } \frac{a}{c} \leq 1.0 \\ 1.0 + 1.465 \left( \frac{c}{a} \right)^{1.65} & \text{for } \frac{a}{c} > 1.0 \end{cases} \quad (9)$$

$a$  = crack depth

$c$  = half crack length

$R_0$  and  $R_i$  = external and internal radii of the pipe

$F$  = net section axial force

$p$  = internal pressure

$\sigma_5$  and  $\sigma_6$  = net section bending stress about the  $x$  and  $y$  axis, respectively

$G_0, G_5,$  and  $G_6$  = influence coefficients of the external crack

In the current work,  $p$ ,  $\sigma_5$ , and  $\sigma_6$  are assumed to be zero, and Eq. 8 simplifies to Eq. 10.

$$K_I = \left[ G_0 \left( \frac{F}{\pi(R_0^2 - R_i^2)} \right) \right] \sqrt{\frac{\pi a}{Q}} \quad (10)$$

Section M.7 of BS 7910 discusses the stress intensity factor solutions for curved shells under internal pressure and mechanical loads. The general form of the stress intensity factor solution is given in the equation M.1 of the document and shown in Eq. 11.

$$K_I = (Y\sigma)\sqrt{\pi a} \quad (11)$$

$(Y\sigma)$  could be the contribution from primary and/or secondary stresses. In the current work, we considered the primary stress due to the axial loading. We also assume that there was no contribution from bending stresses. In essence, we can use Eq. 12 as our governing equation in calculating the stress intensity factor according to BS 7910.

$$K_I = [Mf_w(K_{tm}M_{km}M_mP_m)]\sqrt{\pi a} \quad (12)$$



Where,

$$M = 1$$

$$f_w = \sqrt{\sec\left(\left(\frac{\pi c}{W}\right)\sqrt{\frac{a}{b}}\right)} \quad (13)$$

$B$  = pipe wall thickness

$W$  = circumferential length of the pipe =  $\pi D$

$D$  = outside diameter of the pipe

$P_m$  = the primary stress due to axial load for the current work

$k_{tm}$  and  $M_{tm} = 1$

$M_m$  is defined and given in page 245 of BS 7910

Blade implemented the above stress intensity factor solutions using an application built in-house by using Microsoft Excel. The application has been verified and tested by experts and has been in use for the past 10 years by Blade and its clients. The axial stress used in the calculations was 35,541 psi based on the SS-25 loads at 892 ft (refer to Table 5). The nominal 7 in. casing dimensions for the OD (7.00 in.) and WT (0.317 in.) were used for the calculations. Table 8 shows the  $K_{Ic}$  results for each crack candidate based on the API 579 and BS 7910 fracture mechanics models.

**Table 8:  $K_{Ic}$  for Two Crack Candidates for the Circumferential Parting**

Analysis	Crack Length (mm)	Crack Depth (mm)	Fracture Mechanics Model	Fracture Toughness $K_{Ic}$ (ksi-in <sup>1/2</sup> )
1	14.54	5.22	API 579	27.6
2	14.54	5.22	BS 7910	26.9
3	21.72	5.22	API 579	31.8
4	21.72	5.22	BS 7910	32.1

### 4.3.2 Fracture Toughness Testing

Metcut Research Inc. performed fracture mechanics-based toughness testing under the direction of Blade. Section 7.1.9 discusses the fracture toughness testing specimens, methodology, and results in detail. Fracture toughness testing was performed at five temperatures because the fracture toughness of grade J55 steel has a strong dependence on temperature. The five test temperatures were 75°F (24°C), 32°F (0°C), -13°F (-25°C), -58°F (-50°C), and -148°F (-100°C). The following two ASTM standards were followed due to the anticipated brittleness of grade J55 steel at temperatures below 32°F:

- ASTM E399 ( $K_{Ic}$ ) for brittle behavior [31]
- ASTM E1820 ( $J_{Ic}$  and J-R curve) for ductile behavior [32]

The testing was operated in a single rising load mode by using the direct current potential drop (DCPD) method for crack increment ( $\Delta a$ ) monitoring. The results from the single rising load test were analyzed per ASTM E1820 or ASTM E399, depending on the material behavior.

Two specimen orientations (C-L and L-C) were used as described in Section 7.1.9. Figure 298 shows a diagram of the various specimen orientations. The C-L and L-C orientations have the crack plane in the

longitudinal (L) and circumferential (C) orientations, respectively. The L-C orientation was considered for this analysis due to the orientation of the circumferential parting.

The  $J_{IC}$  values provided by the five test temperatures were not valid because of one or both of the following reasons:

- The occurrence of large pop-ins prior to reaching the 0.2 mm offset line
- Insufficient number of data points to establish the power law regression line

The tests did not meet  $K_{IC}$  requirements due to the small size of the specimens, dictated by the 7 in. casing dimensions. However, the tests did provide conditional  $K_Q$  values per ASTM E399. Figure 197 shows a plot of  $K_Q$  vs. test temperature. In general,  $K_Q$  should decrease with temperature, which is the opposite of what is observed in Figure 197. The discrepancy in trend, which can be attributed to the small specimen size, prevented the use of the  $K_Q$  values.

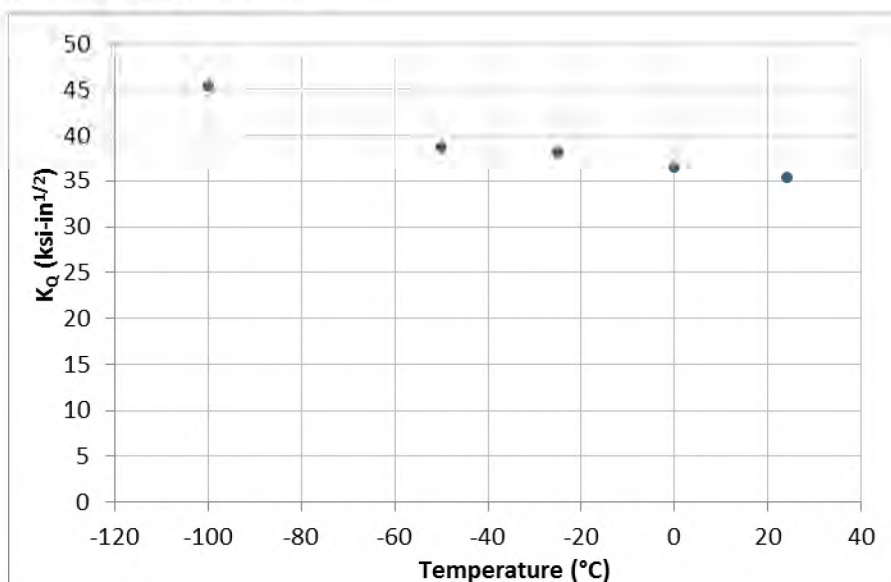


Figure 197:  $K_Q$  Versus Test Temperature

### 4.3.3 Failure Temperature Estimation

The measured fracture toughness values could not be used for failure temperature estimations as described in Section 4.3.2. Fracture toughness values were estimated from CVN impact energies in lieu of using the measured values. Section 4.2.1 describes the method and equations used to convert CVN impact energies into fracture toughness estimates. The DBTT curves were established based on the CVN test data. Section 7.1.8 describes the specimens, methodology, and results for the Element Materials Technology CVN testing. Figure 198 shows the DBTT curve based on the half-size impact energy in the L-C orientation. The figure shows that the CVN values used to establish the fracture toughness of the circumferential parting are located in the transition region adjacent to the lower shelf (blue box). BS 7910 recommends Eq. 6 for estimating fracture toughness from the CVN values in this region. Table 9 shows the estimated fracture toughness values based on the average impact energy at each test temperature.

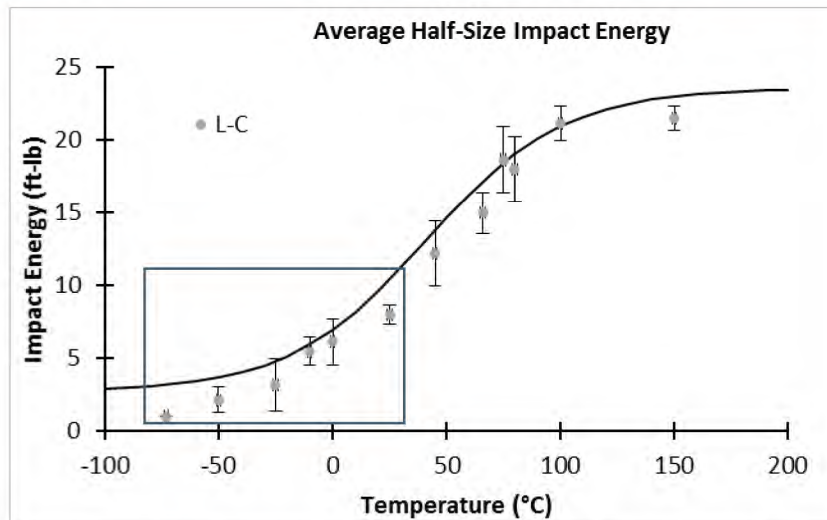


Figure 198: Average Half-Size Charpy Impact Energy Versus Temperature for L-C Orientation

Table 9: Average L-C CVN Results and Estimated  $K_{mat}$  Values for 7 in. Casing

Temperature (°C)	Orientation	Average Half-Size Impact Energy (ft-lb)	Average Full-Size Impact Energy (J)	Estimated $K_{mat}$ (ksi-in <sup>1/2</sup> )
0	L-C	6.12	16.6	53.1
-10	L-C	5.47	14.8	49.9
-25	L-C	3.18	8.6	36.6
-50	L-C	2.12	5.7	28.8
-73	L-C	1.00	2.7	17.9

Regression analysis was used to fit the general DBTT equation (Eq. 21) through the average half-size impact energy data (Figure 198 [black line]). The results from the regression are shown in Eq. 14.

$$C_v = 12.05 + 10.82 \cdot \tanh\left(\frac{T-42.49}{59.54}\right) \tag{14}$$

The lower shelf fracture toughness conversion equation (Eq. 6) was used to convert the results from Eq. 14 into an estimated  $K_{IC}$  value for the casing material at a given temperature. A non-linear solver was used to satisfy the failure condition in Eq. 7, where  $K_I$  values were estimated from the two critical crack candidates (Table 8). The results from the analysis are given in Table 10. The estimated failure temperature in the last column represents the temperature at which the given crack size becomes unstable and propagates.

Table 10: Estimated Failure Temperature for Circumferential Parting

Analysis	Crack Length (mm)	Crack Depth (mm)	Fracture Mechanics Model	Fracture Toughness $K_{IC}$ (ksi-in <sup>1/2</sup> )	Estimated Failure Temperature (°C)
1	14.54	5.22	API 579	27.6	-56.8
2	14.54	5.22	BS 7910	26.9	-60.4
3	21.72	5.22	API 579	31.8	-40.1

Analysis	Crack Length (mm)	Crack Depth (mm)	Fracture Mechanics Model	Fracture Toughness $K_{Ic}$ (ksi-in <sup>1/2</sup> )	Estimated Failure Temperature (°C)
4	21.72	5.22	BS 7910	32.1	-39.1

#### 4.3.4 Comparison and Validation

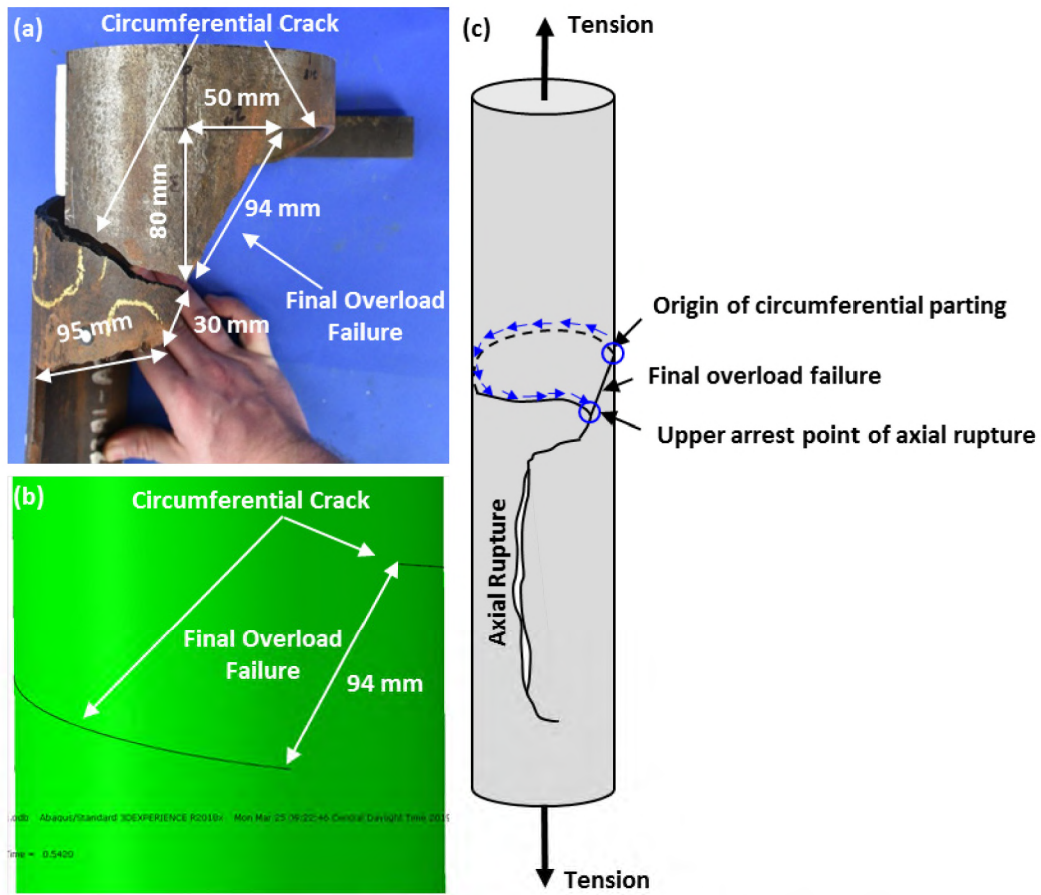
An independent investigation of the failure temperature was performed by using a thermal dynamic model [11], and it concluded that the initial axial rupture was a warm temperature ductile failure, which caused the pressure at the leak point to drop. Because SS-25 was injecting at the time, and the injection pressure was around 2,720 psi, Joule-Thomson [11] [33], cooling could produce injection gas temperature as low as -30°F (-34°C) subsequently to this initial ductile failure.

The comparison of the thermal model prediction (-34°C) with the fracture mechanics prediction (-39°C to -60°C) shows that the second critical crack candidate (21.72 mm × 5.22 mm) was closer and most likely was the critical crack size for the circumferential parting.

#### 4.4 Circumferential Parting Final Overload

The final overload failure occurred after the axial rupture and circumferential cracking events. An FEA was used to determine if the remaining ligament could support the weight of the 7 in. casing string. Figure 199 shows a schematic of the failure sequence and relevant dimensions for the final overload. Figure 199 (a) shows that the circumferential and axial distances between the upper arrest point of the axial rupture and the circumferential parting initiation site was 50 mm and 80 mm, respectively. The linear distance between the two points was 94 mm at approximately 32° from the longitudinal axis of the pipe.

The circumferential crack was modeled as a helical crack, with the arrest points positioned to match the 7 in. casing. Figure 199 (b) shows the FE model with the helical crack. The pipe was modeled as a 100 in. long 7 in. OD cylinder with a wall thickness of 0.321 in., as was done with the axial rupture models in Section 4.1. One end of the pipe was constrained to restrict movement in all directions. A maximum axial force of 236.5 klb was applied to the opposite end of the pipe. The tensile force at the failure location of 892 ft was taken from Table 5.



**Figure 199: Final Overload Schematic and Dimensions**

The pipe model failed to converge beyond an axial force of 128 klbf (54% of the total axial force). A high stress of approximately 180 ksi was observed at both ends of the circumferential crack. Figure 200 shows the various contour plots from the FEA at 54% of the total axial force. High stresses and the model instability at 54% of the total axial force suggest that the remaining ligament could not withstand the tensile force and would tear, causing the final overload failure. This observation is in agreement with the failure sequence described in Section 3.1.

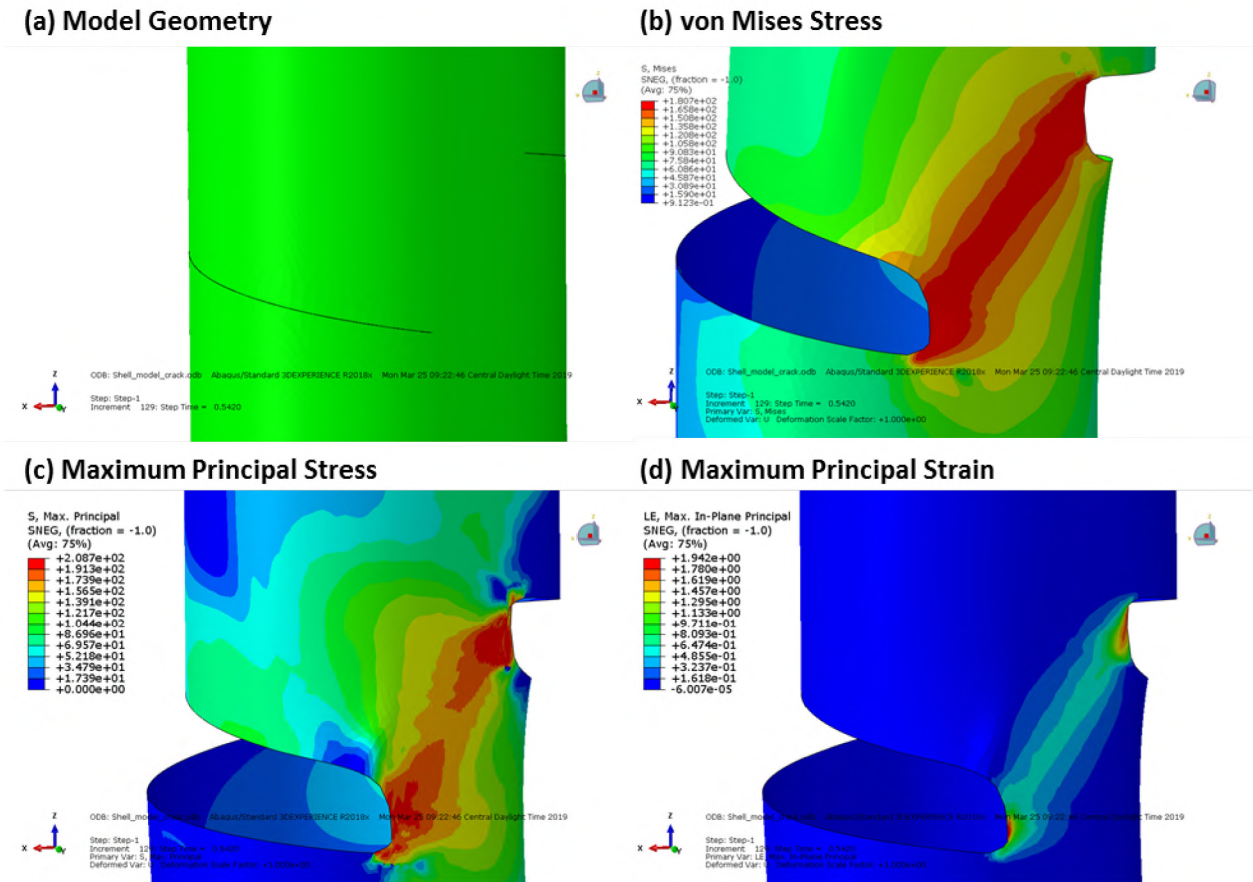


Figure 200: Geometry and FEA Results of the Final Overload Failure

## 4.5 Summary

The axial rupture, circumferential cracking, and final overload failure were validated using FEA and fracture mechanics-based approaches. Summaries for each of the failure events are as follows:

- Axial Rupture
  - The axial rupture was modeled using FEA to estimate the strain-based failure pressure. Three models were constructed to approximate the effects of the corrosion feature and striated grooves:
    - Model 1 approximated the effects of the corrosion feature. The feature was modeled as a semi-elliptical bowl with a major and minor axis of 9.25 in. and 3.72 in., respectively. The center of the bowl was a flat circle with a diameter of 2.13 in. The flat bottom represented the origin of the axial rupture, according to the metallurgical findings.
    - Model 2 approximated the effects of the striated grooves by modeling a 2.13 in. notch in the center of the origin. The corrosion feature was raised so that the bottom of the notch was equal to the minimum remaining wall of 1.26 mm.
    - Model 3 approximated the effects of the striated grooves by modeling a 4.8 in. notch in the center of the origin. The notch was placed so that the bottom was tangent to the flat circular region (origin). This had the effect of generating two notches adjacent to the origin.

The longer notch was based on the macro definition of the origin as described in the metallurgical findings.

- A DFDI value of 1.0 was used to identify the initiation of a crack. Models 1, 2, and 3 predicted pressures of 3,850, 2,836, and 2,327 psi, respectively. The results show that the actual failure pressure was most likely between 2,327 psi (Model 3) and 2,836 psi (Model 2).
- All models showed bulging in the corrosion feature, and this is consistent with the field observations. Model 3 showed the most pronounced bulging, with a measured value of 0.17 in.
- An FE crack model showed that a 2.13 in. long and an 85% deep crack would propagate at a pressure of 1,950 psi, based on fracture mechanics conditions.
- Circumferential Parting
  - The failure temperature for the circumferential parting was determined based on fracture mechanics. Stress intensity factors were determined based on API 579 and BS 7910 for the two critical crack candidates identified during visual examination of the circumferential parting origin.
  - Impact energy values were converted to fracture toughness based on the lower shelf and transition equation from BS 7910.
  - The results showed that the circumferential parting occurred at temperatures between  $-60^{\circ}\text{C}$  and  $-39^{\circ}\text{C}$ . This is consistent with the thermal model prediction of  $-34^{\circ}\text{C}$ .
- Final Overload Failure
  - A ligament remained after the axial rupture and circumferential cracking. The FEA results showed that the model became unstable at 128 klf (54% of the total axial force). The final ligament failed, which is consistent with the metallurgical observations.

The validations were consistent with the field and metallurgical observations. The results were in good agreement with the failure sequence that was determined during the metallurgical investigation.

## 5 Corrosion Feature and Mechanism Related to the 7 in. Casing Failure

---

The SS-25 casing failure sequence included the axial rupture and circumferential parting. Corrosion was identified on the OD of the 7 in. casing beginning at connection 14. The severity of the corrosion appeared to increase with well depth, based on field observations. The deepest corrosion occurred at joint 22 and caused the axial rupture. This section provides a detailed analysis of the corrosion features associated with the 7 in. casing failure, including:

- Corrosion distribution
- Corrosion characterization
- Scale analysis
- Biological analysis

These analyses were integrated and interpreted to determine possible corrosion mechanisms. Other features not related to the 7 in. casing failure are presented in Section 6.

### 5.1 Corrosion Distribution

Corrosion features appeared to have a correlation to depth, based on field observations made during Phase 3. The observations were qualitative rather than quantitative and did not provide an overall picture as to how the corrosion was distributed along the 7 in. casing. One of the main goals during Phase 4 was to generate numerical and graphical representations of the OD corrosion to help identify patterns associated with the corrosion distribution. The data were used to assist with the metallurgical investigation of the RCA and to cross reference with other observations and data sets (log data).

The target output for the distribution was a 2D color map showing corrosion severity as a function of depth and circumferential position. Corrosion severity can be measured with a combination of many different metrics. This analysis used corrosion depth and density as an indication of severity. Corrosion with larger depths or higher feature densities were considered more severe than shallower depths or lower feature densities.

Figure 201 shows the laser scan results for joints 1–25. The map shows that the OD corrosion began around joint 15, and this is consistent with the field observations (connection 14). Furthermore, the color map shows a distinct zone of severe corrosion beginning at 700 ft. Features were identified on the connections and adjacent 3 ft section of pipe above joint 15; however, the pipe bodies did not contain any features. The connections and adjacent 3 ft section of pipe body were not blasted. Features identified in this region were most likely associated with the non-blasted surface condition and handling marks rather than corrosion. Both the visual examination and laser scan data suggested the inexistence of notable corrosion above connection 14.



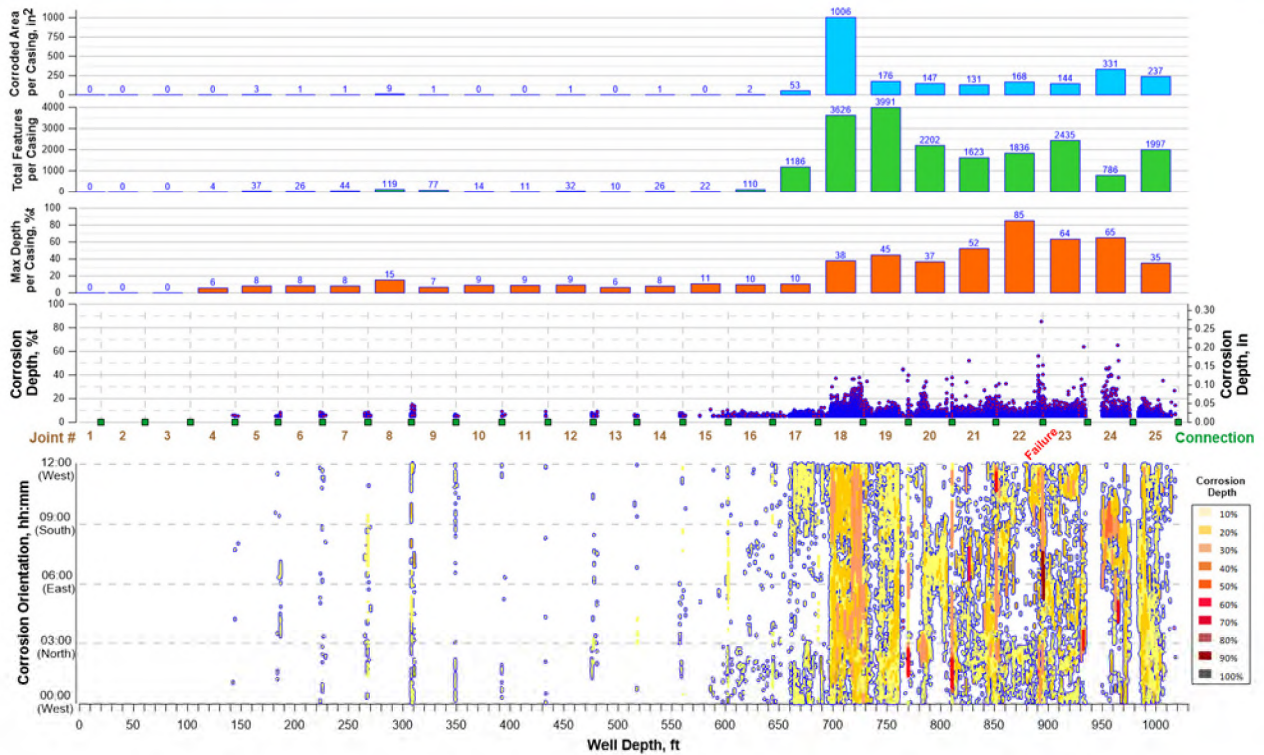


Figure 201: 7 in. Casing OD Corrosion Distribution for Joints 1 to 25

The color plot shows feature depth as a function of well depth and circumferential orientation. The corrosion was present around the entire OD circumference and did not appear to have a preferential orientation.

Figure 202 shows the laser scan results for joints 15–25. The plot above the 2D color map shows the maximum corrosion depth measurement at each well depth location. The abscissa is depth in feet and the ordinate is corrosion depth in percent NWT. The secondary axis on the right side of the plot shows the corrosion depth in inches. The plot reinforces the trends observed in the 2D color map. A spike in the maximum corrosion depth was observed at joint 22 near connection 23. This spike represents the corrosion associated with the axial rupture. This location is identified in the plot by the dark red region in the 2D color map.

The three remaining plots from bottom to top are bar graphs showing max depth, feature count, and corroded area for each joint, respectively. The max depth bar plot shows that joints 21–24 contained features greater than 50% NWT. The feature count bar graph shows how many features were identified for each joint. Joints 18 and 19 contained the most features with counts between 3,000 and 4,000. Feature counts are influenced by clustering parameters within the software. The same clustering parameters were used for all pipe body and connection scans so that the results could be compared. The maximum calculated density was 0.36 features/in<sup>2</sup>, based on the count (4,000 features), nominal dimensions, and joint length for joint 19.

The corroded area bar graph shows the summation of all the corrosion feature areas for each joint. Most of the joints had measured corroded areas of 350 in<sup>2</sup> or less. The maximum value of 1,000 in<sup>2</sup> occurred at joint 18 and is equivalent to a 9% area coverage.

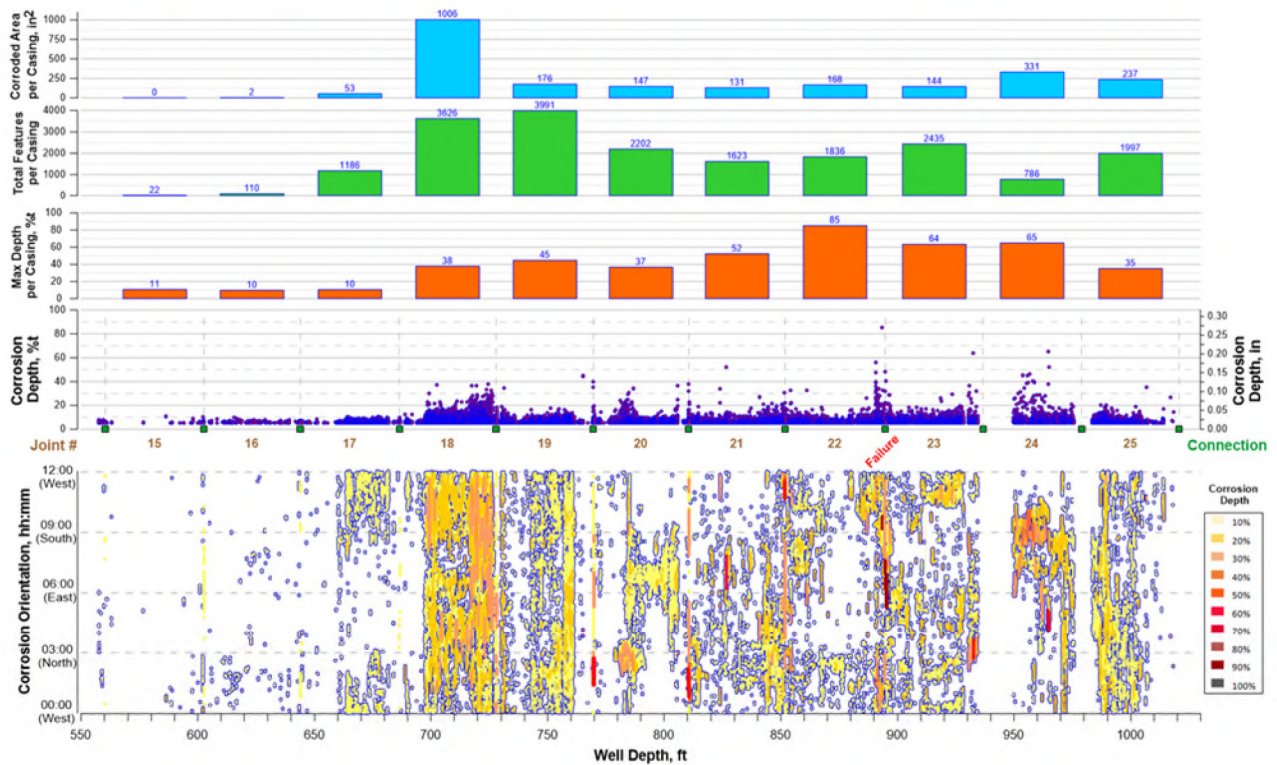


Figure 202: 7 in. Casing OD Corrosion Distribution for Joints 15 to 25

A visual examination was conducted, and three corrosion feature types were identified based solely on morphology (Type I, II, and III). Figure 203 shows examples of each of the following feature types:

- Type I:
  - Characterized by striated grooves with V-shaped tips
  - Typical of joints below 700 ft
  - Associated directly with the axial rupture in joint 22
- Type II:
  - Characterized as corrosion without striated grooves with an appearance similar to general corrosion and pitting
  - Occurred in most joints beginning at joint 15
  - Not associated with the axial rupture
- Type III:
  - Characterized as rectangular-shaped corrosion with little to no attack in the middle region
  - Occurred mostly on connections except for one large feature identified on joint 20
  - Not associated with the axial rupture

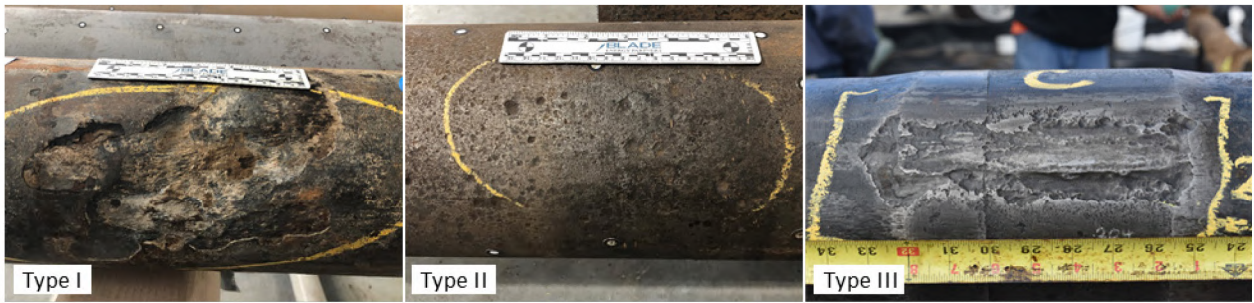


Figure 203: Types I, II, and III Corrosion Features

Table 11 summarizes the distribution of Types I, II, and III based on the visual examination. Joints 1–14 are not included because their corrosion content was little to none.

Table 11: Dominant Corrosion Features in 7 in. Casing

Joint or Connection	Type I	Type II	Type III	Comment
Connection 14	No	No	Yes	Shallow Type III corrosion.
Joint 15	No	Yes	No	Isolated shallow Type II corrosion.
Connection 15	No	No	Yes	Shallow Type III corrosion between the 9:00 and 12:00 o'clock positions.
Joint 16	No	Yes	No	Type II corrosion predominantly between the 3:00 and 9:00 o'clock positions.
Connection 16	No	Yes	No	Shallow Type II corrosion.
Joint 17	No	Yes	No	Type II corrosion predominantly between the 3:00 and 9:00 o'clock positions. Features are more pronounced and clustered as depth increases.
Connection 17	No	No	No	No visible corrosion feature.
Joint 18	Yes	Yes	No	The larger features are primarily Type I. The corrosion is predominantly between the 3:00 and 9:00 o'clock positions. Type I appeared to begin at approximately 9 ft from the cut.

Joint or Connection	Type I	Type II	Type III	Comment
Connection 18	No	Yes	No	Type II corrosion occurred predominantly between the 12:00 and 9:00 o'clock positions.
Joint 19	Yes	Yes	No	Mostly Type II corrosion with large Type I corrosion features.
Connection 19	No	Yes	Yes	The largest–deepest feature was Type III and occurred at 3:00 o'clock. Shallow Type II corrosion occurred between 6:00 and 9:00 o'clock positions.
Joint 20	Yes	Yes	Yes	The largest–deepest feature was Type III and occurred at 3:00 o'clock. Type I and II corrosion began at 12 ft from the cut between the 6:00 and 7:00 o'clock positions.
Connection 20	No	Yes	Yes	The largest–deepest feature was Type III and occurred at 3:00 o'clock. Shallow Type II corrosion occurred between 6:00 and 9:00 o'clock positions.
Joint 21	Yes	Yes	No	Mostly Type II corrosion with large Type I corrosion features.
Connection 21	No	Yes	No	Type II corrosion around the OD of the connection.
Joint 22	Yes	Yes	No	Failed joint. Type I and II corrosion features. The larger features appeared to be Type I.
Connection 22	No	No	Yes	Large Type III corrosion feature between the 3:00 and 6:00 o'clock positions.
Joint 23	Yes	Yes	No	Mostly Type II corrosion with large Type I corrosion features.
Connection 23	No	No	Yes	Large Type III corrosion feature.
Joint 24	Yes	Yes	No	Mostly Type I corrosion features along the 3:00 o'clock position.

Joint or Connection	Type I	Type II	Type III	Comment
Connection 24	No	Yes	No	Possible Type II corrosion feature. Note: Connection was not blasted.
Joint 25	Yes	Yes	No	Type I and II corrosion features along the length of the joint.
Connection 25	No	No	Yes	Type III corrosion feature.

## 5.2 Type I Corrosion Characterization

The axial rupture was caused by a Type I corrosion feature. The feature was 9.25 in. long and 3.72 in. wide and contained striated grooves. Severe wall thinning was observed near the center of the feature. Type I features were observed in many of the joints below 700 ft. Figure 204 (a) shows the Type I feature associated with the axial rupture. Figure 204 (b) shows the V-shaped tips typical of Type I corrosion and small striated grooves within larger striated grooves (groove within groove).

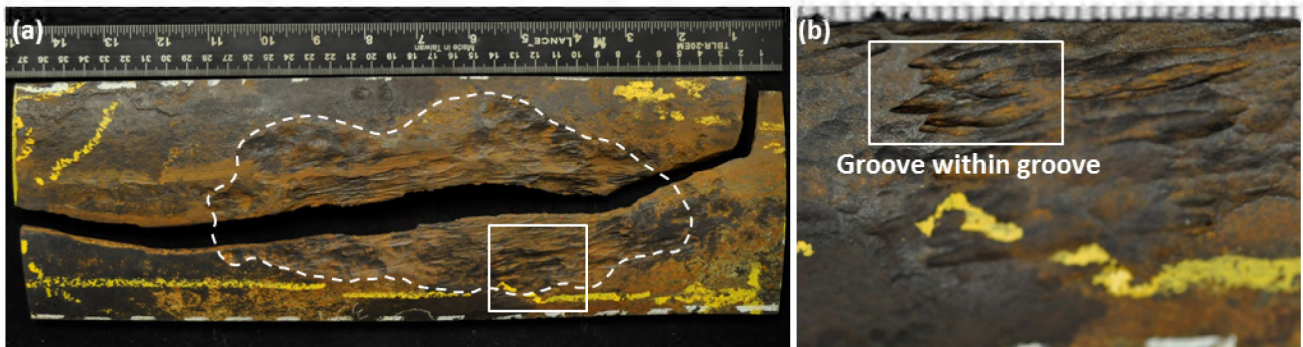


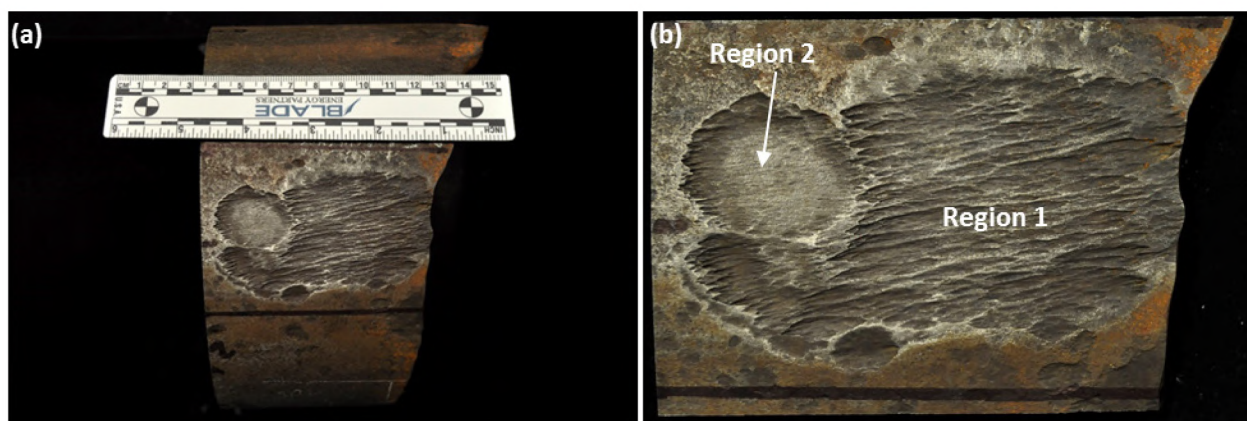
Figure 204: (a) Joint 22 Axial Rupture and (b) Type I Feature Showing V-Shaped Tips

Many Type I corrosion features were extracted from various joints and analyzed with the SEM and EDS. Some specimens were sectioned using the focused ion beam (FIB). Other specimens were subjected to metallographic cross sectioning so that groove profile and groove tips could be investigated. Selected specimens were analyzed using Raman spectroscopy to identify the chemical compounds in the corrosion products and groove deposits. The characterization results of the specimens are presented in this section.

### 5.2.1 Morphology

Corrosion morphology may provide insight into the underlying corrosion mechanism. Many specimens were examined to determine the morphological characteristics for a Type I corrosion.

Specimen C022B1, adjacent to the circumferential parting (Figure 205 [a]), was extracted from the failed joint (joint 22). The corrosion patch was approximately 3.5 in. long in the longitudinal direction and contained two regions. The first region had striated grooves that were present throughout the entire region. The second region contained groove tips along the outer boundary but was relatively flat in the mid-region.



**Figure 205: (a) Specimen C022B1 from Circumferential Parting Showing (b) Regions 1 and 2**

A simple analysis of the morphology was conducted to describe the density of grooves for specimen C022B1 (Figure 205 [b]). An image analysis software (ImageJ) was used to post-process the optical image of the Type I feature and estimate the number of grooves/in<sup>2</sup>. Figure 206 shows the post-processing results. There were 243 grooves within a 3.5 in. × 2.0 in. area, which equated to approximately 35 grooves/in<sup>2</sup>. The procedure for analyzing the groove density was as follows:

1. An optical image of the striated grooves was obtained.
2. The image was cropped showing only the striated grooves.
3. The image was converted into 8-bit using ImageJ.
4. The image thresholding in ImageJ was performed such that the tips of the striated grooves were defined.
5. The ImageJ function was used to count the number of islands with an area threshold of 0.0005 in<sup>2</sup>.



**Figure 206: ImageJ Thresholding for Specimen C022B1**

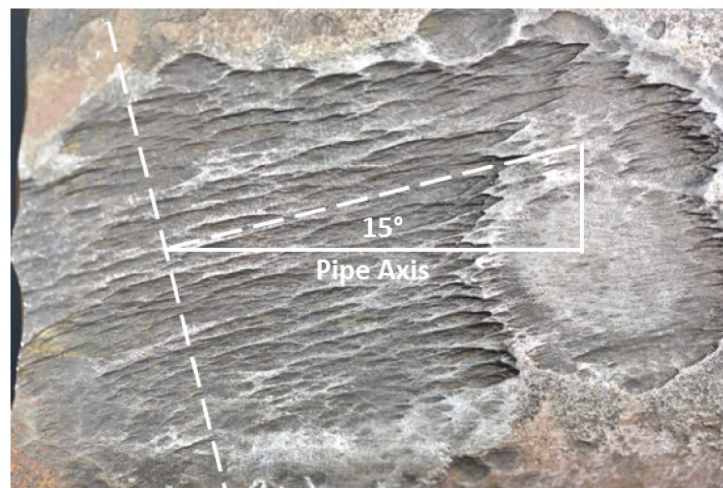
Most of the striated grooves were oriented at 0–15° from the longitudinal axis of the casing (Figure 207). The reason for this phenomenon is unclear. Literature on the subject is limited but suggested that striations could be the result of preferential attack of longitudinally oriented microstructural features, pearlite stringers, coring, and stressed regions. Striations are typically associated with MIC but can be caused by other mechanisms [34] [35].

Blade examined the microstructure of the grade J55 casing material to identify features that could be associated with the formation of the striated grooves. The material has an equiaxed grain microstructure.

Section 7.1.5 describes the 7 in. casing microstructure. The MnS inclusions for the casing steel were oriented parallel to the longitudinal axis (rolling direction); this is consistent with the striated grooves.

Typical MnS inclusion densities are approximately 500–3,500 inclusions/in<sup>2</sup>, based on a paper published by Li, et al. [36] whose study was done with steel containing 0.003 wt% of sulfur. The SS-25 7 in. casing material contained 0.030 wt% sulfur, which suggests that the grade J55 steel has a higher MnS inclusion density than what was found in the study.

The number of grooves per square inch of the metal was low, compared to the number of MnS inclusions per square inch. There was no clear correlation between the density of grooves and MnS inclusions present in the 7 in. casing. The comparison assumed a one-to-one correlation between the striated grooves and the MnS inclusions. However, this may not be an appropriate assumption due to the complexity of the grooving phenomenon. Additional study, which is beyond the scope of this work, is needed to fully understand the correlation between the striated grooves and MnS inclusions.



**Figure 207: Striated Groove Orientation for Specimen C022B1**

Specimen C021A3C extracted from joint 21 of the 7 in. casing has a corrosion patch with similar morphology as specimen C022B1 (Figure 208). The corrosion patch was approximately 3 in. long in the longitudinal direction and contained striated grooves present throughout the entire feature similar to the first region of C022B1 (Figure 205 [b]). Figure 208 [b] shows grooves within grooves, which is typical for Type I corrosion features.

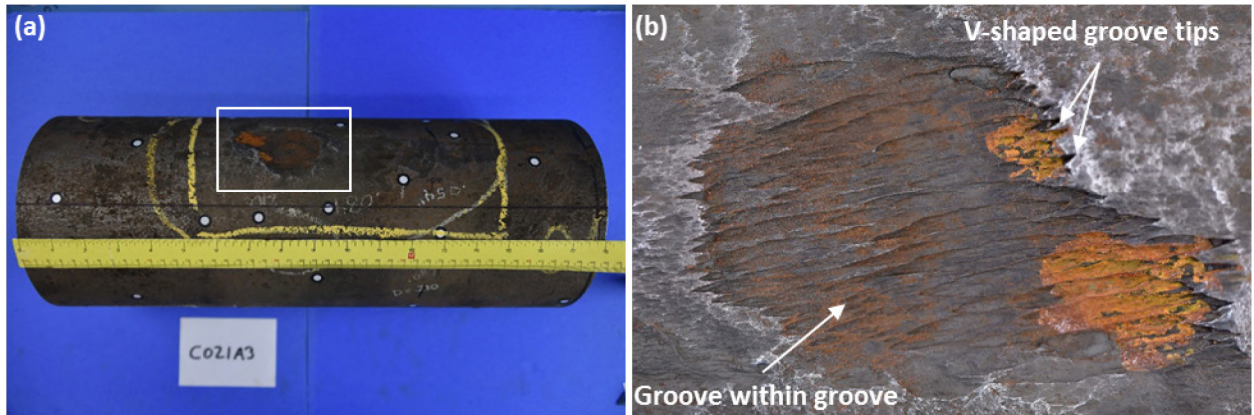


Figure 208: (a) Specimen from Joint 21 and (b) Type I Corrosion Feature

Specimen C021A3C was sectioned in order to investigate the groove profile and V-shaped groove tips (Figure 209 [a]). Figure 209 (b) and (c) show the groove profile within the corrosion patch with respect to the unaffected OD surface of the 7 in. casing. A notch-like profile was observed at each individual groove. The general contour of the corrosion appeared to be semi-elliptical with notches along the bottom of the profile. The general contour of the corrosion patch and notch-like features were incorporated into the FEA for failure pressure prediction. Section 4.1 describes the FEA modeling details.

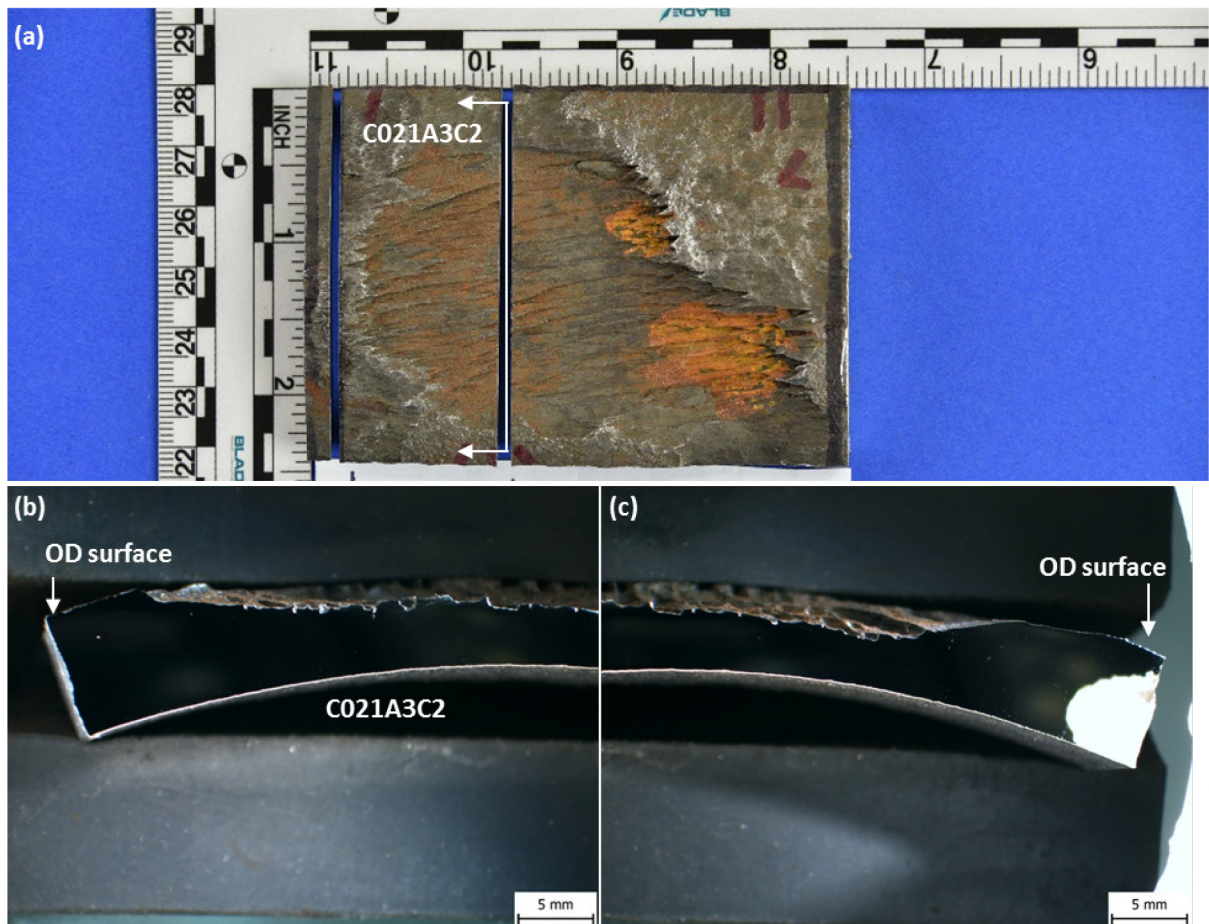


Figure 209: (a) Specimen C021A3C Cross Section and (b) (c) Striated Groove Profile



## 5.2.2 Tunneling

Cross sectioning revealed tunnels extending from the V-shaped groove tips of the Type I corrosion features. Tunnels were generally not observed during visual examination of the OD surface but were identified in some cases. A detailed examination of the tunnels was conducted for the following specimens:

- C021A3C2 and C021A3C3A
- C023A1B2A5 (C023A1B2A5B2 and C023A1B2A5B2A)
- C023A1B2C2

Figure 210 (a) shows the location of a transverse cross section for C021A3C that was made approximately 1 mm ahead of the V-shaped groove tips. Figure 210 (b) identifies two large groove tips designated as tips 1 and 2. Tunnels were observed beneath both groove tips (Figure 210 [c]). Figure 211 (a) and (b) are micrographs of groove tips 1 and 2 after etching with 2% nital. The micrographs clearly show tunnels as black regions ahead of the groove tips. Figure 212 (a) and (b) are metallographs of groove tips 1 and 2 taken at 50 $\times$ . The metallographs show multiple tunnels occurring as deep as 1,300  $\mu\text{m}$  below the OD surface. The inner structure of the tunnels could not be examined due to the limitations of the metallographic microscope. A detailed examination of the tunnels was conducted with the SEM.

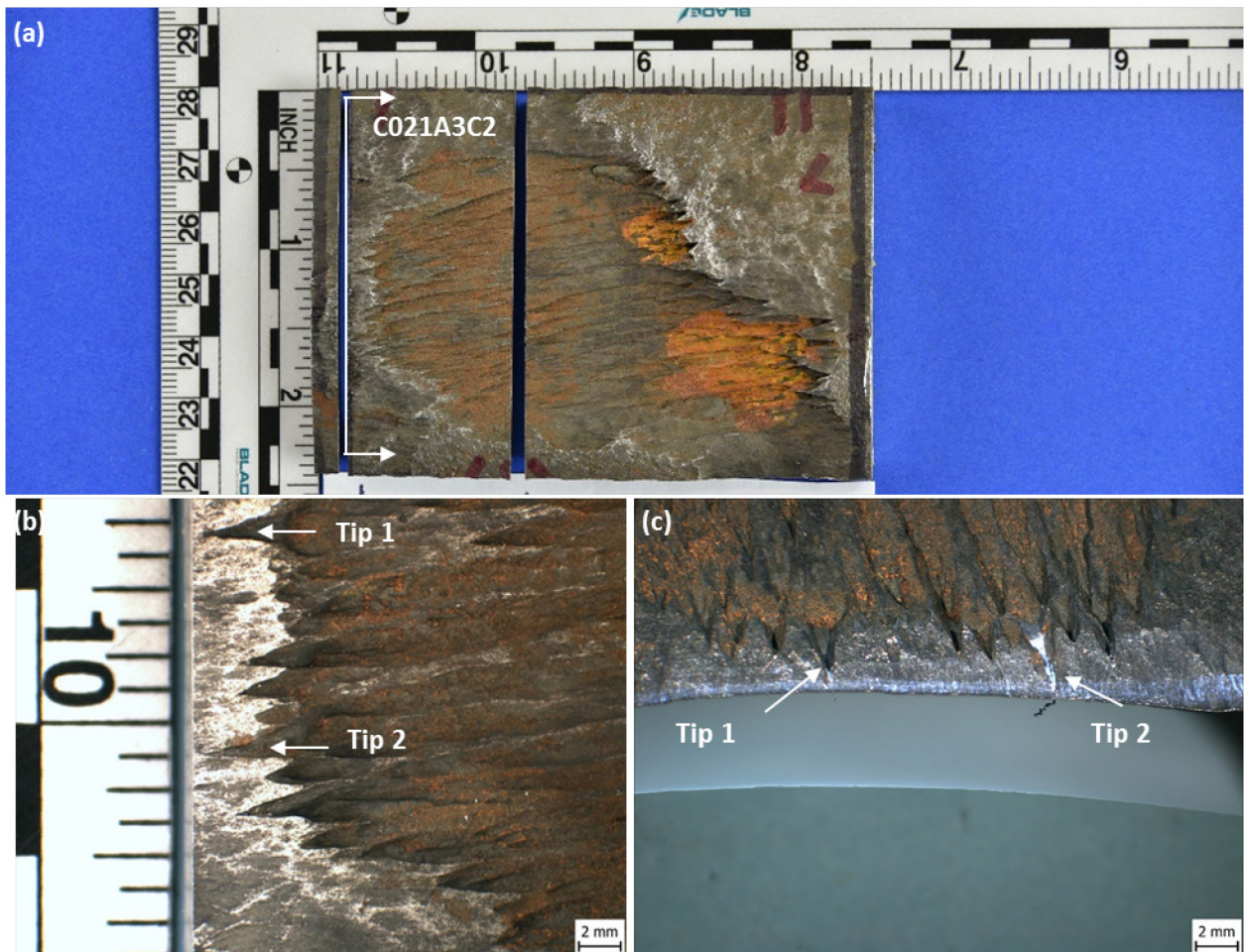


Figure 210: (a) Top and (b) Tilted View of C021A3C2 and (c) Cross Section Showing Tips 1 and 2

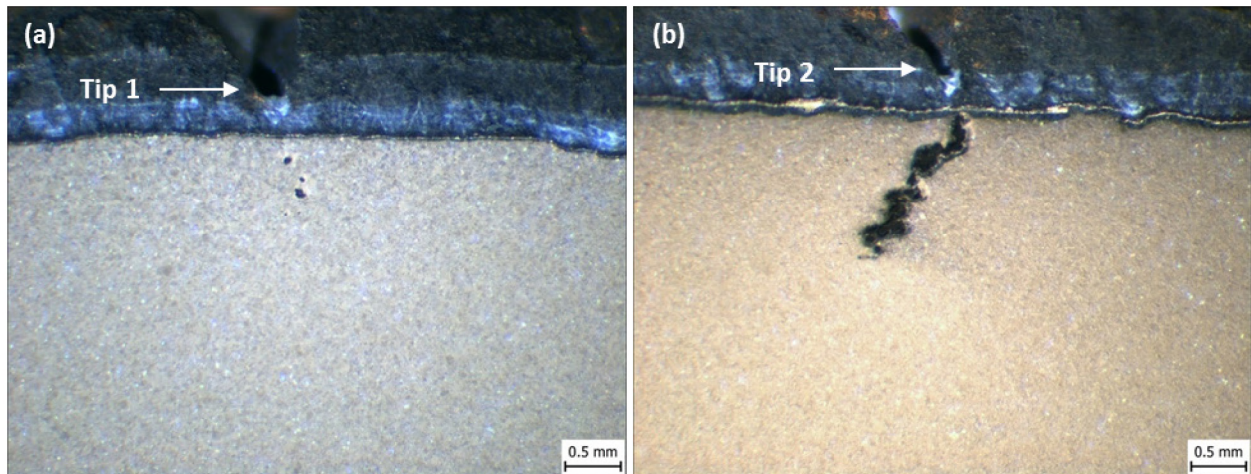


Figure 211: Stereo Microscope Image of (a) Tip 1 and (b) Tip 2

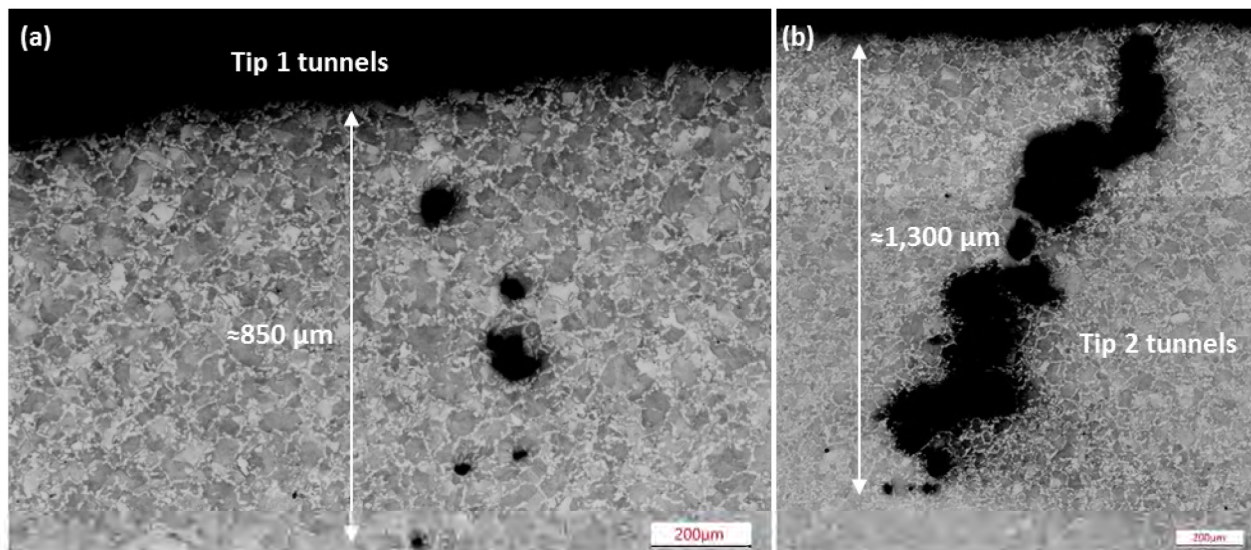


Figure 212: Microstructure Adjacent to (a) Tip 1 and (b) Tip 2 Tunnels

Figure 213 and Figure 214 show SEM images of the tunnels in the C021A3C2 cross section. Corrosion products were present in the tunnels. Figure 215 shows an EDS color map of the corrosion product. The EDS results indicate high levels of oxygen (27–54 at%) and carbon (24–50 at%). The SEM image and EDS maps also show remnants of the original MnS inclusions and plate-like cementite ( $\text{Fe}_3\text{C}$ ) within the corrosion product. There seemed to be a preferential anodic dissolution of ferrite leaving the cementite behind [37]. The presence of the lamellar cementite provided an anchor to the corrosion products [37].

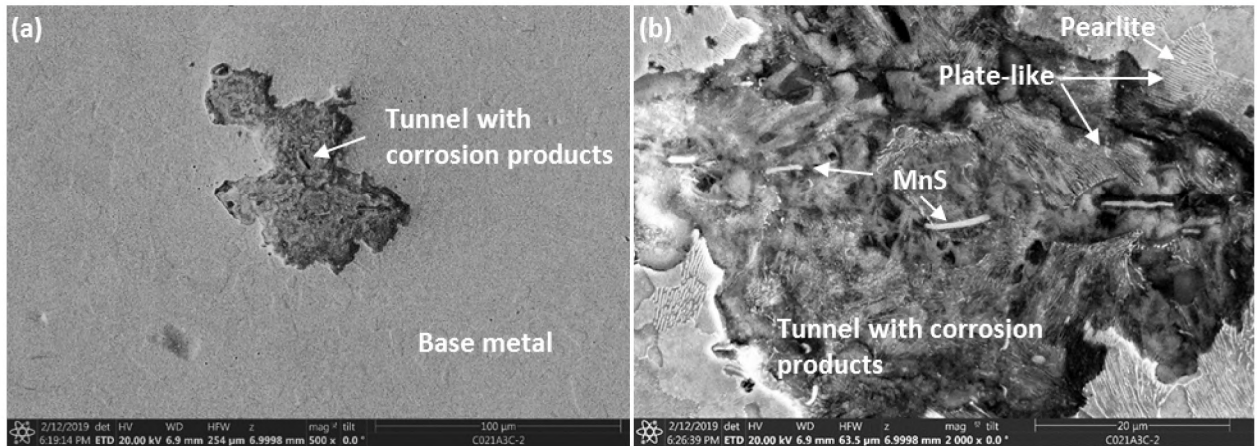


Figure 213: SEM Images of the Largest Tip 1 Tunnel

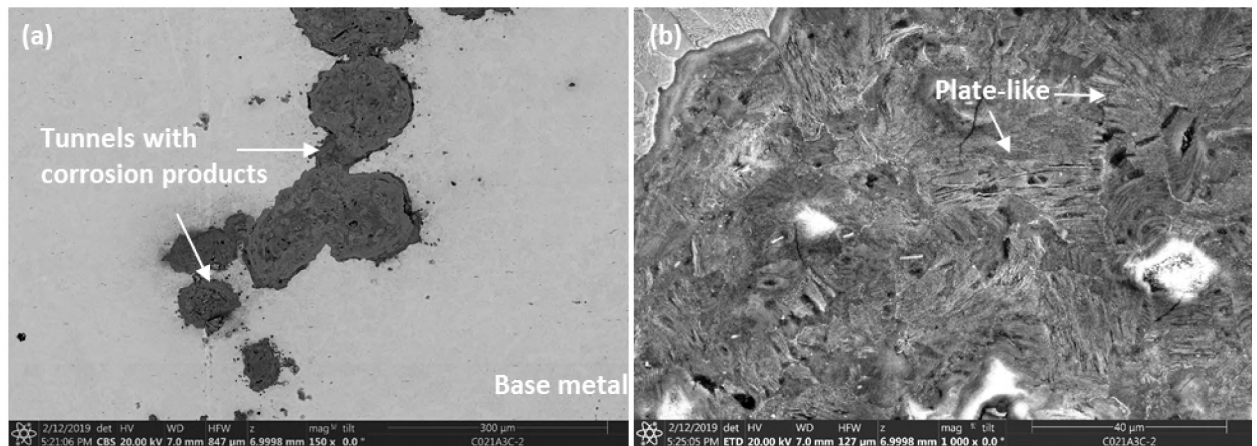


Figure 214: (a) Backscatter and (b) SEM Images of Tip 2 Tunnels

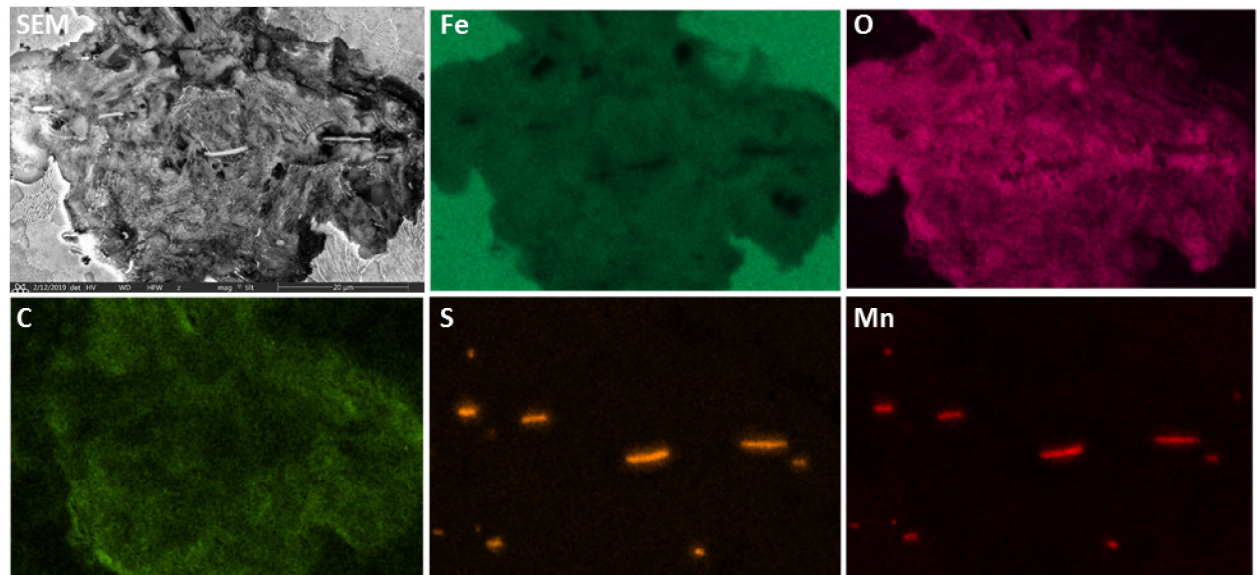


Figure 215: EDS Analysis of Largest Tip 1 Tunnel (C021A3C2)

Specimen C021A3C2 was re-polished towards the V-shaped groove tip by approximately 1 mm.

Figure 216 (a) shows the cross section of tips 1 and 2 after re-polishing. The tunnels under tip 1 increased in size and in depth from the OD surface.

Figure 216 (b) and (c) show metallographs of tips 1 and 2 after etching with 2% nital. The tunnels under tip 2 also increased in size and coalesced into a larger tunnel. Raman spectroscopy identified organic matter, modified hematite ( $\text{Fe}_2\text{O}_3$ ), and magnetite ( $\text{Fe}_3\text{O}_4$ ) in the corrosion products in the tunnel. Figure 217 shows the Raman spectra for the corrosion product in the tip 2 tunnels [38].

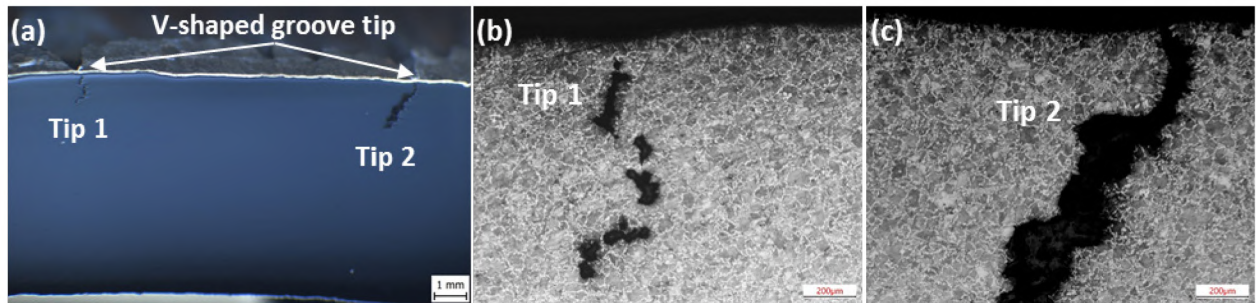


Figure 216: Specimen C021A3C2 after Second Polish

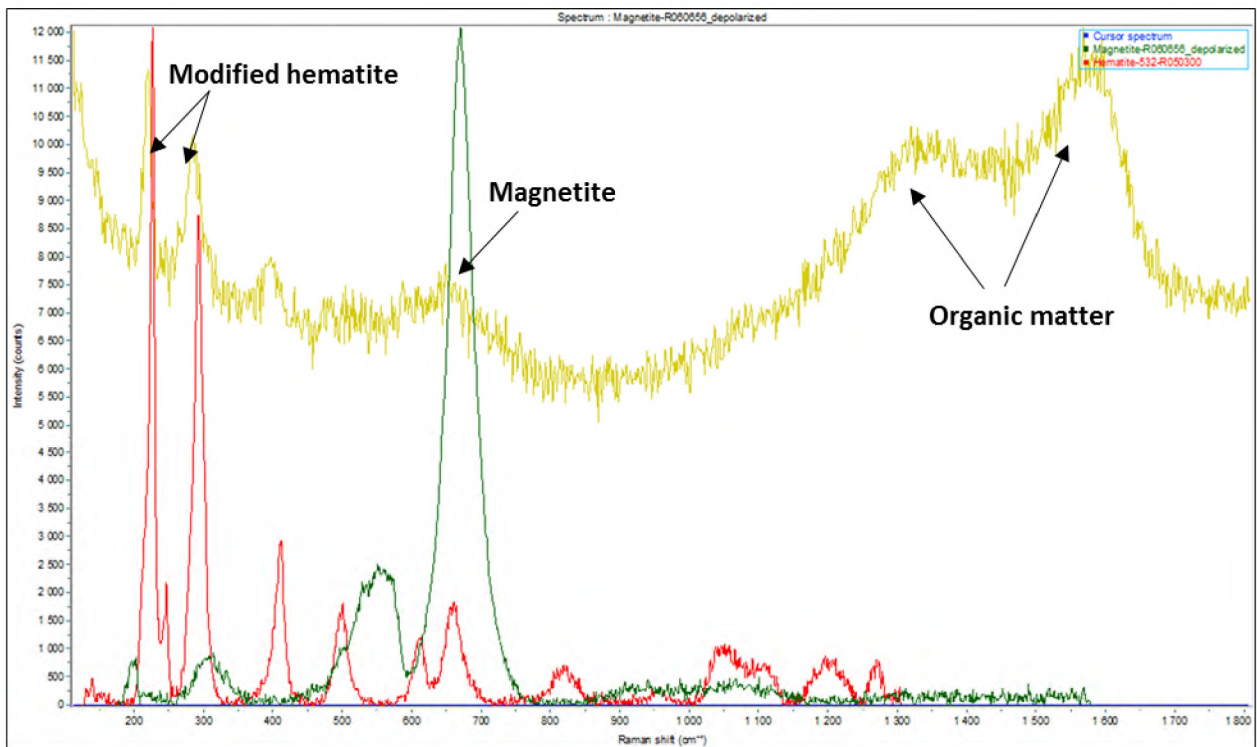


Figure 217: Raman Spectra Showing Organic Matter, Modified Hematite, and Magnetite [38]

A longitudinal cross section was made parallel to the long axis of the striated grooves to reveal the V-shaped groove tips in detail. The primary objective of the cross section was to confirm the presence of tunnels and determine their profile. Figure 218 (a) shows the distinct V-shaped groove tips that were the target for the longitudinal cross section. Figure 218 (b) shows specimen C021A3C3 and the cross section location. Figure 219 shows stereo images of the C021A3C3A cross section. The images show that tunnels penetrated longitudinally into the base metal.

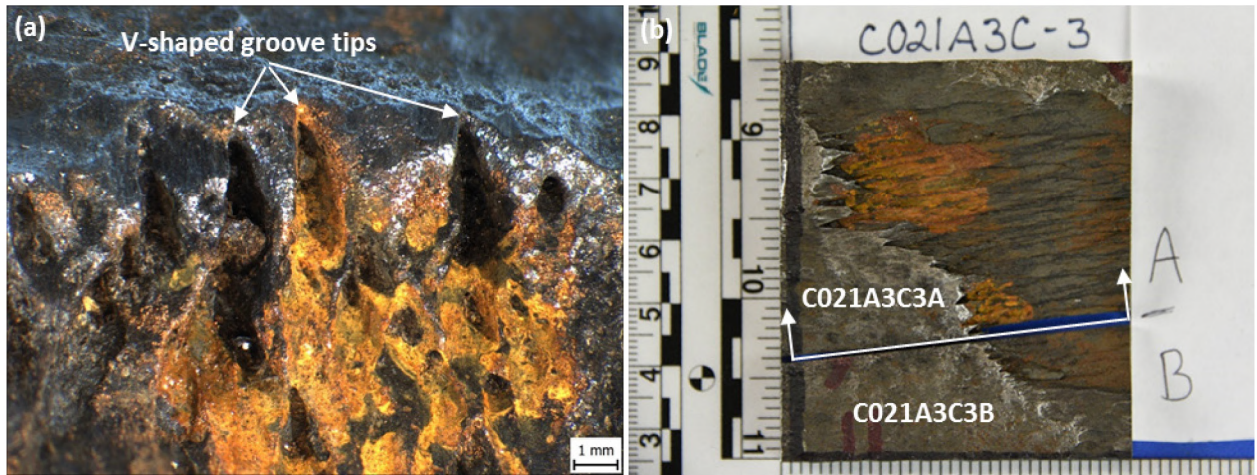


Figure 218: Specimen C021A3C3 (a) V-pointed Groove Tips and (b) Cross Section Location

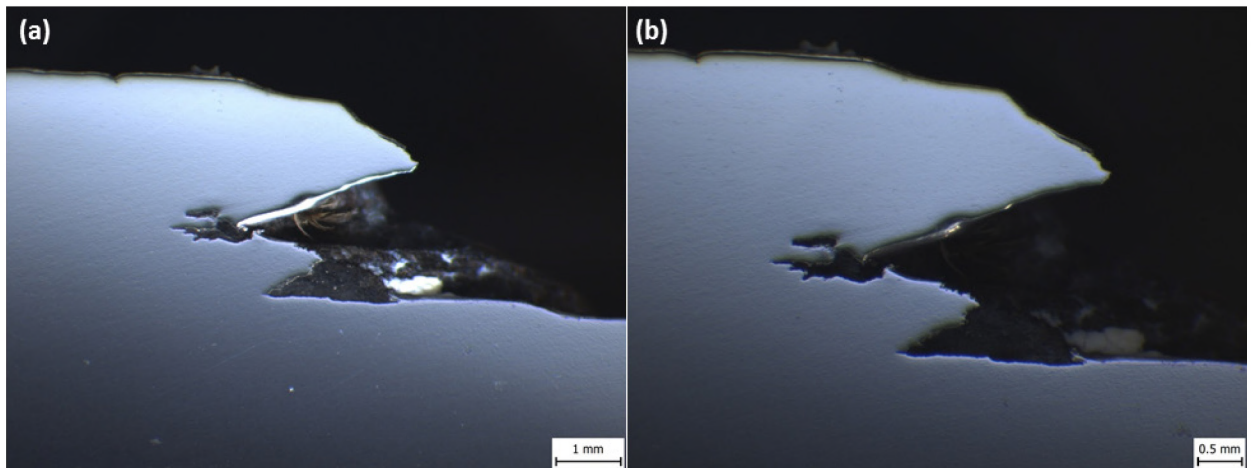


Figure 219: Stereo Images of Specimen C021A3C3A Cross Section Taken at (a) 15 $\times$  and (b) 20 $\times$

Specimen C023A1B2A5 was extracted from the Type I corrosion feature associated with the axial rupture (joint 22). Visual examination of the specimen identified a tunnel adjacent to the axial fracture surface. Figure 220 shows a macro image of the tunnel. This was the only example of a tunnel that was observed by visual examination. Figure 221 (a) shows a low magnification SEM image of the same tunnel as viewed from the top. The tunnel was metallographically cross-sectioned in the longitudinal direction to show the groove profile (Figure 221 [b]). The tunnel had a mouth opening of 0.5 mm and penetrated 1 mm into the base metal.

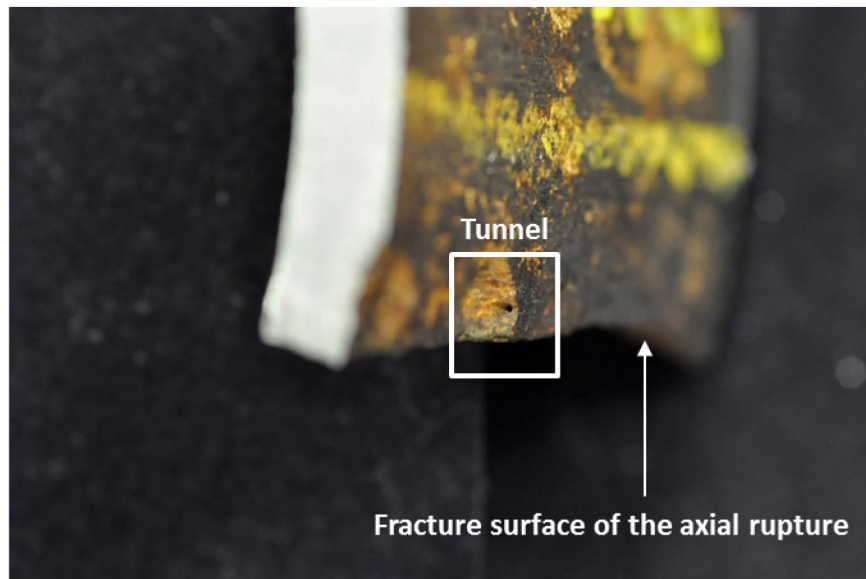


Figure 220: C023A1B2A5 Groove Tunnel Adjacent to Axial Rupture Fracture Surface

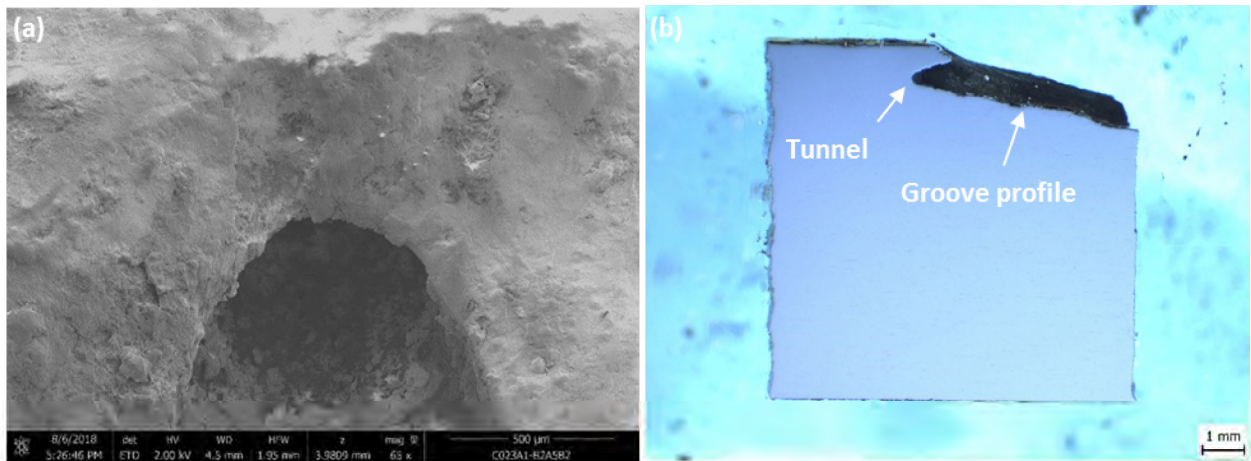


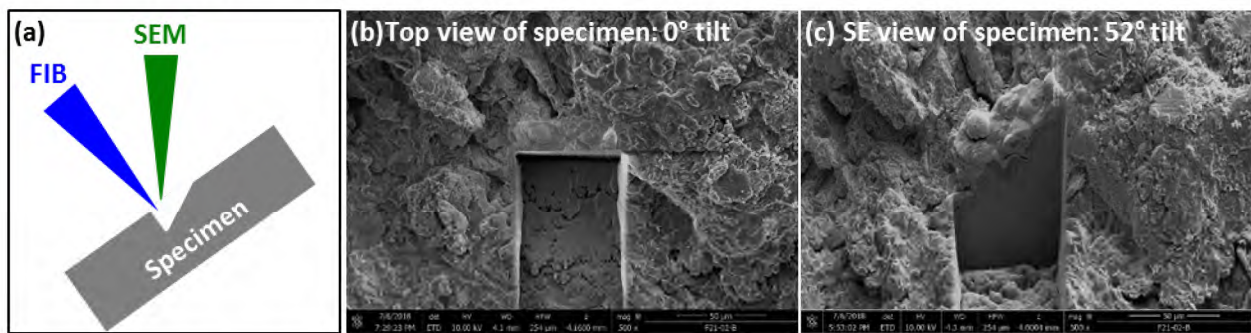
Figure 221: Specimen C023A1B2A5B2's (a) SEM Image and (b) Metallographic Section Showing Tunnel

The chemistry of the corrosion deposits from the V-shaped groove tips were first introduced during the morphology and tunneling investigations. This sub-section provides detailed analysis of these corrosion products. Specimen preparation included metallographic cross sectioning and FIB. SEM, EDS, and Raman techniques were primarily used to conduct the analysis. Corrosion products from the following specimens were analyzed:

- C023A1B2A5B2 and C023A1B2A5B2A
- C023A1B2C2
- C021A3
- C022A2C
- C022B2A5
- C025A3B3

The primary objective of the analysis was to examine the structure and chemistry of corrosion products in the grooves. Metallographic sectioning was the primary technique for preparing the specimens for analysis. FIB was used in cases where metallographic cross sectioning could contaminate, damage, or alter the corrosion products. FIB had the advantage of creating precise small-scale cross sections that preserved the structure of the corrosion product and minimized contamination and damage.

FIB is a tool that uses a gallium (Ga) ion source to section the specimen at an angle while inside the SEM chamber. The specimen is then investigated using the secondary electron (SE) beam. The FIB cross sections and SEM imaging were done at FIB-X Services using Thermo Fisher Helios 660 G3 FIB. Characterization using Raman spectroscopy is quite challenging for the small FIB cross section; therefore, only the EDS characterization was performed on the FIB cross section. Figure 222 shows a schematic of the FIB sectioning technique and the corresponding SEM images of the cut.



**Figure 222: (a) FIB Sectioning Schematic and SEM Image of Cut with a (b) 0° and (c) 52° Tilt**

Specimen C023A1B2A5B2 (extracted from C023A1B2A5 [Figure 220]) was initially sectioned for a detailed analysis using FIB followed by metallographic cross sectioning (C023A1B2A5B2A). The groove wall was cross-sectioned using FIB to look at the deposit morphology. Figure 223 shows a bird's nest formation within the corrosion deposit, as described by various authors [39] [40] [41]. The bird's nest formation is typical of atmospheric corrosion of carbon steel [39].

EDS analysis shows that the corrosion deposit contains approximately 40 at% Fe, 18 at% C, 18 at% O, 9 at% Ca, 0.2 at% S, and small amounts (<1 at%) of other elements. Another FIB cross section at the groove tip (Figure 224) reveals corrosion products that formed just inside the mouth opening of the tunnel. The corrosion product does not appear to be dense. Several layers of deposits were seen inside the tunnel. Figure 225 shows Fe, C, and O EDS color maps of the FIB section. EDS found approximately 60 at% C, 19 at% Fe, 19 at% O, and small amounts of S, K, Mn, Cl, Si, and Al.

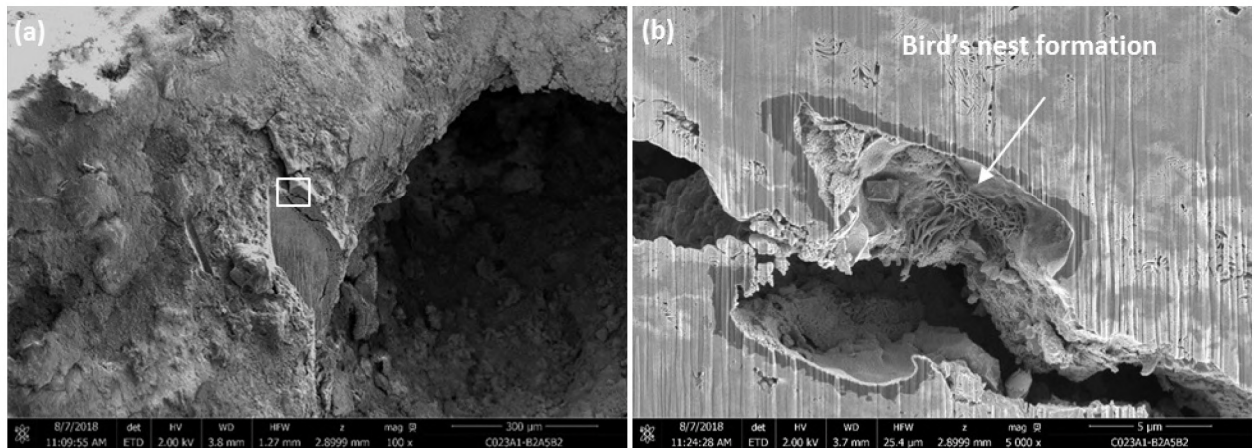


Figure 223: FIB Cross Section of the Groove Wall in C023A1B2A5B2 at (a) 100 $\times$  and (b) 5,000 $\times$

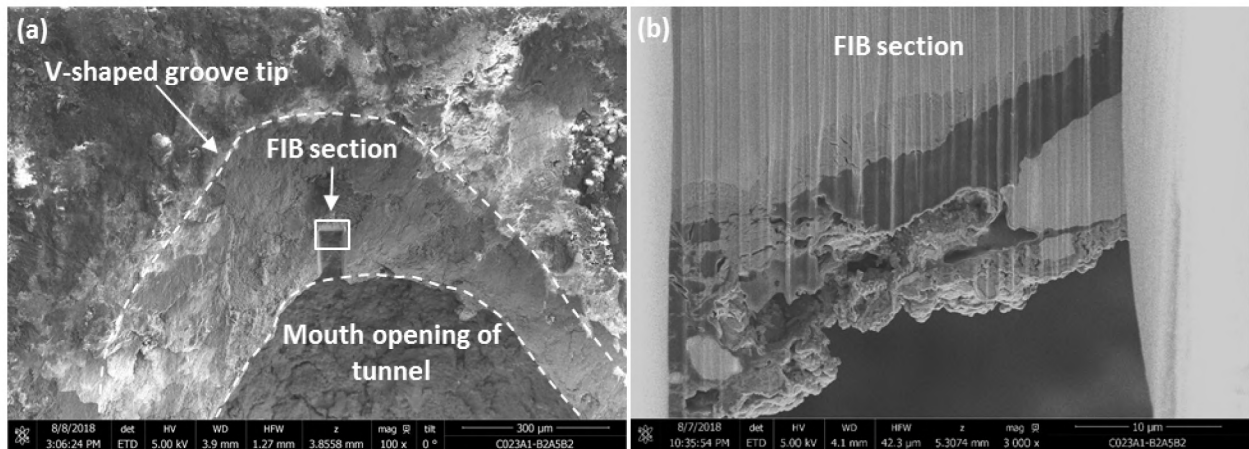
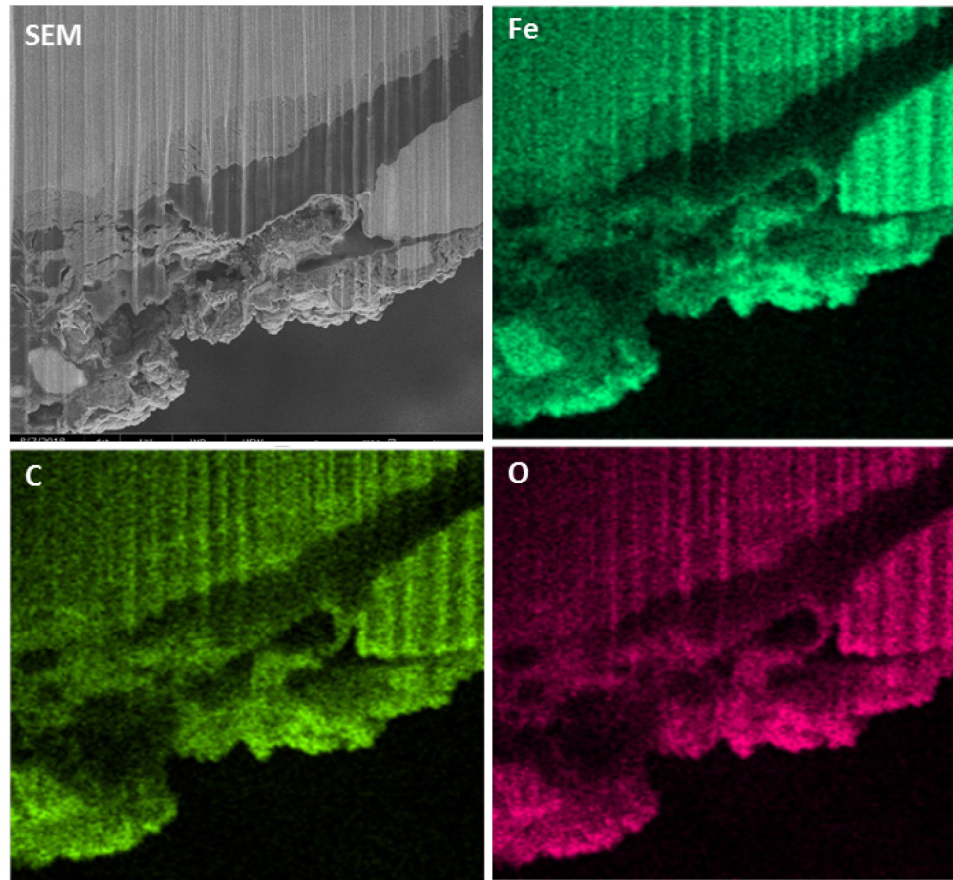


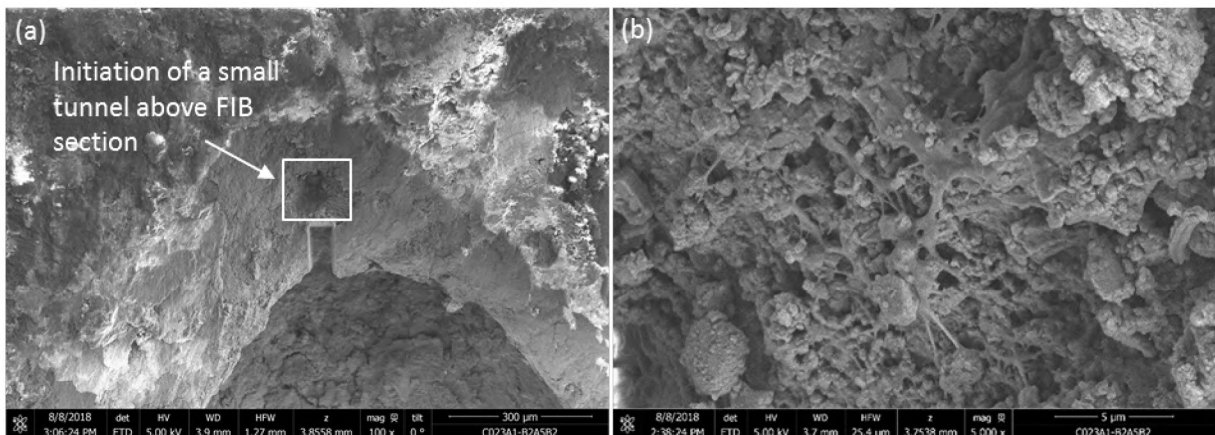
Figure 224: FIB Cross Section of the Groove Tip Viewed at (a) 100 $\times$  and (b) 3,000 $\times$





**Figure 225: EDS Mapping of the Corrosion Deposit Inside the Tunnel**

Figure 226 (a) shows a small, darker circular feature (white box) directly above the FIB section (in the V-shaped groove tip). The circular feature was interpreted as being a small tunnel in its initial stages of forming. Figure 226 (b) shows a high magnification image of the forming tunnel. There is extra-cellular-like material [42] surrounding the forming tunnel. EDS analysis of the area containing the extra-cellular-like material showed high amounts of C ( $\approx 77$  at%), with 10 at% Fe, 9 at% O, and 0.6 at% S. High amounts of carbon may suggest the presence of organic material. The organic matter could have come from different sources, such as microbiological activities, kill fluids, oil, and the surrounding formation.



**Figure 226: (a) Small Tunnel and (b) Extra-Cellular-Like Material**

C023A1B2A5B2A (Figure 221 [b]) was mounted in epoxy, polished, and examined in incremental steps after the FIB investigation. Figure 221 (b) is an image of the specimen after the final polish. Figure 227 shows backscatter images of the cross section after the first polishing step.

Figure 227 (b) shows that the corrosion deposit inside the tunnel is not compact or dense but has some acicular features. A bird's nest formation similar to Figure 227 (b) was observed [39] [40] [41]. EDS analysis of the corrosion product identified high amounts of C (60 at%), Fe (20 at%), and O (17 at%) with trace amount of S and Cl. Raman spectroscopy confirmed the presence of modified hematite ( $Fe_2O_3$ ), magnetite ( $Fe_3O_4$ ), and organic matter inside the tunnel.

Figure 228 shows a corrosion deposit at the tip of the tunnel after the final polish. The corrosion deposit appears denser than what was observed after the first polish. Lamellar (plate-like cementite) features similar to Figure 213 (b) are visible from the high magnification backscatter images (Figure 228). EDS analysis shows that the corrosion product inside the tunnel was rich in O and C. The analysis also revealed that MnS inclusions were present and surrounded by the corrosion product.

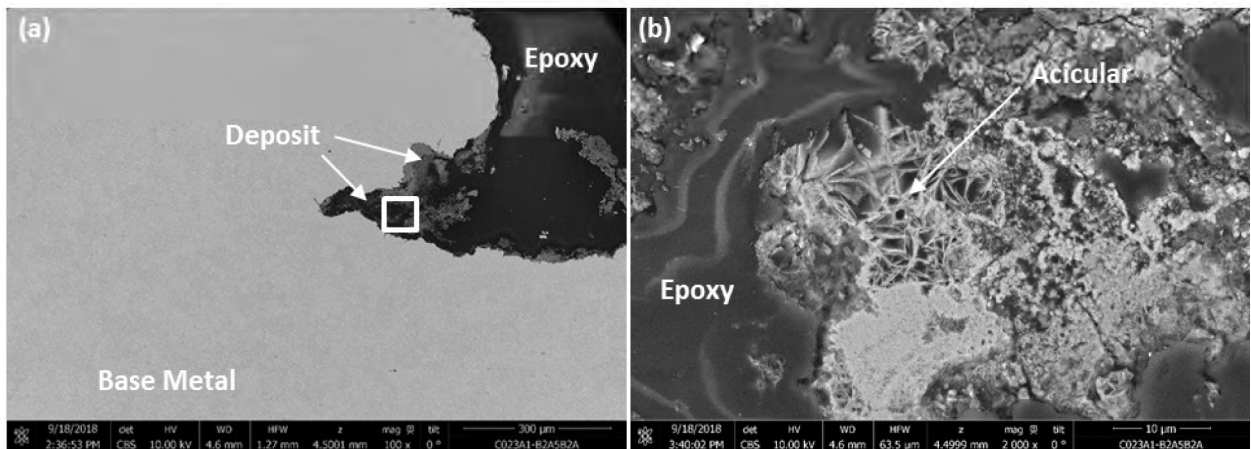


Figure 227: (a) Metallographic Cross Section of C023A1B2A5B2A and (b) High Magnification Image of Corrosion Deposit Inside the Tunnel

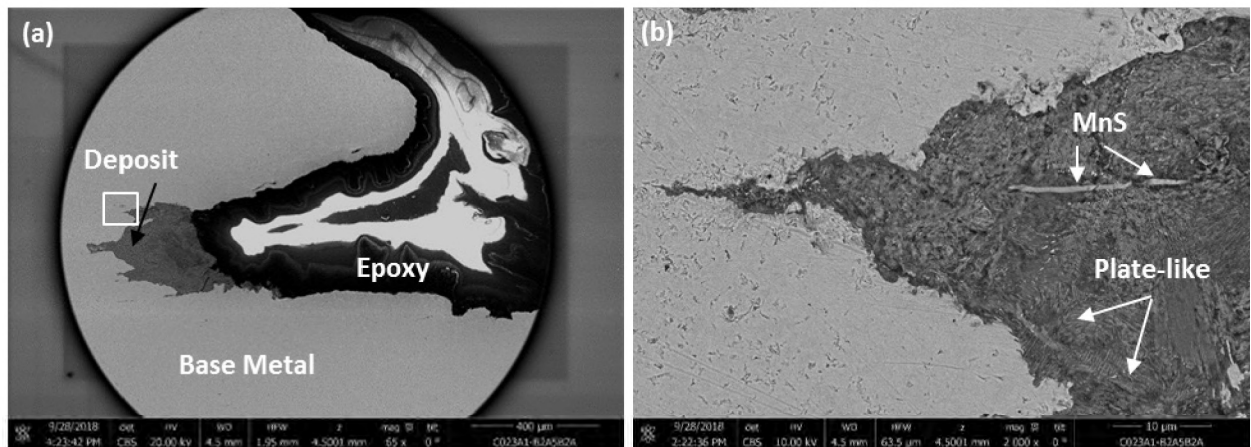


Figure 228: (a) Second Metallographic Cross Section of C023A1B2A5B2A and (b) High Magnification Image of Corrosion Deposit

C023A1B2C2 was extracted from the initiation site of the axial rupture. The specimen was mounted in Bakelite and then polished. Figure 229 shows the presence of tunnels directly below the groove in the Type I corrosion feature. The cross section also shows an acicular corrosion deposit in the tunnel with remnants of MnS inclusions. Figure 230 shows the SEM image of the cross section and the sulfur and manganese mapping obtained with EDS. The corrosion products inside the tunnel are not very dense. Raman spectroscopy identified the corrosion products as hematite ( $\text{Fe}_2\text{O}_3$ ), modified hematite ( $\text{Fe}_2\text{O}_3$ ), magnetite ( $\text{Fe}_3\text{O}_4$ ), and organic matter.

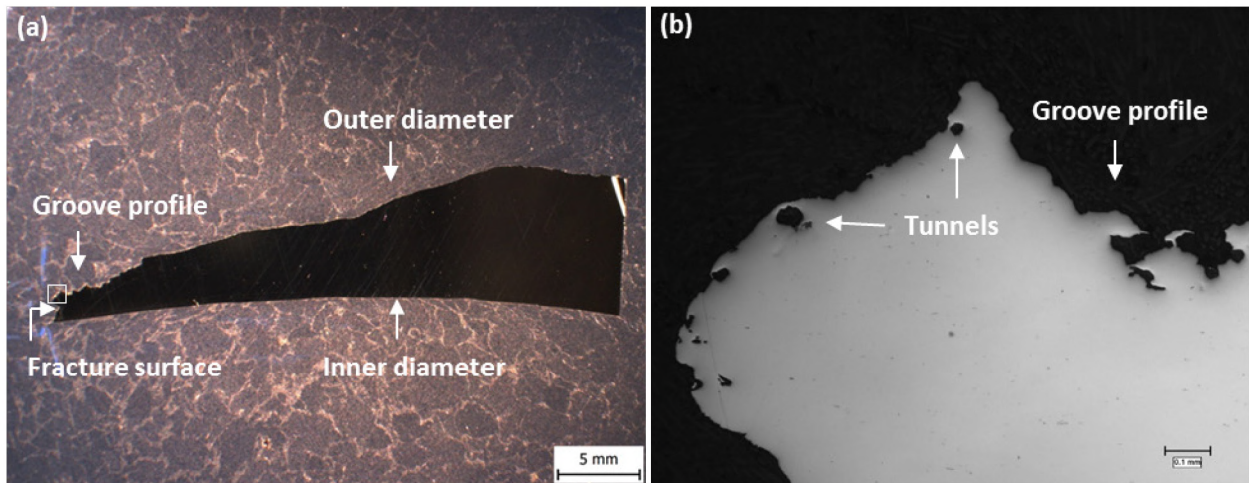


Figure 229: Metallographic Images of C023A1B2C2

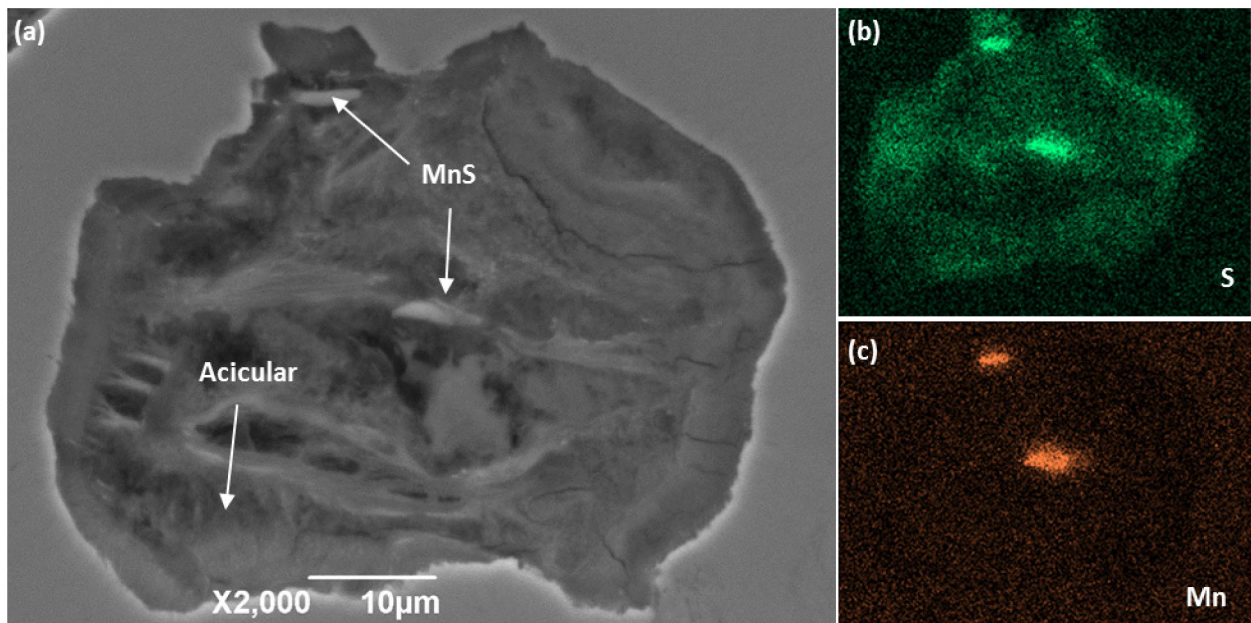


Figure 230: (a) SEM Image of Tunnel with Acicular Deposit and EDS Color Maps for (b) S and (c) Mn Specimen C022B2A5 (Figure 231) was extracted from joint 22 and has a Type I corrosion feature with a length of 2.5 in. along the longitudinal axis. The specimen was subjected to the FIB cross section. The specimen was ultrasonically cleaned in acetone prior to the FIB cross section. Globules are seen mostly inside the groove tips. High magnification imaging of the globules shows details of the globular structure

(Figure 232). The FIB cross section of the globule shows that features that look like bird's nest formation, as described by some authors [39] [40] [41], are present inside the globules (Figure 233). These globules are high in C ( $\approx 50$  at%), Fe ( $\approx 40$  at%), and O ( $\approx 10$  at%). Raman spectroscopy confirmed the presence of modified hematite ( $\text{Fe}_2\text{O}_3$ ), magnetite ( $\text{Fe}_3\text{O}_4$ ), iron oxide combination, and organic matter [38].

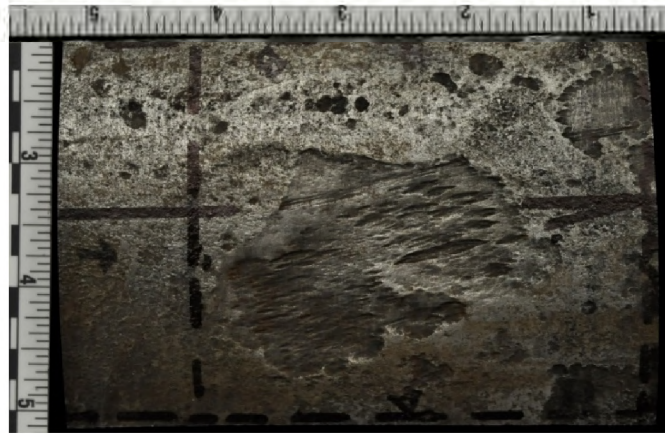


Figure 231: Specimen C022B2A5

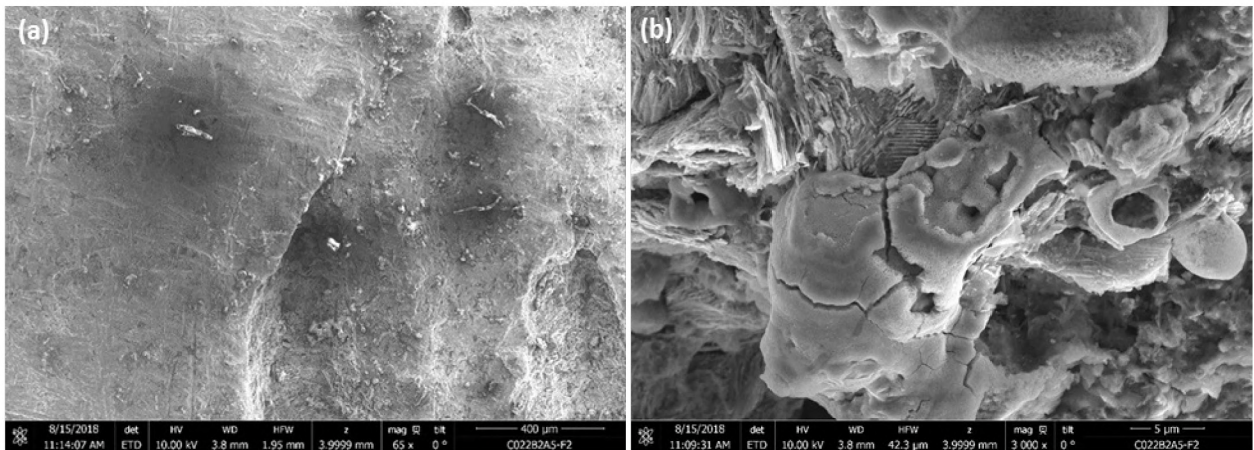


Figure 232: (a) Top View of Groove Tip and (b) High Magnification Image of Globule Cluster

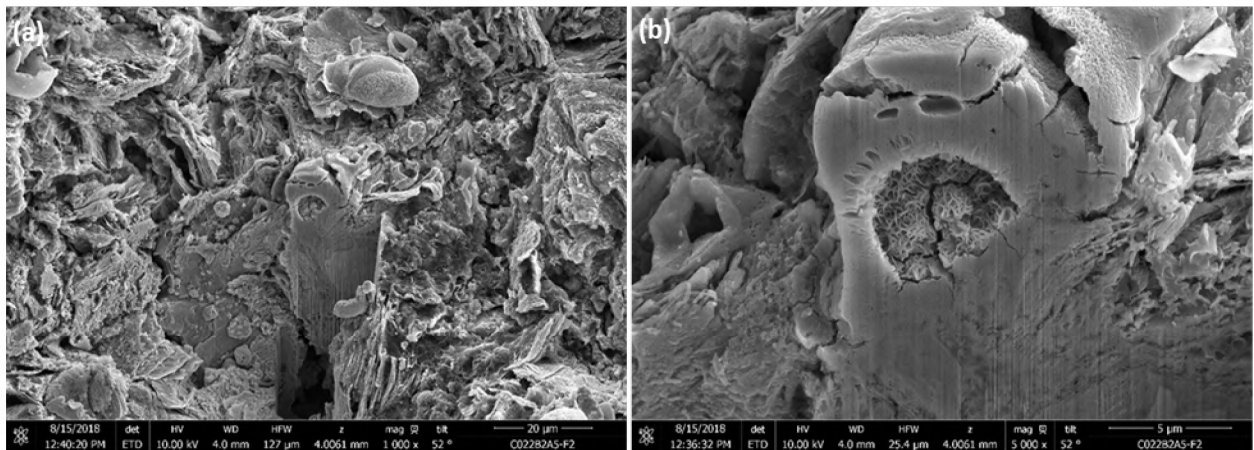


Figure 233: FIB Cross Section of Globules

Specimen C025A3B3 was extracted from a specimen (from joint 24 [Figure 234]) with a large (> 5 in. diameter) corrosion patch. The striated grooves were visible but were covered with what appeared to be white deposits. The white deposits were rich in Ca (10-20 at%), O (30-50 at%), C (20-30 at%), S (2-10 at%). White deposits were also seen in Area 3 (Figure 235), while globules were prominent in Area 4. Raman analysis showed the presence of gypsum ( $\text{CaSO}_4 \cdot \text{H}_2\text{O}$ ) on the surface of specimen C025A3B3 Area 1. Modified hematite ( $\text{Fe}_2\text{O}_3$ ), barite ( $\text{BaSO}_4$ ), and carbonate were identified in Area 1, while barite ( $\text{BaSO}_4$ ), carbonate, and organic matter were found on the surface of Area 4.



Figure 234: Specimen C025A3B Sample (a) Layout and (b) Areas of Investigation

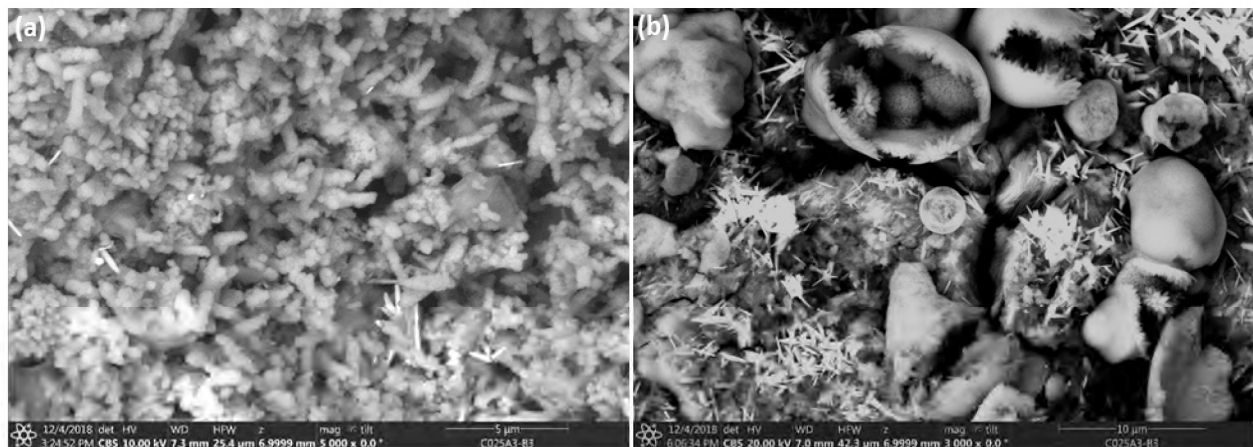


Figure 235: (a) White Deposit on the Surface of C025A3B3 Area 1; (b) Globules on C025A3B3 Area 4

The globules seen on the grooves of Type I corrosion feature were often associated with the morphology of lepidocrocite and goethite [39] [40] [41]. The Raman spectroscopy indicated the presence of iron oxide combination, modified hematite, and magnetite on the specimens with globules. The modified hematite can be an artifact of longer laser scan or higher laser power used during the Raman analysis. The iron oxide combination reported in the Raman analysis were determined from the Raman spectra that indicates presence of hematite, goethite, and ferrihydrite [38]. Acicular or needle-like corrosion products, globules, and corrosion products with birds' nest formations are commonly reported for corrosion in atmospheric environments [39] [40] [41].

Organic matter was also one of the common compounds seen in the OD of the 7 in. casing, based on the results of the Raman spectroscopy. The presence of organic matter on the 7 in. casing, especially those that were seen inside the tunnels, could have been related to microbiological activities. A few authors in

the literature indicated that organic matter can assist in the electron transfer in microbially influenced corrosion [43] [44] [45]. Another study indicated that sessile microorganisms can attach to a thick layer of organic matter adsorbed on the surface [46]. Sources of organic matter, other than those related to microbiological activities and biofilms, could have been contaminated by SS-25 kill fluids, oil, or the surrounding formation.

### 5.3 Scale Analysis

Scale samples were collected from the OD surface of the 7 in. casing for composition analysis. Scale samples were sent to Premier Oilfield Group, a third-party lab in Houston, TX. Premier performed Raman spectroscopy, x-ray diffraction (XRD), inductively coupled plasma (ICP) spectroscopy, and x-ray fluorescence (XRF) analyses on the scale samples. The analyses identified:

- Magnetite— $\text{Fe}_3\text{O}_4$
- Hematite— $\text{Fe}_2\text{O}_3$
- Goethite— $\alpha\text{-FeO(OH)}$
- Lepidocrocite— $\gamma\text{-FeO(OH)}$
- Barite— $\text{BaSO}_4$
- Quartz— $\text{SiO}_2$
- Cristobalite— $\text{SiO}_2$
- Plagioclase— $\text{CaAl}_2\text{Si}_2\text{O}_8$
- Calcite— $\text{CaCO}_3$
- Witherite— $\text{BaCO}_3$
- Siderite— $\text{FeCO}_3$
- Mica (Illite)— $\text{KAl}_3\text{Si}_3\text{O}_{10}(\text{OH})_2$
- Akaganeite— $\beta\text{-Fe}^{3+}\text{O(OH)}$
- Sylvite— $\text{KCl}$

This section summarizes the scale analysis results for samples collected from C001–C025 (joints 1–24). Details of the analysis for C001–C024 can be found in the Premier report [47]. The XRD spectra analysis of the scale samples collected from C025 were completed by Blade at a later date using raw data provided by Premier. The results can be found in Appendix C.

Figure 236 shows the XRD weight percentages of the compounds present in the scale samples collected from C001–C025. It can be seen that barite ( $\text{BaSO}_4$ ) and sylvite ( $\text{KCl}$ ) dominate the weight percentages of the compounds, which were most likely contaminants from the kill fluids. Blade adjusted the weight percentages by removing barite ( $\text{BaSO}_4$ ) and sylvite ( $\text{KCl}$ ) to obtain the graphs shown in Figure 237.

Figure 238 shows a plot of the recalculated weight percentages of iron oxides and iron hydroxides identified in the scale samples for C001–C025. The figure shows that the amount of magnetite ( $\text{Fe}_3\text{O}_4$ ) in the scale samples was higher for joints in the lower portion of the well. In general, scale collected from joints at shallow depths contained higher percentages (>5%) of goethite [ $\alpha\text{-FeO(OH)}$ ] and lepidocrocite

[ $\gamma$ -FeO(OH)], while scale samples collected from deeper locations contained more (>20%) magnetite ( $\text{Fe}_3\text{O}_4$ ). The change in the dominant corrosion product may indicate a possible change in environment.

The OD surface of the 7 in. casing shared the same environment as the ID surface of the 11 3/4 in. casing. The 11 3/4 in.  $\times$  7 in. annulus had a complex environment that was mostly unknown. The annulus was initially filled with drilling fluid during construction. However, the original fluid may have been contaminated or displaced by various fluids throughout the lifetime of the well. Ground water could have entered the annulus through the holes in the upper portion of the 11 3/4 in. casing (Section 2.2.8) or through the shoe at 990 ft. Ground water sources were identified at various depths at the SS-25 site. An investigation of the hydrology [48] showed that the only possible source for the ground water was seasonal precipitation. Blade attempted to understand the 11 3/4 in.  $\times$  7 in. annulus environment by testing fluid samples taken from the annulus. These analyses were complicated by the fact that kill and other fluids were introduced into the annulus environment during and after the blowout. Compounds identified during scale and surface compositional analysis included these contaminants but did not reflect the original corrosion environment inside the annulus.

Section 5.1 discussed a distinct zone of corrosion beginning at 700 ft. Shallow corrosion was observed above 700 ft and comprised only Type II (no striated grooves) and Type III (mostly associated with connections) corrosion. Type I corrosion, which was related to the axial rupture, began at 700 ft. The corrosion below 700 ft was a mix of Types I, II, and III. The zone at 700 ft could indicate a depth at which water was always present. The change in corrosion severity above 700 ft could indicate an environment that was intermittently wet based on seasonal precipitation (changing water level in the annulus).

Magnetite ( $\text{Fe}_3\text{O}_4$ ) is commonly formed in environments with less oxygen. C018–C025 had an adjusted weight percent greater than 20% for magnetite ( $\text{Fe}_3\text{O}_4$ ). These observations suggest a possible change in environment between the upper and lower portion of the extracted 7 in. casing. This change is consistent with the laser scan observations.

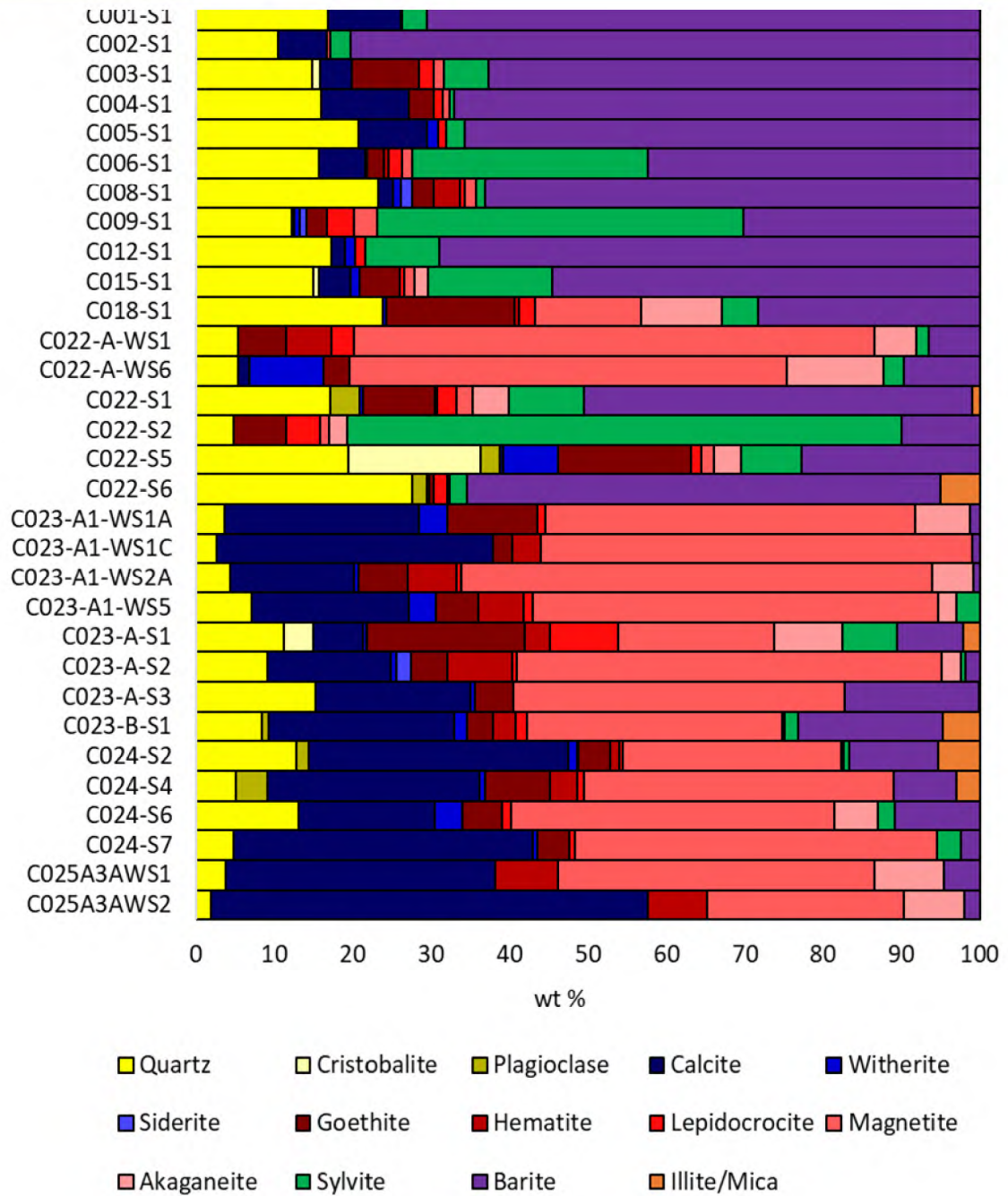


Figure 236: XRD Weight Percentages Before Adjustment



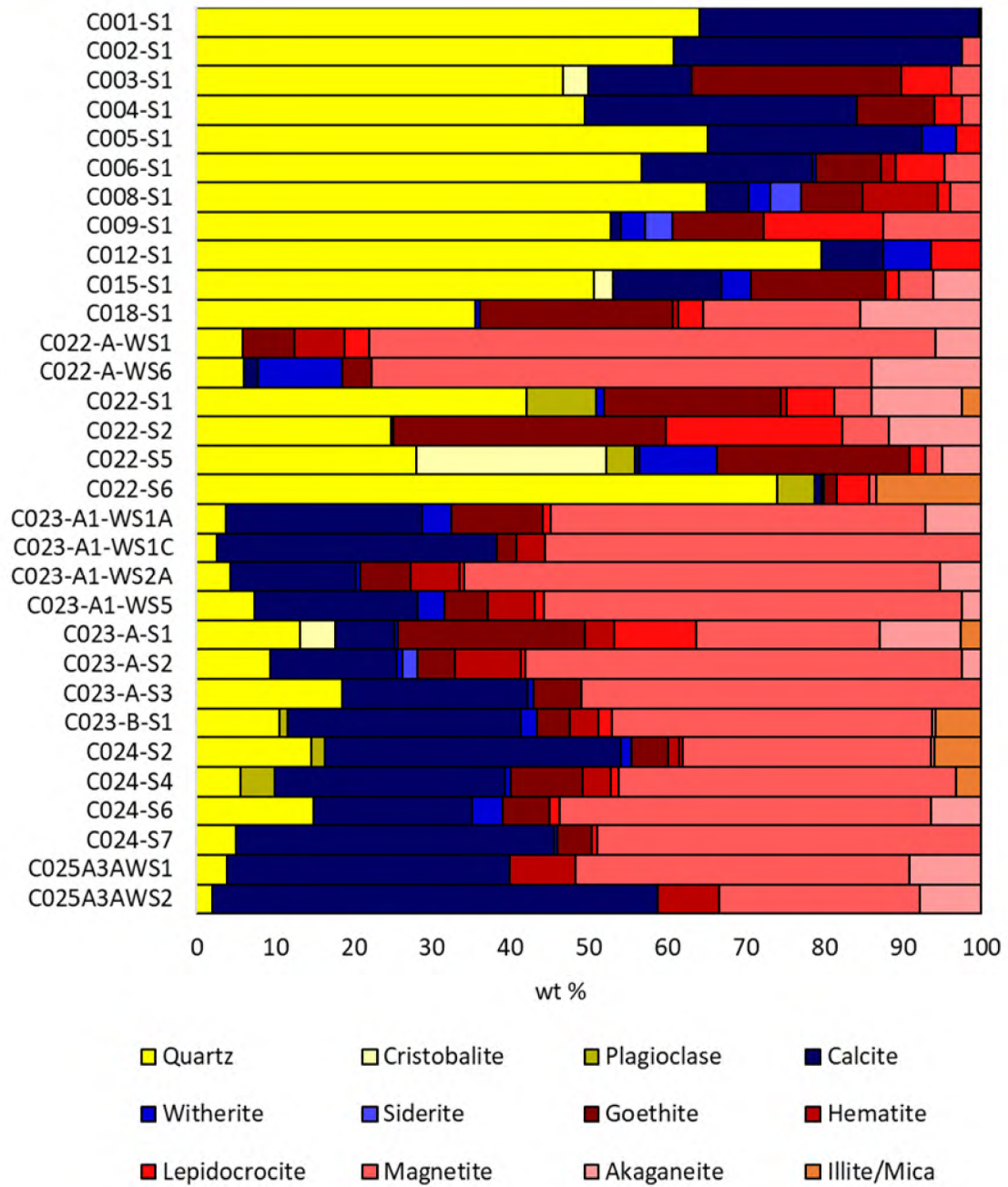
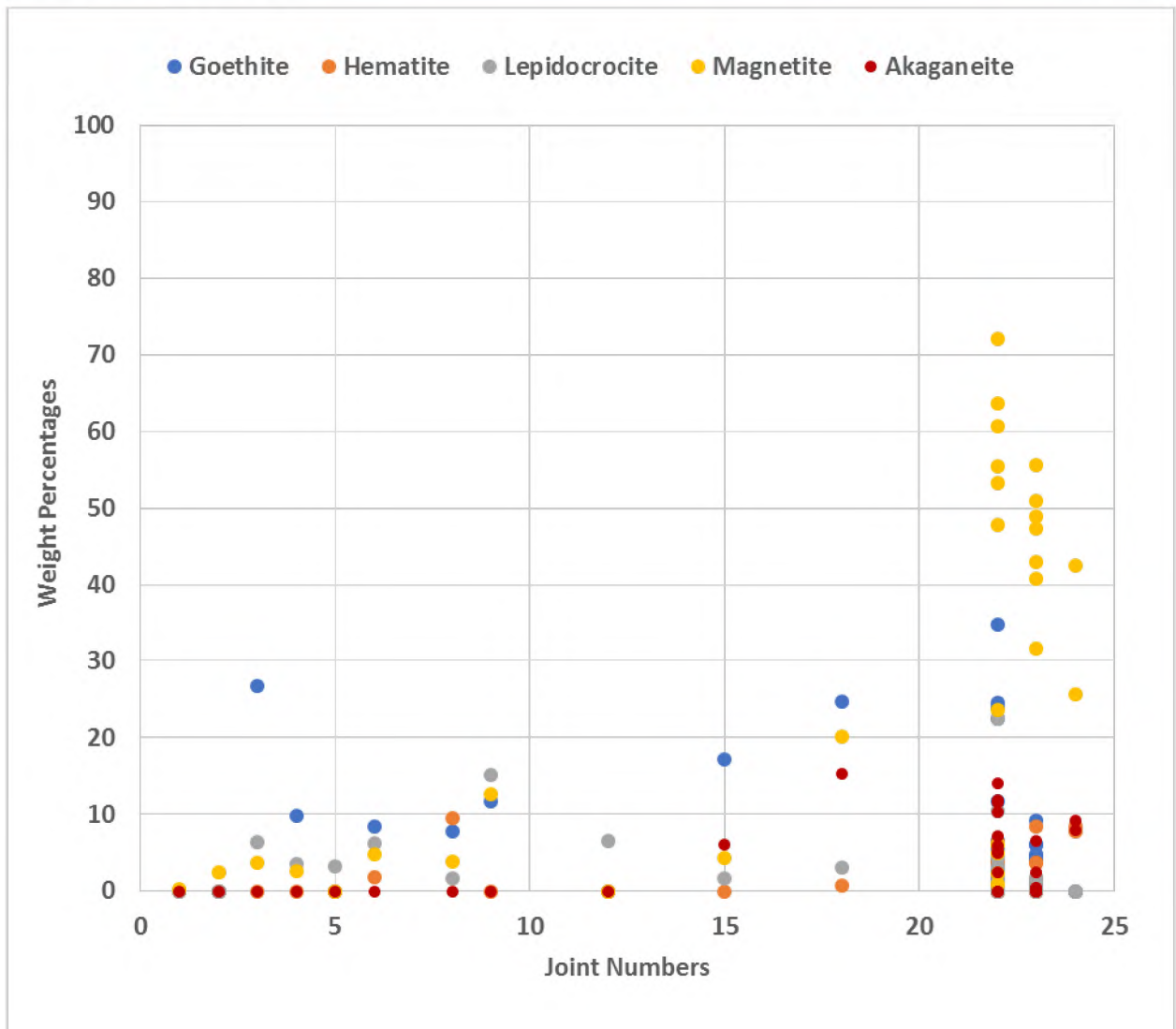


Figure 237: XRD Weight Percentages After Adjustment



**Figure 238: Weight Percentages of Iron Oxides Present in Scale Samples from C001–C025**

Figure 239 shows a bar graph of the weight percentages of iron hydroxides (goethite, lepidocrocite, and akaganeite [red]), iron oxides (magnetite and hematite [green]), carbonates (siderite, barite, aragonite, and witherite [blue]), and formation (quartz, plagioclase, mica [illite], and cristobalite [yellow]). The samples were sorted by depth and examined for trends in the dominate phases as a function of well depth. Iron hydroxides were present in larger amounts at the upper portion of the well, while iron oxides were dominant at the lower portion of the well. High weight percentages of formation were present in scale samples collected from C022 and above. Samples below C022 showed significantly lower weight percentages of formation. This observation reflects the blowout event. Formation was carried by the escaping gas during the blowout and contaminated the OD surface of the joints above the failure (joints 22 and above).

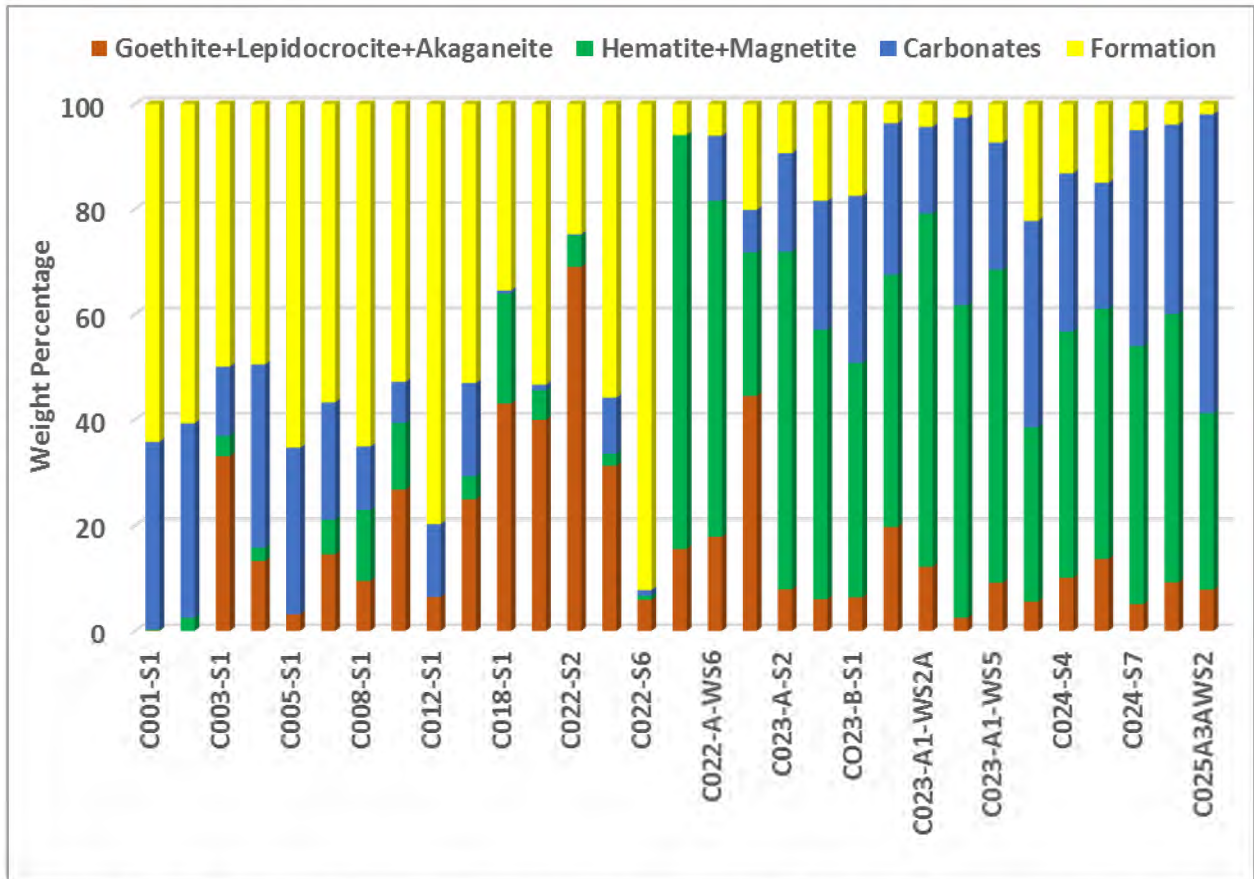


Figure 239: Recalculated Percentages of Iron Hydroxides, Iron Oxides, Carbonates, and Formation

The amount of siderite in the scales from SS-25 was minimal. Premier found Siderite in 3 out of 31 scale samples analyzed from SS-25: C008S1, C009S1, and C023AS2. These samples contained less than 3.9 adjusted weight percent siderite ( $FeCO_3$ ), a common product of  $CO_2$  corrosion, identified on the scale samples from the 7 in. casing.

The formation of siderite ( $FeCO_3$ ) competed with the formation of ferrous hydroxides or ferrous oxides. The competition was determined on the basis of pH and the solubility of either salt. In order to determine which compound might be more stable, Pourbaix diagrams were calculated for two different inputs. Both conditions took into account that the  $CO_2$  concentration would be low and the mineral presence in the water would also be low. The calculations were carried out using OLI software. The input parameters in OLI (Table 12) were used to produce the Pourbaix diagrams and determine the natural pH (red dashed line) of the system (Figure 240 and Figure 241). The Pourbaix diagram is a representation of stability regions for certain phases or compounds in a specific potential (E) and pH range.

Table 12: OLI Software Inputs

Condition	1	2
Stream Amount	55.6797 mol	55.5584 mol
Temperature	78°F (25°C)	78°F (25°C)
Pressure	14.7 psi (1 atm)	14.7 psi (1 atm)
Use Single Titrant	No	No

Condition	1	2
Stream Amount	55.6797 mol	55.5584 mol
pH Acid Titrant	HCl	HCl
pH Base Titrant	NaOH	NaOH
H <sub>2</sub> O	55.5082 mol	55.5082 mol
Fe(OH) <sub>2</sub>	0.100 mol	0.050 mol
CO <sub>2</sub>	0.05 mol	1.50e-4 mol
NaCl	0.02 mol	-
NaHCO <sub>3</sub>	1.50e-3 mol	-

From the calculation of the Pourbaix diagram using condition 1 with high amounts of CO<sub>2</sub> in the system, the ferrous ion in solution is not present in Figure 240. The natural pH is too high (approximately 9.4). The stability domain for siderite (FeCO<sub>3</sub>) extends beyond the natural pH, which means that siderite (FeCO<sub>3</sub>) can coexist with magnetite (Fe<sub>3</sub>O<sub>4</sub>).

The amount of CO<sub>2</sub> concentration was reduced to a more realistic level, and bicarbonate was eliminated in condition 2. The resulting Pourbaix diagram (Figure 241) shows that the natural pH becomes 8.4, and the natural pH is in the magnetite (Fe<sub>3</sub>O<sub>4</sub>) domain. This also means that siderite (FeCO<sub>3</sub>) would not naturally form in the field. The stability diagram confirms that at the location of maximum corrosion there was no siderite (FeCO<sub>3</sub>), or only traces of siderite (FeCO<sub>3</sub>) were observed—it did not naturally occur in this environment. Magnetite (Fe<sub>3</sub>O<sub>4</sub>) formation is qualitatively and quantitatively favored over siderite (FeCO<sub>3</sub>), even if excess CO<sub>2</sub> was present. This also supports that CO<sub>2</sub> corrosion was unlikely.

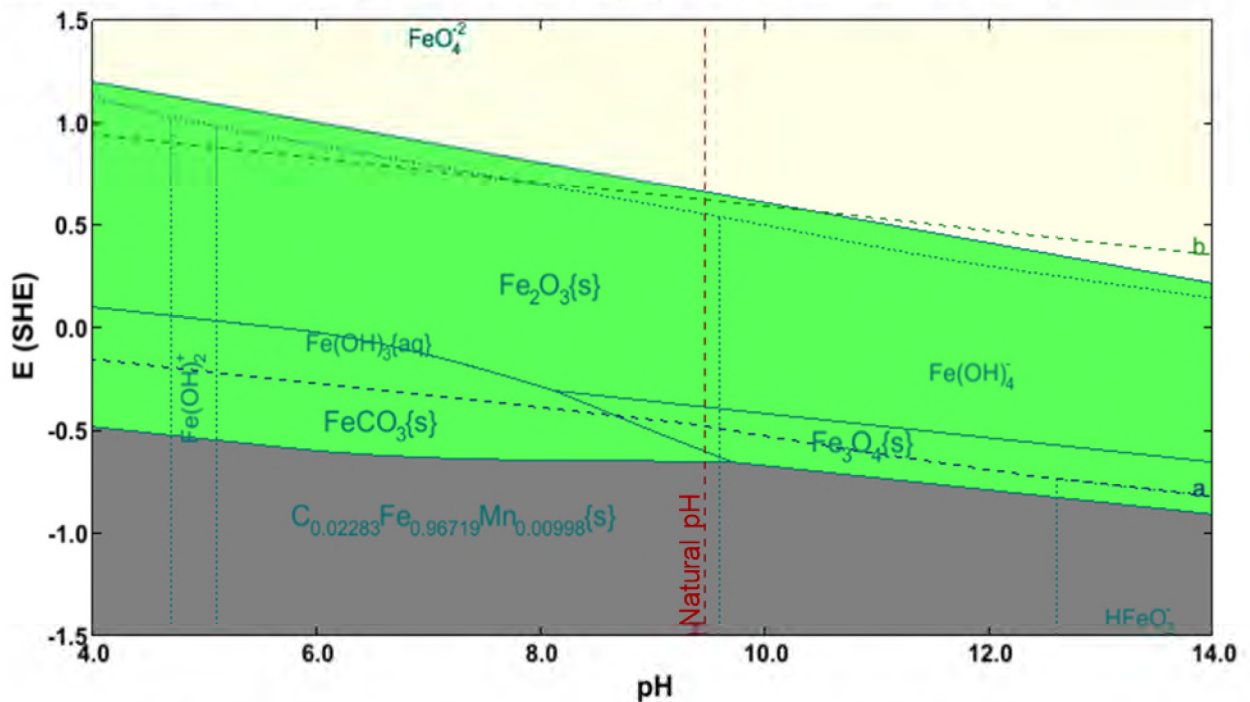


Figure 240: Ferrous/Ferric Hydroxide Stability Domains in the Presence of Carbonate (Condition 1)

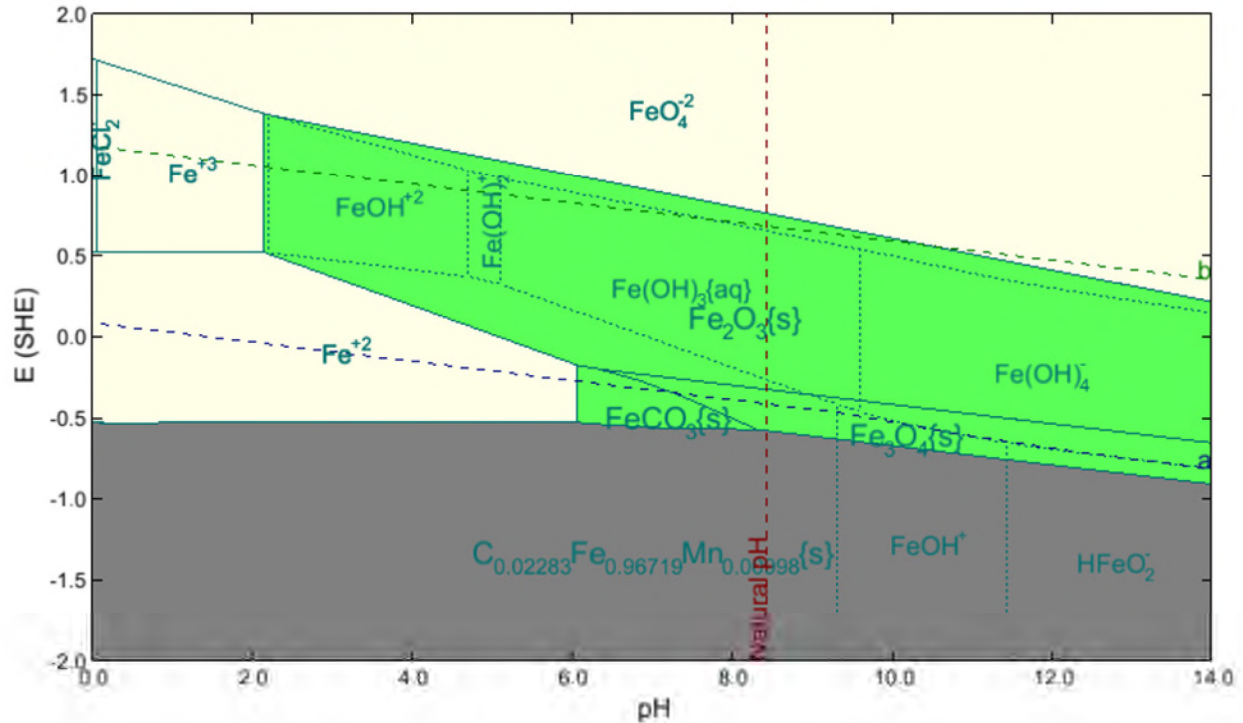


Figure 241: Ferrous/Ferric Hydroxide Stability Domains in the Presence of Carbonate (Condition 2)

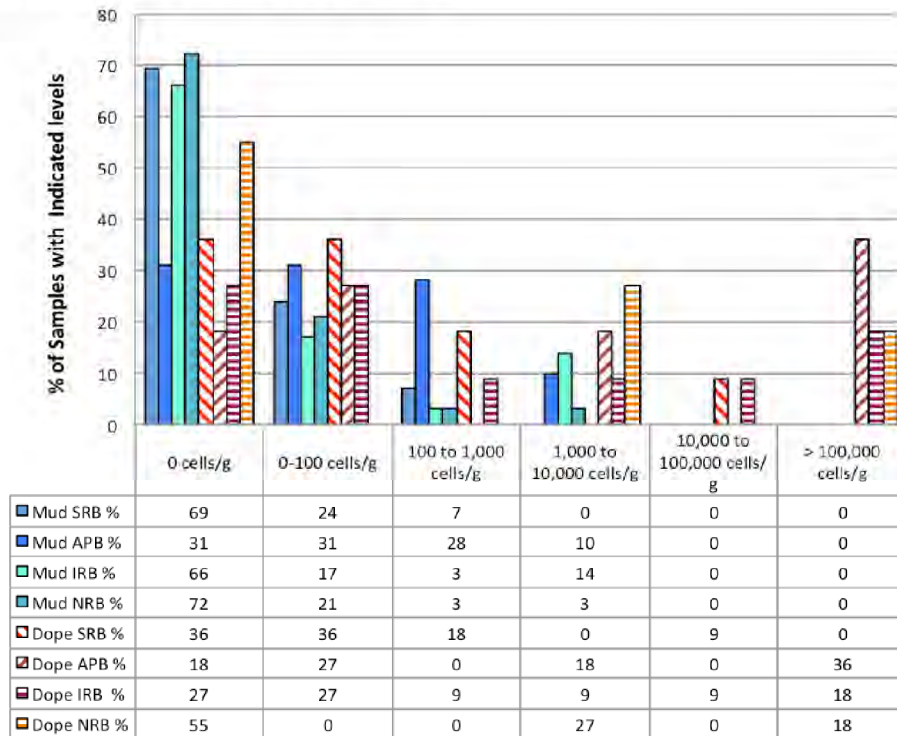
## 5.4 Biological Analysis

The biological evidence was taken from the results of microbial analysis using the most probable number (MPN) and DNA based genetic analysis by qualitative quantitative polymerase chain reaction (qPCR) and amplicon metagenomics technologies. The MPN is used to quantify viable and culturable bacteria through different growth media. These media should be able to identify live cell counts of sulfate-reducing bacteria (SRB), iron-reducing bacteria (IRB), nitrate-reducing bacteria (NRB), acid-producing bacteria (APB), and general heterotrophic bacteria (GHB). qPCR analysis is a DNA based analysis that quantifies the total microbes in a sample. It does not distinguish between living and dead cells and does not give information on the types of cells, but it provides the total cell count assay. Amplicon metagenomics provides information about the types and relative abundance of bacteria samples. It does not distinguish between live and dead cells, and it is not dependent on growth media [49]. It provides a population structure assay.

Ecolyse, a third-party laboratory contracted to perform microbiological analysis, collected samples at Aliso Canyon, the Blade warehouse, and the Schlumberger laboratory in Houston, TX. Qualified laboratory personnel from Ecolyse took the specimens and performed the specimen analysis at their laboratory in College Station, TX. The details of the specimens collected from each sampling trip and the results of the analysis were reported in the Ecolyse project report [50]. However, this section primarily discusses the results of the microbiological analysis of the samples collected from Aliso Canyon on August 8, 2018.

The samples collected from SS-25 in Aliso Canyon (August 8, 2018) did not show great abundance of sulfate-reducing bacteria. Although sulfate-reducing bacteria was present in the scales collected from the 7 in. casing (specifically from C025 and C026), the amount detected was low (less than 1,000 cells/g). GHB and APB were identified in samples taken from areas within Type I corrosion features (C025S06, C025S13,

C025S14, C025S16, C025S17, and C025S19). Cell counts from these samples ranged from 10–2,100 cells/g. APB and GHB were present in 82% of the crude oil samples and 69% of the scale samples. MPN analysis in Figure 242 showed that the bacteria population profile of the scales (mud) collected from the OD of the 7 in. casing and the oily material (dope) were different.



**Figure 242: Culturable Bacteria per Gram of Sample**

From the 42 samples, including scale (29), oily material (11), and background (2) collected at Aliso Canyon on August 8, 2018, 23 specimens yielded DNA using qPCR analysis. Twenty-two samples were positive for 16S primers, five samples were positive for Archaeal-specific primers, and two samples were positive for 18S/Eukaryotic primers. The 16S primers detect the archaea and the bacteria, while Archaeal primers only detect archaea. The 18S primers detect eukaryotes, including fungi, animals, plants, protozoans, and some bacteria, but not archaea.

Based on the analysis, the levels of quantifiable organisms ranged from 1E04 to >1E09 cells/g. The optimal level for DNA isolation was identified to be 1E04 cells/g. Ecolyse indicated that the material composition can interfere with DNA isolation, especially at levels below 1E04 cells/g. Both the scale samples and oily material samples had averages between 1E06 and 1E07 cells/g, based on the 16S primer assay. The microbial concentration of the dried scale samples from C025 based on the 16S primer was 1.63E07 cells/g and based on the Archeal primers was 1.10E08 cells/g. The microbial concentrations of the scale samples from C026 were 4.38E07 cells/g and 7.98E07 cells/g, based on the 16S and Archaeal primers, respectively [51].

Out of the 42 samples tested, only 14 samples yielded amplicon-metagenomic data. These included 14 samples that tested positive for 16S primers, 4 for Archaeal primers, and 2 for Eukaryotic primers. The percent population of the methanogenic archaea and alkaliphiles were significantly higher than the other microbes (such as GHB, APB, SRB, sulfidogens, and IRB) in samples from C025 and C026 (Table 13). The dominate methanogens found in the scale samples were methanobacterium sp., methanobacterium aarhusense, and methanocalculus sp. [51]. Methanogens are archaea that produce methane as a

metabolic byproduct in anoxic conditions. Literature established the contribution of methanogens to corrosion in the oil and gas industry; however, there is limited information about the contribution of alkalibacterium.

**Table 13: Average Abundance and Number of Species of Each Trait**

Species	C025 Avg %	C026 Avg %	Select Traits: Metabolism, Physiology, Ecology, and Taxonomy
Methanobacterium sp.	27.7	34.7	Anaerobe; Archaea; Methanogen
Alkalibacterium sp.	24.3	7.5	Alkaliphile; Firmicutes; Lactobacillales
Unclassified	8.9	11.9	Polytaxonomic Category of Unclassified Organisms
Xanthomonas campestris	9.9	9.3	Gammaproteobacteria; Production of Drilling Mud Component, Xanthan Gum
Methanobacterium aarhusense	0.3	15.2	Anaerobe; Archaea; Methanogen
Methanocalculus sp.	1.4	5.8	Anaerobe; Archaea; Methanogen
Alkalibacter sp.	6.6	0.2	Alkaliphile; BioDeg; Clostridia; Firmicutes
Halolactibacillus halophilus	1.7	4.7	Alkaliphile; Bacilli; Firmicutes; GHB; Halophile
Halomonas sp.	1.9	1.8	Alkaliphile; BioDeg HC; Facultative Anaerobe; Gammaproteobacteria; Halophile; NRB
Alkaliflexus sp.	3.4	0.1	Alkaliphile; Bacteroidetes; Halophile
Ercella succinigenes	1.9	0.01	Anaerobe; Clostridia; Firmicutes; Sulfidogen; Sulfur-Reducing Organism
Synergistes sp.	0.6	1.2	Ferm; Oilfield; Synergistetes
Sedimentibacter sp.	1.2	0.01	BioDeg; NC10
Acetobacterium sp.	1.0	0.1	Acetogen; Anaerobe; APB; Clostridia; Firmicutes
Pseudomonas sp.	0.6	0.3	Aerobe; Gammaproteobacteria; Varies
Anaerobranca sp.	0.8	0.01	Alkaliphile; Anaerobe; Clostridiales; Fermentative; Firmicutes; IRB; Sulfidogen; Thermophile; Thiosulphate-Reducing Bacteria
Methanocorpusculum sinense	0.7	0.1	Anaerobe; Archaea; Methanogen

The mere presence of microbes in the system does not indicate that the corrosion mechanism was microbiologically influenced. SRB were detected but were present at very low levels. Other bacteria, such as IRB, APB, and NRB, were also detected at higher levels using MPN, but the percent population identified using metagenomic amplicon was low. High levels of methanogens were detected in the specimens collected from C025 and C026 with Type I corrosion features. In order to understand the

contribution of these archaea in the degradation of steel, it is important to recognize the mechanisms on how these archaea participate in corrosion.

Most of the literature published on MIC in oil and gas pipelines is about the effects of sulfate-reducing bacteria. Limited literature has been published about MIC due to the presence of methanogens alone [52] [53]. Some authors reported the interaction of methanogens with sulfate-reducing bacteria or other types of microbes causing corrosion in steel [54] [55] [56] [57].

The paper published by Daniels, et al. indicated that methanogens can contribute significantly to the corrosion of iron-containing materials in anaerobic environments [53]. Elemental iron is used as an electron donor for methanogenesis from  $CO_2$  according to the chemical reaction in Eq. 15 [53].



Mand, et al. reported that methanogens can catalyze methanogenesis using either hydrogen and bicarbonate or formate, according to the Eq. 16 and 17 chemical reactions [58]:



Tan, et al. indicated that the methanogens become aggressive to carbon steel, causing increase in corrosion if they are starved from their nutrients [59] [60] [61]. They proposed a mechanism that involves a redox mediator (X) in the extraction of electrons directly from the iron in the absence of traditional electron donor/energy sources. The overall mechanism they presented has the form shown in Eq. 18 and 19.



Tan, et al. also noted that it is possible that the redox mediator is not one of the species in the original media, but it can be a product of metabolic reactions of methanogens [59] [60] [61]. However, they did not present the nature of the metabolic reaction.

SS-25 could have had a varying water level, depending on the seasonal precipitation in Aliso Canyon. The change in the water level could have also affected the local environment in which the microbes lived and attached to the outer diameter of the 7 in. casing. The nutrients present in the ground water could also have been altered by changes in season. If the mechanism presented by Tan, et al. is considered, the methanogens present in the well could have become aggressive to carbon steel when they were starved from their nutrients [59] [60] [61]. Therefore, the changes in the local environment on which the microbes grow and live could affect the corrosion of the steel.

The biological analysis was based on the samples collected roughly 21 months after the blowout (August 8, 2018). Certain changes in the environment could have affected the population of microbes present in the well. There are no previous records that indicate the type of bacteria present in SS-25. Current biological analysis indicated that methanogens most likely influenced the corrosion in the well. Other bacteria not detected by the current biological analyses may also have contributed to the corrosion of the 7 in. casing.



## 5.5 Integration of Evidence

Several forms of corrosion can possibly occur in the OD of the 7 in. casing due to the nature of the environment in the 11 3/4 in. × 7 in. annulus:

- Uniform corrosion
- Pitting corrosion
- Galvanic corrosion
- Crevice corrosion
- CO<sub>2</sub> corrosion
- Under-deposit corrosion
- Microbiologically influenced corrosion (MIC)

The 7 in. casing OD corrosion could have either been governed by a single mechanism or by a combination of possible mechanisms. Uniform corrosion involves damage that shows regular removal of metal from the surface [62]. Pitting corrosion involves localized attack in the nonresistant surface producing pits [62]. Galvanic corrosion involves a corrosion of a more active metal when two dissimilar metals are coupled in the presence of electrolyte [62]. According to Kelly, et al., crevice corrosion is a specific type of localized corrosion involving the creation of a physically occluded region at a particular metal surface [63]. CO<sub>2</sub> corrosion can occur when the environment is rich in CO<sub>2</sub>, forming siderite (FeCO<sub>3</sub>) as a corrosion product. Under-deposit corrosion occurs due to the creation of concentration cells between the areas under a surface deposit and the area without surface deposit. MIC is a form of corrosion caused by the presence or activities of microorganisms [64].

These forms of corrosion were methodologically considered to classify the corrosion features present on the OD of the 7 in. casing. Evidence was collected and evaluated to determine the corrosion mechanism governing the corrosion feature with striated groove, which was related to the 7 in. casing axial rupture. Uniform and pitting corrosion do not represent the corrosion feature with striated groove. CO<sub>2</sub> corrosion product was not identified on the corrosion feature with striated groove. Crevice corrosion may occur at areas where a tight crevice can be formed, in other words, crevice corrosion can happen at areas where the 7 in. casing and the 11 3/4 in. casing are in contact, creating an occluded region. If the corrosion features with striated grooves were due to crevice corrosion, where the 7 in. casing might be leaning to the 11 3/4 in. casing, the corrosion feature with striated grooves should have occurred mostly on one side of the 7 in. casing. Visual inspection and laser scan of the 7 in. casing showed that the corrosion was present around the entire OD circumference and did not appear to have a preferential orientation. Deposits were able to form on the OD surface of the 7 in. casing, forming under-deposit corrosion.

Since the 7 in. casing material (grade J55) is different from the 11 3/4 in. casing material (grade H40), galvanic coupling could also have contributed to the corrosion. However, history shows little evidence that casing string mixed with different carbon steel grades, such as H40, J55, K55, and N80, had galvanic corrosion issues. Moreover, no literature can be found that corrosion with striated groove morphology can be produced by galvanic corrosion. Nevertheless, Blade contracted Materials Research Company to conduct electrochemical experiments to determine the contribution of galvanic corrosion in SS-25. Materials Research Company measured the open circuit potential (OCP) and performed potentiodynamic polarization and zero resistance ammeter (ZRA) measurements between grades J55 and H40. Details of the tests can be found in the Materials Research Company report [65], and the interpretation of the test

results are included in Section 6.1.2. Results showed that from the OCP measurements, grade J55 steel is more active than grade H40 steel. Results also showed that there is a galvanic current density of 0.01–0.1 mA/in<sup>2</sup> flowing from the grade J55 steel anode to the grade H40 steel cathode at a separation distance of 5 mm. The spacing between the 11 3/4 in. surface casing and the 7 in. production casing inside the SS-25 well was about ten times higher than 5 mm. The effect of a larger separation distance on galvanic current would depend on the conductivity of the aqueous medium present in-between the two casings. However, this was not analyzed in the study conducted by Materials Research Company.

Based on the above discussion, the only mechanism left for consideration is MIC. In order to study the influence of microbes in SS-25, several key perspectives need to be considered to determine if microorganisms played a role in the corrosion features with striated groove.

Gas Research Institute published a GRI Field Guide entitled Microbiologically Influenced Corrosion: Methods of Detection in the Field in 1990 [35]. The field guide provides a summary data sheet with a scoring guide for corrosion samples and is presented in Table 14 with the assigned score for the 7 in. casing. A score is assigned based on the points column in Table 14. A total score of 11 was obtained for SS-25 7 in. casing. Based on this total score, the corrosion was very likely to be MIC. There were deposits present on the striated groove. Some of the deposits on the striated grooves were black, and some were brown. There were cup-type corrosion deposits and striated grooves on the OD surface of the 7 in. casing. Tunnels were present and oriented in the rolling direction. Only a limited amount of iron carbonate (FeCO<sub>3</sub>) was identified from the scales analysis, but it was not identified in the corrosion product analysis of Type I corrosion samples; therefore, a score of zero (0) was assigned.

The score of 11 points was mainly influenced by the large number assigned to the presence of tunnels (5 points). Pope reported that the presence of tunnels can often be considered as a metallurgical feature that is fairly definitive for MIC [35]. However, other authors have indicated that the presence of tunnels cannot be solely used in order to determine MIC; therefore, it is necessary to provide additional evidence for MIC [66] [67] [68] [34]. Aside from the presence of tunnels, the shape of the corrosion morphology and the types of corrosion deposits were investigated.

**Table 14: GRI Scoring Sheet for MIC [35]**

Questions	Points	Scores
<b>1. Are deposits present?</b>	Yes=1	1
Approximate number	-	-
Approximate size	-	-
<b>2. Number of positive (turbid) bottles of MC</b>	-	-
Number of positive (black) bottles of SRB or MC media	-	-
Record the higher number of positive bottles above (0-5) (MC or SRB, not both)	-	-
<b>3. Are pit contents grey or black?</b>	Yes=1	1
Is metal surface under the deposit shiny or black?	Yes=1	1
<b>4. Calcium carbonate present?</b>	Yes=0	-
Iron carbonate present?	Yes=2	-
Calcium and iron carbonate?	Yes=1	-
Sulfide present?	Yes=1	-

<b>5. Are cup-type pits present?</b>	Yes=1	1
Are striations present?	Yes=1	1
Are tunnels present?	Yes=5	5
Are tunnels rolling direction?	Yes=1	1
<b>Probability of MIC:</b> ≤ 6 Very unlikely      7-10 Likely      ≥ 11 Very likely	Total Score	11

A review of previous studies showed that there is no specific fingerprint that can indicate if the corrosion mechanism is MIC [64] [66] [67] [68] [69] [34]. The metallurgical, chemical, and biological evidence collected was systematically analyzed in order to determine if the corrosion mechanism was related to MIC.

Based on visual inspection, Type I corrosion features are mostly present between joints 18–25. The Type I corrosion feature is a metal-loss patch containing striated grooves that were slightly angled from the longitudinal direction. The shape of the grooves was not related to the microstructure of the 7 in. casing. The grooves were elongated along the longitudinal axis of the 7 in. casing, but the 7 in. casing had an equiaxed microstructure. Even though MnS inclusions surrounded by corrosion products were seen in the cross section of the groove tips, the striated groove density did not match the reported inclusion number density in grade J55 material. The presence of tunnels and some extra-cellular material (organic matter) in the Type I corrosion features support that the corrosion mechanism could have been related to MIC. The cross section analysis done in specimen C021A3C2 and C021A3C3A proved that tunnels exist at the tip of the striated grooves. Therefore, tunnels could have been present where there were Type I corrosion features.

The Raman characterization in the OD of the 7 in. casing [38] and the XRD analysis of the scales [47] obtained from the OD of 7 in. casing indicate that the common compounds were magnetite (Fe<sub>3</sub>O<sub>4</sub>), hematite (Fe<sub>2</sub>O<sub>3</sub>), modified hematite (Fe<sub>2</sub>O<sub>3</sub>), goethite [α-FeO(OH)], lepidocrocite [γ-FeO(OH)], and barite (BaSO<sub>4</sub>). Barite (BaSO<sub>4</sub>) was commonly found in the kill fluids. Mackinawite (FeS<sub>1-x</sub>) and pyrite (FeS), which are common products in SRB influenced corrosion [70], were not found. Unlike SRB, methanogens do not produce distinctive solid corrosion products [54]. However, authors [54] [71] [72] identified hematite (Fe<sub>2</sub>O<sub>3</sub>), magnetite (Fe<sub>3</sub>O<sub>4</sub>), and goethite [α-FeO(OH)] or lepidocrocite [γ-FeO(OH)] among the corrosion products of the system that had IRB, SRB, or methanogens.

From the chemical evidence, H<sub>2</sub>S corrosion products were not found. SRB was not a culprit either because mackinawite, which is an SRB corrosion product fingerprint, was not identified in the scale analysis. However, there was a minimal amount of CO<sub>2</sub> corrosion product (siderite [FeCO<sub>3</sub>]) found on the OD surface of the 7 in. casing. CO<sub>2</sub> corrosion was not the prevailing corrosion mechanism since only a small amount of CO<sub>2</sub> corrosion products were identified.

The biological evidence showed that different microorganisms were detected on the OD surface of the 7 in. casing. Among the microorganisms identified using MPN analysis of scales obtained from areas with Type I corrosion features are APB and GHB. From qPCR analysis and amplicon metagenomics, high amounts of methanogens were identified in the joints with Type I corrosion features. The probable electrochemical reactions related to the activities of methanogen previously presented showed that electrons from the steel surface were being used by methanogens leading to corrosion of the steel (Fe).

Based on the metallurgical, chemical, and biological evidence, the corrosion mechanism was most likely related to MIC.

## 5.6 Corrosion Rate

The corrosion rates depend on the amount of oxygen present in the system, the pH, the alkalinity, the temperature of the environment, amongst many other factors. Data have been published on the corrosion rates of steel at different environment. The estimated corrosion rate for carbon steel in stagnant air-saturated soft water is roughly 4 mils per year (mpy) [73], while the corrosion rate for carbon steel in immersed sea water is within the range 0.8–14.6 mpy [74]. For a steel pipe buried in soil, the corrosion rate is 40–120 mpy [75]. AlAbbas, et al. reported an increase in corrosion rate by a factor of three for steel specimens immersed in water obtained from an oil well with cultivated SRB compared to specimen immersed in the oil well water without SRB [76]. Usher published a paper that reviews the contribution of microbes in the increase in corrosion rate in buried steel pipes [42].

The exact corrosion rate for the 7 in. casing cannot be predicted because of the limited information about the condition of the well, particularly the pH, alkalinity, temperature, and composition of the fluid in contact with the 7 in. casing OD over the entire life of the well. Also, the start of the corrosion attack is not documented. In addition, the changes in season in Aliso Canyon could have also affected the factors previously mentioned. SS-25 was converted into a gas storage well in 1973, but gas injection started in 1977. If the connections were leaking, CO<sub>2</sub> was seeping into the 11 3/4 in. × 7 in. annulus, and microbes were present, it is rational to assume that the corrosion could have started in 1977. A rough estimate of an 85% wall thickness loss over 38 years (from the time the CO<sub>2</sub> injection started in 1977 up to 2015) leads to a maximum penetration rate of 7 mpy. Assuming that corrosion started after the 7 in. casing had been installed (1954), the maximum penetration rate would have been 4 mpy.

The corrosion rate estimated using controlled laboratory conditions can be different from the corrosion rate in the field. Materials Research Company, LCC used the software EC-Lab, which can estimate the corrosion rate of grade J55 steel tested in a simulated ground water-based Tafel slope fitting of the polarization curves established during electrochemical testing [65]. The corrosion rate of grade J55 material for the aerated and de-aerated conditions were determined to be 11.7 mpy and 5 mpy, respectively [65]. The reported galvanic current density between grades J55 and H40 material can be converted to a galvanic corrosion rate of 0.8–8 mpy [65]. Tan calculated the corrosion rate of coupons immersed in solution with methanogens in the presence of CO<sub>2</sub> to be between 0.9 and 1.2 mpy, based on laboratory experiments [60]. The reported corrosion rates from controlled laboratory experiments involving methanogens were generally lower than the estimated maximum penetration rate in the 7 in. casing. Increased penetration rate in the field conditions could have been due to different factors, such as the presence of types of microorganisms other than methanogens, presence of different ions in the liquid, and actual temperature and pH of the liquid.

## 5.7 Summary

The axial rupture is associated with the Type I corrosion feature present on the OD of the 7 in. casing. Type I corrosion features were characterized, and different corrosion mechanisms were evaluated. The key findings are as follows:

- The Type I corrosion of the 7 in. casing OD was affected by different factors, such as the varying level of fluid inside the 11 3/4 in. × 7 in. annulus, composition of the liquid in the annulus, amount of CO<sub>2</sub> and O<sub>2</sub> dissolved in the liquid, presence of microorganisms, and amount of the galvanic current between grades J55 and H40 steel.
- Different corrosion mechanisms were evaluated with respect to metallurgical, chemical, and biological aspects based on the corrosion environment inside the 11 3/4 in. × 7 in. annulus.

- Metallurgical evidence included tunnels that were seen at the tip of the striated grooves. Extra-cellular looking material that are rich in C were seen in the vicinity of the tunnel. Globules with acicular features were seen as corrosion deposit morphologies.
- Chemical evidence showed that the corrosion products in Type I corrosion features were composed of magnetite ( $\text{Fe}_3\text{O}_4$ ), hematite ( $\text{Fe}_2\text{O}_3$ ), goethite [ $\alpha\text{-FeO(OH)}$ ], lepidocrocite [ $\gamma\text{-FeO(OH)}$ ], and organic matter.
- Scale analysis using XRD and Raman spectroscopy showed the change in the dominant corrosion products based on the depth in the well. Magnetite dominated the lower portion of the well.  $\text{H}_2\text{S}$  corrosion products were not observed on the surface of the 7 in. casing. FeS type compounds, commonly associated with SRB, were not seen on the deposits of the Type I corrosion feature. Although a minute amount of siderite ( $\text{FeCO}_3$ ) was identified in the scales from the OD of 7 in. casing,  $\text{CO}_2$  corrosion was less likely governing, based on the predominance diagram modeling.
- Biological analysis identified APB, GHB, and methanogens as being the microorganisms abundant in the scales collected from 7 in. casing. APB and GHB were identified using MPN analysis, while methanogens (methanobacterium sp., methanobacterium aarhusense, and methanocalculus sp.) were identified using qPCR and amplicon metagenomics.
- The metallurgical, chemical, and biological evidence suggested that the corrosion was likely related to MIC with possible contribution of galvanic coupling.
- A rough estimate of 85% wall thickness loss over 38 years (from the time of  $\text{CO}_2$  injection, 1977, to 2015) led to a maximum penetration rate of 7 mpy. Assuming that corrosion could have started after the 7 in. casing was installed (1954), the maximum penetration rate would have been 4 mpy.

## 6 Additional Features

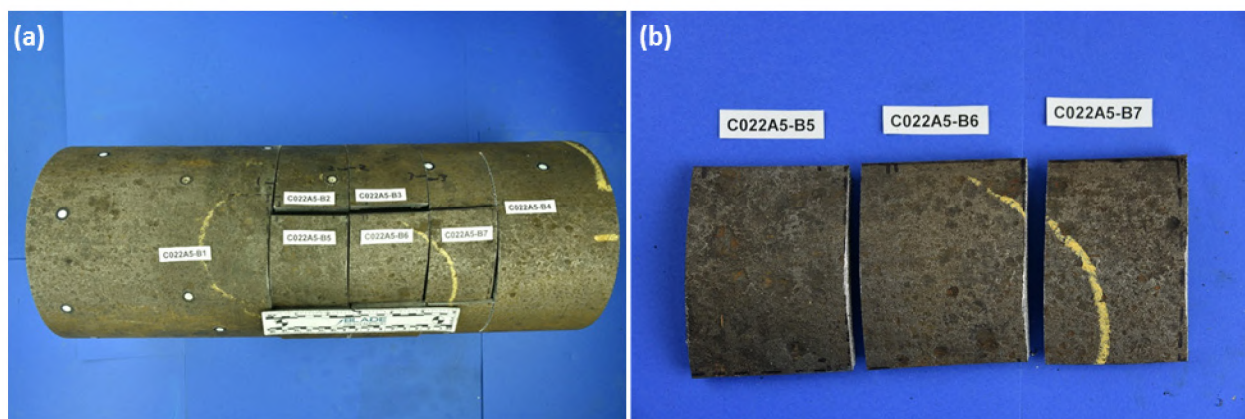
### 6.1 Other Types of Corrosion

Based on the laser scan data presented in Section 5.1, other corrosion features were present on the OD of the 7 in. casing aside from the Type I corrosion feature (striated grooves). Type II corrosion features were characterized by localized metal loss without striated grooves. Type III corrosion features were characterized as rectangular-shaped corrosion with a non-corroded center region. Type III occurred mainly on the 7 in. casing connections, with one feature occurring in the pipe body of joint 20. Details of the metal loss morphology and deposit characteristics for Types II and III corrosion features are discussed in this section.

#### 6.1.1 Type II Corrosion Feature

Type II features were characterized as pit-shaped corrosion without striated grooves. These features were small in diameter (0.05–0.5 in.) and shallow. The depth of the metal loss was less than 20% of the wall thickness, based on the laser scan data. These localized features were distributed along the length of the extracted 7 in. casing, with the highest density occurring between joints 15 and 25.

Three Type II specimens were extracted from joint 22 for a detailed investigation. Figure 243 shows the pipe segment where specimens C022A5B5, C022A5B6, and C022A5B7 were extracted. C022A5B5 contained a combination of large (0.25–0.5 in. diameter) and medium (0.1–0.25 in. diameter) size pits. C022A5B6 mostly contained medium size pits, while C022A5B7 contained both medium and small size pits (<0.1 in. diameter).



**Figure 243: Specimens with Type II Feature Extracted from Joint 22**

Figure 244 shows low magnification (5×) stereoscopic images of Type II corrosion features in C022A5B5 specimens. The Type II features contained smaller pits within larger pits. These were shallow metal-loss pits as compared to the Type I corrosion features. Dark orange, brown, and black deposits were present in the pits. Globules were observed in local pits on specimen C022A5B5. Figure 245 shows small acicular features within a globule. These acicular feature formations are commonly found in atmospheric corrosion of carbon steels and were generally described as flower petals in the literature [39] [40] [41] [77]. Extra-cellular material was not observed on the OD surface of the specimen.

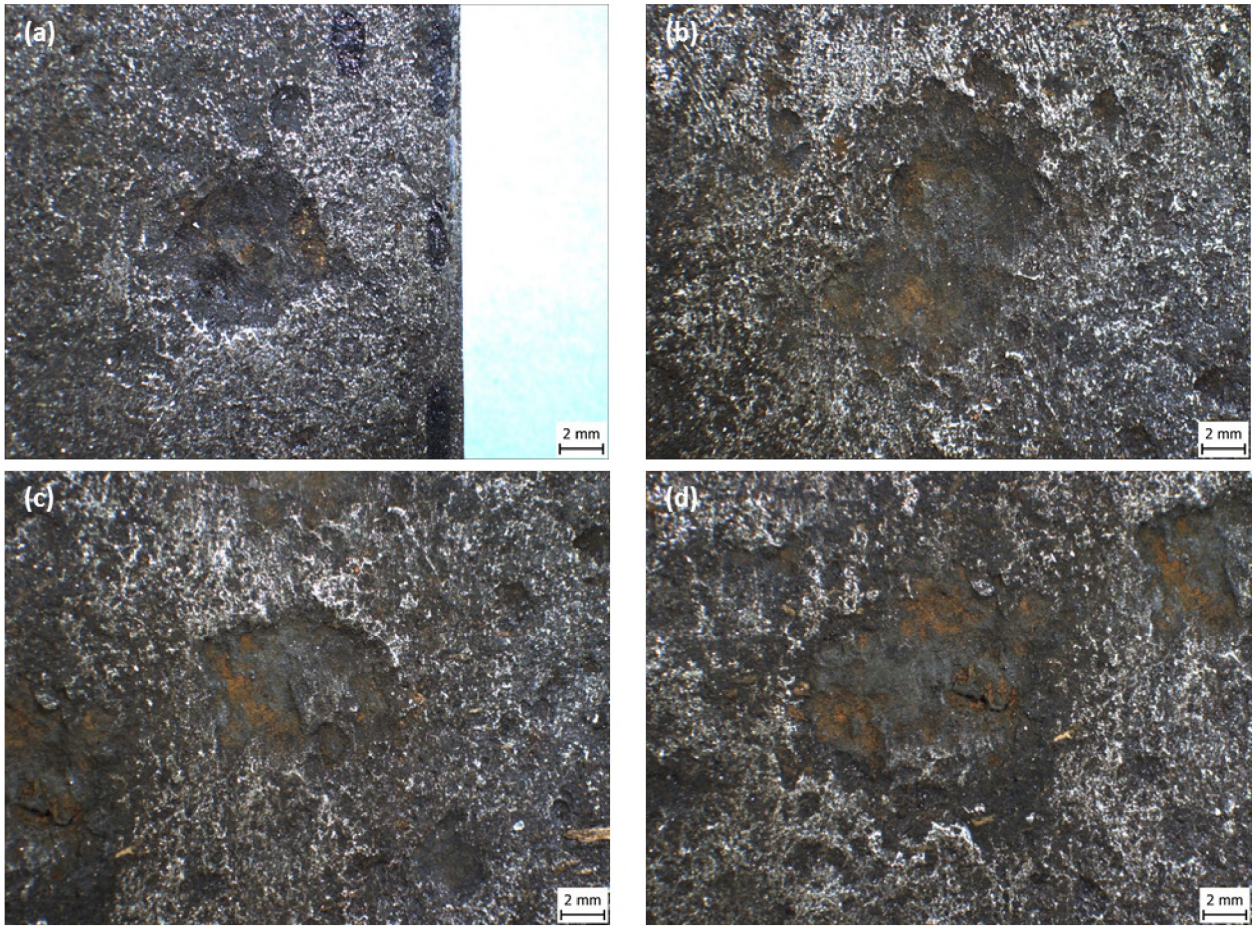


Figure 244: Stereoscopic Image of Specimen C022B2A5B5 Type II Corrosion Feature

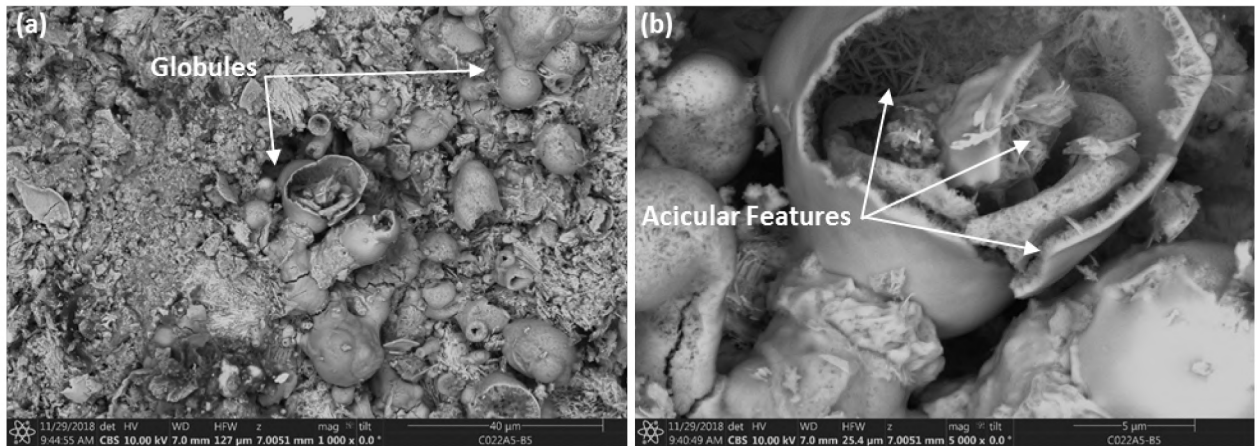
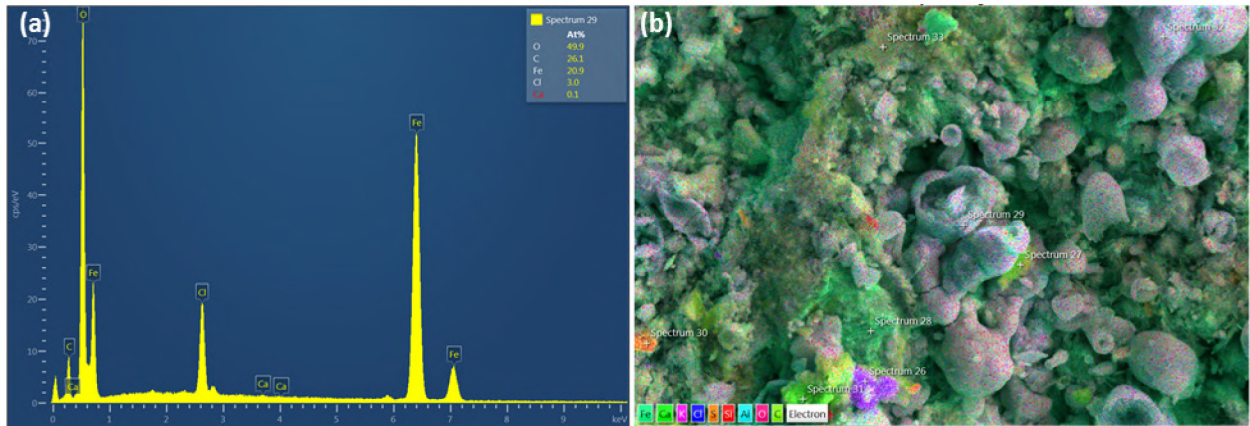


Figure 245: Backscatter Image of (a) Globules and (b) Acicular Features

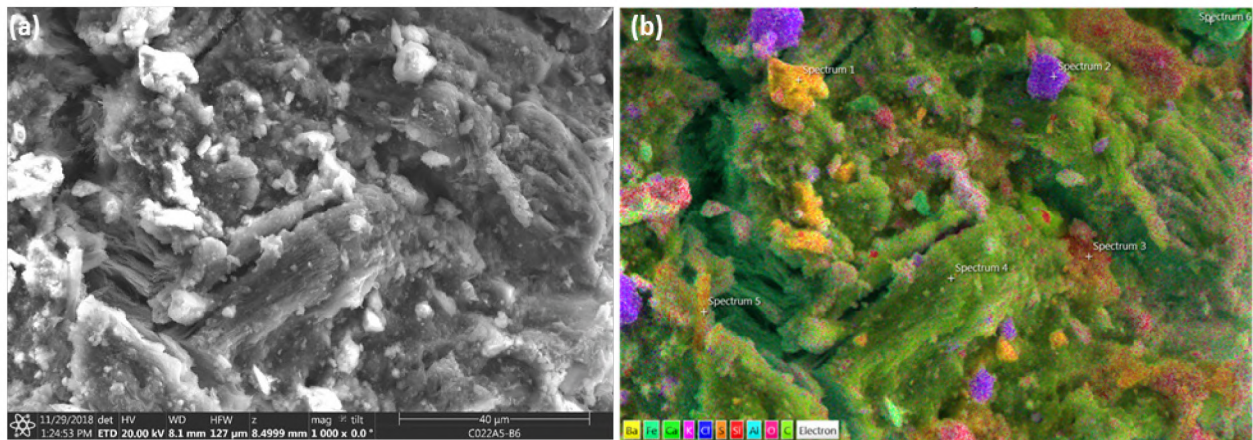
EDS analyses of corrosion deposits on the OD surface showed approximately 35–40 at% O, 35–40 at% C, 20–25 at% Fe, 1–2 at% Cl, 0.2–0.5 at% S, and small amounts (<1 at%) of K, Mn, Al, Si, and Ca. The results show high concentrations of carbon and oxygen. EDS of the small acicular features showed approximately 50 at% O, 26 at% C, 21 at% Fe, and 3 at% Cl (Figure 246). The acicular features were rich in O. Raman spectroscopy identified modified hematite ( $Fe_2O_3$ ), iron oxide combination, and organic matter within the

Type II features on the OD surface of specimen C022A5B5 [38]. Modified hematite ( $\text{Fe}_2\text{O}_3$ ) was identified on the area where most of the globules were found.



**Figure 246: (a) EDS Spectrum and (b) Dot Map Overlay for Corrosion Deposit on Specimen C022A5B5**

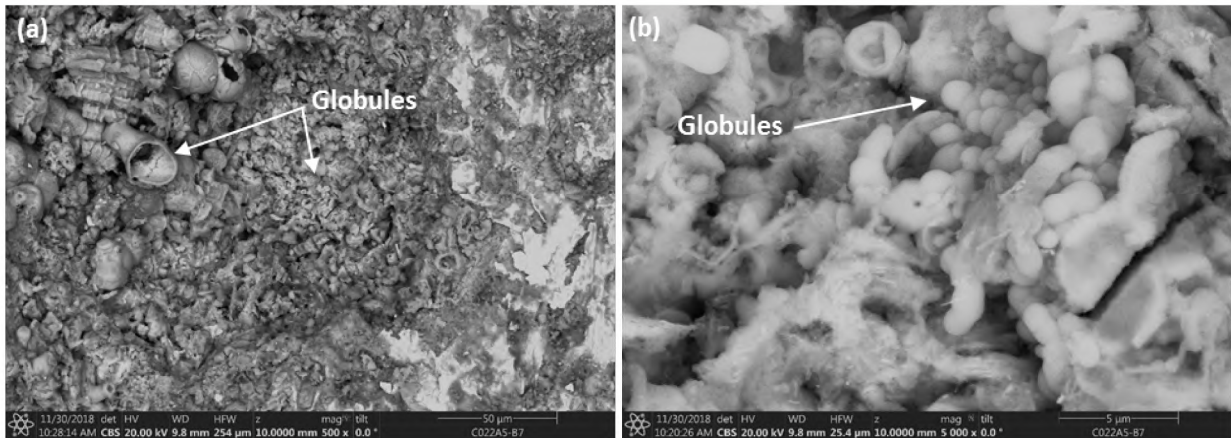
Globules were observed in the corrosion feature on specimen C022A5B6. Extra-cellular material was not observed on the OD surface of the specimen. Particles with Ba (3 at%) and S (3 at%) were identified on the surface, based on the EDS analysis (Figure 247). Raman results confirmed that the particles rich in Ba and S were barite ( $\text{BaSO}_4$ ). Barite was most likely associated with the kill fluids used during the kill attempts (Section 2.1.3). The elevated sulfur in this area was due to the presence of these particles. Aside from barite ( $\text{BaSO}_4$ ), modified hematite ( $\text{Fe}_2\text{O}_3$ ) and some organic matter were identified on the surface of this specimen.



**Figure 247: (a) SEM Image and (b) EDS Dot Map Overlay for the Deposit on Specimen C022A5B6**

Globules were observed on the OD surface of specimen C022A5B7 (Figure 248 [a]). Extra-cellular material was not observed on the OD surface of the specimen. Figure 248 (b) shows a high magnification image revealing the presence of tiny globules ( $< 5 \mu\text{m}$  size). The EDS analysis showed that the tiny globules contained approximately 38 at% Fe, 30 at% C, 29.5 at% O, 2 at% Cl, and 0.5 at% K. Raman spectroscopy confirmed the presence of modified hematite ( $\text{Fe}_2\text{O}_3$ ), iron oxide combination, and organic matter on the surface of specimen C022A5B7.



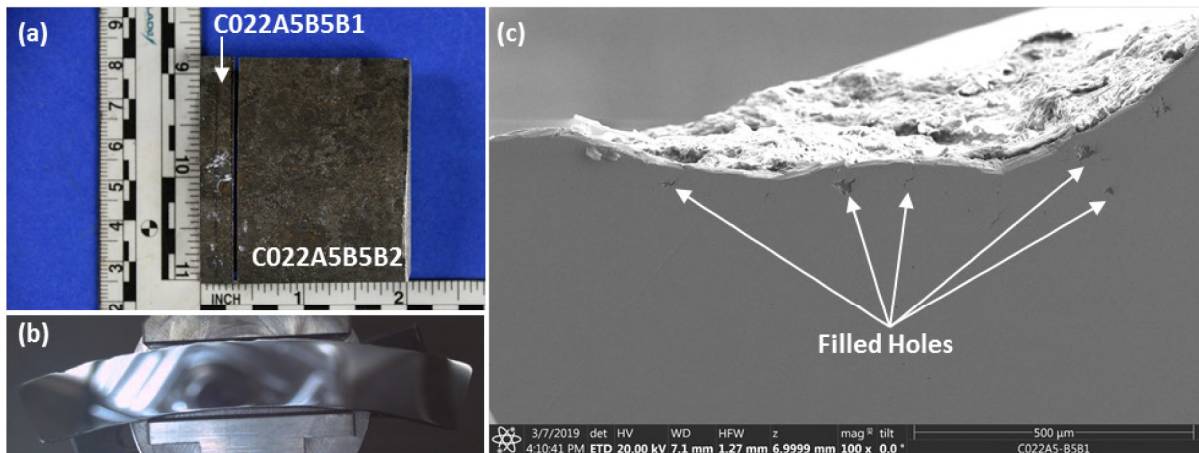


**Figure 248: Backscatter Images of C022A5B7 Taken at (a) 500× and (b) 5,000×**

Tunnels were observed in the striated grooves associated with the Type I corrosion features. The Type II corrosion features did not contain striated grooves. A cross section was made through the local corrosion pits on specimen C022A5B5B to investigate the presence of tunnels within the Type II features. Figure 249 shows the (a) cut location of the (b) metallurgical cross section.

The cross section revealed the corrosion profile and the presence of small filled holes a few microns below the metal surface (Figure 249 [c]). These small holes were between 20 and 50 μm in diameter. Raman spectroscopy identified modified hematite and some organic matter in the deposit inside the holes [38]. The EDS analysis of the same deposits identified 44 at% C, 33 at% O, and 17 at% Fe as well as small amounts of Al, Mn, and Si. These results were consistent with the analyses of the corrosion deposit within the local pits.

Figure 250 (a) shows an SEM image of the small hole below the Type II corrosion feature. Figure 250 (b) shows the FIB cross section of the filled hole. The dashed black lines in Figure 250 represent the metal surface. The FIB cross section shows that the filled holes were not associated with tunnels. These holes were most likely an artifact of cross sectioning an irregular corrosion pit profile. Figure 251 shows a schematic that demonstrates how an irregular corrosion profile can create filled holes on the metallographic cross section. The observations from the FIB cross section, EDS, and Raman analyses suggest that tunnels were not present in the Type II corrosion features. This was consistent with the macroscopic observation that striated grooves were not present in the Type II corrosion features.



**Figure 249: (a) Specimen C022A5B5B Cut Layout (b) C022A5B5B1 Polished Cross Section**

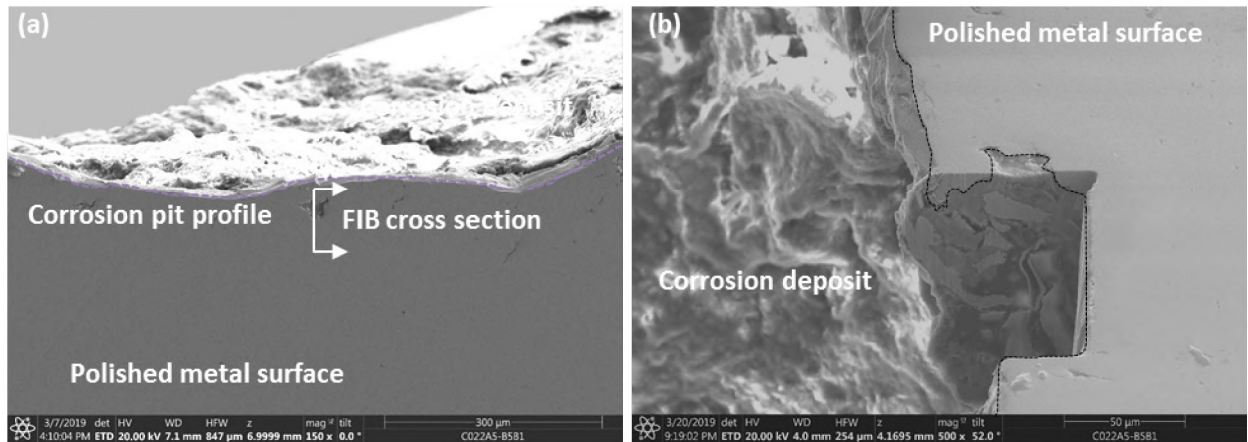


Figure 250: (a) SEM Image of Corrosion Pit and (b) FIB Cross Section of Small Hole

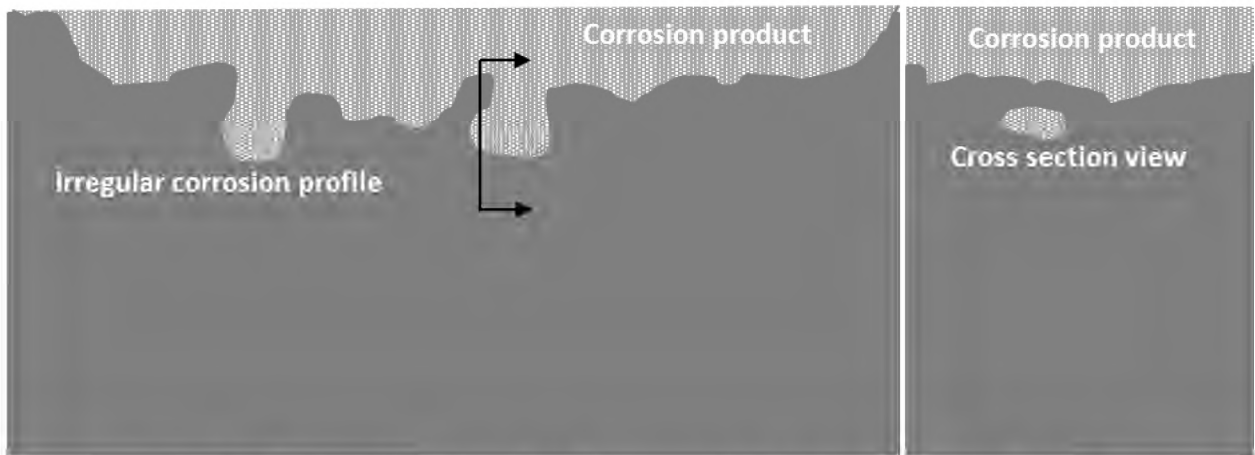
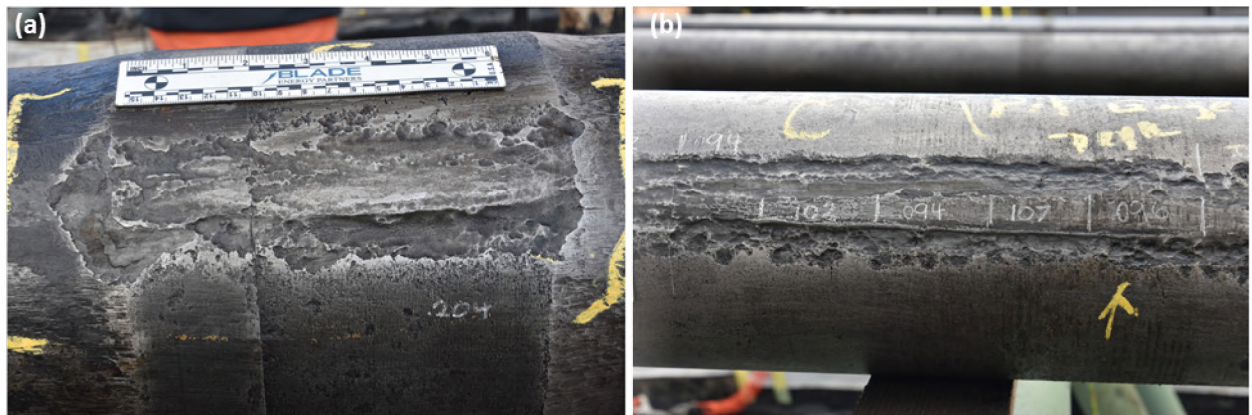


Figure 251: Schematic of Small Hole Generated by Metallographic Cross Section

The corrosion mechanisms for Types I and II appeared to be different, based on the corrosion morphology. The Type II corrosion features did not contain striated grooves, tunnels, or extra-cellular material, which suggests that microbes had a minimal contribution to the localized pitting. The Type II corrosion was a localized attack on the metal surface. The localized pitting was most likely caused by a breakdown of the passive film or by the formation of a local anodic site. However, pits within pits, which can be caused by microbial activity, were observed. Therefore, microbial activity cannot be fully ruled out. To fully understand the contribution of microbes to the formation of the Type II corrosion would require a more detailed investigation, which would be beyond the scope of this work. The detailed investigation was focused on the Type I features that caused the axial rupture.

### 6.1.2 Type III Corrosion Feature

The Type III corrosion feature had a rectangular shape with little to no corrosion attack in the middle region. The rectangular shape of the Type III corrosion consisted of scoop-shaped features. This corrosion occurred mainly on the 7 in. casing connections, with one feature occurring in the pipe body of joint 20. (Figure 252).



**Figure 252: (a) Type III Corrosion Feature on 7 in. Casing Connection and (b) Pipe Body**

Specimen C024B1B was extracted from connection 24 (Figure 253). Stereoscopic images revealed deposits ranging in color from orange to brown (Figure 254). The morphology of the deposit on the surface of specimen C024B1B appeared to be needle-like (Figure 255) [39] [40] [41]. EDS analyses (Figure 256) showed that these small acicular (needle-like) features contained approximately 55 at% C, 30 at% O, 11 at% Fe, and 2 at% Cl, being similar to the Type II corrosion deposits. Raman spectroscopy identified modified hematite ( $Fe_2O_3$ ), barite ( $BaSO_4$ ), iron oxide (FeO) combination, and organic matter within the Type III feature. Elemental analyses of other areas within the feature also showed the presence of Ba and S. Barite was most likely associated with the kill fluids used during the kill attempts (Section 2.1.3). The FIB cross section in Figure 257 shows the details of the corrosion deposit morphology observed on top of the Type III corrosion feature.



**Figure 253: (a) Connection C024B and (b) Type III Corrosion Specimen C024B1B**

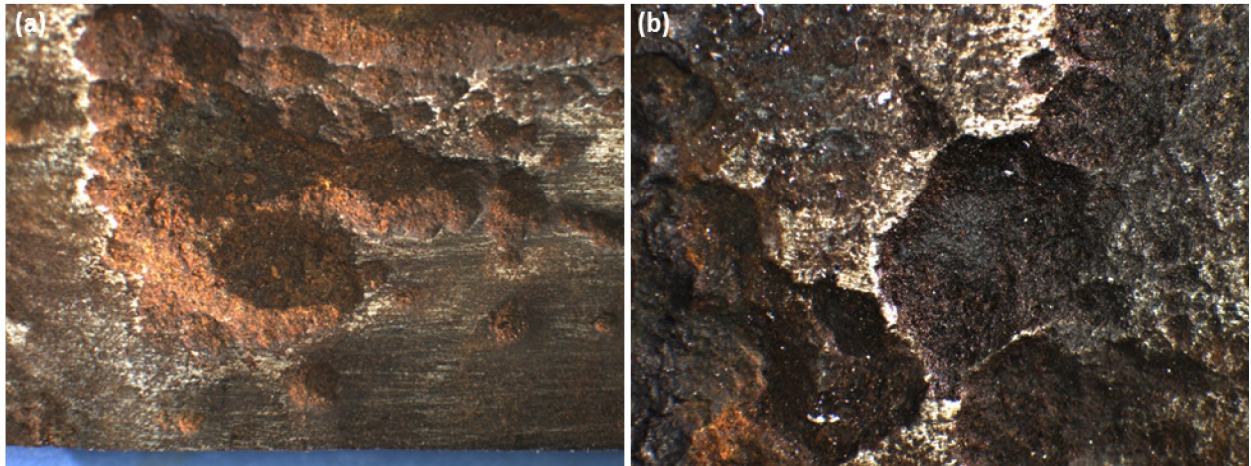


Figure 254: Stereoscopic Images of C024B1B (a) Area 1 and (b) Area 5

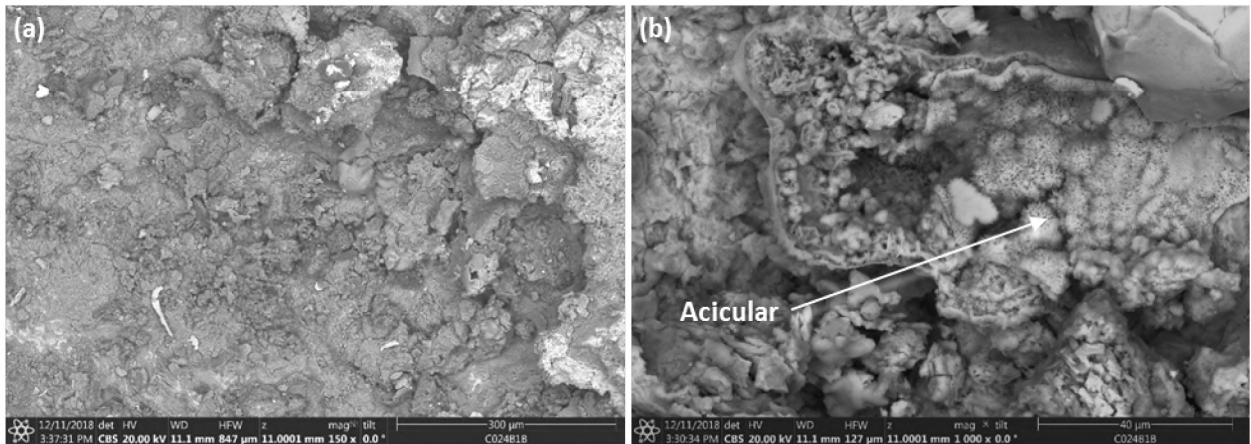


Figure 255: Backscatter Images of Specimen C024B1B A1 Taken at (a) 150 $\times$  and (b) 1,000 $\times$

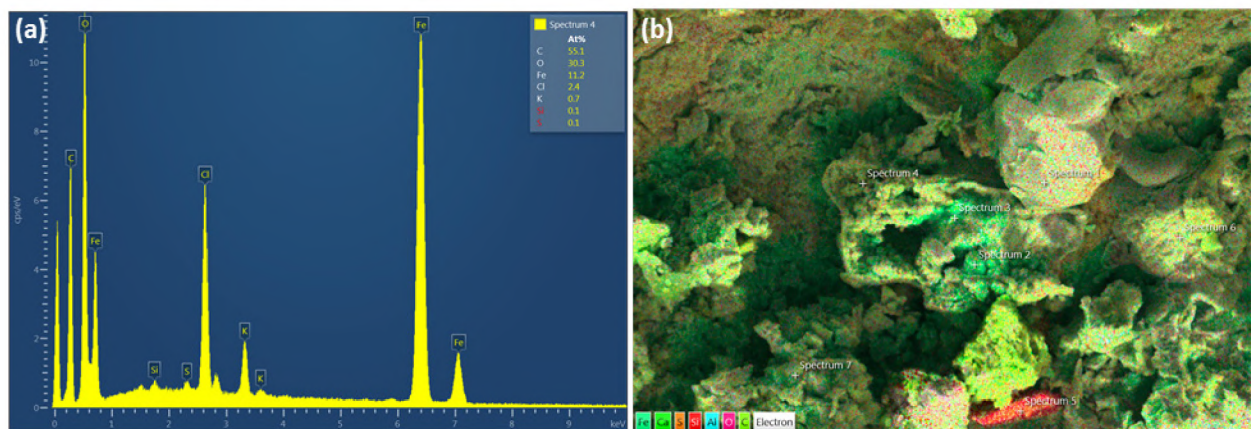
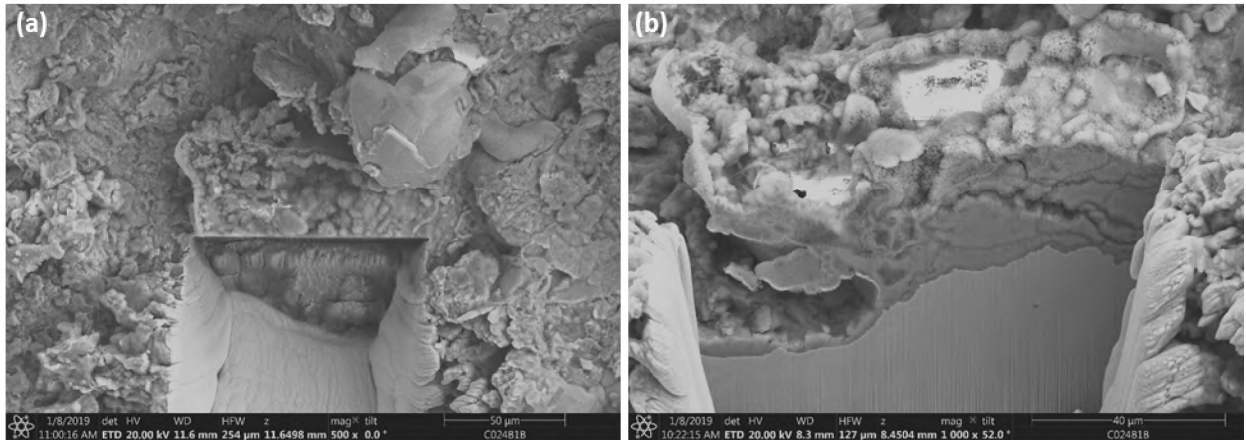
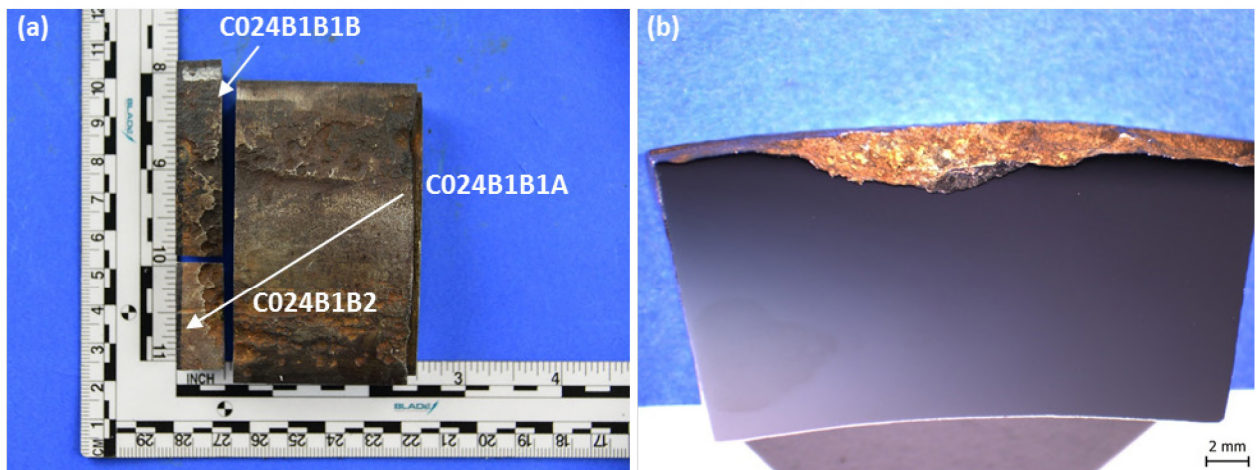


Figure 256: (a) EDS Spectrum and (b) Dot Map Overlay for Type III Small Acicular Features

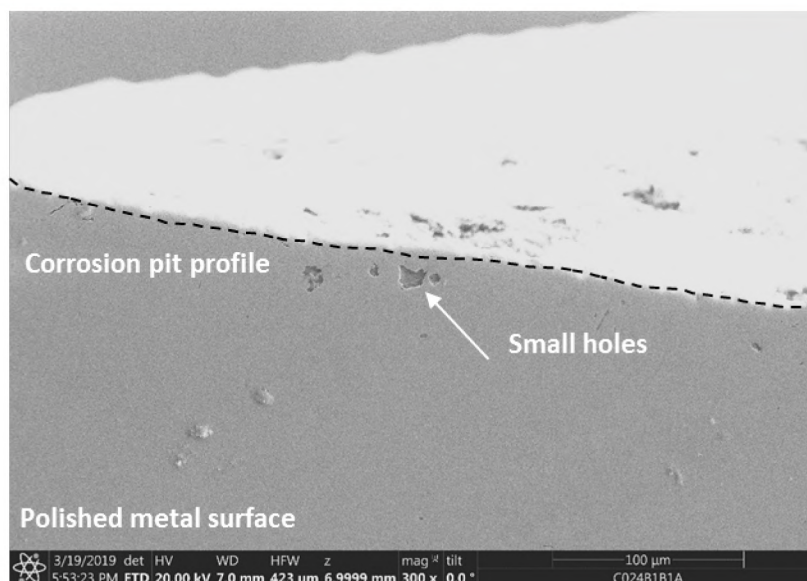


**Figure 257: (a) FIB Cut and (b) Cross Section View of Specimen C024B1B Corrosion Deposit**

Figure 258 (a) shows the cut locations for the cross section of specimen C024B1B1A, revealing the Type III corrosion profile (Figure 258 [b]). Small filled holes were observed below the OD surface of the Type III feature (Figure 259). These small holes were similar to the holes observed in the Type II corrosion feature. They contained corrosion products with approximately 50 at% O, 27 at% Fe, and 20 at% C. Raman spectroscopy indicated that these corrosion products were composed of organic matter, modified hematite ( $\text{Fe}_2\text{O}_3$ ), magnetite ( $\text{Fe}_3\text{O}_4$ ), maghemite ( $\gamma\text{-Fe}_2\text{O}_3$ ), and some carbonates. Raman spectroscopy did not identify siderite ( $\text{FeCO}_3$ ).



**Figure 258: (a) C024B1B Cut Layout and (b) C024B1B1A Corrosion Profile**



**Figure 259: SEM Image of Small Holes Under the Metal Surface of C024B1B1A**

Galvanic corrosion may explain the occurrence of Type III corrosion features. Galvanic corrosion occurs when two different materials are connected in the presence of an electrolyte (liquid). As previously mentioned, the 7 in. casing was of grade J55 steel, while the 11 3/4 in. casing was mostly of grade H40 steel. The two metals have different compositions. When the two casings are in contact, one casing can act as an anode (prone to corrosion) and the other can act as a cathode (more noble). The anodic metal can have an increased corrosion rate.

In order to understand the galvanic corrosion in SS-25, Materials Research Company conducted the open circuit (OCP) measurement and the polarization tests in the following environments:

- Aerated synthetic seawater
- De-aerated synthetic seawater
- Aerated simulated groundwater
- De-aerated simulated groundwater

Grades J55 and H40 steel samples were obtained from specimens taken from SS-25. The as-received specimens were cleaned with ethanol and a nylon brush and then tested in each environment in triplicate. The details of the test can be found in the electrochemical test report [65]. The composition of the simulated groundwater was based on the ground water analysis results from W-TH1-325 [78], and the pH was adjusted to 7.5. This composition was used to simulate the electrolyte in the SS-25 well, assuming that groundwater was present in the 11 3/4 in. × 7 in. annulus. The measured OCP and the corrosion potential ( $E_{\text{corr}}$ ) values are summarized in (Table 15). The OCP and  $E_{\text{corr}}$  values for grade J55 steel were more negative than for grade H40 steel in both aerated and de-aerated conditions for the groundwater, indicating that grade J55 steel is more anodic (active) than grade H40 steel.

Table 16 summarizes the results for the electrochemical tests done with synthetic seawater. The OCP values of grade J55 steel in synthetic seawater were more negative than the OCP of grade H40 in both the aerated and de-aerated conditions.  $E_{\text{corr}}$  values of grade J55 were more negative than the  $E_{\text{corr}}$  values of grade H40 in the de-aerated synthetic seawater. On the other hand, the  $E_{\text{corr}}$  values of the grade H40 steel were more negative than the  $E_{\text{corr}}$  values of grade J55 steel in aerated synthetic seawater. This switch in

the trend could have been due to the presence of existing iron oxide on the surface of the specimens and its interaction with the ions present in the aerated synthetic seawater. More negative OCP or  $E_{corr}$  values indicate that a metal is more active than one with higher OCP or  $E_{corr}$  values. From the ZRA test, a galvanic current density of 0.01–0.1 mA/in<sup>2</sup> was measured, flowing from the grade J55 steel anode to the grade H40 steel cathode. This indicates that a 0.01–0.1 mA/in<sup>2</sup> galvanic current density was present when the grade J55 steel was coupled with the grade H40 steel at a coupling distance of 0.197 in. (5 mm).

**Table 15: Electrochemical Test Results Summary for Simulated Groundwater Testing [65]**

Specimen	Material	OCP		$E_{corr}$	
		Aerated	De-aerated	Aerated	De-aerated
7 in Casing Specimen 1	J55	-0.486	-0.564	-0.460	-0.685
7 in Casing Specimen 2	J55	-0.420	-0.500	-0.456	-0.675
7 in Casing Specimen 3	J55	-0.481	-0.536	-0.421	-0.630
<b>7 in. Casing Average</b>	<b>J55</b>	<b>-0.462 ± 0.037</b>	<b>-0.533 ± 0.037</b>	<b>-0.446 ± 0.021</b>	<b>-0.663 ± 0.029</b>
11 3/4 in. Specimen 1	H40	-0.416	-0.475	-0.3888	-0.6259
11 3/4 in. Specimen 2	H40	-0.396	-0.475	-0.3868	-0.6272
11 3/4 in. Specimen 3	H40	-0.431	-0.493	-0.3725	-0.639
<b>11 3/4 in. Average</b>	<b>H40</b>	<b>-0.414 ± 0.017</b>	<b>-0.481 ± 0.010</b>	<b>-0.383 ± 0.009</b>	<b>-0.631 ± 0.007</b>

**Table 16: Electrochemical Test Results Summary for Synthetic Seawater Testing**

Specimen	Material	OCP		$E_{corr}$	
		Aerated	De-aerated	Aerated	De-aerated
7 in Casing Specimen 1	J55	-0.553	-0.566	-0.644	-0.838
7 in Casing Specimen 2	J55	-0.566	-0.587	-0.5896	-0.854
7 in Casing Specimen 3	J55	-0.564	-0.574	-0.584	-0.872
<b>7 in. Casing Average</b>	<b>J55</b>	<b>-0.561 ± 0.007</b>	<b>-0.576 ± 0.010</b>	<b>-0.606 ± 0.033</b>	<b>-0.854 ± 0.017</b>
11 3/4 in. Specimen 1	H40	-0.494	-0.519	-0.7397	-0.7979
11 3/4 in. Specimen 2	H40	-0.488	-0.518	-0.6251	-0.8137
11 3/4 in. Specimen 3	H40	-0.528	-0.512	-0.6641	-0.818
<b>11 3/4 in. Average</b>	<b>H40</b>	<b>-0.503 ± 0.021</b>	<b>-0.516 ± 0.004</b>	<b>-0.676 ± 0.058</b>	<b>-0.810 ± 0.011</b>

Logs from the SS-25 casings revealed that features on the outer diameter of the 7 in. casing mostly matched the locations on the inner diameter of the 11 3/4 in. casing. Figure 260 shows an overlay of the laser scan data for the 7 in. casing and the HRVRT log data for the 11 3/4 in. casing. Type III corrosion features were often observed in the 7 in. casing connection (connections C014 to C025). The figure identifies some of the Type III feature locations. This observation suggests that crevice corrosion occurred at these locations. Crevice corrosion is a form of corrosion where occluded areas become more anodic with respect to the surrounding metal. The outer diameter of the 7 in. casing, especially the connection (with larger outer diameter compared to the casing body), could have been in contact with the inner diameter of the 11 3/4 in. casing. Figure 261 shows a schematic that demonstrates how a crevice would have formed between the ID of the 11 3/4 in. casing and the OD of the 7 in. casing. The general shape of

the Type III features suggests that crevice corrosion was the most likely corrosion mechanism, with possible contributions from galvanic coupling.

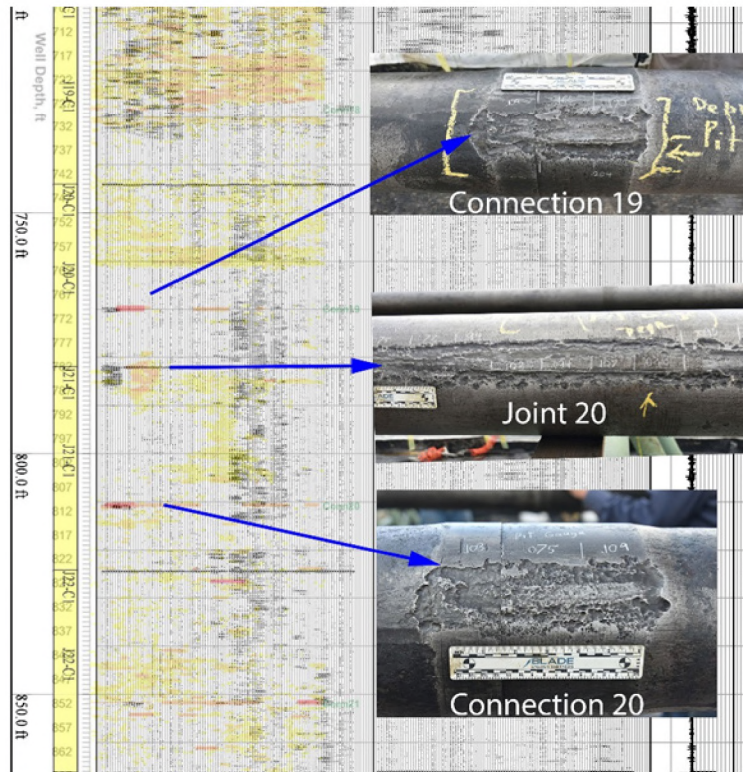


Figure 260: Laser Scan Data Overlaid with HRVRT Log Data

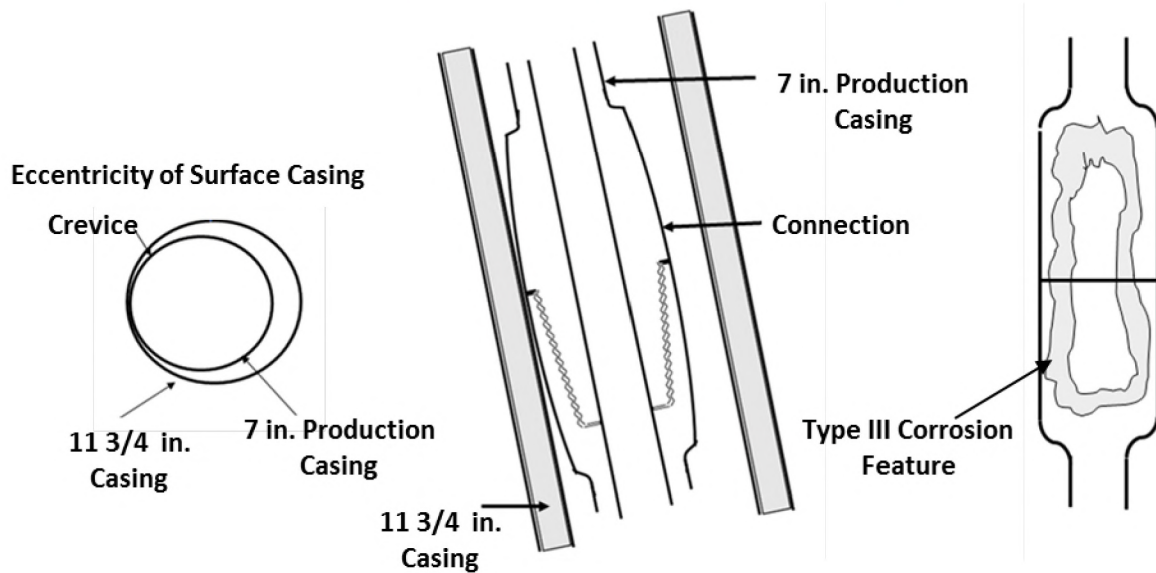
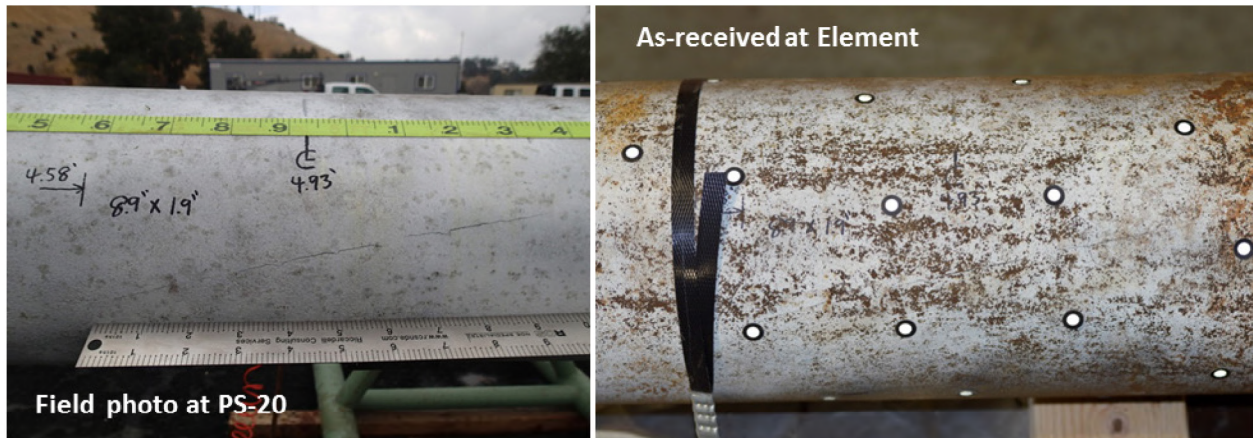


Figure 261: Schematic of 7 in. and 11 3/4 in. Casing Contact



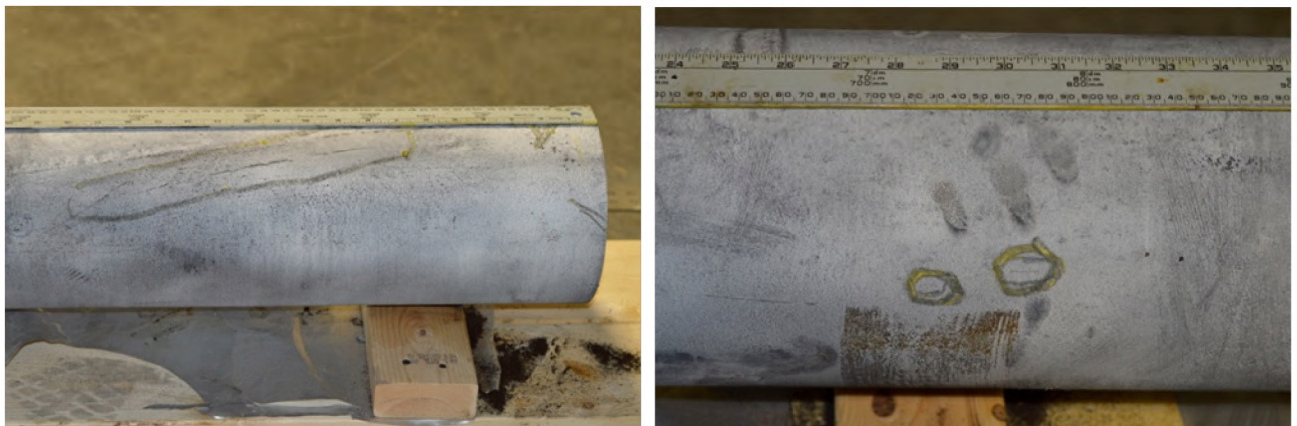
## 6.2 7 in. Casing Linear Indication

Oblique linear indications were identified during the field MPI of the 7 in. casing. Figure 262 shows images of a linear indication after field MPI and in the as-received condition at Element Materials Technology, an ISO 9000 certified lab. The objective was to determine if the linear indication occurred downhole or during the manufacturing process.



**Figure 262: Field and As-Received Images of the C004C Linear Indication**

A linear indication identified on joint 4 was selected for examination. NDE was performed at Element to re-establish the length of the oblique linear indication. Fluorescent MPI identified two additional linear indications but did not detect the original indication. Black and white MPI was repeated in an attempt to confirm the original indication. Both the original indication and two additional indications were confirmed with the black and white MPI. Figure 263 shows the Element MPI results.



**Figure 263: Black and White MPI Results for C004C**

Eddyfy's eddy current technology was used to map the indications [79]. Figure 264 shows a 2D depth color map of the oblique linear indication. The map was used to determine cut locations for sectioning. A section adjacent to the deepest location was selected for metallographic cross sectioning (Figure 265).

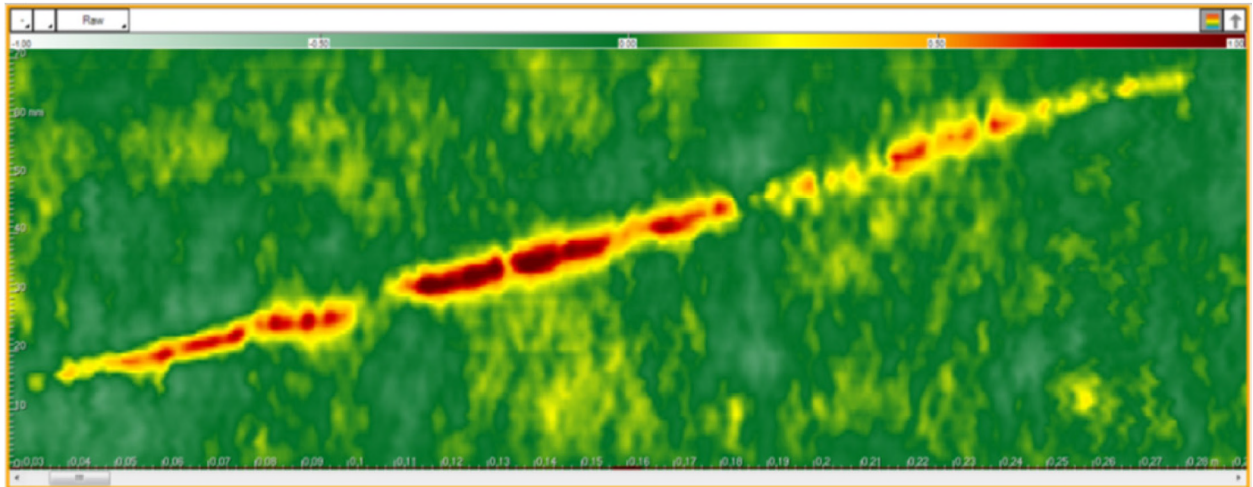


Figure 264: Eddy Current 2D Depth Color Map [79]

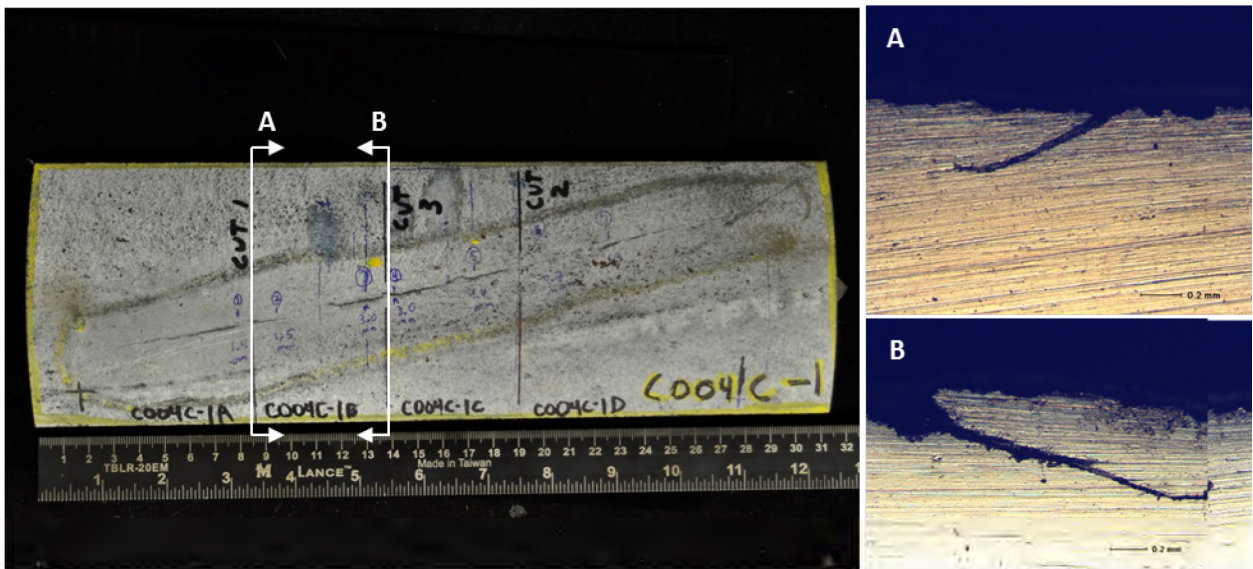
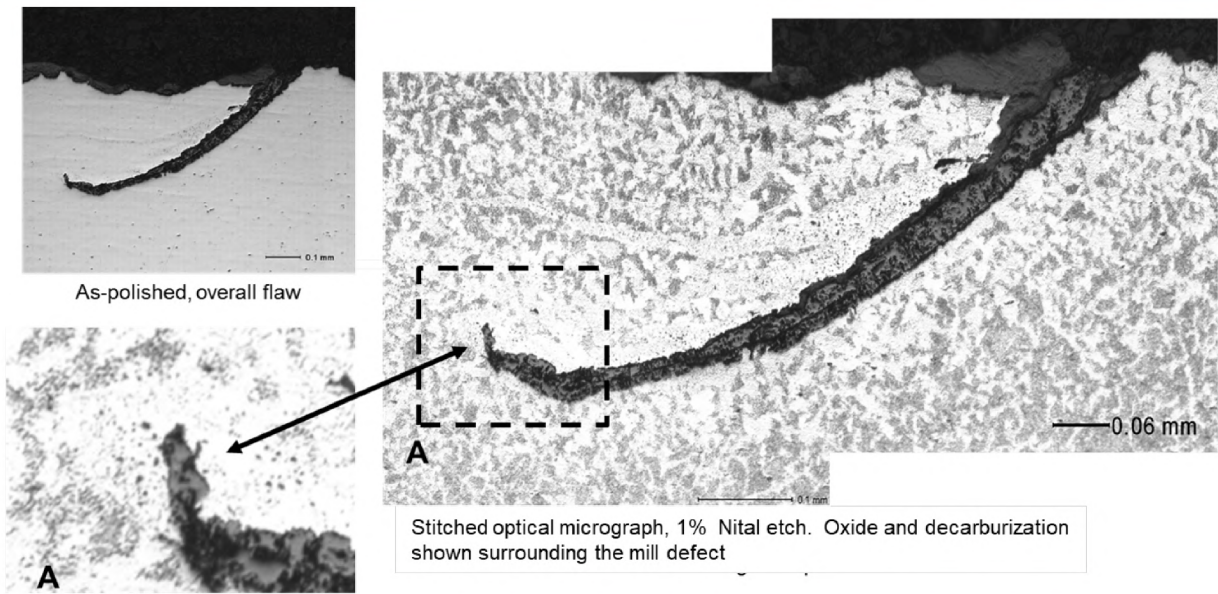


Figure 265: Cut Locations for Metallographic Sections A and B

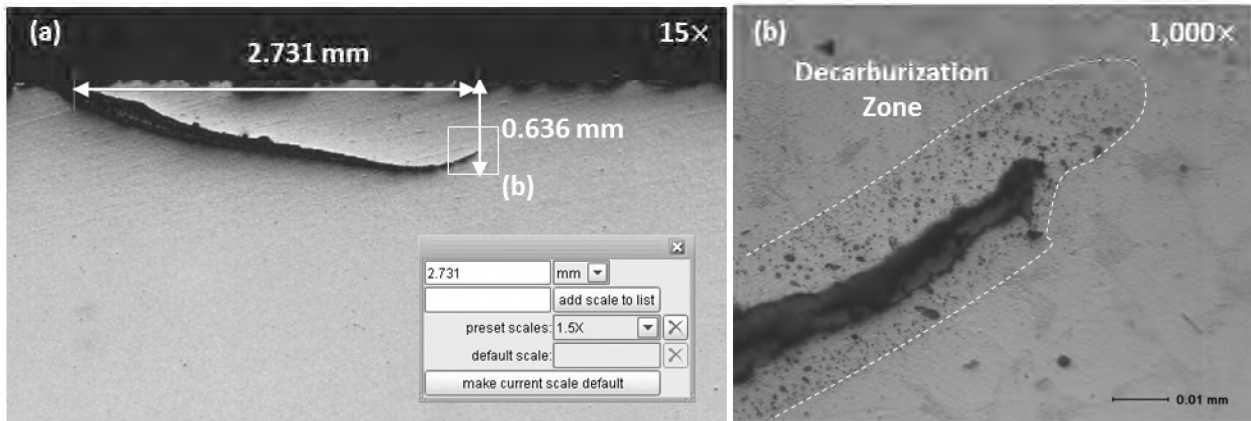
### 6.2.1 Metallographic Sectioning Investigation

The cross sections A and B were examined in the polished and etched conditions. Figure 266 shows the micrographs for cross section B in the polished and etched conditions at low and high magnifications. The indication had a shallow depth of 0.27 mm and a width of 0.57 mm. The indication was surrounded by an oxidation layer and a decarburization layer. This observation suggests that the indication was exposed to high temperatures and is a mill defect (lap, sliver, etc.) that formed during the manufacturing process. Since the tip of the mill defect was surrounded by an oxidation layer and a decarburization layer, crack initiation and growth did not occur during the lifetime of the well.



**Figure 266: Micrographs of Cross Section B (a) Polished and (b) Etched with 1% Nital**

Figure 267 shows micrographs for cross section A in the polished and etched conditions at low and high magnifications. The linear indication has a width of 2.731 mm and a depth of 0.636 mm (7.9% NWT). The 1,000× micrograph in Figure 267 shows oxidation and decarburization around the tip of the indication. Figure 268 is a stitched micrograph of the crack taken at 200× in the etched condition. The stitched micrograph shows that the oxidation and decarburization layer surrounds the entire indication. Again, the oxidation and decarburization layer suggests that the indication was exposed to a high temperature environment and is a mill defect. The high magnification micrograph in Figure 267 shows the mill defect is surrounded by an oxidation layer and a decarburization layer. This observation further confirms that the mill defect did not grow during the lifetime of the well.



**Figure 267: Micrographs of Cross Section B (a) Polished (15×) and (b) Etched with 1% Nital (1,000×)**

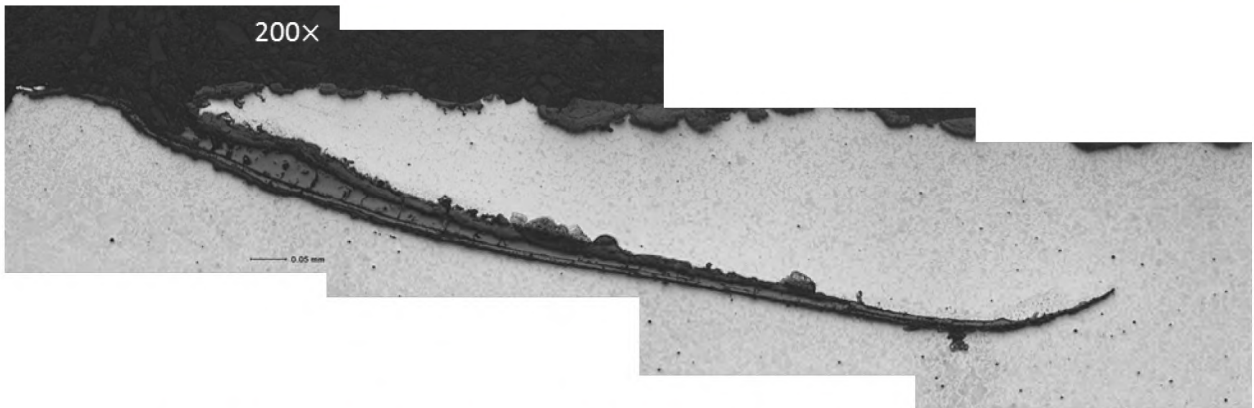


Figure 268: Metallographic Cross Section A Etched with 1% Nital and Taken at 200×

### 6.2.1 Fractographic Analysis

Specimen C004C1C, which contained the deepest point of the mill defect, was extracted. Two notches were made on the back side of the specimen to reduce the remaining ligament of the defect for opening. The specimen was submerged in liquid nitrogen for several minutes. The specimen was then removed from the liquid nitrogen, locked into a vice, and broken open with a steel hammer.

The opened linear indication (mill defect) was stored in a desiccator over the weekend. Flash rust occurred. Figure 269 shows the opened linear indication and flash rust. Most of the flash rust was removed by sonic agitation in a 3% Alconox solution for a total of six minutes. The specimen was cut into smaller pieces for SEM and EDS examination and analysis. The visual examination of the fracture surface showed a black oxide scale (Figure 270).

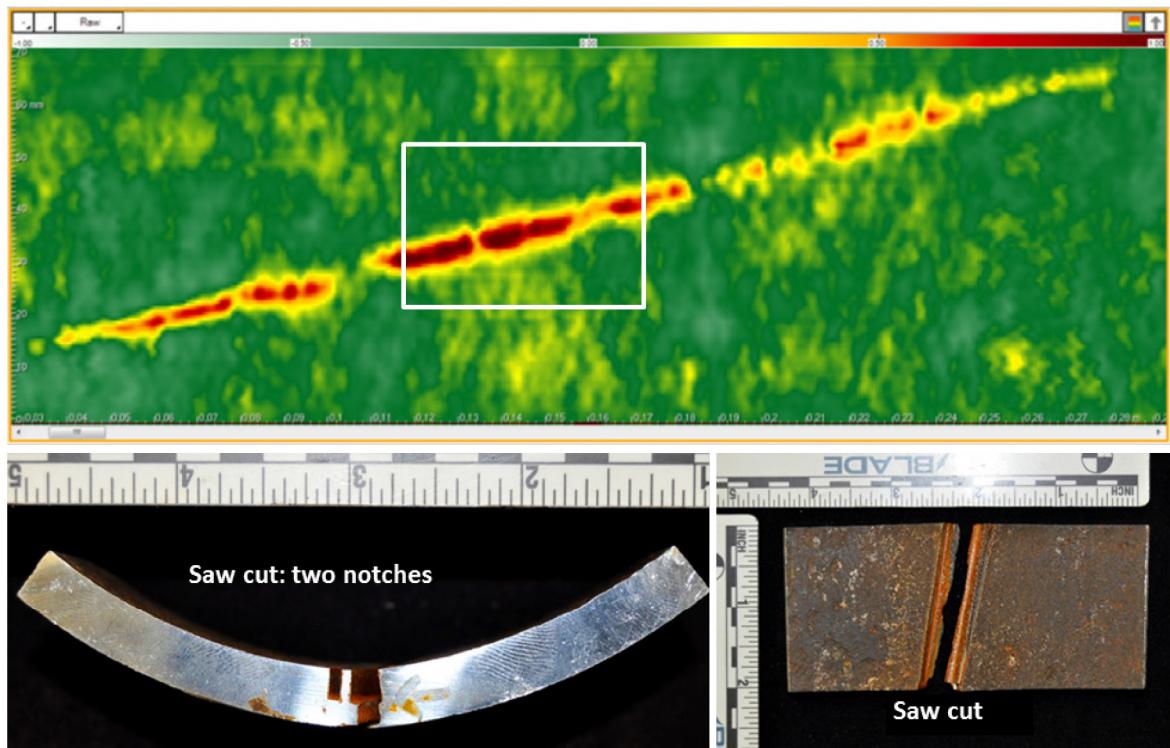
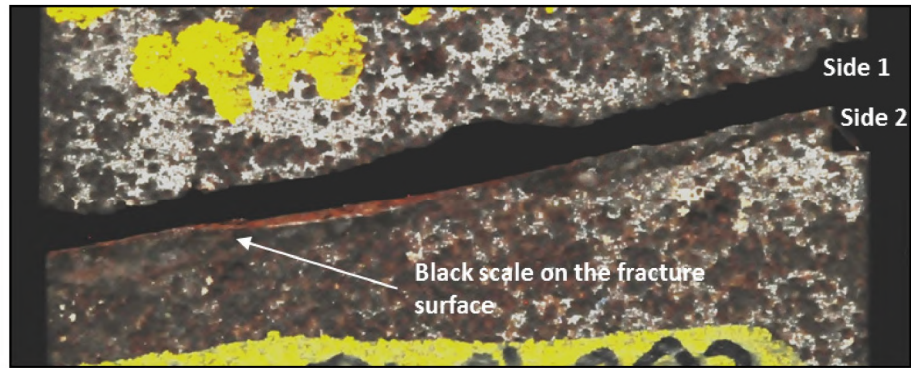


Figure 269: C004C1C After Opening at Liquid Nitrogen Temperature

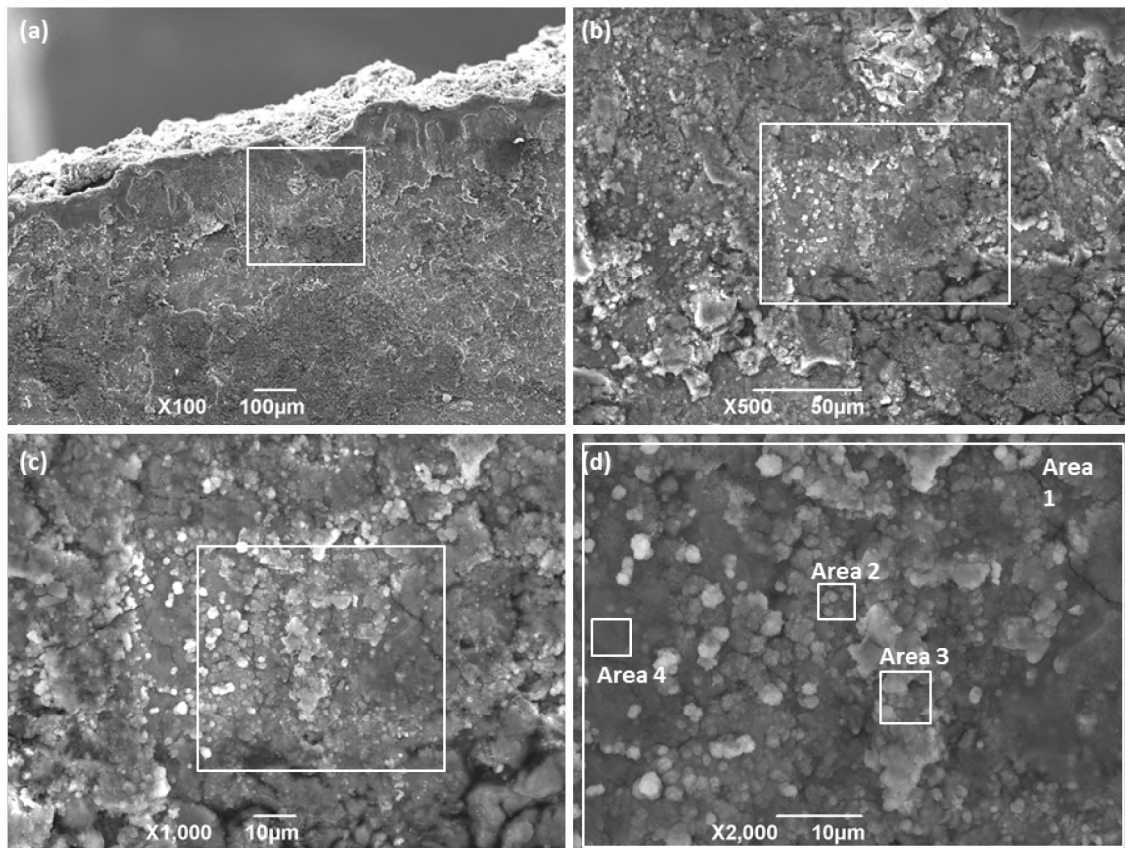


**Figure 270: C004C1C Fracture Surface After Opening at Liquid Nitrogen Temperature**

Figure 271 shows SEM images of the fracture surface after cleaning. The images show an oxide scale with small crystalline particles that are consistent with high temperature oxidation. Figure 271 (d) shows four locations selected for EDS examination. EDS results identified high levels of O and Fe at all four locations. Figure 272 shows the EDS spectra for Area 1.

Table 17 shows the EDS results for C, O, Fe, and Mn for all four locations. The EDS results suggest a mixture of  $Fe_xO_y$  type oxide, which is consistent with high temperature oxidation.

The evidence shows that these features were manufacturing defects. The evidence also shows that these features did not grow over the lifetime of the well and did not pose a threat to the integrity of the 7 in. casing.



**Figure 271: SEM Images of C004C1C Taken at (a) 100×, (b) 500×, (c) 1,000×, and (d) 2,000×**

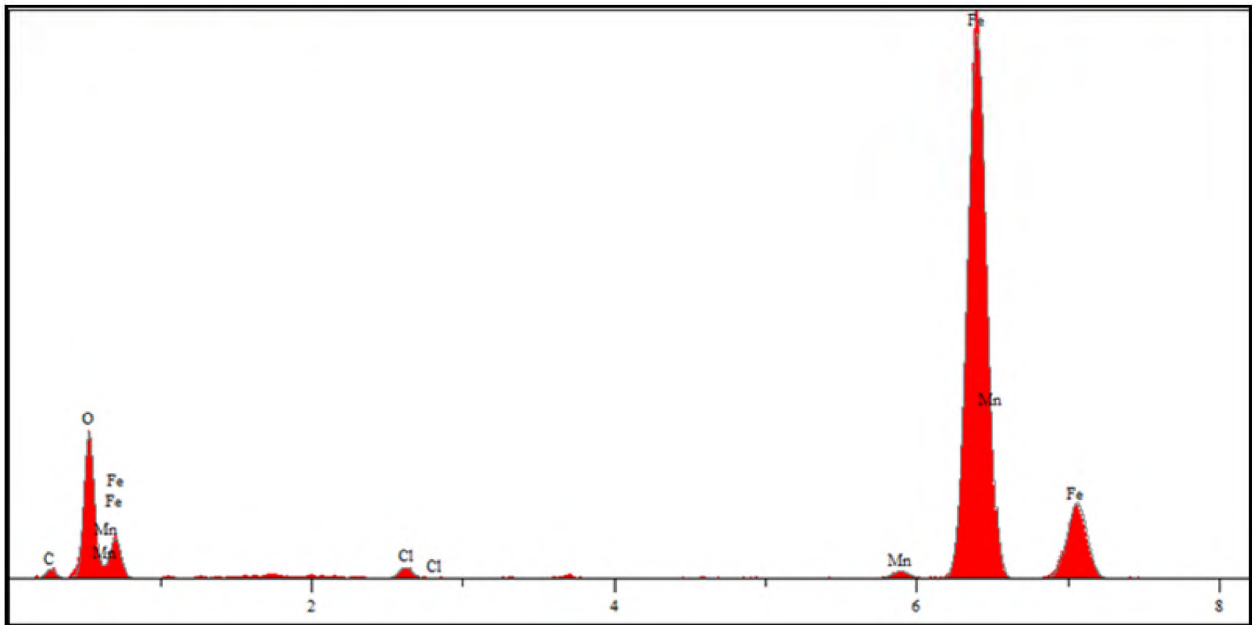


Figure 272: EDS Spectra for C004C1C Area 1

Table 17: EDS Results for Areas 1–4 of C004C1C Showing C, O, Fe, and Mn

Area	C (at%)	O (at%)	Fe (at%)	Mn (at%)
1	12.324	39.628	46.870	0.557
2	14.100	35.610	49.006	0.418
3	26.490	38.452	33.243	0.310
4	15.302	39.004	43.815	0.345

## 7 Material Testing

Testing was conducted on material from the 2 7/8 in. tubing, 7 in. casing, and 11 3/4 in. casing. The goal of material testing was to:

- Identify material deficiencies or anomalies possibly related to the failure.
- Establish a material database to support the failure analysis.
- Evaluate the effects of temperature on material properties and fracture mode.

Material testing focused primarily on the 7 in. casing properties due to the nature of the failure. Every 7 in. casing joint extracted from the well was subjected to material testing (joints 1–25). The 2 7/8 in. tubing and 11 3/4 in. casing were selectively tested to verify nominal properties. Eleven of the 244 extracted 2 7/8 in. tubing joints were randomly selected for material testing. The 11 3/4 in. casing was limited to a 3 ft section below the casing head because extraction of the 11 3/4 in. casing from the well was not possible. Testing was conducted by Element Materials Technology in accordance with the ASTM A370 standard. The Element quality manual was reviewed by Blade to verify that machining and testing practices were both compliant and satisfactory with the goals of the testing.

SS-25 was completed on October 01, 1953. The well contained casing and tubing made from grades H40, J55, and N80 steel. These casing and tubing grades were adopted in 1940 by API. The most relevant API specification that could be found was API Specification 5A, 18<sup>th</sup> edition, 1953 [80]. The only requirements within the specification relevant to material testing were chemistry and tensile properties.

Table 18 shows the chemistry requirements for seamless pipe based on manufacturing process. The specification only limits the amount of phosphorus and sulfur. The other controlling alloys were left up to the manufacturer.

Table 19 was extracted from a paper published in the Journal of Petroleum Technology [81]. The table shows typical carbon, manganese, and alloy composition for various grades of casing and tubing.

Table 20 shows the API 5A tensile requirements for various grades of casing and tubing. The yield strength is taken as the tensile stress required to produce a total elongation of 0.5% of the gauge length. This value is also known as elongation under load (EUL).

**Table 18: API 5A 18<sup>th</sup> Edition Chemical Requirements for Seamless Pipe [80]**

Manufacturing Method	Maximum Phosphorus (%)	Maximum Sulfur (%)
Open-hearth	0.04	0.06
Electric-furnace	0.04	0.06
Bessemer	0.11	0.065

**Table 19: Typical Analyses for API Casing and Tubing [81]**

Grade	Product	Carbon (%)	Manganese (%)	Alloys
H40	Casing and tubing	0.27/0.37	0.70/1.00	None

Grade	Product	Carbon (%)	Manganese (%)	Alloys
J55	Casing and tubing	0.37/0.47	0.80/1.00	None
N80	Tubing (N)	0.38/0.48	1.40/1.70	0.15 Mo Min.

**Table 20: API 5A 18<sup>th</sup> Edition Tensile Requirements for Casing and Tubing [80]**

Grade	Minimum Yield Strength (psi)	Minimum Ultimate Tensile Strength (psi)	Minimum Elongation (%)
F-25	25,000	40,000	40
H-40	40,000	60,000	27
J-55	55,000	75,000	20
N-80	80,000	100,000	16

## 7.1 7 in. Casing Testing

The SS-25 failure occurred in the 7 in. casing, making it the primary focus for material testing. Visual inspection of the tubing suggested that it did not contribute to the failure. The 11 3/4 in. casing visual inspection was limited because the string was not extracted from the well. The 2 7/8 in. tubing and 11 3/4 in. casing were tested with a reduced testing program, based on the relationship to the failure and material quantity. A comprehensive testing program was developed for the 7 in. casing to establish a database for the casing material. Every 7 in. casing joint extracted from the well was subject to the following material testing program:

- Chemistry
- Grain Size—ASTM E112 [82]
- Microcleanliness—ASTM E45 A [83]
- Tensile—ASTM A370 [84]
- Hardness—ASTM E18 [85]
- CVN—ASTM A370 [84] /ASTM E23 [86]
- Toughness (joint 22 only)—ASTM E1820 [32]

Temperature was of primary interest during the initial phases of the investigation. Temperature anomalies were discovered during and after the failure event. Temperatures were deliberately selected for CVN and fracture toughness testing. Fracture surfaces were also examined to determine fracture mode as a function of temperature (Section 3).

Blade purchased a joint of new 7 in. casing material. The material was tested at Element to complement data provided by the material testing report (MTR). The MTR and Element data were compared to the 7 in. casing material to identify similarities and differences.



### 7.1.1 Specimen Preparation and Layout

Two different specimen layouts were created for testing purposes. Figure 273 shows the primary layout used for the majority of the joints. The layout shows the location for the CVN, tensile, and hardness specimens. The locations for chemistry, grain size, and microcleanliness were documented but were not explicitly specified. The layout required a 2 ft section of pipe to provide enough material for testing. The primary layout was used for all joints, except joint 22.

Joint 22 was the failed joint that contained the axial rupture and circumferential parting. Additional testing for joint 22 included sub-size tensile and fracture toughness testing. The sub-size tensile testing was conducted to determine transverse tensile properties. Fracture toughness testing was conducted to determine fracture toughness in both the circumferential and longitudinal directions. Both orientations were required because fractures occurred in both directions. Figure 274 shows the layout for joint 22.

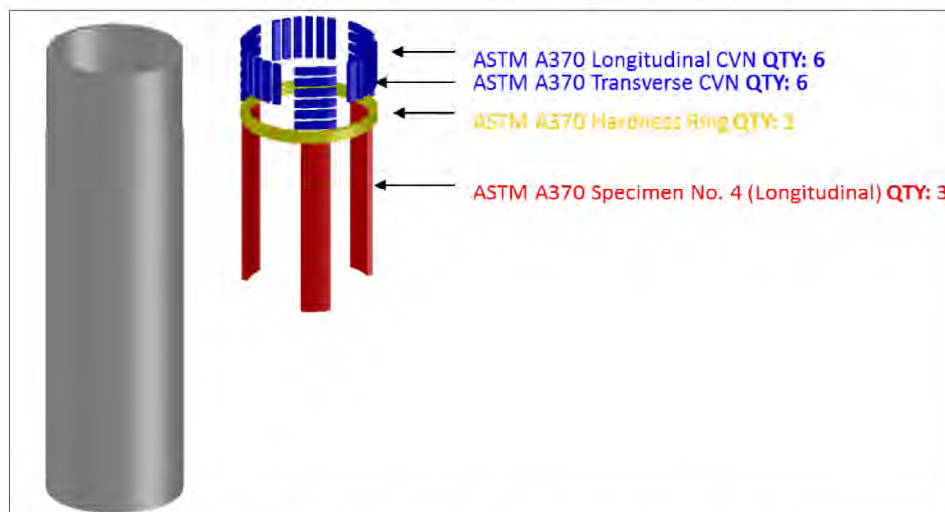


Figure 273: Typical Material Testing Specimen Layout

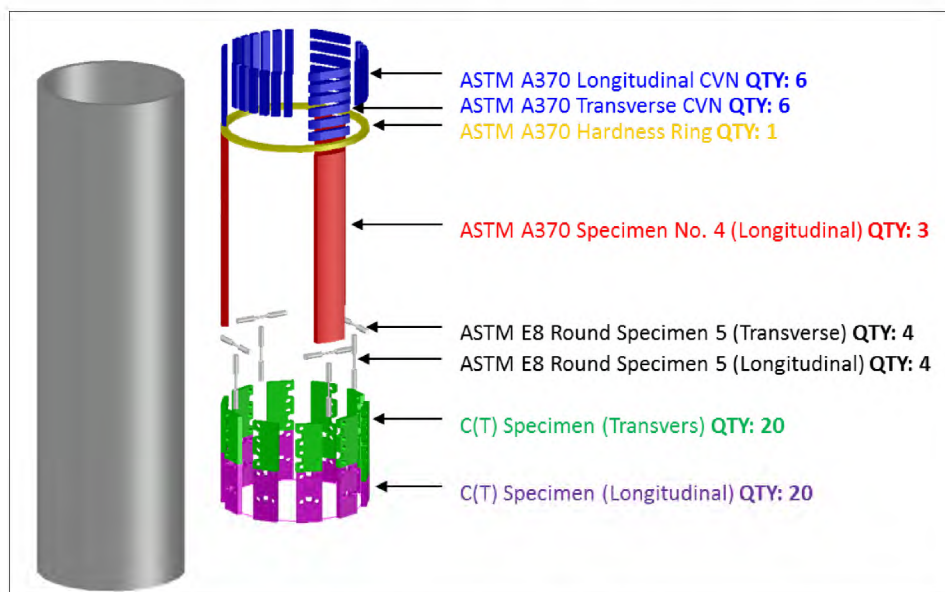


Figure 274: Joint 22 Material Testing Specimen Layout

Casing joints were transported from Aliso Canyon to the Blade warehouse in Houston, TX. They were cleaned, inspected, and coated in the field with Tectyl 846 (a corrosion inhibitor designed to prevent any additional corrosion during transport and storage). Several steps were taken to ensure the material was free of any localized anomalies that might have interfered with the material testing results. Material identified for testing was inspected for corrosion and cracks. Specimen preparation included the following steps:

1. Removal of the Tectyl 846 coating
2. Cleaning of the surface using nylon brushes and rags
3. Abrasive blasting using Black Beauty Extra Fine media (glass bead was used on 5 of the 25 joints)
4. MPI for cracks

Figure 275 shows the as-received condition of joint 6 at Element. Element used Sentinel 909 to remove the Tectyl 846 coating followed by Purple Power degreaser to remove the remaining residue. Figure 276 shows the surface condition after cleaning. Blade transported the material from the warehouse to Superior Shot Peening for abrasive blasting. Blasting was completed within a day, and the material was returned to Element. Figure 277 shows the surface condition of joint 6 after blasting. Black Beauty Extra Fine media was used for the blasting process. This media creates a white metal finish without aggressive removal of the material. This method is ideal for identifying cracks.

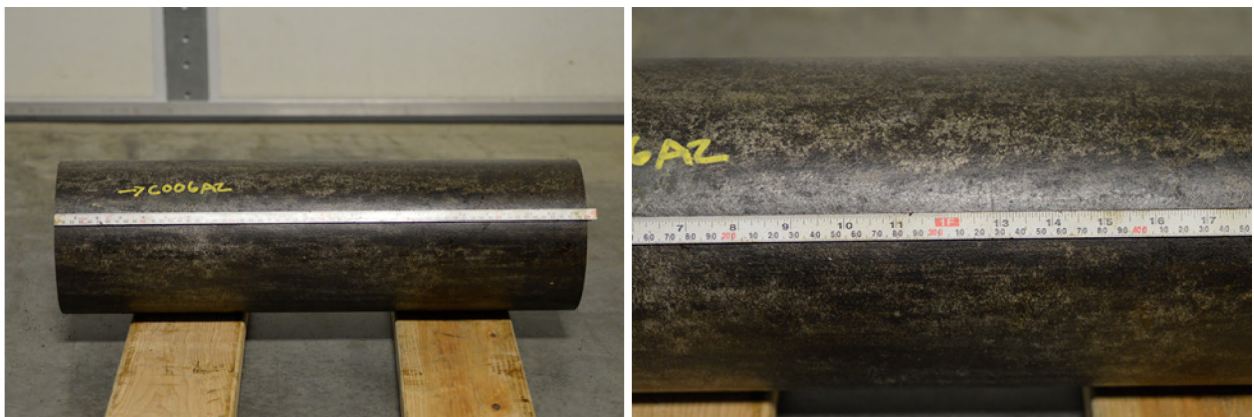


Figure 275: As-Received Condition for Specimen C006A2

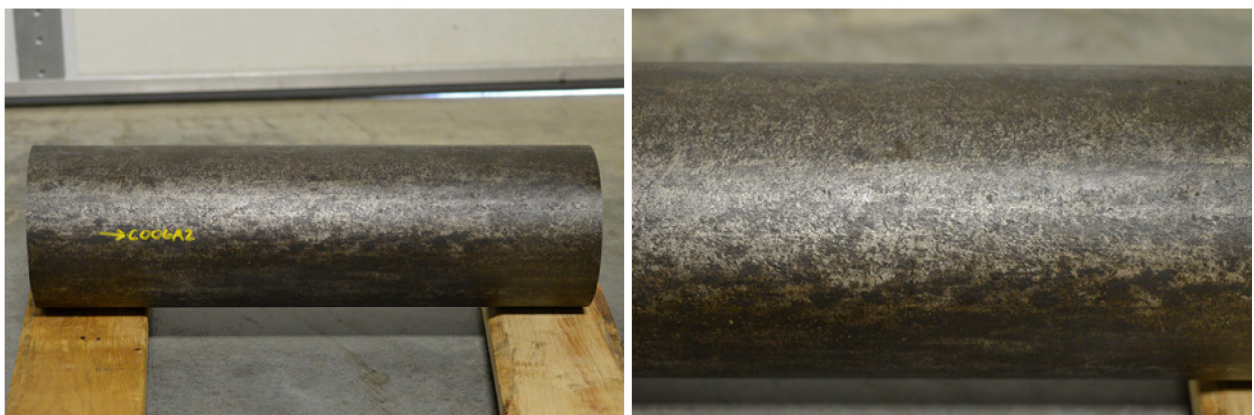
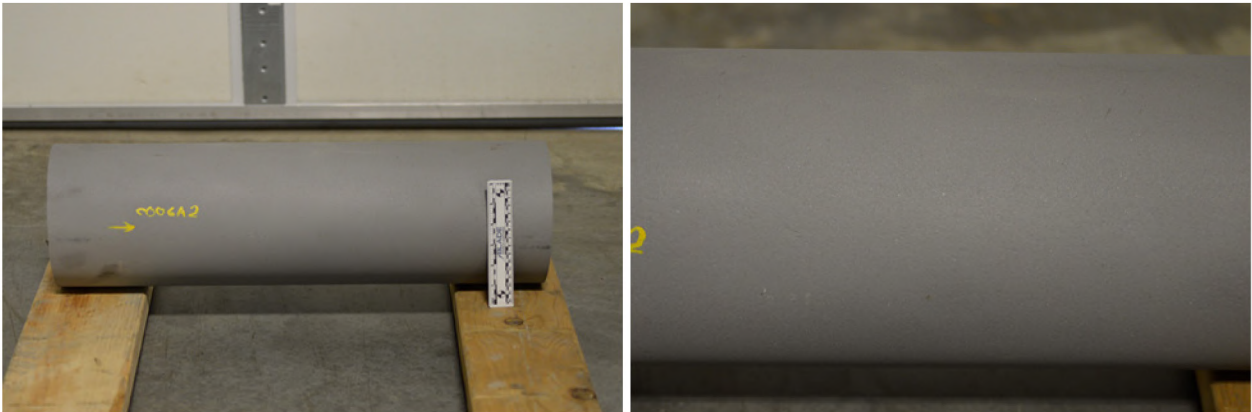


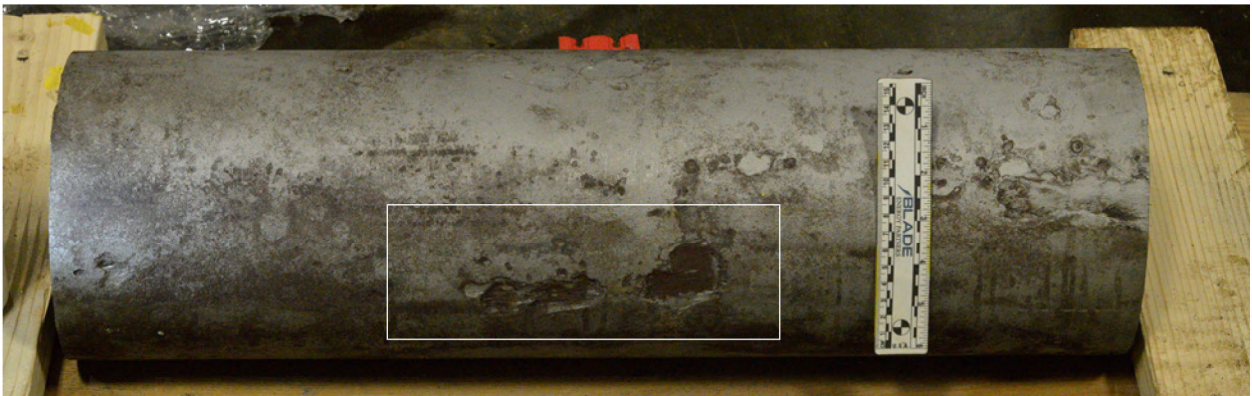
Figure 276: Post-Cleaning Condition for Specimen C006A2



**Figure 277: Post Abrasive Blasting for Specimen C006A2**

MPI was primarily performed at Superior Shot Peening, but in some cases, MPI was completed at Element. The location for performing MPI was solely based on scheduling considerations. Linear indications were not identified in any of the 7 in. casing inspections. This suggests that the pipe specimens were free of any surface breaking cracks.

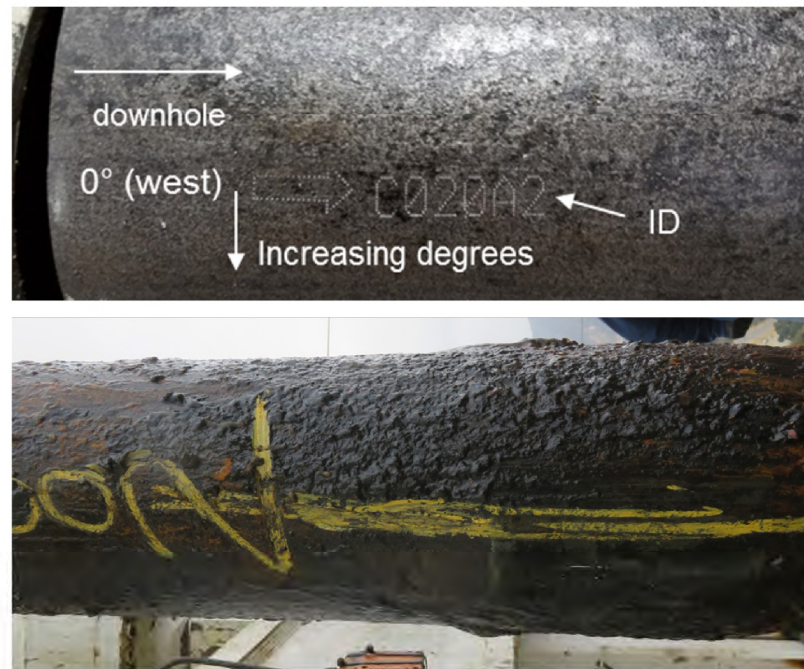
One corrosion feature was identified on joint 24 (Figure 278) during visual examination of the blasted specimens despite efforts to avoid extracting such features. The corrosion feature was not visible during the initial inspection due to the surface condition of the joint. The corrosion feature was extracted and preserved after it had been discovered, and the test layout was shifted to accommodate the feature extraction.



**Figure 278: Joint 24 Features Identified After Abrasive Blasting**

Element laid out each test specimen on the OD surface of the material prior to the machining. Specimens were evenly distributed along the circumference of the casing material. Circumferential orientation was based on the field orientation mark. As the casing was extracted from the well, an orientation mark was placed on the west side of the casing. This practice was consistent with each extracted joint. The temporary field mark was eventually replaced with a permanent dot peen mark representing the west side of the casing. The permanent mark included the specimen identification and an arrow representing the downhole direction. The dot peen was maintained throughout the investigation. The mark was transferred with each cut of the larger specimens. For the purpose of material testing, the west side of the casing was designated as the 0° location, with increasing degrees in the clockwise direction when looking downhole. Figure 279 shows the temporary and permanent field marks made to identify the

orientation of the casing as it was removed from the well. Section 2.2.6 discusses the field orientation mark in detail.



**Figure 279: Field and Permanent Orientation Mark**

Figure 280 shows the distribution of the CVN specimens around the circumference of the 7 in. casing. C-L (transverse) CVN specimens were located at the top of the 2 ft pipe section at 0°, 120°, and 240°. L-C (longitudinal) CVN specimens were located between the tensile specimens at 60°, 180°, and 300°. The hardness ring was located below the CVN specimens. Tensile specimens were located below the hardness ring at 0°, 120°, and 240°. Locations for chemistry, microcleanliness, and grain size were documented but not specified by Blade. Locations for these specimens were determined by Element. Figure 281 shows the specimen layout on the OD surface of joint 6. The image shows the location and Element identification number for each of the specimens.

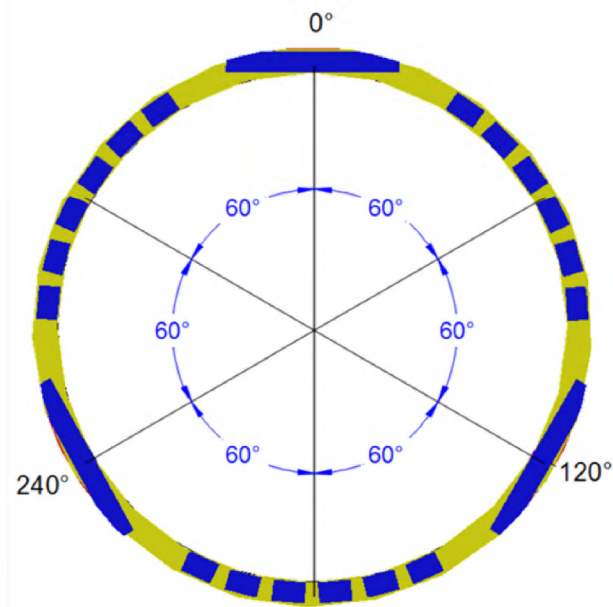


Figure 280: Circumferential Orientation of Specimens



Figure 281: Material Testing Layout for Specimen C006A2

### 7.1.2 Chemistry

Chemical analysis of the 7 in. casing material was conducted using an optical emission spectrometer (OES). An OES works by applying electrical energy in the form of a spark generated between an electrode and a metal sample. The atoms within the metal are brought to an excited state and emit characteristic light or optical emission lines. The emission lines from the vaporized sample pass into a spectrometer where a diffraction grating separates the light into element-specific wavelengths. An additional detector in the spectrometer measures the intensity of the light for each wavelength. The intensity of the light is proportional to the concentration of the element in question. OES is a common analytical method used to determine the elemental composition of metals. The results are accurate and consistent.

Chemistry requirements at the time of installation of SS-25 were limited to phosphorous and sulfur. Other controlling alloys were left up to the manufacturer [81]. Table 21 shows the chemistry results for each joint. The chemical composition was compared to the phosphorous and sulfur limits presented in API 5A 18<sup>th</sup> edition, 1953 [80]. The maximum sulfur percentage was 0.033%, which is below the 0.06% maximum allowed by the specification. Five joints (3, 6, 9, 10, and 13) had phosphorus percentages not significantly higher than the allowable maximum of 0.04%. The higher sulfur values were noted but were not considered significant to the metallurgical investigation.

Table 20, presented at the beginning of the section, indicates that grade J55 steels typically had carbon and manganese compositions between 0.37–0.47% and 0.80–1.00%, respectively. The average values for carbon and manganese are 0.48% and 1.03%, respectively, and are consistent with the typical values from Table 20.

**Table 21: 7 in. Casing Optical Emission Spectroscopy Results**

Joint	C	Mn	P	S	Si	Cr	Ni	Mo	Al	Cu	Fe
1	0.460	1.110	0.018	0.021	0.300	0.050	0.020	0.010	0.020	0.050	97.911
2	0.510	1.090	0.021	0.023	0.290	0.050	0.020	0.010	0.020	0.050	97.916
3	0.520	1.140	0.054	0.022	0.300	0.050	0.010	0.010	0.020	0.050	97.824
4	0.470	1.070	0.038	0.020	0.280	0.050	0.020	0.010	0.020	0.050	97.972
5	0.480	1.060	0.037	0.030	0.250	0.050	0.020	0.010	0.020	0.070	97.973
6	0.510	1.170	0.046	0.023	0.310	0.050	0.020	0.010	0.020	0.050	97.791
7	0.460	0.920	0.025	0.022	0.300	0.050	0.030	0.010	0.010	0.080	98.093
8	0.500	1.080	0.035	0.023	0.280	0.050	0.020	0.010	0.020	0.050	97.932
9	0.520	1.190	0.055	0.022	0.320	0.050	0.020	0.010	0.020	0.050	97.743
10	0.520	1.090	0.041	0.024	0.280	0.050	0.020	0.010	0.020	0.050	97.895
11	0.500	1.060	0.018	0.015	0.280	0.040	0.010	0.010	0.010	0.050	97.977
12	0.450	0.950	0.007	0.024	0.230	0.050	0.020	0.010	0.010	0.070	98.149
13	0.500	1.100	0.041	0.024	0.280	0.050	0.010	0.010	0.020	0.050	97.915
14	0.460	0.890	0.015	0.013	0.290	0.050	0.030	0.020	0.030	0.080	98.092
15	0.480	0.910	0.016	0.024	0.290	0.050	0.030	0.020	0.020	0.080	98.080
16	0.470	0.930	0.029	0.023	0.300	0.050	0.030	0.010	0.020	0.080	98.058
17	0.450	1.010	0.019	0.033	0.240	0.050	0.020	0.010	0.010	0.070	98.088
18	0.510	1.130	0.024	0.023	0.300	0.050	0.020	0.010	0.020	0.050	97.863
19	0.500	1.000	0.026	0.015	0.240	0.050	0.010	0.010	0.010	0.050	98.059
20	0.530	1.020	0.030	0.022	0.240	0.050	0.010	0.010	0.020	0.050	98.018
21	0.460	0.980	0.018	0.031	0.240	0.060	0.020	0.010	0.020	0.070	98.061
22	0.490	1.060	0.023	0.022	0.290	0.050	0.020	0.010	0.020	0.050	97.935
23	0.470	0.900	0.023	0.018	0.300	0.050	0.030	0.020	0.030	0.080	98.049
24	0.450	1.020	0.018	0.030	0.250	0.060	0.030	0.010	0.020	0.070	98.012
25	0.430	0.880	0.014	0.016	0.300	0.050	0.030	0.020	0.020	0.080	98.130
<b>Min</b>	<b>0.430</b>	<b>0.880</b>	<b>0.007</b>	<b>0.013</b>	<b>0.230</b>	<b>0.040</b>	<b>0.010</b>	<b>0.010</b>	<b>0.010</b>	<b>0.050</b>	<b>97.743</b>

Joint	C	Mn	P	S	Si	Cr	Ni	Mo	Al	Cu	Fe
Max	0.530	1.190	0.055	0.033	0.320	0.060	0.030	0.020	0.030	0.080	98.149
Avg	0.484	1.030	0.028	0.023	0.279	0.050	0.021	0.012	0.019	0.061	97.981

### 7.1.3 Grain Size

Grain sizes were measured for each of the 7 in. casing joints and were determined based on ASTM E112 [82]. The general repeatability and reproducibility for the comparison method is approximately  $\pm 1$  grain size. Figure 282 shows a micrograph of joint 22 at 100 $\times$  after etching with 4% picral acid. The ASTM grain size measured for joint 22 using a comparison method was 7.0. Figure 283 shows a histogram for the ASTM grain sizes for all 25 joints. The statistical data for the grain sizes are shown to the right of the histogram. The average grain size for all of the joints is 7.54 with a standard deviation of 0.63. Grain size for grade J55 material is not specified by the current API 5CT. In general, a finer grain size is preferred for better mechanical properties and resistance to corrosion and cracking. The average grain size for the vintage grade J55 material is above 5.0, which is the generally accepted boundary between coarse and fine grain.

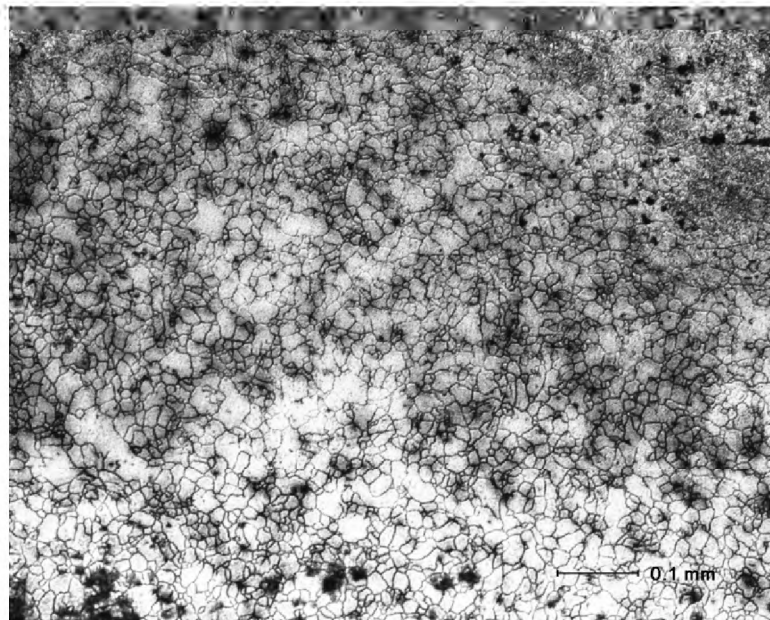


Figure 282: Joint 22 Grain Size 7.0 at 100 $\times$  4% Picral

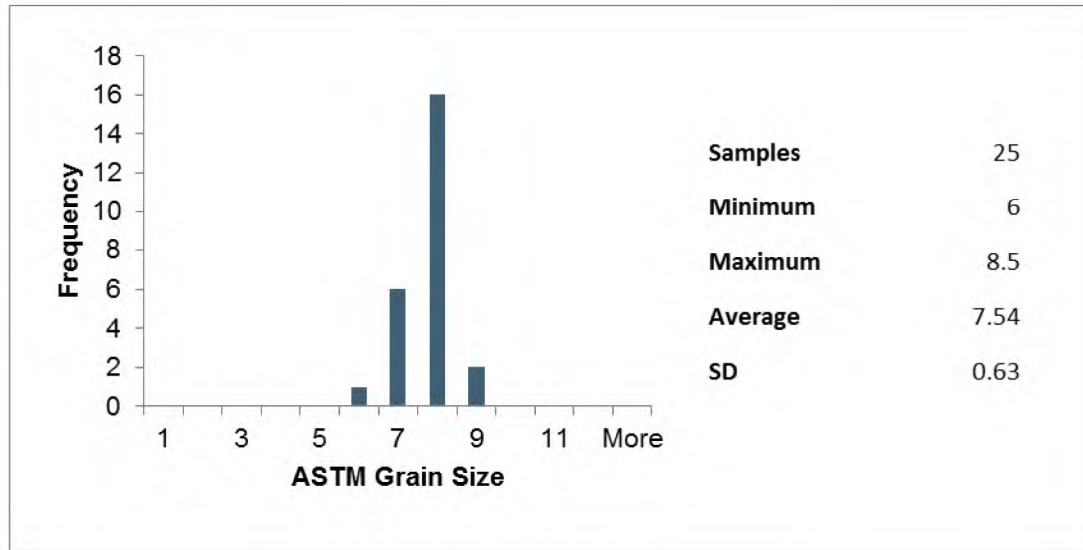


Figure 283: ASTM Grain Size Histogram

### 7.1.4 Microcleanliness (Inclusion Content E45 A)

The objective of ASTM E45 [83] is to characterize inclusions based on size, shape, concentration, and distribution rather than chemical composition. The test method covers five microscopic test methods (A, B, C, D, and E) for describing inclusion content of steel. Element used E45 Method A to characterize the inclusions for the 7 in. casing steel. Method A (Worst Field) is a microscopic comparison method that requires a survey of a polished specimen at 100X. The worst field method is conducted by examining several fields within the specimen and taking the highest severity rating value for each inclusion type. Inclusions are categorized by type and thickness or diameter.

There are four inclusion types based on morphology:

- Type A—Sulfide
- Type B—Alumina
- Type C—Silicate
- Type D—Globular Oxide

Inclusions fall into two additional subcategories (thin and heavy) based on thickness-diameter. Table 22 shows the thickness-diameter limits for each series and inclusion type. The four categories are partitioned into severity levels based on the number or length of the particles present in a 0.50 mm<sup>2</sup> field of view. Table 23 shows the minimum length-count values for each severity level.

Table 22: Inclusion Width and Diameter Parameters (ASTM E45 Methods A and D) [83]

Series	Thin		Heavy	
	Min. Width µm (in.)	Max. Width µm (in.)	Min. Width µm (in.)	Max. Width µm (in.)
A	2 (0.00008)	4 (0.00016)	>4 (0.00016)	12 (0.0005)
B	2 (0.00008)	9 (0.00035)	>9 (0.00035)	15 (0.0006)
C	2 (0.00008)	5 (0.0002)	>5 (0.0002)	12 (0.0005)



Series	Thin		Heavy	
Inclusion Type	Min. Width $\mu\text{m}$ (in.)	Max. Width $\mu\text{m}$ (in.)	Min. Width $\mu\text{m}$ (in.)	Max. Width $\mu\text{m}$ (in.)
D	2 (0.00008)	8 (0.0003)	>8 (0.0003)	13 (0.0005)

Table 23: Minimum Values for Severity Level Numbers [83]

mm (in.) at 100 $\times$ , or Count				
Severity	A	B	C	D
0.5	3.7 (0.15)	1.7 (0.07)	1.8 (0.07)	1
1.0	12.7 (0.50)	7.7 (0.30)	7.6 (0.30)	4
1.5	26.1 (1.03)	18.4 (0.72)	17.6 (0.69)	9
2.0	43.6 (1.72)	34.3 (1.35)	32.0 (1.26)	16
2.5	64.9 (2.56)	55.5 (2.19)	51.0 (2.01)	25
3.0	89.8 (3.54)	82.2 (3.24)	74.6 (2.94)	36
3.5	118.1 (4.65)	114.7 (4.52)	102.9 (4.05)	49
4.0	149.8 (5.90)	153.0 (6.02)	135.9 (5.35)	64
4.5	189.8 (7.47)	197.3 (7.77)	173.7 (6.84)	81
5.0	223.0 (8.78)	247.6 (9.75)	216.3 (8.52)	100

Table 24 shows the Element ASTM E45 Method A results for each joint. It shows that the highest Severity Level of 2.5 occurred in both the thin and heavy series for Type A inclusions. The results are consistent with MnS inclusions, which are typical of carbon steel. Figure 284 shows micrographs at 100 $\times$  of polished specimens taken from joint 10 and 15. The micrographs show the inclusion morphology, size, and distribution.

Table 24: Microcleanliness Results for Joints 1–25

Series	Thin				Heavy			
Joint	Type A (Sulfide)	Type B (Alumina)	Type C (Silicate)	Type D (Globular Oxide)	Type A (Sulfide)	Type B (Alumina)	Type C (Silicate)	Type D (Globular Oxide)
1	2.0	1.0	0.0	1.5	0.0	1.0	0.0	0.5
2	2.0	0.5	1.0	1.5	1.0	0.0	2.0	0.5
3	2.0	0.0	0.0	0.5	0.5	1.0	0.0	0.0
4	2.0	0.5	0.0	1.0	1.0	0.0	0.0	0.0
5	0.5	0.0	0.5	0.5	2.0	0.5	0.0	0.0
6	2.0	0.5	0.0	1.0	0.0	0.5	1.0	1.0
7	1.0	0.0	0.0	0.0	1.0	0.5	2.0	0.5
8	2.0	0.0	0.0	0.5	0.0	0.5	0.0	0.5
9	2.0	0.5	0.0	1.0	0.0	0.0	0.0	0.0
10	2.5	0.0	0.0	1.0	0.5	0.0	0.0	0.0

Series	Thin				Heavy			
Joint	Type A (Sulfide)	Type B (Alumina)	Type C (Silicate)	Type D (Globular Oxide)	Type A (Sulfide)	Type B (Alumina)	Type C (Silicate)	Type D (Globular Oxide)
11	2.5	0.0	0.0	0.5	0.0	0.0	0.0	0.0
12	2.0	0.0	0.0	0.5	0.0	0.0	0.0	0.5
13	0.0	0.0	0.0	1.5	2.5	0.0	0.0	0.5
14	2.0	0.0	0.0	1.5	0.0	0.0	0.0	0.0
15	2.5	0.0	0.0	0.5	0.0	0.5	0.0	0.0
16	2.5	0.0	0.0	0.0	0.0	0.0	0.0	0.5
17	2.5	0.0	0.0	0.5	0.0	0.0	0.0	0.0
18	2.5	0.0	0.0	0.5	0.5	0.0	0.0	0.5
19	2.5	0.0	0.0	0.5	0.0	0.0	0.0	0.0
20	2.5	0.0	0.5	1.0	0.0	0.0	0.5	0.5
21	2.5	0.0	0.0	1.0	0.0	0.0	0.0	0.0
22	2.0	0.5	0.0	1.5	0.0	0.0	0.0	0.0
23	0.5	0.0	0.0	1.0	0.0	0.0	0.0	0.0
24	2.0	0.0	0.0	1.0	1.0	0.0	0.0	0.0
25	2.0	1.0	0.0	1.5	0.0	0.5	0.0	0.5
<b>Min</b>	<b>0.0</b>	<b>0.0</b>	<b>0.0</b>	<b>0.0</b>	<b>0.0</b>	<b>0.0</b>	<b>0.0</b>	<b>0.0</b>
<b>Max</b>	<b>2.5</b>	<b>1.0</b>	<b>1.0</b>	<b>1.5</b>	<b>2.5</b>	<b>1.0</b>	<b>2.0</b>	<b>1.0</b>
<b>Avg</b>	<b>1.9</b>	<b>0.2</b>	<b>0.1</b>	<b>0.9</b>	<b>0.4</b>	<b>0.2</b>	<b>0.2</b>	<b>0.2</b>

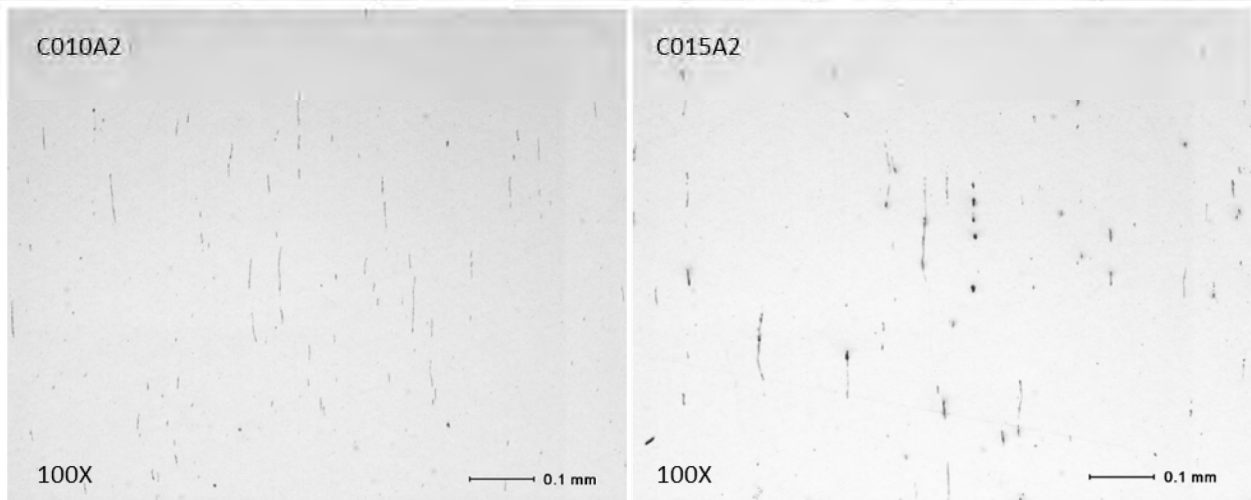


Figure 284: Polished Micrograph for Joints (a) 10 and (b) 15 Showing Inclusions at 100X

### 7.1.5 Microstructure

Element evaluated the microstructure of all the 25 joints extracted from the well. Specimen preparation was performed in accordance with ASTM E3 [87]. Specimens were etched with 2% nital to reveal the

microstructure. The microstructure was examined at 200× and 500× with an inverted stage metallurgical microscope using ordinary reflected light. All evaluations revealed pearlite and grain boundary ferrite. Figure 285 shows images from the metallurgical evaluation for joints 21, 22, and 23 with a similar microstructure for all three joints. This microstructure was typical for all 25 joints.

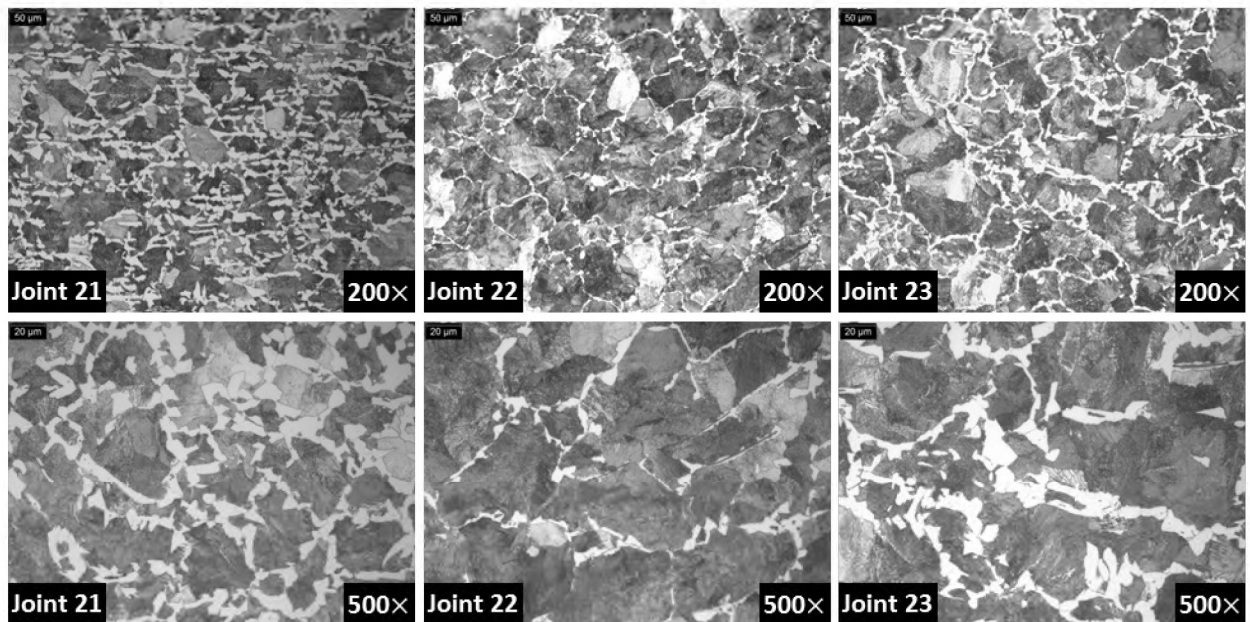


Figure 285: Micrographs of Joints 21, 22, and 23 Microstructure at 200× and 500×

### 7.1.6 Tensile

Tensile tests were performed on the 7 in. casing extracted from SS-25. Testing was conducted per ASTM A370 [84]. The standard allows for the use of longitudinal strip test specimens as an alternative to full-size longitudinal test specimens. The standard recommends the use of specimen no. 4 from Figure A2.3 in Appendix A of the specification, unless the capacity of the testing equipment or the dimensions and nature of the tubular product to be tested require the use of another specimen. The testing equipment at Element had sufficient capacity, and the casing material was of sufficient size for the use of specimen no. 4, as recommend by ASTM A370 [84]. Figure 286 shows the standard dimensions for specimen no. 4 reproduced from ASTM A370 [84].

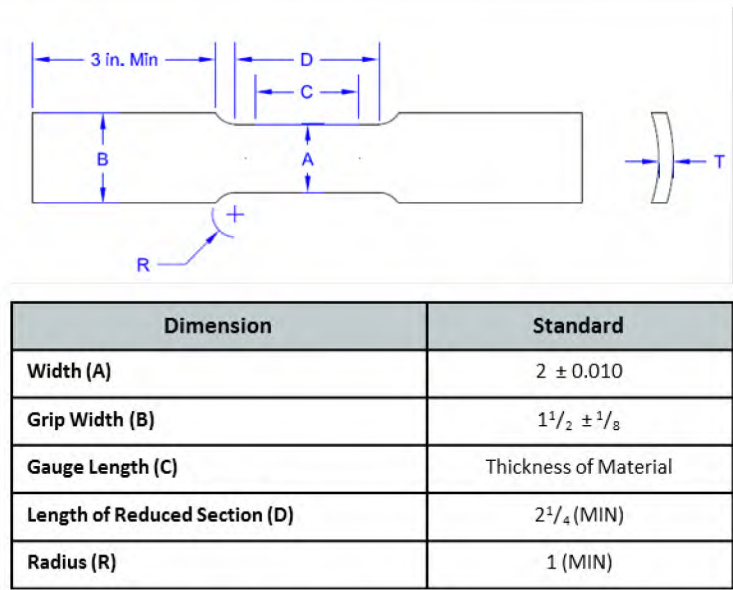


Figure 286: ASTM A370 Specimen No. 4 [84]

ASTM A370 [84] permits the use of grips that are either flat or have a surface contour corresponding to the curvature of the tubular product. Casing material was tested using flat grips and inserts machined to the curvature of the casing. The inserts had grooves machined into the curved surfaces to provide grip for the specimen. The steel used for the inserts was hardened to allow the inserts to deform into the surface of the specimen while simultaneously allowing the harder flat grips to deform into the inserts. The design goal was to prevent slip between the flat grips and curved inserts and between the curved inserts and specimen.

One triplicate from each joint (25 triplicates total) were tested using the flat grips. One additional triplicate from joint 19 was tested using the curved inserts for comparison to the flat grip results. The goal of the comparison was to identify possible effects that flattening could have on tensile properties. Figure 287 shows one of the tensile specimens from joint 19 in the test frame. The enlarged image of the bottom grip shows the curved inserts between the specimen and the flat grips.

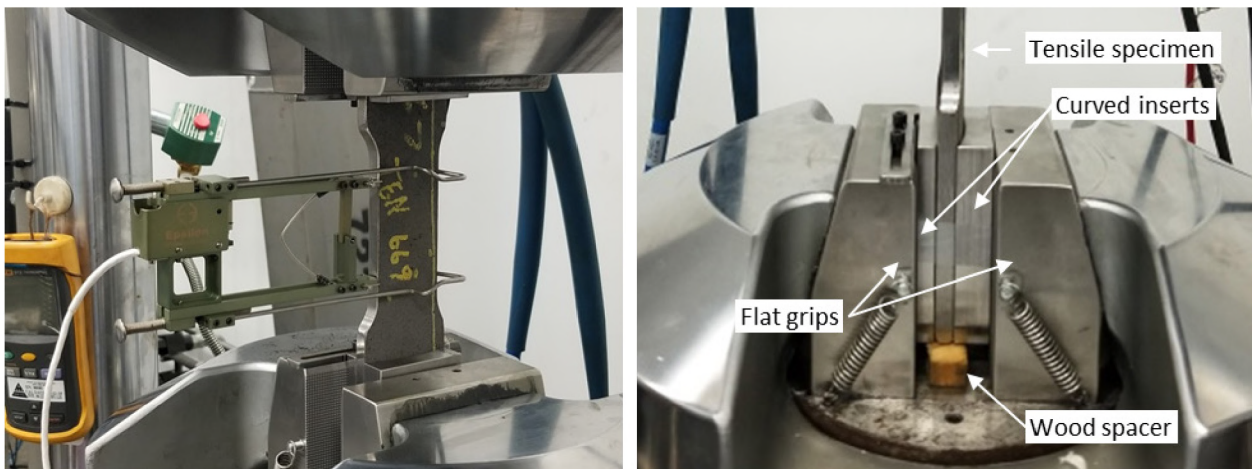


Figure 287: Curved Grip Tensile Specimens

Table 25 shows the flat grip tensile test results. The table includes the minimum, maximum, and average values for 0.5% EUL, ultimate tensile strength, elongation, and reduction in area. All values were taken directly from the Element reports, except for reduction in area. Reduction in area is the difference between the original and final cross-sectional area, expressed as a percentage of the original cross-sectional area. Blade calculated the reduction in area using the initial dimensions and the post-failure stereo micrographs as per ASTM A370 [84].

**Table 25: 7 in. Casing A370 Flat Grip Tensile Results**

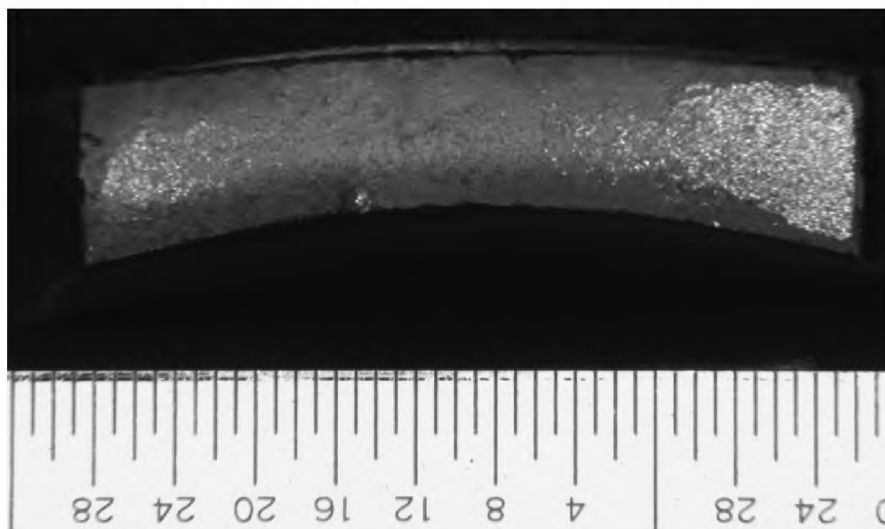
Joint	0.5% EUL (psi)			Ultimate Tensile Strength (psi)			Elongation (%)			Reduction in Area (%)		
	Min	Max	Avg	Min	Max	Avg	Min	Max	Avg	Min	Max	Avg
1	62,000	65,500	63,500	108,000	111,000	109,000	20	26	23.3	32	41	38.1
2	59,500	61,000	60,500	108,000	110,000	109,333	25	27	26.0	35	40	37.1
3	60,500	64,000	62,500	111,000	114,000	112,333	22	24	23.3	36	39	37.3
4	54,500	56,000	55,333	99,000	100,000	99,667	28	30	29.3	42	46	43.7
5	58,000	68,500	65,000	99,000	112,000	107,000	25	28	26.3	36	46	39.9
6	62,500	63,500	63,000	109,000	111,000	110,000	25	27	26.0	41	43	41.7
7	59,500	61,000	60,000	99,000	102,000	100,667	25	29	27.3	42	46	43.4
8	59,500	61,500	60,833	108,000	110,000	108,667	25	27	26.0	38	39	38.3
9	66,000	72,000	69,667	115,000	120,000	117,333	25	26	25.7	37	43	41.2
10	62,500	65,000	63,500	112,000	117,000	113,667	19	25	22.7	30	43	37.4
11	65,000	66,000	65,667	113,000	114,000	113,333	23	28	25.0	31	39	33.9
12	62,500	64,500	63,333	104,000	105,000	104,333	24	28	26.3	39	41	39.9
13	64,500	64,500	64,500	112,000	112,000	112,000	25	27	25.7	38	41	39.9
14	60,500	61,000	60,833	102,000	104,000	103,000	27	28	27.3	41	43	42.3
15	60,500	61,500	61,000	102,000	104,000	103,000	26	29	27.3	36	42	39.0
16	58,000	59,000	58,500	99,500	101,000	100,167	29	31	30.0	44	45	44.6
17	61,000	63,000	62,000	103,000	105,000	104,000	25	31	28.0	34	44	39.7
18	62,000	64,000	63,000	109,000	112,000	110,333	26	28	27.0	38	42	39.3
19	61,500	62,000	61,833	107,000	108,000	107,667	21	27	24.7	36	37	36.2
20	60,000	61,000	60,500	107,000	110,000	108,667	24	26	25.0	40	43	41.0
21	57,500	59,000	58,167	97,000	98,500	97,833	29	32	31.0	44	47	45.3
22	62,500	65,500	63,833	112,000	113,000	112,333	23	26	25.0	31	39	34.8
23	59,000	62,500	60,500	102,000	105,000	103,000	26	28	27.0	40	43	41.5
24	61,000	62,500	61,667	102,000	103,000	102,333	23	30	26.7	36	42	39.8
25	60,500	64,000	61,833	102,000	102,000	102,000	16	30	24.3	30	43	38.2
<b>Totals</b>	<b>54,500</b>	<b>72,000</b>	<b>62,040</b>	<b>97,000</b>	<b>120,000</b>	<b>106,867</b>	<b>16</b>	<b>32</b>	<b>26.3</b>	<b>30</b>	<b>47</b>	<b>39.7</b>

Note A2.2 of A370 [84] states that an exact formula for calculating the cross-sectional area of specimens taken from circular tubes can be found in ASTM E8 [88]. Eq. 20 is the area calculation for a circular tube

with a D/W ratio less than 6. Eq. 20 was used to calculate the tensile specimen's initial cross-sectional area.

$$A = \left[ \frac{W}{4} \times (D - W^2)^{\frac{1}{2}} \right] + \left[ \left( \frac{D^2}{4} \right) \times \arcsin \frac{W}{D} \right] - \left[ \frac{W}{4} \times ((D - 2T)^2 - W^2)^{\frac{1}{2}} \right] - \left[ \left( \frac{(D - 2T)^2}{2} \right) \times \arcsin \frac{W}{(D - 2T)} \right] \quad (20)$$

The final cross-sectional area was calculated using an image processing software and a scaled image of the final cross section. The reduction in area was calculated using the measured original and final cross-sectional areas. Figure 288 shows an example of the scaled image used to calculate the final cross-sectional area. The image processing software calculated the cross-sectional area in pixel units. Pixel units were converted to real world units using the image scale for reference.



**Figure 288: Final Cross-Sectional Area for Specimen 862 from Joint 20**

Figure 289 shows histograms for each of the properties calculated from the flat grip tensile test data. The total specimen count shown in the histograms is 75. The 0.5% EUL, elongation, and reduction in area histograms appeared to be normally distributed, while the ultimate tensile strength histogram did not.

The normally distributed properties suggest that the average property values of 62,040 psi, 26.3%, and 39.7% are good representative values for the 0.5% EUL, elongation, and reduction in area, respectively. The ultimate tensile strength average of 106,867 psi is also a good representation of the 7 in. casing but with a slightly larger margin of error.

The absolute minimum value for 0.5% EUL occurred in joint 4 and was 54,500 psi. This value was slightly below the minimum requirement of 55,000 psi, but the average 0.5% EUL value for joint 4 was 55,333 psi, which is over the minimum requirement. The failure joint (joint 22) had a minimum value of 62,500 psi, which is greater than the minimum requirement.

The sample average value was used to evaluate the 0.5% EUL of the 7 in. casing. A 95% confidence interval was constructed to estimate how close the 7 in. casing sample mean was to the population. The results show that the average value for the 0.5% EUL is greater than 59,476 psi, with a 0.95 degree of confidence. This value is greater than the required minimum of 55,000 psi. The results suggest that the yield strength of the 7 in. casing meets specifications and did not contribute to the failure.

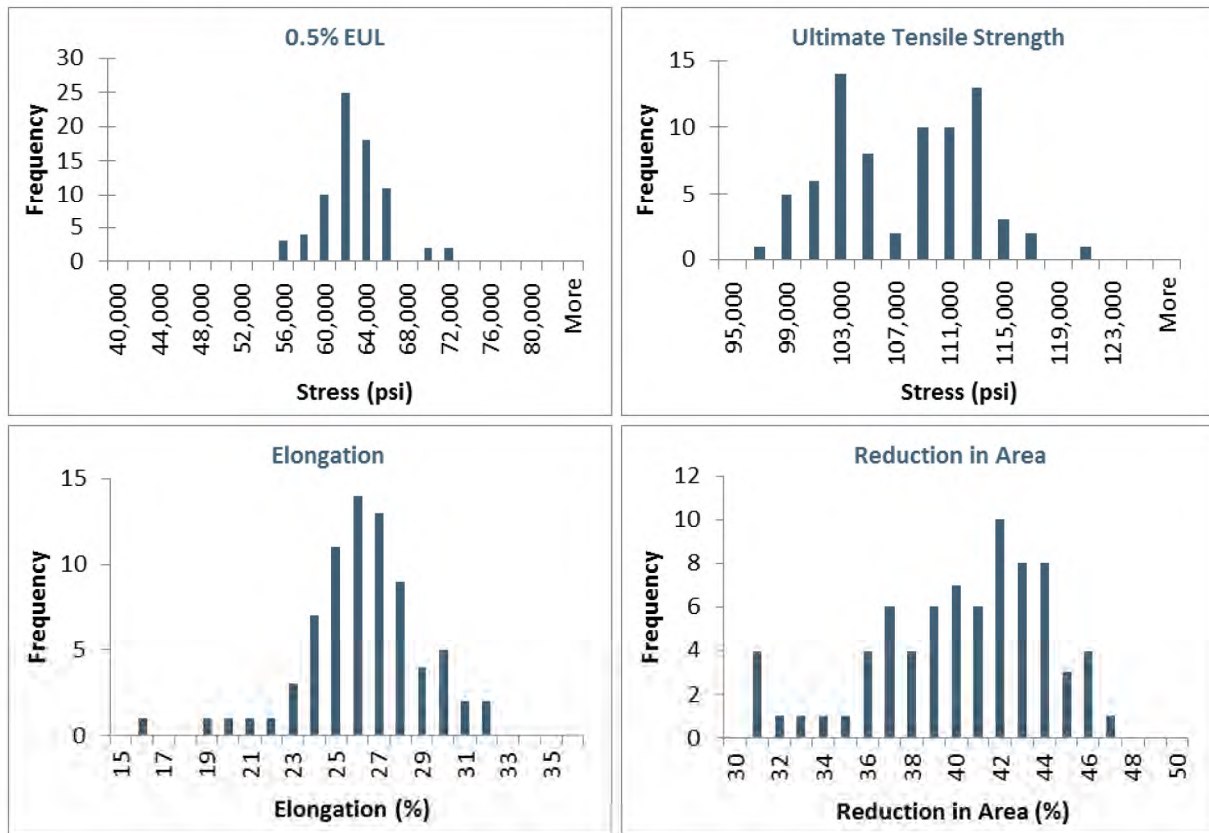


Figure 289: Tensile Property Frequency Plots

Table 26 shows the comparison of the tensile properties for the joint 19 specimens tested using the flat grips and curved inserts. The average 0.5% EUL for the flat and curved grip was 61,833 psi and 63,667 psi, respectively. The difference was just under 2,000 psi, which was less than the standard deviation for the 0.5% EUL in Table 25. Similar observations were made for the other tensile properties, suggesting that the curved grip results were in good agreement with the flat grip results. The results suggest that using flat grips when testing curved specimens does not have a significant impact on the tensile properties. The results validate the properties presented in Table 25.

Table 26: ASTM A370 Flat Grips Versus Curved Inserts Results

Joint	ID	Grip	0.2% Offset Yield Strength (psi)	0.5% EUL (psi)	Ultimate Tensile Strength (psi)	Elongation (%)	RIA (%)
19	1	Flat	60,500	62,000	108,000	26	36
19	2	Flat	58,500	61,500	108,000	27	37
19	3	Flat	60,000	62,000	107,000	21	36
19	1	Curved Inserts	63,500	65,000	108,000	26	42
19	2	Curved Inserts	61,500	63,000	108,000	23	37
19	3	Curved Inserts	61,500	63,000	108,000	22	34

The failure in joint 22 contained an axial rupture and a circumferential parting. Properties in the transverse direction were required to model the failure events. ASTM A370 [84] defines transverse as the

orientation that is at right angles to the direction of the greatest extension of the steel during extrusion. Therefore, the transverse orientation corresponded to the circumferential orientation of the casing. Transverse properties were used when analyzing the circumferential parting.

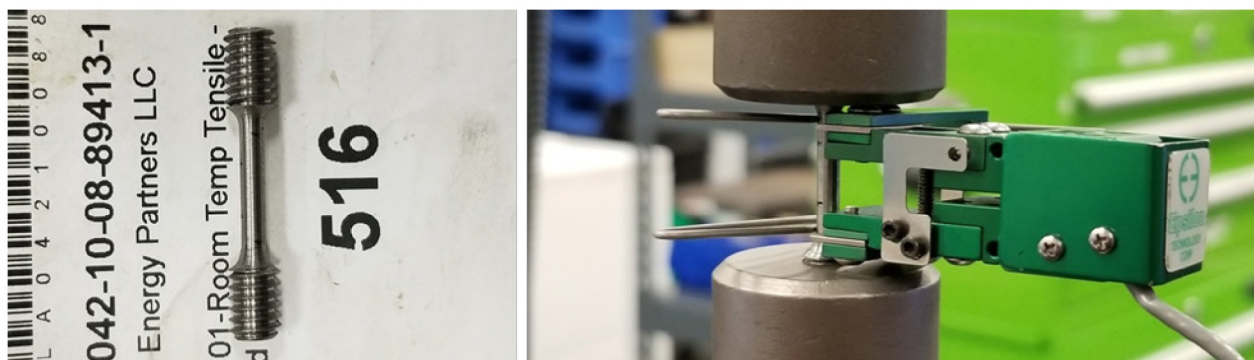
The size of the 7 in. casing limited the options for determining the transverse tensile properties. Flattening, which allows for larger transverse specimens, is permitted by ASTM A370 [84]. However, Blade chose not to flatten the pipe section for the transverse specimens because flattening would have introduced stresses in the gauge section. Blade chose to use sub-sized round specimens that could be machined directly from the transverse orientation of the pipe. The smallest sub-size specimen permitted by ASTM E8 [88] was chosen for testing.

Table 27 shows the results from the sub-size specimen tests. Figure 290 shows the sub-size round specimen and test setup. The results suggest that a size effect was associated with the sub-size rounds. The longitudinal values for 0.5% EUL were not in line with the results from the strip specimens. The average yield and UTS for the longitudinal sub-size rounds were 53,900 psi and 115,667 psi as compared to the strip specimen results of 63,833 psi and 112,333 psi. The yield was significantly lower for the sub-size rounds and even below the specified yield of 55,000 psi. The UTS values were also different but not by a significant amount. The transverse properties were considered invalid based on the fact that they were comparable with the longitudinal sub-size rounds, which were not in good agreement with the strip specimen properties.

Additional testing was conducted at Blade’s lab to measure transverse properties and critical strain of the specimen. Critical strain is a material property used in the DFDI model to determine the initiation of a crack. Section 4.1.2 discusses DFDI as it relates to FEA modeling and pressure predictions.

**Table 27: ASTM E8 Sub-Size Tensile Specimen Results for Joint 22**

No.	Orientation	0.2% Offset Yield (psi)	0.5% EUL (psi)	Ultimate Tensile Strength (psi)	Elongation (%)	RIA (%)
1	Longitudinal	45,500	49,200	115,000	27	51
2	Longitudinal	54,500	59,500	115,000	25	50
3	Longitudinal	47,100	53,000	117,000	22	46
1	Transverse	45,900	52,500	115,000	-	-
2	Transverse	43,600	48,600	113,000	20	38
3	Transverse	48,800	56,000	115,000	23	38
4	Transverse	51,000	58,000	117,000	18	36



**Figure 290: Sub-Size Tensile Specimens**



Critical strain testing is a tensile test that records the true stress and strain of the specimen. True stress and strain were recorded using a machine vision system developed by Blade. Figure 292 shows an image of the Blade vision system. A camera with an LED back light was used to measure the instantaneous diameter of the specimen during the test. Telecentric lenses were used to polarize the light and minimize distortions as the light passed around the specimen. The camera-lens system used the backlighting to capture a silhouette of the specimen.

Figure 291 shows silhouette images of a tensile specimen taken with the Blade vision system. The specimen edges in the gauge area were detected by the software and used to measure diameters along the length of the specimen. The minimum diameter was recorded and tracked by the system. The instantaneous diameter was used to calculate the true stress and strain of the specimen during the tensile test. The true stress-strain curves and tensile properties from the testing were used as inputs for the FE models.

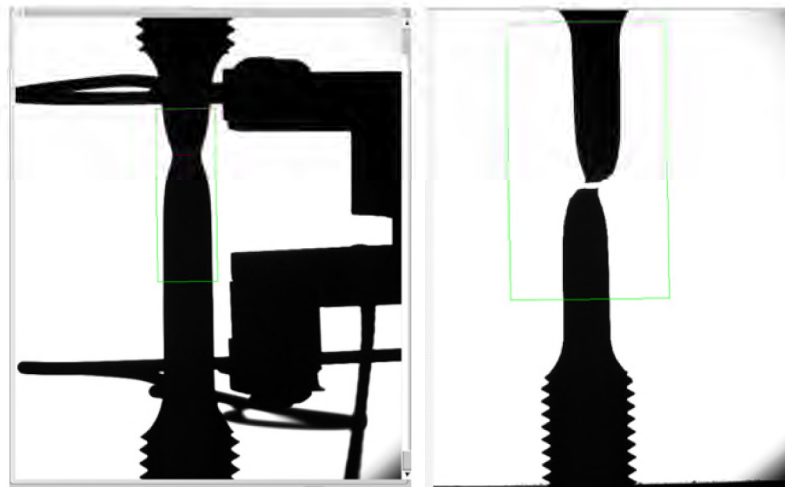


Figure 291: Silhouette Image of Tensile Specimen from Blade Vision System

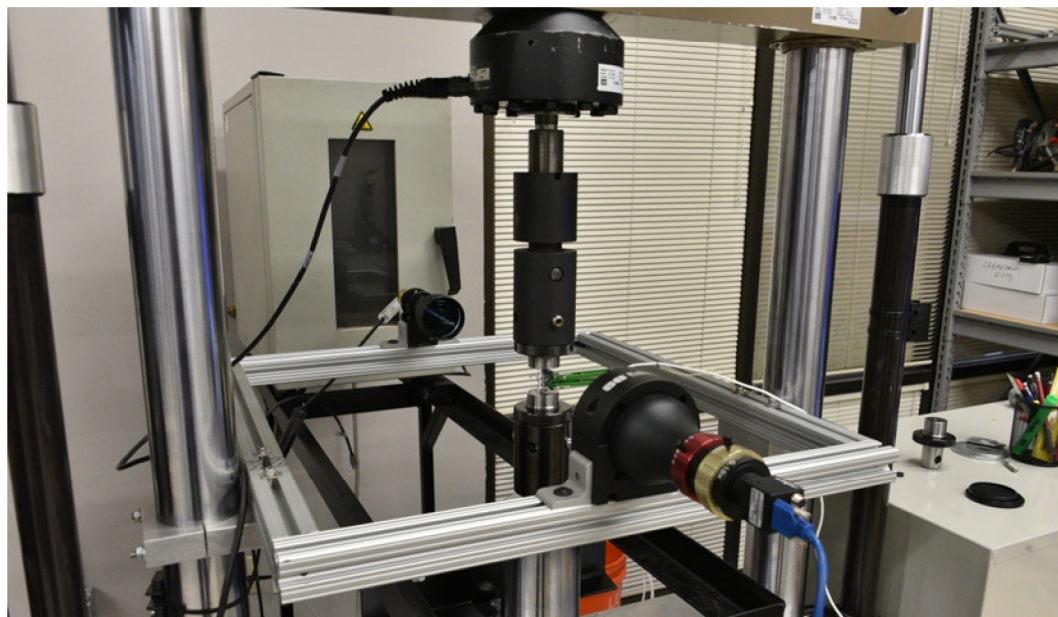


Figure 292: Blade Critical Strain Test Setup

Larger transverse tensile specimens were required based on the size effect discovered by the previous sub-size testing at Element. The pipe wall thickness limited the specimen size to ASTM E8 [88] round specimen 4 (0.16 in. diameter). Transverse specimen lengths were limited due to the curvature of the casing. Additional material was welded to the ends of the specimen to acquire a long enough grip section to support the load. Electron beam welding (EBW) was used to weld additional steel to the ends of the parent material. EBW has the advantage of precision, full penetration, and a limited heat-affected zone (HAZ). Figure 293 shows a schematic of the transverse tensile specimen and the approximate weld locations. The schematic was used to ensure that the weld location was outside the gauge section. The joint 22 parent material is indicated in red. The 0.25 in. steel plate, which was purchased to extend the parent material, is indicated in blue.

The steps taken to create the transverse sub-size round specimens were as follows:

1. A 0.25 in. thick by 4 in. long plate was machined from the joint 22 parent material.
2. An extra 0.25 in. plate was EBW'd to the machined parent material.
3. Blanks from the welded plates were extracted and round tensile specimens were machined.

Table 28 shows the results from the critical strain tests for both the longitudinal and transverse orientations. The average 0.5% EUL for the longitudinal and transverse orientations was 65,899 psi and 66,276 psi, respectively. These values are in good agreement with the average strip specimen 0.5% EUL value of 63,833 psi. The average UTS for the longitudinal and transverse orientations were 118,429 psi and 114,828 psi, respectively. These values are slightly higher than the strip specimen UTS value of 112,333 psi but are consistent. The average critical strain value for the longitudinal and transverse orientations was 0.37 and 0.32, respectively. The results show a slightly higher critical strain value for the longitudinal orientation.

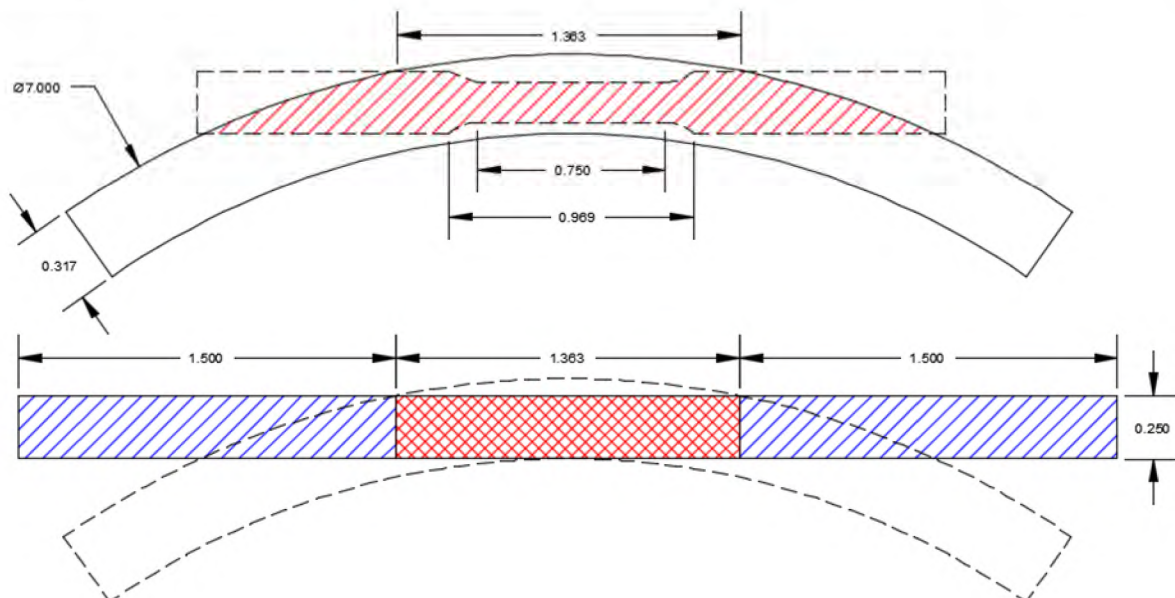


Figure 293: Transverse Tensile Specimen Schematic and Approximate Weld Locations

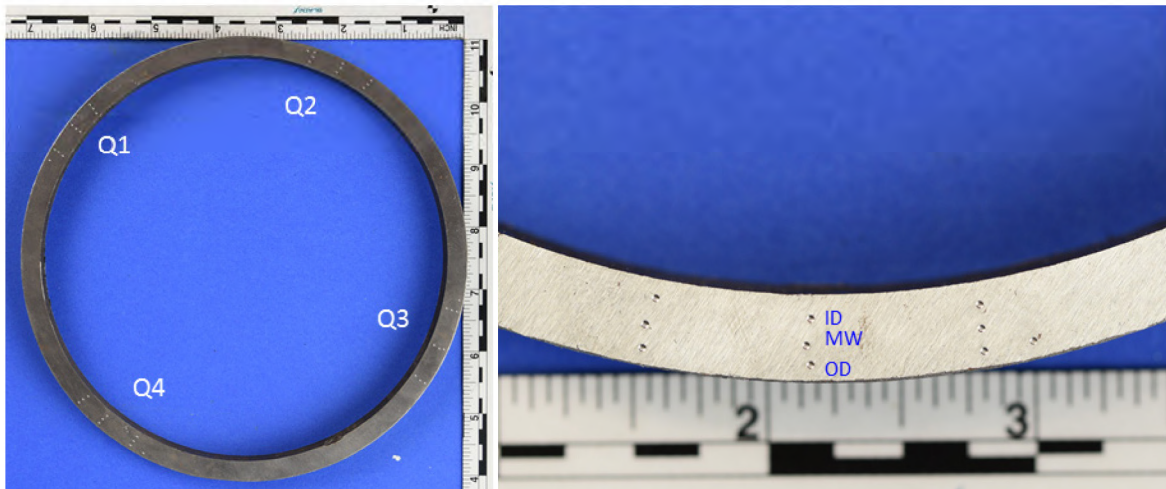
**Table 28: Critical Strain Tensile Test Results**

Joint	ID	Orientation	0.5% EUL (psi)	Ultimate Tensile Strength (psi)	Elongation (%)	RIA (%)	Critical Strain (in./in.)
22	1	Longitudinal	66,832	117,767	23	47.3	0.38
22	2	Longitudinal	67,259	117,461	22	45.3	0.36
22	3	Longitudinal	67,097	119,006	23	47.1	0.38
22	4	Longitudinal	67,087	119,480	23	47.0	0.38
22	1	Transverse	65,523	112,663	20	40.2	0.32
22	2	Transverse	67,573	116,162	21	39.0	0.31
22	3	Transverse	66,928	115,659	21	39.2	0.32

### 7.1.7 Hardness

Element conducted Hardness Rockwell B (HRB) tests per ASTM E18 [85] on hardness rings extracted from each casing joint. Three indentations were made at the OD, MW, and ID locations at four quadrants. The goal of the testing was to identify possible variations in hardness based on through thickness or circumferential position. Figure 294 shows examples of the indentation locations for a typical hardness ring.

Table 29 shows a summary of the results. The minimum and maximum HRB values for all indentations were 82 and 98, respectively. The average and standard deviation HRB values for all indentations were 93.5 and 2.75, respectively. Figure 295 shows the HRB value distributions. The left plot shows the distribution for all the hardness indentations. The right plot shows the same data separated by through thickness position. The results show that the hardness for the 7 in. casing is consistent.



**Figure 294: Hardness Ring with Three Indentations at the OD, MW, and ID in Four Quadrants**

Table 29: 7 in. Casing Hardness Rockwell B Results

Joint	Outside Diameter			Mid-Wall			Inside Diameter		
	Min	Max	Avg	Min	Max	Avg	Min	Max	Avg
1	96	98	96.8	96	98	96.8	96	98	97.0
2	93	97	95.2	91	96	94.5	94	97	95.7
3	96	98	97.3	96	98	96.9	97	98	97.4
4	92	94	92.8	92	94	93.1	93	94	93.4
5	94	95	94.5	93	94	93.8	94	95	94.7
6	91	95	93.6	91	96	93.9	93	97	95.3
7	90	94	92.1	92	93	92.8	94	95	94.6
8	96	97	96.8	96	97	96.3	95	97	96.7
9	96	97	96.7	96	97	96.1	96	97	96.8
10	93	97	95.8	95	97	95.8	96	97	96.8
11	93	96	95.0	94	96	95.3	95	97	96.1
12	87	94	91.4	91	94	92.8	93	95	94.3
13	82	96	92.4	93	96	94.8	95	97	96.0
14	85	94	91.7	90	93	92.0	92	95	93.7
15	90	95	93.1	92	94	92.7	93	95	94.3
16	88	94	91.8	92	94	92.8	93	95	93.9
17	82	94	90.6	88	95	92.8	92	96	94.3
18	94	96	95.4	95	96	95.6	95	97	96.3
19	91	95	93.4	93	96	94.3	93	96	94.7
20	91	95	92.9	91	94	92.8	92	96	94.4
21	85	93	89.6	86	93	89.1	85	92	89.3
22	96	98	97.1	97	98	97.1	94	97	96.4
23	91	95	93.4	86	95	92.8	90	96	93.3
24	94	96	95.0	94	96	95.3	94	96	94.8
25	90	95	93.9	92	96	94.2	93	95	94.1
Totals	82	98	93.9	86	98	94.2	85	98	95.0

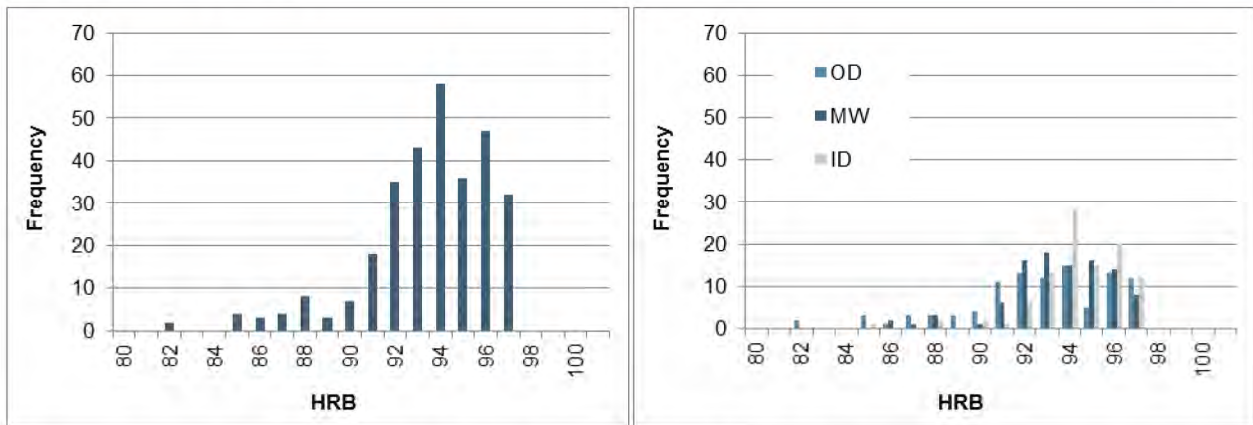


Figure 295: Hardness Rockwell B Value Distribution

### 7.1.8 Charpy V-Notch Testing

Element conducted CVN tests on the extracted 7 in. casing joints per ASTM E23 [86]. CVN testing is a three-point bend impact test that uses a pendulum with a weighted hammer to fracture a notched specimen.

Figure 296 shows the CVN testing apparatus and concepts relevant to the test method. The image on the left is the actual apparatus and setup used at Element.

The goal of CVN testing is to measure the amount of energy absorbed during fracture of a standard specimen. The CVN specimen is positioned so that the hammer impacts the specimen at the bottom of its arch. This is the point at which the hammer is at its maximum velocity (maximum kinetic energy). The hammer is released from a known height (maximum potential energy) and allowed to impact the specimen. The hammer completes its swing and reaches a height that is below the starting height (final potential energy). The difference in height is a measure of the energy absorbed during impact of the CVN specimen. Energy is lost through the fracture of the CVN specimen, with some losses contributed to heat.

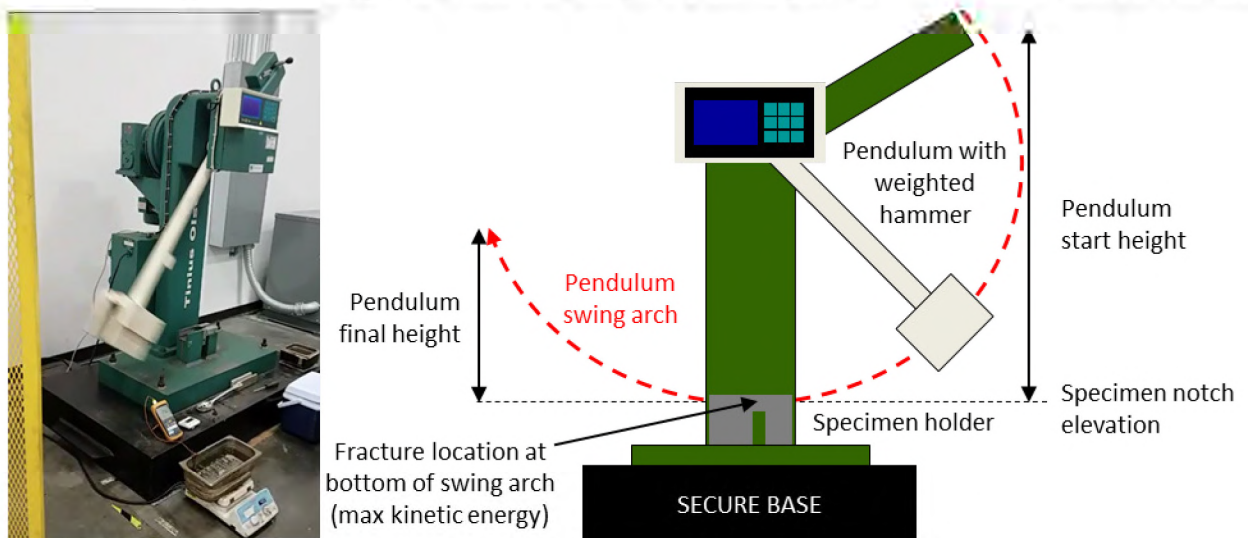


Figure 296: CVN Testing Apparatus

The measured absorbed energy is sensitive to specimen geometry. Figure 297 shows the standard specimen geometry according to ASTM E23 [86]. The full-size specimen is 10 mm wide, 10 mm thick, and 55 mm long. The notch is located at the center of the specimen with a depth of 2 mm. The other specimens shown in Figure 297 are sub-sized specimens that are typically used when geometric limitations prevent the use of full-size specimens.

The most commonly used sub-sized specimens are three-quarter, half, and quarter-size specimens. Sub-sized specimens differ from full-size—the widths of the sub-sized specimens are a fraction of the full-size. For example, the half-size specimen has a width of 5 mm, which is half of the full-size width of 10 mm. The length, thickness, and notch size of the sub-sized specimen are the same as the full-size. Half-size specimens were used for the 7 in. casing due to geometric limitations caused by the wall thickness.

Specimens from the 7 in. casing CVN testing were extracted with the notch plane in two orientations. This was based on the fact that the failure sequence included fracture paths in both the longitudinal and circumferential orientations. Figure 298 shows the nomenclature for specimen orientation based on ASTM E1823 [89] (fracture mechanics) and API 5CT [90] (CVN for tubulars). The ASTM E1823 [89] nomenclature shall be used throughout this section for consistency. Transverse and longitudinal Charpy orientations from API 5CT [90] correspond with the C-L and L-C ASTM E1823 [89] orientations, respectively.

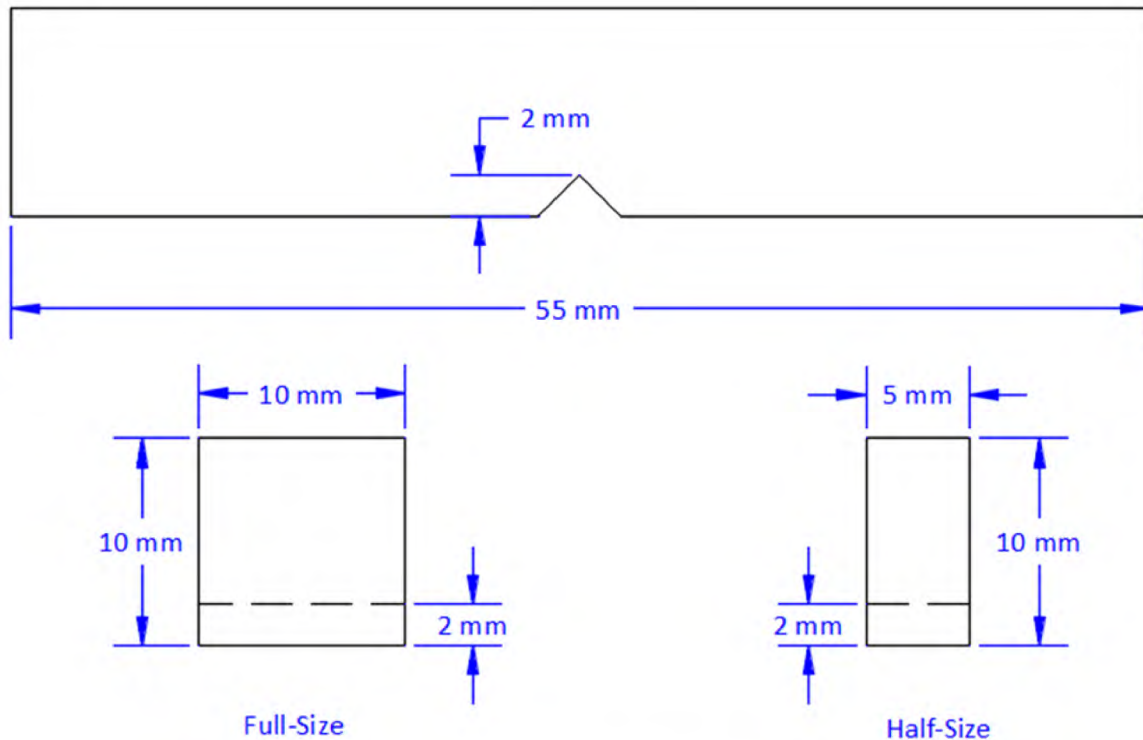


Figure 297: ASTM E23 CVN Specimen Dimensions [86]

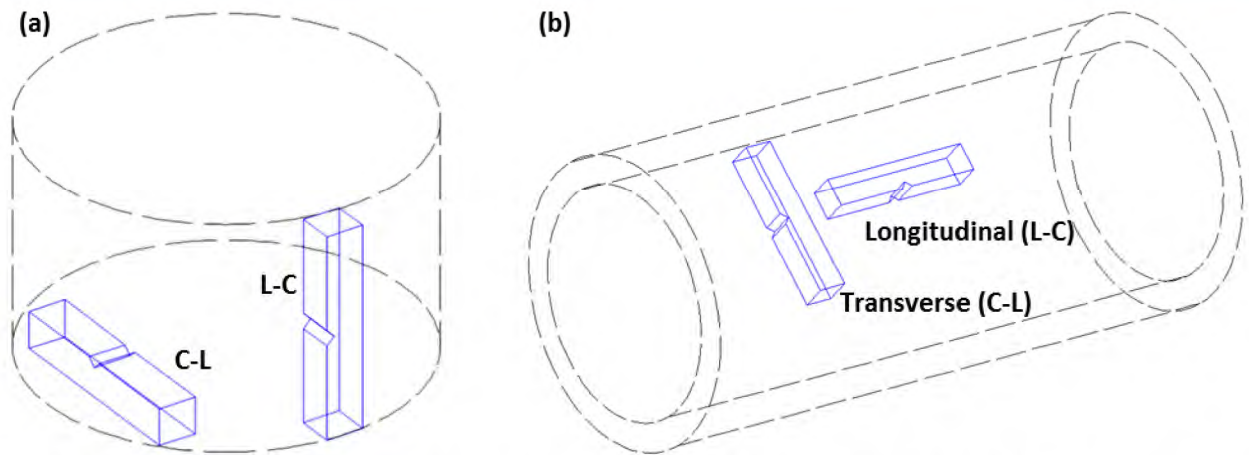


Figure 298: (a) ASTM E1823 Crack Plane Orientation [89] and (b) API 5CT CVN Orientations [90]

Figure 299 shows a cross section of the full, three-quarter, and half-size specimens in relation to the 7 in. casing wall thickness. The schematic shows that half-size specimens were required for testing. The NWT of 0.317 in. was not thick enough to accommodate larger sizes. This was the case for both the L-C and C-L orientations.

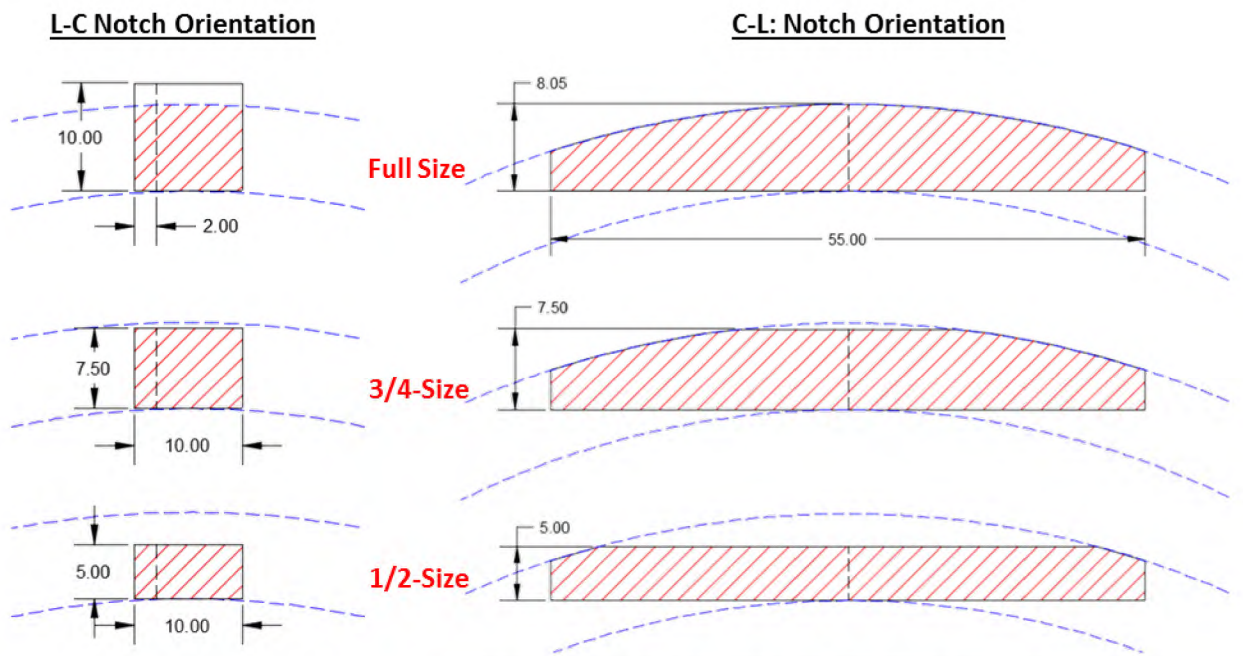


Figure 299: Full, Three-Quarter, and Half-Size CVN Specimen Layout

CVN specimens experience a high strain rate during impact, which promotes fracture rather than flow (plastic deformation). Fracture is further promoted by the triaxial stress state created by the notch on the back side of the specimen. These conditions are severe for measuring toughness. It is for that reason that CVN results do not represent the exact behavior of material in service but will give a general indication as to the performance.

A material’s behavior during fracture is influenced by several factors including temperature, stress state, material cleanliness, and microstructure. These factors influence the material’s ability to flow. The factor of primary concern for this metallurgical investigation is temperature.

A phenomenon typical of BCC materials is a transition from ductile fracture to brittle when temperature is lowered. A common parameter used to indicate the transition point is the DBTT, which is the temperature at which the fracture mode transitions from ductile to brittle. Figure 300 shows a typical ductile-to-brittle transition curve for mild steel. The transition zone represents temperatures at which the fracture mode is a combination of brittle and ductile fracture. The lower plateau (lower shelf) to the left of the transition zone is pure brittle fracture, while the upper plateau to the right (upper shelf) is pure ductile fracture.

The DBTT is shown by the red dashed lines in the middle of the transition zone. This is based on the NIST definition for DBTT [91]. The point represents the temperature at which the fracture transitions from primarily ductile to primarily brittle. The ordinate of the ductile-to-brittle transition curve can be impact energy (Figure 300) or percent shear. The plots can give different values for the DBTT. Percent shear is the ratio of the ductile fracture surface area to the total fracture surface area expressed as a percentage.

The percent shear reported by Element was measured using a comparison method. Results from the comparison are somewhat subjective and can show significant scatter. Image analysis was used to refine the percent shear calculations and limit the amount of scatter within the data sets. Figure 301 shows a typical image of a CVN fracture surface. The shiny area in the middle of the specimen is caused by cleavage facets, which are typical of brittle fracture. The dull woody area surrounding the brittle area is typical of ductile fracture. The total fracture surface and ductile fracture areas were measured using image processing software. The software calculated the areas within a polygon defined by the user. The areas were calculated in pixel units and converted into real world units based on a calculated scale factor. This method proved to be more consistent and less subjective than the comparison method. The percent shear as reported in this section is in reference to values calculated using this method.

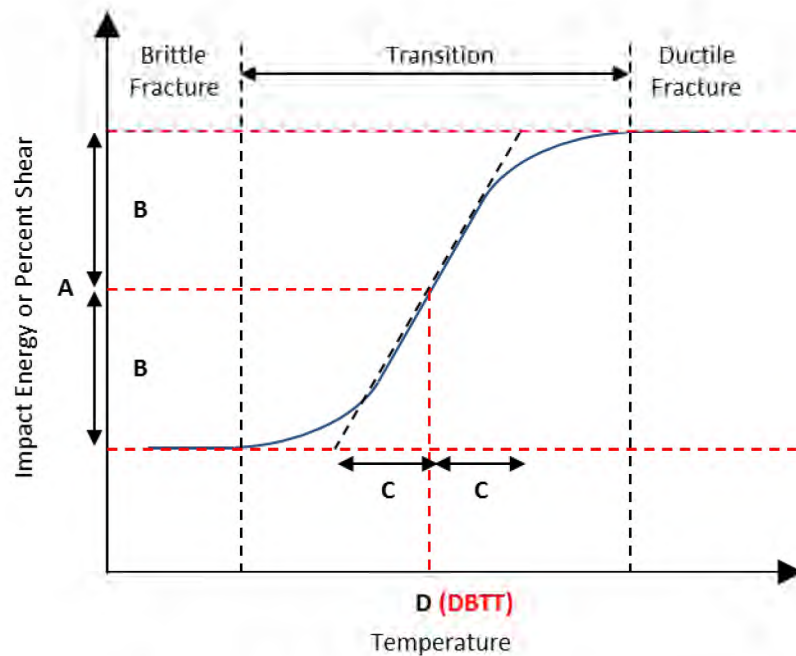
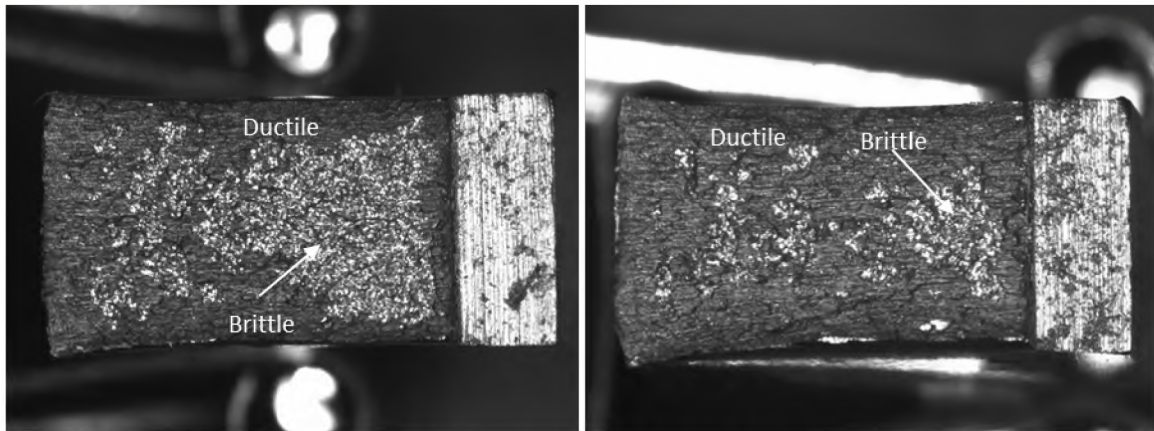


Figure 300: Ductile-to-Brittle Transition Curve





**Figure 301: CVN Fracture Surface Image**

Initial observations from the SS-25 temperature logs suggested that temperature could have played a role in the failure sequence. CVN specimens were tested at various temperatures in an effort to calculate the DBTT. Ductile-to-brittle transition curves were established by testing CVN specimens at several temperatures. The number of selected temperatures should be sufficient enough to capture the shape of the DBTT curve.

Two specimens were selected for a 10-point DBTT curve, which used 10 temperatures to establish the curve shape. Five temperatures were selected first to establish an initial curve. Additional temperatures were selected to accurately capture the upper and lower shelf and transition zones.

The test temperatures for the 10-point curve were  $-73$ ,  $-50$ ,  $-25$ ,  $0$ ,  $25$ ,  $45$ ,  $66$ ,  $80$ ,  $100$ , and  $150^{\circ}\text{C}$ . Joints 2 and 20 were selected for the 10-point DBTT curves. The remaining joints were tested at five temperatures, based on the results from the 10-point curves. The DBTT was determined by the regression function in Eq. 21 [91] using the least-squares method. Figure 300 shows the physical significance of the constants A–D.

$$Y = A + B \cdot \tanh\left(\frac{T-D}{C}\right) \quad (21)$$

Figure 302 shows the 10-point DBTT curves for joints 2 and 20 for impact energy and percent shear. The impact energy curves show a difference between the C-L and L-C orientations. The C-L orientation has lower impact energy values as compared to the L-C orientation. The C-L and L-C impact energy DBTT for joint 2 is  $39.4^{\circ}\text{C}$  and  $49.1^{\circ}\text{C}$ , respectively. This is a difference of  $9.7^{\circ}\text{C}$ . The upper shelf impact energy for the C-L orientation is approximately 11 ft-lb, whereas the L-C orientation is approximately 23 ft-lb. The upper shelf for the L-C orientation is approximately twice as large as the C-L orientation.

The percent shear DBTT curves show comparable results for both orientations. The C-L and L-C percent shear DBTT for joint 2 is  $52.7^{\circ}\text{C}$  and  $56.8^{\circ}\text{C}$ , respectively. This is a difference of  $4.1^{\circ}\text{C}$ , which is less than the difference observed with the impact energy DBTT. The percent shear DBTT plots suggest that the fracture mode at each temperature is similar for both orientations.

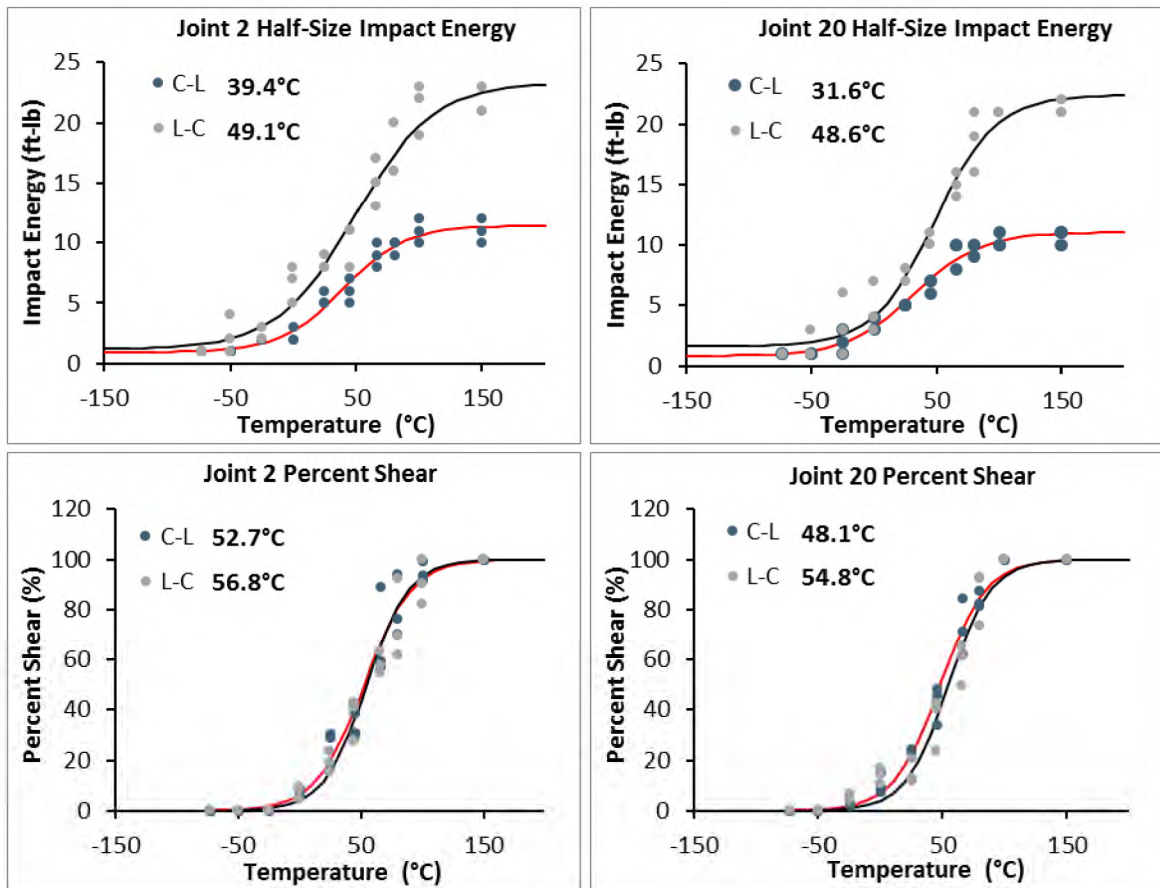


Figure 302: DBTT Curves for Joints 2 and 20

DBTT curves for the remaining joints were constructed using five temperatures based on the results for the 10-point curves for joints 2 and 20. The chosen temperatures were -50, 0, 45, 75, and 100°C. Triplicates were tested at each temperature for all 25 joints. Figure 303 shows the average results for each property at every tested temperature. The points represent averaged values obtained from the CVN testing, and the lines represent the best fit curve for the points based on Eq. 21. Values at each temperature vary over how many specimens were used to obtain the average at that point.

Values for -50, 0, 45, and 100°C were averaged over 75 specimens (all joints), and 75°C was averaged over 69 specimens (joints 2 and 20 were not tested at this temperature). Values for -73, 25, 66, 80, and 150°C were averaged over six specimens (joints 2 and 20 only). Values for -10°C were averaged over three specimens (joint 22 only). The DBTT values for impact energy, reported percent shear, and measured percent shear are included in the plots. The results are consistent with the observations made for joints 2 and 20. The upper shelf impact energy for the L-C orientation is approximately double the C-L orientation. The upper shelf value for the L-C and C-L orientations is approximately 21 ft-lb and 10 ft-lb, respectively. The lower shelf for both orientations is approximately 1 ft-lb.

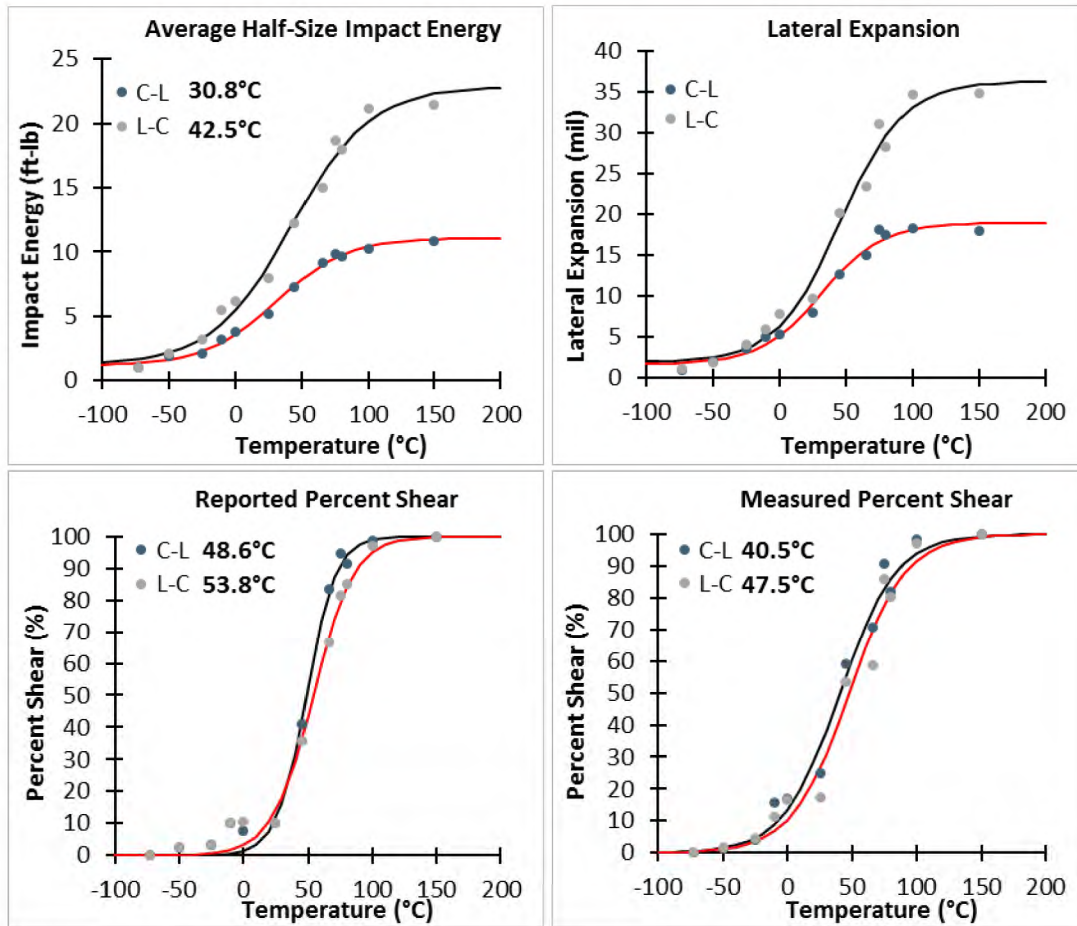


Figure 303: Average CVN Properties Plotted Against Temperature

DBTT for impact energy and percent shear were calculated for all 25 joints. Figure 304 shows histograms of the results. The average impact energy DBTT in the C-L and L-C orientations is 31.2°C and 39.5°C, respectively. The average percent shear DBTT in the C-L and L-C orientations is 35.5°C and 40.3°C, respectively.

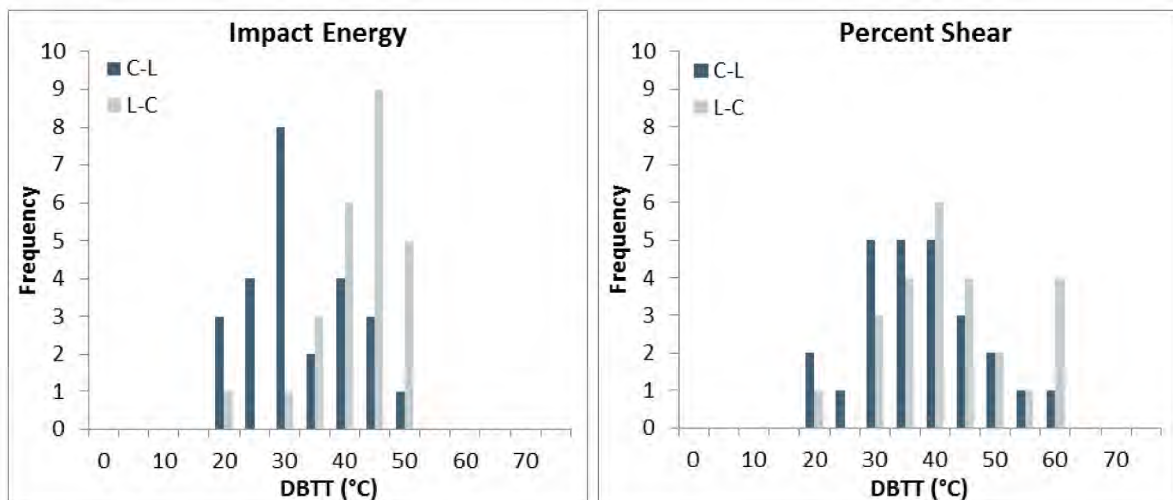


Figure 304: Impact Energy and Percent Shear DBTT Histograms

### 7.1.9 Fracture Toughness

Fracture toughness is a measure of a material's resistance to fracture. A material with higher toughness has an increased ability to resist cracking. Fracture toughness was a primary concern for the circumferential parting due to the temperature drop caused by the Joule-Thomson effect [33]. Decreasing temperatures have the general effect of decreased ductility and toughness. CVN testing showed that the grade J55 material transitioned from a ductile fracture mode to a brittle fracture mode as the testing temperature was decreased. CVN testing is a simple method for material quality and indirect toughness evaluation. Materials with a higher toughness generally have higher impact energies and percent shear [17]. The testing showed that the toughness of the material decreased with the decreasing temperature. Blade conducted fracture toughness testing at Anderson and Associates and Metcut in an attempt to directly measure fracture toughness of the grade J55 7 in. casing material as a function of temperature.

$K_{IC}$  and  $J_{IC}$  are quantitative measurements of a material's resistance to cracking.  $K_{IC}$  is a fracture parameter used when a material behaves in a linear elastic manner prior to failure. The plastic zone ahead of a crack must remain small when compared to specimen dimensions for  $K_{IC}$  to be valid.  $K_{IC}$  represents the critical point of unstable crack growth under Mode I loading [17].

$J_{IC}$  is another fracture parameter that accounts for elastic-plastic material behavior.  $J_{IC}$  is determined from the resistance curve of a material. Most ductile materials exhibit a rising resistance curve. This means that the material's resistance to crack propagation increases with crack growth. The crack driving force also increases with crack growth.  $J_{IC}$  is the initiation toughness near the onset of stable crack growth [92].

Fracture toughness testing was conducted at  $-100$ ,  $-50$ ,  $-20$ ,  $0$ , and  $24^{\circ}\text{C}$  (room temperature). The focus of the testing was at the lower temperatures because of the brittle nature of the circumferential parting. Section 3.3 presents fractographic evidence and discusses the brittle nature of the circumferential parting.

Compact tension, C(T), specimens were machined from joint 22 (failed joint) in the C-L and L-C orientations. Figure 298 shows a schematic of the specimen orientations. The first letter represents the orientation of the tensile load, and the second letter represents the orientation of the crack plane. Figure 274 shows the layout location of the specimens on the material extracted from joint 22. Testing was conducted at five temperatures and two orientations (30 tests total). Twenty specimens were machined for each orientation (15 tests plus five extra specimens per orientation). The 40 specimens were distributed into 4 rows (2 rows for C-L and two for L-C), with 10 specimens in each row. The ten specimens were distributed equally around the circumference of the pipe (Figure 274).

Specimen identification included a letter for orientation, a number representing the row, and the circumferential location expressed in degrees. The origin ( $0^{\circ}$ ) corresponded to the west face of the pipe as described in Section 7.1.1. As an example, specimen L1036 specified a longitudinal (C-L) compact tension specimen extracted from the first row at the  $36^{\circ}$  orientation. T3000 specified a transverse (L-C) compact tension specimen extracted from the third row at the  $0^{\circ}$  orientation.

Material was sent to Anderson and Associates for machining and testing. Blade reviewed the data as they became available to guide future testing. Anderson performed  $J_{IC}$  testing per ASTM E1820 [32] using a compliance-based method to measure crack growth. Compliance-based testing requires systematic loading and unloading of the specimen to generate the resistance curve. Table 30 shows the results for the testing completed at Anderson and Associates. The last column indicates that the  $J_{IC}$  values were invalid, based on the ASTM E1820 criteria [32]. The data showed that the material was susceptible to pop-ins during loading and unloading cycles. Blade decided to switch to a DCPD approach for measuring the crack extension. DCPD can be used with a single rising load during testing and does not require loading and unloading of the specimen.

Table 30: Anderson Fracture Toughness Results Summary

Specimen Number	Orientation	Test Temperature (°C)	J <sub>Q</sub> (in. lbf/in <sup>2</sup> )	Valid J <sub>IC</sub>
L3036	C-L	24	172.0	No
L4000	C-L	24	168.3	No
L4288	C-L	24	110.9	No
L3072	C-L	0	162.5	No
L3108	C-L	0	102.6	No
L3324	C-L	0	35.4	No
L3144	C-L	-50	178.3	No
T1144	L-C	24	294.6	No
T1216	L-C	24	341.0	No
T1252	L-C	24	238.0	No
T1108	L-C	0	158.4	No
T2216	L-C	0	314.3	No
T2288	L-C	0	107.8	No

Anderson and Associates did not have the capability to perform DCPD measurements. Metcut was chosen to complete the fracture toughness testing. Table 31 shows the testing results from Metcut. The last column indicates that the J<sub>IC</sub> values were invalid. Tests were invalid because of material behavior (early pop-in). The test data were then analyzed per ASTM E399 for K<sub>IC</sub> evaluation. The values were invalid based on the plane strain condition caused by the small specimen size. The specimen size was limited by the wall thickness of the 7 in. casing.

Table 31: Metcut Fracture Toughness Results Summary

Specimen Number	Orientation	Test Temperature (°C)	J <sub>Q</sub> (in. lbf/in <sup>2</sup> )	K <sub>JIC</sub>	K <sub>Q</sub>	Valid J <sub>IC</sub>
L3000	C-L	24	156.5	71.8	34.0	No
L3180	C-L	24	253.9	90.7	35.9	No
L4036	C-L	0	224.8	86.1	34.8	No
L4180	C-L	0	238.9	88.7	34.9	No
L4324	C-L	0	101.8	57.9	34.9	No
L3252	C-L	-25	271.4	94.6	38.7	No
L3288	C-L	-25	62.3	45.3	39.4	No
L3216	C-L	-50	-	-	42.3	No
L4072	C-L	-50	-	-	39.3	No
L4144	C-L	-50	-	-	37.1	No
L4108	C-L	-100	-	-	41.9	No
L4216	C-L	-100	-	-	44.0	No

Specimen Number	Orientation	Test Temperature (°C)	J <sub>Q</sub> (in. lbf/in <sup>2</sup> )	K <sub>JIC</sub>	K <sub>Q</sub>	Valid J <sub>IC</sub>
L4252	C-L	-100	30.4	31.7	34.7	No
T2072	L-C	24	400.4	114.9	34.8	No
T2108	L-C	24	431.1	119.2	36.1	No
T1000	L-C	0	455.7	122.6	35.9	No
T1324	L-C	0	426.5	118.6	35.5	No
T2180	L-C	0	420.1	117.1	38.2	No
T1072	L-C	-25	-	-	35.5	No
T2000	L-C	-25	-	-	39.0	No
T2144	L-C	-25	378.3	111.7	39.9	No
T1180	L-C	-50	-	-	40.7	No
T1288	L-C	-50	-	-	37.6	No
T2036	L-C	-50	-	-	30.8	No
T1036	L-C	-100	-	-	41.5	No
T2252	L-C	-100	-	-	43.2	No
T2324	L-C	-100	-	-	41.5	No

### 7.1.10 Grade J55 for the 7 in. Casing Vintage Versus New Comparison

The grade J55 steel used for the SS-25 7 in. casing was manufactured prior to its installation in October 1953. Improvements to steel quality and performance are expected to have happened over the last six decades. A newly manufactured steel joint of grade J55 for the 7 in. casing was investigated and compared with the vintage J55 used in the SS-25 well. The new grade J55 7 in. casing was manufactured by Vallourec Star LP in Youngstown, OH, USA, in 2017 in accordance with API 5CT J55 PSL1, 9th Edition, 2012 [90].

Review of the Vallourec MTR and the Element material testing results [93], Houston, TX, found that the grain size (ASTM 7.46 vs. 8.0) and yield strength (62.0 ksi vs. 63.4 ksi) are comparable, while the UTS is slightly higher (106.8 ksi vs. 97.2 ksi) between the vintage and the new grade J55 7 in. casing steel, respectively.

The major differences between the new and the vintage J55 7 in. casing were:

- Phosphorus and sulfur contents;
- Carbon content;
- Microstructure;
- Charpy impact toughness.

Each of these differences is discussed in detail in this section.

## Phosphorus and Sulfur Contents

API standards only specify the maximum limit for phosphorus and sulfur for grade J55 casing and tubing. Table 32 shows the API-specified maximum limits and the actual phosphorus and sulfur contents for vintage and new grade J55 material.

**Table 32: Vintage and New J55 Phosphorous and Sulfur Comparison**

Manufacturing Method	Vintage J55		New J55	
	API 5A, 1953 Maximum	SS-25 7 in. Casing	API 5CT, 2012 Maximum	Vallourec (2017)
<b>Phosphorous (Mass Fraction %)</b>				
Open-hearth	0.04	Average 0.028 Maximum 0.055	0.03	MTR 0.008 Element 0.008
Electric-furnace	0.04			
Bessemer	0.11			
<b>Sulfur (Mass Fraction %)</b>				
Open-hearth	0.06	Average 0.023 Maximum 0.033	0.03	MTR 0.007–0.008 Element 0.019
Electric-furnace	0.06			
Bessemer	0.065			

The table shows that the phosphorus content limit was reduced from 0.04% (vintage open-hearth and electric-furnace) to 0.03% (new), while the sulfur content limit was reduced from 0.06% (vintage open-hearth and electric-furnace) to 0.03% (new). More importantly, even though both vintage and new steels met their respective specifications, the actual contents of phosphorus and sulfur in the new grade J55 were significantly lower. The contents in the new grade J55 were 0.007–0.008%, which are approximately three times lower than the vintage grade J55.

Phosphorus increases strength and hardness at the expense of ductility and impact toughness. The phosphorus content in most steel is limited to a maximum of 0.05% [94] [95], but OCTG casing and tubing limits sulfur to 0.03%. Sulfur lowers transverse ductility and notched impact toughness. Sulfur is detrimental to the surface quality in low carbon and low manganese steels. Lower contents of phosphorus and sulfur are always desirable in OCTG steel grades for better ductility and notched impact toughness. This is achievable with modern steel making technology, without significantly increasing the cost.

## Carbon Content

The early and current versions of the API standards do not specify contents for carbon, manganese, and other controlling alloying elements for Group 1 OCTG steel grades, including H40, J55, K55, and N80. The contents of these alloying elements are left up to the manufacturer. This is traditionally done for this group of API steel grades because mechanical properties are of primary importance, while chemistry is secondary. The chemistries obtained at different steel mills typically do not exactly agree because each mill must tailor its chemical limits to some extent to suit its own particular manufacturing practices [81]. Typical analyses of grade J55 API casing and tubing used in the early 1960s reported carbon contents in the range of 0.37%–0.47% [81].

Analyses of the 25 grade J55 casing joints extracted from SS-25 reported carbon contents in the range of 0.43%–0.53%, with an average value of 0.484%. The average value is slightly over the typical value of 0.47%. However, based on the MTR [93], the carbon content of the new grade J55 7 in. casing provided by

Vallourec is in the range of 0.36%–0.37%, which is on the lower end of the typical carbon content range of 0.37–0.47%. The carbon content between the vintage and new grade J55 has a difference of 0.13%. This could result in a 17% difference in volume fraction of pearlite, according to the level rule under the equilibrium condition (i.e., annealing condition), by neglecting the difference in molar volume among austenite, ferrite, and pearlite [94].

The strength and hardness of grade J55 increases with increasing carbon content due to an increase in pearlite. This also has the effect of lowering the Charpy impact toughness.

## Microstructure

Both vintage and new grade J55 have fine grains, with an average size of ASTM 7.45 and ASTM 8.0, respectively, per ASTM E112 [82]. Despite the similarity in grain size, the difference in microstructure is significant. Figure 305 and Figure 306 are micrographs of the vintage and the new grade J55 microstructure in longitudinal direction, respectively. The major difference in microstructure can be identified as follows:

- The microstructure of the vintage grade J55 consisted of a network of pro-eutectoid grain boundary ferrite ( $\alpha$ -Fe), while the new grade J55 microstructure appeared as typical banded ferrite.
- The amount of pearlite in the vintage grade J55 is higher than in the new grade J55.

The difference in microstructure may reflect the difference in metallurgical processes, including:

- Difference in manufacturing process—rolling temperature, reduction rate, and cooling control.
- Difference in heat treatment—as a rule, even in the 1960s or earlier, grade J55 casing and tubing products were supplied as-rolled and were not heat treated unless necessary. For example, grade J55 casing could be heat treated to combat “ring worm” corrosion [81]. It is not clear if the vintage grade J55 was post-heat treated.
- Difference in carbon contents—the carbon content in vintage grade J55 is 13% higher than the new grade J55, which resulted in a higher amount of pearlite.

As a consequence, the performance between the vintage and new grade J55 should be significantly different.

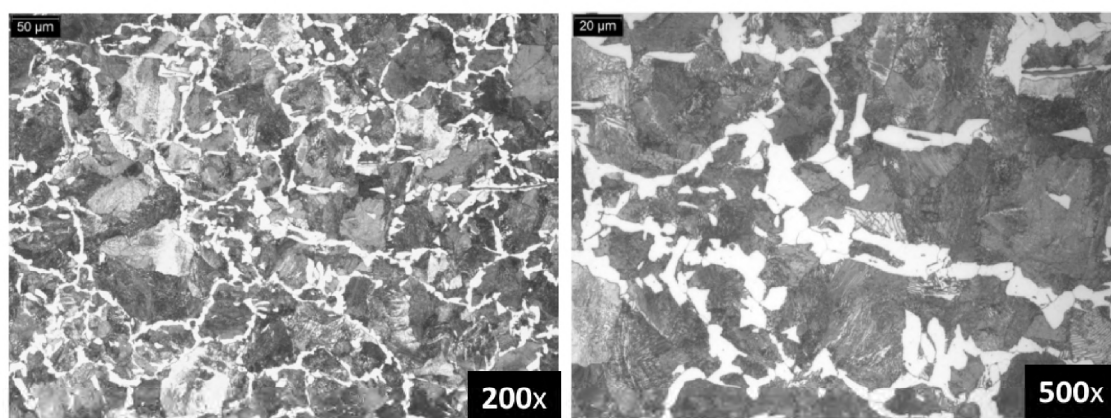


Figure 305: Vintage J55 Microstructure in the Longitudinal Direction (Joint 23)



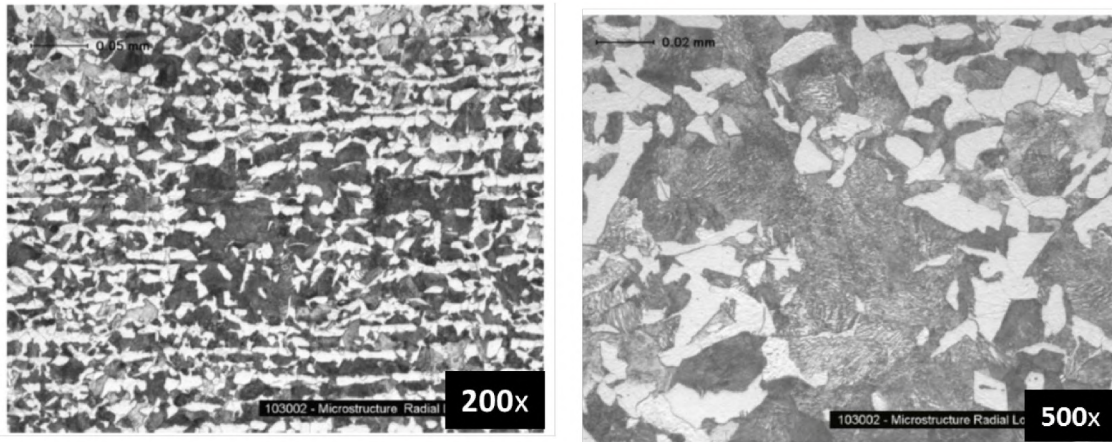


Figure 306: New J55 Microstructure in the Longitudinal Direction

### Charpy Impact Toughness

The Element CVN tests (Table 33) reported room temperature values twice as high for the new grade J55 as compared to the vintage grade J55. The difference is significant and may reflect a combined effect of the impurities content, carbon content, and microstructural difference (e.g., grain boundary ferrite).

Table 33: Vintage and New Grade J55 Charpy V-Notch Comparison

Orientation	Temperature (°C)	Number of Tests	Minimum	Maximum	Average
<b>Vintage Grade J55</b>					
Longitudinal	25	6	7	9	8.0
Transverse	25	6	5	6	5.2
<b>New Grade J55</b>					
Longitudinal	25	3	19	21	20
Transverse	25	3	17	17	16

In summary, the new grade J55 7 in. casing steel grade has a significantly higher CVN impact energy than the vintage grade J55. This improvement may be attributed to the low impurity concentration of phosphorus and sulfur, lower carbon content, and an improved microstructure. It is noted that there are some limitations to the comparison. The information on the new grade J55 is limited to the MTR and test results from one joint. On the other hand, the difference in corrosion behavior between the vintage and new grade J55 steels was not evaluated because of limited data.

### 7.1 2 7/8 in. Tubing Testing

Initial observations conducted in the field and at the warehouse suggested the tubing did not contribute to the 7 in. casing failure. Section 2.2.4 discusses the tubing field observations. The tubing OD surface appeared clean with minor features identified on some of the joints. The objective of the testing was to verify that the 2 7/8 in. tubing material properties were consistent and within specifications in place at the time of installation. Material testing for the tubing included similar tests as the 7 in. casing, with the exception of fracture toughness. Fracture toughness was not considered for the tubing.

Two hundred and forty-four tubing joints were extracted from SS-25. The tubing string consisted of six joints of grade N80 and 265 joints of grade J55 from the hangar to 8,393 ft. Section 2.1.2 describes the tubing string and provides a schematic of the well. Ten grade J55 joints and one grade N80 joint were randomly selected for material testing. A 3 ft section from the pin end of each joint was extracted for testing. The extracted material was cleaned, blasted, and inspected by MPI using the same procedures as the 7 in. casing. Superior Shot Peening performed the abrasive blasting using Black Beauty Extra Fine blasting media.

Linear indications were identified by MPI on the material extracted from joint 21 (T021B). Figure 307 (a) shows mechanical testing layouts for the joints. Figure 307 (c) and (d) show the T021B linear indications identified by MPI. The indications were aligned axially and spanned most of the 3 ft section. The mechanical testing layout was modified to avoid the linear indications. Figure 307 (b) shows a schematic of the extraction location for the tubing testing material.

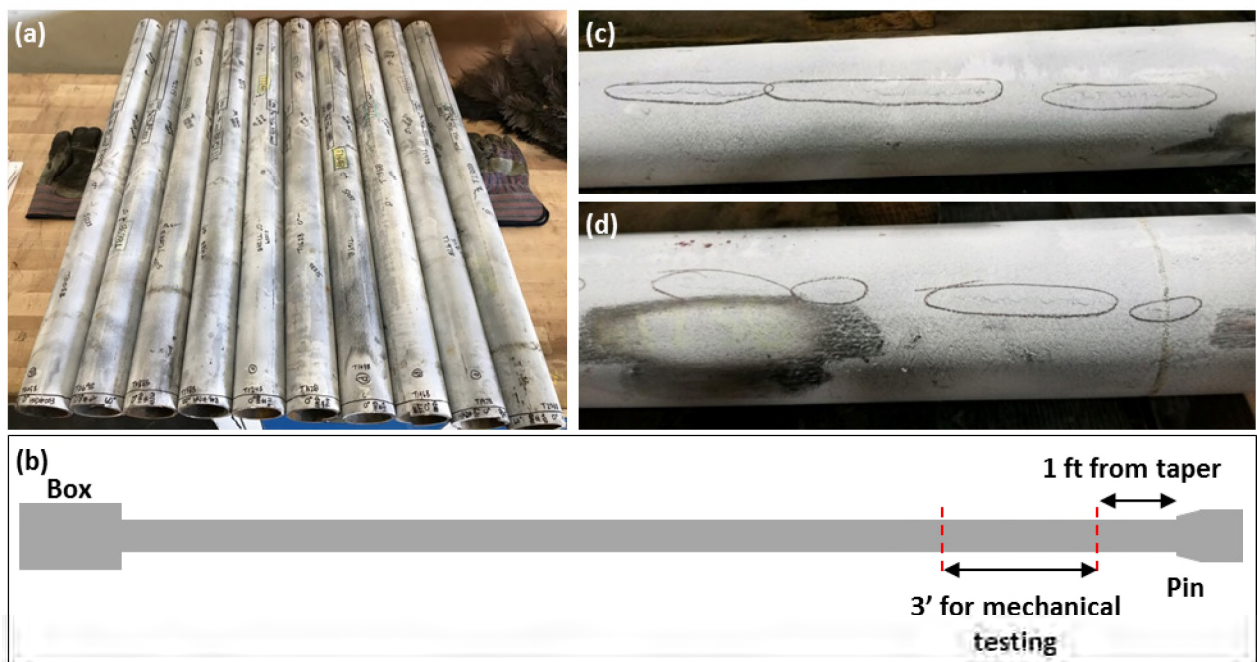


Figure 307: (a) 2 7/8 in. Layout, (b) Schematic, and (c)(d) T021B MPI Features

### 7.1.1 Chemistry

Chemistry of the joints' material was determined using OES. Three locations were analyzed for each joint. Table 34 shows the average values for each. The average content for grade N80 joints was 0.373%. This is slightly below but consistent with the typical range of 0.38-0.48%. The average carbon content for grade J55 joint was 0.40%, which is consistent with the typical range of 0.37-0.47%. The average phosphorous and sulfur content for grade N80 joint was 0.011% and 0.144%, respectively. The phosphorous content is below the maximum value of 0.04%, but the sulfur content is above the maximum allowable value of 0.06%. The average phosphorous and sulfur content for grade J55 was 0.024% and 0.03%, respectively. These values are below the maximum allowable values of 0.04% and 0.06%. The higher sulfur content identified in the grade N80 material did not contribute to the failure and was not considered significant to the failure investigation.

**Table 34: 2 7/8 in. Tubing Optical Emission Spectroscopy Results (wt%)**

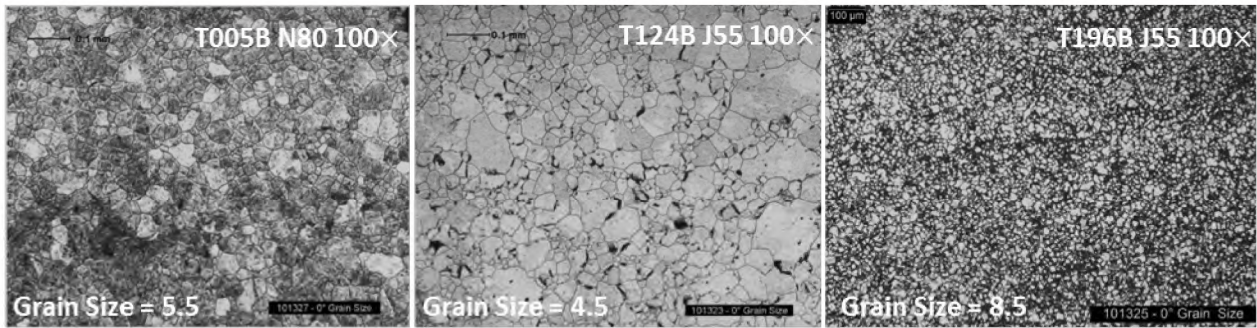
Joint	Grade	C	Mn	P	S	Si	Cr	Ni	Mo	Al	Cu	Fe
5	N80	0.373	1.127	0.011	0.144	0.160	0.010	0.060	0.010	0.010	0.060	98.005
21	J55	0.463	1.373	0.013	0.031	0.033	0.020	0.013	0.010	0.030	0.020	97.963
69	J55	0.373	1.190	0.015	0.030	0.293	0.040	0.020	0.010	0.040	0.050	97.908
88	J55	0.390	0.923	0.020	0.036	0.210	0.060	0.040	0.010	0.010	0.200	98.071
124	J55	0.403	0.847	0.022	0.031	0.187	0.050	0.030	0.010	0.013	0.140	98.238
158	J55	0.410	1.277	0.014	0.027	0.250	0.030	0.010	0.010	0.040	0.097	97.806
162	J55	0.410	1.293	0.014	0.027	0.250	0.033	0.020	0.010	0.043	0.100	97.769
164	J55	0.437	0.850	0.017	0.031	0.217	0.050	0.030	0.010	0.010	0.140	98.179
196	J55	0.433	1.280	0.015	0.028	0.247	0.033	0.013	0.010	0.040	0.100	97.770
197	J55	0.367	0.997	0.029	0.043	0.230	0.050	0.030	0.010	0.017	0.200	97.998
238	J55	0.313	0.793	0.083	0.018	0.270	0.053	0.010	0.010	0.050	0.070	98.298

### 7.1.2 Grain Size, Microcleanliness, and Microstructure

The grain size was determined based on ASTM E112 [82]. Section 7.1.3 briefly describes the ASTM method. Table 35 shows the grain size results for the 2 7/8 in. tubing. The grade N80 grain size was found to be 5.5. The grain sizes for the grade J55 joints ranged from 4.5 to 8.5 and had an average value of 6.88. The standard deviation for the grade J55 grain sizes was 1.70. Figure 308 shows grain size micrographs for the (a) 5.5 grade N80 material, (b) 4.5 grade J55 material, and (c) 8.5 grade J55 material.

**Table 35: 2 7/8 in. Tubing Grain Size Results**

Joint	Grade	Grain Size
5	N80	5.5
21	J55	8.0
69	J55	8.0
88	J55	5.0
124	J55	4.5
158	J55	8.5
162	J55	8.5
164	J55	5.0
196	J55	8.5
197	J55	6.5
238	J55	7.0



**Figure 308: Grain Size Micrographs for (a) T005B, (b) T124B, and (c) T196B Taken at 100×**

Microcleanliness was based on ASTM E45 A [83]. Section 7.1.4 briefly describes the method used to determine the microcleanliness for the tubing materials. Table 36 summarizes the results for each tubing joint. The maximum severity level for grade N80 was 2.5 for Heavy Type A. The maximum severity level for grade J55 was 2.0 for Heavy Type A. The results are consistent with MnS inclusions typical of carbon steel. Figure 309 shows micrographs of (a) T005B, (b) T124B, and (c) T196B in the polished condition at 100×. The micrographs show the MnS inclusions typical of carbon steel.

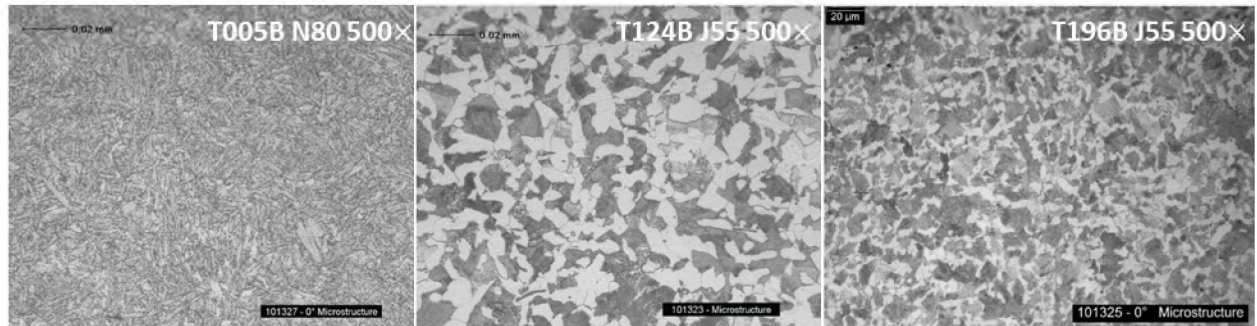
**Table 36: 2 7/8 in. Tubing Microcleanliness Results**

Series		Thin				Heavy			
Joint	Grade	Type A (Sulfide)	Type B (Alumina)	Type C (Silicate)	Type D (Globular Oxide)	Type A (Sulfide)	Type B (Alumina)	Type C (Silicate)	Type D (Globular Oxide)
5	N80	0.0	0.0	0.0	0.0	2.5	0.0	0.0	0.5
21	J55	0.0	0.0	0.0	0.5	2.0	0.0	0.0	1.0
69	J55	1.0	0.0	0.0	0.5	2.0	0.0	0.0	0.5
88	J55	0.0	0.0	0.0	0.0	2.0	0.0	0.0	1.0
124	J55	1.0	0.0	0.0	1.5	2.0	0.0	0.0	1.0
158	J55	0.0	0.0	0.0	0.0	1.5	0.0	0.0	1.0
162	J55	0.0	0.0	0.0	0.0	1.5	0.0	0.0	1.0
164	J55	1.0	0.0	0.0	0.5	2.0	0.0	0.0	1.0
196	J55	1.0	0.0	0.0	0.5	2.0	0.0	0.0	1.0
197	J55	0.0	0.0	0.0	0.0	1.0	0.0	0.0	1.5
238	J55	0.0	0.0	0.0	0.0	1.5	0.0	0.0	1.5



**Figure 309: Microcleanliness Micrographs for (a) T005B, (b) T124B, and (c) T196B Taken at 100×**

The microstructure was evaluated for the selected tubing joints. Specimens were etched with 3% Nital, and micrographs were taken at 200× and 500×. Micrographs of the grade N80 material revealed tempered martensite. Micrographs of the grade J55 material revealed ferrite and pearlite. These observations are consistent with typical grades N80 and J55 microstructures. Figure 310 shows examples of the microstructure micrographs for grades (a) N80 and (b)(c) J55 material.



**Figure 310: Microstructural Micrographs for (a) T005B, (b) T124B, and (c) T196B Taken at 500×**

### 7.1.3 Tensile

Element conducted tensile testing per ASTM A370 [84]. Table 37 shows a summary of the tensile testing results. Blade calculated the reduction in area following the procedure discussed in Section 7.1.6. The remaining tensile properties were reported by Element. Tensile properties reported in Table 37 are for grade J55 (except joint 5, which is grade N80 material).

The overall minimum, maximum, and average yield strength values for the grade J55 2 7/8 in. tubing material were 61,000, 77,500, and 70,133 psi, respectively. The minimum yield strength was above the minimum allowed value of 55,000 psi. The overall minimum, maximum, and average UTS values were 99,500, 121,000, and 108,783 psi, respectively. The minimum UTS was also above the minimum allowed value of 75,000 psi. The reported percent elongation values ranged from 18% to 26% and had an average value of 21.6%. Five joints reported values below the minimum allowable elongation of 20%, however the average elongation was above the limit. The elongation percentages appeared to be consistent and did not contribute to the failure.

The minimum, maximum, and average tensile properties for grade N80 (joint 5) were also reported in Table 37. The minimum values for 0.5% EUL, UTS, and percent elongation were all above the allowed minimums.

**Table 37: 2 7/8 in. Tubing Flat Grip Tensile Results**

Joint	0.5% EUL (psi)			Ultimate Tensile Strength (psi)			Elongation (%)			Reduction in Area (%)		
	Min	Max	Avg	Min	Max	Avg	Min	Max	Avg	Min	Max	Avg
5	90,500	93,000	91,833	105,000	108,000	106,667	19	24	21.0	49	56	53.2
21	70,500	72,000	71,500	112,000	115,000	113,333	24	26	24.7	39	48	43.8
69	71,000	77,500	74,167	113,000	121,000	118,000	19	23	21.0	43	46	44.8
88	67,500	69,500	68,500	99,500	103,000	100,833	18	21	19.3	36	46	41.0
124	69,500	72,000	70,333	105,000	107,000	106,000	20	24	22.3	40	43	41.0
158	70,500	71,000	70,667	112,000	113,000	112,333	21	22	21.7	47	50	48.7
162	69,000	72,000	70,500	109,000	112,000	110,667	22	23	22.3	48	50	49.4
164	70,500	72,500	71,333	105,000	108,000	106,000	19	22	20.3	36	41	39.0
196	70,500	72,500	71,500	111,000	112,000	111,667	21	22	21.7	44	48	46.3
197	69,000	71,000	70,000	105,000	106,000	105,667	19	22	20.0	34	36	35.0
238	61,000	64,000	62,833	102,000	104,000	103,333	22	23	22.7	39	42	40.5

### 7.1.4 Hardness

Element conducted hardness testing for the 2 7/8 in. tubing per ASTM E384 [96] and ASTM E18 [85]. ASTM E384 [96] describes the standard test method for microindentation hardness testing. ASTM E18 [85] describes the standard test method for Rockwell hardness testing. Through-wall hardness values were not acquired using the HRB scale due to the size limitations imposed by the wall thickness. Hardness testing has spacing requirements for indentations in relation to adjacent indentations and the specimen edge. The HRB scale could not be used because the indenter size did not permit three indentations from the ID to the OD based on the spacing requirements.

Blade selected Vickers microhardness to analyze the through-wall hardness values for joints 5 and 88. Joints 5 and 88 were selected as a representative sample for grades N80 and J55, respectively. Vickers microhardness uses a smaller indenter that allowed for three indentations from the ID to OD. Table 38 shows the Vickers microhardness results for both joints with the min, max, and average values of the four quadrants for the OD, MW, and ID. The hardness was consistent from the ID to the OD for both grades N80 and J55 material. The remaining joints were tested using the HRB indenter at the MW.

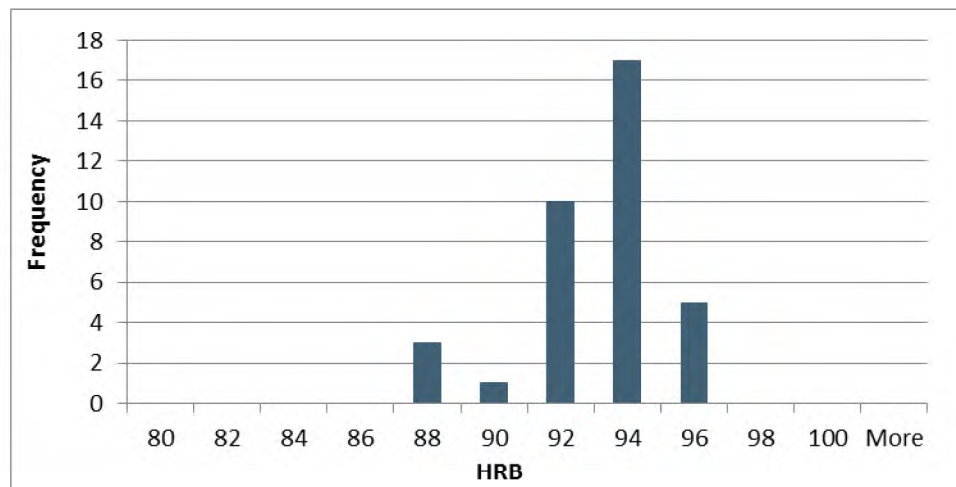
Table 39 shows the HRB results for the remaining grade J55 specimens—the values ranged from 88 to 96 HRB, and the average value was 93.5 HRB. Figure 311 shows a histogram of the HRB values. The distribution appears to be normal, with a standard deviation of 2.0 HRB. The results show consistent HRB values for the sampled grade J55 joints, with no hardness anomalies.

**Table 38: 2 7/8 in. Tubing Vickers Hardness Results**

Joint	Grade	Outside Diameter			Mid-Wall			Inside Diameter		
		Min	Max	Avg	Min	Max	Avg	Min	Max	Avg
5	N80	231	243	236.4	227	237	231.7	229	240	235.2
88	J55	201	214	208.8	200	212	205.8	201	214	207.9

**Table 39: 2 7/8 in. Tubing Hardness Rockwell B Results**

Joint	Grade	Mid-Wall		
		Min	Max	Avg
21	J55	88	95	92.1
69	J55	88	95	92.1
124	J55	91	96	94.0
158	J55	92	96	94.7
162	J55	94	96	95.0
164	J55	93	96	94.5
196	J55	92	96	93.8
197	J55	92	96	94.3
238	J55	88	92	90.8
<b>Totals</b>		<b>88</b>	<b>96</b>	<b>93.5</b>



**Figure 311: Hardness Rockwell B Distribution for J55 Joints**

### 7.1.5 Charpy V-Notch

Element performed CVN testing for the 2 7/8 in. tubing per ASTM E23 [86]. Testing was conducted on quarter-size specimens due to the size limitations imposed by the pipe wall thickness. The tubing was tested at a single temperature; the DBTT curves were not constructed. Testing was conducted at 0°C for comparison with the 7 in. casing. Toughness was not a concern for the tubing because the tubing did not fracture and did not contribute to the 7 in. casing failure. CVN was conducted to verify the properties of the grades N80 and J55 material. Table 40 shows the CVN results for the 2 7/8 in. tubing.

**Table 40: 2 7/8 in. Charpy V-Notch Results**

Joint	Grade	Impact Energy			Lateral Expansion			Percent Shear		
		Min	Max	Avg	Min	Max	Avg	Min	Max	Avg
5	N80	14	16	15.0	22	45	36.3	100	100	100.0
21	J55	8	10	8.7	18	23	20.7	60	80	70.0

Joint	Grade	Impact Energy			Lateral Expansion			Percent Shear		
		Min	Max	Avg	Min	Max	Avg	Min	Max	Avg
69	J55	5	8	7.0	11	23	18.3	40	90	70.0
88	J55	6	10	8.3	17	21	19.7	60	100	83.3
124	J55	3	4	3.3	10	11	10.7	10	20	13.3
158	J55	11	13	11.7	17	24	21.3	100	100	100.0
162	J55	12	13	12.7	14	17	15.3	100	100	100.0
164	J55	4	5	4.3	7	10	8.3	10	20	13.3
196	J55	11	13	12.3	14	16	15.0	100	100	100.0
197	J55	6	8	6.7	15	16	15.7	40	60	53.3
238	J55	4	5	4.3	11	14	12.3	20	20	20.0

## 7.2 11 3/4 in. Casing Testing

The 11 3/4 in. casing material testing was limited to a 2 ft section extracted from the top of the string. The 11 3/4 in. casing string could not be extracted due to safety risks and a risk to damaging the evidence during the extraction procedures.

### 7.2.1 Chemistry

Element performed OES analysis at three locations on the 11 3/4 in. casing sample. Table 41 shows the OES results for each of the three locations. The average phosphorus and sulfur are 0.011% and 0.025%, respectively. These are below the API 5A 18<sup>th</sup> Edition [80] maximum requirements of 0.04% and 0.06%. The average carbon and manganese contents are 0.373% and 0.650%, respectively. These values are consistent with the typical values of 0.27–0.37% and 0.70–1.00% presented in Table 19.

**Table 41: 11 3/4 in. Casing Optical Emission Spectroscopy Results (wt%)**

ID	C	Mn	P	S	Si	Cr	Ni	Mo	Al	Cu	Fe
1	0.370	0.650	0.010	0.020	0.040	0.050	0.030	0.010	0.010	0.100	98.710
2	0.400	0.650	0.011	0.021	0.040	0.050	0.030	0.010	0.010	0.100	98.678
3	0.350	0.650	0.011	0.035	0.040	0.050	0.030	0.010	0.010	0.100	98.714
Avg	0.373	0.650	0.011	0.025	0.040	0.050	0.030	0.010	0.010	0.100	98.701

### 7.2.2 Grain Size, Microcleanliness, and Microstructure

Element measured the grain size for the 11 3/4 in. casing. The results for the three locations were 2.5, 2.5, and 2.0 resulting in an average value of 2.33. Figure 312 shows micrographs from the three locations taken at 100×. The micrographs show a consistently coarse grain size.

Figure 313 shows the micrographs of the polished specimens used for the microcleanliness investigation. Table 42 summarizes the results from three locations. The severity levels were low for all four Types. The highest severity occurred in Type A, which most likely corresponded to manganese sulfides. Figure 314 shows microstructural micrographs taken from three different locations. The specimens were etched with 4% picral to reveal the microstructure. The images show a typical pearlite–ferrite microstructure.



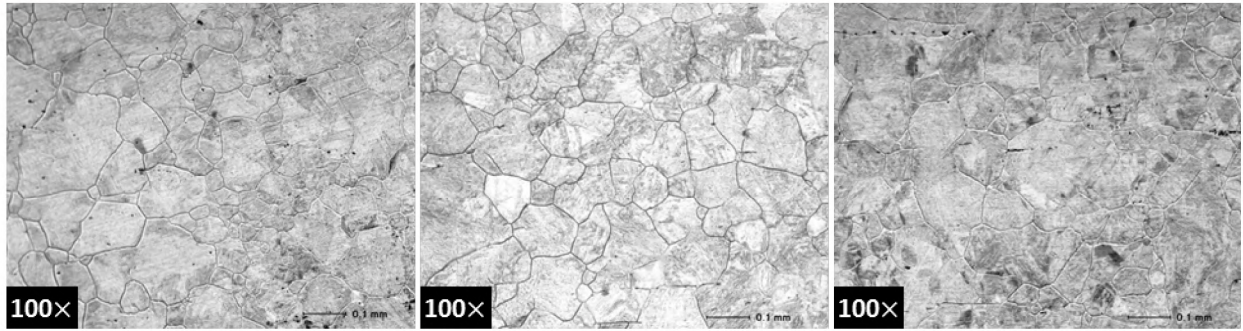


Figure 312: 11 3/4 in. Casing Grain Size Micrographs Taken at 100×

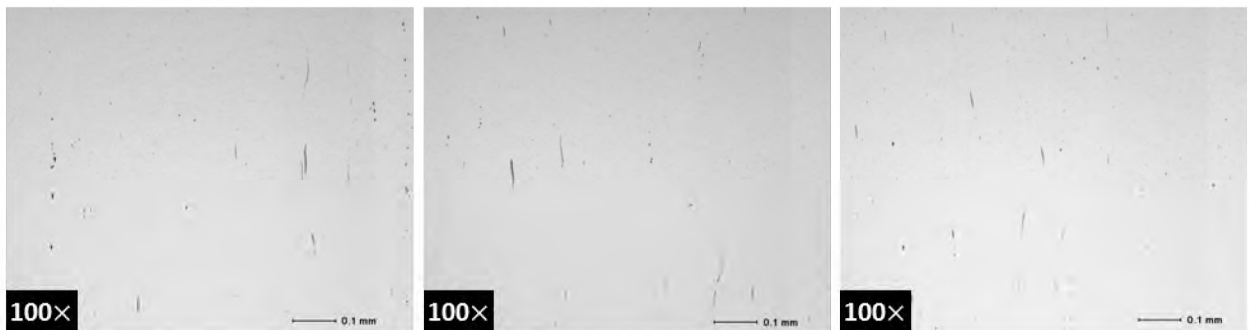


Figure 313: 11 3/4 in. Casing Micrographs from Three Locations Taken at 100×

Table 42: 11 3/4 in. Casing Microcleanliness Results

Series	Thin				Heavy			
	Type A (Sulfide)	Type B (Alumina)	Type C (Silicate)	Type D (Globular Oxide)	Type A (Sulfide)	Type B (Alumina)	Type C (Silicate)	Type D (Globular Oxide)
1	1.50	0.00	0.00	1.00	1.00	0.50	0.00	0.50
2	1.50	0.00	0.00	1.00	1.00	0.50	0.00	0.50
3	1.50	0.00	0.00	1.00	1.00	0.50	0.00	0.50
<b>Avg</b>	<b>1.50</b>	<b>0.00</b>	<b>0.00</b>	<b>1.00</b>	<b>1.00</b>	<b>0.50</b>	<b>0.00</b>	<b>0.50</b>

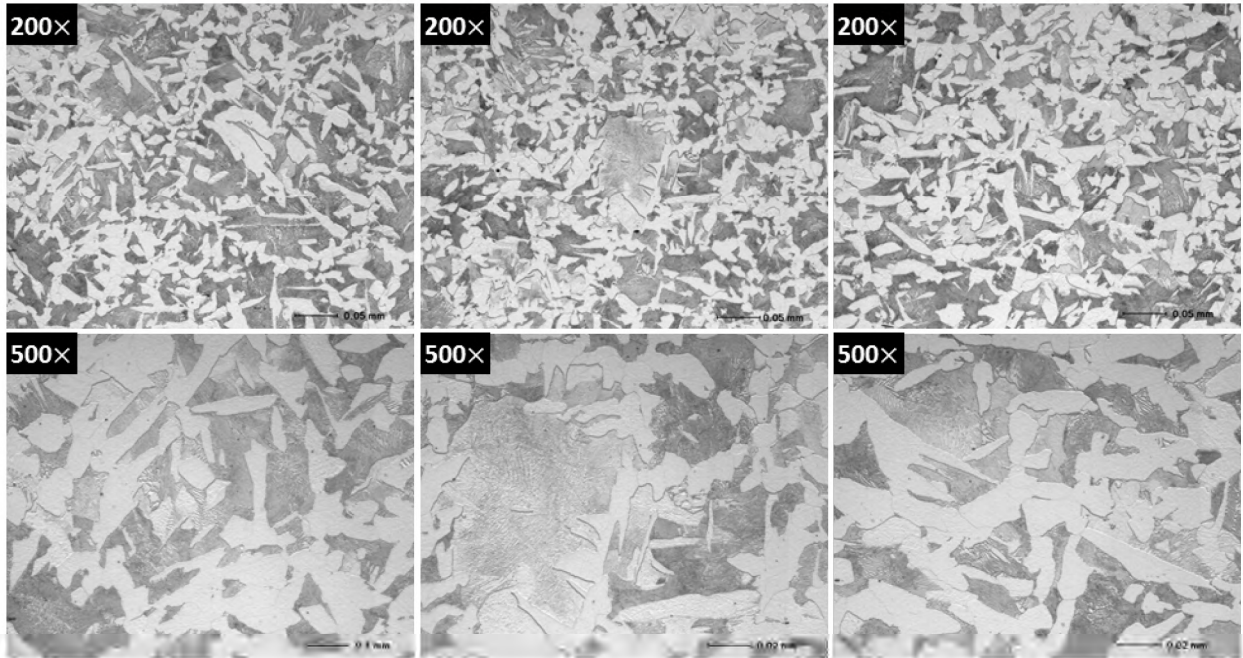


Figure 314: 11 3/4 in. Casing Microstructural Micrographs Etched and Taken at 200x and 500x

### 7.2.3 Tensile

Element performed tensile testing per ASTM A370 [84]. Table 43 is a summary of the results. The average 0.5% EUL and UTS are 48,533 psi and 84,000 psi, respectively. These are greater than the API 5A 18<sup>th</sup> Edition [80] minimum requirements of 40,000 psi and 60,000 psi. Percent elongation for specimen 181 was 26%, which is slightly below the API 5A 18<sup>th</sup> Edition [80] minimum requirement of 27%. This is not significant and did not contribute to the failure.

Table 43: 11 3/4 in. Tensile Results

Specimen ID	0.5% EUL (psi)	Ultimate Tensile Strength (psi)	Elongation (%)	Reduction in Area (%)
181	49,200	86,000	26	20
182	49,600	83,500	30	31
183	47,900	82,500	32	29

### 7.2.4 Hardness

Element performed HRB testing per ASTM E18 [85]. A hardness ring was extracted from the 11 3/4 in. casing. Triplicate indentations were made at the OD, MW, and ID at four quadrants. Table 44 shows the results from the HRB testing—they are consistent both through-wall and around the circumference. The average HRB value for the OD, MW, and ID was 83, 82, and 81, respectively.

Table 44: 11 3/4 in. Hardness Rockwell B Results

Quadrant	Indentation	OD	MW	ID
1	1	82	81	80
1	2	82	82	81
1	3	82	81	80
2	1	82	81	80
2	2	82	81	80
2	3	81	81	79
3	1	82	82	82
3	2	82	82	81
3	3	81	81	81
4	1	85	86	87
4	2	86	84	84
4	3	86	85	85

### 7.2.5 Charpy V-Notch

Element performed CVN testing on half-size specimens per ASTM E23 [86]. Testing was performed at five temperatures (100, 75, 45, 0, and -50°C) and two orientations (L-C and C-L). Table 45 shows the Charpy results. The impact energy values are higher for both orientations as compared to the 7 in. casing.

Table 45: 11 3/4 in. Charpy V-Notch Results

Temperature (°C)	Orientation	Impact Energy (ft-lb)	Lateral Expansion (mil)	Percent Elongation (%)
100	L-C	50.7	50.0	100.0
75	L-C	51.3	50.0	100.0
45	L-C	44.0	42.3	86.7
0	L-C	14.0	17.3	10.0
-50	L-C	2.7	4.3	10.0
100	C-L	34.0	40.7	100.0
75	C-L	32.7	39.0	100.0
45	C-L	34.0	37.7	100.0
0	C-L	10.7	13.3	10.0
-50	C-L	2.7	4.7	10.0

## 8 Conclusions

---

A blowout of the SS-25 well occurred on October 23, 2015. Logging identified that the 7 in. casing was potentially parted at 892 ft. Temperature logs during the blowout showed a cold temperature anomaly at the suspected failure location. The downhole camera confirmed that the 7 in. casing had parted at joint 22 (approximately 892 ft). A total of twenty-five 7 in. casing joints were extracted from the well, including the failed casing segments. Visual inspection of the failed casing segments showed that both an axial rupture and a circumferential parting had occurred.

Examination of the failed joint showed that the axial rupture originated from an 85% metal loss due to corrosion. The internal pressure inside the 7 in.  $\times$  2 7/8 in. annulus caused slow ductile tearing of the thinnest region. The unstable crack propagation, after ductile tearing, resulted in a 2 ft long axial rupture. The release of cold gas [11] from the opening formed by the axial rupture resulted in rapid cooling of the adjacent casing material. The rapid cooling resulted in the circumferential parting, which comprised an initiation, a propagation of a circumferential crack, followed by a final overload failure.

The corrosion causing the axial rupture was characterized by striated grooves with V-shaped tips. A distinct zone of severe corrosion was identified with laser scan and logging data beginning at 700 ft and extending below the 11 3/4 in. casing shoe (990 ft). Observations during the visual inspection showed that corrosion with a similar morphology (striated grooves with V-shaped tips) as the axial rupture corrosion feature began at 700 ft. Corrosion was observed above 700 ft but was less severe and did not contain striated grooves with V-shaped tips. The ID surface of the 11 3/4 in. casing shared the same environment as the OD surface of the 7 in. casing. Logging of the 11 3/4 in. casing confirmed the corrosion zone to be between 700 and 990 ft. Visual inspection with a downhole camera suggested that the corrosion on the ID surface of the 11 3/4 in. casing appeared to be similar to the 7 in. corrosion, which contained striated grooves. Other features, such as localized pitting and crevice corrosion with possible galvanic effects, were also observed on the OD surface of the 7 in. casing during visual inspection; however, these features were not related to the failure of the 7 in. casing and were not limited to below 700 ft.

The corrosion features with striated grooves contained tunnels that penetrated longitudinally into the base metal from the V-shaped tips. Characterization of the OD scale and the corrosion deposits inside the tunnels confirmed the presence of iron oxides and organic matter. Extra-cellular material, which is normally associated with the activities of microbes, was found in the developing tunnel. DNA-based amplicon metagenomics confirmed high amounts of methanogens on the OD surface of joint 24 of the 7 in. casing. Literature data indicated that methanogens can influence the corrosion of steel. The corrosion feature containing striated grooves with V-shaped tips was most likely MIC.

Material testing from the twenty-five 7 in. casing joints from SS-25 well showed that the chemistry, grain size, microcleanliness, microstructure, tensile, and hardness were consistent with the vintage grade J55 properties. CVN and fracture toughness tests were conducted, and the results were used for FEA and fracture mechanics analysis. FEA was used to estimate the failure pressure of the 7 in. casing axial rupture based on the geometry from the corrosion feature and striated grooves.

Three models were used to predict failure pressure. The first model represented the 9.25 in.  $\times$  3.72 in. and 85% deep corrosion feature without striated grooves. The model predicted a differential pressure of 3,850 psi, which is above the estimated differential pressure (2,405 psi) at the time of the failure. The other two models incorporated notches to simulate the effects of the striated grooves. These models predicted differential pressures of 2,327–2,836 psi, which were reasonably consistent with the estimated differential failure pressure. The models also showed bulging in the corrosion feature consistent with the field observations. Two possible initiation sizes were identified during the metallurgical investigation of

the circumferential parting. The failure temperature for the circumferential parting was estimated based on fracture mechanics as per API 579 and BS 7910. The results suggested that the circumferential parting would occur at temperatures between  $-60^{\circ}\text{C}$  and  $-39^{\circ}\text{C}$ . This is consistent with the thermal model, which estimated a failure temperature of  $-34^{\circ}\text{C}$ . Charpy toughness results indicated that the grade J55 material (7 in. casing) had a high full-size impact energy DBTT of approximately  $53.6^{\circ}\text{C}$ . This is consistent with the observation that the 7 in. casing circumferentially parted in a brittle manner when the material reached a temperature between  $-60^{\circ}\text{C}$  and  $-39^{\circ}\text{C}$ .

The metallurgical investigation of the circumferential parting showed that a circumferential crack formed, which left behind a final ligament. FEA was used to evaluate if the final ligament could have sustained the axial force. A helical circumferential crack was modeled based on dimensions measured in the lab. The model became unstable at 128 kbf (54% of the total axial force), indicating that the ligament would have failed due to the axial force. This is consistent with the proposed sequence of events based on metallurgical observations.

In summary, an interdisciplinary approach was used for the investigation, including metallurgical, mechanical, chemical, and biological analyses. This interdisciplinary failure investigation established that an axial rupture occurred in the SS-25 7 in. casing due to an 85% deep corrosion on the OD surface, most likely influenced by microbes. Rapid cooling due to the release of cold gas from the axial rupture led to the circumferential parting.

## 9 References

---

- [1] Blade Energy Partners, "Aliso Canyon RCA Phase 4 Protocol for Metallurgical Investigation of the SS-25 Failure," Houston, TX, 2018.
- [2] Blade Energy Partners, "Aliso Canyon RCA SS-25 Site Evidence Collection and Documentation Protocol," Houston, TX, 2017.
- [3] Blade Energy Partners, "Phase 1 Summary," Houston, TX, 2019.
- [4] Blade Energy Partners, "Aliso Canyon RCA: SS-25 Phase 3 Tubing, Casing, Wellhead Extraction Protocol," Houston, TX, 2017.
- [5] Blade Energy Partners, "Aliso Canyon RCA: SS-25 Phase 3 Wellsite Tubulars Handling Protocol," Houston, TX, 2017.
- [6] Blade Energy Partners, "Phase 3 Summary," Houston, TX, 2019.
- [7] Blade Energy Partners, "Phase 4 Summary," 2019.
- [8] Blade Energy Partners, "SS-25 7 in. Speedtite Connection Testing and 11 3/4 in. STC Assessment," Houston, TX, 2019.
- [9] Blade Energy Partners, "SS-25 Transient Kill Analysis," Houston, TX, 2019.
- [10] Blade Energy Partners, "SS-25 Temperature, Pressure, and Noise Log Analysis," Houston, TX, 2019.
- [11] Blade Energy Partners, "Analysis of the Post-Failure Gas Pathways and Temperature Anomalies at the SS-25 Site," Houston, TX, 2019.
- [12] Blade Energy Partners, "Aliso Canyon RCA: Phase 1 Versa-Line MID Validation Report," Houston, TX, 2019.
- [13] Blade Energy Partners, "Phase 2 Summary," Houston, TX, 2019.
- [14] Blade Energy Partners, "SS-25 2 7/8 in. Tubing Field Documentation," Houston, TX, 2019.
- [15] Blade Energy Partners, "SS-25 Inspection Log Analysis," Houston, TX, 2019.
- [16] Blade Energy Partners, "SS-25 7 in. Casing Documentation," Houston, TX, 2019.
- [17] T. L. Anderson, *Fracture Mechanics Fundamentals and Applications*, 2nd ed., Boca Raton, FL: CRC Press, 2004.
- [18] M. Janssen, J. Zuidema and R. Wanhill, *Fracture Mechanics*, Delft, The Netherlands: VSSD, 2002-2006.
- [19] ASM International, *ASM Handbook Vol. 11 Failure Analysis and Prevention*, Materials Park, Ohio, USA: ASM International, 2011.
- [20] ASM International, *ASM Handbook Vol. 12 Fractography*, ASM, 9th Edition, 1987.
- [21] G. M. Boyd, "The Propagation of Fractures in Mild Steel Plates," *Engineering*, vol. 175, no. 16 Jan and 23 Jan, pp. pp 65-69, pp100-102, 1953.
- [22] Alconox, Inc., "Citranox Technical Bulletin," Alconox, Inc, 2018.
- [23] *ASM Handbook Volume 9 Metallography and Microstructure*, 9 ed., Materials Park, OH: ASM International, 2013.
- [24] A. Ghosh, P. Modak, R. Dutta and D. Chakrabarti, "Effect of MnS Inclusions and Crystallographic Texture on Anisotropy in Charpy Impact Toughness of Low Carbon Steel," *Materials Science and Engineers A*, pp. 298-308, 2016.

- [25] J. Chen and R. Cao, *Micromechanism of Cleavage Fracture of Metals - A Comprehensive Microphysical Model for Cleavage Cracking in Metals*, Elsevier Inc., 2015.
- [26] J. M. Barsom and S. T. Rolfe, ASTM STP 466, p.281, Philadelphia: ASTM, 1970.
- [27] American Petroleum Institute, *Fitness-For-Service*, API 579 Washington, DC: API Publishing Services, 2007.
- [28] J. W. Hancock and A. C. McKenzie, "On the Mechanisms of Ductile Failure in High-Strength Steels Subjected to Multi-axial Stress-states," *Journal of Mechanical and Physical Solids*, vol. 24, pp. 147-169, 1976.
- [29] J. R. Rice and D. M. Tracey, "On the Ductile Enlargement of Voids in Tri-axial Stress Fields," *Journal of Mechanical and Physical Solids*, vol. 17, pp. 201-217, 1969.
- [30] British Standards Institute, *Guide to Methods for Assessing the Acceptability of Flaws in Metallic Structures*, BSI Standards Limited, 2015.
- [31] "Standard Test Method for Linear-Elastic Plane-Strain Fracture Toughness K<sub>IC</sub> of Metallic Materials," ASTM E399, 2009.
- [32] *Standard Test Method for Measurement of Fracture Toughness*, ASTM E1820, 2011.
- [33] F. Reif, Chapter 5 - Simple Application of Macroscopic Thermodynamics Fundamentals of Statistical and Thermal Physics, McGraw-Hill, 1965.
- [34] H. Herro, "MIC Myths- Does Pitting Cause MIC?," in *Corrosion*, San Diego, CA, 1998.
- [35] D. Pope, *Microbiologically Influenced Corrosion (MIC): Methods of Detection in the Field*, Chicago, IL: Gas Research Institute, 1990.
- [36] H. Li, D.-w. Zhao, G.-s. Zhu, C.-l. Bao and J. Yang, "Influence of Inclusions on Impact Properties of J55 Steel," *Journal of Iron and Steel Research International*, vol. 22, no. Supplement 1, pp. 36-41, 2015.
- [37] M. Ueda and H. Takabe, "Effect of Environmental Factor and Microstructure on Morphology of Corrosion Products in CO<sub>2</sub> Environments," in *Corrosion*, San Antonio, TX, 1999.
- [38] Premier Oilfield Group, "Technical Services Report Raman Consultation Samples SS-25," Houston, TX, 2019.
- [39] M. Morcillo, B. Chico, J. Alcantara, I. Diaz, R. Wolthuis and D. de la Fuente, "SEM/Micro-Raman Characterization of the Morphologies of Marine Atmospheric Corrosion Products Formed on Mild Steel," *Journal of The Electrochemical Society*, vol. 163, no. 8, pp. C426-C439, 2016.
- [40] J. Alcantara, B. Chico, D. Diaz, D. de la Fuente and M. Morcillo, "Airborne Chloride Deposit and its Effect on Marine Atmospheric Corrosion of Mild Steel," *Corrosion Science*, vol. 97, pp. 74-88, 2015.
- [41] M. Morcillo, D. de la Fuente, I. Diaz and y. H. Cano, "Atmospheric Corrosion of Mild Steel," *Revista de Metalurgia*, vol. 47, no. 5, pp. 426-444, 2011.
- [42] K. Usher, A. Kaksonen, I. Cole and D. Marney, "Critical Review: Microbially Influenced Corrosion on Buried Carbon Steel Pipes," *International Biodeterioration and Biodegradation*, vol. 93, pp. 84-106, 2014.
- [43] L. L. Machuca, K. Lepkova and A. Petroski, "Corrosion of Carbon Steel in the Presence of Oilfield Deposit and Thiosulphate-Reducing Bacteria in CO<sub>2</sub> Environment," *Corrosion Science*, vol. 129, pp. 16-25, 2017.
- [44] B. J. Little and J. S. Lee, "Microbiologically Influenced Corrosion," in *Oil and Gas Pipelines Integrity and Safety Handbook*, Hoboken, NJ, John Wiley & Sons, 2015, pp. 387-398.

- [45] K. M. Al-Nabulsi, F. M. A-Abbas, T. Y. Rizk and A. E. M. Salameh, "Microbiologically Assisted Stress Corrosion Cracking in the Presence of Nitrate Reducing Bacteria," *Engineering Failure Analysis*, vol. 58, pp. 165-172, 2015.
- [46] F. Jacob, "The Role of Sulfur Oxidizing Bacteria on Corrosion of X65 Low carbon Steels and Its Mitigation Using Sodium Tungstate and Nickel Biocides," African University of Science and Technology, Abuja, Nigeria, 2013.
- [47] Premier Oilfield Group, "Technical Services Report Well SS-25 Scale Characterization," Houston, TX, 2019.
- [48] Blade Energy Partners, "Aliso Canyon Field: Hydrology," Houston, TX, 2019.
- [49] J. Fichter, E. Summer, C. Janes and G. Hamblen, "Direct Comparison of Microbial Population Analysis using ATP Quantification, Culture Based Enumeration in Bug Bottles, Epifluorescence Microscopy and Shotgun Population Analysis by Sequencing 16S Amplicons," in *Corrosion*, Houston, TX, 2015.
- [50] Ecolyse, Inc., "Microbial Population Analysis of Well SS25 7" Casing Samples: 170721\_LA5 WellSS25 7" Casing Samples," College Station, TX, 2019.
- [51] Blade Energy Partners, "SS-25 Analysis of Microbial Organisms on 7 in. Production Casing," Houston, TX, 2019.
- [52] H. Dinh, J. Kuever, M. MuBmann, A. Hassel, M. Stratmann and F. Widdel, "Iron Corrosion by Novel Anaerobic Microorganisms," *Nature*, vol. 427, pp. 829-832, 2004.
- [53] L. Daniels, N. Belay, B. Rajagopal and P. Weimer, "Bacterial Methanogenesis and Growth from CO<sub>2</sub> with Elemental Iron as Sole Source of Electrons," *Science*, pp. 509-511, 1987.
- [54] J. Larsen, K. Rasmussen, H. Pedersen, K. Sorensen, T. Lundgaard and T. Skovhus, "Consortia of MIC Bacteria and Archaea Causing Pitting Corrosion in Top Side Oil Production Facilities," in *Corrosion*, Houston, TX, 2010.
- [55] T. Zhang and H. K. B. Fang, "Methanogen Population in a Marine Biofilm Corrosive to Mild Steel," *Applied Microbiology and Biotechnology*, vol. 63, pp. 101-106, 2003.
- [56] R. Liang, R. Grizzle, K. Duncan, M. McInerney and J. Suflita, "Roles of Thermophilic Thiosulfate-Reducing Bacteria and Methanogenic Archaea in the Biocorrosion of Oil Pipelines," *Frontiers in Microbiology*, vol. 5, p. 89, 6 March 2014.
- [57] J. Mand, H. Park, T. Jack and G. Voordouw, "The Role of Acetogens in Microbially Influenced Corrosion of Steel," *Frontiers in Microbiology*, 03 June 2014.
- [58] J. Mand, H. Park, C. Okoro, B. Lomans, S. Smith, L. Chiejina and G. Voordouw, "Microbial Methane Production Associated with Carbon Steel Corrosion in a Nigerian Oil Field," *Frontiers in Microbiology*, 11 January 2016.
- [59] J. Tan, P. Goh and D. Blackwood, "Influence of H<sub>2</sub>S Producing Chemical Species in Culture Medium and Energy Source Starvation on Carbon Steel Corrosion Caused by Methanogens," *Corrosion Science*, vol. 119, pp. 102-111, 2017.
- [60] J. Tan, *The Role of Methanogens in Microbiologically Influenced Corrosion*, Singapore: National University of Singapore, 2017.
- [61] D. Blackwood, "An Electrochemist Perspective of Microbiologically Influenced Corrosion," *Corrosion and Materials Degradation*, vol. 1, pp. 59-76, August 2018.
- [62] D. A. Jones, *Principles and Prevention of Corrosion* 2nd ed., Upper Saddle River, NJ: Prentice Hall, Inc., 1996.



- [63] R. G. Kelly and J. S. Lee, "Localized Corrosion: Crevice Corrosion," in *Encyclopedia of Interfacial Chemistry: Surface Science and Electrochemistry*, Elsevier, 2018, pp. 291-301.
- [64] B. J. Little and J. S. Lee, *Microbiologically Influenced Corrosion*, Hoboken, NJ: Wiley & Sons, 2007.
- [65] Materials Research Company, LLC, "A Report on Corrosion Tests of J55 and H40 Steel Pipe in Simulated Groundwater and Artificial Seawater," Houston, TX, 2019.
- [66] *Detection, Testing, and Evaluation of Microbiologically Influenced Corrosion on Internal Surfaces of Pipelines*, NACE TM0212-2018, 2018.
- [67] *Detection, Testing and Evaluation of Microbiologically Influenced Corrosion (MIC) on External Surfaces of Buried Pipelines*, NACE TM0106-2016, 2016.
- [68] B. Little, J. Lee and R. Ray, "Diagnosing Microbiologically Influenced Corrosion: A State-of-the-Art Review," *Corrosion*, vol. 62, no. 11, pp. 1006-1017, 2006.
- [69] J. S. Lee and B. J. Little, "Diagnosing Microbiologically Influenced Corrosion," in *Microbiologically Influenced Corrosion in the Upstream Oil and Gas Industry*, Boca Raton, FL, CRC Press, 2017, pp. 157-175.
- [70] B. J. Little, P. Wagner and Z. Lewandowski, "The Role of Biomineralization in Microbiologically Influenced Corrosion," in *Corrosion*, San Diego, CA, 1998.
- [71] H. Almahadmedh, J. Spear, D. Olson, C. Williamson and B. Mishra, "Identification of Microorganisms and Their Effects on Corrosion of Carbon Steels Pipelines," in *Corrosion*, Houston, TX, 2011.
- [72] T. Rao, T. Sairam, B. Viswanathan and K. Nair, "Carbon Steel Corrosion by Iron Oxidizing and Sulphate Reducing Bacteria in Freshwater Cooling System," *Corrosion Science*, vol. 42, no. 8, pp. 1417-1431, 2000.
- [73] I. Matsushima, "Carbon Steel- Corrosion in Freshwaters," in *Uhlig's Corrosion Handbook Third Ed.*, Hoboken, NJ, John Wiley & Sons, 2011, pp. 589-600.
- [74] I. Matsushima, "Carbon Steel- Corrosion by Seawater," in *Uhlig's Corrosion Handbook Third Ed.*, Hoboken, NJ, John Wiley & Sons, 2011, pp. 601-607.
- [75] I. Matsushima, "Carbon Steel- Corrosion by Soils," in *Uhlig's Corrosion Handbook Third Ed.*, Hoboken, NJ, John Wiley & Sons, 2011, pp. 609-613.
- [76] F. AlAbbas, C. Williamson, S. Bhola, J. Spear, O. D.L., B. Mishra and A. Kakpovbia, "Microbial Corrosion in Linepipe Steel Under the Influence of a Sulfate-Reducing Consortium Isolated from an Oil Field," *Journal of Materials Engineering and Performance*, vol. 22, no. 11, pp. 3517-3529, 2013.
- [77] R. Antunes, I. Costa and D. de Faria, "Characterization of Corrosion Products Formed on Steels in the First Months of Atmospheric Exposure," *Materials Research*, vol. 6, no. 3, pp. 403-408, 2003.
- [78] Geosyntec Consultants, "Subsurface Assessment Report, Investigative Order R4-2016-0035, Aliso Canyon Gas Storage Facility, Los Angeles County, California," Los Angeles, CA, 2018.
- [79] Eddify NDT Inc., "Detection and Depth Sizing of Surface Breaking Linear Indication on a 5ft 7" Casing," Houston, 2018.
- [80] *Specification for Casing, Tubing, and Drill Tubing*, API 5A 18 Ed., 1953.
- [81] P. D. Thomas, "Steels for Oilwell Casing and Tubing - Past, Present and Future," *Journal of Petroleum Technology*, pp. 495-500, 1963.
- [82] *Standard Test Methods for Determining Average Grain Size*, ASTM E112, 1996.
- [83] *Standard Test Methods for Determining the Inclusion Content of Steel*, ASTM E45, 1997.
- [84] *Standard Test Methods and Definitions for Mechanical Testing of Steel Products*, ASTM A370, 2017.

- [85] *Standard Test Methods for Rockwell Hardness of Metallic Materials*, ASTM E18, 1998.
- [86] *Standard Test Methods for Notched Bar Impact Testing of Metallic Materials*, ASTM E23, 2007.
- [87] *Standard Practice for Preparation of Metallographic Specimens*, ASTM E3, 1995.
- [88] *Standard Test Method for Tension Testing of Metallic Materials*, ASTM E8, 2011.
- [89] *Standard Terminology Relating to Fatigue and Fracture Testing*, ASTM E1823, 2000.
- [90] *Specification for Casing and Tubing*, API 5CT, 2011.
- [91] E. Lucon, C. N. McCowan and R. L. Santoyo, "NIST Technical Note 1865," 10 February 2015. [Online]. Available: <https://www.nist.gov/publications/impact-characterization-line-pipe-steels-means-standard-sub-size-and-miniaturized>. [Accessed 01 May 2019].
- [92] X.-K. Zhu and J. A. Joyce, "Review of Fracture Toughness (G, K, J, CTOC, CTOA) Testing and Standardization," *Engineering Fracture Mechanics*, vol. 85, pp. 1-46, May 2012.
- [93] Blade Energy Partners, "Material Testing Laboratory Reports," 2019.
- [94] Z. Q. Liu, G. Miyamoto, G. Yang and T. Furuhashi, "Volume Fraction of Proeutectoid Ferrite/Pearlite and Their Dependence on Prior Austenite Grain Size in Hypoeutectoid Fe-Mn-C Alloys," *Metallurgical and Materials Transactions A*, vol. 44A, p. 5456.
- [95] ASM International, *ASM Handbook Vol. 6 Welding, Brazing, and Soldering*, 10 ed., vol. 6, ASM International, 1993.
- [96] *Standard Test Method for Microindentation Hardness of Materials*, ASTM Standard E384, 2000.

## Appendix A 2 7/8 in. Tubing Samples

### A.1 Field Samples

**Table 46: Field Samples Collected from 2 7/8 in. Tubing**

Line	Sample Identification	Sampling Date	Description
1	T001S1	August 22, 2017	ID Swab
2	T003S1	August 23, 2017	Scale sample
3	T003S2	August 23, 2017	ID Swab
4	T006S1	August 23, 2017	Oil sample
5	T008S1	August 23, 2017	Oil sample
6	T008S2	August 23, 2017	ID Swab
7	T014S1	August 23, 2017	Oil sample
8	T020S1	August 23, 2017	Oil sample
9	T021S1	August 23, 2017	Solid Sample
10	T021S2	August 23, 2017	ID Swab
11	T022S1	August 23, 2017	Scale sample
12	T023S1	August 23, 2017	Scale sample
13	T024S1	August 23, 2017	Scale sample
14	T025S1	August 23, 2017	oily scale sample
15	T026S1	August 23, 2017	Scale sample
16	T026S2	August 23, 2017	ID swab
17	T028S1	August 23, 2017	Scale sample
18	T028S2	August 23, 2017	sample
19	T029S1	August 23, 2017	Scale sample
20	T029S2	August 23, 2017	sample
21	T030S1	August 23, 2017	Oil sample
22	T032S1	August 23, 2017	Oil sample
23	T038S1	August 23, 2017	Oil sample
24	T038S2	August 23, 2017	Oil sample
25	T044S1	August 24, 2017	Oil sample
26	T050S1	August 24, 2017	Oil sample
27	T056S1	August 24, 2017	Oil sample
28	T068S1	August 25, 2017	ID swab
29	T077S1	August 25, 2017	Solid Sample
30	T079S2	August 25, 2017	solid sample
31	T080S1	August 25, 2017	Liquid sample w/solids

Line	Sample Identification	Sampling Date	Description
32	T081S1	August 25, 2017	Solid Sample
33	T087S1	August 25, 2017	ID Swab
34	T089S1	August 25, 2017	Solid sample
35	T094S1	August 26, 2017	wet mud sample
36	T098S1	August 26, 2017	ID swab
37	T102S1	August 26, 2017	mud sample
38	T113S1	August 26, 2017	mud sample
39	T123S1	August 27, 2017	Oil sample
40	T125S1	August 27, 2017	Solid Sample
41	T128S1	August 27, 2017	ID swab
42	T142S1	August 27, 2017	Solid Sample
43	T157S1	August 28, 2017	Solid Sample
44	T158S1	August 28, 2017	Solid Sample
45	T158S2	August 28, 2017	Solid Sample
46	T170S1	August 28, 2017	Liquid sample
47	T177S1	August 28, 2017	Solid Sample
48	T180S1	August 28, 2017	Solid Sample
49	T187S1	August 29, 2017	Solid Sample
50	T188S1	August 29, 2017	Viscous sample
51	T188S2	August 29, 2017	ID swab
52	T191S1	August 29, 2017	Solid Sample
53	T204S1	August 29, 2017	Solid Sample
54	T221S1	September 1, 2017	ID swab
55	T233S1	September 1, 2017	Solid Sample
56	T244S1	September 1, 2017	Solid Sample

## Appendix B 7 in. Casing Samples

### B.1 Field Samples

Table 47: Field Samples Collected from 7 in. Casing

Line	Sample Identification	Sampling Date	Description	Analyzed By
1	C001S1	October 12, 2017	OD Solid	Premier
2	C001S2	October 12, 2017	ID Scale	Premier
3	C002S1	October 30, 2017	OD Solid	Premier
4	C003S1	October 31, 2017	OD Solid	Premier
5	C003S2	October 31, 2017	ID Solid	Premier
6	C004S1	October 31, 2017	OD Solid	Premier
7	C004S2	October 31, 2017	ID Solid	Premier
8	C005S1	October 31, 2017	OD Solid	Premier
9	C005S2	October 31, 2017	ID Solid	Premier
10	C006S1	November 1, 2017	OD Solid	Premier
11	C008S1	November 1, 2017	OD Solid	Premier
12	C009S1	November 2, 2017	OD Solid	Premier
13	C009S2	November 2, 2017	ID Solid	Premier
14	C012S1	November 3, 2017	OD Solid	Premier
15	C015S1	November 4, 2017	OD Solid	Premier
16	C015S2	November 4, 2017	ID Solid	Premier
17	C018S1	November 5, 2017	OD Solid	Premier
18	C018S2	November 5, 2017	OD Solid	Premier
19	C018S3	November 5, 2017	ID Solid	Premier
20	C021S1	November 6, 2017	OD Solid	Premier
21	C021S2	November 6, 2017	OD Solid	Premier
22	C022S1	November 7, 2017	OD Solid	Premier
23	C022S2	November 7, 2017	OD Solid	Premier
24	C022S3	November 7, 2017	ID Solid	Premier
25	C022S4	November 7, 2017	OD Solid	Premier
26	C022S5	November 7, 2017	OD Solid	Premier
27	C022S6	November 7, 2017	OD Solid	Premier
28	C022S7	November 7, 2017	OD Solid	Premier
29	C022S8	November 7, 2017	OD Solid	Premier
30	C023AS1	November 14, 2017	OD Solid	Premier
31	C023AS2	November 14, 2017	OD Solid	Premier

Line	Sample Identification	Sampling Date	Description	Analyzed By
32	C023AS3	November 14, 2017	OD Solid	Premier
33	C023AS4	November 15, 2017	ID Solid	Premier
34	C023BS1	November 14, 2017	OD Solid	Premier
35	C024S1	November 15, 2017	OD Solid	Premier
36	C024S2	November 15, 2017	OD Solid	Premier
37	C024S3	November 15, 2017	OD Solid	Premier
38	C024S4	November 15, 2017	OD Solid	Premier
39	C024S5	November 16, 2017	OD Solid	Premier
40	C024S6	November 16, 2017	OD Solid	Premier
41	C024S7	November 16, 2017	OD Solid	Premier

## Appendix C X-Ray Diffraction Results for C025 Scale Samples

Blade obtained raw XRD spectra from Premier (Figure 315) for scale samples collected from C025. Blade identified the compounds present in the scale samples. The results of the post-processed XRD data are reported in Table 48. These data were compared with the data analyzed by Premier for C001–C024.

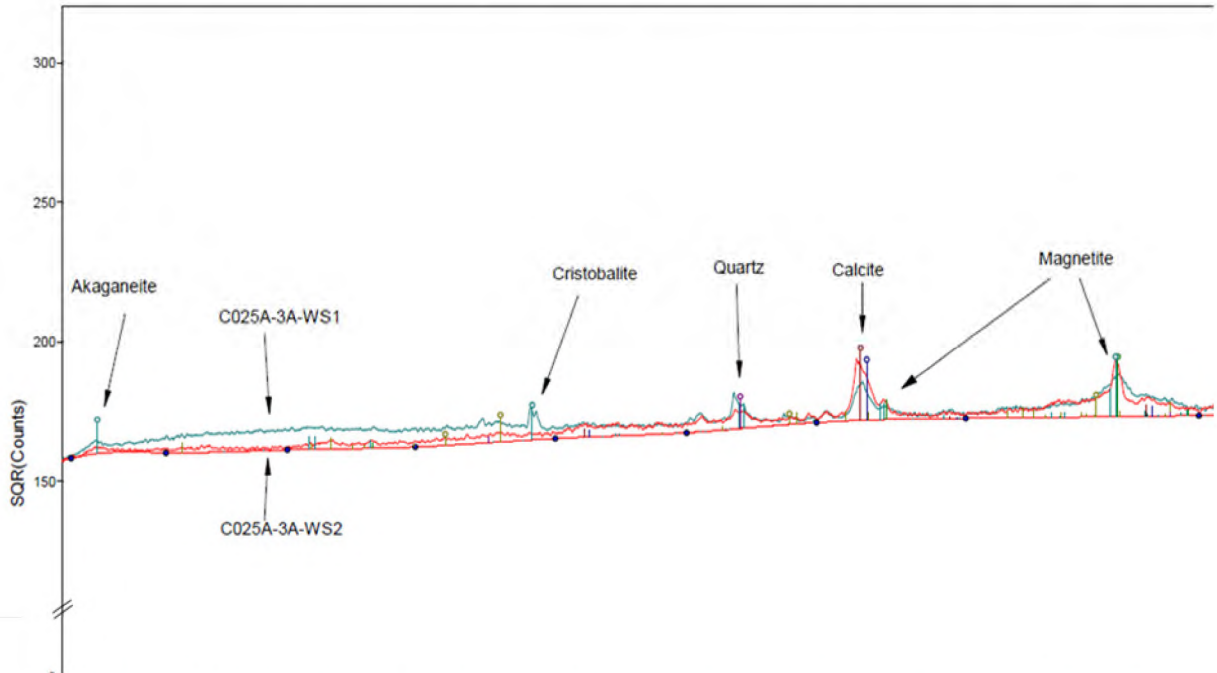


Figure 315: X-Ray Diffraction Spectra Used to Determine the Compounds Present in C025

Table 48: X-Ray Diffraction Data from C025 Scale Analysis

	Original Weight Percentage		Adjusted Weight Percentage	
	C025A3AWS1	C025A3AWS2	C025A3AWS1	C025A3AWS2
Quartz	3.7	1.9	3.9	1.9
Plagioclase	0	0	0	0
Cristobalite	0	0	0	0
Mica (Illite)	0	0	0	0
Calcite	34.4	55.7	36.1	56.8
Aragonite	0	0	0	0
Witherite	0	0	0	0
Siderite	0	0	0	0
Goethite	0	0	0	0
Hematite	8	7.6	8.4	7.8
Lepidocrocite	0	0	0	0

	Original Weight Percentage		Adjusted Weight Percentage	
	C025A3AWS1	C025A3AWS2	C025A3AWS1	C025A3AWS2
Magnetite	40.5	25.1	42.5	25.6
Akaganeite	8.8	7.7	9.2	7.9
Sylvite	Tr	Tr	0	0
Barite	4.6	2	0	0
Total	100%	100%	100%	100%



# SS-25 RCA Supplementary Report

# SS-25 7 in. Speedtite Connection Testing and 11 3/4 in. STC Assessment



2600 Network Boulevard, Suite 550  
Frisco, Texas 75034

+1 972-712-8407 (phone)  
+1 972-712-8408 (fax)

16285 Park Ten Place, Suite 600  
Houston, Texas 77084

1-800-319-2940 (toll free)  
+1 281-206-2000 (phone)  
+1 281-206-2005 (fax)

[www.blade-energy.com](http://www.blade-energy.com)

## Purpose:

Document the results of the connection testing program for the twenty-five 7 in. Speedtite connections extracted from SS-25 and assess the 11 3/4 in. STC connections.

## Date:

May 31, 2019

Blade Energy Partners Limited, and its affiliates ('Blade') provide our services subject to our General Terms and Conditions ('GTC') in effect at time of service, unless a GTC provision is expressly superseded in a separate agreement made with Blade. Blade's work product is based on information sources which we believe to be reliable, including information that was publicly available and that was provided by our client; but Blade does not guarantee the accuracy or completeness of the information provided. All statements are the opinions of Blade based on generally-accepted and reasonable practices in the industry. Our clients remain fully responsible for all clients' decisions, actions and omissions, whether based upon Blade's work product or not; and Blade's liability solely extends to the cost of its work product.

## Abstract

The gas storage well Standard Sesnon 25 (SS-25) in the Aliso Canyon Gas Storage Field located in Los Angeles County, California started leaking gas in October 2015. A relief well was drilled, and SS-25 was brought under control. The leak stopped in February 2016.

In January 2016, as part of their investigation of the leak, the California Public Utilities Commission (CPUC) and the Division of Oil, Gas, and Geothermal Resources (DOGGR) selected and gave provisional authority to Blade Energy Partners (Blade) to perform an independent Root Cause Analysis (RCA). The Blade Team and parties under Blade's direction were responsible for directing the work of subcontractors who performed the extraction of SS-25's wellhead, tubing, casing, and the preservation and protection of associated evidence. Blade's RCA Reports, including this one, document and describe the key activities undertaken in support of the RCA effort.

Blade tested the 7 in. 23 ppf J55 Speedtite connections that were extracted from SS-25. The purpose of the connection testing was to determine whether the connections would maintain internal pressure equivalent to the highest gas storage operating pressure without leaking. Twenty-five connections were tested at the Blade RCA Storage Facility in Houston, TX, and nine leaked. After testing, select connections were broken out, and all of them had breakout torques that were lower than the estimated recommended makeup torque. The pin and box threads were cleaned, visually inspected, and found to be in very good condition. There was no obvious thread galling, metal burrs, seal area damage, or erosion paths. Two connections having the highest leak rates were retested to see if the original test results were repeatable. The connections were made up to the estimated recommended makeup torques and then tested using the same procedures as before. Both connections leaked.

The testing results suggest that over time some of the connections leaked very small amounts of gas into the 11 3/4 in. × 7 in. annulus and that the volume of gas would vary depending on the internal pressure the casing was exposed to during the various storage operations (injection or withdrawal). A review of the Short Thread Casing (STC) connection design that was used on the 11 3/4 in. casing shows that the connections were not gas-tight and were susceptible to leaking gas at very low internal pressure.

## Table of Contents

<b>1</b>	<b>Introduction.....</b>	<b>5</b>
1.1	Abbreviations and Acronyms .....	7
1.2	Speedtite Connection Description.....	8
<b>2</b>	<b>Connection Test Methodology .....</b>	<b>10</b>
2.1	Connection Test Equipment and Operation.....	12
2.2	Connection Leak Definition .....	13
<b>3</b>	<b>Connection Test Results.....</b>	<b>14</b>
3.1	Post Connection Test Operations.....	16
3.2	Supplemental Testing.....	18
3.3	Connection Thread Magnetic Particle Inspection .....	21
<b>4</b>	<b>Short Thread Casing Leak Resistance Review .....</b>	<b>23</b>
<b>5</b>	<b>Conclusions.....</b>	<b>24</b>
<b>6</b>	<b>References.....</b>	<b>26</b>
Appendix A	<b>Performance Data .....</b>	<b>A-1</b>
Appendix B	<b>Photos .....</b>	<b>B-1</b>
Appendix C	<b>Connection Test Data Sheets .....</b>	<b>C-1</b>
Appendix D	<b>Breakout and Makeup Torque Data .....</b>	<b>D-1</b>
Appendix E	<b>Pipe Thread compound X-Ray Diffraction Analysis.....</b>	<b>E-1</b>

## List of Figures

Figure 1:	Uncratering the Connections the Houston Warehouse.....	5
Figure 2:	7 in. Casing and Connection Locations .....	6
Figure 3:	Super EU (Speedtite) Connection Configuration .....	9
Figure 4:	Ideal ‘No Leak’ Pressure Test Example .....	12
Figure 5:	C001B Pin Threads Condition after Cleaning .....	18
Figure 6:	C023A1C Blueing Results .....	19
Figure 7:	C023A1C Before Breakout (left) and after Power Makeup (right) .....	20
Figure 8:	Ultraviolet Magnetic Particle Inspection of Threads .....	21
Figure 9:	SS-25 Casing Pressure History ( $P_{w,csg}$ ) .....	25
Figure 10:	Conex Trailer Used for Connection Testing .....	B-1
Figure 11:	Inside the Conex—Pressure Cabinet and Control Box .....	B-1
Figure 12:	Inside the Conex—Test Specimen Secured in the Test Fixture .....	B-2
Figure 13:	Inside the Conex—Instrumented Test Specimen .....	B-2
Figure 14:	Test Control Panel and Test Data Display.....	B-3
Figure 15:	Camera View of Test.....	B-3
Figure 16:	Connection Test Specimens after Testing .....	B-4



Figure 17: Breaking Out a Connection with the Horizontal Bucking Machine ..... B-4  
Figure 18: Representative Pin Condition after Break out and Cleaning ..... B-5  
Figure 19: Representative Box Condition after Break out and Cleaning ..... B-5  
Figure 20: Representative Full Blueing Transfer on C002B ..... B-6

## List of Tables

Table 1: Test Specimen List..... 7  
Table 2: Connection Test Nominal Loads ..... 10  
Table 3: Injection at 2,700 psi with the Worst Case Cool Down Loads ..... 10  
Table 4: Connection Test Load Schedule ..... 11  
Table 5: Connection Test Results Summary ..... 14  
Table 6: Connection Test Results Detail ..... 15  
Table 7: Connection Breakout Summary ..... 17  
Table 8: Connection Makeup Torque for Retests ..... 19  
Table 9: Connection Retest Results Details ..... 20  
Table 10: Final Testing Results Summary ..... 20  
Table 11: 7 in. Casing Details ..... A-1  
Table 12: 7 in. Casing Nominal Performance ..... A-1

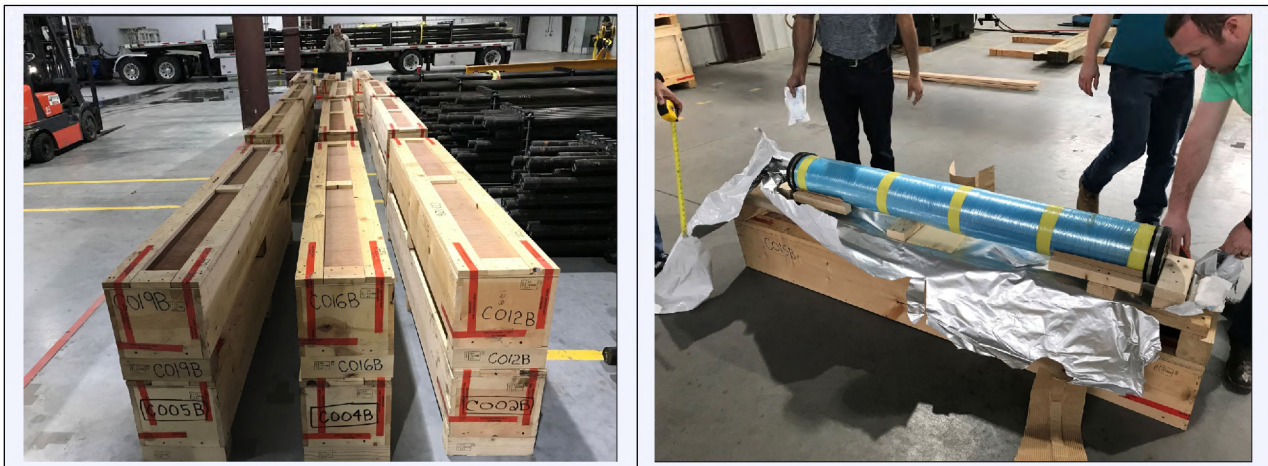
# 1 Introduction

The purpose of this document is to summarize the results of the connection testing performed on the 7 in. 23.0 ppf J55 Speedtite casing connections extracted from SS-25. The objective was to apply internal pressure to the connection equivalent to the highest gas storage operating pressure the 7 in. casing had been exposed to and determine if it would maintain the pressure without leaking. The testing was done in accordance with the Blade Connection Testing Protocol [1] at the Blade RCA storage facility (warehouse) in Houston, TX.

The 7 in. production casing string was run in SS-25 on February 10, 1954. The well served as an oil producer for the next 19 years and was converted to a gas storage well in June 1973. SS-25 served as a gas storage well for the next 42 years until October 2015, and it was primarily for gas injection through the 7 in. x 2 7/8 in. annulus.

During the Phase 3 well site operations, the 7 in. casing was cut at 939 ft in August 2017, and 23 joints of 7 in. casing were extracted from SS-25. In September 2018, the 7 in. casing was cut at 1,040 ft, and two additional joints were extracted. The Speedtite connections were not broken out during the extraction operations. Instead, the casing was cut approximately 2 1/2 ft on either side of the connection to allow the connection to remain intact. The connections were handled in accordance with the Blade Tubulars Handling Protocol [2], wrapped in a volatile corrosion inhibitor (VCI) sheet, sealed in a Mylar moisture barrier bag, and individually crated. The first 23 connections were transferred from Aliso Canyon to the Blade warehouse in Houston on December 05, 2017, and the final two connections on September 21, 2018. The connection testing was conducted between August 15 and October 24, 2018.

Figure 1 shows the crated connections after unloading at the warehouse and an example of a VCI-wrapped connection after the uncrating and removal of the Mylar bag.



**Figure 1: Uncrating the Connections the Houston Warehouse**

Figure 2 shows the measured depths of where the 7 in. casing joints and the corresponding Speedtite connections were located in the SS-25 wellbore. Table 1 lists the connection specimens that were tested. The Joint Sequence Number (JSN) is the unique Blade serial number used for internal traceability purposes.

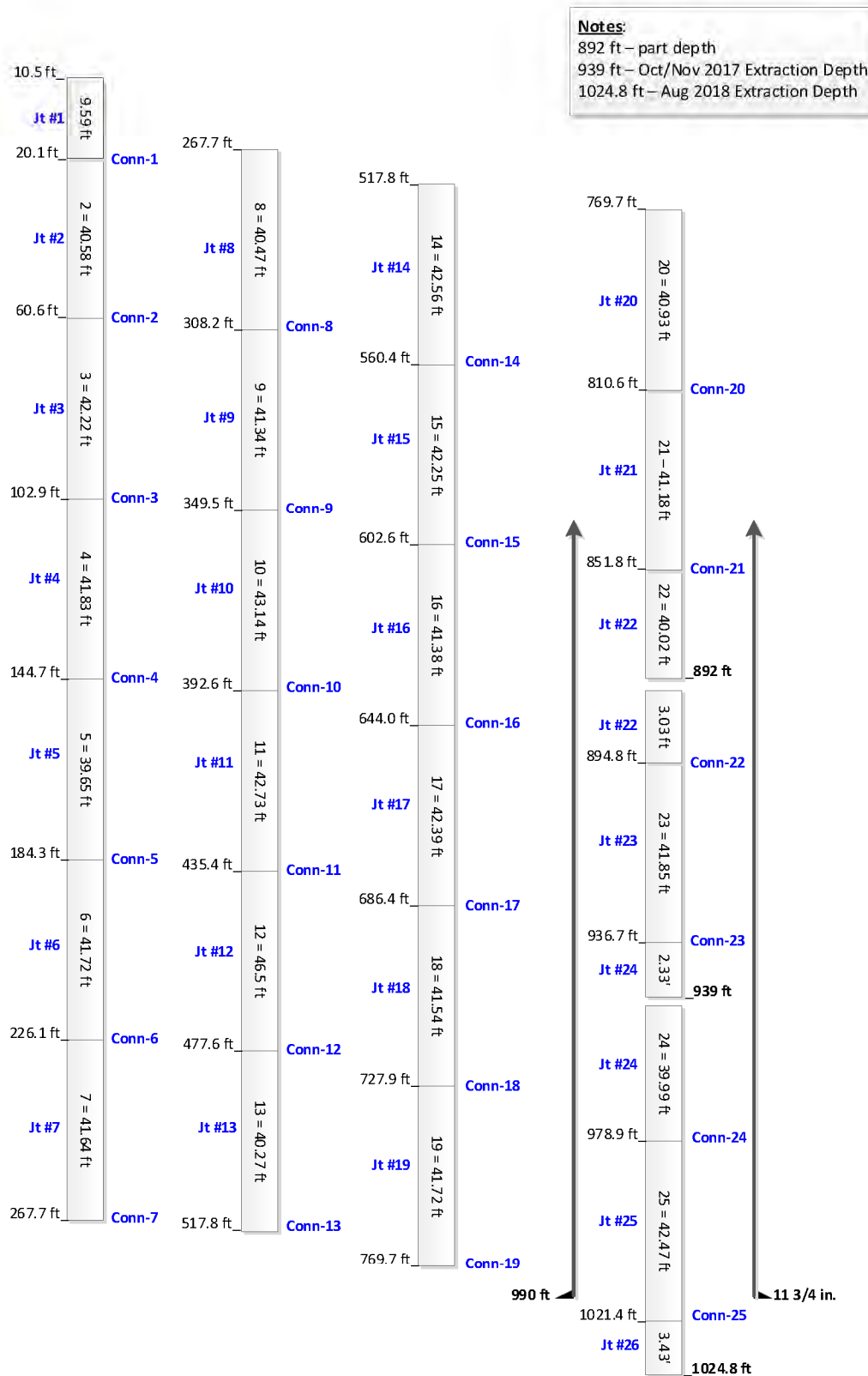


Figure 2: 7 in. Casing and Connection Locations

Table 1: Test Specimen List

Connection No.	Location in Well (ft)	JSN	Length (ft)
1	20.1	C001B	4.99
2	60.6	C002B	4.95
3	102.9	C003B	5.01
4	144.7	C004B	4.99
5	184.3	C005B	5.03
6	226.1	C006B	5.01
7	267.7	C007B	4.99
8	308.2	C008B	5.00
9	349.5	C009B	5.00
10	392.6	C010B	4.99
11	435.4	C011B	5.00
12	477.6	C012B	5.82
13	517.8	C013B	4.98
14	560.4	C014B	5.26
15	602.6	C015B	5.17
16	644.0	C016B	4.89
17	686.4	C017B	5.01
18	727.9	C018B	5.38
19	769.7	C019B	5.00
20	810.6	C020B	4.99
21	851.8	C021B	6.31
22	894.8	C023A1C	5.80
23	936.7	C024B	4.63
24	978.9	C025B	5.69
25	1,021.4	C026B1	5.00

## 1.1 Abbreviations and Acronyms

Term	Definition
API	American Petroleum Institute
Blade	Blade Energy Partners
CAL	Connection Application Level Test
CPUC	California Public Utilities Commission
cc	Cubic centimeters
DOGGR	Division of Oil, Gas, and Geothermal Resources
EU	External Upset

Term	Definition
GTC	General Terms and Conditions
ID	Internal Diameter
JSN	Joint Sequence Number
kips	Thousand pounds
ksi	Thousand pounds per square inch
MMscf/D	Million Standard Cubic Feet per Day
MPI	Magnetic Particle Inspection
OD	Outside Diameter
ppf	Pounds Per Foot
RCA	Root Cause Analysis
RP	Recommended Practice
SCCM	Standard Cubic Centimeters per Minute
SCFD	Standard Cubic Feet per Day
SLM	Standard Liters per Minute
SS	Standard Sesnon
STC	Short Thread Casing
UV	Ultraviolet
VCI	Volatile Corrosion Inhibitor
VME	Von Mises Equivalent
XRD	X-Ray Diffraction

## 1.2 Speedtite Connection Description

Speedtite connections are no longer commercially available, and the limited public information describing them suggests that Speedtite connections are identical to Hydril's Super EU connections and that Youngstown Steel (the manufacturer of the 7 in. casing run in SS-25) was licensed to cut Super EU connections and market them under the name 'Speedtite'. Super EU connections are no longer commercially available either, but some information is publicly accessible regarding the connection features and design.

Super EU is a proprietary internally upset, two-step connection. The connection outside diameter (OD) at 7.444 in. is slightly larger than the 7 in. pipe OD. During manufacturing, pin threads are cut at the bottom end of each ~42 ft long joint, and the box threads are cut on the upper end of each joint. In the field, the pin from one joint is made-up into the box from another joint when the casing string is run in the well. Internal pressure leak resistance is provided by the post-makeup contact pressure from radial interference in the metal-to-metal seal labeled 'A' in Figure 3. When the casing is exposed to internal pressure, the seal contact pressure increases as the pin expands radially into the box, thereby increasing the internal leak resistance of the connection. The connection is also designed to provide external pressure resistance via another metal-to-metal seal labeled 'B' in Figure 3 and functions similarly to that of seal 'A.' The torque shoulder where the pin and box meet after the connection is made up is located between the 'B' seal and the OD of the pin. This torque shoulder is the only source of torque during



makeup because the threads are free running and therefore do not provide resistance to internal or external pressure.

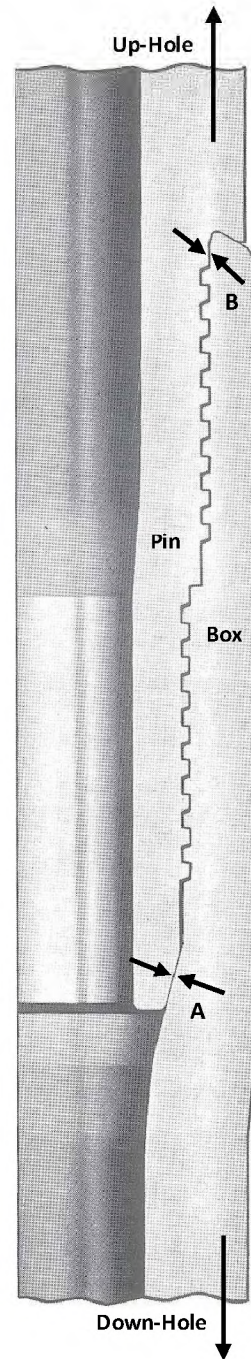


Figure 3: Super EU (Speedtite) Connection Configuration

## 2 Connection Test Methodology

The overall objective of the connection testing was to determine if any of the connections leaked gas at an internal pressure equivalent to the maximum operating pressure the 7 in. casing was exposed to during withdrawal and injection. Historical data show that the maximum operating pressure the casing was exposed to was 3,300 psi. The internal pressure rating of the Speedtite connection is estimated to have been 4,360 psi for the 7 in. 23 ppf J55 casing based on the 7 in. pipe body capacity. During testing, nitrogen gas was used to simulate the methane gas pressure that was seen at SS-25.

Blade's connection testing protocol was based on the relevant sections of American Petroleum Institute (API) Recommended Practice (RP) 5C5 - *Recommended Practice on Procedures for Testing Casing and Tubing Connections* [3], and testing was done at the Blade warehouse in Houston. No attempt was made to do a complete API RP 5C5 Connection Application Level (CAL) IV combined load type of test because the purpose of the testing was not to determine the connection's performance limits but only to see if these connections leaked under normal gas storage operating conditions.

Table 2 lists the nominal loads placed on the 7 in. connections when subjected to an internal pressure of 3,300 psi during the connection test. These loads were lower than the actual loads listed in Table 3, which shows the loads that the 7 in. casing was subjected to during injection at 2,700 psi while the casing was cooled as gas expanded through the leak at 892 ft. [4].

**Table 2: Connection Test Nominal Loads**

Nominal Load	Value
Internal Pressure	3,300 psi
Axial Load	105.04 kips
Axial Stress	15,780 psi
Hoop Stress	34,790 psi
VME Stress	33,050 psi

**Table 3: Injection at 2,700 psi with the Worst Case Cool Down Loads**

Nominal Load	At 0 ft MD	At 892 ft MD
Internal Pressure	2,700 psi	2,791 psi
External Pressure	0 psi	388 psi
Axial Load	266.5 kips	245.9 kips
Axial Stress	40,041 psi	36,950 psi
Hoop Stress	30,075 psi	28,778 psi
VME Stress	39,611 psi	36,747 psi

The basic connection test procedure includes:

- Measuring the OD, inside diameter (ID), and wall thickness for each test specimen.
- Attaching strain gauges and thermocouples to the test specimen to allow strain and temperature measurements to be continuously monitored and recorded during the test. Strain gauges allow the test operator to monitor for the onset of plasticity in the specimen during the test that could lead to a catastrophic failure. In the event of a leak, the thermocouple can monitor the specimen temperature and ensure it does not create an unsafe environment due to Joule-Thomson cooling.
- Attaching the flexible boot leak-trap device to the connection to trap any gas leaking from the connection during the test. The boot consisted of neoprene sheets wrapped around the connection and affixed to the specimen OD with superglue and contact cement. A 1/8 in. vinyl hose was inserted between the boot and the connection OD to convey any gas leaking from the connection to a flow meter that measured leak flow rate and volume.
- Installing the test specimen onto the test fixture that held the specimen in place during the test. A 6 in. diameter filler bar was inserted into the specimen to reduce the internal volume and thereby minimize the volume of nitrogen required for the test. High pressure end-caps were then attached to either end of the test specimen.
- Installing a mass flow meter that continuously monitored, measured, and recorded any gas flow leaking from the connection and through the boot. Gas flow readings are measured in units of standard cubic centimeters per minute (SCCM).
- Testing the flexible boot using a syringe pump and a 4 SCCM flow meter. Air was pumped into the boot, and the volume of flow out of the boot was compared to the flow in volume. If at least 95% of the air pumped into the boot was collected, the boot was deemed to provide a satisfactory seal around the connection.
- Testing the connection by increasing the internal pressure in the specimen by increments according to the load schedule shown in Table 4. The resulting test data (pressures, rates, strains, temperatures) were continuously monitored and recorded.

**Table 4: Connection Test Load Schedule**

Pressure (psi)	Hold Time (minutes)
500	15
1,000	5
1,500	5
2,000	5
2,500	2
3,300	240

If the connection leaked during the test, then the internal pressure was maintained in order to allow for a volumetric flow rate to be calculated based on the internal pressure and mass flow sensor. This required slowly metering compressed nitrogen gas into the specimen at a comparable rate to that of the leak.

Figure 4 shows what an ideal pressure test would be expected to look like. The graph shows internal test pressure and gas flow rate through the boot vs. time. The load step increments and hold periods are clear.

The flow rate through the boot is zero SCCM. The minor pressure variations can be attributed to temperature effects and pressure-related expansion.

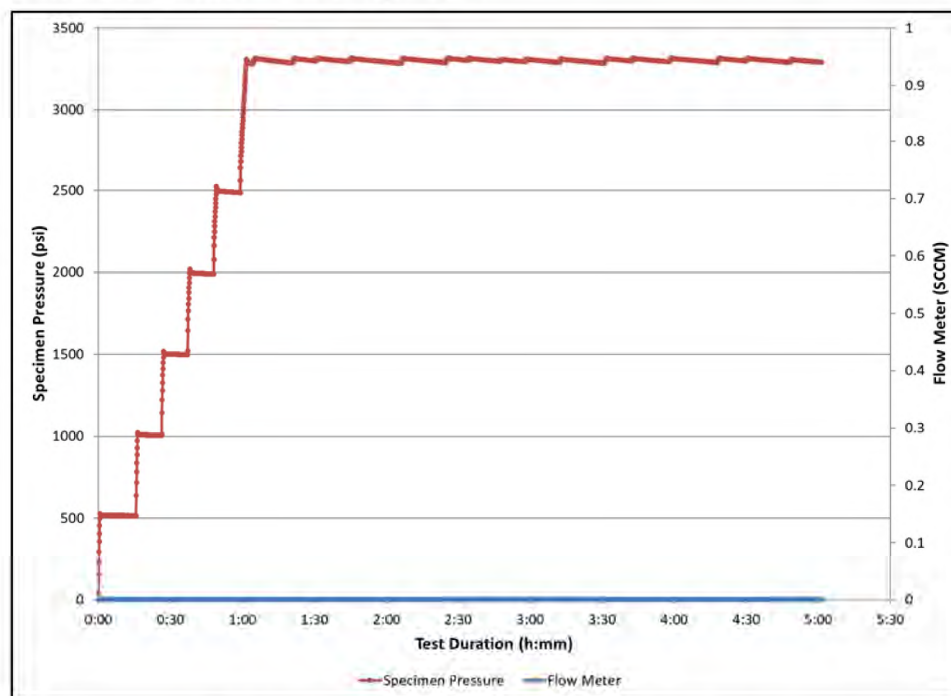


Figure 4: Ideal 'No Leak' Pressure Test Example

Blade obtained seven 7 in. 23 ppf J55 Speedtite connection test specimens from casing recovered from the Aliso Canyon well P-34 and then transported them to Houston, TX on April 26, 2018. Several of these specimens were used to validate the test equipment and testing procedures before any testing was done on the connections from SS-25.

## 2.1 Connection Test Equipment and Operation

Blade designed and built the connection testing equipment and control system. Photographs of the test facility and an instrumented test specimen are shown in Appendix B. The key components were the:

- Conex trailer, which served as a safety containment vessel in the event of a catastrophic failure, and as the primary barrier between debris and personnel. The Conex housed the test specimen, pressure cabinet, control box, and other instrumentation, such as an O<sub>2</sub> sensor and a webcam for remote observation.
- Pressure cabinet, which contained pneumatic gate and metering valves that allowed for a semi-automated test sequence.
- Test stand, which restrained the specimen during testing in the event of rupture.
- Control system and software, which allowed automated testing and monitors for leak detection. The data collection rate was automatically increased if a leak was detected, but it could also be changed by the test operator.
- Test pump, which was an air-driven boost pump used to increase the pressure from the nitrogen tanks that was then pumped into the pressure cabinet and subsequently into the test specimen.

After testing, the thread attributes and seal dimensions were not able to be measured or gauged to identify any deviations from nominal because Speedtite connections are no longer commercially available.

## 2.2 Connection Leak Definition

For this testing program, a leak was defined as a quasi-steady state and repeatable volume of gas exiting the connection testing boot. Due to the testing set-up, it was possible for a flow meter to register false positives for a leak rate due to the differential expansion of the steel connection and the flexible outer boot. Since these indications were over a very short duration (seconds in some cases), they were only considered a leak when they occurred for a prolonged time period.

### 3 Connection Test Results

Twenty-five connections were tested. Table 5 lists the details of the results. Nine connections leaked and 16 did not. The highlighted rows indicate the connections that leaked.

**Table 5: Connection Test Results Summary**

Connection No.	Depth in Well (ft)	JSN	Leak?
1	20.1	C001B	No
2	60.6	C002B	Yes
3	102.9	C003B	No
4	144.7	C004B	Yes
5	184.3	C005B	No
6	226.1	C006B	No
7	267.7	C007B	No
8	308.2	C008B	No
9	349.5	C009B	No
10	392.6	C010B	No
11	435.4	C011B	Yes
12	477.6	C012B	Yes
13	517.8	C013B	No
14	560.4	C014B	No
15	602.6	C015B	No
16	644.0	C016B	Yes
17	686.4	C017B	No
18	727.9	C018B	No
19	769.7	C019B	Yes
20	810.6	C020B	No
21	851.8	C021B	Yes
22	894.8	C023A1C	Yes
23	936.7	C024B	No
24	978.9	C025B	Yes
25	1,021.4	C026B1	No

The tests began by using a 4 SCCM flow meter. If during the test the flow meter range was not sufficient to measure the flow rate, then the test was stopped. A higher capacity flow meter was installed, and the test was re-started. In several cases a 50,000 SCCM meter had to be used. Therefore, some connections required multiple individual tests to complete the test program.

Connections that leaked were generally characterized by constant and repeatable flow rates. Connections that didn't leak typically acted in accordance with what is shown in Figure 4. The highest leak rates came

from C016B and C023A1C, which leaked at 1,120 SCCM (57 SCFD) and 196 SLM (9,967 SCFD), respectively. Connection C023A1C was located in the well 2.3 ft above where the 7 in. casing parted.

Table 6 provides detailed information about the individual tests. The individual connection data sheets showing the pressure, flow rate, and flow volume data vs. time are provided in Appendix C.

**Table 6: Connection Test Results Detail**

Connection	Leak?	Flow Meter (SCCM)	Pressure (psi)	Max Leak Rate	Volume Leaked (cc)
C001B	1. No	1. 4	1. 3,300	1. 0 SCCM	1. 0.24
C002B	1. Yes	1. 4	1. 1,500	1. > 4 SCCM	1. > 112
	2. Yes 3. Yes	2. 50 3. 500	2. 2,500 3. 3,300	2. > 50 SCCM 3. 101 SCCM	2. > 550 3. > 11,200
			Rate after 2.5 hours at 3,300 psi was ~78 SCCM		
C003B	1. No	1. 4	1. 3,300	1. 0 SCCM	1. 0
C004B	1. Yes	1. 4	1. 2,000	1. > 4 SCCM	1. 124
	2. Yes 3. Yes	2. 4 3. 500	2. 2,000 3. 3,300	2. > 4 SCCM 3. 200 SCCM	2. 630 3. > 17,100
			Rate after 1 hour at 3,330 psi was 140 SCCM		
C005B	1. No	1. 4	1. 3,300	1. 3.4 SCCM	1. 70
	2. No	2. 50	2. 3,300	2. 0 SCCM	2. 0
C006B	1. No	1. 4	1. 3,300	1. 0 SCCM	1. 0
C007B	1. No	1. 4	1. 3,300	1. 0.4 SCCM	1. 9.6
C008B	1. No	1. 500	1. 3,300	1. 0 SCCM	1. 0
	2. No	2. 4	2. 3,300	2. 0 SCCM	2. 0.078
C009B	1. No	1. 4	1. 3,300	1. 0 SCCM	1. 0.08
C010B	1. No	1. 4	1. 3,300	1. 0 SCCM	1. 0
C011B	1. Yes	1. 4	1. 1,200	1. > 4 SCCM	1. > 18
	2. Yes	2. 500	2. 3,300	2. 90 SCCM	2. > 6,500
C012B	1. Yes	1. 4	1. 3,300	1. 1.7 SCCM	1. 183
			Rate after 2 hours at 3,300 psi was 1.1 SCCM		
C013B	1. No	1. 4	1. 3,300	1. 0.7 SCCM	1. 6.1
C014B	1. No	1. 4	1. 3,300	1. 0.84 SCCM	1. 7.5
C015B	1. No	1. 4	1. 3,300	1. 0.17 SCCM	1. 0.48
C016B	1. Yes	1. 4	1. 1,000	1. > 4 SCCM	1. > 2
	2. Yes	2. 500	2. 2,500	2. > 500 SCCM	2. > 5,000
	3. Yes	3. 50,000	3. 3,300	3. 1,120 SCCM	3. 117,500

Connection	Leak?	Flow Meter (SCCM)	Pressure (psi)	Max Leak Rate	Volume Leaked (cc)
			Rate after 2 hours at 3,300 psi was 945 SCCM		
C017B	1. No	1. 4	1. 3,300	1. 4 SCCM	1. 67.7
C018B	1. No	1. 4	1. 3,300	1. 0.14 SCCM	1. 0.74
C019B	1. Yes	1. 4	1. 1,000	1. > 4 SCCM	1. > 90
	2. Yes	2. 500	2. 3,300	2. > 500 SCCM	2. > 700
C019B	3. No	3. 50,000	3. 3,300	3. 0 SCCM	3. 0
	4. Yes	4. 500	4. 3,300	4. 137 SCCM	4. >4900
			Rate after 4 hours at 3,330 psi was 15 SCCM		
C020B	1. No	1. 4	1. 3,300	1. 0.3 SCCM	1. 6.9
C021B	1. Yes	1. 4	1. 1,000	1. > 4 SCCM	1. > 80
	2. Yes	2. 500	2. 3,300	2. 128 SCCM	2. > 5200
			Rate after 2 hours at 3,330 psi was 91 SCCM		
C023A1C	1. Yes	1. 4	1. 500	1. > 4 SCCM	1. > 7
	2. Yes	2. 50,000	2. 2,500	2. > 50,000 SCCM	2. > 350,000
	3. Yes	3. 1,000,000	3. 2,800	3. 195 SLM	3. > 1,180,000
C024B	1. No	1. 4	1. 3,300	1. 0.65 SCCM	1. > 18
C025B	1. Yes	1. 4	1. 1,400	1. > 4 SCCM	1. > 27
	2. Yes	2. 500	2. 3,300	2. 237 SCCM	2. > 35,000
			Rate after 4 hours at 3,330 psi was 110 SCCM		
C026B1	1. No	1. 4	1. 3,300	1. 0.17 SCCM	1. 0.48

It should be noted that the tests are not quantitatively repeatable. If a connection leaked during a test and was retested at a later date, it would still leak, but the leak rates may not have been the same.

### 3.1 Post Connection Test Operations

All nine of the connections that leaked and five of the connections that did not were broken out using a horizontal bucking machine. Table 7 shows the resulting breakout torques that were uniformly low—ranging from 3,614 to 8,708 ft-lb—which was unexpected. Publicly-available information suggests that the makeup torque for these connections would be approximately 8,000 ft-lb. The breakout torque for a correctly made-up connection can be expected to be much higher than the makeup torque, especially if the connection has been in place for an extended period of time. For comparison, Table 7 includes the breakout torques from five P-34 connections that are significantly higher and more in line with what would normally be expected. The individual breakout torque charts are provided in Appendix C.



Table 7: Connection Breakout Summary

Connection No.	JSN	Leak?	Breakout Torque (ft-lb)
1	C001B	No	3,614
2	C002B	Yes	4,732
4	C004B	Yes	4,910
6	C006B	No	4,452
10	C010B	No	6,477
11	C011B	Yes	5,237
12	C012B	Yes	8,708
16	C016B	Yes	6,734
17	C017B	No	6,318
19	C019B	Yes	8,313
21	C021B	Yes	6,148
22	C023A1C	Yes	5,649
23	C024B	No	7,093
24	C025B	Yes	5,822
P-34 C002	P-34 C002	N/A	22,707
P-34 C003	P-34 C003	N/A	16,620
P-34 C005	P-34 C005	N/A	21,506
P-34 C006	P-34 C006	N/A	19,610
P-34 C007	P-34 C007	N/A	23,457

After break out, the pin and box threads were cleaned and visually inspected. The threads were found to be in very good condition with no obvious galling, metal burrs, erosion paths, or damage to the threads and seal areas. There was no obvious relationship between the thread condition, the breakout torque, and whether or not a particular connection leaked. Figure 5 is a representative photo of the condition of the threads after break out and cleaning. The original machined surface condition is still visible.



**Figure 5: C001B Pin Threads Condition after Cleaning**

Six thread compound samples from SS-25 connections and one sample of modern API Modified pipe thread compound were sent to Premier Oilfield Labs for X-ray Diffraction (XRD) analysis. The results are provided in Appendix E with the units in percent mass. While there is a large variance in the chemistry found in each of the samples, there was no correlation between the thread compound composition and connection test results. A significant quantity of barite ( $\text{BaSO}_4$ ) was found in the thread compound from casing connection C023A1C. This is likely attributed to the mud used during several of the kill attempts.

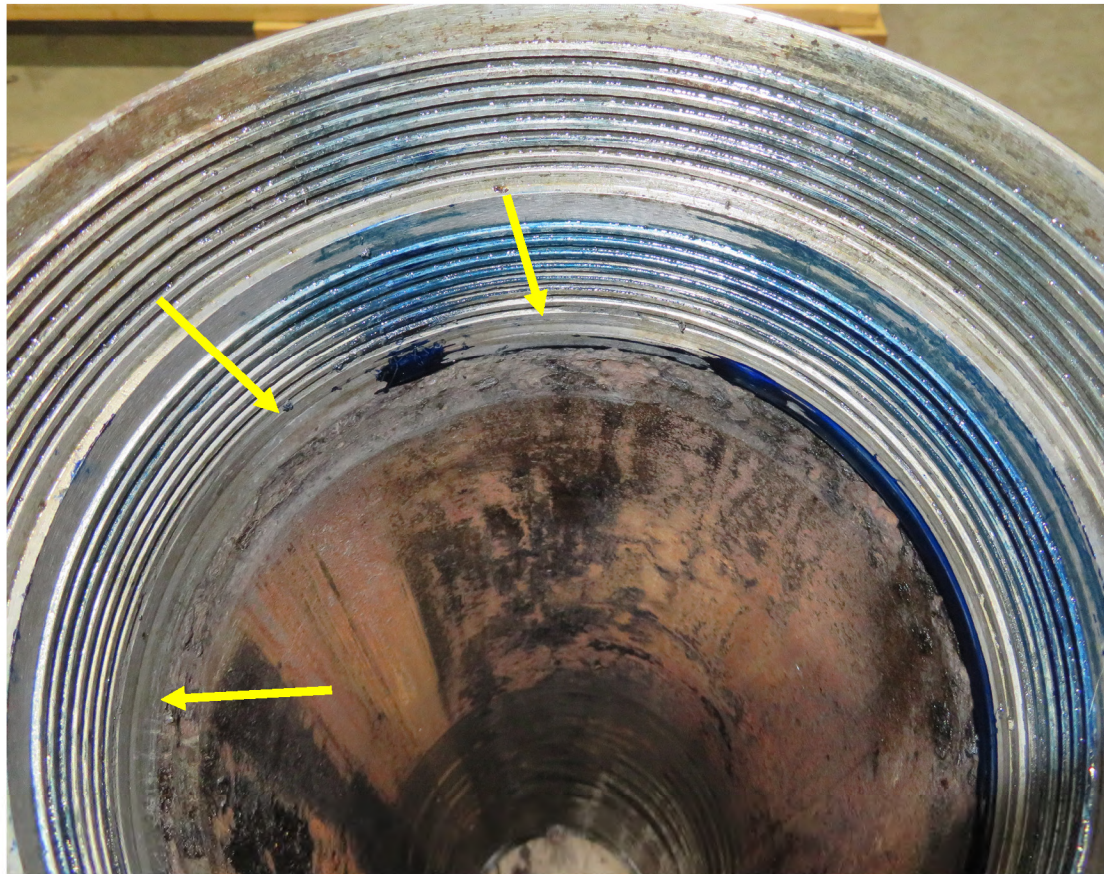
### 3.2 Supplemental Testing

After reviewing the breakout data and thread inspection results, Blade decided to retest connections C016B and C023A1C after making them up to the estimated recommended torque (8,000 ft-lb) using the horizontal bucking machine to see if the original test results were repeatable.

A paste-like blue dye was first applied to the pin nose seal before carefully making the connections up to hand-tight torque. This type of blueing process is commonly used as a quality check to detect high-spots or gaps during machining and assembly processes through the transfer of the dye from one surface to another when the surfaces contact. The connections were then carefully backed out by hand so that the blueing transfer from the pin nose seal to the box seal area could be observed. The transfer of the dye from the pin nose seal to the box seal was incomplete for both connections. Figure 6 shows the blueing

results for C023A1C where the arrows in the picture point to areas where the dye was not transferred to the box seal.

While results of the blueing process are qualitative in nature, they can be helpful for identifying areas where there is a gross lack of seal contact at hand-tight makeup. However, even if the dye transfers completely across the seal surfaces at hand-tight makeup, the connection may still leak. Therefore, blueing results can be used to identify connections that have a high probability of leaking, but they will not definitively identify connections that will not leak.



**Figure 6: C023A1C Blueing Results**

The connections were next made up to the estimated recommended makeup torque using modern API Modified pipe thread compound and tested again using the same procedures as before. Both connections leaked. Table 8 shows the original breakout torques and the actual makeup torques when the connections C016B and C023A1C were retested. Table 9 shows the retest results.

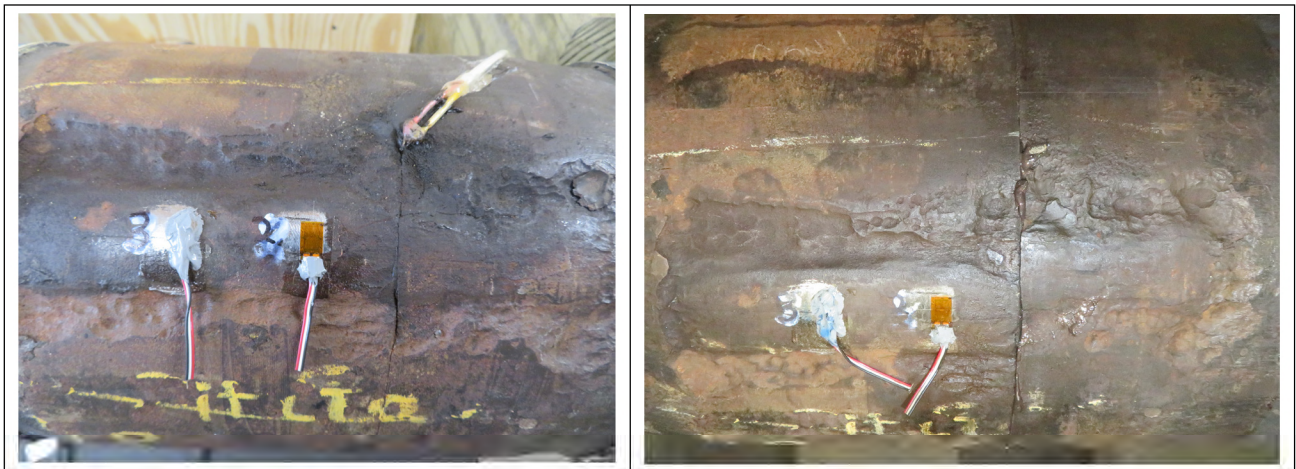
**Table 8: Connection Makeup Torque for Retests**

Connection	Original Breakout (ft-lb)	Makeup for Retest (ft-lb)
C016B	6,734	8,396
C023A1C	5,649	8,009

**Table 9: Connection Retest Results Details**

Connection	Leak?	Flow Meter (SCCM)	Pressure	Max Leak Rate	Volume Leaked (cc)
C016B	1. Yes	1. 4	1. 3,300 psi	1. > 4 SCCM	1. > 9
	2. Yes	2. 50	2. 3,300 psi	2. 35 SCCM	2. > 530
C023A1C	1. Yes	1. 500	1. 2,200 psi	1. > 500 SCCM	1. > 1,090
	2. Yes	2. 50,000	2. 2,400 psi	2. > 50,000 SCCM	2. > 140,000
	3. Yes	3. 1,000,000	3. 2,906 psi	3. 306 SLM	3. > 2,820,000

The fact that the connections had been made up to the estimated recommended torque and still leaked demonstrates that the leaks were not associated with the low breakout torques and that the low breakout torques were therefore not a consequence of any mechanisms associated with the parting of the 7 in. casing. The left panel in Figure 7 shows the how the corrosion on connection C023A1C was aligned in the original condition before being broken out. The right panel shows the corrosion misaligned after C023A1C was broken-out, cleaned and then made-up to 8,000 ft-lb. These results also indicate that the original makeup torque was less than 8,000 ft-lb.



**Figure 7: C023A1C Before Breakout (left) and after Power Makeup (right)**

The blue dye was also applied to the remaining seven connections that leaked and to three of the connections that did not leak during the original testing. Some of the connections that leaked had small areas of no blue transfer while others had full blue transfer across the ID seal area. The results from the connections that did not leak had full blueing transfer across the ID seal area. Table 10 shows a final summary of the connection test results.

**Table 10: Final Testing Results Summary**

Connection No.	Depth in Well (ft)	JSN	Leak?	Breakout Torque (ft-lb)	Fully Blued?
1	20.1	C001B	No	3,614	No
2	60.6	C002B	Yes	4,732	Yes
3	102.9	C003B	No	-	No
4	144.7	C004B	Yes	4,910	Yes

Connection No.	Depth in Well (ft)	JSN	Leak?	Breakout Torque (ft-lb)	Fully Blued?
5	184.3	C005B	No	-	No
6	226.1	C006B	No	4,452	Yes
7	267.7	C007B	No	-	No
8	308.2	C008B	No	-	No
9	349.5	C009B	No	-	No
10	392.6	C010B	No	6,477	Yes
11	435.4	C011B	Yes	5,237	Yes
12	477.6	C012B	Yes	8,708	Yes
13	517.8	C013B	No	-	No
14	560.4	C014B	No	-	No
15	602.6	C015B	No	-	No
16	644.0	C016B	Yes - twice	6,734	Yes
17	686.4	C017B	No	6,318	Yes
18	727.9	C018B	No	-	No
19	769.7	C019B	Yes	8,313	Yes
20	810.6	C020B	No	-	No
21	851.8	C021B	Yes	6,148	Yes
22	894.8	C023A1C	Yes - twice	5,649	Yes
23	936.7	C024B	No	7,093	No
24	978.9	C025B	Yes	5,822	Yes
25	1,021.4	C026B1	No	-	No

### 3.3 Connection Thread Magnetic Particle Inspection

After the connection testing was completed, the connections identified in Table 7 were broken out and their threads were cleaned. The pins of four chosen connections underwent ultraviolet (UV) magnetic particle inspection (MPI) for detection of fatigue cracks within the threads. Figure 8 shows a picture of the UV MPI inspection.

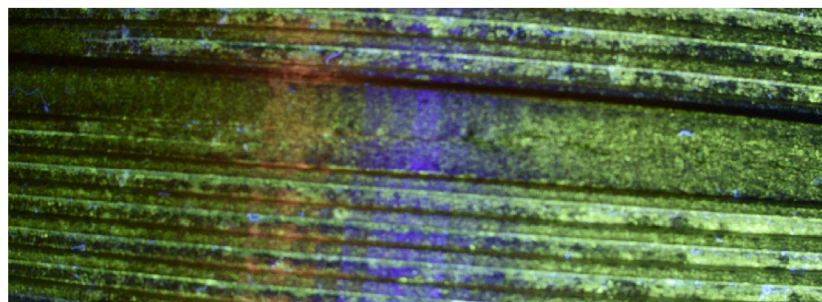


Figure 8: Ultraviolet Magnetic Particle Inspection of Threads

**SS-25 7 in. Speedtite Connection Testing and 11 3/4 in. STC Assessment**

---

The four connections chosen were C001B, C011B, C019B, and C025B. None of the pins had any surface-breaking defects (cracks).

## 4 Short Thread Casing Leak Resistance Review

---

The surface casing string run on SS-25 was 11 3/4 in. 42 ppf H40 with STC connections set at 990 ft in October 1953. STC is a non-proprietary connection whose design and manufacturing requirements are specified in *API 5B - Specification for Threading, Gauging and Thread Inspection of Casing, Tubing, and LinePipe Threads* [5]. STC connections do not have metal-to-metal seals and instead rely on the interference bearing pressure created between the pin and box threads during makeup. These threads also have a void at the thread root and crest areas that create a helical leak path through the connection, which must be plugged with thread compound to provide the possibility of any leak resistance.

Internal yield pressure of the 11 3/4 in. casing is 1,980 psi. The calculated, or design, leak resistance of STC connections for 11 3/4 in. casing is also 1,980 psi. However, as recognized by the industry since the 1940s, the actual leak resistance for STC connections run in the field can be significantly lower. The original API tubular specifications were established with the intent to standardize pipe sizes and connections so that material from one mill could be used interchangeably with material from other sources. The specifications did not focus on leak resistance. The leak resistance equations provided by API do not account for many threading variables either, including dimensional tolerances and tension. The variables that affect STC leak resistance include the pipe OD and pipe yield strength, the thread attributes (lead, taper, pitch diameter), the thread compound (which degrades over time), the tension load (which reduces the thread bearing pressure), and the field makeup practices (which impacts the thread bearing pressure).

Research on API threads conducted by T. H. Hill Associates in 1989 demonstrated that “the average pin screwed into the average coupling to the nominal power-tight position will have about 25%–45% less leak resistance than supposed” [6]. Due to pipe manufacturing practices and allowances and practical limitations on machining, a bias towards small pins and large boxes is built into the API pitch diameter gauging method. This leads to most connections not achieving design leak resistance. The research showed that at least 2.5% of the STC connections in a string will have an actual leak resistance at least 67% lower than the design leak resistance [6].

Enertech Engineering conducted research for API that concluded that leak resistance is strongly influenced by: loading sequence, makeup conditions, and dimensional tolerances (taper, thread lead, and ovality). In the study it was found that lower yield strengths of both the pipe body and coupling result in lower connector leak pressures due to the material in the connector reaching yield stress at makeup. Tension causes a significant reduction in leak resistance due to reduced stab flank contact pressure [7].

The actual STC leak resistance is expected to be lower than the design value and can be significantly lower with respect to gas leak resistance, which is much more challenging than leak resistance to a fluid (e.g., water, drilling fluids). This is why most proprietary connections utilize a metal-to-metal seal to provide leak resistance and do not rely on the threads and thread compound. STC connections are not gas-tight. A great deal of industry work has been done since SS-25 was drilled to understand and improve the leak resistance and reliability of STC and similar API connections. This knowledge was unavailable in 1953.

STC connections are perfectly acceptable in the right application, such as for surface casing strings where the setting depths are relatively shallow, downhole pressures are low, and gas is rarely encountered. The main function of surface casing is to isolate fresh water, provide structural support for the rest of the well, and not to provide a gas-tight barrier to a production string.

Considering the amount of time the 11 3/4 in. casing had been in place and the known limitations of STC regarding leak resistance, exacerbated in the presence of gas, it is highly probable that the 11 3/4 in. casing could have leaked gas at a very low pressures.

## 5 Conclusions

---

The purpose of the connection testing was to determine whether the connections would maintain internal pressure equivalent to the highest gas storage operating pressure without leaking. Twenty-five connections were tested and nine leaked. After testing, select connections were broken out and all had breakout torques that were lower than the estimated recommended makeup torque. In contrast, five connections from the P-34 well were broken out and all had breakout torques higher than the recommended makeup torque, which would have been expected. However, there was no apparent relationship between breakout torque and the susceptibility of a particular connection to leak because, for example, test specimen C001B had the lowest breakout torque and did not leak during testing. The pin and box threads were cleaned, visually inspected, and found to be in very good condition. There was no obvious thread galling, metal burrs, seal area damage, or erosion paths. The thread attributes and seal dimensions could not be measured or gauged to identify any deviations from nominal because Speedtite connections are no longer commercially available.

The two connections with the highest leak rate (C016B and C023A1) were retested. A blue dye was first applied to the pin seal areas, and the connections were made up to a hand tight position and then broken out. On both connections there were sections of the box seal area where the dye had not been transferred from the pin seal area, suggesting a lack of seal contact. The connections were then made up to the estimated recommended makeup torque with modern API modified thread compound and retested. Both connections leaked again.

It should be noted that the tests were not quantitatively repeatable. If a connection leaked during a test and was retested at a later date, it would still leak, but the leak rates may not have been the same. For example, during the testing of C019B, the connection leaked beyond the capacity of the 500 SCCM meter. The connection was retested with the 50,000 SCCM flow meter and no leaks appeared. It was then retested with the 500 SCCM flow meter and had a peak leak rate of 137 SCCM. Most of the leak rates were quite low, ranging from 1.2 to 237 SCCM for seven tests. The two joints with the highest leak rates were C016B and C023A1C, which leaked at 1,120 SCCM (57 SCFD) and 196 SLM (9,967 SCFD), respectively, during initial testing. To put this in context, while the C023A1C leak rate was 0.01 million standard cubic feet of gas per day (MMscf/D), it is estimated that during the blowout the well rate exceeded 90 MMscf/D.

The capped end load during testing was 105 kips, which is approximately 44% of the load seen by the 7 in. casing at 892 ft. Due to this difference in axial load, the downhole leak rates may have been greater than those observed during testing due to tension decreasing the primary seal energy.

The testing results suggest that some of the Speedtite connections leaked very small amounts of gas into the 7 in. × 11 3/4 in. annulus over time. It can be concluded that the volume of gas would also have varied over time, depending on the internal pressure that the casing was exposed to, which was a function of the ongoing storage operation (injection or withdrawal). Figure 9 shows the SS-25 casing pressure history from 1977 to 2016.



STANDARD SESNON 25 WELL

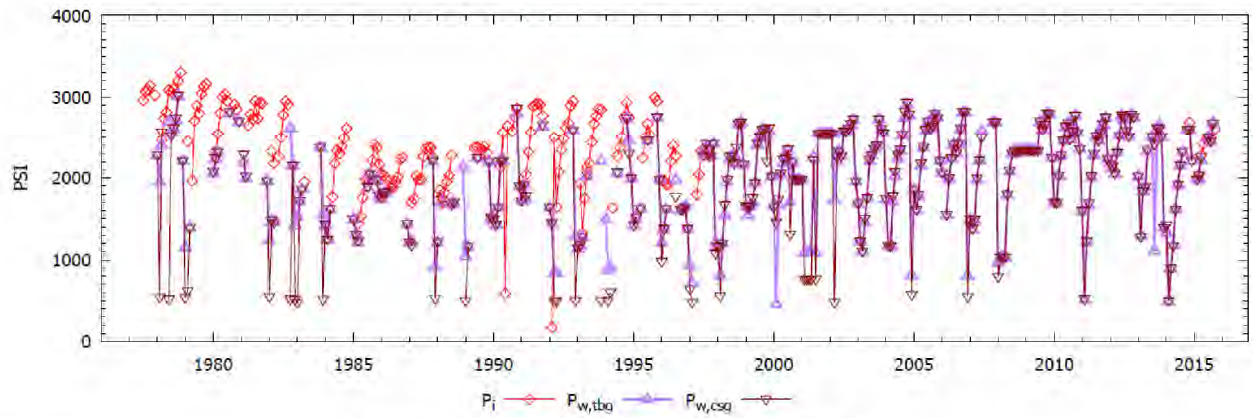


Figure 9: SS-25 Casing Pressure History ( $P_{w,csq}$ )

The STC connection design, and the recognized issues around the leak resistance of the connection, demonstrate that the connection was not gas-tight and suggests that the connection would have leaked gas at very low internal pressures.

## 6 References

---

- [1] Blade Energy Partners, "Aliso Canyon RCA: Protocol for 7" Casing Connection Testing, Rev 000," 2018.
- [2] Blade Energy Partners, "Phase 3 Tubulars Handling Protocol (AC-RCA Phase 3 Tubulars Handling Protocol Rev 004, 31-July-2017.pdf)".
- [3] American Petroleum Institute, "API RP 5C5 - Recommended Practice on Procedures for Testing Casing and Tubing Connections," 2003.
- [4] Blade Energy Partners, "SS-25 7 in. Casing Load Analysis," 2019.
- [5] American Petroleum Institute, "API Specification 5B - Specification for Threading, Gauging, and Thread Inspection of Casing, Tubing and Line Pipe Threads".
- [6] T. H. Hill and R. C. Money, "Caution: API Gaging Practices Can Be Hazardous To Your Leak Resistance," Petroleum Engineer International, 1989.
- [7] Eneritech Engineering and Research Company, "Investigation of Leak Resistance of API 8-Round Connector," 1985.

## Appendix A Performance Data

Table 11: 7 in. Casing Details

String	OD (in.)	Nom. Wt. (ppf)	Grade	Nom. Wall (in.)	Nom. ID (in.)	Drift ID (in.)	Top (ft)	Bottom (ft)	Length (ft)	Conn.
Production	7.000	23.00	J55	0.317	6.366	6.241	0	2,398	2,398	Speedtite
		23.00	N80	0.317	6.366	6.241	2,398	6,308	3,910	Speedtite
		26.00	N80	0.362	6.276	6.151	6,308	8,282	1,974	Speedtite
		29.00	N80	0.408	6.184	6.059	8,282	8,585	303	Speedtite

Table 12: 7 in. Casing Nominal Performance

String	OD (in.)	Nom. Wt. (ppf)	Grade	Pipe Body Data				Connection Data		
				Nom. Wall (in.)	Burst (psi)	Collapse (psi)	Tension (lbf)	OD (in.)	ID (in.)	Burst (psi)
Production	7.000	23.00	J55	0.317	4,360	3,270	366,000	7.444	6.285	4,360
		23.00	N80	0.317	6,340	3,830	532,000	7.444	6.285	6,340
		26.00	N80	0.362	7,240	5,410	604,000	7.444	6.196	7,240
		29.00	N80	0.408	8,160	7,030	676,000	7.572	6.104	8,160

## Appendix B Photos



Figure 10: Conex Trailer Used for Connection Testing



Figure 11: Inside the Conex—Pressure Cabinet and Control Box



Figure 12: Inside the Conex—Test Specimen Secured in the Test Fixture



Figure 13: Inside the Conex—Instrumented Test Specimen

# SS-25 7 in. Speedtite Connection Testing and 1 3/4 in. STC Assessment



Figure 14: Test Control Panel and Test Data Display

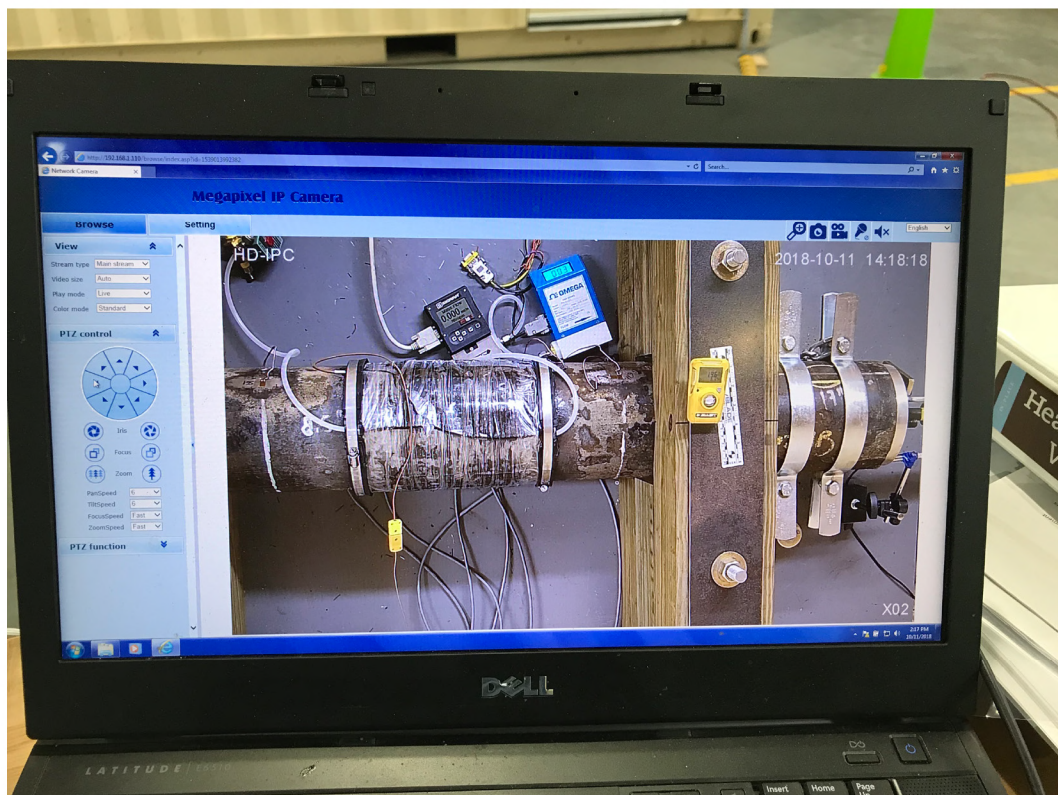


Figure 15: Camera View of Test



Figure 16: Connection Test Specimens after Testing



Figure 17: Breaking Out a Connection with the Horizontal Bucking Machine



Figure 18: Representative Pin Condition after Break out and Cleaning




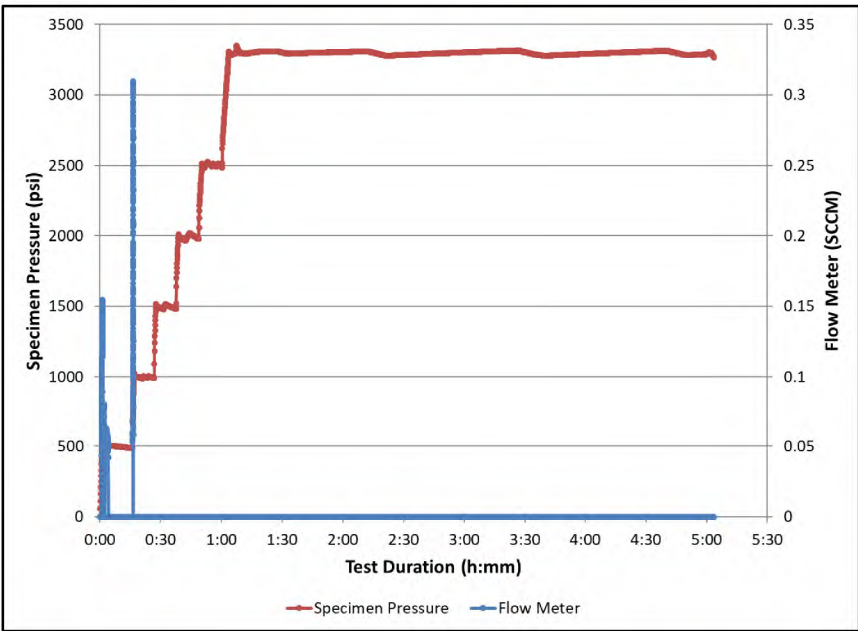
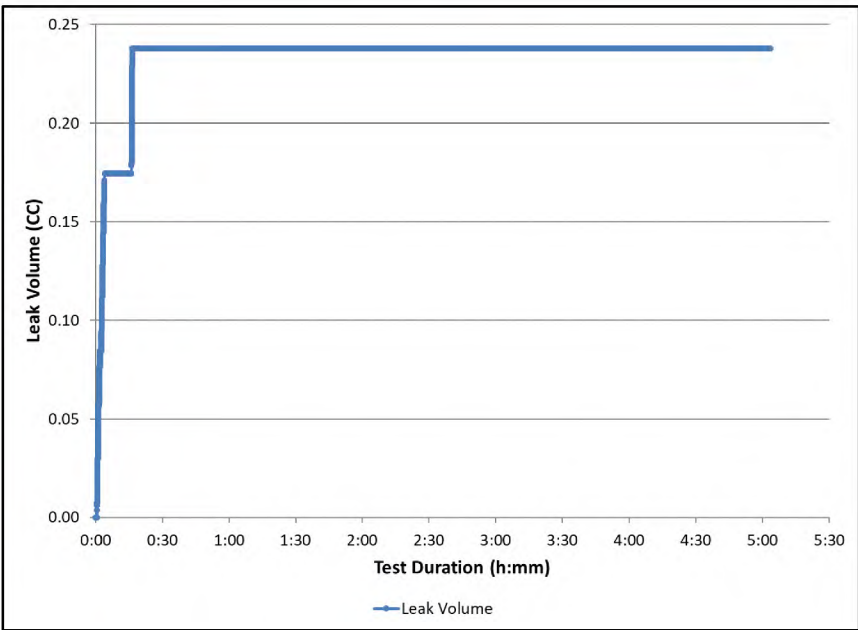
Figure 19: Representative Box Condition after Break out and Cleaning





Figure 20: Representative Full Blueing Transfer on C002B


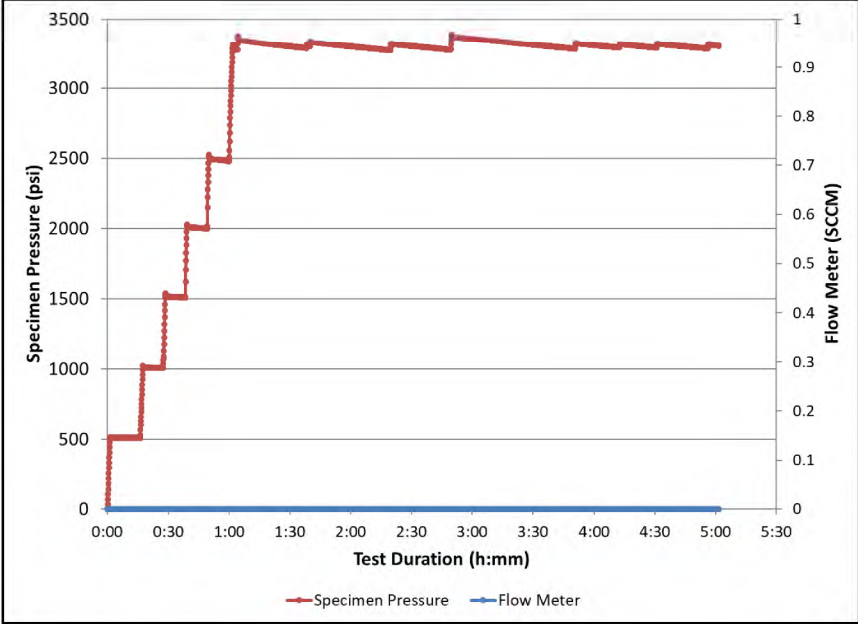
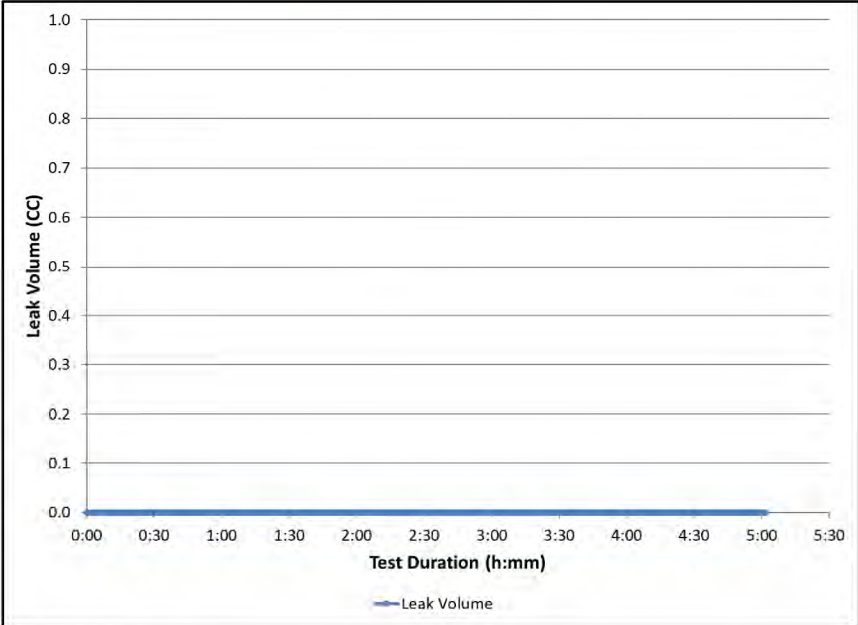
## Appendix C Connection Test Data Sheets


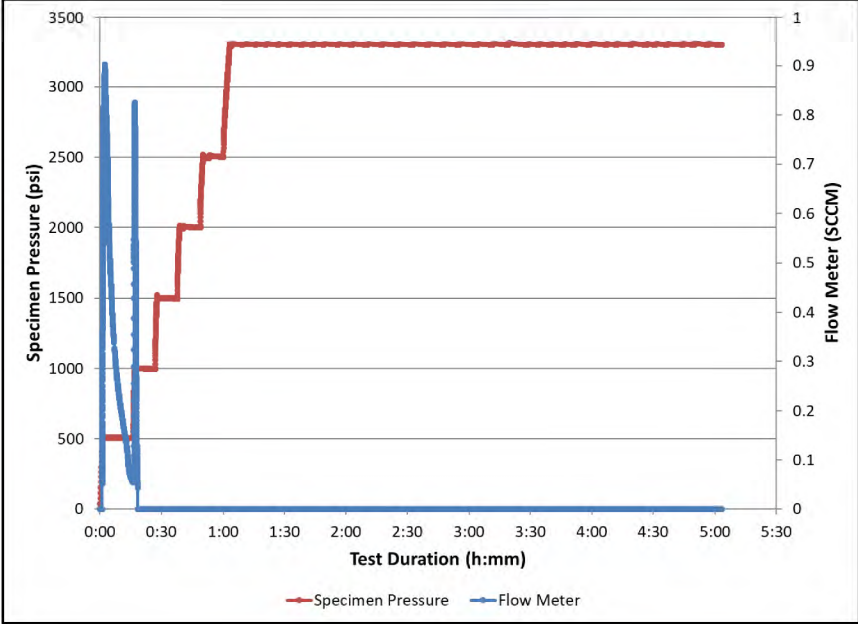
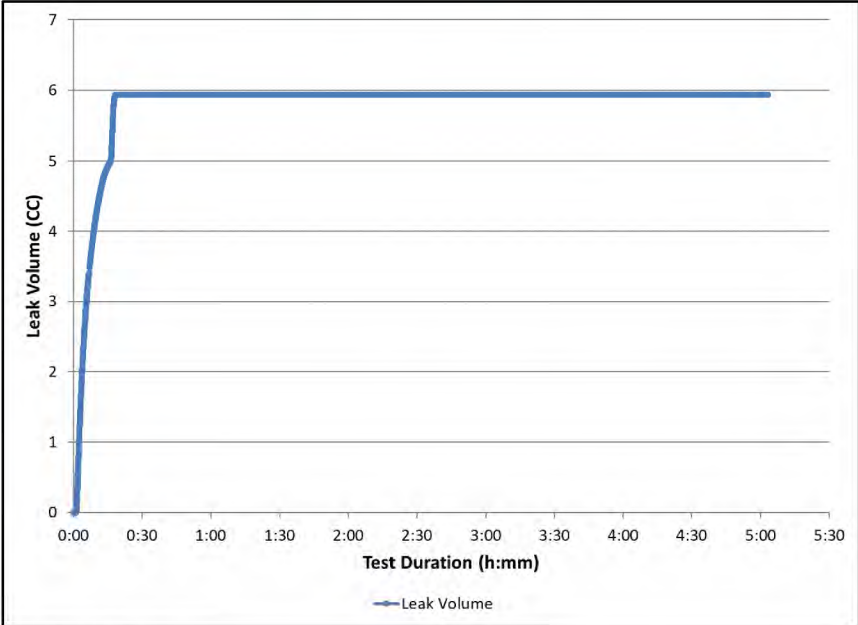
 <b>Connection Test Data Sheet</b> SS-25 7" 23.0 ppf J55 Casing, Speedtite Connection Connection: <u>C001B</u>		No Leak
		
		
<b>Test Date:</b>	<b>Comments:</b>	
1. 12, Sept. 2018	1.) Test conducted with 4 SCCM flow meter; No Leak.	

<b>Connection Test Data Sheet</b> SS-25 7" 23.0 ppf J55 Casing, Speedtite Connection Connection: <u>C002B</u>		Leak
<p><b>Test Date:</b></p> <ul style="list-style-type: none"> <li>1. 20, Aug 2018</li> <li>2. 23, Aug 2018</li> <li>3. 27, Aug 2018</li> </ul>	<p><b>Comments:</b></p> <p>1.) Tested with 4 SCCM flow meter, leak detected at 1,000psi. 2.) Tested with 50 SCCM flow meter and leaked beyond flow meter range. 3.) Tested with 500 SCCM flow meter. Maximum leak rate was approximately 101 SCCM.</p>	

<b>Connection Test Data Sheet</b> SS-25 7" 23.0 ppf J55 Casing, Speedtite Connection Connection: <u>C003B</u>		No Leak
<b>Test Date:</b> 1. 30, Aug 2018	<b>Comments:</b> 1.) Tested with 4 SCCM flow meter; No Leak.	


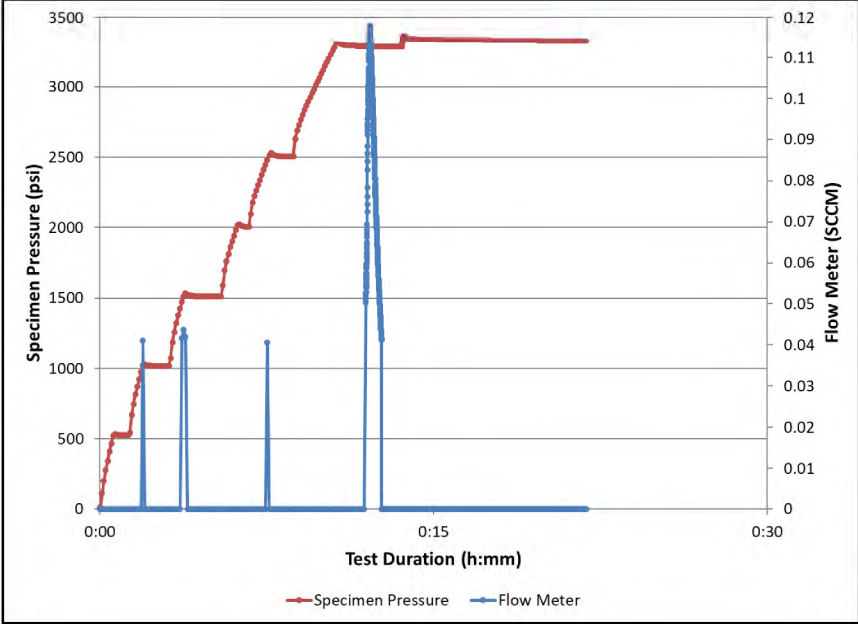
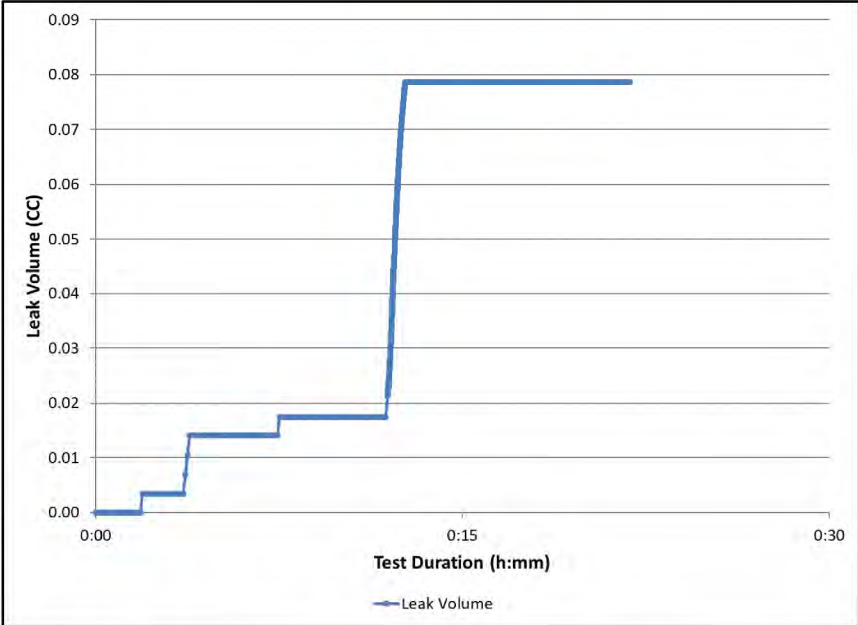
<b>Connection Test Data Sheet</b> SS-25 7" 23.0 ppf J55 Casing, Speedtite Connection Connection: <u>C004B</u>		Leak
<p><b>Test Date:</b></p> <ul style="list-style-type: none"> <li>1. 15, Aug 2018</li> <li>2. 17, Aug 2018</li> <li>3. 27, Aug 2018</li> </ul>	<p><b>Comments:</b></p> <p>1.) Tested with 4 SCCM flow meter, leaked beyond range of flow meter. 2.) Re-tested with 4 SCCM flow meter to verify initial test. 3.) Tested with 500 SCCM flow meter. Maximum leak rate was approximately 200 SCCM.</p>	


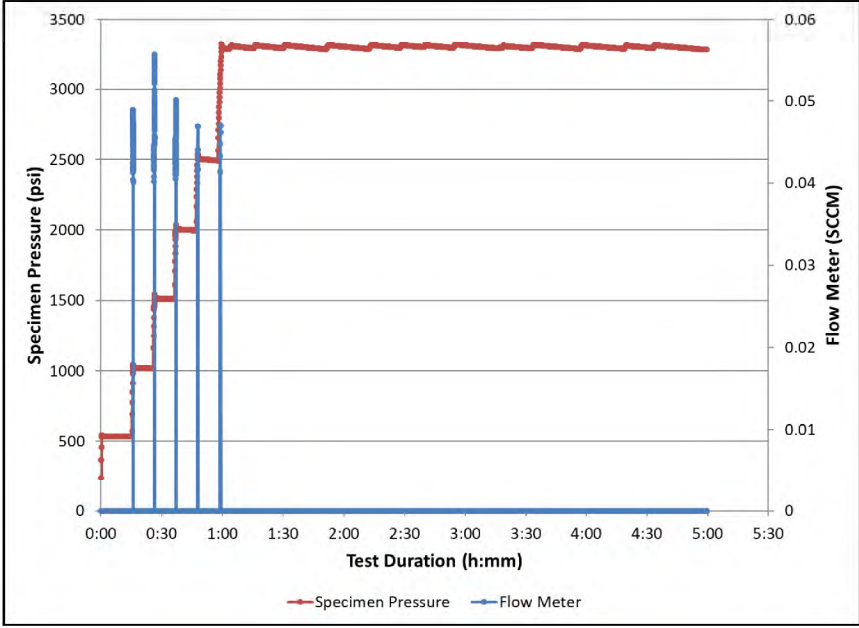
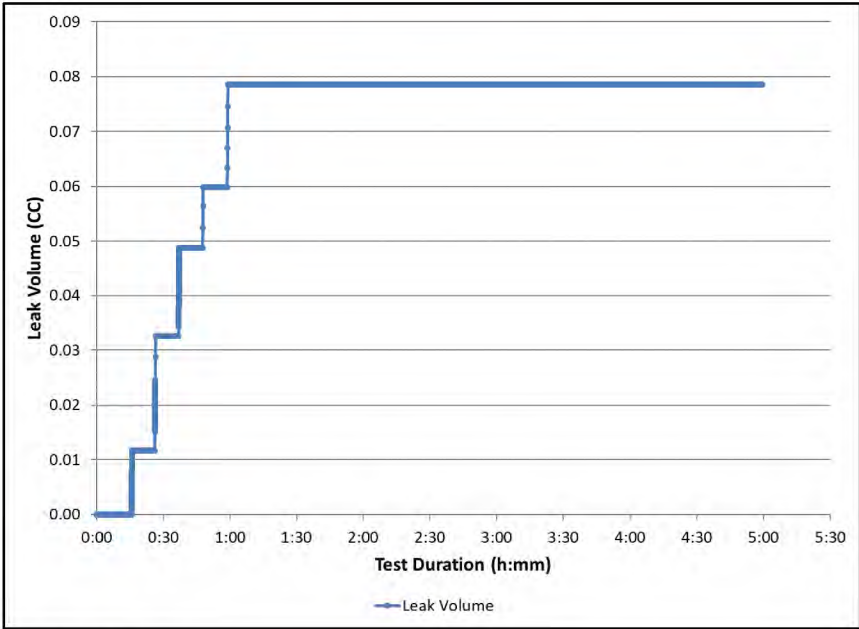
 <b>Connection Test Data Sheet</b> SS-25 7" 23.0 ppf J55 Casing, Speedtite Connection Connection: <u>C005B</u>		No Leak
		
		
<p><b>Test Date:</b>                  1. 16, Aug 2018                  2. 24, Aug 2018</p>	<p><b>Comments:</b>                  1.) Tested with 4 SCCM flow meter. Flow through the meter peaked at 3.4 SCCM and was determined to be from differential expansion of the connection and external sealing boot. 2.) Retested with 50 SCCM flow meter; No Leak.</p>	


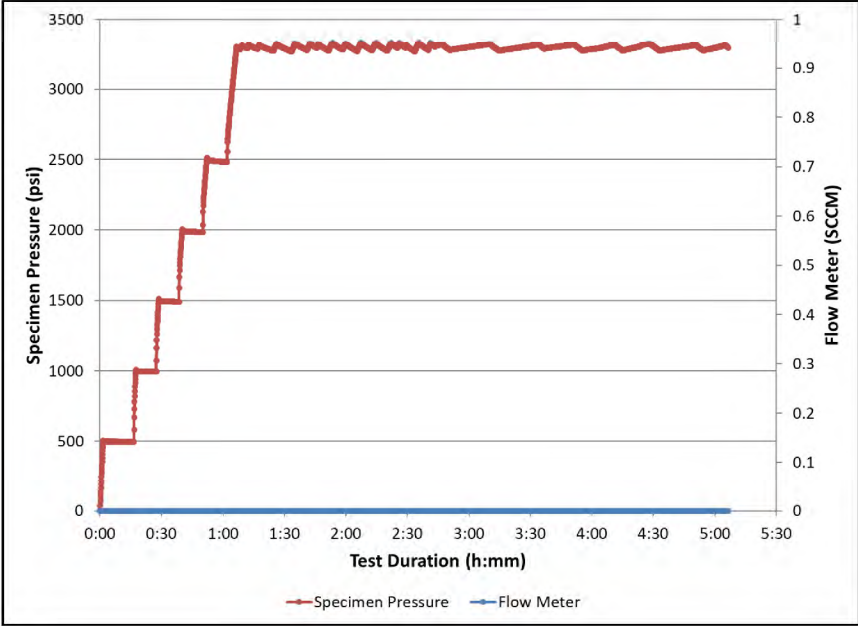
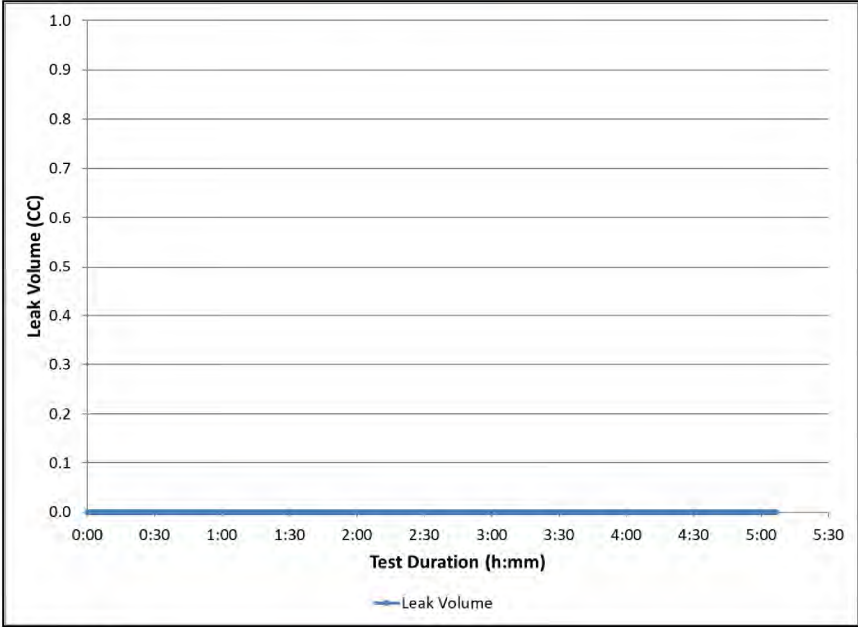
 <b>Connection Test Data Sheet</b> SS-25 7" 23.0 ppf J55 Casing, Speedtite Connection Connection: <u>C006B</u>		No Leak
		
		
<b>Test Date:</b> 1. 30, Aug 2018	<b>Comments:</b> 1.) Tested with 4 SCCM flow meter; No Leak.	

<b>Connection Test Data Sheet</b> SS-25 7" 23.0 ppf J55 Casing, Speedtite Connection Connection: <u>C007B</u>		No Leak
<b>Test Date:</b> 1. 29, Aug 2018	<b>Comments:</b> 1.) Tested with 4 SCCM flow meter; No Leak.	



 <b>Connection Test Data Sheet</b> SS-25 7" 23.0 ppf J55 Casing, Speedtite Connection Connection: <u>C008B</u>		No Leak
		
		
<p><b>Test Date:</b> 1. 28, Aug 2018 2. 28, Aug 2018</p>	<p><b>Comments:</b> 1.) Tested with 500 SCCM flow meter; No Leak. 2.) Retested with 4 SCCM flow meter, no leak.</p>	

 <b>Connection Test Data Sheet</b> SS-25 7" 23.0 ppf J55 Casing, Speedtite Connection Connection: <u>C009B</u>		No Leak
		
		
<b>Test Date:</b> 1. 29, Aug 2018	<b>Comments:</b> 1.) Tested with 4 SCCM flow meter; No Leak.	

 <b>Connection Test Data Sheet</b> SS-25 7" 23.0 ppf J55 Casing, Speedtite Connection Connection: <u>C010B</u>		No Leak
		
		
<b>Test Date:</b> 1. 29, Aug 2018	<b>Comments:</b> 1.) Tested with 4 SCCM flow meter; No Leak.	

<b>Connection Test Data Sheet</b> SS-25 7" 23.0 ppf J55 Casing, Speedtite Connection Connection: <u>C011B</u>		Leak
<p><b>Test Date:</b>                  1. 05, Sept 2018                  2. 05, Sept 2018</p>	<p><b>Comments:</b>                  1.) Tested with 4 SCCM flow meter leaked beyond flow meter range. 2.) Tested with 500 SCCM flow meter. Flow rate peaked at approximately 363 SCCM.</p>	


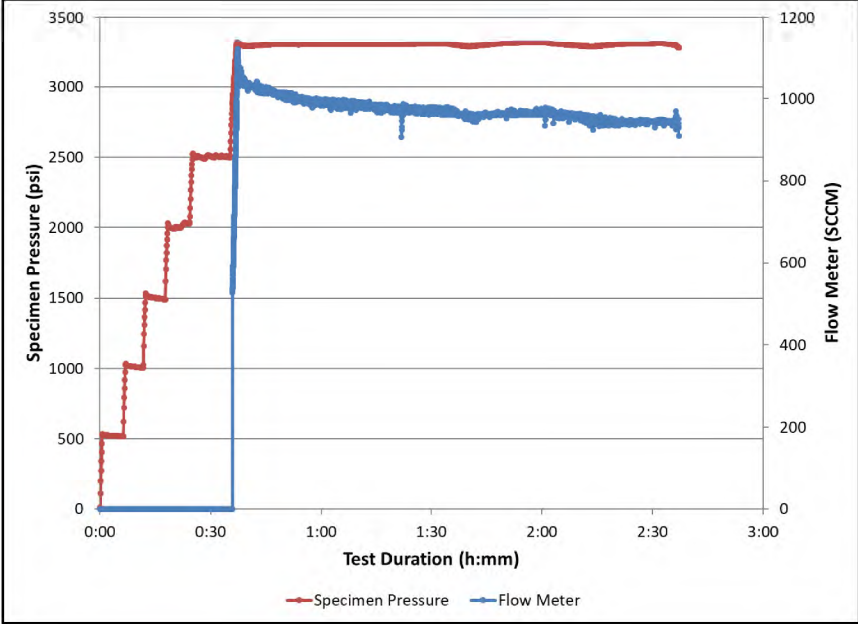
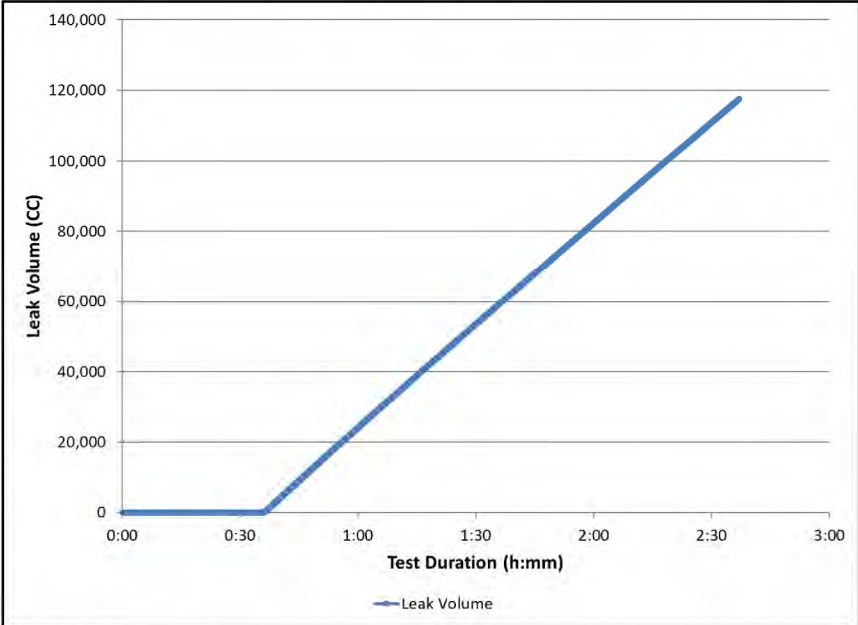
<b>Connection Test Data Sheet</b> SS-25 7" 23.0 ppf J55 Casing, Speedtite Connection Connection: <u>C012B</u>		Leak
<p><b>Test Date:</b> 1. 05, Sept 2018</p>	<p><b>Comments:</b> 1.) Tested with 4 SCCM flow meter. Flow rate peaked at approximately 1.7 SCCM.</p>	

<b>Connection Test Data Sheet</b> SS-25 7" 23.0 ppf J55 Casing, Speedtite Connection Connection: <u>C013B</u>		No Leak
<p><b>Test Date:</b> 1.06, Sept 2018</p>	<p><b>Comments:</b> 1.) Tested with 4 SCCM flow meter; No Leak.</p>	

<b>Connection Test Data Sheet</b> SS-25 7" 23.0 ppf J55 Casing, Speedtite Connection Connection: <u>C014B</u>		No Leak
<b>Test Date:</b> 1. 07, Sept 2018	<b>Comments:</b> 1.) Tested with 4 SCCM flow meter; No Leak.	

<b>Connection Test Data Sheet</b> SS-25 7" 23.0 ppf J55 Casing, Speedtite Connection Connection: <u>C015B</u>		No Leak
<b>Test Date:</b> 1. 11, Sept 2018	<b>Comments:</b> 1.) Tested with 4 SCCM flow meter; No Leak.	



 <b>Connection Test Data Sheet</b> SS-25 7" 23.0 ppf J55 Casing, Speedtite Connection Connection: <u>C016B</u>		Leak
		
		
<b>Test Date:</b> 1. 10, Sept 2018 2. 10, Sept 2018 3. 10, Sept 2018	<b>Comments:</b> 1.) Tested with 4 SCCM flow meter. Leaked beyond flow meter range. 2.) Tested with 500 SCCM flow meter. Leaked beyond flow meter range. 3.) Tested with 50,000 SCCM flow meter. Flow rate peaked at 1,120 SCCM.	

<b>Connection Test Data Sheet</b> SS-25 7" 23.0 ppf J55 Casing, Speedtite Connection Connection: <u>C016B – After Make-Up</u>		Leak
<b>Test Date:</b> 1. 24, Jan 2019 2. 24, Jan 2019	<b>Comments:</b> All testing done after connection was broken out, cleaned, re-doped with API modified dope and made-up to 8,396 ft-lb 1.) Tested with 4 SCCM flow meter. Leaked beyond flow meter range. 2.) Tested with 50 SCCM flow meter. Flow rate peaked at 34.9 SCCM.	

<b>Connection Test Data Sheet</b> SS-25 7" 23.0 ppf J55 Casing, Speedtite Connection Connection: <u>C017B</u>		No Leak
<p><b>Test Date:</b> 1. 13, Sept 2018</p>	<p><b>Comments:</b> 1.) Tested with 4 SCCM flow meter; No Leak. Readings on flow meter are due to differential expansion between the connection and external sealing boot.</p>	

<b>Connection Test Data Sheet</b> SS-25 7" 23.0 ppf J55 Casing, Speedtite Connection Connection: <u>C018B</u>		No Leak
<p><b>Test Date:</b> 1. 17, Sept 2018</p>	<p><b>Comments:</b> 1.) Tested with 4 SCCM flow meter; No Leak.</p>	

<b>Connection Test Data Sheet</b> SS-25 7" 23.0 ppf J55 Casing, Speedtite Connection Connection: <u>C019B</u>		Leak
<p><b>Test Date:</b></p> <ul style="list-style-type: none"> <li>1. 19, Sept 2018</li> <li>2. 19, Sept 2018</li> <li>3. 8, Oct 2018</li> <li>4. 9, Oct 2018</li> </ul>	<p><b>Comments:</b></p> <p>1.) Tested with 4 SCCM flow meter, leaked beyond flow meter range. 2.) Tested with 500 SCCM flow meter, leaked beyond flow meter range. 3.) Tested with 50,000 SCCM flow meter, no flow recorded. 4.) Retested with 500 SCCM flow meter. Peak flow was approximately 137 SCCM.</p>	

<b>Connection Test Data Sheet</b> SS-25 7" 23.0 ppf J55 Casing, Speedtite Connection Connection: <u>C020B</u>		No Leak
<p><b>Test Date:</b> 1. 14, Sept 2018</p>	<p><b>Comments:</b> 1.) Tested with 4 SCCM flow meter; No Leak.</p>	

<b>Connection Test Data Sheet</b> SS-25 7" 23.0 ppf J55 Casing, Speedtite Connection Connection: <u>C021B</u>		Leak
<p><b>Test Date:</b>                  1. 20, Sept 2018                  2. 20, Sept 2018</p>	<p><b>Comments:</b>                  1.) Tested with 4 SCCM flow meter, leaked beyond flow meter range. 2.) Tested with 500 SCCM flow meter. Flow rate peaked at approximately 128 SCCM.</p>	

<b>Connection Test Data Sheet</b> SS-25 7" 23.0 ppf J55 Casing, Speedtite Connection Connection: <u>C023A1C</u>		Leak
<p><b>Test Date:</b></p> <ul style="list-style-type: none"> <li>1. 15, Oct 2018</li> <li>2. 15, Oct 2018</li> <li>3. 24, Oct 2018</li> </ul>	<p><b>Comments:</b></p> <p>1.) Tested with 4 SCCM flow meter, leaked beyond flow meter range. 2.) Tested with 50,000 SCCM flow meter, leaked beyond flow meter range. 3.) Tested with 1,000 SLM. Flow rate peaked at approximately 196 SLM at which point the leak rate was too great to continue to build pressure. Also, during the peak leak rate the resulting temperature drop was approaching an unsafe limit.</p>	



<b>Connection Test Data Sheet</b> SS-25 7" 23.0 ppf J55 Casing, Speedtite Connection Connection: <u>C023A1C – After Make-Up</u>		Leak
<p><b>Test Date:</b></p> <ul style="list-style-type: none"> <li>1. 24, Jan 2019</li> <li>2. 24, Jan 2019</li> <li>3. 24, Jan 2019</li> </ul>	<p><b>Comments:</b></p> <p>All testing done after connection was broken out, cleaned, re-doped with API modified dope and made-up to 8,009 ft-lb. 1.) Tested with 500 SCCM flow meter, leaked beyond flow meter range. 2.) Tested with 50,000 SCCM flow meter, leaked beyond flow meter range. 3.) Tested with 1,000 SLM. Flow rate peaked at approximately 306 SLM at which point the leak rate was too great to continue to build pressure.</p>	

<b>Connection Test Data Sheet</b> SS-25 7" 23.0 ppf J55 Casing, Speedtite Connection Connection: <u>C024B</u>		No Leak
<b>Test Date:</b> 1. 22, Oct 2018	<b>Comments:</b> 1.) Tested with 4 SCCM flow meter; No Leak.	

<b>Connection Test Data Sheet</b> SS-25 7" 23.0 ppf J55 Casing, Speedtite Connection Connection: <u>C025B</u>		Leak
<b>Test Date:</b> 1. 10, Oct 2018 2. 10, Oct 2018	<b>Comments:</b> 1.) Tested with 4 SCCM flow meter, leaked beyond flow meter range. 2.) Tested with 500 SCCM flow meter. Maximum leak rate was approximately 240 SCCM.	

<b>Connection Test Data Sheet</b> SS-25 7" 23.0 ppf J55 Casing, Speedtite Connection Connection: <u>C026B1</u>		No Leak
<b>Test Date:</b> 1. 10, Oct 2018	<b>Comments:</b> 1.) Tested with 4 SCCM flow meter; No Leak.	

## Appendix D Breakout and Makeup Torque Data

---

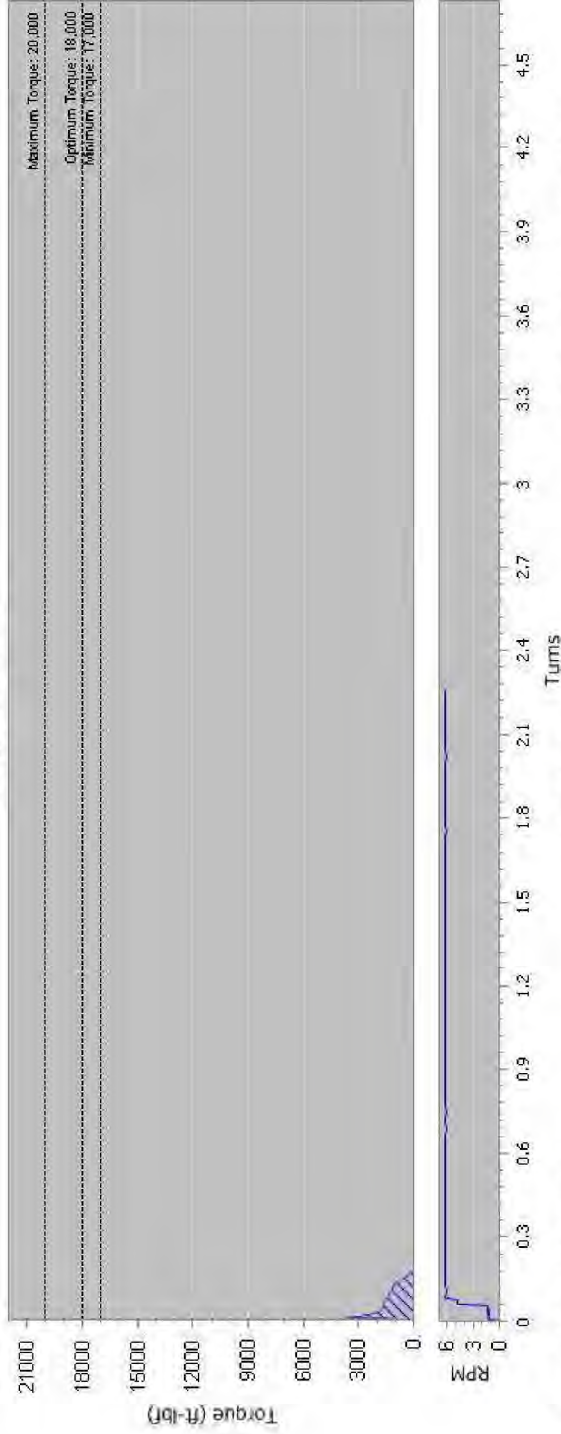
The breakout torque charts for the SS-25 7 in. Speedtite connections are included in this section. The charts show the torque and revolutions per minute vs. turns. The joint and connection numbers are shown in the lower left-hand corners. Other details are shown below the charts.

# BREAK OUT REPORT

Date: 23/10/2018

Operator: MILLIGAN

Torque vs Turns



## BREAK OUT INFORMATION

Job Reference SC-G-16-001-SS25  
Sequence No. 4  
Operator MILLIGAN  
Customer SoCalGas  
Description SS-25 C001B

## JOINT DETAILS

Start Time 13:02:00  
End Time 13:02:26  
Achieved Torque 3,614  
Shoulder Torque -  
Delta Torque -  
Achieved Turns 2,253  
Delta Turns -  
Delta Slope -

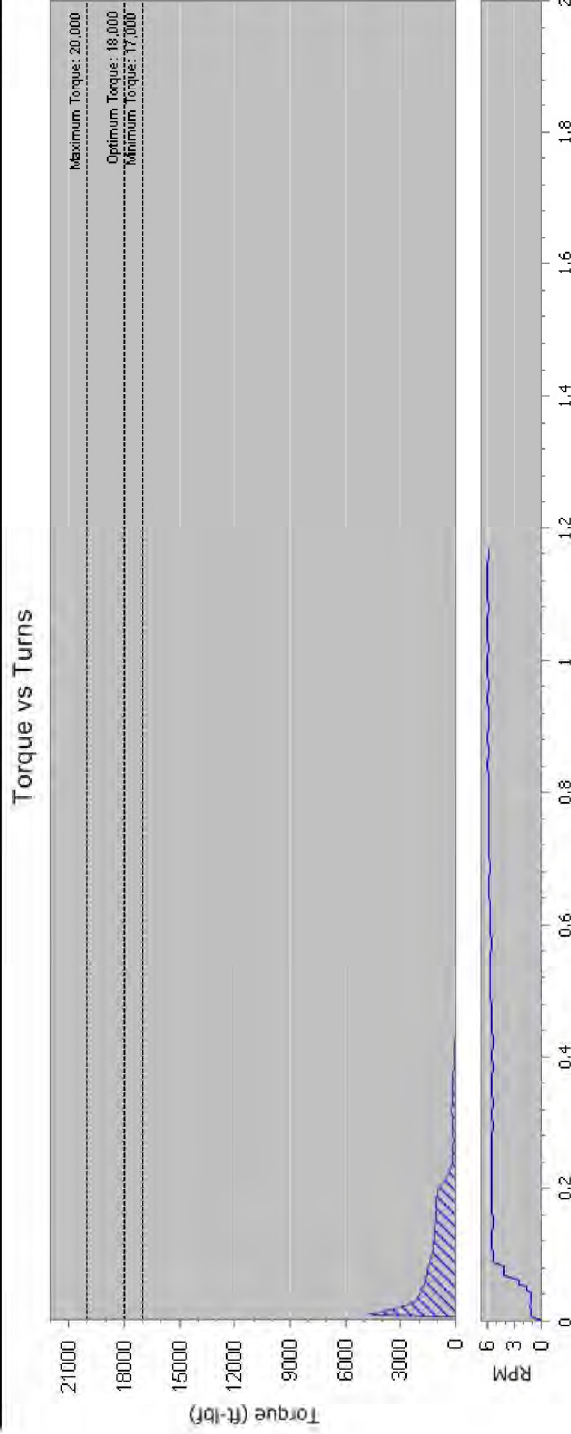
## PIPE DETAILS / PARAMETERS

Thread Direction Right Hand Thread  
Thread Type SpeedTite  
Size 7"  
Weight 23.0  
Grade J55  
Thread Compound Unknown

# BREAK OUT REPORT

Date: 06/11/2018

Operator: JS,BW,BS



### BREAK OUT INFORMATION

Job Reference: SoCal  
 Sequence No.: 1  
 Operator: JS,BW,BS  
 Customer: SOCALGAS  
 Description: SS-25 C002B

### JOINT DETAILS

Start Time: 14:26:28  
 End Time: 14:26:45  
 Achieved Torque: 4,732  
 Shoulder Torque: -  
 Delta Torque: -  
 Achieved Turns: 1.167  
 Delta Turns: -  
 Delta Slope: -

### PIPE DETAILS / PARAMETERS

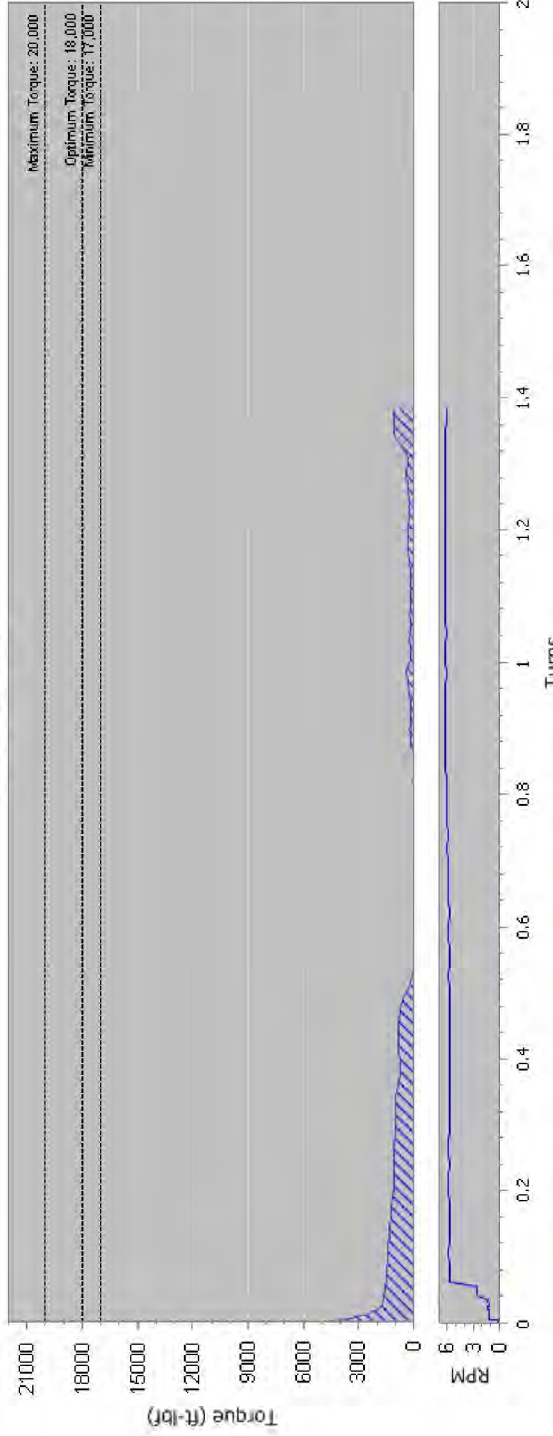
Thread Direction: Right Hand Thread  
 Thread Type: SpeedTite  
 Size: 7"  
 Weight: 23.0  
 Grade: J55  
 Thread Compound: Unknown

# BREAK OUT REPORT

Date: 06/11/2018

Operator: JS,BW,BS

Torque vs Turns



### BREAK OUT INFORMATION

Job Reference SoCal  
 Sequence No. 2  
 Operator JS,BW,BS  
 Customer SOCALGAS  
 Description SS-25 C004B

### JOINT DETAILS

Start Time 14:36:13  
 End Time 14:36:31  
 Achieved Torque 4,910  
 Shoulder Torque -  
 Delta Torque -  
 Achieved Turns 1.385  
 Delta Turns -  
 Delta Slope -

### PIPE DETAILS / PARAMETERS

Thread Direction Right Hand Thread  
 Thread Type SpeedTite  
 Size 7"  
 Weight 23.0  
 Grade J55  
 Thread Compound Unknown

www.eqtorque.com

Generated by AMC Rotational Torque on machine serial RT10:100/8656

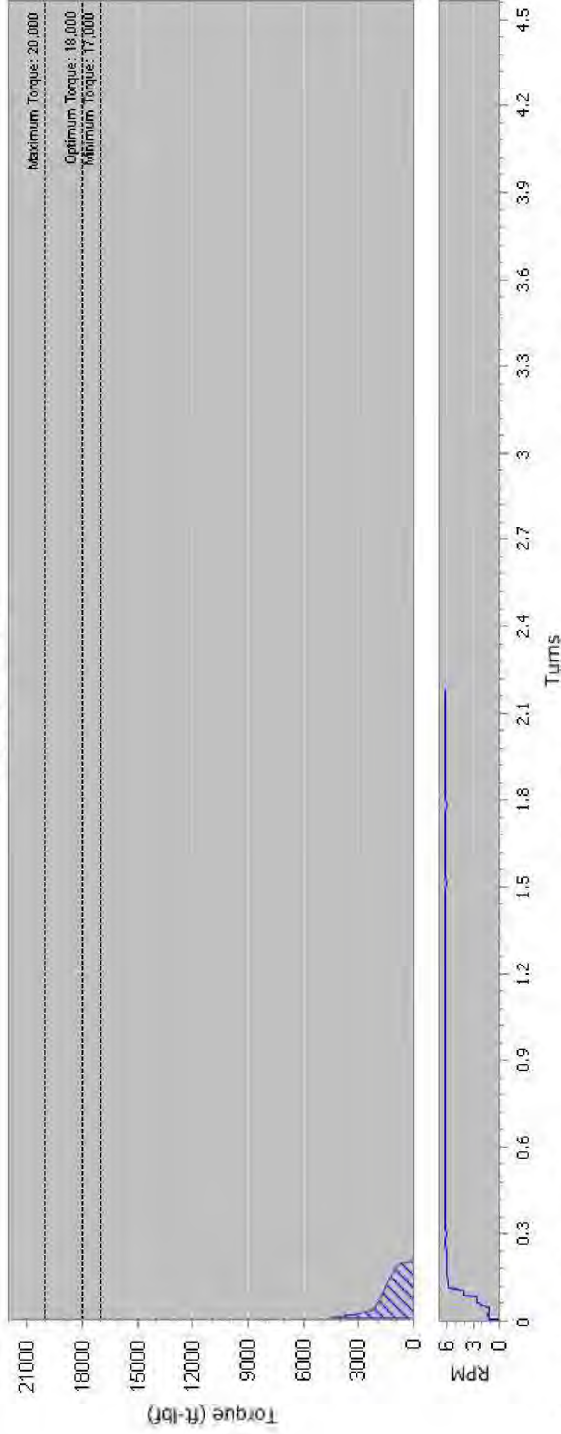


# BREAK OUT REPORT

Date: 23/10/2018

Operator: MILLIGAN

Torque vs Turns



## BREAK OUT INFORMATION

Job Reference SC-G-16-001-SS25  
 Sequence No. 3  
 Operator MILLIGAN  
 Customer SoCalGas  
 Description SS-25 C006B

## JOINT DETAILS

Start Time 12:54:10  
 End Time 12:54:36  
 Achieved Torque 4,452  
 Shoulder Torque -  
 Delta Torque -  
 Achieved Turns 2.174  
 Delta Turns -  
 Delta Slope -

## PIPE DETAILS / PARAMETERS

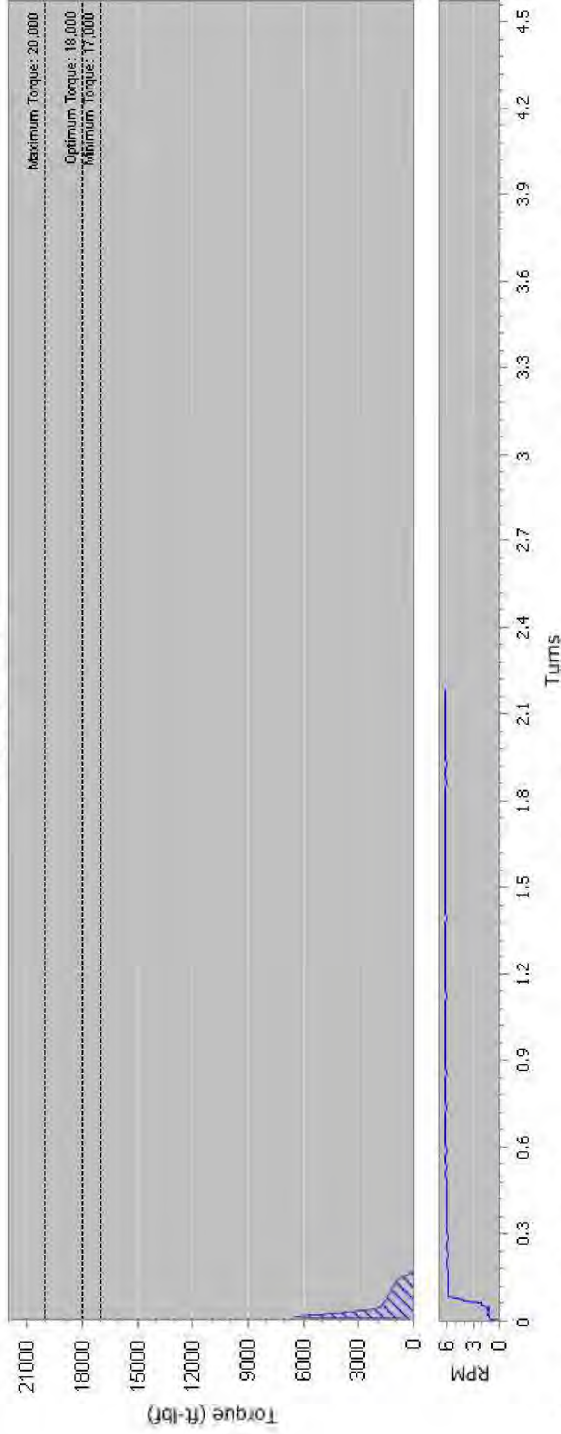
Thread Direction Right Hand Thread  
 Thread Type SpeedTite  
 Size 7"  
 Weight 23.0  
 Grade J55  
 Thread Compound Unknown

# BREAK OUT REPORT

Date: 23/10/2018

Operator: MILLIGAN

Torque vs Turns



### BREAK OUT INFORMATION

Job Reference SC-G-16-001-SS25  
Sequence No. 2  
Operator MILLIGAN  
Customer SoCalGas  
Description SS-25 C010B

### JOINT DETAILS

Start Time 12:46:26  
End Time 12:46:52  
Achieved Torque 6,477  
Shoulder Torque -  
Delta Torque -  
Achieved Turns 2.178  
Delta Turns -  
Delta Slope -

### PIPE DETAILS / PARAMETERS

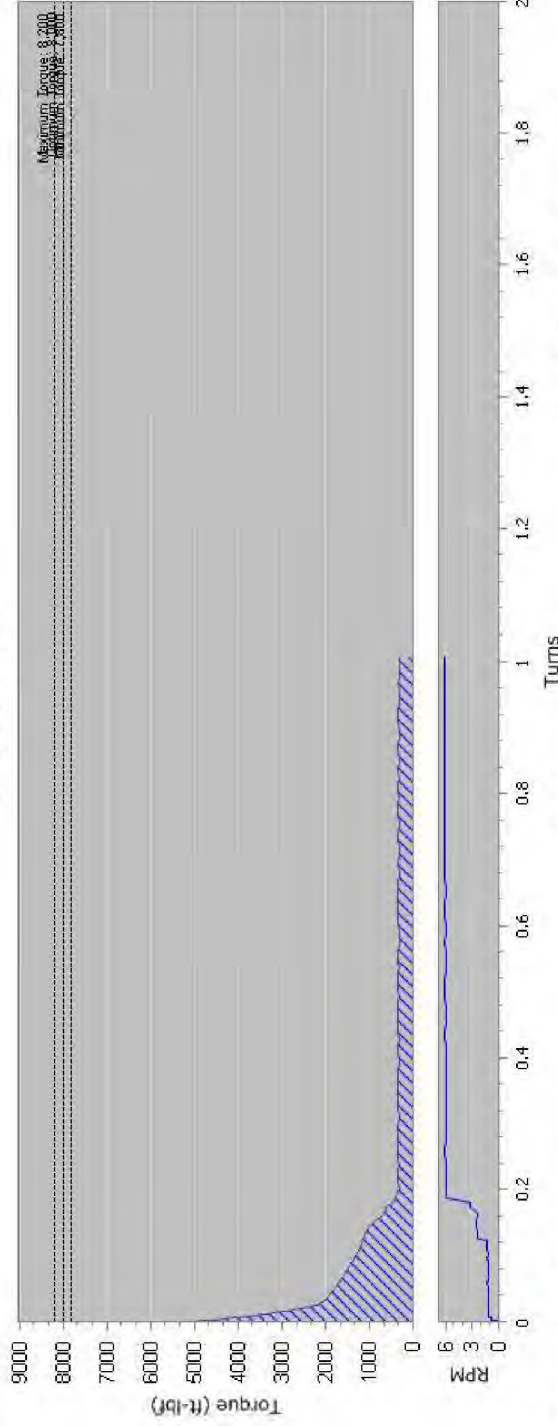
Thread Direction Right Hand Thread  
Thread Type SpeedTite  
Size 7"  
Weight 23.0  
Grade J55  
Thread Compound Unknown

# BREAK OUT REPORT

Date: 30/01/2019

Operator: JS,GC

Torque vs Turns



### BREAK OUT INFORMATION

Job Reference: SoCal  
 Sequence No.: 12  
 Operator: JS,GC  
 Customer: SOCALGAS  
 Description: C011B

### JOINT DETAILS

Start Time: 09:03:12  
 End Time: 09:03:30  
 Achieved Torque: 5,237  
 Shoulder Torque: -  
 Delta Torque: -  
 Achieved Turns: 1.005  
 Delta Turns: -  
 Delta Slope: -

### PIPE DETAILS / PARAMETERS

Thread Direction: Right Hand Thread  
 Thread Type: SpeedTite  
 Size: 7"  
 Weight: 23.0  
 Grade: J55  
 Thread Compound: API Modified

www.eqtorque.com

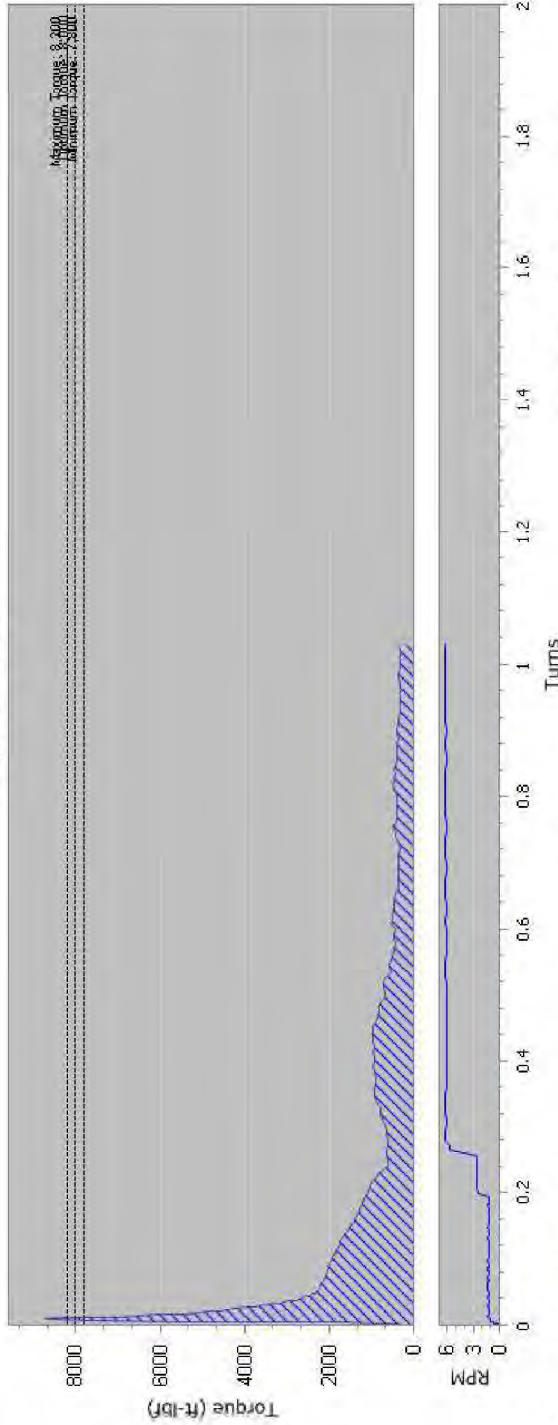
Generated by AMC Rotational Torque on machine serial RT10:100/8656

# BREAK OUT REPORT

Date: 30/01/2019

Operator: JS,GC

Torque vs Turns



Maximum Torque: 8,000  
Minimum Torque: 7,500

### BREAK OUT INFORMATION

Job Reference: SoCal  
 Sequence No.: 13  
 Operator: JS,GC  
 Customer: SOCALGAS  
 Description: C012B

### JOINT DETAILS

Start Time: 09:07:57  
 End Time: 09:08:18  
 Achieved Torque: 8,708  
 Shoulder Torque: -  
 Delta Torque: -  
 Achieved Turns: 1.029  
 Delta Turns: -  
 Delta Slope: -

### PIPE DETAILS / PARAMETERS

Thread Direction: Right Hand Thread  
 Thread Type: SpeedTite  
 Size: 7"  
 Weight: 23.0  
 Grade: J55  
 Thread Compound: API Modified

www.eqtorque.com

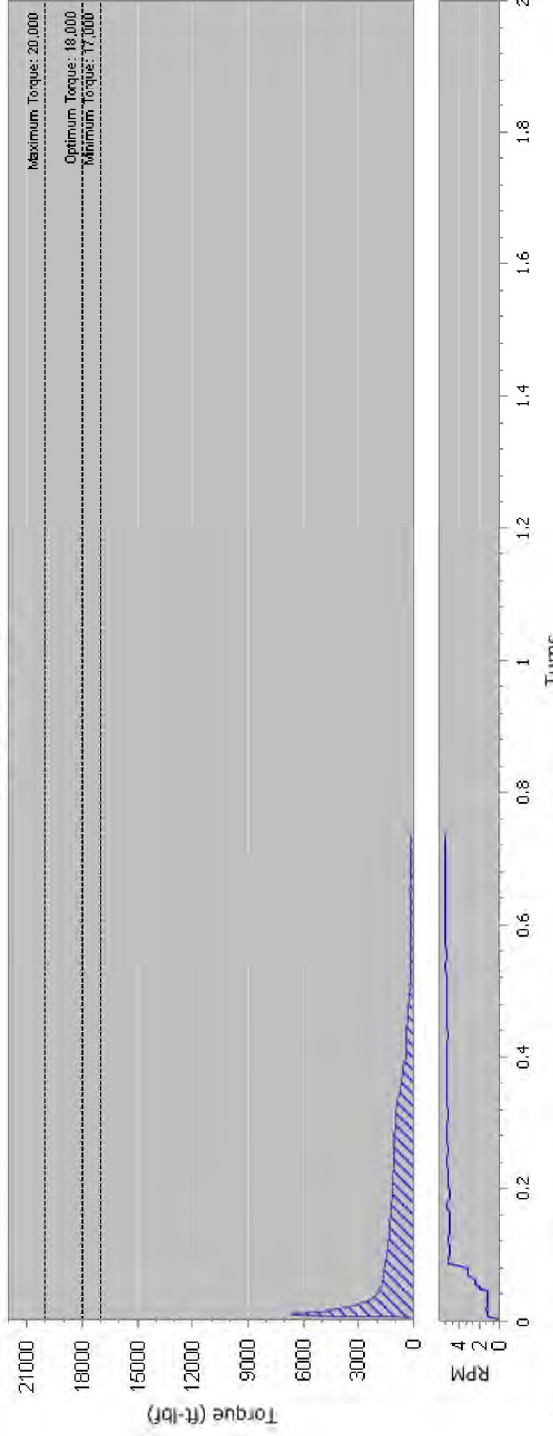
Generated by AMC Rotational Torque on machine serial RT110:100/8656

# BREAK OUT REPORT

Date: 10/01/2019

Operator: JS,GC

Torque vs Turns



### BREAK OUT INFORMATION

Job Reference: SoCal  
 Sequence No.: 6  
 Operator: JS,GC  
 Customer: SOCALGAS  
 Description: C016B

### JOINT DETAILS

Start Time: 11:46:55  
 End Time: 11:47:08  
 Achieved Torque: 6,734  
 Shoulder Torque: -  
 Delta Torque: -  
 Achieved Turns: 0.735  
 Delta Turns: -  
 Delta Slope: -

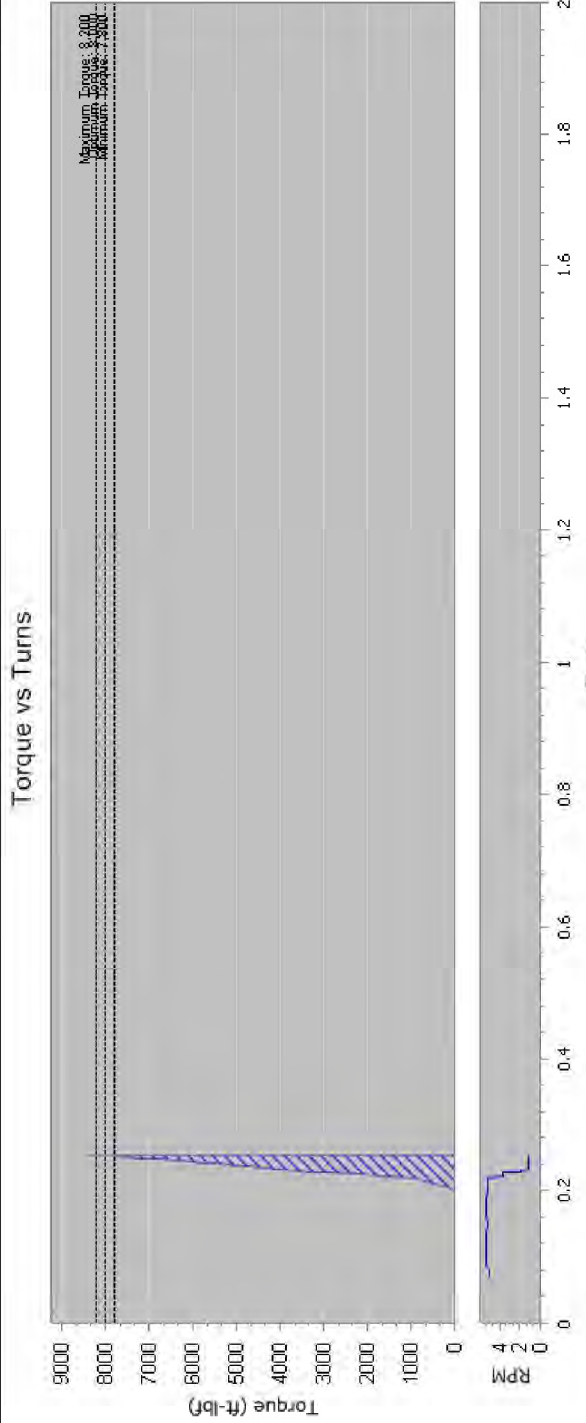
### PIPE DETAILS / PARAMETERS

Thread Direction: Right Hand Thread  
 Thread Type: SpeedTite  
 Size: 7"  
 Weight: 23.0  
 Grade: J55  
 Thread Compound: Unknown

# MAKE UP REPORT

Date: 16/01/2019

Operator: JS,GC



### MAKE UP INFORMATION

Job Reference SoCal  
 Sequence No. 8  
 Operator JS,GC  
 Customer SOCALGAS  
 Description C016B

### JOINT DETAILS

Start Time 15:19:49  
 End Time 15:19:53  
 Achieved Torque 8,396  
 Shoulder Torque 8,396 ft.lb  
 Delta Torque 0.253  
 Achieved Turns 0.056  
 Delta Turns 149,929 ft.lb/turn  
 Delta Slope

### PIPE DETAILS / PARAMETERS

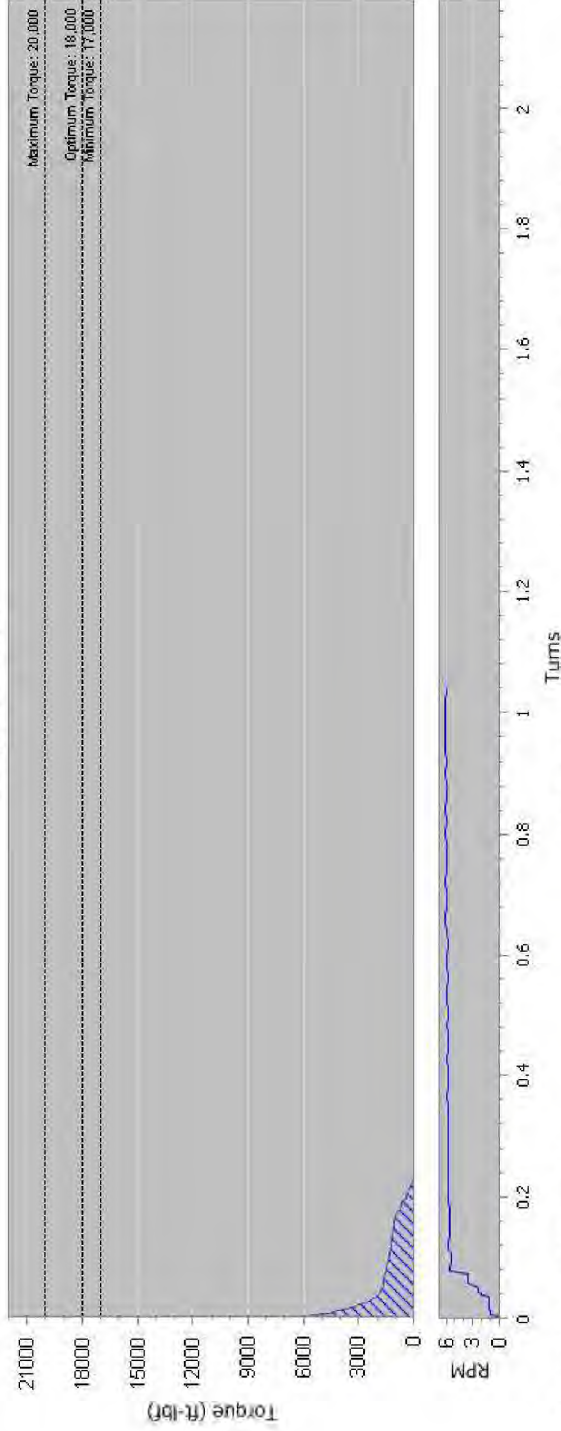
Thread Direction Right Hand Thread  
 Thread Type SpeedTite  
 Size 7"  
 Weight 23.0  
 Grade J55  
 Thread Compound API Modified

# BREAK OUT REPORT

Date: 23/10/2018

Operator: MILLIGAN

Torque vs Turns



### BREAK OUT INFORMATION

Job Reference SC-G-16-001-SS25  
 Sequence No. 1  
 Operator MILLIGAN  
 Customer SoCalGas  
 Description SS-25 C017B

### JOINT DETAILS

Start Time 12:37:24  
 End Time 12:37:39  
 Achieved Torque 6,318  
 Shoulder Torque -  
 Delta Torque -  
 Achieved Turns 1.040  
 Delta Turns -  
 Delta Slope -

### PIPE DETAILS / PARAMETERS

Thread Direction Right Hand Thread  
 Thread Type SpeedTite  
 Size 7"  
 Weight 23.0  
 Grade J55  
 Thread Compound Unknown

www.eqtorque.com

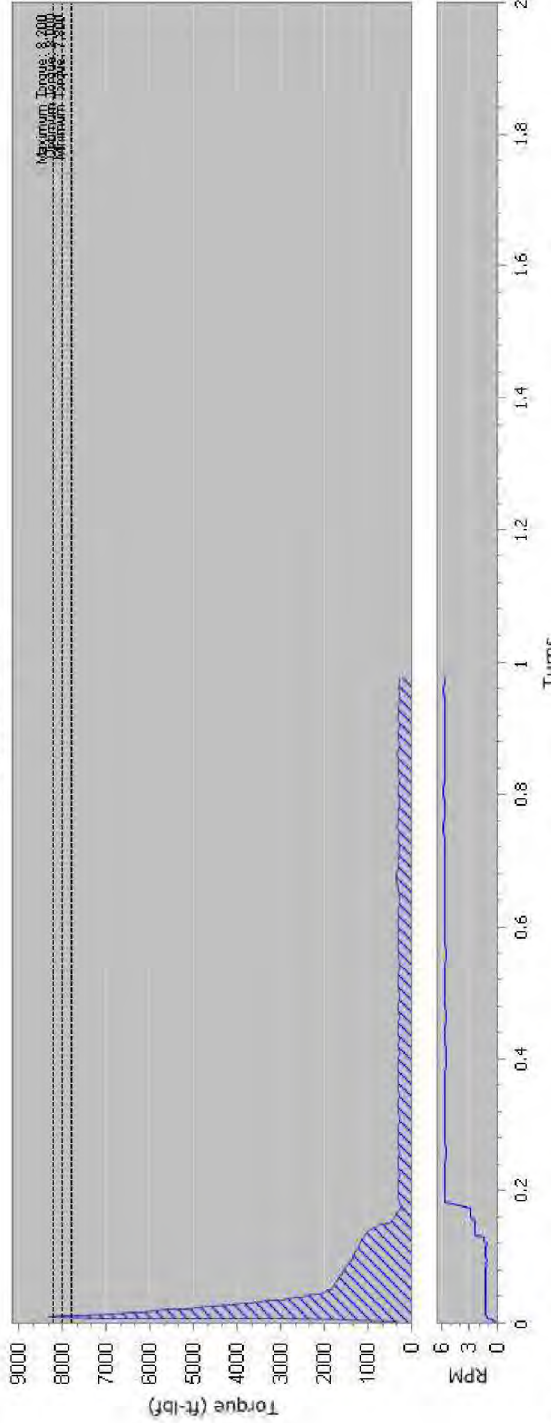
Generated by AMC Rotational Torque on machine serial RT10:100/8656

# BREAK OUT REPORT

Date: 30/01/2019

Operator: JS,GC

Torque vs Turns



### BREAK OUT INFORMATION

Job Reference SoCal  
 Sequence No. 10  
 Operator JS,GC  
 Customer SOCALGAS  
 Description C019B

### JOINT DETAILS

Start Time 08:53:31  
 End Time 08:53:49  
 Achieved Torque 8,313  
 Shoulder Torque -  
 Delta Torque -  
 Achieved Turns 0.977  
 Delta Turns -  
 Delta Slope -

### PIPE DETAILS / PARAMETERS

Thread Direction Right Hand Thread  
 Thread Type SpeedTite  
 Size 7"  
 Weight 23.0  
 Grade J55  
 Thread Compound API Modified

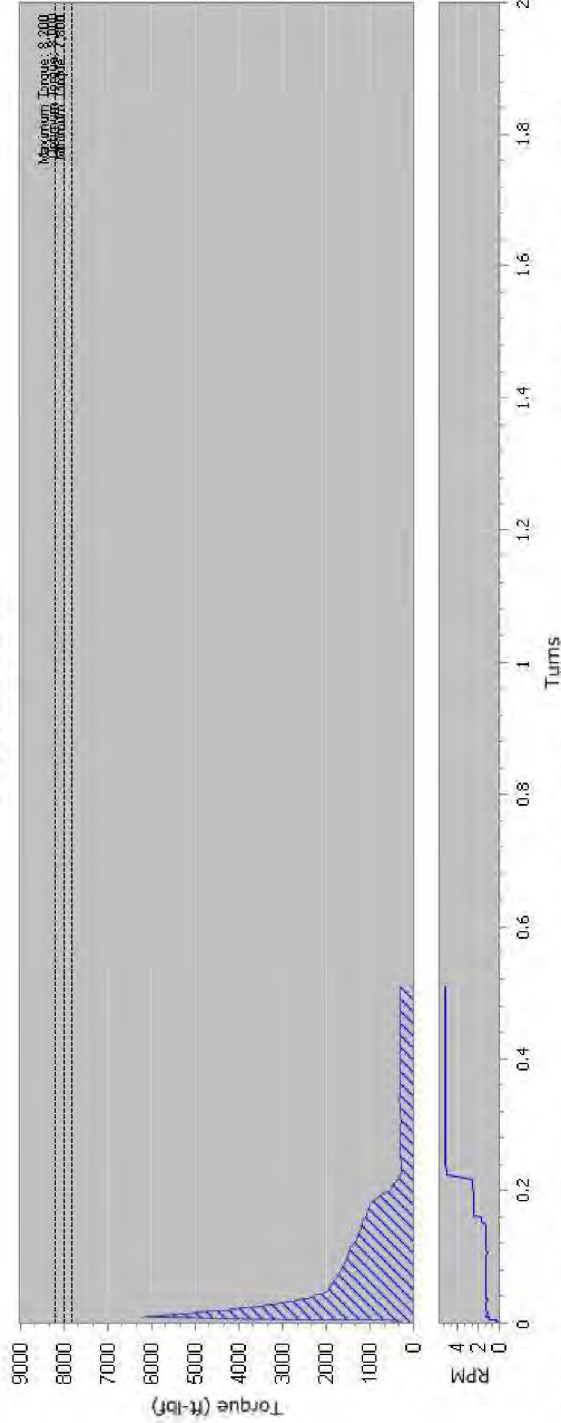


# BREAK OUT REPORT

Date: 30/01/2019

Operator: JS,GC

Torque vs Turns



### BREAK OUT INFORMATION

Job Reference SoCal  
 Sequence No. 9  
 Operator JS,GC  
 Customer SOCALGAS  
 Description C021B

### JOINT DETAILS

Start Time 08:47:22  
 End Time 08:47:37  
 Achieved Torque 6,148  
 Shoulder Torque -  
 Delta Torque -  
 Achieved Turns 0.509  
 Delta Turns -  
 Delta Slope -

### PIPE DETAILS / PARAMETERS

Thread Direction Right Hand Thread  
 Thread Type SpeedTite  
 Size 7"  
 Weight 23.0  
 Grade J55  
 Thread Compound API Modified

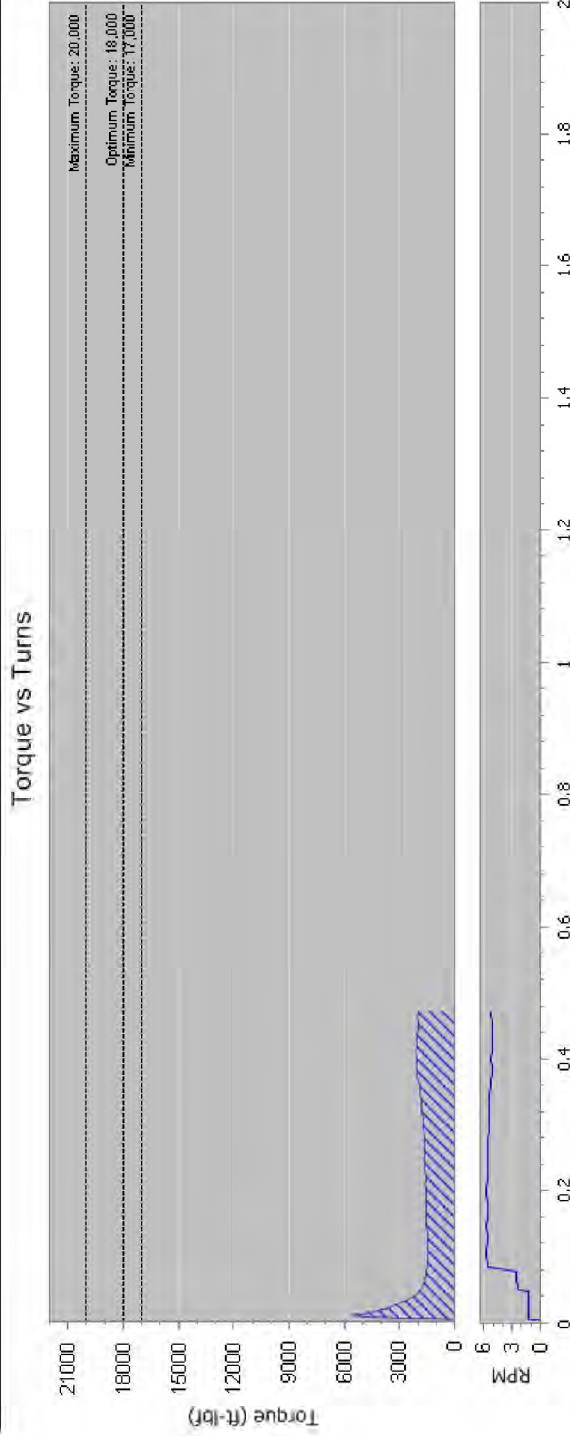
www.eqtorque.com

Generated by AMC Rotational Torque on machine serial RT10:100/8656

# BREAK OUT REPORT

Date: 06/11/2018

Operator: JS,BW,BS



## BREAK OUT INFORMATION

Job Reference: So Cal  
 Sequence No.: 3  
 Operator: JS,BW,BS  
 Customer: SOCALGAS  
 Description: SS-25 C023A1C

## JOINT DETAILS

Start Time: 15:07:28  
 End Time: 15:07:38  
 Achieved Torque: 5,649  
 Shoulder Torque: -  
 Delta Torque: -  
 Achieved Turns: 0.470  
 Delta Turns: -  
 Delta Slope: -

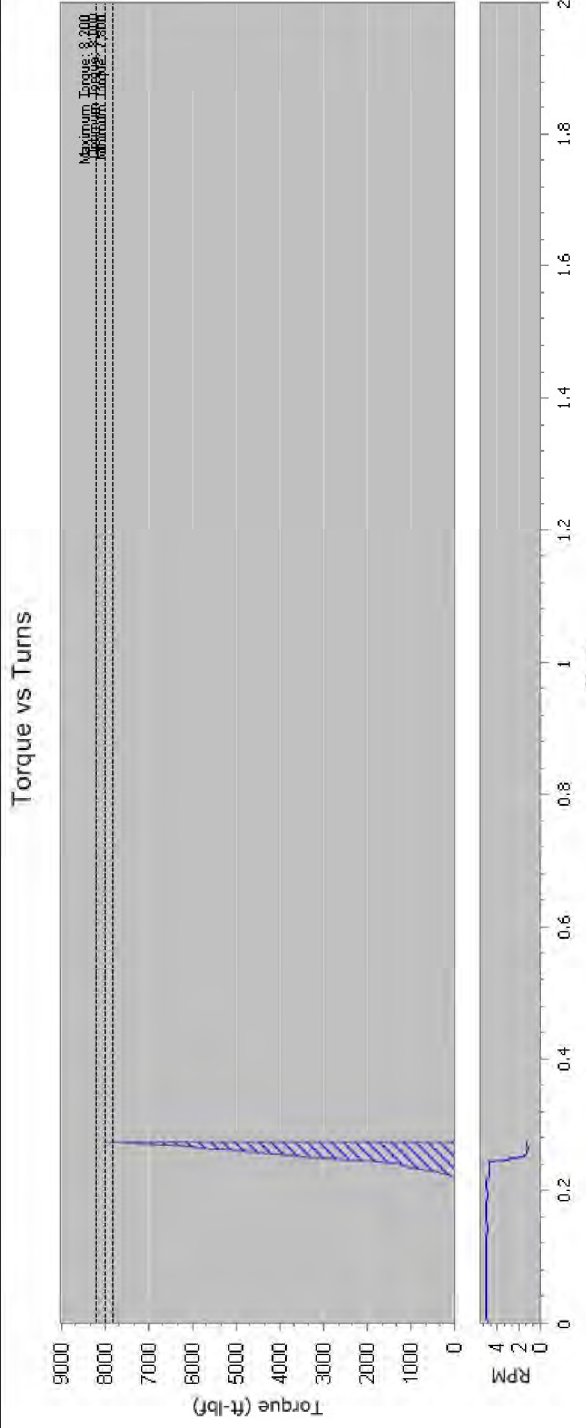
## PIPE DETAILS / PARAMETERS

Thread Direction: Right Hand Thread  
 Thread Type: SpeedTite  
 Size: 7"  
 Weight: 23.0  
 Grade: J55  
 Thread Compound: Unknown

# MAKE UP REPORT

Date: 16/01/2019

Operator: JS,GC



## MAKE UP INFORMATION

Job Reference SoCal  
 Sequence No. 7  
 Operator JS,GC  
 Customer SOCALGAS  
 Description C023A1C

## JOINT DETAILS

Start Time 14:56:27  
 End Time 14:56:33  
 Achieved Torque 8,009  
 Shoulder Torque 8,009 ft.lb  
 Delta Torque 0.274  
 Achieved Turns 0.058  
 Delta Turns 138.086  
 Delta Slope ft.lb/turn

## PIPE DETAILS / PARAMETERS

Thread Direction Right Hand Thread  
 Thread Type SpeedTite  
 Size 7"  
 Weight 23.0  
 Grade J55  
 Thread Compound API Modified

www.eqtorque.com

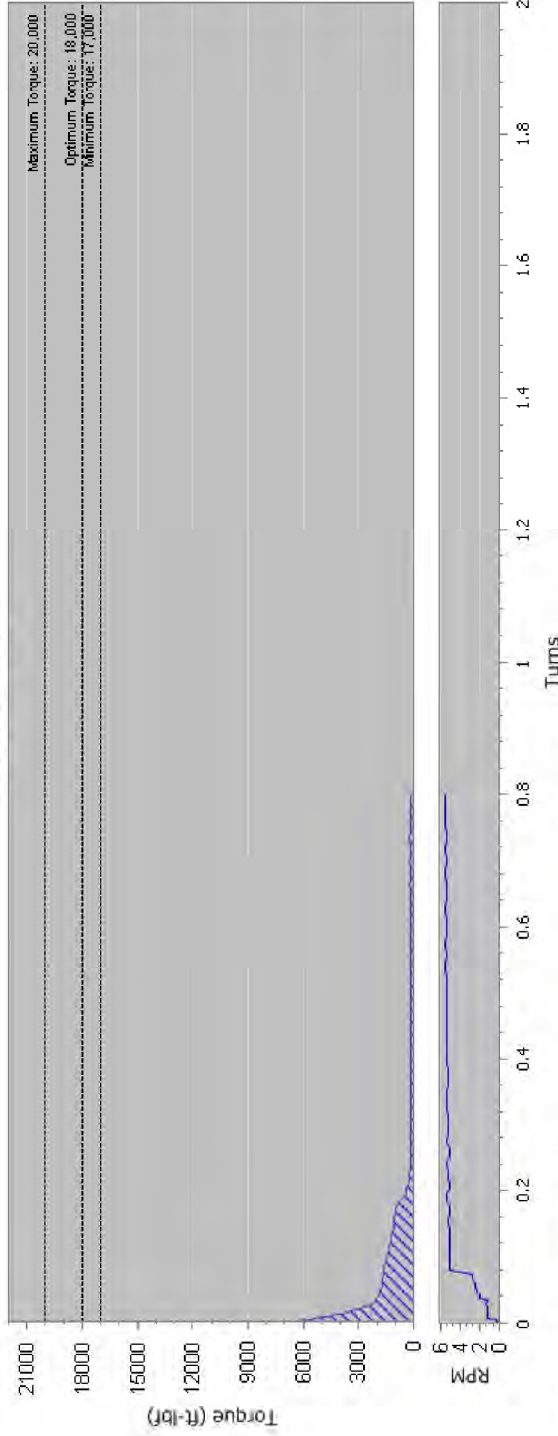
Generated by AMC Rotational Torque on machine serial RT10:100/8656

# BREAK OUT REPORT

Date: 16/11/2018

Operator: JS,GC

Torque vs Turns



### BREAK OUT INFORMATION

Job Reference: SoCal  
 Sequence No.: 5  
 Operator: JS,GC  
 Customer: SOCALGAS  
 Description: C024B

### JOINT DETAILS

Start Time: 10:46:31  
 End Time: 10:46:45  
 Achieved Torque: 7,093  
 Shoulder Torque: -  
 Delta Torque: -  
 Achieved Turns: 0.799  
 Delta Turns: -  
 Delta Slope: -

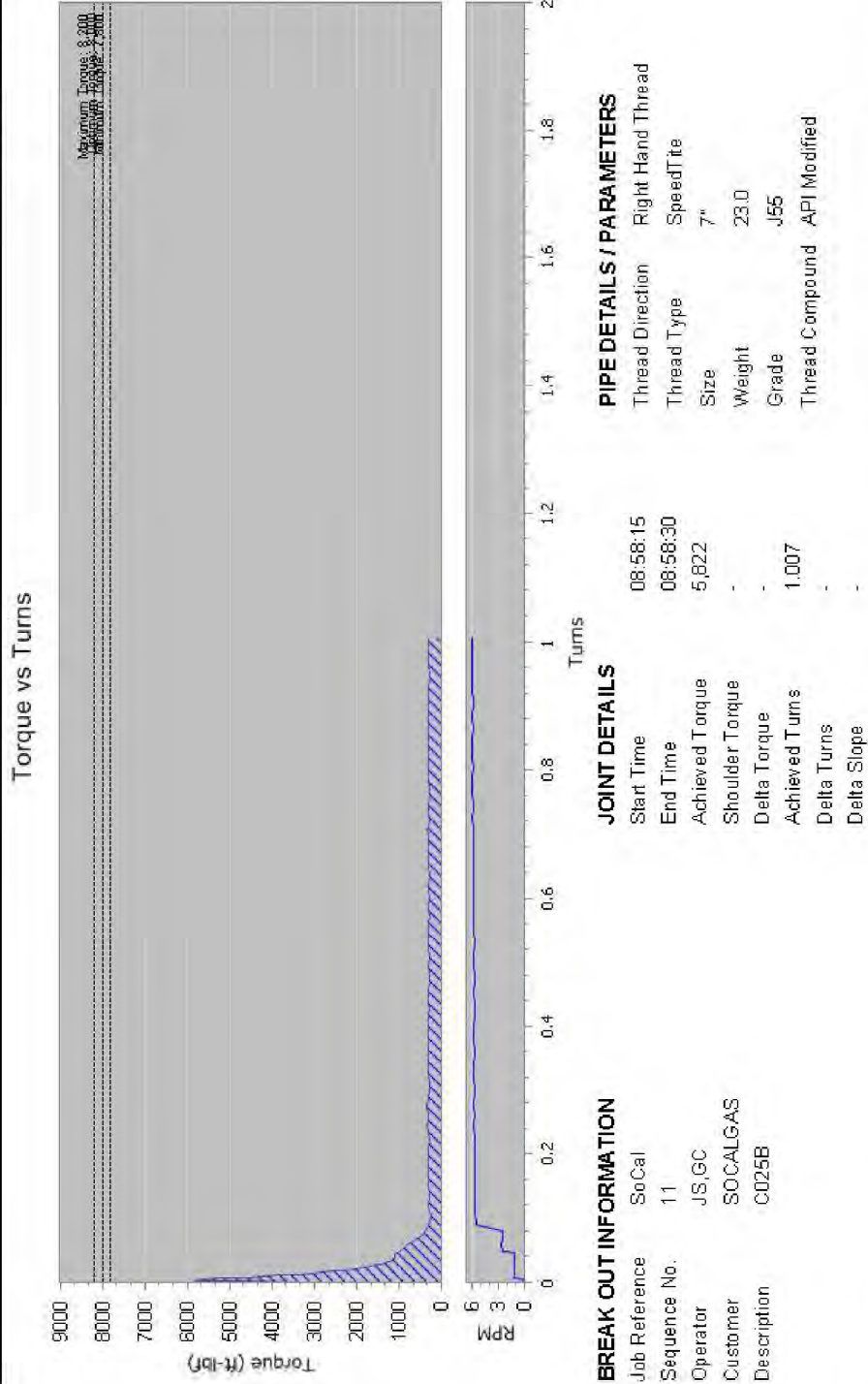
### PIPE DETAILS / PARAMETERS

Thread Direction: Right Hand Thread  
 Thread Type: SpeedTite  
 Size: 7"  
 Weight: 23.0  
 Grade: J55  
 Thread Compound: Unknown

# BREAK OUT REPORT

Date: 30/01/2019

Operator: JS,GC



### BREAK OUT INFORMATION

Job Reference: SoCal  
 Sequence No.: 11  
 Operator: JS,GC  
 Customer: SOCALGAS  
 Description: C025B

### JOINT DETAILS

Start Time: 08:58:15  
 End Time: 08:58:30  
 Achieved Torque: 5,822  
 Shoulder Torque: -  
 Delta Torque: -  
 Achieved Turns: 1.007  
 Delta Turns: -  
 Delta Slope: -

### PIPE DETAILS / PARAMETERS

Thread Direction: Right Hand Thread  
 Thread Type: SpeedTite  
 Size: 7"  
 Weight: 23.0  
 Grade: J55  
 Thread Compound: API Modified

www.eqtorque.com

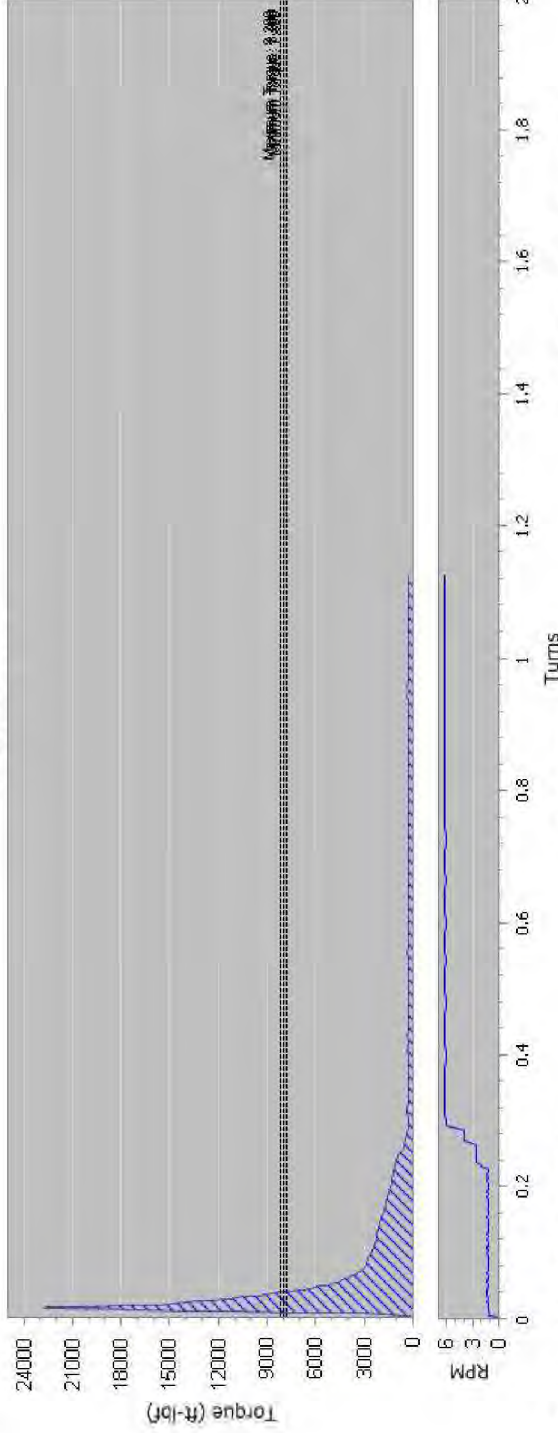
Generated by AMC Rotational Torque on machine serial RT10:100/8656

# BREAK OUT REPORT

Date: 30/01/2019

Operator: JS,GC

Torque vs Turns



Maximum Torque: 22,700

### BREAK OUT INFORMATION

Job Reference SoCal-P34  
 Sequence No. 2  
 Operator JS,GC  
 Customer SOCALGAS  
 Description P34 C002

### JOINT DETAILS

Start Time 11:30:03  
 End Time 11:30:26  
 Achieved Torque 22,707  
 Shoulder Torque -  
 Delta Torque -  
 Achieved Turns 1.124  
 Delta Turns -  
 Delta Slope -

### PIPE DETAILS / PARAMETERS

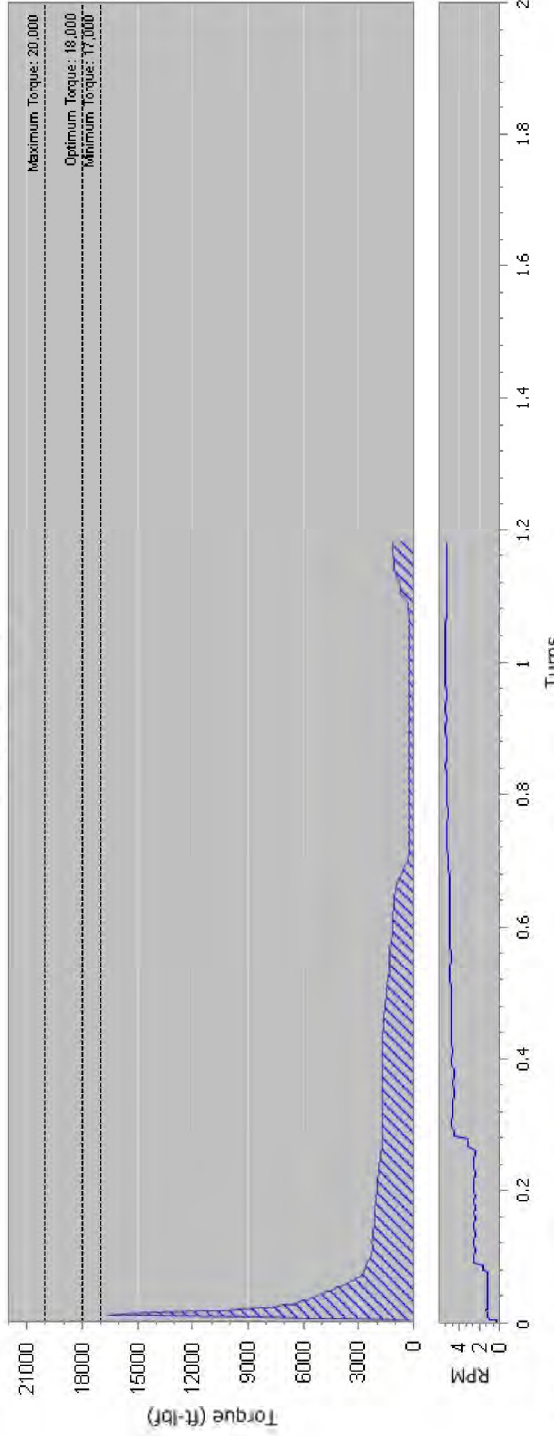
Thread Direction Right Hand Thread  
 Thread Type SpeedTite  
 Size 7"  
 Weight 23.0  
 Grade J55  
 Thread Compound API Modified

# BREAK OUT REPORT

Date: 14/11/2018

Operator: JS,GC

Torque vs Turns



### BREAK OUT INFORMATION

Job Reference: SoCal  
Sequence No.: 4  
Operator: JS,GC  
Customer: SOCALGAS  
Description: P34 C003

### JOINT DETAILS

Start Time: 15:17:58  
End Time: 15:18:20  
Achieved Torque: 16,620  
Shoulder Torque: -  
Delta Torque: -  
Achieved Turns: 1.179  
Delta Turns: -  
Delta Slope: -

### PIPE DETAILS / PARAMETERS

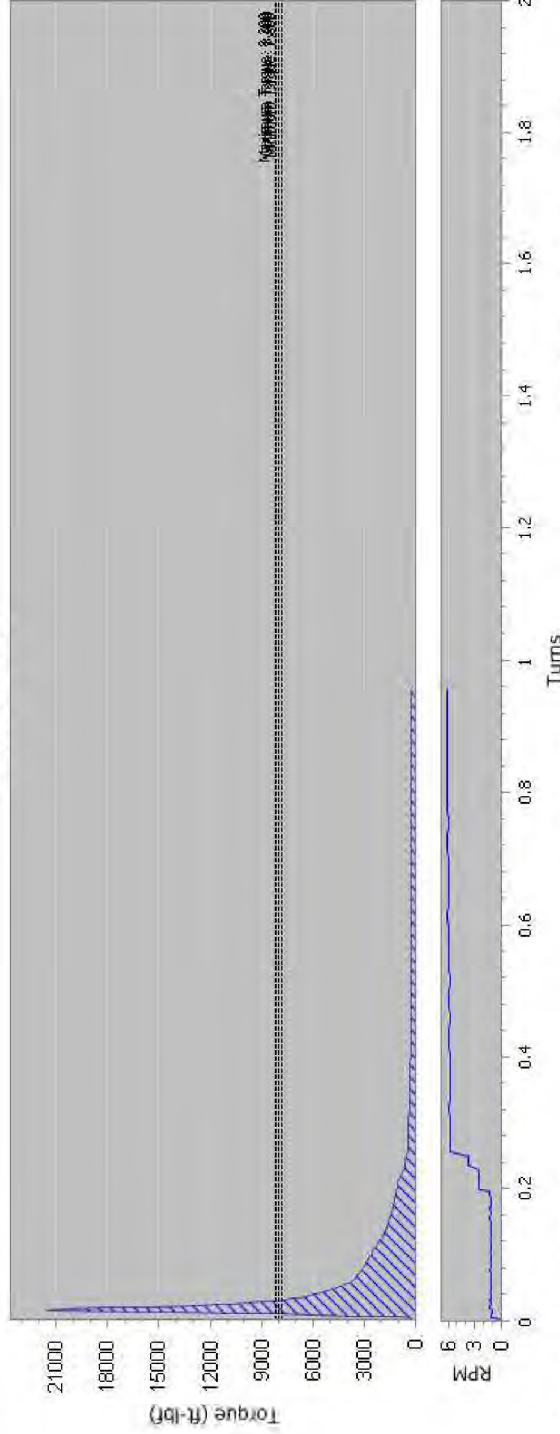
Thread Direction: Right Hand Thread  
Thread Type: SpeedTite  
Size: 7"  
Weight: 23.0  
Grade: J55  
Thread Compound: Unknown

# BREAK OUT REPORT

Date: 30/01/2019

Operator: JS,GC

Torque vs Turns



### BREAK OUT INFORMATION

Job Reference SoCal-P34  
 Sequence No. 1  
 Operator JS,GC  
 Customer SOCALGAS  
 Description P34 C005

### JOINT DETAILS

Start Time 11:25:11  
 End Time 11:25:31  
 Achieved Torque 21,506  
 Shoulder Torque -  
 Delta Torque -  
 Achieved Turns 0.955  
 Delta Turns -  
 Delta Slope -

### PIPE DETAILS / PARAMETERS

Thread Direction Right Hand Thread  
 Thread Type SpeedTite  
 Size 7"  
 Weight 23.0  
 Grade J55  
 Thread Compound API Modified

www.eqtorque.com

Generated by AMC Rotational Torque on machine serial RT10:100/8656

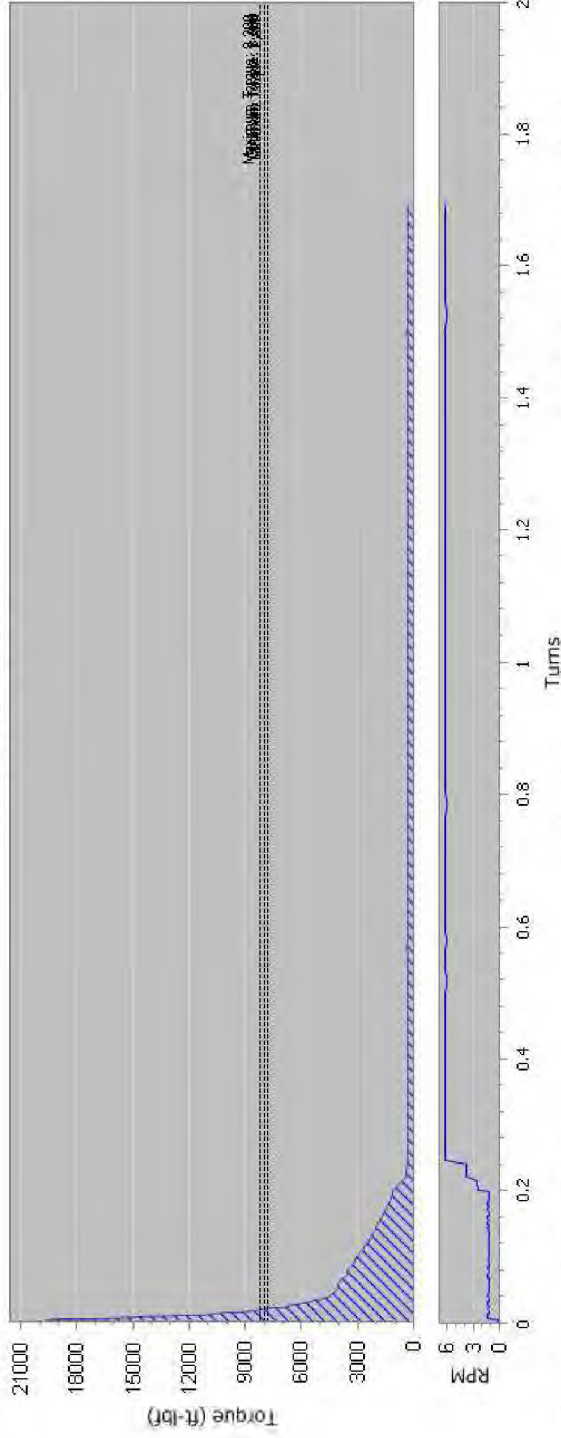


# BREAK OUT REPORT

Date: 30/01/2019

Operator: JS,GC

Torque vs Turns



### BREAK OUT INFORMATION

Job Reference SoCal-P34  
 Sequence No. 3  
 Operator JS,GC  
 Customer SOCALGAS  
 Description P34 C006

### JOINT DETAILS

Start Time 11:35:46  
 End Time 11:36:13  
 Achieved Torque 19,610  
 Shoulder Torque -  
 Delta Torque -  
 Achieved Turns 1.691  
 Delta Turns -  
 Delta Slope -

### PIPE DETAILS / PARAMETERS

Thread Direction Right Hand Thread  
 Thread Type SpeedTite  
 Size 7"  
 Weight 23.0  
 Grade J55  
 Thread Compound API Modified

www.eqtorque.com

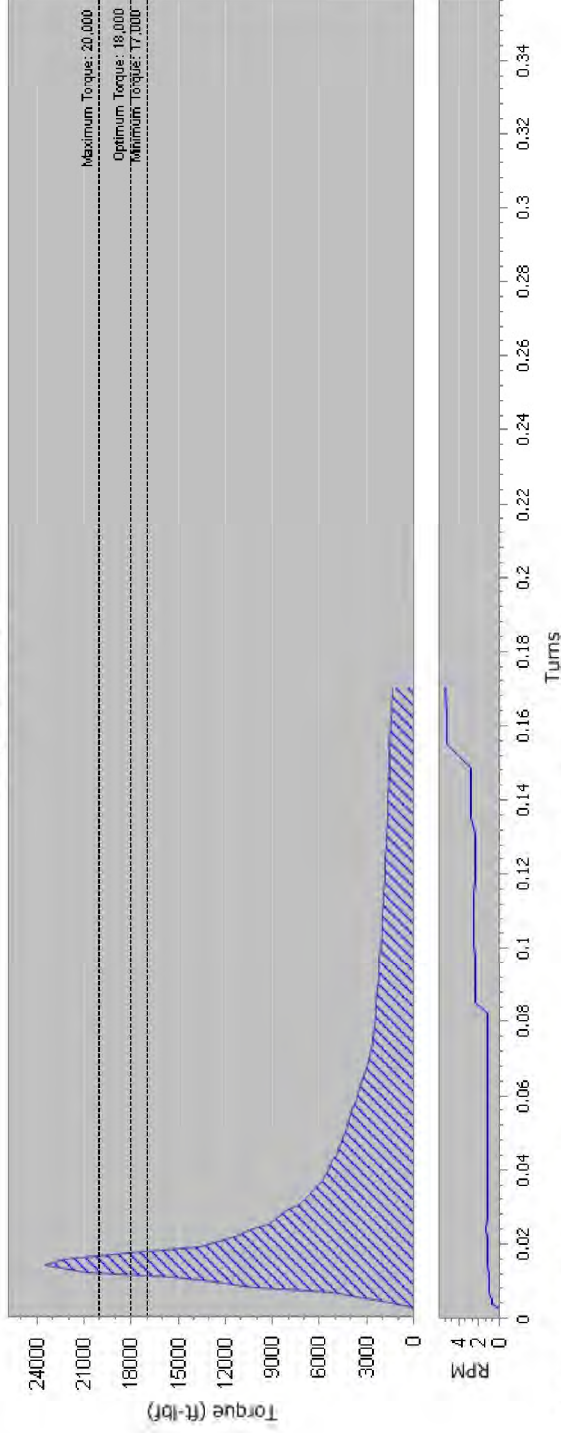
Generated by AMC Rotational Torque on machine serial RT10:100/8656

# BREAK OUT REPORT

Date: 23/10/2018

Operator: MILLIGAN

Torque vs Turns



### BREAK OUT INFORMATION

Job Reference SC-G-16-001-P34  
 Sequence No. 1  
 Operator MILLIGAN  
 Customer SoCalGas  
 Description P34 C007

### JOINT DETAILS

Start Time 11:01:03  
 End Time 11:01:11  
 Achieved Torque 23,457  
 Shoulder Torque -  
 Delta Torque -  
 Achieved Turns 0.170  
 Delta Turns -  
 Delta Slope -

### PIPE DETAILS / PARAMETERS

Thread Direction Right Hand Thread  
 Thread Type SpeedTite  
 Size 7"  
 Weight 23.0  
 Grade J55  
 Thread Compound Unknown

# Appendix E Pipe Thread compound X-Ray Diffraction Analysis

## X-Ray Diffraction (XRD) - Summary

Operator: Blade Energy Partners

Sample: Pipe Dope

County, State: \_\_\_\_\_



Date: 02/26/19

Premier Job No.: P399\_201802

Joint ID	Sample ID	TECTOSILICATES			CARBONATES			PHYLLOSILICATES			ADDITIONAL							TOTAL		
		Quartz	Kaolinite	Illite	Siderite (FeCO <sub>3</sub> )	Magnesite	Hydroxide (Ca(OH) <sub>2</sub> )	Stentite	Illite/Musc	Magnesite	Hematite	Mg7(SO4)5(OH)4(H2O)	MnO3	Baryte	TECTOSILICATES	PHYLLOSILICATES	CARBONATES	ADDITIONAL		
C001B	C001B-DS1	22.8	0.0	0.0	0.0	0.0	0.0	0.0	0.0	0.0	12.5	0.0	0.0	22.8	0.0	0.0	0.7	76.6		
C002B	C002B-DS1	14.0	0.0	0.0	0.0	0.0	0.0	0.0	Tr	0.0	0.0	0.0	0.0	14.0	Tr	0.0	0.0	86.0		
C006B	C006B-DS1	29.9	0.0	0.0	4.6	0.0	0.0	0.0	0.0	0.0	0.0	0.0	0.0	29.9	0.0	0.0	4.6	65.5		
C010B	C010B-DS1	20.8	0.0	0.0	0.3	0.0	0.0	0.0	0.0	0.0	0.0	0.0	0.0	20.8	0.0	0.0	0.3	78.9		
C016B	C016B-DS1	26.6	0.0	0.0	10.7	1.7	12.0	23.6	0.0	0.0	4.3	0.0	0.0	26.6	0.0	0.0	48.0	25.4		
C023A1C	C023A1C-DS1	30.3	0.0	0.0	0.0	0.0	0.0	0.0	Tr	0.0	0.0	0.0	0.0	30.3	0.0	0.0	0.0	69.7		
API Modified	API Modified	45.8	0.0	0.0	3.1	0.0	0.0	0.0	0.0	0.0	1.0	0.0	0.0	45.8	5.7	3.1	0.0	45.4		

\*Mineral is a Copper compound with mixed elements

Note: All quantities are in percent mass.

# SS-25 RCA Supplementary Report

# Analysis of Microbial Organisms Associated with the SS-25 Production Casing



2600 Network Boulevard, Suite 550  
Frisco, Texas 75034

+1 972-712-8407 (phone)  
+1 972-712-8408 (fax)

16285 Park Ten Place, Suite 600  
Houston, Texas 77084

1-800-319-2940 (toll free)  
+1 281-206-2000 (phone)  
+1 281-206-2005 (fax)

[www.blade-energy.com](http://www.blade-energy.com)

## Purpose:

Overview of results from all samples with particular focus on the analysis of the corrosion potential of microorganisms on the surface of the SS-25 well 7 in. casing

## Date:

May 31, 2019

Blade Energy Partners Limited, and its affiliates ('Blade') provide our services subject to our General Terms and Conditions ('GTC') in effect at time of service, unless a GTC provision is expressly superseded in a separate agreement made with Blade. Blade's work product is based on information sources which we believe to be reliable, including information that was publicly available and that was provided by our client; but Blade does not guarantee the accuracy or completeness of the information provided. All statements are the opinions of Blade based on generally-accepted and reasonable practices in the industry. Our clients remain fully responsible for all clients' decisions, actions and omissions, whether based upon Blade's work product or not; and Blade's liability solely extends to the cost of its work product.

## Abstract

The gas storage well Standard Sesnon 25 (SS-25) in the Aliso Canyon Gas Storage Field located in Los Angeles County, California started leaking gas in October 2015. A relief well was drilled, and SS-25 was brought under control. The leak stopped in February 2016.

In January 2016, as part of their investigation of the leak, the California Public Utilities Commission (CPUC) and the Division of Oil, Gas, and Geothermal Resources (DOGGR) selected and gave provisional authority to Blade Energy Partners (Blade) to perform an independent Root Cause Analysis (RCA). The Blade Team and parties under Blade's direction were responsible for directing the work of subcontractors who performed the extraction of the SS-25's wellhead, tubing and casing, and the preservation and protection of associated evidence. Blade RCA Reports, including this report, document and describe the key activities undertaken in support of the RCA effort.

Microbiologically Influenced Corrosion (MIC) is known to be a root cause of pipeline failures within many areas of the oil and gas industry. As a result, microbial analysis was included in the SS-25 RCA.

The catastrophic nature of the initial failure event required an immediate well control effort to contain the leak. This effort precluded direct analysis of the population of microbes at the time of the failure.

For this project, samples were collected from locations chosen to give a broad picture of the microbial activity at Aliso Canyon. A total of 204 samples were collected and analyzed by a combination of growth-based Most Probably Number (MPN) testing, DNA-based genetic analysis using quantitative polymerase chain reaction (qPCR), and amplicon metagenomics population analysis technologies.

Samples from casing surface material, casing fluids, drilling fluids, surfaces of sampling tools, and equipment were collected. Three of the sample sets consisted of material removed from the outer surface of the casing of three different wells as the casing was being extracted from the wells. This sampling was done to gain an understanding of the microbial population that might have been on the casing surface at the time of rupture.

This report contains an overview of all samples, with particular focus on the analysis of the corrosion potential of microorganisms on the surface of the SS-25 7 in. casing. It was found that the population of microorganisms on the surface of joints located below the rupture site was heavily dominated by methanogenic archaea. These methanogenic archaea include representatives of the hydrogenotrophic genera *Methanobacterium* and *Methanocalculus* that are related to isolates shown to be capable of metal corrosion. Therefore, the population of microorganisms is consistent with the potential that MIC can occur in this field.

Full reports containing the data from all samples are available as reference information, and are listed in Appendix A .

## Table of Contents

<b>1</b>	<b>Introduction.....</b>	<b>5</b>
1.1	Abbreviations and Acronyms .....	5
1.2	Sample Sets .....	6
<b>2</b>	<b>Overview of Approach Used for Microbial Population Analysis .....</b>	<b>8</b>
2.1	MIC Standard Test Methods References.....	8
2.2	Methods Used in this Study.....	8
2.3	Overview of Each Method Used.....	9
<b>3</b>	<b>Analysis of Microbial Populations from SS-25 7 in. Casing OD .....</b>	<b>15</b>
3.1	Well SS-25 Sampling Details .....	15
3.2	MPN Analysis of the Microbial Population of Well SS-25. ....	16
3.3	qPCR Analysis of the Microbial Population of Well SS-25.....	16
3.4	Amplicon Metagenomics Analysis of the Microbial Populations of Well SS-25.....	18
<b>4</b>	<b>Identification of Localized Variations in the Microbial Population .....</b>	<b>21</b>
4.1	Marker Organisms Identified for Each Sample Type.....	21
4.2	Scale Samples are Representative of Casing Surface Microbiology.....	21
4.3	Identifying the Most Abundant Organisms in the Well SS-25 Casing Scale Samples.....	22
4.4	Variations in the Microbial Population Along the Surface of the Casing from Well SS-25 .....	24
<b>5</b>	<b>Conclusions.....</b>	<b>26</b>
<b>6</b>	<b>References.....</b>	<b>27</b>
Appendix A	<b>Detailed Reference Reports List.....</b>	<b>A-1</b>
Appendix B	<b>Background on Methanogens and MIC .....</b>	<b>B-1</b>
Appendix C	<b>Methods.....</b>	<b>C-1</b>
Appendix D	<b>Overview of Select Metabolic Processes .....</b>	<b>D-1</b>

## List of Figures

Figure 1: Diagram of Biochemical Reactions Occurring During (A) Hydrogenotrophic, and (B) Methylo-trophic Methanogenesis. Green Ovals: Energy-Conserving Reactions. Red Ovals: Energy-Consuming Reaction. [19] .....	B-1
Figure 2: Energetics of Methanogenesis Compared to Other Respiratory Pathways .....	B-2
Figure 3: (a) Sytrophic Relationship Involving the Sharing of Acetate and Methane Between <i>S. multivorans</i> and the Methanogen, <i>M. voltae</i> . (b) Growth Curve of <i>S. multivorans</i> with lactae in the Presence (Squares) and Absence (Circles) of <i>M. voltae</i> . [20] .....	B-3
Figure 4: Model of Hydrogenotrophic Methanogen Mediated Metal Corrosion [6] [25].....	B-3
Figure 5: Diagram of Extracellular Hydrogenases Responsible for Fe Oxidation [27] .....	B-4



## List of Tables

Table 1: Project Ecolyse 170721 List of Sample Sets Analyzed for Microbial Populations.....	7
Table 2: NACE Standard Test Methods Documents .....	8
Table 3: Overview of Microbial Population Analysis Method .....	9
Table 4: Bacterial Culture Medias Used for MPN Analysis .....	10
Table 5: Wells SS-25, Casing Joint and Background Samples Set Details .....	15
Table 6: Well SS-25 MPN Microbial Populations Analysis Summary.....	16
Table 7: qPCR Analysis of the Microbial Populations of Wells SS-25 and P35 .....	17
Table 8: Well SS-25 16S Amplicon Metagenomic Population Profile Overview.....	18
Table 9: Population Profile of Well SS-25 Samples.....	20
Table 10: Marker Organisms for Each Sample Type.....	21
Table 11: Well SS-25 Casing Joints C025 and C026 Most Abundant Organisms .....	22
Table 12: Microbial Populations in each Well SS-25 7 in. Casing OD Samples .....	25

# 1 Introduction

This report presents the results of analysis of the microbial population present in samples originating from Aliso Canyon gas wells. The microbial population was analyzed with the intention of gaining an understanding of the potential the population has for participation in MIC.

Over 200 samples were collected and analyzed, including materials removed from the surface of the 7 in. casing of three wells (SS-25, P-35, and P-34) while the casing was being extracted from the well. Other sample sets included fluids collected from the casing annulus, dried scale collected from cleaned casing joints, and various drilling muds, fluids, and background samples.

The full analysis of all sample sets is provided in the reference reports listed in Appendix A. This report focuses specifically on results obtained from analysis of the material collected from the outside of the SS-25 7 in. casing joint numbers 24 and 25, referred to in this document by their Joint Sequence Numbers (JSN) C025 and C026, respectively. It was found that the population of microorganisms on the surface of these two joints, located below the rupture site, were heavily dominated by methanogenic archaea. These methanogenic archaea include representatives of the hydrogenotrophic genera *Methanobacterium* and *Methanocalculus* that are related to isolates shown to be capable of metal corrosion. Therefore, the population of microorganisms is consistent with the potential that MIC can occur in this field.

## 1.1 Abbreviations and Acronyms

Term	Definition
APB	Acid Producing Bacteria
CHDT	Cased Hole Dynamics Tester
COC	Chain of Custody
CT	Cycle Threshold
DNA	Deoxyribonucleic Acid
GHB	General Heterotrophic Bacteria
g	gram
H <sub>2</sub> S	Hydrogen Sulfide
ID	Pipe Inner Diameter
IRB	Iron Reducing Bacteria
KCl	Potassium Chloride
<LOD	Below limit of detection
MIC	Microbiologically Influenced Corrosion
ml	milliliter
MPB	Modified Postgate's B media
MPN	Most Probable Number
NACE	National Association of Corrosion Engineers
NRB	Nitrate Reducing Bacteria
NRSOB	Nitrate-Reducing, Sulfur Oxidizing Bacteria



Term	Definition
OD	Pipe Outer Diameter
O&G	Oil and Gas
OTU	Operational Taxonomic Unit
PBS	Phosphate Buffered Saline
PRD	Phenol Red Dextrose Media
qPCR	Quantitative Polymerase Chain Reaction
RCA	Root Cause Analysis
Sp.	Species, the most narrowly defined taxa or taxonomic grouping
SS	Standard Sesnon
SoCalGas	Southern California Gas Company
SRB	Sulfate Reducing Bacteria

## 1.2 Sample Sets

The purpose of this project was to evaluate the potential role of microorganisms in the casing failure of well SS-25. This evaluation requires an understanding of the general microbiology of the area and what is found on casing surfaces downhole.

Rupture dynamics and subsequent actions taken to shut down the leak meant that unaltered material collected from the rupture site was not available for testing. In the absence of unaltered materials from the rupture site, material was collected from the surrounding areas off of surfaces that corresponded to the rupture site conditions as closely as feasible.

In addition to samples from the casing outer diameter (OD), samples were collected of various drilling fluids, muds, and materials on tool surfaces of collection tools. Various samples of materials that had been removed from the field location at earlier dates were also collected.

These samples provide additional information about the microbial populations associated with various drilling activities.

Because microbial populations change with both time and environmental shifts and are prone to contamination from outside sources, fresh samples analyzed soon after acquisition are considered to be the most indicative of the population in Aliso Canyon at the time of collection from the primary location.

There were 10 different sample sets that encompass 204 individual samples obtained for this analysis (Table 1):

- Three of the sample sets (Sample Set ID LA4, LA5, LA6) were taken from the surface of casings as the casing joints were being extracted from the well. Casing samples are included from wells P-34, P-35, and SS-25. These samples were collected on location in Aliso Canyon.
- Two of the sample sets (Sample Set ID LA3 and LA1) were taken with a downhole wireline fluid sampler from SS-25. Drilling mud and fluid samples were also analyzed.
- One sample set (Sample Set ID LA2) included primarily material that had been collected from SS-25 and SS-25A at Aliso Canyon at an earlier date and stored on location. Weather conditions interfered with sample collection.

## Analysis of Microbial Organisms Associated with the SS-25 Production Casing

- Two of the sample sets (Sample Set ID H1 and H2) were collected from the casing stored in the Blade Warehouse in Houston, TX. Loose surface material had been previously removed from the casing. Casing was stored dry in a warehouse in Houston. Samples consisted of very dry, red scale from the SS-25 casing.
- Two of the sample sets (Sample Set ID H3 and H4) were wells P-35 and SS-25 casing annular fluids. These fluids were initially collected using a cased hole dynamic tester (CHDT) device. The samples were transported to Houston and stored for 3 to 108 days prior to acquisition of material for microbial analysis.

Samples were initially processed in the field and shipped via FedEx to the Ecolyse laboratories in College Station, TX for full analysis.

Table 1 provides details of each sample set. The focus of this report is on the microbial organism population of the 7 in. casing surfaces from well SS-25. In some cases, references to other sample sets will be made. Refer to specific sample set reports for full details and analysis of all samples (Appendix A).

**Table 1: Project Ecolyse 170721 List of Sample Sets Analyzed for Microbial Populations**

Sample Set ID	Sample Types	Sample Set	Collection Date	Sample Location <sup>a</sup>	Well	# Samples
170721-LA1	Fresh Wireline Samples	SS-25 Wireline Samples	July, Aug 2017	Aliso Canyon, CA	SS-25	13
170721-LA2	Stored Pipe Solids	SS-25 and SS-25A Scale and Pipe Solids	Aug, 2017	Aliso Canyon, CA	SS-25, SS-25A	21
170721-LA3	Fresh Wireline Samples	SS-25 Wireline Samples	Nov, 2017	Aliso Canyon, CA	SS-25	6
170721-H1	Stored Casing Scale	SS-25 Casing Dried Scale	Mar, 2018	BLADE TX	SS-25	22
170721-LA4	Fresh Casing Surface Material	P-34 Casing, SS-9 Muds	Mar, 2018	Aliso Canyon, CA	P-34, SS-9	15
170721-H2	Stored Casing Scale	SS-25 Casing Dried Scale	May, 2018	Blade TX	SS-25	4
170721-H3	CHDT Casing Annulus Liquids	SS-25 CHDT Fluid	July, Aug, 2018	Schlumberger TX	SS-25	11
170721-LA5	Fresh Casing Surface Material	SS-25 Casing OD	Aug, 2018	Aliso Canyon, CA	SS-25	42
170721-LA6	Fresh Casing Surface Material	P-35 Casing OD	Nov, 2018	Aliso Canyon, CA	P-35	56
170721-H4	CHDT Casing Annulus Liquids	P-35 and SS-25 CHDT Fluids	Nov, Dec 2018	Schlumberger TX	P-35 SS-25	14

<sup>a</sup> Sample Location is where samples were at the time of acquisition for microbial analysis. Aliso Canyon, CA samples were located at the SolCalGas field. Blade TX samples were located at the Blade warehouse, 5404 Clara Rd, Houston, TX 77041. Schlumberger TX samples were located at 6350 W Sam Houston Pkwy N Suite 200, Houston, TX 77041.

## 2 Overview of Approach Used for Microbial Population Analysis

### 2.1 MIC Standard Test Methods References

Testing microbial populations for corrosion potential is based on recommendations and guidelines established by the National Association of Corrosion Engineers (NACE). NACE Standard Test Methods include those described in the documents listed in Table 2.

**Table 2: NACE Standard Test Methods Documents**

NACE ID	Item	Standard Test Method
TM0194	21224	Field Monitoring of Bacterial Growth in Oil and Gas Systems [1]
TM0212	21260	Detection, Testing, and Evaluation of Microbiologically Influenced Corrosion on Internal Surfaces of Pipeline [2]
TM0106	21248	Detection, Testing, and Evaluation of Microbiologically Influenced Corrosion (MIC) on External Surfaces of Buried Pipeline [3]

NACE recognizes that the subsurface and infrastructure systems being sampled vary greatly with respect to accessibility, as well as physical, chemical, and biological traits; therefore, it is impossible to give an exact list of methods or protocols that must be followed absolutely.

Guidelines have to be adapted to the given situation and system.

### 2.2 Methods Used in this Study

Microbial populations of Aliso Canyon samples were analyzed by a combination of three methods:

- MPN
- qPCR
- Amplicon Metagenomics

All three methods were used on most, but not all, of the samples. MPN was not conducted when sufficient material was not available.

Each approach provides different and complementary data. Each approach also has strengths and limitations.

Table 3 shows an overview of each method. Methodological details are provided in Appendix C.

**Table 3: Overview of Microbial Population Analysis Method**

Method	Approach and Data	Strength	Limitations
<b>MPN</b>	<b>Culture-Based</b> <ul style="list-style-type: none"> <li>Number of culturable bacteria per g or ml sample</li> </ul>	<ul style="list-style-type: none"> <li>Provides absolute quantitation</li> <li>Traditional method</li> <li>Viable cell assay</li> <li>Phenotype assay</li> </ul>	<ul style="list-style-type: none"> <li>Low percentage of culturable organisms</li> <li>Choice of media and incubation temperature biases results</li> <li>Usually underestimates levels</li> </ul>
<b>qPCR</b>	<b>DNA-Based</b> <ul style="list-style-type: none"> <li>Total number of microorganisms per g or ml sample</li> </ul>	<ul style="list-style-type: none"> <li>Provides absolute quantitation</li> <li>Not growth-dependent</li> <li>Detects live and dead cells</li> </ul>	<ul style="list-style-type: none"> <li>Does not tell identity of individual organisms.</li> <li>Does not provide phenotype information</li> <li>DNA isolation efficiency reduced by sample composition, leading to underestimation</li> </ul>
<b>Amplicon Meta-Genomics</b>	<b>DNA-Based</b> <ul style="list-style-type: none"> <li>Types of microorganisms in sample</li> <li>Relative abundance of each organism to other organisms in sample</li> </ul>	<ul style="list-style-type: none"> <li>Provides relative abundance</li> <li>Provides details about population structure</li> <li>Phenotypes determined</li> <li>Not growth dependent</li> <li>Detects live and dead cells</li> </ul>	<ul style="list-style-type: none"> <li>Does not provide absolute quantification</li> <li>DNA isolation efficiency reduced by sample composition, leading to samples for which no data is obtained</li> <li>Analysis-intensive</li> <li>Bioinformatics skills required</li> </ul>

## 2.3 Overview of Each Method Used

### 2.3.1 MPN Method

The Most Probably Number (MPN) method is a culture-based quantification of bacteria in a sample. Data generated is “bacteria per ml” or “bacteria per g” of sample.

This method is based on culturing the bacteria in the sample in artificial growth media. The sample is subject to serial 10X dilutions, typically to a dilution factor of 10<sup>7</sup>, in selective, indicator bacterial culture medias. Indicator medias contain substrates that undergo a visible chemical change when certain types of bacteria grow in them. Selective medias contain substrates that promote the growth of certain types of bacteria preferentially over other types of bacteria in the sample.

Dilutions are set up in triplicate to allow for more robust statistical quantification. After 28 days of incubation, the highest dilution for which growth is observed is used to calculate the starting concentration of bacteria in the sample.

#### MPN Method Advantages

The MPN method has the following advantages:

- Determines the number of living, culturable bacteria in the sample
- Provides phenotypic data
- Provides information on viability of bacteria in sample
- Traditional method, recommended by NACE as a standard method

- Historical approach that is widely used throughout the industry
- Can be used for the analysis of anaerobic organisms
- Requires minimal sample manipulation to set up assay
- Easy to set up and interpret results

### MPN Method Disadvantages

The following are well-known limitations inherent in culture-based analysis, as described in NACE TM0194 [1]:

*3.1.1 Bacterial culturing in artificial growth media is accepted as the standard technique for the estimation of bacteria numbers. However, users should be aware of the limitations of the culture technique:*

*3.1.1.1 Any culture medium grows only those bacteria able to use the nutrients provided.*

*3.1.1.2 Culture medium conditions (pH, osmotic balance, redox potential, etc.) prevent the growth of some bacteria and enhance the growth of others.*

*3.1.1.3 Conditions induced by sampling and culturing procedures, such as exposure to oxygen, may hamper the growth of strict anaerobes.*

*3.1.1.4 Only a small percentage of the viable bacteria in a sample can be recovered by any single medium; i.e., culture media methods may underestimate the number of bacteria in a sample.*

*3.1.1.5 Some bacteria cannot be grown on culture media at all.*

### MPN Condition Used for Project Ecolyse 170721

Four media were chosen for this project. Each one provides information on a different phenotypic population (Table 4).

**Table 4: Bacterial Culture Medias Used for MPN Analysis**

Media	Full Name	Type of Organisms Detected
MPB	Modified Postgate's Medium B	Sulfidogen, SRB (sulfate reducing bacteria)
PRD	Phenol Red Dextrose	APB (acid producing bacteria) and GHB (general heterotrophic bacteria)
IRB	Iron Reducing Bacteria Media	IRB (iron reducing bacteria)
NRB	Nitrate Reducing Bacteria Media	NRB (nitrate reducing bacteria)

- Media salinities were all set at 2.5%.
- Culturing temperature was set at 30°C.
- Final readings were taken after full 28 days of incubation.

### 2.3.2 qPCR Method

As used in this project, the quantitative polymerase chain reaction (qPCR) method is used to quantify microorganisms in the sample based on the number of copies of the ribosomal RNA (rRNA) gene isolated from the sample.

The specificity of the qPCR reaction (e.g, what organisms are quantified) is conferred by primers choice. Primers chosen for this project were those known to detect as wide a range of microorganisms as possible in the sample. qPCR with primers that target ribosomal gene sequences were used to quantify bacteria, archaea, and eukaryotic cells. Genes for rRNA are present in all cellular life forms. Sequence variations in the rRNA genes are used to design primers with broader or narrower target specificities.

qPCR is based on using fluorescence probes to indicate the first cycle at which a positive reading above background fluorescence is obtained. The lower the cycle number, the more target sequences were present in the starting sample. These values are related back to the amount of sample from which the DNA was isolated. This ultimately provides the number of cells per ml or g of starting sample.

#### qPCR Method Advantages

The qPCR method has the following advantages:

- Widely used method to quantify bacteria in environmental samples
- Detects both living and non-living cells
- Sensitive and can be used for many sample types
- Primers can be designed to detect specific cell types or broad cell types
- Not limited by the ability to grow in specific media or conditions

#### qPCR Method Disadvantages

The qPCR method has the following disadvantages:

- Samples sometimes contain components that carryover during the DNA isolation procedure, and these can inhibit the qPCR reaction. This can cause values to be lower than what is really present.
- Because microorganisms are ubiquitous, when broad-specificity primers are used, such as the ones in this project, qPCR is prone to contamination.
- qPCR does not differentiate between living and non-living cells.
- qPCR primers have to be designed for each target group.
- qPCR requires specialty equipment and expertise.
- qPCR, as used in this study, only provides quantitative data and does not provide phenotypic data.

## qPCR Assay Used for Project Ecolyse 170721

Samples were processed to obtain a bacterial fraction separated away from other material in the sample. Total DNA was isolated from each sample using standardized protocols.

qPCR was set up by using the following three different primer sets:

- Universal 16S Primers 515F- and 806R-, which detect Bacterial and Archaeal 16S genes
- Archaeal Primers Arch517F and Arch909R, which detect the Archaeal 16S gene but not the Bacterial 16S gene. Increased specificity results in less Archaeal 16S sequences being detected than with the 16S primers.
- Eukaryotic 18S Primers Euk1391F and EukBR, which detect Eukaryotic 18S gene and some bacterial 16S genes

Refer to Appendix C for primer sequences and reaction conditions.

### 2.3.3 Amplicon Metagenomics Method

Amplicon metagenomics is a method that can be used to provide information on the different types of organisms in a sample. It also provides the relative abundance of each organism as compared to the other organisms present in the same sample.

Amplicon metagenomics is an involved process, requiring DNA isolation steps, gene amplification steps, DNA sequencing steps, and several levels of bioinformatics analysis of the resulting sequences. After sample collection, the material is processed in order to fractionate cells from other materials (dirt, soil, oils, etc.) in the sample. Total DNA is then isolated from the sample. Target genes of interest, in this case the rRNA gene, are amplified in a PCR reaction. Amplicons are further amplified using tagged primers in a DNA sequencing reaction, and the DNA sequences are determined.

Primary data resulting from these steps are tens of thousands of DNA sequences. These sequences are then subject to quality control procedures. Resulting sequences that pass quality control are compared to rRNA gene sequences in a ribosomal sequence database library. Based on similarity to sequences in the database, each sequence obtained from the sample is assigned a species annotation.

Information is then gathered about each of the identified organisms by searching the scientific literature. Based on the available level of published information, each organism is assigned metabolic, physiological, and ecological traits, with particular focus being on traits of relevance to corrosion. After all organisms are assigned traits, the microbial profile of the sample is evaluated with respect to the prevalence of each of the traits. Resulting data is then processed into a report containing identities of the organisms, their relative (%) abundance in the sample, information on what similar organisms are known to do, and the overall composition of the sample with regard to the key metabolic, physiological, and ecological characteristics found to dominate the sample.

### Amplicon Metagenomics Method Advantages

The Amplicon metagenomics method has the following advantages:

- Information gathered includes the types of organism and the % in the population.
- It is the only method that provides broad species-level identification.
- It is less biased than culture-based approaches.

- It is much more detailed and inclusive than qPCR approaches.
- It is not as subject to bias as the alternative population analysis methods that were not used in this study.
- It provides the most details of the microbial population structure of the three methods.
- The 16S sequence data can be independently analyzed, and then reanalyzed as new analysis tools become available.
- The list of organisms identified in the sample can be related to scientific information published about each organism.
- In some cases, taxonomic proximity to an organism with a known function is enough to assign functionality. For example, any organism assigned the Genus designation *Desulfovibrio* is assigned the metabolic trait of being an SRB [4].
- It provides a large data set that can be mined for information in many ways.

### Amplicon Metagenomics Method Disadvantages

The Amplicon metagenomics method has the following disadvantages:

- Samples sometimes contain components that carryover during the DNA isolation procedure, and these can inhibit the Amplicon metagenomics analysis. As a result, it is common that not all samples submitted for analysis yield data.
- Amplicon metagenomics does not provide absolute quantification, only relative quantification. This is why the qPCR method is still required.
- Amplicon metagenomics does not provide experimental evidence for physiological or phenotypic activity. This is what MPN data provides.
- Amplicon metagenomics requires advanced understanding of bioinformatics and a detailed database to be established and maintained.
- Many organisms are identified whose exact role in the environment is not known.
- Not every organism has been studied enough to understand its metabolism.
- Even for organisms that have been studied, analysis is typically incomplete with regards to the traits of specific interest to potentiating corrosion.

### Amplicon Metagenomics as Used for Project Ecolyse 170721

Samples were processed to obtain a bacterial fraction separated away from other material in the sample. Total DNA was isolated from each sample using standardized protocols.

rRNA amplification reactions and DNA sequencing reactions were set up by using the following three different primer sets:

- Universal 16S Primers 515F- and 806R-, which detect Bacterial and Archaeal 16S genes.
- Archaeal Primers Arch517F and Arch909R, which detect the Archaeal 16S gene but not the Bacterial 16S gene. Increased specificity results in less Archaeal 16S sequences being detected than with the 16S primers.



## Analysis of Microbial Organisms Associated with the SS-25 Production Casing

---

- Eukaryotic 18S Primers Euk1391F and EukBR, which detect Eukaryotic 18S gene and some bacterial 16S genes.
  1. Sequences were generated with each primer set, and subject to quality control.
  2. Sequences that passed quality control were compared against a ribosomal RNA database.
  3. Based on similarity to sequences in the ribosomal database, each sequence was assigned a taxonomic designation.
  4. The list of species was compared against a list of traits assigned to each species based on what is known about close relatives and is available in the published scientific literature.

Examples of traits assigned include sulfidogenesis, acid production, methanogenesis, iron reduction, anaerobe, aerobe, spore-forming, etc. Not every trait is known for every bacteria, so the list is incomplete.
  5. The resulting data was evaluated to identify microbial population profiles in each sample.
  6. The profile is used to make predictions about the MIC potential of the population in that sample.
  7. The profiles of each sample are compared to other samples to make general population structure analysis.
  8. Trends and patterns that emerge are evaluated and discussed.

An inherent assumption of this approach is that organisms comprising the majority of a sample are both an indicator of the sample characteristics as well as having a significant impact on the localized environment.

There are limitations to this assumption. In particular, there are no absolute % cutoff points below and above which it can be stated absolutely whether an organism will be problematic.

## 3 Analysis of Microbial Populations from SS-25 7 in. Casing OD

The most informative samples analyzed during the course of this project were those collected from the outer diameter (OD) of the 7 in. casing joints pulled from well SS-25.

Sample collection occurred on the rig floor as the casing was being pulled out. Multiple samples were removed from each joint. Clean collection tools were used to scrape material into plastic receptacles.

Samples were documented and shipped back to the lab for analysis. Each sample was processed and analyzed separately. Data from each casing joint sample was then pooled to allow for a general picture of the microbial population along the vertical structure of the joints. Populations from each casing joint were compared to those from the other casing joints, and similarities and differences are discussed. A discussion on the elucidated population structures, as well as information on whether the casing colonizing organisms include those associated with MIC, is provided.

### 3.1 Well SS-25 Sampling Details

For well SS-25, 40 casing OD samples and two control samples were collected and analyzed separately (Table 5). Samples originated from two casing joints, 24 and 25, with casing joint sequence numbers, JSN C025 and C026, respectively. Joints C025 and C026 originated at depths of 939 ft and 981.47 ft, respectively.

Joints C025 and C026 samples were further broken down into “Casing OD Scale” and “Oily Material”:

- “Casing OD Scale” was the dried, gray layer of mud, pipe scale, and possible microbial biofilms that coated much of the casing surface. Because it was a warm, dry, windy day, any moisture on the casing dried quickly during casing extraction.
- “Oily Material” consisted of occasional globules of greasy black material, presumably from tar and crude oil originating in the well. These did not dry due to their greasy nature. Deposits of oil accumulated on the end of the cut pipe and the gripper tool.

Two background samples were collected on the same day (Table 5):

- A sample of dirt from the road at the rig site
- Drilling fluids pooling on the rig floor drip pad

Well SS-25 samples were analyzed by MPN, qPCR, and Amplicon metagenomics. Due to sample drying during collection, DNA isolation efforts were successful for only 14 of the 42 samples. Amplicon metagenomic analysis was conducted on all of these samples.

**Table 5: Wells SS-25, Casing Joint and Background Samples Set Details**

Sample Set	Number of Samples	Sample Details
SS-25 Oily Material	11	Crude oil accumulated on casing OD
SS-25 Casing JSN C025	16	7 in. casing joint 24 OD material, sampling depth 978.9 ft

Sample Set	Number of Samples	Sample Details
SS-25 Casing JSN C026	13	7 in. casing joint 25 OD material, sampling depth 1021.4 ft
SS-25 Background	2	Dirt from rig area, fluids on rig floor drip pad

## 3.2 MPN Analysis of the Microbial Population of Well SS-25.

### 3.2.1 Well SS-25 MPN Analysis

MPN analysis in MPB, PRD, NRB, and IRB media was set up with 42 samples. Of these 168 media/sample combinations, less than 50% exhibited any growth. This result indicates that the microbial activity in the samples is low or that the media/incubation conditions were incompatible with organisms in the sample.

The average cells per g sample were calculated for each of the well SS-25 sample types. Table 6 shows the results of population analysis by MPN method using the four different culture medias.

Culturable microbial activity was on average 1 to 3 log orders higher in the Oily Material samples as compared to the OD Scale samples.

Microbial activity was lowest in the Background samples.

**Table 6: Well SS-25 MPN Microbial Populations Analysis Summary**

Well	Sample Set	Media Type/Phenotype Detected by Media			
		MPB/SRB	PRD/APB	IRB/IRB	NRB/NRB
SS-25	C025 and C026, Oil	7.76E+03	3.07E+05	6.39E+04	3.26E+04
SS-25	C025 OD Scale	3.04E+01	3.51E+02	6.68E+02	6.64E+01
SS-25	C026 OD Scale	4.81E+00	5.43E+02	3.13E+02	7.90E+01
SS-25	Background Materials	0.00E+00	2.00E+03	0.00E+00	4.75E+02

Values are the average number of culturable bacteria per g of sample for each sample set.  
 Red > 10<sup>4</sup> cells/g. Yellow > 10<sup>3</sup> cells/g. Gray is no activity.  
 MPB–Modified Postgate’s Broth B. SRB–Sulfate-Reducing Bacteria. PRD–Phenol Red Dextrose. APB–Acid Producing Bacteria. IRB–Iron Reducing Bacteria. NRB–Nitrate Reducing Bacteria.

## 3.3 qPCR Analysis of the Microbial Population of Well SS-25

### 3.3.1 Well SS-25 qPCR Analysis

Well SS25 qPCR reactions were set up with primer sets 16S, Arch, and 18S. The majority of the sample/primer combinations gave negative results that were below the limit of detection.

Due to poor DNA isolation efficiency from dried samples, most samples did not yield detectable DNA. Samples that did not yield DNA as a result of technical challenges with the material are excluded from the analysis of the results.

Note that if enough DNA was isolated for one analysis, there was enough DNA for all analysis. This means that the results are significant when there are positive results for 16S analysis and negative results from

18S analysis. This indicates that there are log-order differences in the levels of the two target populations in the sample.

Table 7 shows the average for each sample type that was calculated.

**Table 7: qPCR Analysis of the Microbial Populations of Wells SS-25 and P35**

Well	Sample Sets	qPCR Primer Set		
		16S	Arch	18S
SS-25	Oily Samples	2.64E+07	<LOD	1.11E+05
SS-25	C025 OD Scale	1.63E+07	1.10E+08	<LOD
SS-25	C026 OD Scale	4.38E+07	7.98E+07	<LOD
SS-25	SS-25 Background	6.20E+07	<LOD	<LOD

Values are the average number of cells per g of sample for each sample set.  
 Primers used were: 16S (detect bacteria and archaea), Arch (detect only archaea), 18S (detect eukaryotes, including fungi, animals, plants, protozoans as well as some bacteria).  
 Cells are color-coded by value: green ( $10^4 - 10^6$ ), yellow ( $>10^6$ ). <LOD indicates below limit of detection.

qPCR values indicate that for many samples the microbial load is as much as 8 log orders higher than what was cultured during MPN analysis. This result indicates the presence of uncultured organisms in the samples. This can be due to cell viability or culture conditions.

The 16S primers detected organisms for each sample set, with values 6.9E+06 and 2.8E+07 cells per g.

The 18S primers detected organisms in the casing oily sample but not in any of the casing OD scale samples or background samples.

The Arch primers detected organisms in both joints C025 and C026 OD scale material. Archaeal signatures were identified only in the casing samples and not in the background or the oily samples. Joints C025 and C026 contained Archaeal signatures at an average cell density of 9.5E+07 cells per g sample.

Results indicate that the SS-25 casing OD scale contains a population of bacteria and archaea that is greater than 1E+08 cells per g, and that this population does not include significant levels of eukaryotes such as fungi or protozoans.

## 3.4 Amplicon Metagenomics Analysis of the Microbial Populations of Well SS-25

### 3.4.1 Amplicon Metagenomics: Overview of Unique Bacterial and Archaeal Taxa Identified

Amplicon metagenomic population profiles reactions were conducted on DNA isolated from the samples. Over 356,883 individual sequences were generated (Table 8). These sequences were aligned to sequences in a ribosomal database. Each sequence was assigned a taxonomic identity, referred to here as a “species.”

Note that many of these were annotated only to the Genus level. Any organism not assigned at least a Genus level designation is listed under “Unclassified,” which is actually a composite classification containing numerous taxonomically unrelated organisms.

**Table 8: Well SS-25 16S Amplicon Metagenomic Population Profile Overview**

Project	Well	Sample Set	# DNA Sequences	# Bacterial Species	# Archaeal Species	Total # Species
LA5	SS-25	SS25-C025	115,468	113	12	125
LA5	SS-25	SS25-C026	146,406	124	11	135
LA5	SS-25	SS25 Oily	72,388	120	6	126
LA5	SS-25	Background	22,621	75	4	79
LA5	SS-25	<i>SS25 Total</i>	<i>356,883</i>	<i>210</i>	<i>13</i>	<i>223</i>

The # DNA Sequences is the number of 16S library sequence reads obtained for that sample set. The # Bacterial Species is the number of unique bacterial taxa elucidated for each sample set. The # Archaeal Species is the number of Archaeal taxa elucidated for each sample set. The Total # Species is the number of unique taxa elucidated for each sample set.

A total of 223 organisms were assigned species designation (Table 8). 210 were identified as belonging to the Domain Bacteria. 13 were identified as belonging to the Domain Archaea.

Even though Archaeal qPCR did not detect archaea in the Oily and Background samples, low levels of archaea were identified in the Amplicon metagenomics. This result is probably due to the broader coverage of Archaea conferred by 16S primers relative to Archaeal primers. Increased specificity comes at the cost of being less sensitive.

Over all, the number of species identified from each sample is within the typical range obtained from oil and gas (O&G) samples using this approach.

### 3.4.2 Trait Profiling of Well SS-25

Each of the 223 different organisms identified in the sample was assigned traits that include physiological, ecological, metabolic, and taxonomic associations.

Each of these traits was broken down by the number of species of the 223 different species that had that trait, as well as the percent of the total population of organisms they occupied (Table 9).

The data was screened, and the traits for which the highest percentage of organisms fit were used to generate population profiles for each sample set (Table 9).

From this data, distinct differences between the Oily Samples, Casing Joint C025, Casing Joint C026, and the Background Sample emerged.

From population profiling, the following three distinct population profiles emerged from the analysis:

1. **Oily Samples:** Metabolically dominated by NRB, alkaliphiles, and hydrocarbon biodegrading bacteria

These are primarily from the Bacterial Class, Gammaproteobacteria.

2. **Casing Joint Scale Samples:** Metabolically dominated by alkaliphiles and anaerobic methanogens

- Archaeal methanogens were from the Archaeal Class Methanobacteria and Methanomicrobia.
- Predominant Alkaliphiles were from the Bacterial Class Bacilli.
- Scale from C025 additionally contained significant levels of Clostridia.
- C025 and C026 scale samples also contained significant levels of Gammaproteobacteria.

3. **Background Sample:** Metabolically dominated by biodegrading bacteria, but not hydrocarbon biodegrading Bacteria

These are primarily represented by members of Bacterial Phylum Actinobacteria, a bacterial clade that includes many aerobic soil isolates.

Traits associated with MIC that were not found in great abundance in the samples include IRB (iron reducing bacteria) and sulfidogens, including SRB (sulfate reducing bacteria). For the C025 and C026 samples, the percentage of sulfidogens in the samples was less than 5% of the population.

Despite low abundance, the diversity of sulfidogens was quite high, with 28 and 27 different sulfidogenic species in each sample set, respectively. This suggests that under the right environmental conditions, there is a potential for sulfidogens to become dominant members of the microbial community.

**Table 9: Population Profile of Well SS-25 Samples**

Selected Metabolic, Physiological, Ecological Traits, % of Population; # of Species				
Selected Traits	Oily Samples	C025 Scale	C026 Scale	Background
Alkaliphile	58.6 ; 9	37.2 ; 7	17.1 ; 8	0.2 ; 3
Methanogen	0.1 ; 6	33.2 ; 13	57.0 ; 11	1.3 ; 4
Anaerobe	4.4 ; 31	39.1 ; 48	59.3 ; 50	1.5 ; 12
NRB	52.8 ; 10	2.4 ; 8	1.4 ; 10	3.0 ; 4
Sulfidogen	2.1 ; 21	3.3 ; 27	1.4 ; 28	0.03 ; 3
IRB	1.0 ; 6	0.9 ; 7	0.1 ; 8	0.01 ; 1
BioDeg	55.2 ; 38	10.1 ; 28	2.7 ; 34	23.9 ; 20
<i>BioDeg HC</i>	53.5 ; 14	2.4 ; 11	1.5 ; 12	0.3 ; 3
Halophile	53.0 ; 9	7.2 ; 5	6.7 ; 7	2.6 ; 4
Higher Taxonomic Level Profiles, % of Population ; # of Species				
Taxonomic Group	Oily Samples	C025 Scale	C026 Scale	Background
Firmicutes	11.8 ; 36	37.2 ; 39	16.9 ; 35	0.8 ; 13
<i>Clostridia</i>	3.3 ; 19	9.8 ; 28	1.1 ; 23	0.1 ; 5
<i>Bacilli</i>	8.0 ; 17	27.8 ; 12	15.9 ; 13	0.4 ; 6
Gammaproteobacteria	78.8 ; 17	12.8 ; 12	9.4 ; 14	1.2 ; 7
Euryarchaeota	0.1 ; 6	33.2 ; 13	57.0 ; 11	1.3 ; 4
<i>Methanobacteria</i>	0.2 ; 5	30.4 ; 2	46.4 ; 2	1.2 ; 2
<i>Methanomicrobia</i>	0.1 ; 1	2.7 ; 9	10.6 ; 9	0.06 ; 2
Actinobacteria	1.1 ; 11	0.01 ; 7	0.01 ; 7	48.3 ; 21
Bacteroidetes	2.1 ; 5	3.9 ; 6	0.5 ; 6	1.4 ; 8
<p>Trait and Taxonomic Profiles.                      First value is % of population; second value is # of species.                      Values add up to &gt; 100% because each organism can be categorized under more than one trait (e.g., all Methanogens and SRB are also Anaerobes).                      Indented traits indicate the following subcategories: BioDeg HC (hydrocarbon biodegrading) is a subcategory of BioDeg (biodegrading). Clostridia and Bacilli are Classes within the Bacterial Phylum, Firmicutes.                      Methanobacteria and Methanomicrobia are Classes within the Archaeal Phylum, Euryarchaeota.                      Yellow indicates values &gt; 10% of the population.</p>				

## 4 Identification of Localized Variations in the Microbial Population

### 4.1 Marker Organisms Identified for Each Sample Type

The majority of organisms constituted less than 1% of the population of any samples. When the data was sorted by % abundance in each of the samples, organisms characteristic of each sample type were identified (Table 10).

Markers for each sample type were identified, defined as abundance of more than 1% of each sample time, and greater than 10-fold higher in that sample type than the other two sample types (Table 10).

**Table 10: Marker Organisms for Each Sample Type**

Organism	Average %, Oil	Average %, Scale	%, Dirt
<i>Methanobacterium sp</i>	0.049	31.62	0.614
<i>Methanobacterium aarhusense</i>	0.008	8.649	0.685
<i>Methanocalculus sp</i>	0.033	3.874	0
<i>Halomonas sp</i>	58.04	1.892	0.115
<i>Pseudomonas sp</i>	6.886	0.469	0.097
<i>Nocardioides sp</i>	0	0	20.229
<i>Sphingomonas sp</i>	0.007	0.001	9.177
<i>Dietzia sp</i>	0.090	0.011	8.974

Values are the % of the population averaged for each sample type. Yellow are marker species for that sample.

By this method, organisms whose abundance is indicative of that sample type were identified:

- Crude oil: two organisms, the Gammaproteobacteria *Halomonas* and *Pseudomonas*
- Scale Samples: three organisms, all methanogenic archaea
  - *Methanobacterium sp*
  - *Methanobacterium aarhusense*
  - *Methanocalculus sp*
- Dirt sample: nine species (three are shown), all are organisms commonly isolated from soil samples

### 4.2 Scale Samples are Representative of Casing Surface Microbiology

The population profile suggested that at least some of the oily material originated from higher in the well rather than solely from joints C025 and C026. Results of analysis of the background dirt sample indicated that background material found on site was not significantly impacting the analysis of the casing joint samples.

Organisms present in the scale samples from joints C025 and C026; therefore, are of the most relevance to understanding the potential role of microorganisms in MIC within the subsurface environment of well



SS-25. The organisms present in the Scale Samples from joints C025 and C026 were further evaluated for corrosion potential.

### 4.3 Identifying the Most Abundant Organisms in the Well SS-25 Casing Scale Samples

163 different organisms were identified on the SS-25 joints C025 and C026 samples. Of these organisms, 149 occupied less than 1% of the total population from either sample. Only 14 different organisms were found to be present in more than 1% of the total population (Table 11). This included Archaeal methanogens, alkaliphiles, and sulfidogens, as well as organisms associated with subsurface samples.

**Table 11: Well SS-25 Casing Joints C025 and C026 Most Abundant Organisms**

Species	C025 Avg	C026 Avg	Select Traits: Metabolism, Physiology, Ecology, Taxonomy
<i>Methanobacterium sp</i>	27.7	34.7	Anaerobe; Archaea; Methanogen
<i>Alkalibacterium sp</i>	24.3	7.5	Alkaliphile; Firmicutes; Lactobacillales
Unclassified	8.9	11.9	Polytaxonomic category of unclassified organisms
<i>Xanthomonas campestris</i>	9.9	9.3	Gammaproteobacteria; Production of Drilling Mud Component, Xanthan Gum
<i>Methanobacterium aarhusense</i>	0.3	15.2	Anaerobe; Archaea; Methanogen
<i>Methanocalculus sp</i>	1.4	5.8	Anaerobe; Archaea; Methanogen
<i>Alkalibacter sp</i>	6.6	0.2	Alkaliphile; BioDeg; Clostridia; Firmicutes
<i>Halolactibacillus halophilus</i>	1.7	4.7	Alkaliphile; Bacilli; Firmicutes; GHB; Halophile
<i>Halomonas sp</i>	1.9	1.8	Alkaliphile; BioDeg HC; Facultative Anaerobe; Gammaproteobacteria; Halophile; NRB
<i>Alkaliflexus sp</i>	3.4	0.1	Alkaliphile; Bacteroidetes; Halophile
<i>Ercella succinigenes</i>	1.9	0.01	Anaerobe; Clostridia; Firmicutes; Sulfidogen; SuRB
<i>Synergistes sp</i>	0.6	1.2	Ferm; Synergistetes
<i>Sedimentibacter sp</i>	1.2	0.01	BioDeg; NC10
<i>Acetobacterium sp</i>	1.0	0.1	Acetogen; Anaerobe; APB; Clostridia; Firmicutes
<i>Pseudomonas sp</i>	0.6	0.3	Aerobe; Gammaproteobacteria; Varies
<i>Anaerobranca sp</i>	0.8	0.01	Alkiliphile; Anaerobe; Clostridiales; Firmicutes; IRB; Sulfidogen; Thermophile; TRB
<i>Methanocorpusculum sinense</i>	0.7	0.1	Anaerobe; Archaea; Methanogen

Percent of the population of the top 17 most abundant organisms in well SS-25 casing joints C025 and C026.

This table includes all organisms present in more than 1% of the total population of the sample.

Averages: Yellow are >10% of the population. Green shows 1–10% of the population.

Trait abbreviations (details of each trait are in Appendix C): BioDeg HC–Hydrocarbon biodegrading organisms; BioDeg–Biodegrading organisms; NRB–Nitrate Reducing Bacteria; TRB–Thiosulfate Reducing Bacteria; APB–Acid Producing Bacteria; SuRB–Sulfur Reducing Organism.

Traits are highlighted: Red, Methanogens; yellow, Alkaliphiles; and green, Sulfidogens.

### 4.3.1 Characteristics of Most Abundant Organisms in Well SS-25 Casing Samples

#### Methanogens

***Methanobacterium sp.*** *Methanobacterium sp.*, together with the related *Methanobacterium aarhusense*, were the most abundant organism overall in well SS-25 joints C025 and C026 samples. *Methanobacterium* species are hydrogenotrophic methanogens from the Archaeal Class, Methanobacteria commonly found in anaerobic digestors and hot springs. *Methanobacterium sp.* have also been shown to dominate cathodic biofilms [5]. *Methanobacterium*-related organisms have been demonstrated to be more active in the presence of iron, suggesting they can utilize iron directly, which contributes to a direct role in metal corrosion [6].

Additional methanogenic genera detected at levels greater than 1% of the population were *Methanocalculus* and *Methanocorpusculum*. *Methanocalculus* is a genus of hydrogenotrophic methanogens from the Archaeal class, Methanomicrobia. Members include alkaliphilic methanogens, such as *Methanocalculus natronophilus*. *Methanocalculus* species are associated with corrosion in oil and gas operations [7] [8] [9].

*Methanocorpusculum sinense* are methanogens from the Archaeal class, Methanomicrobia. *Methanocorpusculum* species are commonly found in anaerobic digestors activated sludges [10]. They are not currently known to be associated with corrosion.

There is an increasing recognition of the role of methanogens in corrosion specifically in oil and gas operations. Methanogens specifically related to the ones identified on the surface of the SS-25 casing have been demonstrated to cause iron corrosion. See Appendix B for details on the role of methanogens and corrosion.

#### Non-Methanogens

***Alkalibacterium sp.*** *Alkalibacterium* species were particularly widespread and abundant across many samples originating from Aliso Canyon. As such, they are probably important components of the local microbiology. *Alkalibacterium* is a genus of alkaliphilic, anaerobes of the bacterial Phylum Firmicutes. *Alkalibacterium* are members of the Lactobacillaceae, a bacterial family that includes the well known, common lactic acid bacteria (LAB) found in fermented dairy and plant materials, such as yogurts and sauerkraut [11]. There are eight species within the *Alkalibacterium*. Members are noted for their growth under alkaline conditions, meaning they grow at elevated pH, greater than 8.5. Some strains are obligate alkaliphiles in that an elevated pH is required for growth. Some strains are also halophiles, e.g. they grow under elevated salt conditions. Most *Alkalibacterium* strains in the literature were isolated from fermented waste products, including shrimp processing waste, olive waste, rotting marine algae, as well as alkaline soda lakes. *Alkalibacterium* species were widely present in samples collected from Aliso Canyon and were the dominant organisms in many samples. *Alkalibacterium* are not typical components of O&G systems microbial populations, which suggests they are simply organisms native to the region around Aliso Canyon, reflective of the geological influence on the environment, rather than being promoted specifically by the natural gas activities in the area. A role of *Alkalibacterium* in MIC has not been reported or established.

***Alkalibacter sp., Halolactibacillus sp. and Alkaliflexus.*** *Alkalibacter*, *Halolactibacillus*, and *Alkaliflexus* are alkaliphilic anaerobes initially isolated from soda lakes, but they have been found in diverse environments such as muds. *Halolactibacillus* and *Alkaliflexus* are genera within the bacterial Phylum Firmicutes, while *Alkaliflexus* is from the bacterial Phylum Bacteroidetes. *Alkalibacter* has been identified in microbial

populations of gas-water separators from gas gathering systems [12]. A direct role in corrosion is not known for *Alkaliflexus*, *Alkalibacter*, or *Halolactibacillus*.

**Unclassified.** Unclassified includes all sequences that could not be identified to the Genus level. This is a polytaxonomic category, e.g., it includes unrelated sequences. Evaluation of these sequences did not identify majority components of the population, although the data suggests additional, novel Archaeal methanogens might be present at low levels.

***Xanthomonas campestris*.** Just under 10% of the signatures from well SS-25 originated from *Xanthomonas campestris*. The presence of these aerobic, plant pathogenic members of the bacterial class, Gammaproteobacteria is most likely due to the presence of xanthan gum in the drilling fluids. *Xanthomonas* species are widely used during the commercial production of xanthan gum, which is a component of drilling fluids used in the well [13]. The signatures most likely reflect the presence of residual DNA in the drilling fluids applied to the well. While not directly tested, it is unlikely that there were viable *Xanthomonas* cells in the system because *Xanthomonas* species are noted for growth under aerobic conditions only. It is unlikely that there is any association between *Xanthomonas* signatures and MIC.

***Halomonas sp.*** *Halomonas sp* are members of the Gammaproteobacteria, a class that includes many common Gram–organisms, such as *E. coli* and *Pseudomonas*. Many *Halomonas* species are capable of degrading oil and gas hydrocarbons produced by oil and gas operations [14], and thus are frequently associated with oil and gas activities [15]. They are often identified as prominent components of samples originating from O&G operations. *Halomonas* are facultative anaerobes, halophilic, and alkaliphilic organisms. Their association is often observed with samples experiencing product degradation, rather than corrosion. This hydrocarbon biodegradation capacity has been evaluated for use in oil contamination bioremediation. Because they are widespread in O&G samples, *Halomonas* species are sometimes found in MIC associated populations. It was proposed that one species, *H. titanicae*, was in part responsible for the corrosion of a wreck [16]. The presence of *Halomonas* in these samples is reflective of their origin in a natural gas field.

## 4.4 Variations in the Microbial Population Along the Surface of the Casing from Well SS-25

A more detailed analysis of the population in each sample originating from the surface of the casing from well SS-25 was conducted.

Each sample was analyzed individually, and the most abundant organisms in each sample were identified (Table 12).

It was found that *Methanobacterium sp* was the most abundant organism in all samples. Samples C026-S12 and S16 were also found to be dominated by the methanogen, *Methanobacterium aarhusense*. Sample C026-S01 was also found to be dominated by the methanogen, *Methanocalculus sp*.

Taken together, this data indicated that there are local variations in microbial population structure. Because potentially corrosion-associated organisms vary in distribution along the casing surface, it suggests that there are localized differences in the corrosive capacity of microbial populations along the surface of the casing joints.

**Table 12: Microbial Populations in each Well SS-25 7 in. Casing OD Samples**

Distribution of Alkaliphiles and Methanogens									
Select Traits	CO25-S07	CO25-S08	CO25-S17	CO25-S21	CO26-S01	CO26-S04	CO26-S06	CO26-S12	CO26-S16
Alkaliphiles, % and # sp (species)	43.9%; 6 sp	53.2%; 5 sp	31.1%; 6 sp	24.2%; 4 sp	27.8%; 6 sp	21.6%; 6 sp	9.7%; 6 sp	9.5%; 5 sp	2.8%; 6 sp
Methanogens, % and # sp (species)	24.2%; 3 sp	22.5%; 4 sp	42.7%; 12 sp	32.2%; 6 sp	52.6%; 8 sp	59.5%; 8 sp	45.6%; 7 sp	76.9%; 9 sp	48.9%; 6 sp
Sulfidogen, % and # sp (species)	10.4%; 8 sp	1.4%; 4 sp	1.5%; 24 sp	0.7%; 8 sp	1.8%; 10 sp	2.3%; 14 sp	3.8%; 18 sp	0.2%; 9 sp	0.5%; 10 sp
Predominant Species Composition of Individual Casing CO25 and CO26 Samples, % of Microbial Population									
Individual Species	CO25-S07	CO25-S08	CO25-S17	CO25-S21	CO26-S01	CO26-S04	CO26-S06	CO26-S12	CO26-S16
<i>Methanobacterium aarhusense</i>	0.4	0.004	0.06	1.0	0.1	7.6	0.9	42.5	24.9
<i>Methanobacterium sp</i>	23.7	22.4	37.9	26.5	26.6	48.0	42.3	34.1	22.6
<i>Methanocalculus sp</i>	0	0	1.3	4.4	25.5	2.9	0.5	0.02	0.04
<i>Methanocorpusculum sinense</i>	0	0	2.9	0	0.01	0.6	0	0.01	0
<i>Alkalibacter sp</i>	5.8	20.4	0.1	0	0.04	0.1	0.5	0.5	0.09
<i>Alkalibacterium sp</i>	24.0	31.8	24.1	17.2	19.7	6.4	2.8	8.3	0.2
<i>Alkaliflexus sp</i>	12.6	0.6	0.2	0.4	0.01	0.1	0.3	0.02	0.013
<i>Halolactibacillus halophilus</i>	1.1	0.2	3.0	2.6	7.6	11.08	2.4	1.1	1.3
<i>Ercella succinigenes</i>	6.8	0.8	0.02	0.1	0.01	0.02	0.05	0	0
Select traits and list of organisms found to be present in greater than 1% of the total population of Well SS-25 casing joints CO25 and CO26									
Values are the percent abundance and are color-coded as such: Yellow are >10% and green are 1%–10%.									

## 5 Conclusions

---

- The SS-25 casing samples were shown to have average microbial levels of  $9.5E+07$  cells per gram dried casing mud.
- Between 22% and 77% of all microorganisms were determined to be methanogenic archaea, which indicates a casing surface population of methanogenic archaea of over  $1E+07$  per g sample.
- Two genera, *Methanobacterium* and *Methanocalculus*, were the predominant archaea identified in the samples.
- *Methanocalculus* and *Methanobacterium* species have been shown to be directly associated with metal corrosion in oil and gas systems.
- The combination of high cell density on the casing surface, along with the identity of methanogens related to those known to cause metal corrosion, suggests that the microbial population present at the time of sampling has the potential to cause corrosion.
- The microbial population on the surface of the SS-25 casing is consistent with a microbial population able to cause metal corrosion.
- It should be noted that a diagnosis of MIC requires more evidence than genus or species identification.
- Physical evidence, including identification of corrosion features associated with MIC, as well as through elimination of non-MIC causes of corrosion, must also be provided before a diagnosis of MIC can be made.

## 6 References

---

- [1] NACE International, Field Monitoring of Bacterial Growth in Oil and Gas Systems. NACE-TM0194-2014, NACE International, 2014.
- [2] NACE International, Detection, Testing, and Evaluation of Microbiologically Influenced Corrosion on Internal Surfaces of Pipeline. NACE-TM0212-2018, NACE International, 2018.
- [3] NACE International, Detection, Testing, and Evaluation of Microbiologically Influenced Corrosion (MIC) on External Surfaces of Buried Pipeline. NACE-TM0106-2016, NACE International, 2016.
- [4] L. L. Barton and G. D. Fauque, "Biochemistry, physiology and biotechnology of sulfate-reducing bacteria," *Adv Appl Microbiol*, vol. 68, pp. 41-98, 2009.
- [5] M. Siegart, M. D. Yates, D. F. Call, X. Zhu, A. Spormann and B. E. Logan, "Comparison of Nonprecious Metal Cathode Materials for Methane Production by Electromethanogenesis," *ACS Sustain Chem Eng*, vol. 2, no. 4, pp. 910-917, 2014.
- [6] H. T. Dinh, J. Kuever, M. Mußmann, A. W. Hassel, M. Stratmann and F. Widdel, "Iron corrosion by novel anaerobic microorganisms," *Nature*, vol. 427, pp. 829-32, 2004.
- [7] B. Ollivier, M. L. Fardeau, J. L. Cayol, M. Magot, B. K. Patel, G. Prensier and J. L. Garcia, "Methanocalculus halotolerans gen. nov., sp. nov., isolated from an oil-producing well," *Int. J. Syst. Bacteriol*, vol. 48, no. 3, pp. 821-8, 1998.
- [8] T. J. Tidwell, R. De Paula, Z. Broussard and V. V. Keasler, "Mitigation of Severe Pitting Corrosion Caused by MIC in a CDC Biofilm Reactor," in *NACE-2017-9604*, 2017.
- [9] T. Zhang, H. H. Fang and B. C. KO, "Methanogen population in a marine biofilm corrosive to mild steel," *Appl Microbiol Biotechnol.*, vol. 63, no. 1, pp. 101-6, 2003.
- [10] G. Zellner, E. Stackebrandt, P. Messner, B. J. Tindall, E. Conway de Macario, H. Kneifel, U. B. Sleytr and J. Winter, "Methanocorpusculaceae fam. nov., represented by *Methanocorpusculum parvum*, *Methanocorpusculum sinense* spec. nov. and *Methanocorpusculum bavaricum* spec. nov.," *Arch Microbiol*, vol. 151, no. 5, pp. 381-390, 1989.
- [11] I. Yumoto, K. Hirota and K. Nakajima, "The genus *Alkalibacterium*," in *Lactic Acid Bacteria: Biodiversity and Taxonomy*, W. H. Holzapel and B. J. Wood, Eds., John Wiley & Sons, Ltd, 2014.
- [12] Y. Zhang, Z. Yu, H. Zhang and I. P. Thompson, "Microbial distribution and variation in produced water from separators to storage tanks of shale gas wells in Sichuan Basin, China," *Environ. Sci.: Water Res. Technol*, vol. 3, pp. 340-351, 2017.
- [13] Z. Wang, J. Wu, M. J. Gao, L. Zhu and X. B. Zhan, "High production of xanthan gum by a glycerol-tolerant strain *Xanthomonas campstris* WXLB-006," *Prep Biochem Biotechnol*, vol. 47, no. 5, pp. 468-472, 2017.
- [14] S. D'Ippolito, R. E. de Castro and S. K. Herrera, "Chemotactic responses to gas oil of *Halomonas* spp. strains isolated from saline environments in Argentina," *Rev Argent Microbiol*, vol. 43, no. 2, pp. 107-10, 2011.
- [15] B. Z. Fathepure, "Recent studies in microbial degradation of petroleum hydrocarbons in hypersaline environments," *Frontiers in Microbiology*, vol. 5, p. 173, 2014.
- [16] C. Sanchez-Porro, B. Kaur, H. Mann and A. Ventosa, "*Halomonas titanicae* sp. nov., a halophilic bacterium isolated from the RMS Titanic," *Int J Syst Evol Microbiol*, vol. 60, no. 12, pp. 2768-2774,

- 2010.
- [17] G. D. Vogels, J. T. Keltjens and C. Van Der Drift, "Biochemistry of methane production," in *Biology of anaerobic microorganisms*, A. J. B. Zehnder, Ed., New York, Wiley, 1988, pp. 707-770.
- [18] W. E. Balch, G. E. Fox, L. J. Magrum, C. R. Woese and R. S. Wolfe, "Methanogens: reevaluation of a unique biological group," *Microbiol*, vol. 43, no. 2, pp. 260-296, 1979.
- [19] D. J. Lieber, J. Catlett, N. Madayijpathiya, R. Nandakumar, M. M. Lopez, W. W. Metcalf and N. R. Buan, "A Multienzyme Complex Channels Substrates and Electrons through Acetyl-CoA and Methane Biosynthesis Pathways in Methanosarcina," *PLoS One*, vol. 9, no. 9, 2014.
- [20] S. Kruse, T. Goris, M. Westermann, L. Adrian and G. Kiekert, "Hydrogen production by *Sulfurospirillum* species enables syntrophic interactions of Epsilonproteobacteria," *Nature communications*, vol. 9, no. 1, 2018.
- [21] C. R. Hubert, T. B. Oldenburg, M. Fustic, N. D. Gray, S. R. Larter, K. Penn, A. K. Rowan, R. Seshardri, A. Sherry, R. Swainsbury, G. Voordouw, J. K. Voordouw and I. M. Head, "Massive dominance of Epsilonproteobacteria in formation waters from a Canadian oil sands reservoir containing severely biodegraded oil," *Environ Microbiol*, vol. 14, no. 2, pp. 387-404, 2012.
- [22] L. Daniels, N. Belay, B. S. Rajagopal and P. J. Weimer, "Bacterial Methanogenesis and Growth from CO<sub>2</sub> with Elemental Iron as the Sole Source of Electrons," *Science*, vol. 237, no. 4814, pp. 509-11, 1987.
- [23] K. Mori, H. Tsurumaru and S. Harayama, "Iron corrosion activity of anaerobic hydrogen-consuming microorganisms isolated from oil facilities," *Journal of Bioscience and Bioengineering*, vol. 110, no. 4, pp. 426-30, 2010.
- [24] J. Mand, H. S. Park, C. Okoro, B. P. Lomans, S. Smith, L. Chiejina and G. Voordouw, "Microbial Methane Production Associated with Carbon Steel Corrosion in a Nigerian Oil Field," *Front Microbiol*, vol. 6, no. 1538, 2016.
- [25] T. Uchiyama, K. Ito, K. Mori, H. Tsurumaru and S. Harayama, "Iron-corroding methanogen isolated from a crude-oil storage tank," *Appl Environ Microbiol*, vol. 76, no. 6, pp. 1783-8, 2010.
- [26] S. Kato, "Microbial extracellular electron transfer and its relevance to iron corrosion," *Microb Biotechnol*, vol. 9, no. 2, pp. 141-8, 2016.
- [27] H. Tsurumaru, N. Ito, K. Mori, S. Wakai, T. Uchiyama, T. Lino, A. Hosoyama, H. Ataku, K. Nishijima, M. Mise, A. Shimizu, T. Harada, H. Horikawa, N. Ichikawa, T. Sekigawa, K. Jinno, S. Tanikawa, J. Yamazaki, K. Sasaki, S. Yamazaki, N. Fujita and S. Harayama, "An extracellular [NiFe] hydrogenase mediating iron corrosion is encoded in a genetically unstable genomic island in *Methanococcus maripaludis*," *Sci Rep*, vol. 8, no. 1, p. 15149, 2018.
- [28] R. Liang, R. S. Grizzle, K. E. Duncan, M. J. McInerney and J. M. Suflita, "Roles of thermophilic thiosulfate-reducing bacteria and methanogenic archaea in the biocorrosion of oil pipelines," *Front Microbiol*, vol. 6, no. 5, p. 89, 2014.
- [29] I. B. Beech and J. A. Sunner, "Sulphate-reducing bacteria and their role in corrosion of ferrous materials," in *Sulphate-Reducing Bacteria*, L. L. Barton and W. A. Hamilton, Eds., Cambridge University Press, 2007, pp. 459-482.
- [30] N. Kip, S. Jansen, M. Leite, M. de Hollander, M. Afanasyev, E. E. Kuramae and J. Veen, "Methanogens predominate in natural corrosion protective layers on metal sheet piles," *Sci Rep*, vol. 7, no. 1, p. 11899, 2017.
- [31] D. J. Lonergan, H. L. Jenter, J. D. Coates, E. J. Phillips, T. M. Schmidt and D. R. Lovley, "Phylogenetic analysis of dissimilatory Fe(III)-reducing bacteria," *J Bacteriol*, vol. 178, no. 8, pp. 2402-8, 1996.

- [32] D. R. Lovley, D. E. Holmes and K. P. Nevin, "Dissimilatory Fe(III) and Mn(IV) reduction," *Adv Microb Physiol*, vol. 49, pp. 219-86, 2004.
- [33] A. Gittel, K. B. Sørensen, T. L. Skovhus, K. Ingvorsen and A. Schramm, "Prokaryotic community structure and sulfate reducer activity in water from high-temperature oil reservoirs with and without nitrate treatment," *Appl. Environ. Microbiol*, vol. 75, no. 22, pp. 7086-7096, 2009.
- [34] C. Hubert and G. Voordouw, "Oil Field Souring Control by Nitrate-Reducing *Sulfurospirillum* spp. That Outcompete Sulfate-Reducing Bacteria for Organic Electron Donors," *Appl Environ Microbiol*, vol. 73, no. 8, pp. 2644-2652, 2007.
- [35] Y. Kodama and K. Watanabe, "Sulfuricurvum kujiense gen. nov., sp. nov., a facultatively anaerobic, chemolithoautotrophic, sulfur-oxidizing bacterium isolated from an underground crude-oil storage cavity," *Int J Syst Evol Microbiol*, vol. 54, no. 6, pp. 2297-300, 2004.
- [36] K. Finster, W. Liesack and B. J. Tindall, "Sulfurospirillum arcachonense sp. nov., a new microaerophilic sulfur-reducing bacterium," *Int. J. Syst. Bacteriol*, vol. 47, no. 4, pp. 1212-1217, 1997.
- [37] L. L. Barton and A. Hamilton, Eds., *Sulphate-Reducing Bacteria: Environmental and Engineered Systems*, Cambridge University Press, 2007.
- [38] W. Sand, "Importance of hydrogen sulfide, thiosulfate and methylmercaptan for growth of Thiobacilli during simulation of concrete corrosion," *Appl Environ Microbiol*, vol. 40, pp. 183-190, 1987.
- [39] E. Vincke, N. Boon and W. Verstraete, "Analysis of the microbial communities on corroded concrete sewer pipes – a case study," *Appl Microbiol Biotechnol*, vol. 57, pp. 776-785, 2002.
- [40] J. C. Hulecki, J. M. Foght, M. R. Gray and P. M. Fedorak, "Sulfide persistence in oil field waters amended with nitrate and acetate," *J Ind Microbiol Biotechnol*, vol. 36, pp. 1499-1511, 2009.
- [41] M. Magot, M. L. Fardeau, O. Arnauld, C. Lanau, B. Ollivier, P. Thomas and B. K. Patel, "Spirochaeta smaragdinae sp. nov., a new mesophilic strictly anaerobic spirochete from an oil field," *FEMS Microbiol Lett*, vol. 155, no. 2, pp. 185-91, 1997.
- [42] A. Agrawal, K. Vanbroekhoven and B. Lal, "Diversity of culturable sulfidogenic bacteria in two oil-water separation tanks in the north-eastern oil fields of India," *Anaerobe*, vol. 16, no. 1, pp. 12-8, 2010.
- [43] C. Angeles-Chavez, J. L. Mora-Mendoza, R. Garcia-Esquivel, A. A. Padilla-Viveros, R. Perez, O. Flores and L. Martinez, "Microbiologically influenced corrosion by *Citrobacter* in sour gas pipelines," *Mater Perform*, vol. 41, pp. 50-55, 2002.



## Appendix A Detailed Reference Reports List

---

The reference reports containing the data from all samples analyzed for the RCA are listed below.

- Ecolyse 170721\_LA1 SS25 Wirelines Final Report
- Ecolyse 170721\_LA2 SS25A SS25 Scale Pipe Solids Final Report
- Ecolyse 170721\_LA3 SS25 Wireline Samples Final Report
- Ecolyse 170721\_LA4 P34 Casing SS9 Mud Samples Final Report
- Ecolyse 170721\_LA5 SS25 Casing Samples Final Report
- Ecolyse 170721\_LA5 SS25 Casing Samples Final Report
- Ecolyse 170721\_LA6 Well P35 Casing Samples Final Report
- Ecolyse 170721\_H1 SS25 Dried Casing Scale Final Report
- Ecolyse 170721\_H2 SS25 Dried Casing Scale Final Report
- Ecolyse 170721\_H3 \_H4 SS25 P35 CHDT Samples Final Report

## Appendix B Background on Methanogens and MIC

The most abundant organisms in the casing scale samples were identified as methanogens. Methanogens are all members of the Domain Archaea [17] [18]. Methanogens produce methane as a metabolic byproduct under strictly anaerobic conditions. During methanogenesis, methanogens use CO<sub>2</sub> (hydrogenotrophic methanogenesis) or small molecules, such as acetate (acetotrophic methanogens) as electron acceptors during respiration, releasing methane as a waste product. Some methanogens couple CO oxidation to CO<sub>2</sub> and H<sub>2</sub> generation and methanogenesis, and one organism has been shown to produce organic acids as well as methane via CO oxidation mechanisms. While the mass-balance equation of Methanogenesis looks simple, like most respiratory pathways, the number of steps, the energetics, and the molecular machinery are quite involved, with multiple steps occurring in a membrane-associated protein complex (Figure 1).

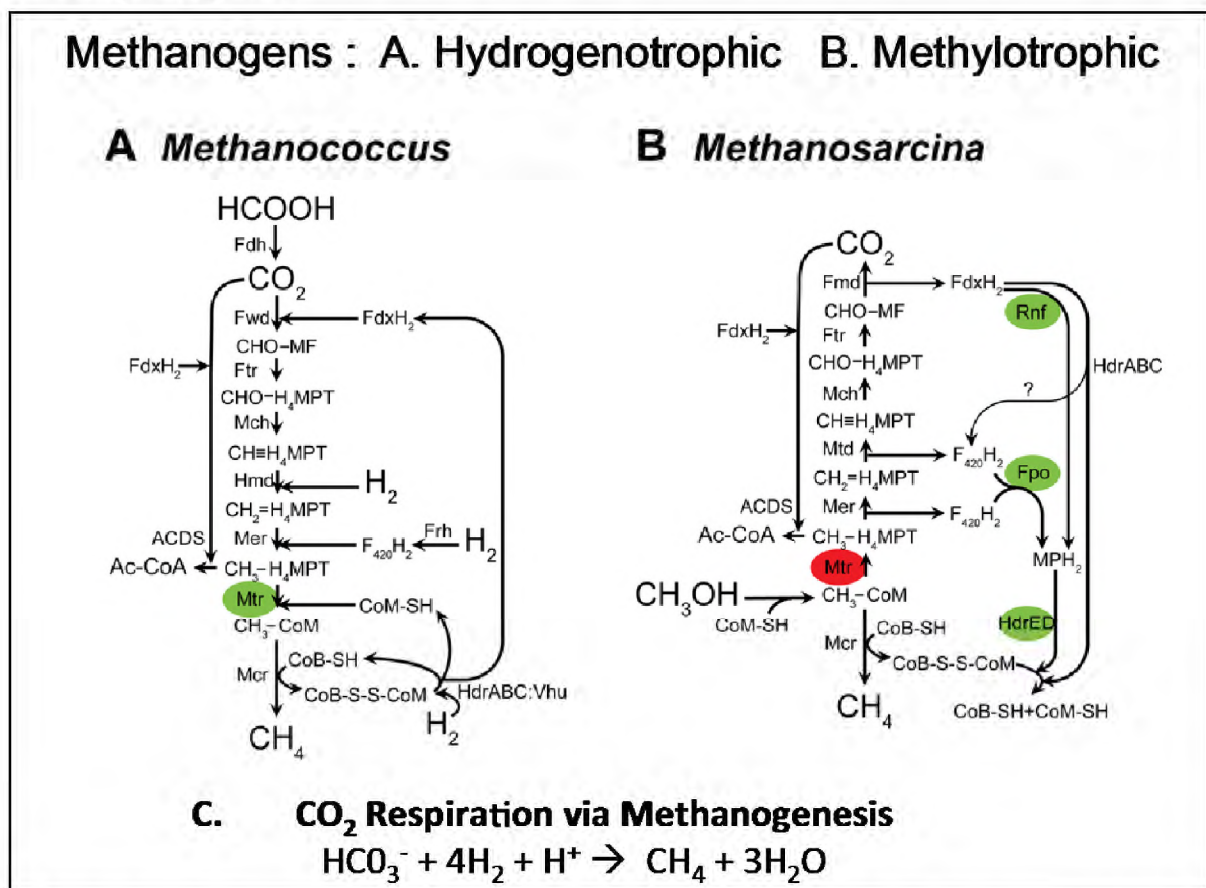



Figure 1: Diagram of Biochemical Reactions Occurring During (A) Hydrogenotrophic, and (B) Methylo trophic Methanogenesis. Green Ovals: Energy-Conserving Reactions. Red Ovals: Energy-Consuming Reaction. [19]

Methanogens are found in different environments including wetlands (marsh gas), animal digestive tracts (for example, methanogens are responsible for methane in cattle flatulence), and the anaerobic digester sludges of wastewater treatment systems. Some methanogens are extremophiles and can be found in hot springs, sub-marine hydrothermal vents, and in the "solid" rock of the Earth's crust kilometers below the surface.

Compared to other anaerobic respiratory pathways, methanogenesis is a low-energy yielding pathway (Figure 2). In many aquatic sediment environments, it has been observed that methanogens are stratified, occurring in a zone below organisms able to use more energetically favorable substrates, such as sulfates. Other methanogens are able to establish syntrophic communities in which hydrogen is transferred between bacteria and methanogens; for example, *Methanobacillus*, *Ruminococcus*, and *Wolinella* in cattle rumen, to the advantage of both members. This allows for complex community survival under conditions in which single species could not propagate.

<b>Environmentally Important Organic Matter Oxidation Reactions</b>		
<b>Reducing Half-reaction</b>	<b><math>E_h</math> (V)</b>	<b><math>\Delta G</math></b>
Reduction of $O_2$		
$O_2 + 4H^+ + 4e^- \rightarrow 2H_2O$	+0.812	-29.9
Reduction of $NO_3^-$		
$2NO_3^- + 6H^+ + 6e^- \rightarrow N_2 + 3H_2O$	+0.747	-28.4
Reduction of Mn (IV)		
$MnO_2 + 4H^+ + 2e^- \rightarrow Mn^{2+} + 2H_2O$	+0.526	-23.3
Reduction of Fe (III)		
$Fe(OH)_3 + 3H^+ + e^- \rightarrow Fe^{2+} + 3H_2O$	-0.047	-10.1
Reduction of $SO_4^{2-}$		
$SO_4^{2-} + 10H^+ + 8e^- \rightarrow H_2S + 4H_2O$	-0.221	-5.9
Reduction of $CO_2$		
$CO_2 + 8H^+ + 8e^- \rightarrow CH_4 + 2H_2O$	-0.244	-5.6



**Figure 2: Energetics of Methanogenesis Compared to Other Respiratory Pathways**

A recently discovered example of syntrophy occurs between *Sulfurospirillum* and *Methanococcus*, where there is sharing of  $H_2$ , acetate, lactate, and succinate (Figure 3) [20]. Importantly, *Sulfurospirillum* are Epsilonproteobacteria abundant in some oil fields [21]. Taken together, these data indicate complex and unexpected relationships between organisms and the subsurface environment.

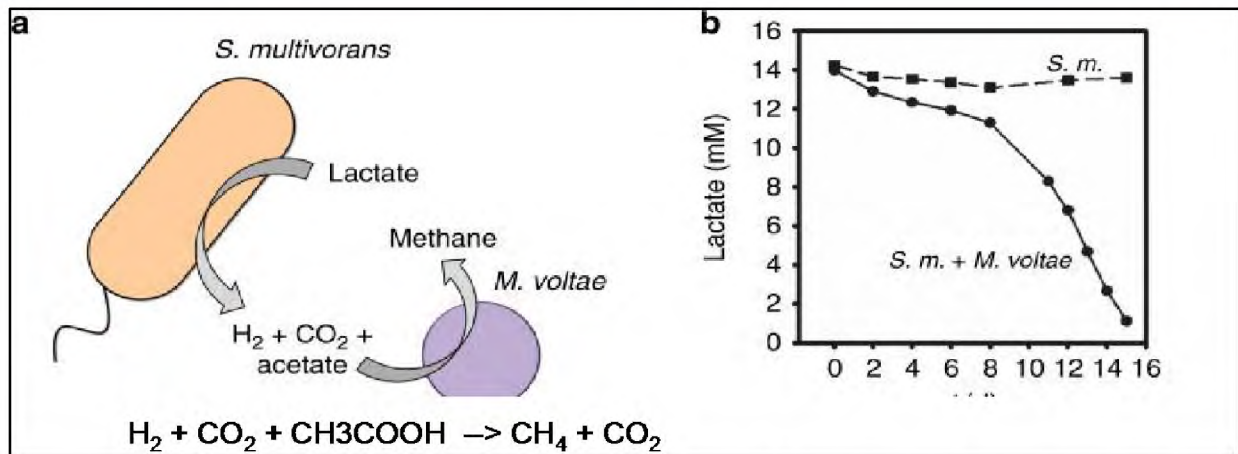


Figure 3: (a) Sytrophic Relationship Involving the Sharing of Acetate and Methane Between *S. multivorans* and the Methanogen, *M. voltae*. (b) Growth Curve of *S. multivorans* with lactae in the Presence (Squares) and Absence (Circles) of *M. voltae*. [20]

Hydrogenotrophic methanogens are able to use hydrogen on the surface of steel pipelines to reduce bicarbonate to either methane [22] [23] [24]. Recently, strains capable of using the steel directly as an electron donor have also been isolated [5] [6] [25] [26]. Hydrogenotrophic methanogens can contribute to MIC by catalyzing the following reaction (Figure 4):

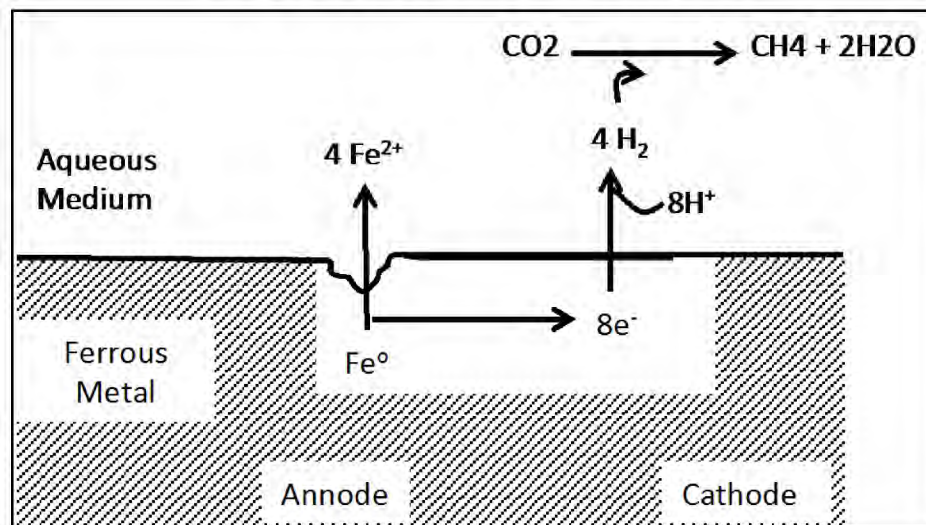
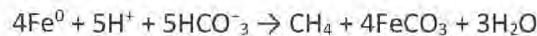


Figure 4: Model of Hydrogenotrophic Methanogen Mediated Metal Corrosion [6] [25]

The capacity for MIC is not a general feature of all methanogens, just like MIC is also not a general feature of all sulfidogens. MIC is an active process, requiring additional genes [27]. In the case of MIC causing *Methanococcus maripaludis* strain OS7, MIC-deficient derivatives were created, and the genes responsible for MIC identified. The MIC-associated genes encode extracellular hydrogenases capable of zerovalent iron oxidation (Figure 5).

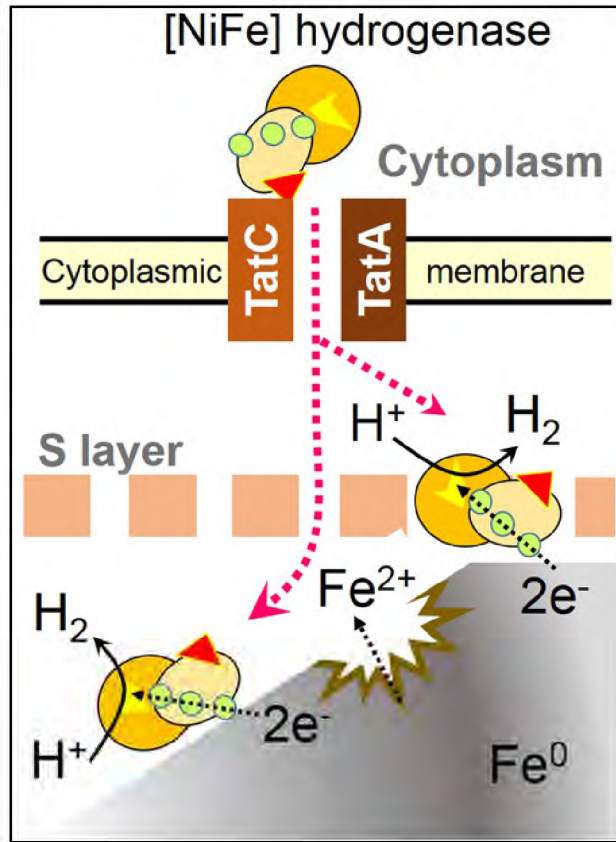


Figure 5: Diagram of Extracellular Hydrogenases Responsible for Fe Oxidation [27]

Over the past decade, increasing evidence has mounted for a direct role of Methanogens in O&G system MIC [28]. Historically, MIC in oil and gas operations has been considered primarily from the standpoint of SRB activity (reviewed in [29]). The correlation between SRB and corrosion is very robust and well supported by experimental evidence. Additionally, compared to other groups of anaerobic organisms, it is relatively easy to screen for SRB by culture-based approaches, genetic assays, as well as various biochemical and immunological tests. In contrast, methanogens have presented more of a challenge to detect and document. To complicate the relationship between methanogens and corrosion, there are also reports that describe a role of methanogens in the formation of corrosion-protective biofilms [30]. While data on all methanogens is not available, evidence indicates that at least some methanogens participate in MIC.

## Appendix C Methods

---

### C.1 Microbial Population Analysis Methods for Project 170721

The microbial population of each sample was analyzed by each of the three following methods, each of which provides a different perspective:

1. MPN analysis following NACE corrosion industry standard methods is used to quantify viable and culturable bacteria able to grow in five different growth media preparations. It has the following qualities:
  - Quantifies cells/ml of SRB, IRB, NRB, APB, and GHB
  - Dependent on bacteria being alive and able to grow in the media
  - Viable cell count assay
2. qPCR analysis is a DNA-based analysis that quantifies total microbes in a sample. It has the following qualities:
  - Quantifies cells/ml of all microbes in a sample
  - Does not distinguish between living and dead cells
  - Does not give information on types of cells
  - Total cell count assay
3. Amplicon metagenomics provides information on the types and relative abundance of bacteria and archaea in a sample. It has the following qualities:
  - Provides a list of all bacteria in the sample
  - Does not distinguish between live and dead cells
  - Does not provide cells/ml quantification
  - Provides relative abundance
  - Very detailed
  - Is not dependent on growth in media
  - Population structure assay

### C.2 MPN Analysis

MPN analysis is carried out by serially diluting 1 mL of sample eightfold in selective media. Selective media used for this project were Modified Postgate's B Broth (MPB) for the growth of Sulfate-Reducing Bacteria, Phenol Dextrose Red Broth (PRD) for the enumeration of acid-producing bacteria, Iron-Reducing Broth (IRB) for the enumeration of iron-reducing bacteria, and Nitrogen-Reducing Broth (NRB) for the enumeration of nitrogen-reducing bacteria. Dilutions were carried out in triplicate. All medias were at 2.5% salinity. Incubations were conducted at 30°C. Growth was assayed every 7 days, for a total of 28 days. Growth was compared to the FDA Bacterial Analytical Manual to determine the most probable number. It should be noted that the MPN is an estimate of growth units or colony-forming units and not individual bacterial cells.

### C.3 Primers for qPCR and Amplicon Metagenomics

For microbial analysis, DNA was subject to qPCR and/or amplicon metagenomic analysis using any combination of the following primer pairs:

- Universal 16S Primers (detects Bacteria and Archaea)
- 515F-GTGCCAGCMGCCGCGGTAA and 806R-GGACTACHVGGGTWTCTAAT
- Archaeal Primers (detects Archaea but not Bacteria)
- Arch517F-GCYTAAAGSRNCCGTAGC and Arch909R TTTCAGYCTTGCGRCCGTAC
- Euk 18S Primers (detects Eukaryotes, including Fungi)
- Euk1391F GTACACACCGCCCGTC EukBR TGATCCTTCTGCAGGTTACCTAC

### C.4 Quantitative PCR (qPCR)

qPCR reactions are performed as such: DNA was run on the Roche Light Cycler 480 (LC480; Roche Life Sciences) for quantitative real-time PCR (qPCR). Roche LC480 master mix (Roche Life Sciences) was used with each of the specific primers and probes (TACAAGGCCCGGAACGTATTCACCG) in a 10ul reaction and the following cycling conditions: 1 cycle of 50°C for 2 minutes, 1 cycle of 95°C for 10 minutes, followed by 35 cycles of 95°C for 15 seconds, 60°C for 1 minute, and a final cycle at 40°C for 30 seconds. Results of qPCR were scored based on cycle threshold (CT) score. The CT is the first cycle at which a reading above background is detected. A positive result was recorded if the CT was  $\leq 30$  cycles, negative if  $CT > 30$  cycles).

### C.5 Amplicon Metagenomics

#### C.5.1 Ion Torrent Sequencing

Samples were amplified for semi-conductor sequencing using a forward and reverse fusion primer. The forward primer was constructed with (5'-3') the Ion A linker (CCATCTCATCCCTGCGTGTCTCCGACTCAG), an 8–10bp barcode, and the 515F primer (GTGCCAGCMGCCGCGGTAA). The reverse fusion primer was constructed with (5'-3') a biotin molecule, the Ion P5 linker (CCTCTCTATGGGAGTCGGTGAT), and the 806R primer (GGACTACHVGGGTWTCTAAT). Amplifications were performed in 25ul reactions with Qiagen HotStar Taq master mix (Qiagen Inc, Valencia, California), 1ul of each 5uM primer, and 1ul of template. Samples were amplified on ABI Veriti thermocyclers (Applied Biosystems, Carlsbad, California) under the following thermal profile: 95°C for 5 minutes, then 35 cycles of 94°C for 30 seconds, 54°C for 40 seconds, 72°C for 1 minute, followed by one cycle of 72°C for 10 minutes and 4°C hold.

Amplification products were visualized with eGels (Life Technologies, Grand Island, New York). Products were then pooled equimolar and each pool was size selected using Agencourt AMPure XP (BeckmanCoulter, Indianapolis, Indiana) following Life Technologies protocols (Life Technologies, Grand Island, New York). Size selected pools were quantified using a Qubit 2.0 fluorometer and the Qubit High Sense kit (Life Technologies, Grand Island, New York), then diluted to 23pM. Diluted pools were emPCR'd and enriched using the OneTouch2 system and sequenced using the Ion Torrent PGM following manufacturer protocols (Life Technologies, Grand Island, New York).

### C.5.2 Illumina Two-Step MiSeq Sequencing.

Samples were amplified for sequencing in a two-step process. The forward primer was constructed with (5'-3'), the Illumina i5 sequencing primer (TCGTCGGCAGCGTCAGATGTGTATAAGAGACAG), and the indicated forward primer. The reverse primer was constructed with (5'-3'), the Illumina i7 sequencing primer (GTCTCGTGGGCTCGGAGATGTGTATAAGAGACAG), and the indicated reverse primer. Amplifications were performed in 25ul reactions with Qiagen HotStar Taq master mix (Qiagen Inc, Valencia, California), 1ul of each 5uM primer, and 1ul of template. Reactions were performed on ABI Veriti thermocyclers (Applied Biosystems, Carlsbad, California) under the following thermal profile: 95°C for 5 minutes, then 35 cycles of 94°C for 30 seconds, 54°C for 40 seconds, 72°C for 1 minute, followed by one cycle of 72°C for 10 minutes and 4°C hold.

Products from the first stage amplification were added to a second PCR based on qualitatively determined concentrations. Primers for the second PCR were designed based on the Illumina Nextera PCR primers as follows: Forward - AATGATACGGCACCACCGAGATCTACAC[i5index]TCGTCGGCAGCGTC and Reverse - CAAGCAGAAGACGGCATACGAGAT[i7index]GTCTCGTGGGCTCGG. The second stage amplification was run the same as the first stage except for 10 cycles.

Amplification products were visualized with eGels (Life Technologies, Grand Island, New York). Products were then pooled equimolar, and each pool was size selected in two rounds using SPRIselect (BeckmanCoulter, Indianapolis, Indiana) in a 0.7 ratio for both rounds. Size selected pools were then run on a Fragment Analyzer (Advanced Analytical, Ankeny, Iowa) to assess the size distribution, quantified using the Qubit 3.0 fluorometer (Life Technologies), and loaded on an Illumina MiSeq (Illumina, Inc. San Diego, California) 2x300 flow cell at 10pM and sequenced.

## C.6 Notes on Taxonomic and Metabolic Assignment

Organisms are referred to by the identity of the most closely matched organism in the database. However, this does not indicate 100% identity. In most cases, the most closely matched organisms are referred to as “uncultured organisms” and as such there is no physiological or metabolic information for them. Organisms that fall below the cutoff for taxonomic assignment at the genus level are listed as unclassified. Due to the unusual source of samples, a large number of organisms in the samples may be unclassified. This indicates that they are novel organisms that have not been described in the scientific literature.

Metabolic assignments are inferred by the metabolic characteristics of the most closely related organism for which experimental data has been provided. Some metabolic groupings are overlapping and non-exclusive, e.g. many fermentative organisms generate organic acids or are capable of sulfidogenesis under some conditions. An overview of select metabolism is provided in Appendix D.



## Appendix D Overview of Select Metabolic Processes

---

### D.1 APB: Acid-Producing Bacteria

Acid-producing bacteria are of specific interest to the oilfield community as acid production directly and aggressively promotes corrosion. Several metabolic pathways result in the production of acids, including fermentation pathways that generate organic acids such as lactic acid and acetic acid, as well as those that generate inorganic acids such as sulfuric acid as a byproduct of the oxidation of inorganic sulfur compound. Note that not all fermentative pathways that yield acid as a byproduct result in acidification of the surrounding environment. The identification of bacteria as acid-producing does not necessarily indicate acidification of bulk fluids.

### D.2 Biodeg: Biodegradation

Some bacterial genera and species have the capacity to utilize “atypical” or “unusual” substrates as carbon sources. These bacteria are loosely referred to as Biodeg, for “Biodegradation”. The definition used here for “atypical or unusual substrates” with reference to bacterial metabolism includes compounds that most bacteria cannot utilize as a food source. Unusual compounds Biodeg organisms utilize include disinfectants, antibiotics, xenobiotics, and detergents. Some degrade long chain polymers of sugars and carbohydrates, such as those found in cell wall materials. Others are able to degrade hydrocarbons. Hydrocarbons, including alkanes, alkenes, aromatic hydrocarbons, and waxes, are found naturally in great variety in crude oil and other petroleum compounds. Due to their structural diversity, most bacteria lack the capacity to utilize petroleum hydrocarbons as food sources. Each type of hydrocarbon-degrading microorganism is likely to be capable of metabolizing a few specific types of hydrocarbons.

### D.3 IRB: Iron-Reducing Bacteria

Some microbes can use Fe(III) as an electron acceptor, reducing it to Fe(II). Iron reduction has been observed under both acidophilic and neutrophilic conditions. Two common iron-reducing genera are *Shewanella* and *Geobacter* [31] [32]. Many IRB, such as isolates of the genus *Desulfuromonas*, are also sulfidogens. IRB should not be confused with iron oxidizing bacteria, which are aerobes responsible for a rust brown staining and slimy growth in surface waters.

### D.4 NRB: Nitrate Reducing Bacteria

NRB reduce nitrates to nitrites, nitrous oxide, or nitrogen under anaerobic conditions in a process termed denitrification. Most are heterotrophic facultative anaerobic bacteria including such common bacteria as *Paracoccus*, *Pseudomonas*, *Alcaligenes*, and *Bradyrhizobium*. A few bacteria use such reduction processes as hydrogen acceptor reactions and hence as a source of energy; in this case, the end product is ammonia. Denitrification is a normal part of nitrogen cycling, and not all NRB are of concern to O&G infrastructure. A subcategory of NRB is the Nitrate-Reducing Sulfur-Oxidizing Bacteria (NRSOB). NRSOB are a specific subgroup of NRB whose levels are increased in reservoirs following nitrate injections [33] [34]. Growth of NRSOB suppresses the activity of SRB, and thus reducing sulfidogenesis. Some Epsilonproteobacteria can also oxidize petroleum sulfur compounds and utilize nitrate as an electron acceptor for growth, and thus may be considered hydrocarbon degrading. Massive dominance of related Epsilonproteobacteria has been observed in other petroleum samples, for example in formation waters

from a Canadian oil sands reservoir containing severely biodegraded oil [35] [21]. *Sulfurospirillum* are nitrate-reducing, sulfur oxidizing bacteria (NRSOB) members of the class Epsilonproteobacteria and are sometimes referred to as “*Campylobacter*” in older publications. The way in which nitrate addition can affect the SRB population involves several pathways. First, nitrate is a thermodynamically more favorable electron acceptor than sulfate, thus NRB have a competitive advantage. To emphasize the complexity of the metabolism in oilfield samples, it should be noted that under some conditions, these bacteria are also sulfidogens capable of reducing sulfur and thus producing H<sub>2</sub>S [36].

## D.5 Sulfidogenesis: (e.g. SRB, TRB, SuRB)

The metabolic pathways of most historical interest to the oilfield community are sulfidogenic pathways that generate significant levels of hydrogen sulfide (H<sub>2</sub>S). Bacteria that evolve hydrogen sulfide are commonly referred to as “sulfidogens”. Sulfate-reducing bacteria (SRB) are particularly aggressive at sulfide production and are the group of bacteria most commonly implicated in oil field biogenic sulfide production [4]. Hydrogen sulfide formation by sulfate-reducing bacteria (SRB) under strict anaerobic circumstances is a common problem in sediments, sewer systems, oil reservoirs, and anaerobic effluents (reviewed in [37]). The emission of H<sub>2</sub>S into the atmosphere of sewer systems implies odor nuisances and possible health risks. Sulfide can also be converted into sulfuric acid in the aerobic zones, causing severe corrosion of the inner surface of concrete sewer structures [38] [39]. Hence, preventive or curative actions are needed.

While SRB are traditionally associated with O&G system sulfide generation, sulfur- and thiosulfate-reducing bacteria (SuRB and TRB, respectively) can also generate significant levels of H<sub>2</sub>S and contribute to corrosion and souring [40] [41] [42]. Compared to SRB, the TRB are harder to classify taxonomically, as they are members of bacterial genera that can include non-tSRB members. Examples of sulfidogenic TRB commonly found in oilfield samples include *Halanaerobium congolense*, as well as some *Thermoanaerobacter*, and *Spirochaeta*. Additionally, many common enteric bacteria are sulfidogenic, including *Citrobacter* and *Salmonella* [43].

## D.6 Thermophiles

A thermophile is an organism that can survive and often thrives in environments having relatively high temperatures, usually ranging between 45 and 122°C.

# SS-25 RCA Supplementary Report

# SS-25 7 in. Casing Internal Corrosion Assessment



2600 Network Boulevard, Suite 550  
Frisco, Texas 75034

+1 972-712-8407 (phone)  
+1 972-712-8408 (fax)

16285 Park Ten Place, Suite 600  
Houston, Texas 77084

1-800-319-2940 (toll free)  
+1 281-206-2000 (phone)  
+1 281-206-2005 (fax)

[www.blade-energy.com](http://www.blade-energy.com)

## Purpose:

Analyze the internal corrosion rates due to injection/withdrawal gas environments for the SS-25 7 in. production casing.

## Date:

May 31, 2019

Blade Energy Partners Limited, and its affiliates ('Blade') provide our services subject to our General Terms and Conditions ('GTC') in effect at time of service, unless a GTC provision is expressly superseded in a separate agreement made with Blade. Blade's work product is based on information sources which we believe to be reliable, including information that was publicly available and that was provided by our client; but Blade does not guarantee the accuracy or completeness of the information provided. All statements are the opinions of Blade based on generally-accepted and reasonable practices in the industry. Our clients remain fully responsible for all clients' decisions, actions and omissions, whether based upon Blade's work product or not; and Blade's liability solely extends to the cost of its work product.

## Abstract

The gas storage well Standard Sesnon 25 (SS-25) in the Aliso Canyon Gas Storage Field located in Los Angeles County, California started leaking gas in October 2015. A relief well was drilled, and SS-25 was brought under control. The leak stopped in February 2016.

In January 2016, as part of their investigation of the leak, the California Public Utilities Commission (CPUC) and the Division of Oil, Gas, and Geothermal Resources (DOGGR) selected and gave provisional authority to Blade Energy Partners (Blade) to perform an independent Root Cause Analysis (RCA). The Blade Team and parties under Blade's direction were responsible for directing the work of subcontractors who performed the extraction of the SS-25's wellhead, tubing, and casings and the preservation and protection of associated evidence. Blade's RCA Reports, including this report, document and describe the key activities undertaken in support of the RCA effort.

In February 2016, a study was undertaken to assess the corrosion that might have occurred on the inner surface of the 7 in. production casing during the time the SS-25 well served as a gas storage well. It was clear that the dry pipeline gas injected for storage could not have contributed to corrosion. However, during the withdrawal process, the gas would have carried some water which could have condensed and resulted in corrosion. It was also established that the cumulative time the well served as a gas producer was minimal.

Estimating the corrosion rate in the traditional way from the gas composition, temperature, and pressure led to unrealistically high corrosion rates. Several alternate models were developed based on the water content in the produced gas, the temperature-pressure profile during production, and a description of the environmental chemistry prevailing in the production conduits during gas flow. Using corrosion modeling, the results of a caliper run, and finally a laser scan study on the internal surface of the 7 in. production casing, it was demonstrated that all results converged on the conclusion that the internal corrosion of the 7 in. production casing was too low to have contributed to the 7 in. casing failure.

## Table of Contents

<b>1</b>	<b>Introduction.....</b>	<b>4</b>
1.1	Abbreviations and Acronyms .....	5
<b>2</b>	<b>SS-25 Operating History Overview .....</b>	<b>6</b>
2.1	Water Production History.....	6
2.2	Nature of the Production .....	8
<b>3</b>	<b>Assessment of Corrosion Rates .....</b>	<b>11</b>
3.1	Traditional Corrosion Rate Modeling.....	11
3.2	Non-Traditional Corrosion Rate Modeling .....	12
<b>4</b>	<b>Corrosion Rate Assessment Summary .....</b>	<b>19</b>
<b>5</b>	<b>Inside Diameter Laser Scan Results .....</b>	<b>21</b>
5.1	Laser Scans Results Overview.....	21
5.2	Laser Scan Results Summary .....	22
<b>6</b>	<b>References.....</b>	<b>23</b>
Appendix A	<b>Evaluation of the Laser Scan Data .....</b>	<b>A-1</b>

## List of Figures

Figure 1:	SS-25 Production—Historical Water Cut.....	6
Figure 2:	SS-25 Production—Historical Water Cut (Expanded Scale).....	7
Figure 3:	SS-25 and SS-9 Water Cut Comparison, 2011–2015.....	8
Figure 4:	SS-25 Production—Oil/Water Ratio .....	9
Figure 5:	Traditional Corrosion Rate Model Results.....	12
Figure 6:	COPRA Correlation Corrosion Model Basis.....	13
Figure 7:	SS-25 Production Dew Point Profile .....	14
Figure 8:	Iso-Corrosion-Rates Contour Model.....	15
Figure 9:	Iso-Corrosion-Rate Contour Model with Iron Carbonate .....	16
Figure 10:	Frequency Distribution of Maximum Corrosion Feature Penetration on Pipe Body .....	A-3
Figure 11:	Frequency Distribution of Average Corrosion Feature Penetration on Pipe Body .....	A-4
Figure 12:	Frequency Distribution of Maximum Corrosion Feature Penetration on Connection Body.....	A-5
Figure 13:	Frequency Distribution of Average Corrosion Feature Penetration on Connection Body .....	A-6
Figure 14:	Probability Distribution of Pit Depth for Pipe and Connection Bodies.....	A-7
Figure 15:	Probability Distribution of Average Corrosion on Pipe Body .....	A-8
Figure 16:	Comparison of Maximum Feature Penetrations on Pipe Body for Each Pipe Segment.....	A-9
Figure 17:	Comparison of Average Feature Penetration on Pipe Body for Each Pipe Segment .....	A-10
Figure 18:	Comparison of Maximum Feature Penetration on Connection Body for Each Pipe Segment .	A-11
Figure 19:	Comparison of Average Feature Penetration on Connection Body for Each Pipe Segment ....	A-12



## List of Tables

Table 1: Reservoir Gas Analysis Results (values in mol%) .....	9
Table 2: Corrosion Rate Estimate Based on Iron Counts .....	17
Table 3: Summary Statistics of Laser Scan on 7 in. Casing Inside Diameter .....	22

# 1 Introduction

---

The purpose of this report is to document the study that Blade conducted to understand and estimate the potential cumulative metal loss that could have occurred through internal corrosion in the SS-25 well during its life of serving as an injection and withdrawal well from 1977 to 2015.

Key considerations:

1. The injected gas was pipeline gas (i.e., dry) and containing less than 2 mol% CO<sub>2</sub>, which is the upper limit for pipeline quality gas.
2. Originally, the reservoir drive mechanism was pressure depletion and not water drive. It can be expected that, eventually, the return gas would be less than saturated in water under downhole conditions.
3. As a consequence, no matter what the production conditions were, the water content in the gas would have been very small.
4. Corrosion cannot occur during injection because pipeline quality gas is dry. Therefore, whatever corrosion might have occurred would have been during times of withdrawal, and it would have been intermittent. The record shows that over the 38 years the well served as gas storage well, the cumulative time the well was used for withdrawal was 1,468 days or 4.02 years.
5. Blade's interpretation of the water production records shows that the water production was less than a few bbl/MMscf, which is also consistent with a pressure depletion reservoir.
6. From a corrosion perspective, water production is important, because:
  - Corrosion rate assessments are usually made for systems with a small metal surface and a comparatively large and moving (replenishing) liquid reservoir. Therefore, the water composition is not subject to change in space and time.
  - In a well where a thin water film is flowing upwards with the gas flow, as would be the case for SS-25, the composition of the water will change in space and time, depending upon the flow rate of the gas, and the flow regime in particular. This is the condition that needs to be analyzed to assess the potential for the 7 in. casing to have undergone corrosion during the time it served as a gas storage well.

The corrosion assessment was done by:

- Using the classical corrosion approach.
- Assessing the phase behavior in the production string (tubing and casing) and the flow regime, using the production data to identify the water content in the produced gas.
- Using the corrosion rate based on iron counts approach (COPRA Correlation) which considers buffered condensed water.

## 1.1 Abbreviations and Acronyms

Term	Definition
bbbl	Barrel
BHT	Bottomhole Temperature
Blade	Blade Energy Partners
CPUC	California Public Utilities Commission
DOGGR	Division of Oil, Gas, and Geothermal Resources
ID	Internal Diameter
mil	One Thousandth of an Inch
MMscf	Million Standard Cubic Feet
MMscf/D	Million Standard Cubic Feet per Day
mpy	Mils per Year
OD	Outside Diameter
ppm	Parts Per Million
psi	Pounds per Square Inch
RCA	Root Cause Analysis
SS	Standard Sesnon
TDS	Total Dissolved Solids



## 2 SS-25 Operating History Overview

SS-25 was completed as a gas storage well in the Aliso Canyon field in 1973. Injection and withdrawal continued off and on through 2015. During this time, the well was used mainly for injection, and was used for gas withdrawal for a cumulative total of 4.02 years, or about 10.6% of the time. This means that whatever internal corrosion rate that might be predicted, it would have been cumulatively operative, for only a little over four years over this period of time. The average gas production rate was approximately 20.5 MMscf/D during this time.

### 2.1 Water Production History

Figure 1 shows all recorded data concerning water production in terms of water cut (bbl water/MMscf gas). The data were based on cumulative monthly production volumes. This, however, does not mean that the well was producing gas back for the entire month. Rather, production times varied randomly during each month from a few days to as much as 25 days.

There are two distinct periods of withdrawal operations recognizable. From 1977 to 1997 the water cut was almost consistently above saturation of 0.57 bbl/MMscf, and the ten-day moving average seems to indicate gradually increasing water production. Then in early 1997, the water cut fell below 1 bbl/MMscf. The reason for this abrupt change is unclear.

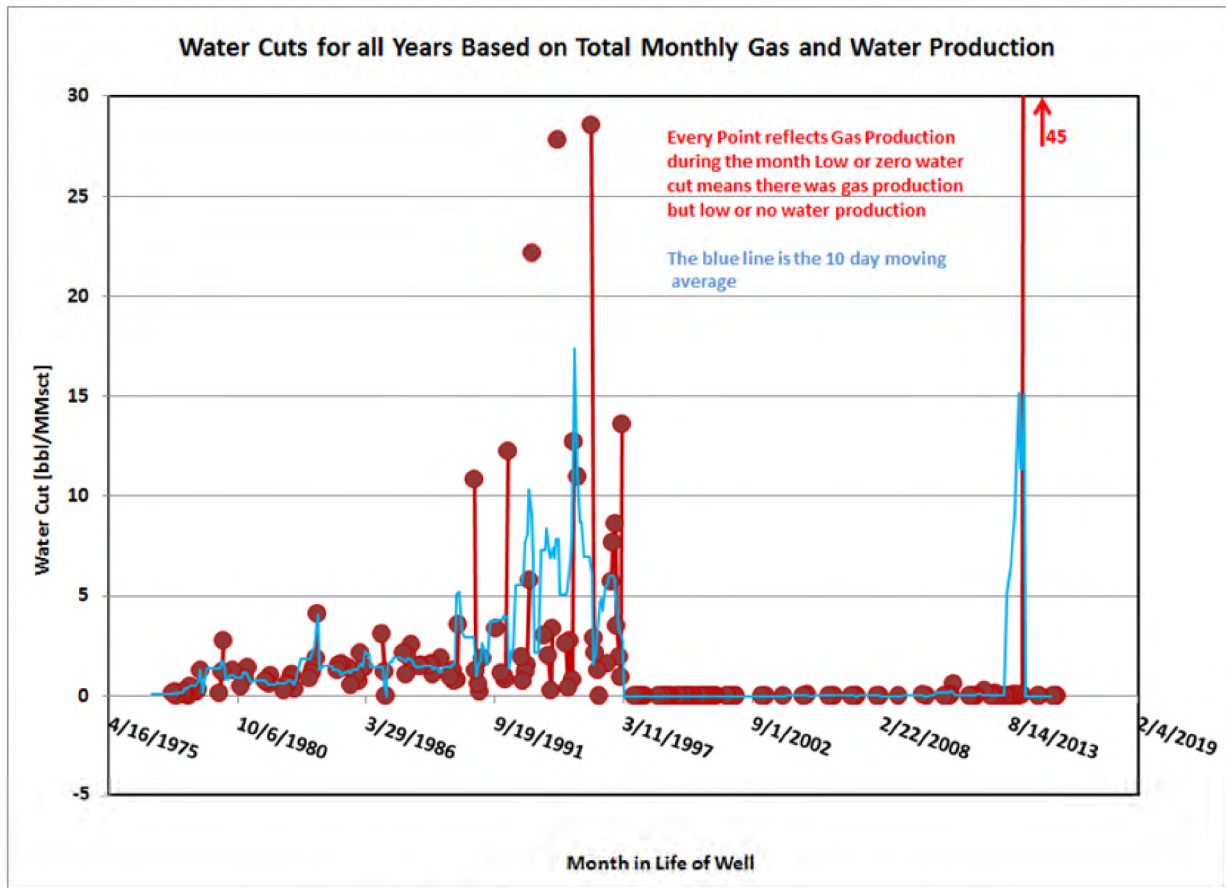


Figure 1: SS-25 Production—Historical Water Cut

Figure 2 shows the same data on an expanded vertical scale in order to highlight the water cut differences before and after 1997.

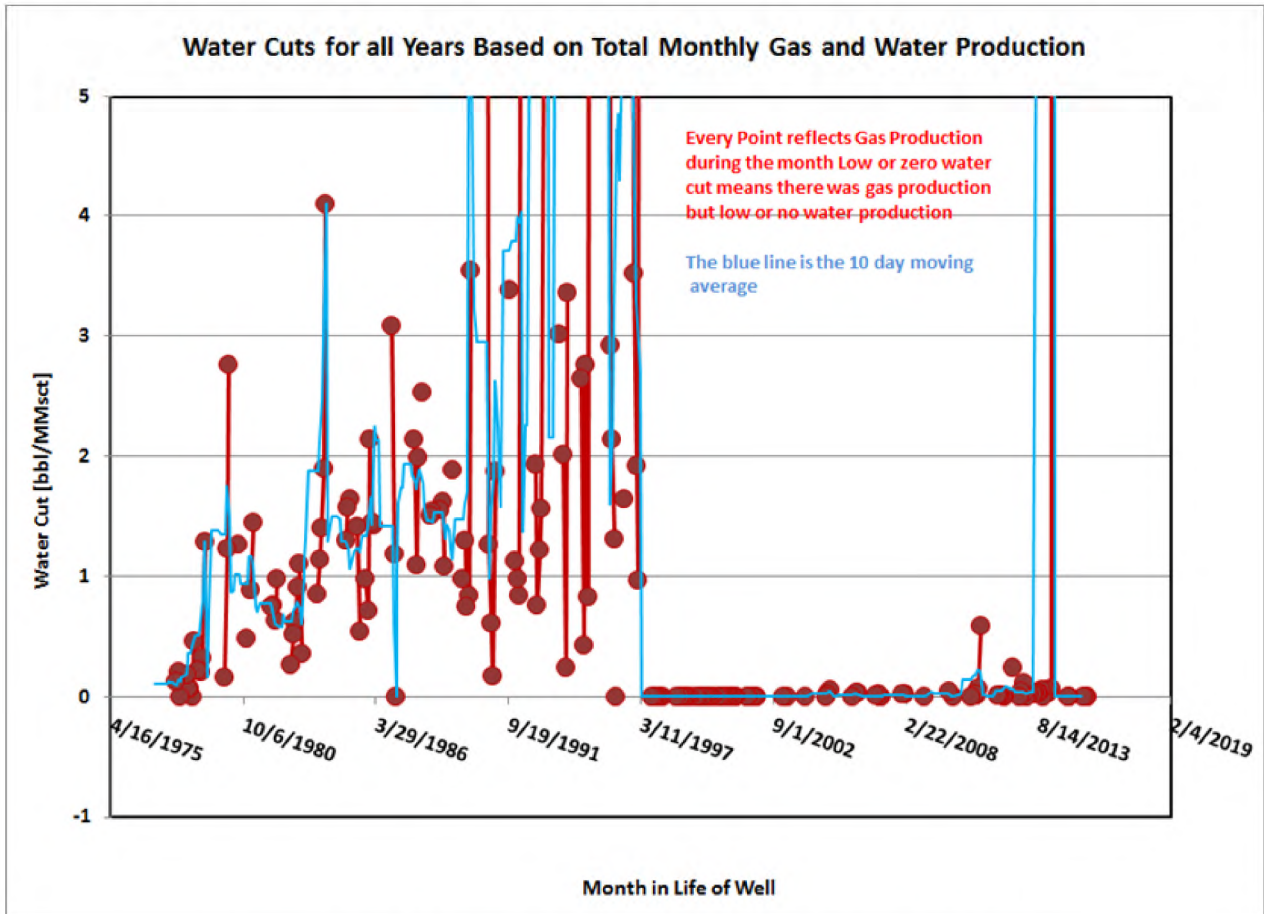


Figure 2: SS-25 Production—Historical Water Cut (Expanded Scale)

Figure 3 shows details of the water cut data for the most recent withdrawal from 2011 to mid-2015 for SS-25 and SS-9. With two exceptions, the water cut for both wells is below 0.1 bbl/MMscf, as measured in the separator. Even accounting for the water content carried out with the gas, the saturation level of 0.57 bbl/MMscf is not reached. Therefore, it can be concluded that, except for occasional well intervention procedures, the produced gas is totally under-saturated under downhole conditions.

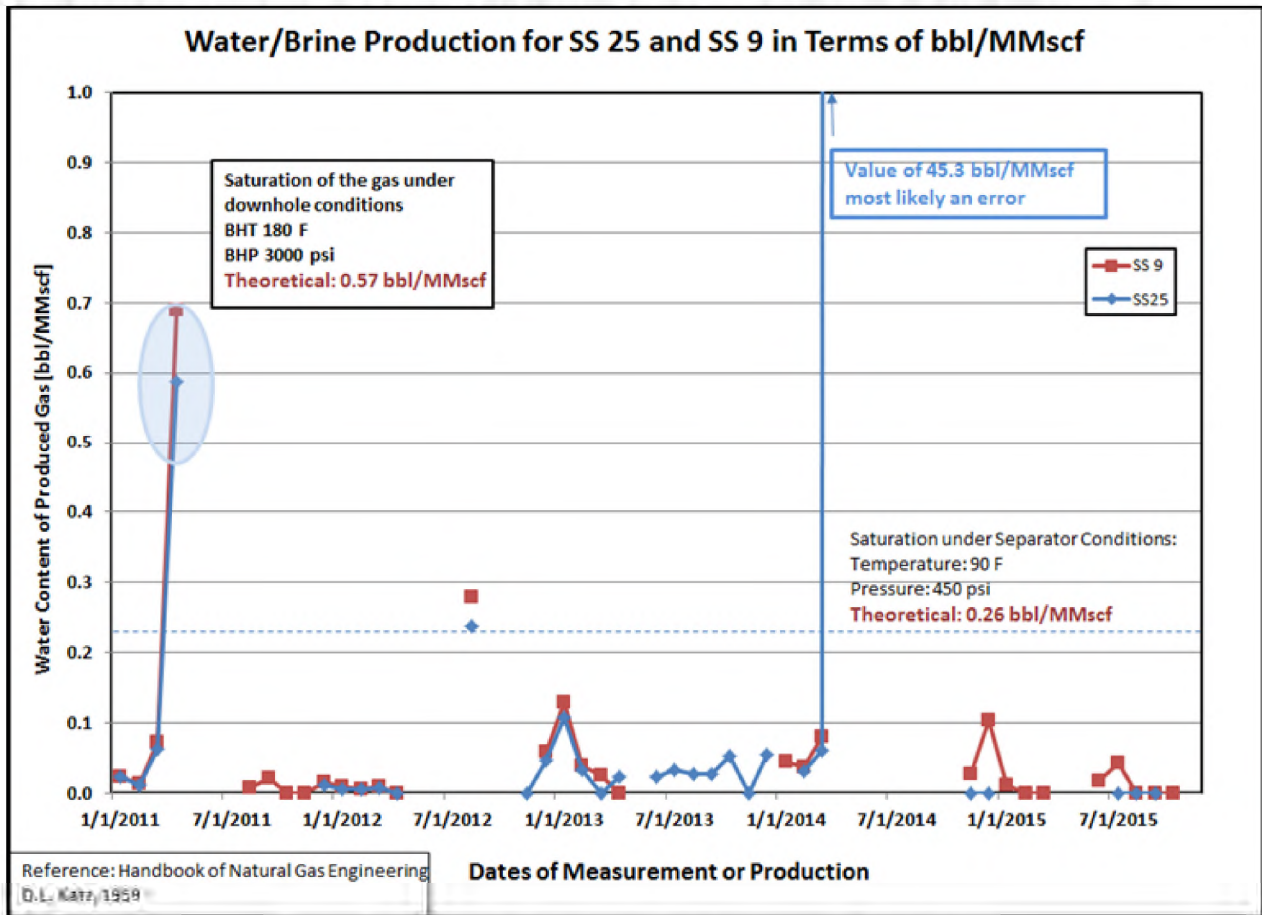


Figure 3: SS-25 and SS-9 Water Cut Comparison, 2011–2015

## 2.2 Nature of the Production

Even though the field is now used for gas storage, a small amount of oil is still produced during withdrawal. Figure 4 shows the SS-25 oil production data in terms of oil/water ratios for the entire 38-year period. On average, the oil production is twice the water production with some large variations. As a consequence, given the nature of this residual oil, corrosion in the production casing and tubing was very likely retarded through corrosion inhibition provided by the oil.

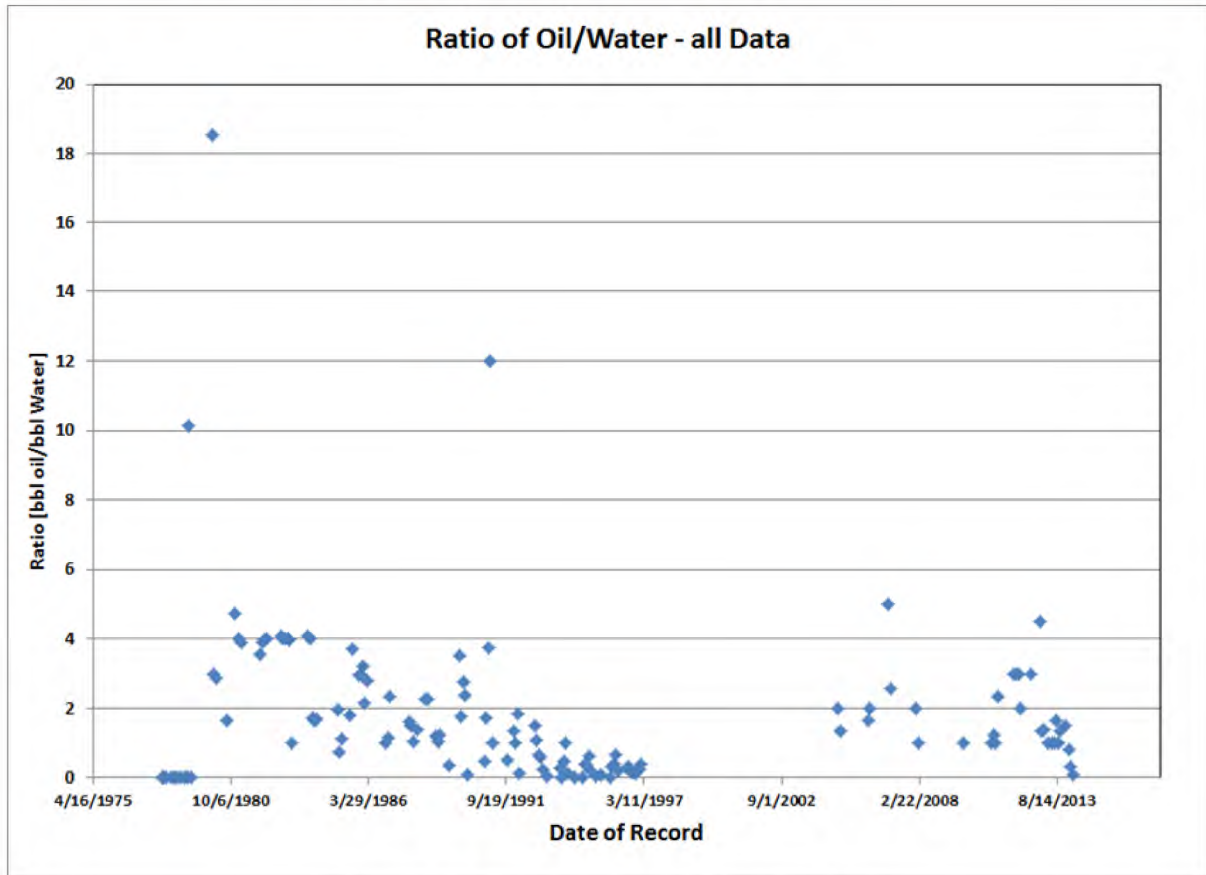


Figure 4: SS-25 Production—Oil/Water Ratio

Blade took several samples of the Sesnon reservoir gas from several different wells in February 2016. A compositional analysis was done on the gas samples to determine what influence the gas might have had on internal corrosion susceptibility. Table 1 shows the analysis results.

Table 1: Reservoir Gas Analysis Results (values in mol%)

Well Name	Number of Samples	Methane		Carbon Dioxide		Hydrogen Sulfide (ppm)		Other Hydrocarbons	
		Average	Standard Deviation	Average	Standard Deviation	Average	Standard Deviation	Average	Standard Deviation
P-47	3	94.9	0.012	0.99	0.0015	<0.05	0	3.78	0.008
P-69	3	94.7	0.042	0.73	0.0036	0.22	0.035	4.24	0.039
SS-25	3	94.8	0.017	0.94	0.0019	0.06	0	3.97	0.0131
SS-31	3	94.7	0.014	0.82	0.0036	0.22	0.046	4.25	0.17
SS-5	3	95.1	0	0.84	0.003	0.1	0	3.71	0.001
SS-9	3	94.8	0.026	0.81	0.0051	0.14	0.035	4.13	0.027
Average		94.833		0.855		0.148		4.013	
Standard Deviation		0.1505		0.0943		0.0716		0.2320	

## SS-25 7 in. Casing Internal Corrosion Assessment

---

The reservoir gas is made up of 99% hydrocarbons, of which 95% is methane. Carbon dioxide and hydrogen sulfide, which are involved with the majority of corrosion issues in downhole tubulars, are present in only very small quantities.

## 3 Assessment of Corrosion Rates

---

The composition of the produced gas for computational purposes was assumed to be 99 mol% methane, 1 mol% CO<sub>2</sub>, and 0.5 ppm H<sub>2</sub>S). The gas composition reflects the model input. Calculations were made with 55.5 mol water (1 liter). The amount of gas present together with the water for the calculations is such that:

- A gas phase exists under all conditions.
- There is enough gas present such that the overall composition is not measurably altered by the mixing with water under the chosen temperature and pressure condition(s).

The produced water is assumed to be fresh (i.e., condensed) water. The pH, with 50 psi CO<sub>2</sub> partial pressure (3.4 bar), was approximately 3.8 (varying somewhat with temperature).

OIL Studio software developed by OLI Systems; Inc. was used for the corrosion modelling.

### 3.1 Traditional Corrosion Rate Modeling

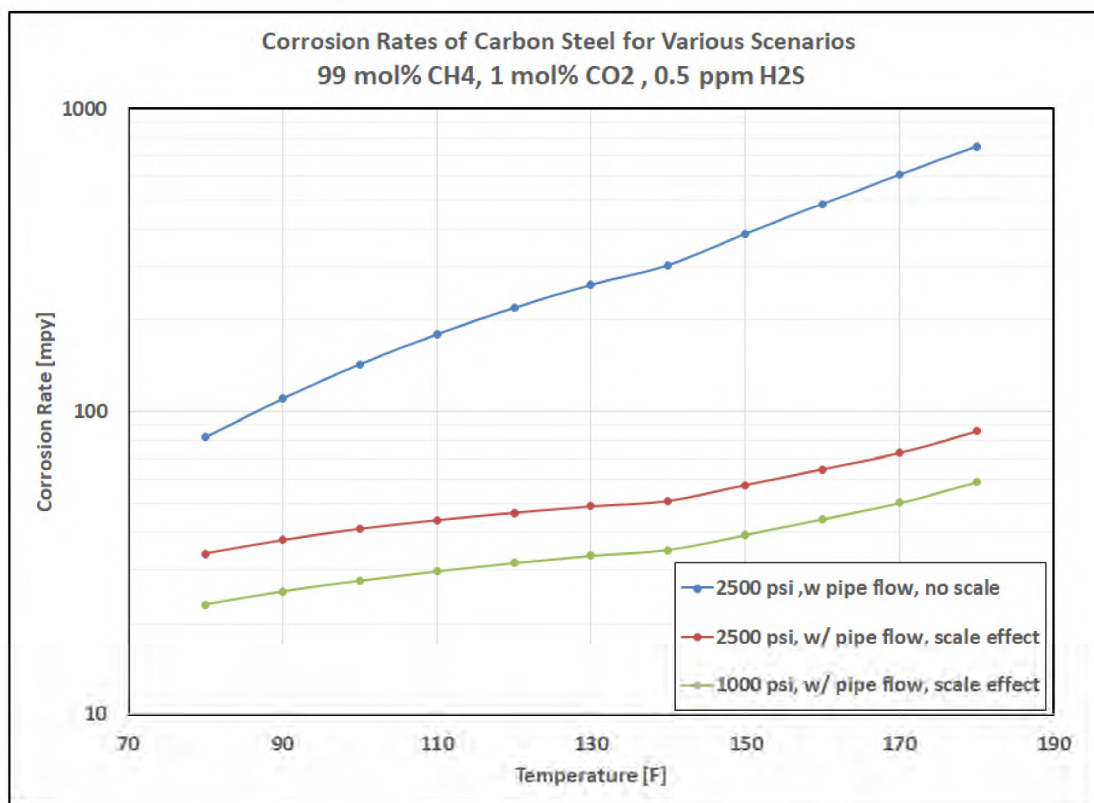
CO<sub>2</sub> corrosion usually entails the formation of a corrosion product layer consisting of siderite (FeCO<sub>3</sub>), unless the water volume is large enough and the pH is low enough that the siderite formation cannot occur. The OLI software contains a switch whereby scale formation can be excluded. Exclusion resulted in the highest corrosion rate—about 300 to 400 mpy at 140°F, which is a number that can be experimentally supported.

Figure 5 shows the temperature behavior of the corrosion rate for the three major effects:

- Corrosion in the presence and absence of scale formation
- The effect of pressure
- The effect of flow

A special feature of these calculations is that no bicarbonate was added for buffering the pH in the water.

If scale is allowed to form, the corrosion rate decreases by a factor of ten, and can be supported by experimental data where the effect depends on the liquid volume to surface area ratio.



**Figure 5: Traditional Corrosion Rate Model Results**

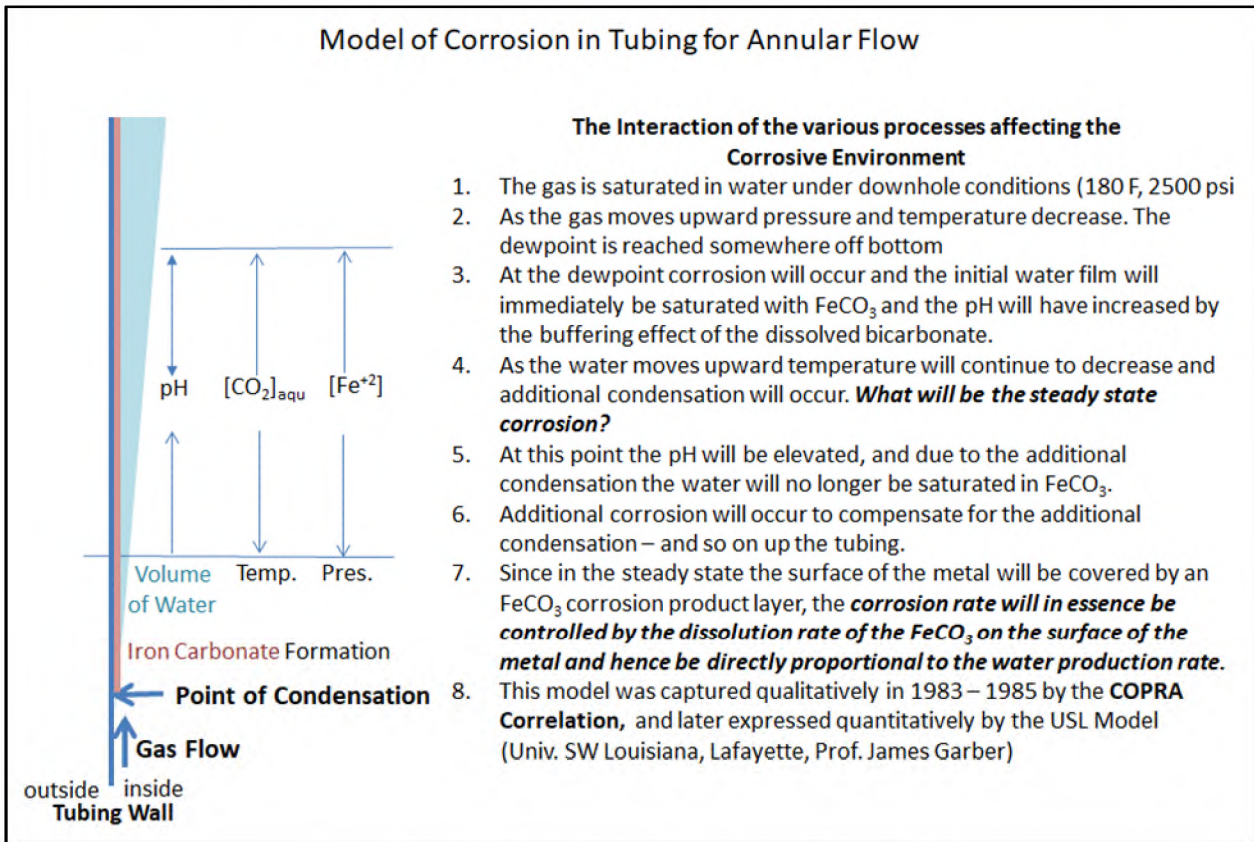
Furthermore, if the pressure were reduced to cut the CO<sub>2</sub> partial pressure in half, the corrosion rate responds by being reduced by 30 to 40%. The corrosion rates modeled by the OLI software may have occurred in SS-25 even when accounting for scale formation. This would result in a maximum cumulative corrosion loss downhole of over 200 mils, which would have destroyed the tubing and a significant portion of the casing.

Even at the 1,000 ft depth in the well, the corrosion rate (at 100°F) would likely have been 30 to 40 mpy, or enough to have resulted in serious damage over the four-year withdrawal time. This is not what was observed on the caliper and wall thickness logs run in the 7 in. casing, as well as subsequent laser scan of the casing ID.

The above calculations and conclusions assume that the aqueous volume to corroding surface area is large. Such a system reduces the rate of corrosion product build-up in the water and assures more or less constant corrosion kinetics which are relatively easily modeled. The system where the liquid to surface area ratio is reversed will be examined in following sections.

## 3.2 Non-Traditional Corrosion Rate Modeling

The classical approach to corrosion modeling as shown in Figure 5 did not result in corrosion rates which would maintain the integrity of the production tubing and casing for 40, or even 20 years. An alternate approach to corrosion modeling of gas wells was developed in the mid-1980s and called the COPRA Correlation [1] [2] [3] [4]. The COPRA correlation was based on the observation that the corrosion rate in gas producing tubulars, measured by means of iron counts, and the amount of brine produced, could be correlated with gas production rates. Figure 6 describes the COPRA correlation.



**Figure 6: COPRA Correlation Corrosion Model Basis**

Even though the COPRA Correlation is empirical, the underlying principle is that the corrosion rate could not be larger than the amount of iron removed from the entire surface, limited only by the solubility of iron carbonate.

Alternatively, it was also argued that because the formation of the protective iron carbonate scale was fast while the dissolution was slow (laboratory observations), the overall corrosion rate would be controlled by the dissolution rate of iron carbonate, the maximum possible iron carbonate concentration in solution, and the brine production rate.

### 3.2.1 Discussion of the Gas Phase behavior

Determining the corrosion rate using the principle of the COPRA Correlation also required an assessment of the wetted surface area. It was necessary to assess the dewpoint characteristic in the tubing and casing, and the production temperature-pressure profile.

Figure 7 shows dewpoint curves as a function of temperature and pressure. The two curves differ in the assumption of the downhole conditions (150°F and two pressures). Temperature-pressure characteristics are also inserted into this graph for four different production rates based on Blade's PROSPER production model. It turns out that the flowing bottomhole temperature (BHT) was consistently lower than the reported static BHT due to the Joule-Thomson effect at the face of the formation. Consequently, one must assume that the tubing was wet from the bottom to the surface.



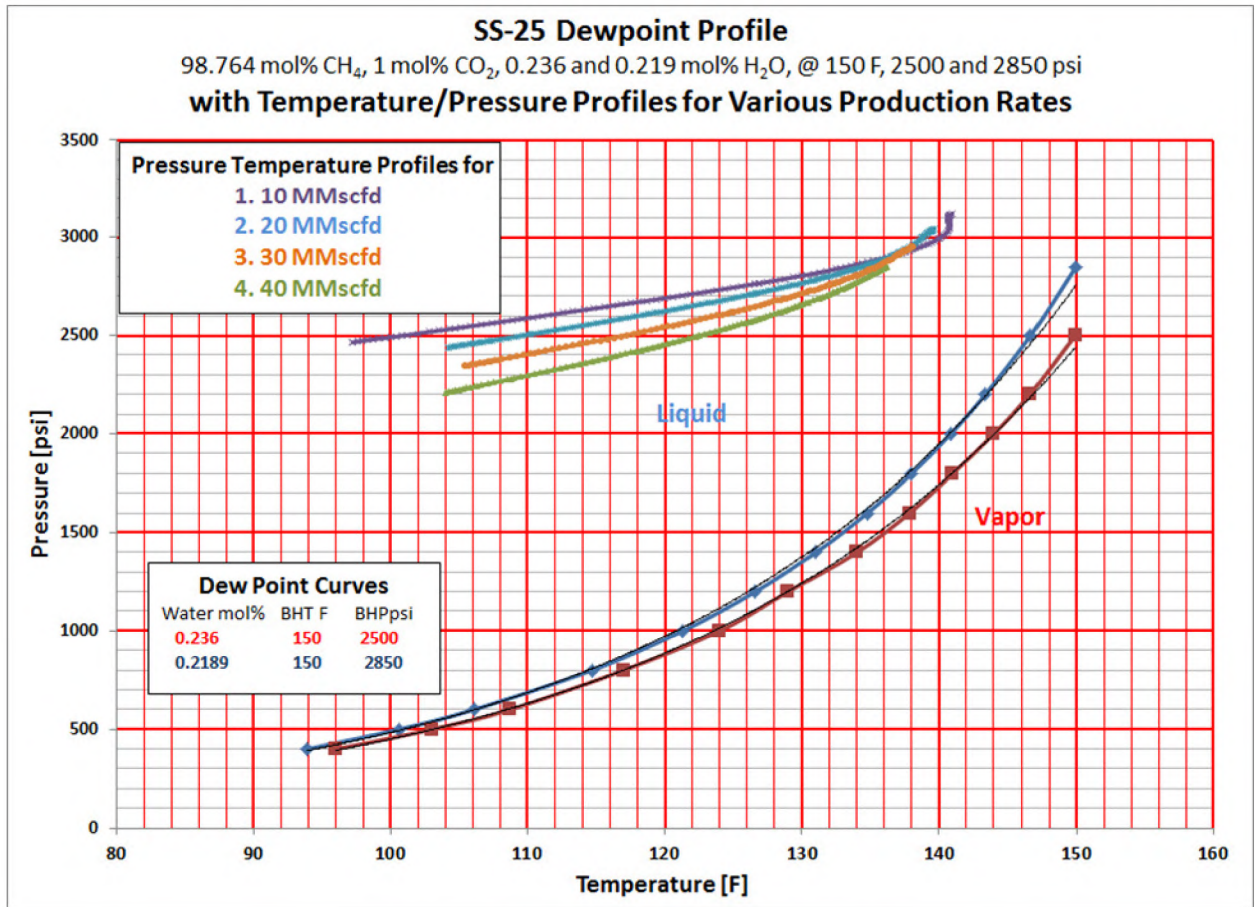
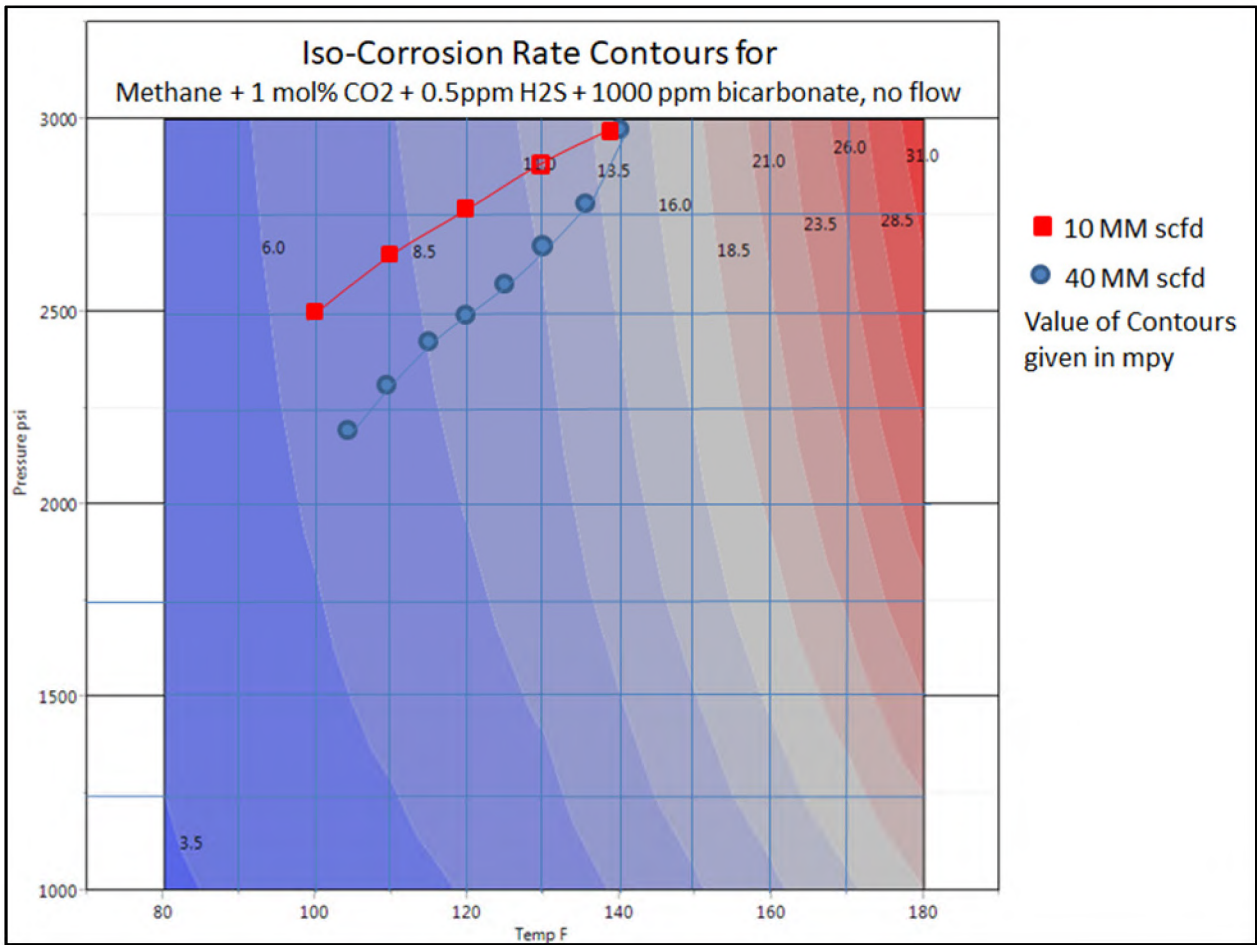


Figure 7: SS-25 Production Dew Point Profile

### 3.2.2 Corrosion Modeling

In order to illustrate the change of the corrosion rate along the tubing, the OLI software was used to generate corrosion rates within a grid of temperature and pressure. Subsequently, the results were used to generate a contour plot of Iso-Corrosion Rates as shown in Figure 8.

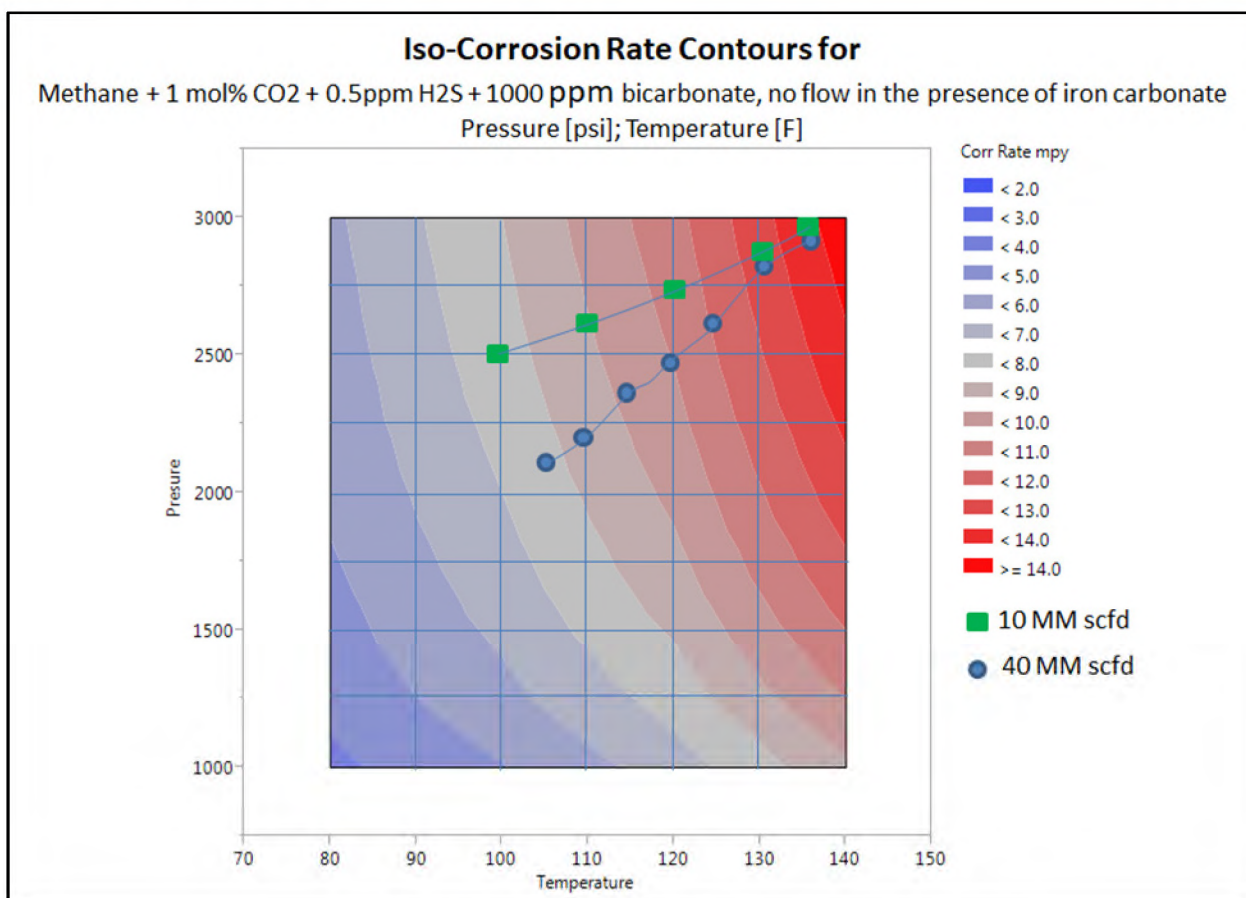


**Figure 8: Iso-Corrosion-Rates Contour Model**

This figure illustrates Iso-Corrosion Rate domains in the temperature-pressure grid applicable to SS-25 downhole conditions. The numbers in the graph are the corrosion rates within the specific contour areas. Superimposed are the temperature–pressure characteristics for two extreme production rates: 20 and 40 MMscf/D (Figure 7).

The results show that the gas flow rate has little effect on the corrosion rate. This may be because the higher flow rate is compensated for by the lower pressure which results in a higher water content in the flowing gas. What is important is the fact that these rates had been calculated with bicarbonate present in the condensed water. These data are justified because, as soon as CO<sub>2</sub> saturated condensed water touches the steel surface, the corrosion process generates the bicarbonate. At the point of condensation, only a very thin film of condensate exists. It becomes saturated in CO<sub>2</sub> immediately, and an iron carbonate film quickly forms at this location, thereby retarding the corrosion process. The observed corrosion rates are comparable to those observed in the laboratory [5].

Because of the importance attributed to the iron carbonate (the presence of iron ions in solution), the same calculations were repeated with some iron carbonate in the solution at the start. This modification had little effect on the overall results (Figure 9).



**Figure 9: Iso-Corrosion-Rate Contour Model with Iron Carbonate**

In summary, corrosion rate calculations were first made with bicarbonate present in the brine. This was done to account for the fact that the condensed water flowing up the 7 in. × 2 7/8 in. annulus during the production of gas becomes enriched with bicarbonate (a buffer) which increases the pH from about 3.8 to over 5. The results were shown as a function of pressure and temperature in Figure 8.

In order to show the corrosion rates along the casing, a hypothetical temperature-pressure gradient was inserted in the contour plot (Figure 9). The temperature-pressure gradient depends on the flow rate, which is why the results of these calculations only serve to illustrate orders of magnitude and trends. With respect to the magnitude, it is concluded that 1,000 ppm bicarbonate had not reduced the corrosion rate sufficiently to account for the low corrosion rates reflected in the caliper log and laser scan measurements.

However, if consideration is given to the fact that iron carbonate is formed in the corrosion process, and iron carbonate is added to the brine, the corrosion rates are further depressed, as was shown in Figure 9, to levels which begin to reflect what might have occurred inside the tubulars of SS-25. 12 mpy over four years of continuous service, or 48 mil total wall loss at the most corrosive locations is within the range of observed caliper data and the laser scan results.

### 3.2.3 Corrosion Rates Based on Iron Counts

Estimating corrosion rates based on iron counts assumes that the produced condensed water cannot take up more iron carbonate than its saturation value, which varies depending on temperature and pressure.

Table 2 shows the results assuming an over-saturation level of 1 bbl water/MMscf gas and daily production rates of 5, 12, 15, and 20 MMscf/D resulting in water production rates of 5, 12, 15 and 20 bbl/day. The total iron carry-out was calculated in terms of cubic-inches per day based on the total surface area of tubing and casing from where the iron may come from, and then converted to mpy. The corrosion rates for nominal SS-25 production rates of 5 and 12 MMscf/D varied from 0.092 to 0.221 mpy.

**Table 2: Corrosion Rate Estimate Based on Iron Counts**

Total Iron Contained in Produced (Condensed) Water				
Iron in Water:		150 ppm		
Water Production bbl/day	Water Production liters/day	Total Iron Produced (grams/day)	Total Iron Produced (cubic centimeters)	Total Iron Produced (cubic inches/day)
5	794.9	119.24	15.17	0.9257
12	1,907.8	286.18	36.41	2.2217
15	2,384.8	357.72	45.51	2.7771
20	3,179.7	476.96	60.68	3.7028
Total Wetted Surface Area Top to Bottom				
Total Depth	8,200 ft 2,499.36 meters	Total Area	25,480 square ft 3,669,090 square in.	
Tubing ID	2.5 in.			
Tubing OD	2.875 in.	<b>Corrosion Rate Calculation</b>		
Tubing Area ID	5,364.17 square ft	Iron lost per year:	0.092 mpy	
Tubing area OD	6,168.8 square ft		0.221 mpy	
Casing ID	6.5 in.		0.276 mpy	
Casing area ID	13,947 ft		0.368 mpy	
(1 cubic centimeter = 0.06124 cubic inches)				

There is a perceived difficulty with this approach. If it is presumed that the produced brine consisted of condensate water only (zero TDS), because the gas under downhole conditions is either saturated or under-saturated in water, then there must be a dewpoint at some location in the 7 in. x 2 7/8 in. annulus. At that point, there would not yet be any bicarbonate in the condensate. Because of this, the local corrosion rate would be high, and highly localized, but the amount of water at the point of condensation would be very low—a thin film at the most. Consequently, the point of saturation would be reached fast and a protective iron carbonate film would be established quickly as well. Subsequently, most of the water would condense on the way up the tubing as the temperature decreased. Hence, even though the corrosion rate at the point of condensation may be high, the total metal loss would remain very small.

An alternate scenario could occur when the gas flow rates are low and annular flow reverts to slug flow. At that point, the water would percolate up the tubing and the corrosion rate could be much higher. Even in this scenario, the basic idea would hold, which is that the cumulative metal loss would have been limited by the solubility of iron carbonate.

## SS-25 7 in. Casing Internal Corrosion Assessment

---

The caliper and wall thickness log results and the laser scan data showed no significant localized corrosion which substantiates these conclusions.

## 4 Corrosion Rate Assessment Summary

---

The present discussion focuses on the internal corrosion rates as they might have occurred during the life of the SS-25 well at the Aliso Canyon gas storage facility. Several different corrosion scenarios were examined by means of the OLI software and the results were compared with field and laboratory data. Additionally, the water/gas phase behavior was evaluated for several production scenarios and uncertainties in downhole water saturation.

- The well had been in service as a gas storage well (injection and withdrawal) for 38 years 1977–2016. However, during this time the well only served as a producer for a cumulative total of 4 years. The rest of the time it was an injection well or was shut in.
- The reservoir serving for gas storage had previously been an oil producing formation and was not known as a water drive reservoir. Since the injection gas was essentially pipeline quality, it can be presumed to have been dry. The gas contained 1 mol% CO<sub>2</sub>, less than 0.5 ppm H<sub>2</sub>S and some higher molecular weight hydrocarbons.
- It can be safely presumed that the gas produced back was nearly dry, or, as has been observed during the past 20 years, under-saturated in water.
- It turns out that during withdrawal, the well produced some oil, and measurements indicate about twice as much as water with large variations in this ratio. The importance of the oil is that it is very heavy oil, with a point of condensation at temperatures higher than the water dewpoint and would therefore act as a natural corrosion inhibitor.
- Several different approaches were used in the attempt to model the corrosion of carbon steel in the most likely production environment of SS-25.
  - In the first instance, steel was exposed to condensed water in equilibrium with the gas phase as defined above. The maximum corrosion rate was >1,000 mpy (at 180°F and 2,500 psi). Allowing for an iron carbonate scale to build up reduced the maximum corrosion rate by a factor of 10, and lowering the CO<sub>2</sub> content from 2 to 1 mol% resulted in another 30% reduction of the corrosion rate. These were not realistic corrosion rates.
  - A second approach accounted for the corrosion process producing alkalinity, and 1,000 ppm of bicarbonate was added to the condensed water. At this point, the maximum corrosion rate had decreased to 36 mpy (at 180°F and 3,000 psi): still considerably higher than what could be justified by the observations. The results were presented as corrosion contour plots in a temperature-pressure grid and the modeled temperature-pressure profile was superimposed.
  - Finally, in order to fully account for field conditions, the solution was saturated in iron by adding iron carbonate. The maximum corrosion rate was then 12 mpy (at 140°F and 3,000 psi). This result is of an order of magnitude that begins to account for what might have happened in the field.
  - A different approach calculated the corrosion rate caused by the condensed liquid film moving up the tubing based solely on the amount of iron that can be dissolved in the water under surface conditions. It was postulated that it would not be likely to carry out more iron from the tubing than corresponds to the iron saturation in the liquid. Using this saturation value multiplied by the total water production reduced to the total corrosion iron carried out of the tubing and was

averaged over the total surface area<sup>i</sup>), the final corrosion rates were very low and practically negligible.

These corrosion estimates were in part confirmed by evaluating the results obtained from laser scans of the ID of the 7 in. casing.

---

<sup>i</sup> The 'total surface area' consisted of the outside diameter (OD) area of the tubing and the ID area of the casing (forming the 7 in. × 2 7/8 in. annulus in the well).

## 5 Inside Diameter Laser Scan Results

---

### 5.1 Laser Scans Results Overview

The upper 20 joints of the 7 in. casing extracted from SS-25 underwent an ID laser scan inspection at the Blade warehouse in Houston, TX. The inspection was done by Laserstream, L.P. in July 2018. The purpose of the inspection was to assess the extent of internal corrosion in the casing and to complement the ID corrosion rate study.

Because the ID of the casing was different between the pipe body and the connections, the data for the pipe body and connection were reported separately. Only features in excess of 5% of wall thickness penetration were considered corrosion-related. This limited the data realistically accepted as corrosion features to a depth of 0.015 in. (15 mils) on the lower end. Considering that the inherent roughness of the 1954 vintage casing may have been 0.006 in. (6 mils)<sup>ii</sup>, and taking into consideration a reasonable error (standard deviation) due to the variation of the internal pipe diameter, a lower cut-off of retained data was 15 mils was therefore considered reasonable.

The results of the laser scan are reported in the form of the length and width of any feature above the limiting minimum depth. However, since the surface of the feature was not uniform, an average surface area was determined by measurement within the length and width boundaries. The maximum depth and the average depth were determined within this feature area. The average depth was based on multiple depth measurements. The volume of the feature was determined from the average surface area and the average feature depth.

The laser scan results were used to estimate a corrosion rate by assuming, as a first order approximation, that the volume of iron removed from the feature was likely a better measure for the overall corrosion rate than the maximum depth<sup>iii</sup>.

Each data set was evaluated statistically in several ways in order to ascertain the general randomness of the nature of the corrosion features vs. occasional unordered events. The statistical analysis involved:

- Determining the kind of frequency distribution represented by the laser data as corrosion pit distribution. For pipe body and connections segments, the laser essentially detected localized depth variation from the general surface—hence, pit penetration. Note that this is not strictly correct, but there are no data available with respect to the original surface other than what the pipe specifications recognize as the nominal ID what the laser may recognize as an average most likely pipe diameter. These frequency distribution results are shown in Figure 10 through Figure 13 in Appendix A.
- Transforming the data to a probability distribution, such as the Weibull distribution, in order to estimate the probability of an extreme value. These results are shown in Figure 14 in Appendix A.
- Comparing all corrosion features for pipe body or connection as a function of depth into the well. These results are shown in Figure 15 through Figure 19 in Appendix A.

---

<sup>ii</sup> this assessment is based on assumptions made in the CO<sub>2</sub> corrosion model development at the University of Southern Louisiana (Lafayette) during the years of 1980 through 1983.

<sup>iii</sup> This is a first order approximation because it is a significant step from the feature corrosion rate to the general surface corrosion rate.



The maximum pitting on the pipe body (Figure 10) appeared to be nearly normally (Gaussian) distributed, with an average pit depth of 0.027 in. (27 mils). The variability is represented by the standard deviation which is 0.0068 in. (6.8 mils). However, the standard deviation of the mean value was only 0.00018 in. (~0.2 mils), which makes the mean penetration an almost absolute value.

By comparison, the mean maximum pit penetration on the connections (Figure 11) is 0.0378 in. (39 mils) with a larger standard deviation of 0.0008 in. (0.8 mils). The comparison between the two means is significant, which at this time only means that pitting on the connections are higher by an average of 44% over the pipe body penetration.

Table 3 shows the results for the pit depth frequency distributions.

**Table 3: Summary Statistics of Laser Scan on 7 in. Casing Inside Diameter**

Location	Maximum Penetration (in.)			Average Penetration (in.)		
	Mean	std dev. of Mean	std. dev. of Data	Mean	std dev. of Mean	std. dev. of Data
Pipe Body	0.0271	0.00018 (0.67%)	0.0068 (25%)	0.0172	0.000073 (0.43%)	0.00283 (16.5%)
Connection	0.0378	0.0008 (2.0%)	0.0164 (43%)	0.0195	0.000203 (1.04%)	0.00417 (21.4%)

## 5.2 Laser Scan Results Summary

It has been shown by laser scans of the internal surface of the 7 in. casing from the SS-25 well that:

- Pitting attacks on the pipe body were relatively frequent but marginal in depth. The distributions for maximum and average penetrations were essentially the same, albeit different by a factor of about two.
- Pitting on the connections was more frequent and occurred with a greater depth of penetration<sup>iv</sup>). The maximum observed penetration (0.117 in.) was about one-third of the pipe wall thickness. Hence, corrosion or pitting was more severe on the connections.
- There was no observable correlation between depth in the well and pit penetration depth.
- The pitting phenomenon was different for the pipe body and the connections.
- The average depths of the features better reflected the removal rate of iron by corrosion as determined in model calculations.

<sup>iv</sup> While the absolute number of pits observed on the connections was only one-third of those on the pipe body, the much smaller surface of the connections made the pit density proportionately much higher.

## 6 References

---

- [1] R. Hausler, "The COPRA Correlation - A Quantitative Assessment of Deep Hot Gas Well Corrosion and Its Control," in *NACE: Corrosion/83 1983, Paper No. 48*, 1983.
- [2] R. Hausler and T. Garber, "The COPRA Correlation Revisited," in *CORROSION/90, NACE 1990, Paper #90045.*, 1990.
- [3] S. Weeks and R. Hausler, "Low Cost, Low Volume, Continuous Inhibition of Gas Production Tubulars," *NACE Materials Performance*, no. June 1986, p. 28, 1986.
- [4] S. Weeks and R. Hausler, "Low-Volume Continuous Inhibition Technique, At Nominal Expense, For High Wellbore Temperature, CO<sub>2</sub> And Mildly Sour Gas Procedures," in *SPE, Las Vegas, Sept. 1985, Paper #14404*, 1985.
- [5] R. Hausler, "Laboratory Investigations of The Corrosion Mechanism as Applied to Hot Deep Gas Wells," in *NACE: Corrosion/83 1983, Paper No. 47*, 1983.

## Appendix A Evaluation of the Laser Scan Data

---

### Analysis of the Extreme Value Distribution

The analysis and summary (Table 3) of the overall frequency distribution provided a limited picture of the corrosion phenomena. Figure 10 and Figure 12 show the extreme value (Weibull) plots for the two sets of maximum penetration data from the pipe and connection segments.

For the correlation for the pipe body pit depths, one observes the expected straight-line behavior up to a penetration of about 0.05 or 0.055 in. Above this value, there were about 10 to 12 individual points which defy the extreme value prediction and rose much faster in value. It was noted that these outlier points represented only 0.8% of the entire data set collected on the pipe body segments.

Considering that the corrosion rate on the connections was higher than on the pipe body, it can be speculated that these points belong to the connection data set. It would have been difficult for the laser scanner to achieve a clean separation between the end of a pipe section and the beginning of the connection.

The extreme value correlation for the connection pit penetrations showed a slightly different picture. At the low end of penetration values, it appeared that one could observe an approach toward a constant low value. Subsequently, the correlation followed a fairly predictable course toward a maximum penetration value of 117 mils.

Where the differences between pitting in the pipe body and the connection become obvious is when the two curves are superimposed, as in Figure 14. There is a certain amount of fine structure in both curves, and the argument for either curve (the Weibull Plotting number) is different for each of them. What this means is that the frequency of occurrence of a given pit depth is not the same in each of the curves. However, this inherent difference between the two data sets, which is based on the number of observations and not on the nature of these observations, clearly highlights the fact that corrosion-pitting-localized attack was materially different for the two types of corroding surfaces.

The laser scan results are presented in multiple formats. The above discussions are based only on the reported maximum depth of each feature with a penetration larger than 5% of wall thickness. Features were also characterized by the average area of the feature as well as an average depth from which the volume of metal loss of the singular feature was calculated. Therefore, the average depth of the feature represents an average surface corrosion rate. Such corrosion rate is more likely to represent the corrosion rate calculated by the overall iron loss based on 'iron counts' (a common measure for general surface corrosion rate in CO<sub>2</sub>-containing systems). Figure 14 and Figure 15 show the statistical Weibull correlation of the average corrosion rate calculated for each feature.

### Analysis of Pitting Frequency along all 21 Pipe and Connection Sections

Finally, the question was asked if the extent (magnitude) of the corrosion phenomena depended on the depth of the casing in the well. Figure 16 through Figure 19 report the pitting frequency (number of features) returned by the laser scan for each joint. These are separated in pipe features and connection features for maximum (Figure 16 and Figure 18) and average (Figure 17 and Figure 19) penetration rates, respectively. These figures show correlations of all the pits occurring in each joint with the joint number in increasing depth toward the right-hand side. Therefore, the argument on the horizontal axis is the joint number, and pit depth is plotted on the vertical axis. The statistics are calculated for each batch of features in each corresponding pipe section. The mean for each individual batch is plotted in relationship to the overall mean, and the height of the diamond represents the standard variability for each mean. The

width of the diamond is a measure for the number of features found in the particular joint to which the diamond belongs.

The circles on the right of the graph denote the statistical significance of each set of data such that each set of data can be compared in a Student's t-test at the 5% significance level with each other set of feature depths. What this means in a practical sense is that the pitting in some pipe sections may be different from another. Applied to all of the pitting observed in the pipe body, the conclusion is that the pitting is quite uniform along all the 7 in. joints pulled from the well. The spread of pit penetrations within each pipe section may be large, but it is uniformly large, and there is no discernable trend from the top to the bottom or vice versa.

The width of each diamond indicates the pitting frequency for each particular section. Therefore, sections C003A1 and C004A1 show an overwhelmingly larger pit frequency over any other section. This knowledge, however, does not permit the conclusion that corrosion is more severe toward the top of the casing string due to the fact that the pit depth distribution is comparable to any of the other pipe sections, and is also reasonably well confirmed by the overlapping circles where no particular outlier is found.

Figure 18, the individual frequency distribution correlation with each connection, mirrors the conclusion that had been reached earlier by comparing the Weibull correlation in Figure 12, which is that there is a certain overlap in the frequency distribution before the divergence occurs. We now find that this overlap was essentially confined to joint C003A1 and connection C004A1.

Figure 17 and Figure 19 lead to the same conclusions by means of the average penetration rather than the maximum ones. In Figure 17, one finds that the mean for the average depth of the corrosion features on pipe segment C017A1 is significantly above the global average of all pipe segments. The reason is not clear since no significant differences between the pipe segments have been reliably established.

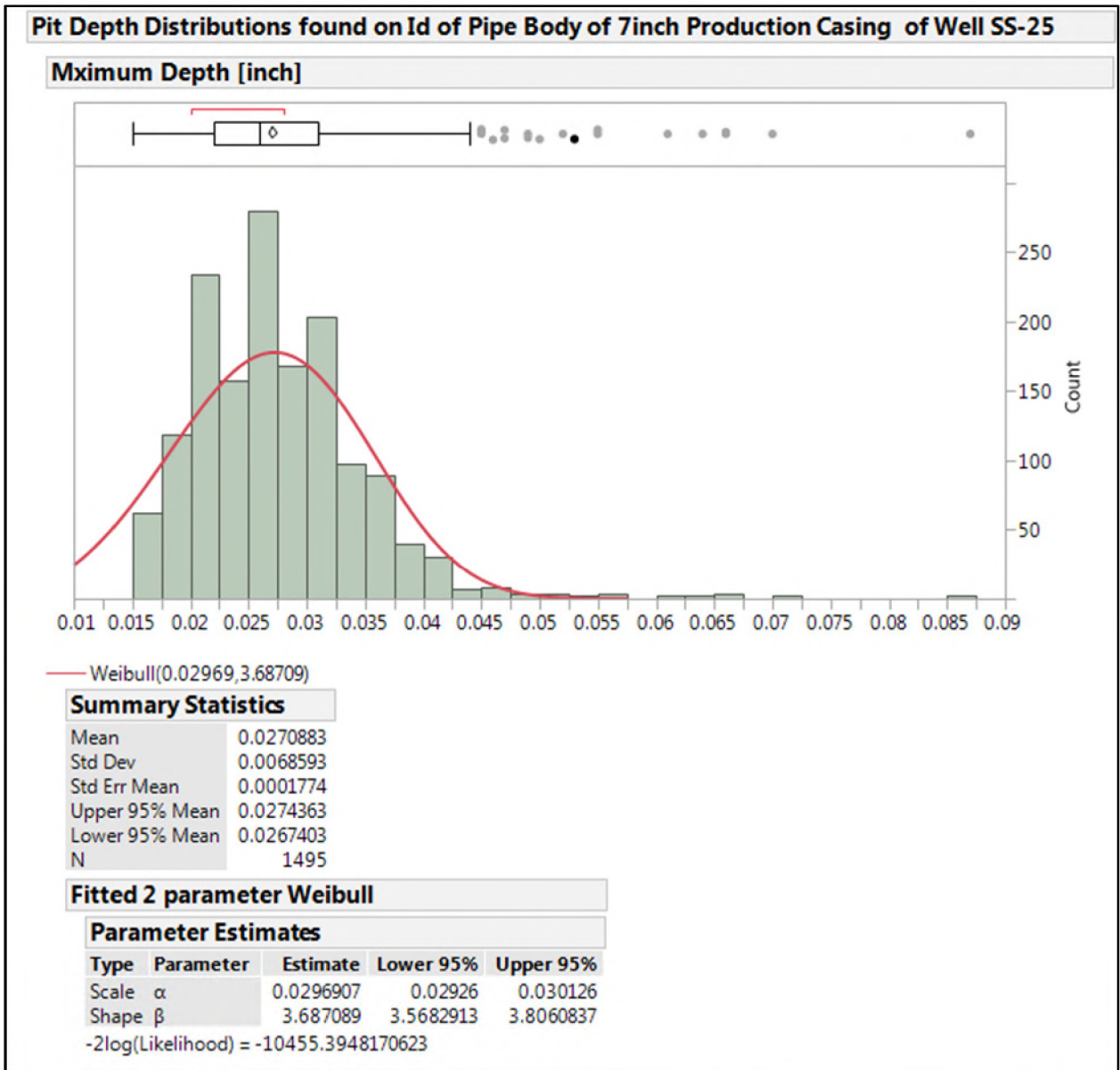


Figure 10: Frequency Distribution of Maximum Corrosion Feature Penetration on Pipe Body

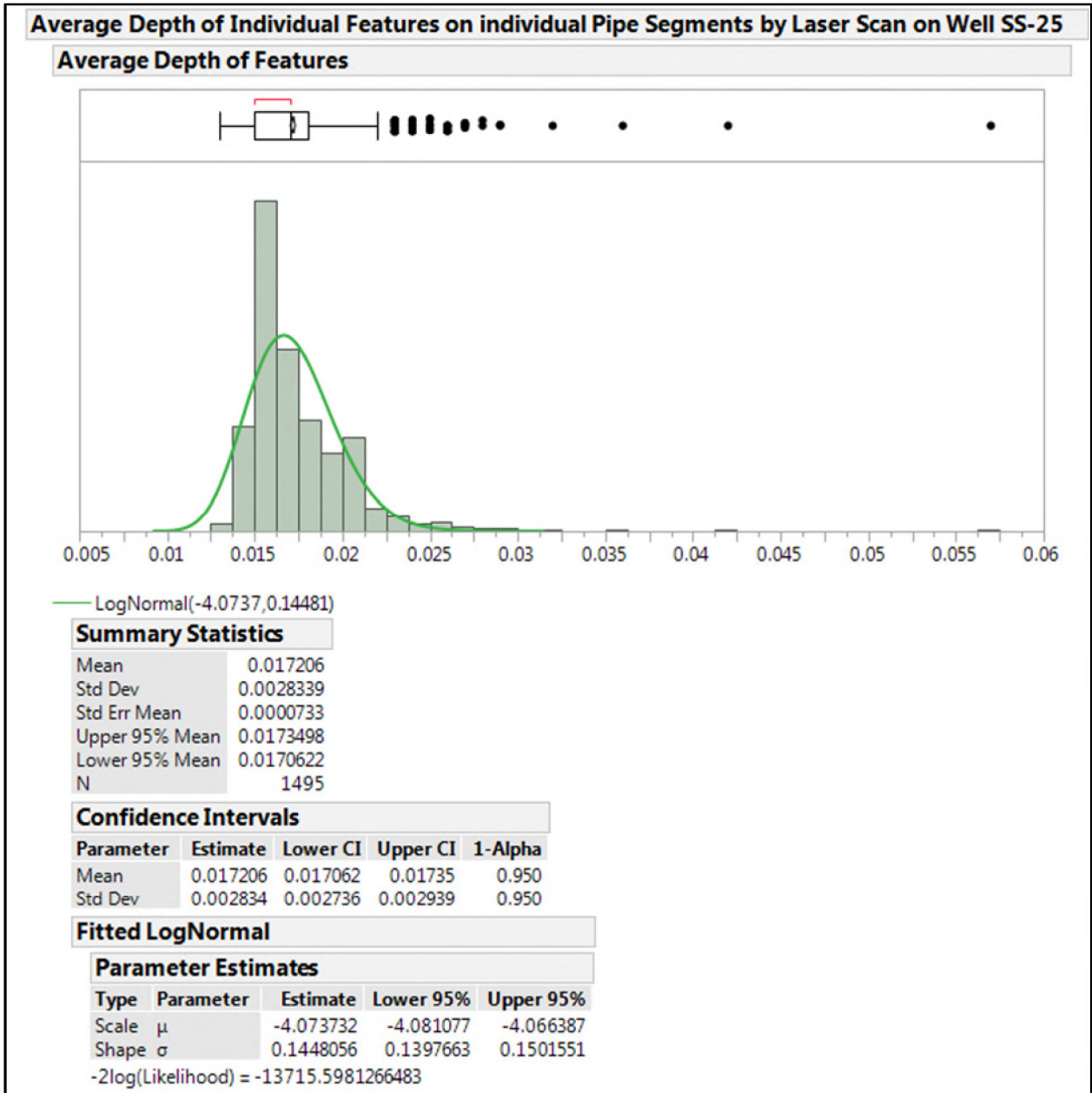


Figure 11: Frequency Distribution of Average Corrosion Feature Penetration on Pipe Body

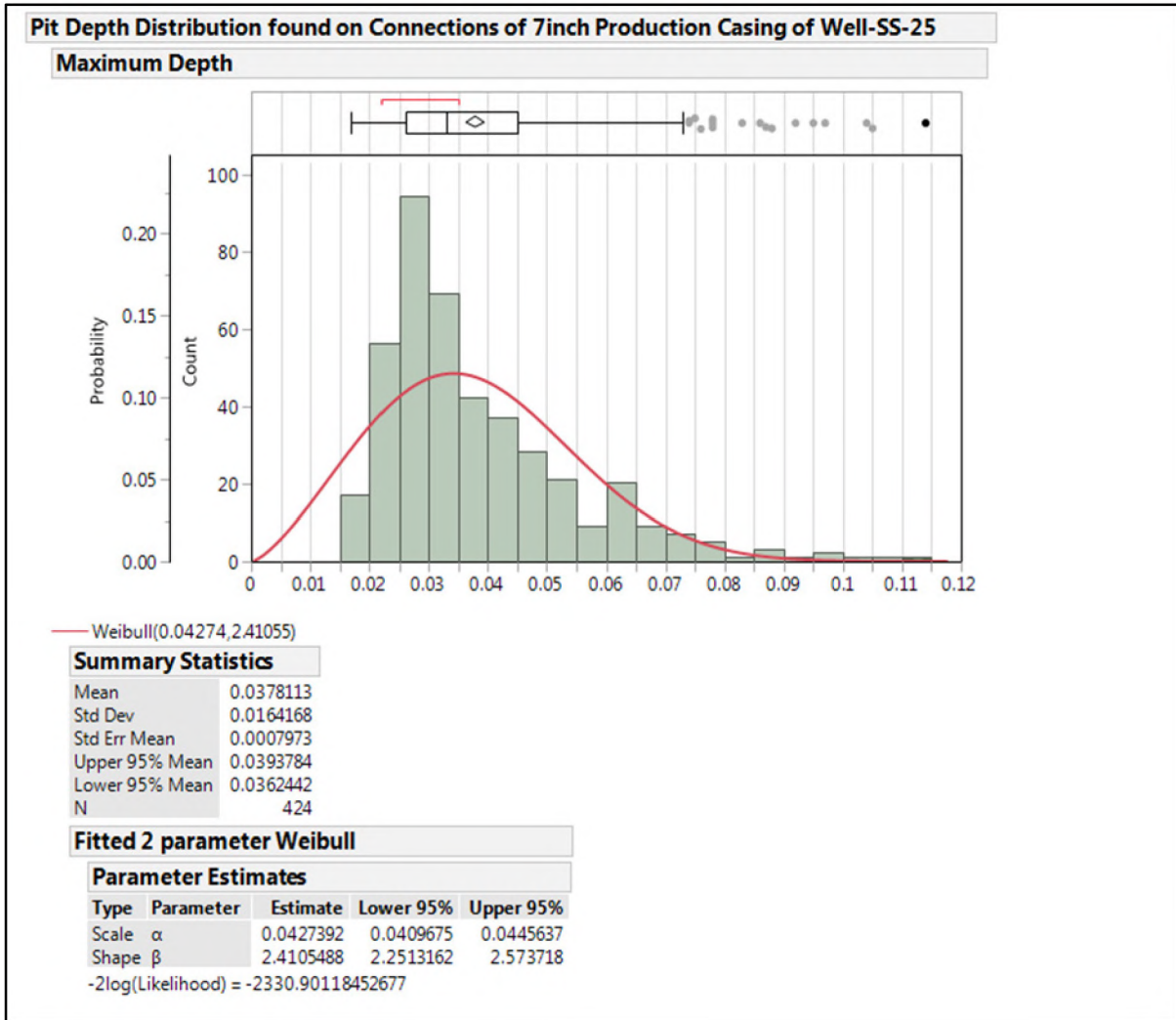


Figure 12: Frequency Distribution of Maximum Corrosion Feature Penetration on Connection Body

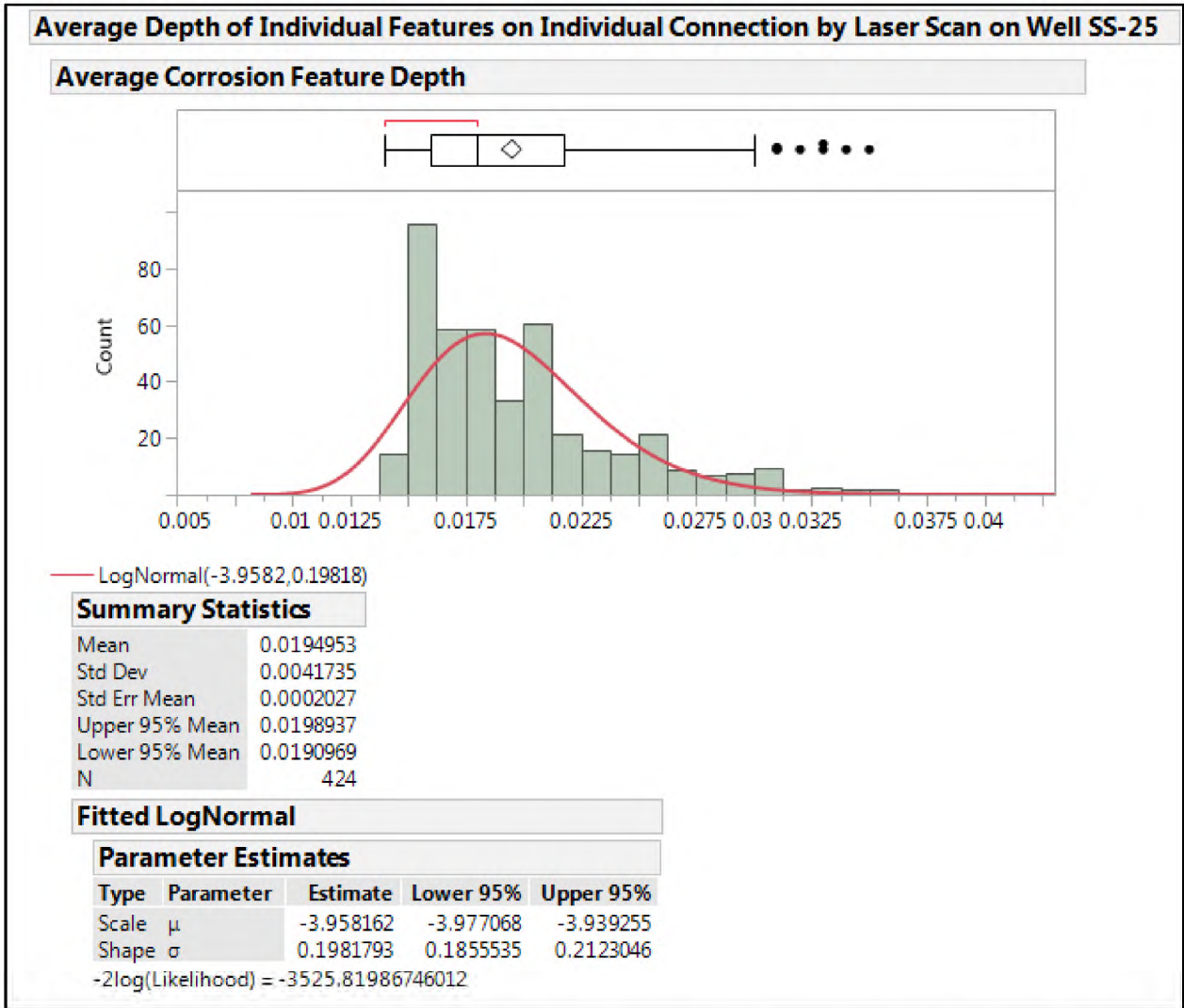


Figure 13: Frequency Distribution of Average Corrosion Feature Penetration on Connection Body



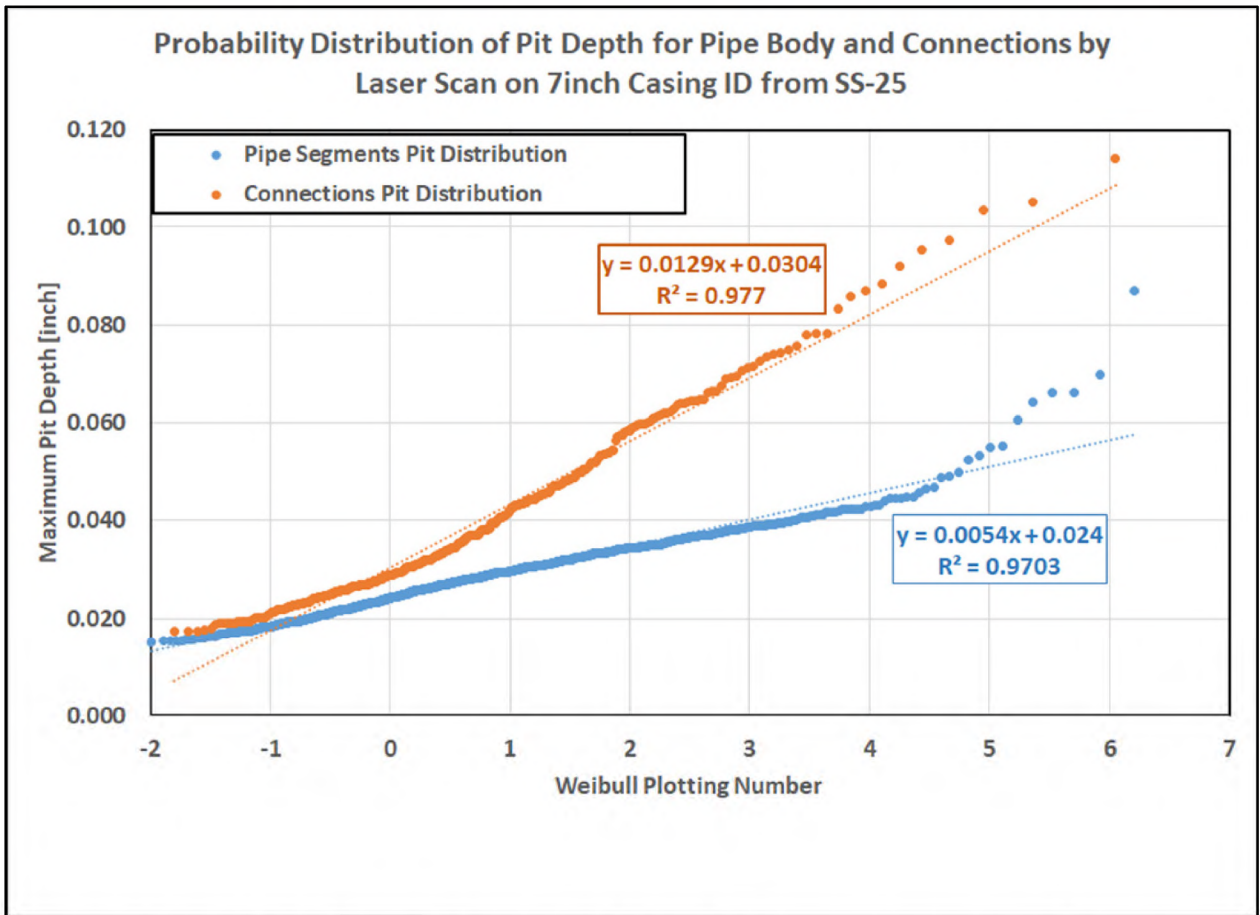


Figure 14: Probability Distribution of Pit Depth for Pipe and Connection Bodies

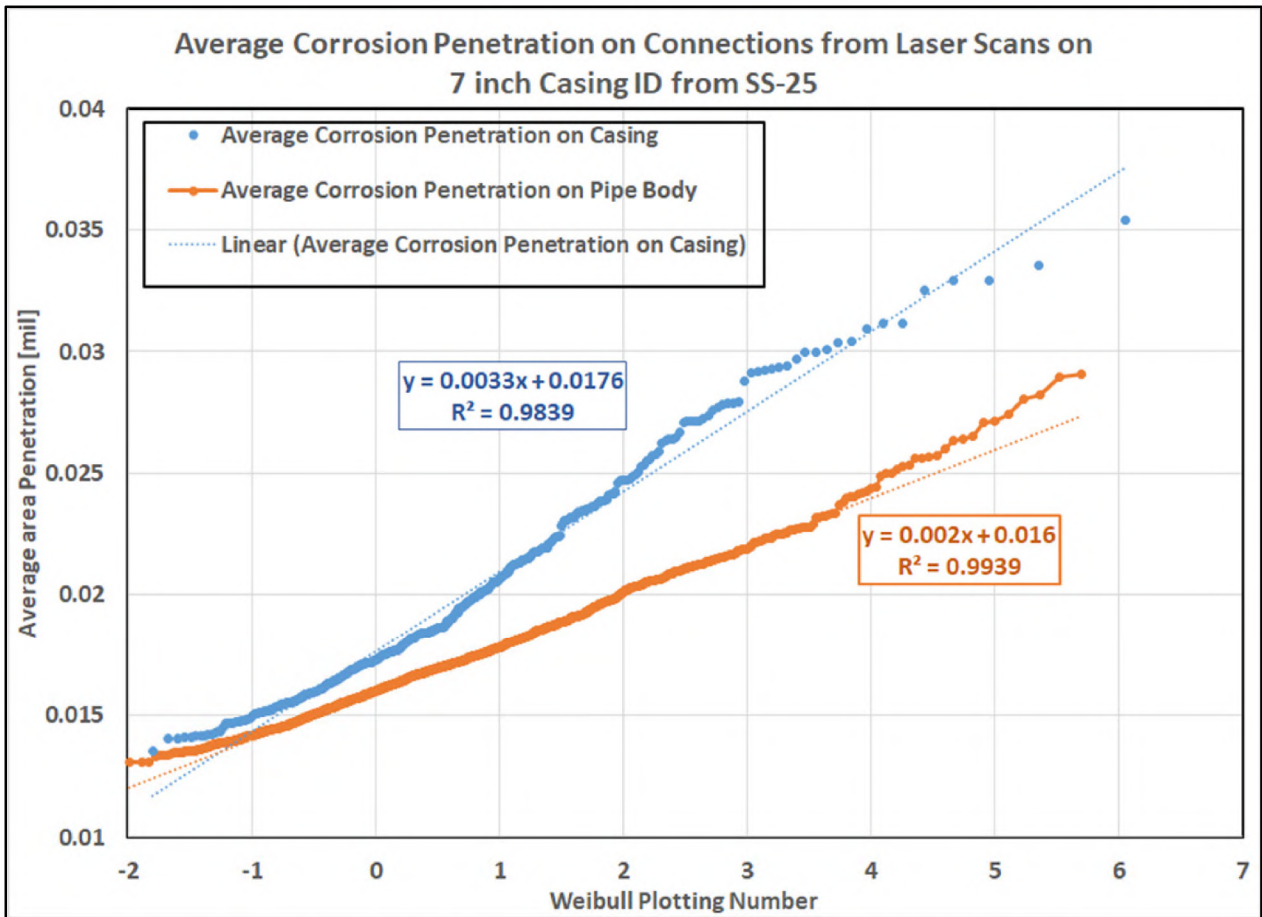


Figure 15: Probability Distribution of Average Corrosion on Pipe Body

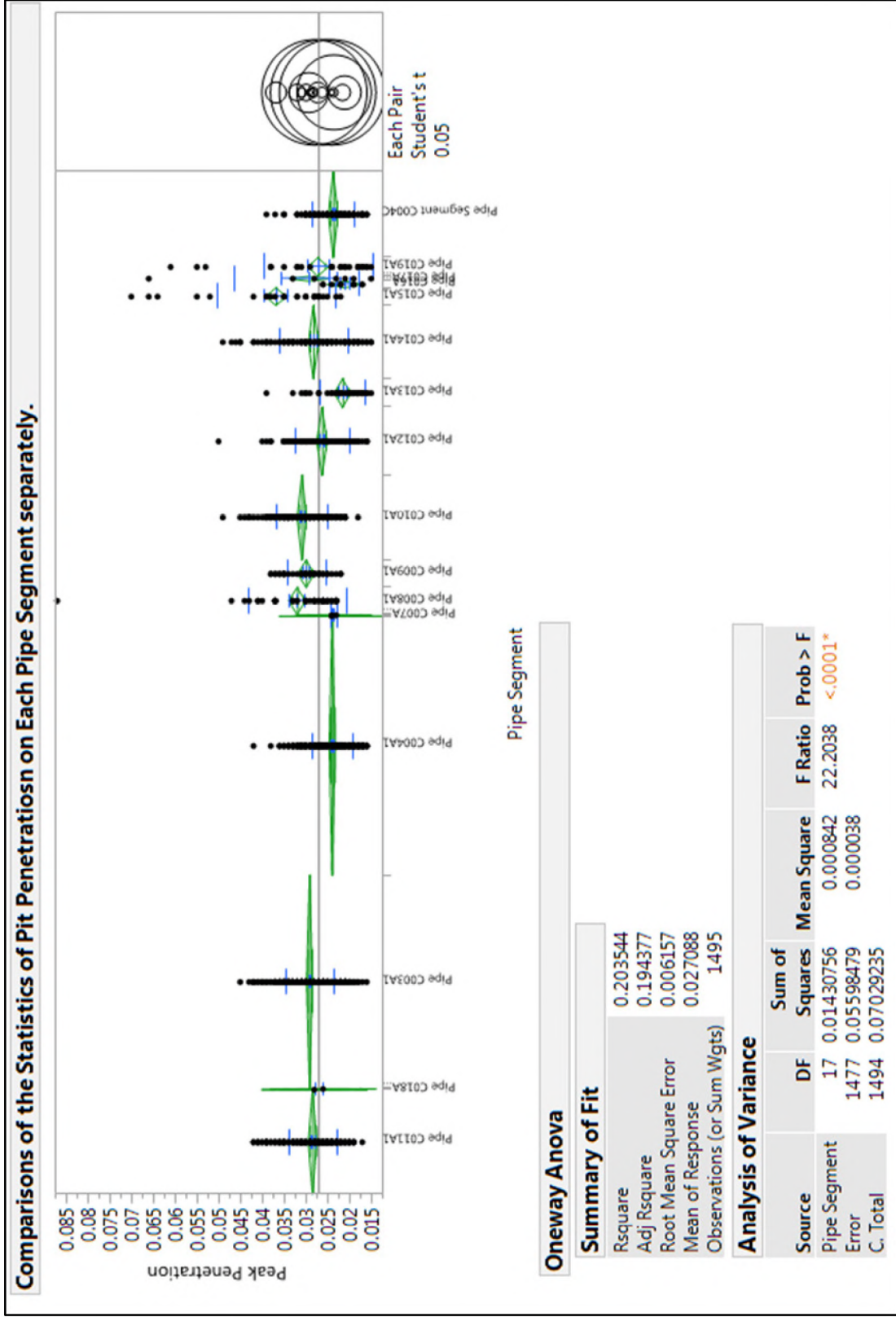


Figure 16: Comparison of Maximum Feature Penetrations on Pipe Body for Each Pipe Segment

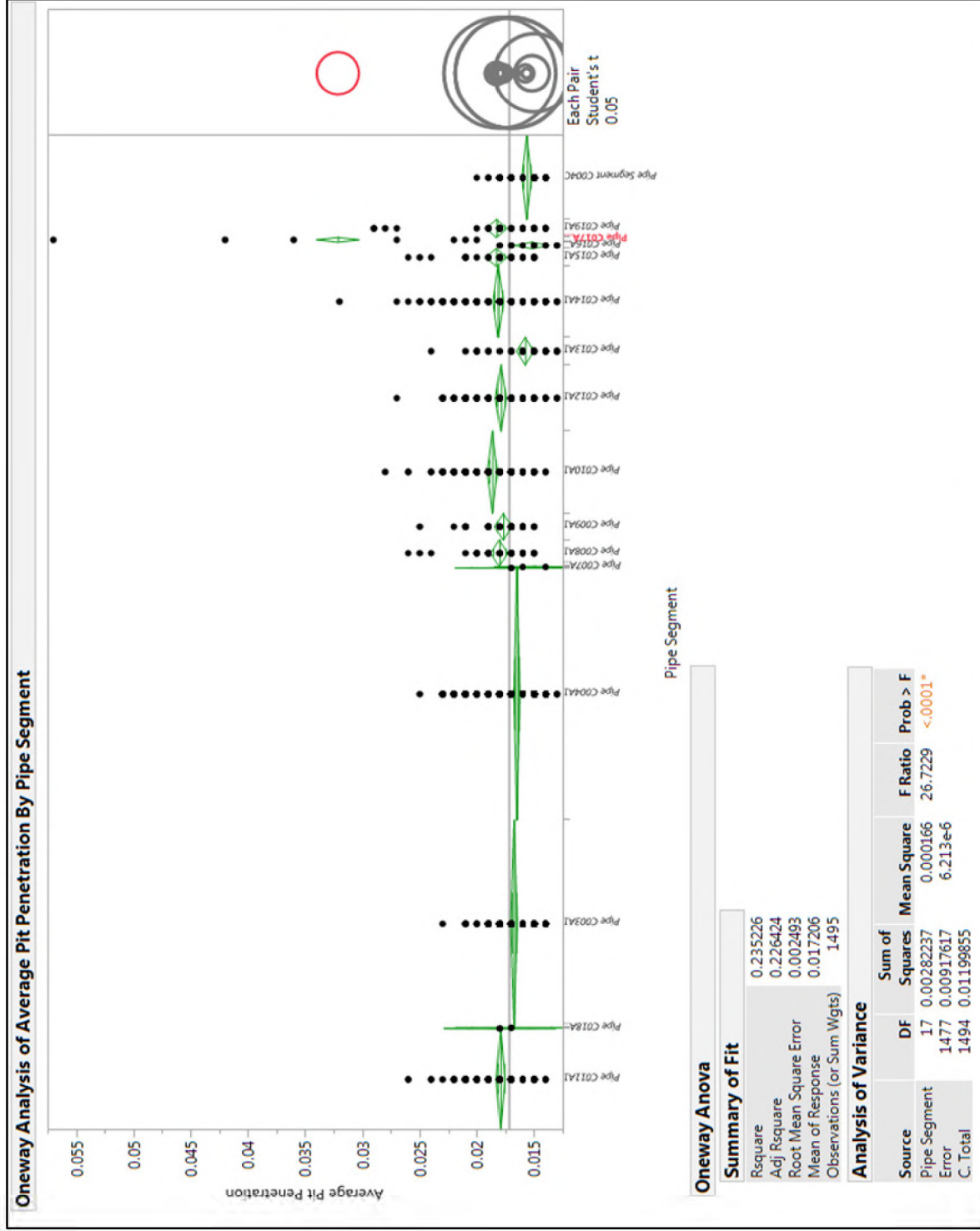


Figure 17: Comparison of Average Feature Penetration on Pipe Body for Each Pipe Segment

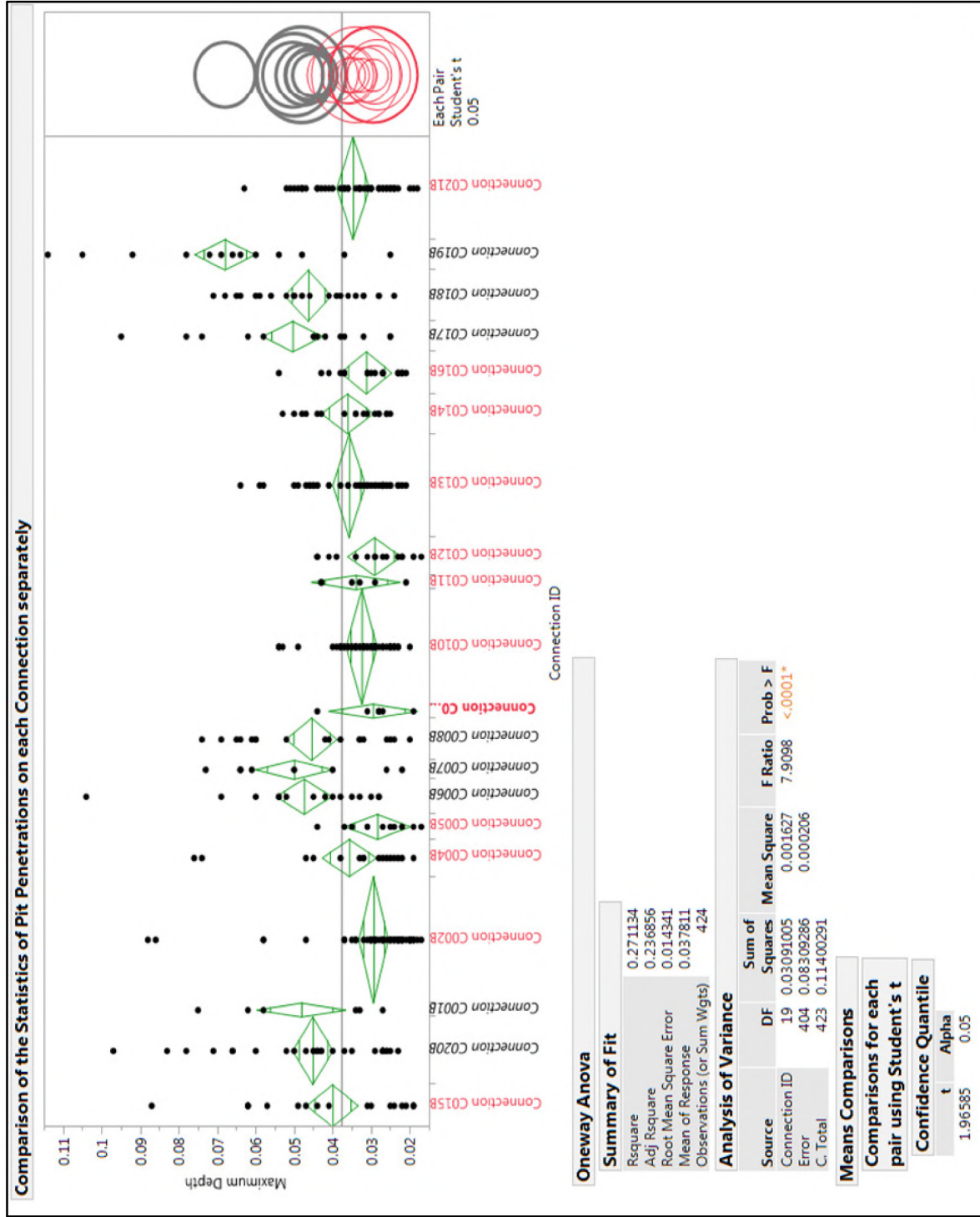


Figure 18: Comparison of Maximum Feature Penetration on Connection Body for Each Pipe Segment



# SS-25 RCA Supplementary Report

# SS-25 Inspection Logs Analysis



2600 Network Boulevard, Suite 550  
Frisco, Texas 75034

+1 972-712-8407 (phone)  
+1 972-712-8408 (fax)

16285 Park Ten Place, Suite 600  
Houston, Texas 77084

1-800-319-2940 (toll free)  
+1 281-206-2000 (phone)  
+1 281-206-2005 (fax)

[www.blade-energy.com](http://www.blade-energy.com)

## Purpose:

Report on the condition of the tubing, production and surface casings, and annuli of SS-25 from downhole logging operations.

## Date:

May 31, 2019

Blade Energy Partners Limited, and its affiliates ('Blade') provide our services subject to our General Terms and Conditions ('GTC') in effect at time of service, unless a GTC provision is expressly superseded in a separate agreement made with Blade. Blade's work product is based on information sources which we believe to be reliable, including information that was publicly available and that was provided by our client; but Blade does not guarantee the accuracy or completeness of the information provided. All statements are the opinions of Blade based on generally-accepted and reasonable practices in the industry. Our clients remain fully responsible for all clients' decisions, actions and omissions, whether based upon Blade's work product or not; and Blade's liability solely extends to the cost of its work product.

## Abstract

The gas storage well Standard Sesnon 25 (SS-25) in the Aliso Canyon Gas Storage Field located in Los Angeles County, California started leaking gas in October 2015. A relief well was drilled, and SS-25 was brought under control. The leak stopped in February 2016.

In January 2016, as part of their investigation of the leak, the California Public Utilities Commission (CPUC) and the Division of Oil, Gas, and Geothermal Resources (DOGGR) selected and gave provisional authority to Blade Energy Partners (Blade) to perform an independent Root Cause Analysis (RCA). The Blade Team and parties under Blade's direction were responsible for directing the work of subcontractors who performed the extraction of the SS-25's wellhead and tubing and casing and the preservation and protection of associated evidence. This report is a supplementary report to the main RCA report.

This report provides details of Blade's examination and interpretation of all the downhole inspection logs run after the SS-25's blowout. These logs were wireline conveyed to inspect the 2 7/8 in. tubing, 7 in. casing, and 11 3/4 in. casing. The inspection logs utilized were caliper, ultrasonic, magnetic flux leakage, and video imaging.

The following are Blade's key observations:

- The 2 7/8 in. tubing was in good condition.
- The 7 in. casing had external corrosion, and the most severe, in terms of penetration, was present from 700 ft to 1,015 ft. Numerous indications of internal corrosion were present from 1,700 to 2,300 ft, mostly of shallow penetration. The internal corrosion was related to a gas-lift mandrel at 1,965 ft when SS-25 was an oil producer. Deformations in the form of minor ovality were 1-2%, except at the whipstock area, which were 6%.
- The 7 in. casing annulus was cemented to 6,980 ft. Varying ratios of gas, liquid, and solids were present in the annulus above the cement.
- The 11 3/4 in. casing had external corrosion, and the most severe, in terms of penetration, was from 90 to 385 ft. Fifty-eight holes were present in the depth range of 134–300 ft; the majority of the holes were present in joint 5, which was 152–195 ft. Present in many joints were internal metal loss, such as casing wear, pitting, erosion, and other features that appeared mechanical in nature. Internal pitting was present between 700 and 990 ft. Some of the deepest features were at the same depth as the corrosion found on the 7 in. casing connections. Circumferential and longitudinal wall thinning of the 11 3/4 in. casing was present at the location of the 7 in. casing failure; this was interpreted as erosion. Deformations in the form of minor ovality were present in numerous 11 3/4 in. joints; only 1% ovality was present in the location of the 7 in. casing failure.
- Good cement was observed in only a small portion of the 11 3/4 in. annulus, specifically at 606–660 ft and 950-985 ft. Cement was not observed above 400 ft. Areas without cement were filled with liquids, gases, and solids of varying percentages.



## Table of Contents

<b>1</b>	<b>Introduction.....</b>	<b>6</b>
1.1	Abbreviations and Acronyms .....	7
<b>2</b>	<b>Inspection Logs Run in SS-25.....</b>	<b>9</b>
2.1	2 7/8 in. Summary .....	9
2.2	7 in. Summary.....	15
2.3	Openhole Summary.....	40
2.4	11-3/4 in. Summary.....	40
<b>3</b>	<b>Conclusions.....</b>	<b>60</b>
<b>4</b>	<b>References.....</b>	<b>61</b>
<b>Appendix A</b>	<b>Log Headers.....</b>	<b>A-1</b>
<b>Appendix B</b>	<b>7 in. EV Camera Pictures.....</b>	<b>B-1</b>
<b>Appendix C</b>	<b>11 3/4 in. EV Camera Pictures November 7, 2017 .....</b>	<b>C-1</b>
<b>Appendix D</b>	<b>Comparison of 7 in. Laser Scan Data and 11 3/4 in. High-Resolution Vertilog .....</b>	<b>D-1</b>
<b>Appendix E</b>	<b>11 3/4 in. Composite Log.....</b>	<b>E-1</b>

## List of Figures

Figure 1: Example of Bulging and Circumferential Features (Red Arrows) Observed on Numerous 2 7/8 in. Tubing Joints [6] .....	10
Figure 2: MicroVertilog Classification Summary of 2 7/8 in. Tubing [6].....	10
Figure 3: MicroVertilog Log of 2 7/8 in. Tubing, 830–1,020 ft [6] .....	11
Figure 4: 7 in. Casing Defect Observed by the April 18, 2016, MID Logs at 894.7 ft (Later Revised to 892 ft) .....	12
Figure 5: Metal Loss Defects Found by the April 18, 2016, MID-3 Log in the 11 3/4 in. Casing.....	13
Figure 6: (a) Side View and (b) Down View Cameras.....	13
Figure 7: Camera Screenshots of Tubing ID.....	14
Figure 8: 2 7/8 in. Tubing Joint 116 After Extraction.....	15
Figure 9: 7 in. Casing Defects by Depth, Joint Number, and Percent Penetration.....	17
Figure 10: 7 in. Caliper Summary [7] to 866 ft.....	18
Figure 11: 7 in. Caliper Summary [7] with Tieback Installed .....	18
Figure 12: 7 in. Caliper Data [7] Showing Ovalization at 3,834 ft.....	19
Figure 13: Drilling Record; Highlighted Section Shows the Placement of a Whipstock above 3,860 ft. ....	20
Figure 14: SS-25 Trajectory [8] (Whipstock Area in Black Box) .....	21
Figure 15: 7 in. HRVRT Log [9], December 2, 2017, External Corrosion at 939–1,015 ft - Green Bracket, Extracted August 8, 2018 – Red Bracket .....	22
Figure 16: 7 in. Summary of External Metal Loss by HRVRT [9]; Extracted Top 1,024 ft .....	23
Figure 17: 7 in. UCI Log [10], December 2, 2017, External Corrosion at 939–980 ft - Green Bracket.....	24
Figure 18: 7 in. Casing Joint 26, HRVRT [9] Flux Leakage Tracks (left), Laser Scan (right).....	25
Figure 19: 7 in. HRVRT [9] Summary of Internal Corrosion .....	26

Figure 20: 7 in. Caliper Log [7] Showing Internal Corrosion at 1,850–1,985 ft..... 27

Figure 21: 7 in. HRVRT [9] Log Showing Internal Corrosion at 1,850–1,985 ft..... 27

Figure 22: Gas-lift Mandrel at 1,965 ft Related to Internal Corrosion ..... 29

Figure 23: Well Configuration for Through-Tubing Camera Run to View 7 in. Failure Area ..... 30

Figure 24: Video Imaging from August 31, 2017, Parted 7 in. Casing ..... 31

Figure 25: Video Imaging from August 31, 2017, Parted 7 in. Casing (Upper Portion) ..... 32

Figure 26: Video Imaging from August 31, 2017, Parted 7 in. Casing (Lower Portion) ..... 33

Figure 27: December 11, 2017 EV Camera (Images Above) and December 2 Caliper Log (Bottom), 7 in. Casing Connection 177 at 7,488.1 ft, Minor Gouges..... 35

Figure 28: Historical Count [13] of the Number of Trips Through the 7 in. Casing, 19 Trips ..... 36

Figure 29: December 12, 2017, EV Camera, Example of Internal Corrosion on 7 in. Casing for 1,818–1,775 ..... 37

Figure 30: 7 in. IBC and CBL [10] Log Showing Top of Cement at 6,980 ft ..... 38

Figure 31: 7 in. IBC and CBL [10] Log Showing Annulus Condition 940–1,070 ft ..... 39

Figure 32: 4-Arm Caliper [15] Log, 940–1,070 ft ..... 40

Figure 33: 11 3/4 in. Caliper Log, Mean Average ID Changes (Green Line) Joints 12–13 (Arrow) ..... 43

Figure 34: 11 3/4 in. HRVRT [16] and Isolation Scanner [17], External Corrosion Observed (Green Box) . 44

Figure 35: 11 3/4 in. IBC [17] Summary of Maximum Penetration by Wall Thickness for Joints 6–25 ..... 45

Figure 36: 11 3/4 in. HRVRT [16] and IBC [17] Log, Joints 16–18, Isolated External Corrosion at Joint 17 (Blue Box) ..... 45

Figure 37: 11 3/4 in. Caliper Log [7] and Pictures from Video Imaging at 145 ft and 147 ft ..... 46

Figure 38: Picture of Hole in 11 3/4 in Casing with Dimensions from Video Imaging at 145 ft ..... 46

Figure 39: Caliper Log [7] Example of Internal Metal Features (Blue Rectangles) at 11 3/4 in. Joint 13 ... 47

Figure 40: UCI Log [17] Example of Internal Metal Features (Blue Rectangles) at 11 3/4 in. Joint 13..... 47

Figure 41: HRVRT Log [16], Examples of Internal Metal Loss Features (Highlighted Blue), Joints 10–15.. 48

Figure 42: 11 3/4 in. Caliper Logs and HRVRT Log [16] (Right), Internal Metal Loss as Pitting from 700–990 ft ..... 50

Figure 43: 11 3/4 in. Video Imaging at ~731 ft, Example of Pitting Observed ..... 51

Figure 44: 11 3/4 in. HRVRT Log [16], Nonrandom Internal Metal Loss (Blue Rectangle) ..... 52

Figure 45: Type III Corrosion Feature, Photograph of 7 in. Casing Connection No. 19 [2]..... 53

Figure 46: Trajectory [18] and Estimated 7 in. and 11 3/4 in. Casings Contact Locations ..... 54

Figure 47: UCI Log [7] of 11 3/4 in. Longitudinal Feature in 11 3/4 in. Casing Resembling 7 in. Rupture.. 55

Figure 48: Caliper Log [7] of 11 3/4 in. Casing Joint 23 ..... 56

Figure 49: Caliper [7] Log of 11 3/4 in. Casing Joint 23, 888–898 ft, Mean ID Highlighted Green, 3D Inset 56

Figure 50: Caliper Log [7] of 11 3/4 in. Casing, Ovality (Right Track) Displayed Range 0–0.4 in. (0–3.6%) 57

Figure 51: UCI Log [17] of 11 3/4 in., Joints 13–14, Casing Wear (Red Box) and Internal Metal Loss Feature (Blue Boxes) ..... 58

## List of Tables

Table 1: Vendors, Logs, and Category of Logging Tools ..... 6

Table 2: SS-25 Tubing Inspection Logs..... 9

Table 3: Average Inside Diameters from April 8, 2016 Caliper Log, Surface to 8,181.7 ft ..... 10

Table 4: 7 in. Casing Inspection Logs ..... 15

Table 5: Operations Summary for August 31, 2017 ..... 30

Table 6: Operations Summary for October 10, 2017..... 34

Table 7: Operations Summary for December 10–13, 2017 ..... 34



**SS-25 Inspection Logs Analysis**

---

Table 8: Openhole Inspection Logs.....	40
Table 9: 11 3/4 in. Casing Inspection Logs.....	41
Table 10: 11 3/4 in. Defect Summary .....	42

# 1 Introduction

At the request and under supervision of Blade, various vendors collected data from the tubing (2 7/8 in.), production (7 in.) casing, surface (11 3/4 in.) casing, and annuli using wireline-conveyed inspection logging tools. These data were collected in situ, i.e., with the tubulars in place.

The purpose of this document is to present the findings of the SS-25 inspections logs. Additional data on the extracted tubulars were collected during Phase 4 and are presented in separate reports [1] [2]. No inspection logs had been run in SS-25 before the October 23, 2015 incident; therefore, no comparisons could be made to historic logs.

The approach was multifaceted—it utilized a combination of technologies, such as mechanical, electromagnetic, ultrasonic, and downhole camera logs. Table 1 shows the vendors, logs, and categories of the logging tools run in SS-25 related to the inspection of the 2 7/8 in. tubing and 7 in. and 11 3/4 in. casings.

**Table 1: Vendors, Logs, and Category of Logging Tools**

Vendor	Log Name	Category
Baker Hughes GE	24-arm Caliper	Mechanical
Baker Hughes GE	56-arm Caliper	Mechanical
Baker Hughes GE	High-Resolution Vertilog	Electromagnetic
Baker Hughes GE	Micro Vertilog	Electromagnetic
Baker Hughes GE	Integrity eXplorer	Ultrasonic
Versa-Line/TGT	Micro Imaging Defectoscope-2	Electromagnetic
Versa-Line/TGT	Micro Imaging Defectoscope-3	Electromagnetic
Schlumberger	Ultrasonic Corrosion Imager	Ultrasonic
Schlumberger	Isolation Scanner	Ultrasonic
Schlumberger	Sonic Scanner	Ultrasonic
Schlumberger	Corrosion Protection Evaluation Tool	Electromagnetic
EV Camera	Camera	Visual

The different logs complement each other and provide a thorough and complete review of the tubular condition. Each tool has its own individual strengths and weaknesses in identifying certain types of defects:

- The High-Resolution Vertilog (HRVRT), a magnetic flux leakage and eddy current inspection tool (generically, electromagnetic), detects pitting with high repeatability and accuracy but may not detect ovality or shallow casing wear.
- The ultrasonic tools are affected by the surface condition of the tubular ID and may not detect reliably small pits that are less than the transmitter beam width, but they are exceptional at detecting ovality and casing wear.
- The caliper log does not detect features that fall in the gap between its fingers, but it is the only log that provides direct measurements of the radius.

Protocol [3] [4] and Work Plan [5] documents include the tool specifications, operations parameters, and run order. In some figures, the log data is presented without the log header information, which displays the track and curve information. Appendix A shows the log header information.

## 1.1 Abbreviations and Acronyms

Term	Definition
CBL	Cement Bond Log
CPET	Corrosion and Protection Evaluation Tool
CPUC	California Public Utilities Commission
DE	diatomaceous earth
DOGGR	Division of Oil, Gas, and Geothermal Resources
EOT	End of Tubing
FMI	Formation Micro Imager
GNPT	Global New Petro Tech, Inc.
GR-JB	Gamma Ray Junk Basket
HPT	High Precision Temperature
HRVRT	High-Resolution Vertilog Service
IBC	Isolation Scanner
ID	Internal Diameter
INTeX	Integrity eXplorer Cement Evaluation Service
KCL	Potassium Chloride
LD	Lay down
MID	Magnetic Imaging Defectoscope
MPC	Mechanical Pipe Cutter
MU	Make Up
MVRT	MicroVertilog Tool
NDE	Nondestructive Evaluation
NOV	National Oilwell Varco
OD	Outside Diameter
P&A	Plug and Abandon
POH	Pull Out of Hole
POOH	Pull Out Of Hole
RCA	Root Cause Analysis
RD	Rig Down
RIH	Run In Hole
RU	Rig Up
SD	Set Down
SO	Slack Off

## SS-25 Inspection Logs Analysis

Term	Definition
SoCalGas	Southern California Gas Company
SS	Standard Sesnon
SSCAN	Sonic Scanner
TOF	Top of Fish
UCI	Ultrasonic Corrosion Imager
WL	Wireline

## 2 Inspection Logs Run in SS-25

### 2.1 2 7/8 in. Summary

Table 2 shows the inspection logs run in the 2 7/8 in. tubing of SS-25. All the logs listed were performed under the request and supervision of Blade, except the earliest log performed by Western Wireline—it was conducted during the blowout at the direction of SoCalGas or Boots & Coots. No historical tubing inspection logs were found prior to the ones listed. The MicroVertilog, caliper, MID-2, and MID-3 logs were run to quantify the metal loss, shape, and other damage in the tubing. Additionally, the MID-2 and MID-3 logs quantified metal loss in the 7 in. and 11 3/4 in. casings prior to extraction. These logs provided early insight into the condition of SS-25 prior to the extraction activity consisting of valuable data to the planning documents, such as protocols, work plans, hazard identification, notice of intent, extract tubulars on paper exercise. The tubing was extracted and sent for nondestructive examination (NDE). The log and NDE results agree well; the NDE results are contained in a separate report.

**Table 2: SS-25 Tubing Inspection Logs**

Date	Vendor	Log	Top (ft)	Bottom (ft)
January 21, 2016	Western Wireline	Caliper - 24 arm	3,000	6,000
April 8, 2016	Baker Hughes GE	Caliper - 24 arm	0	8,186
April 18, 2016	TGT, Versa-line, GNPT	MID-2, MID-3	0	8,187
April 22, 2016	Baker Hughes GE	MicroVertilog	0	8,186
August 30, 2017	EV	Camera	0	1,040
August 31, 2017	EV	Camera	0	892

#### 2.1.1 Bulging and Circumferential Anomalies

Figure 1 shows an example of the bulging phenomenon and circumferential features. The individual traces of each caliper finger are shown on the left, and the calculated minimum, average, and maximum diameters are shown in blue, green, and red respectively. Smaller diameters are to the left, and larger diameters are to the right. The tubing pipe body seems to be radially flared out or bulged, i.e., the ID in the middle is larger than at the ends of each joint. This was evident in joints 83–234 (2,564–7,250 ft). Circumferential features were also observed. They are denoted by red arrows pointing to short lengths with a small reduction in diameter.

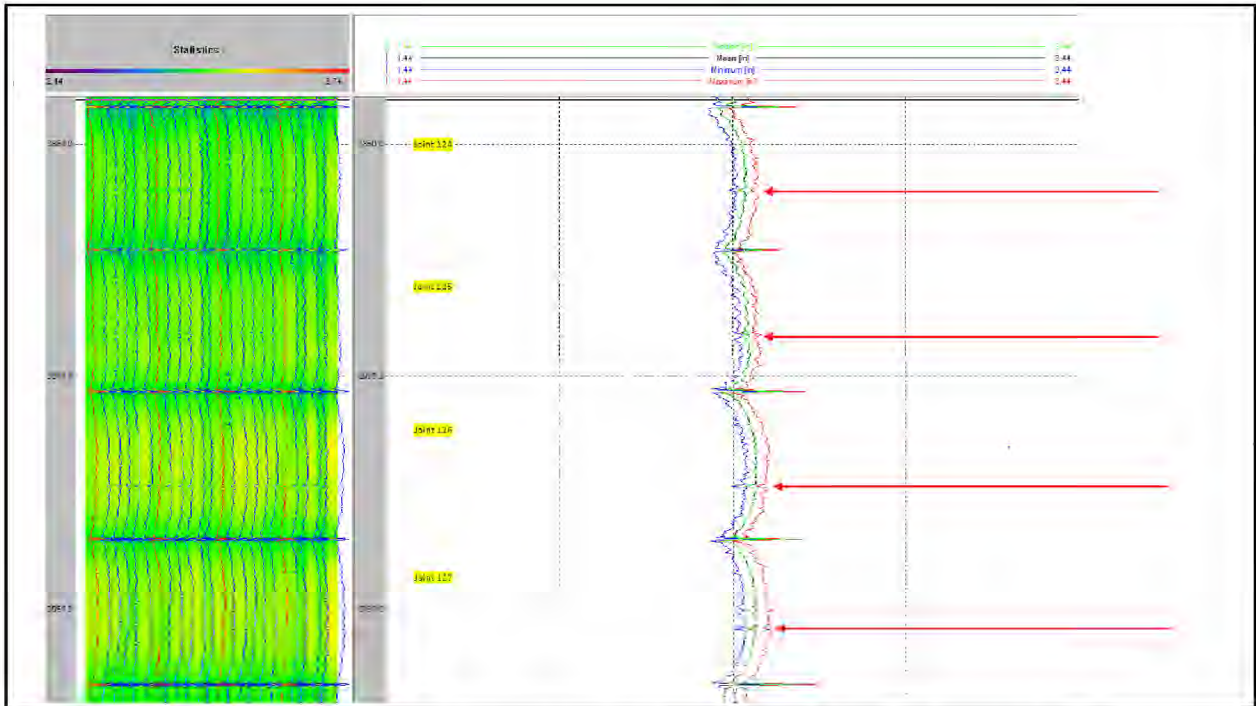


Figure 1: Example of Bulging and Circumferential Features (Red Arrows) Observed on Numerous 2 7/8 in. Tubing Joints [6]

Table 3 shows the average minimum ID, average ID, and average maximum ID obtained by the April 8, 2016, caliper log calculated from the entire log interval, i.e., from surface to 8,181.7 ft. The range of average IDs calculated was within 0.5–2.1% of the nominal ID of the 2 7/8 in. 6.5 lb tubing, which was 2,441 in.

Table 3: Average Inside Diameters from April 8, 2016 Caliper Log, Surface to 8,181.7 ft

Average Minimum ID	Average ID	Average Maximum ID
2.454 in.	2.473 in.	2.492 in.

### 2.1.2 Tubing Metal Loss Features

Significant pitting was not observed in the MID-2, MID-3, MicroVertilog logs, or caliper logs. Figure 2 shows the summary from the MicroVertilog log; *no defects were found that exceeded 20% depth.*

Class	Defect Range	Joints	Total Length	Percentage
1	0 - 20	264	8139.70	100.0
2	20 - 40	0	0.00	0.0
3	40 - 60	0	0.00	0.0
4	60 - 100	0	0.00	0.0
Total		264	8139.70	100.0

Figure 2: MicroVertilog Classification Summary of 2 7/8 in. Tubing [6]



Figure 3 shows the portion of the MicroVertilog log for the depths 830–1,020 ft. Metal loss features are not present. At ~891 ft, denoted by a green box, we see the call-out by Baker Hughes “Not a metal loss feature – probable hardware.” The way we interpret this is that the parted 7 in. casing was in contact with the tubing at this location, and the MicroVertilog registered this as an external hardware.

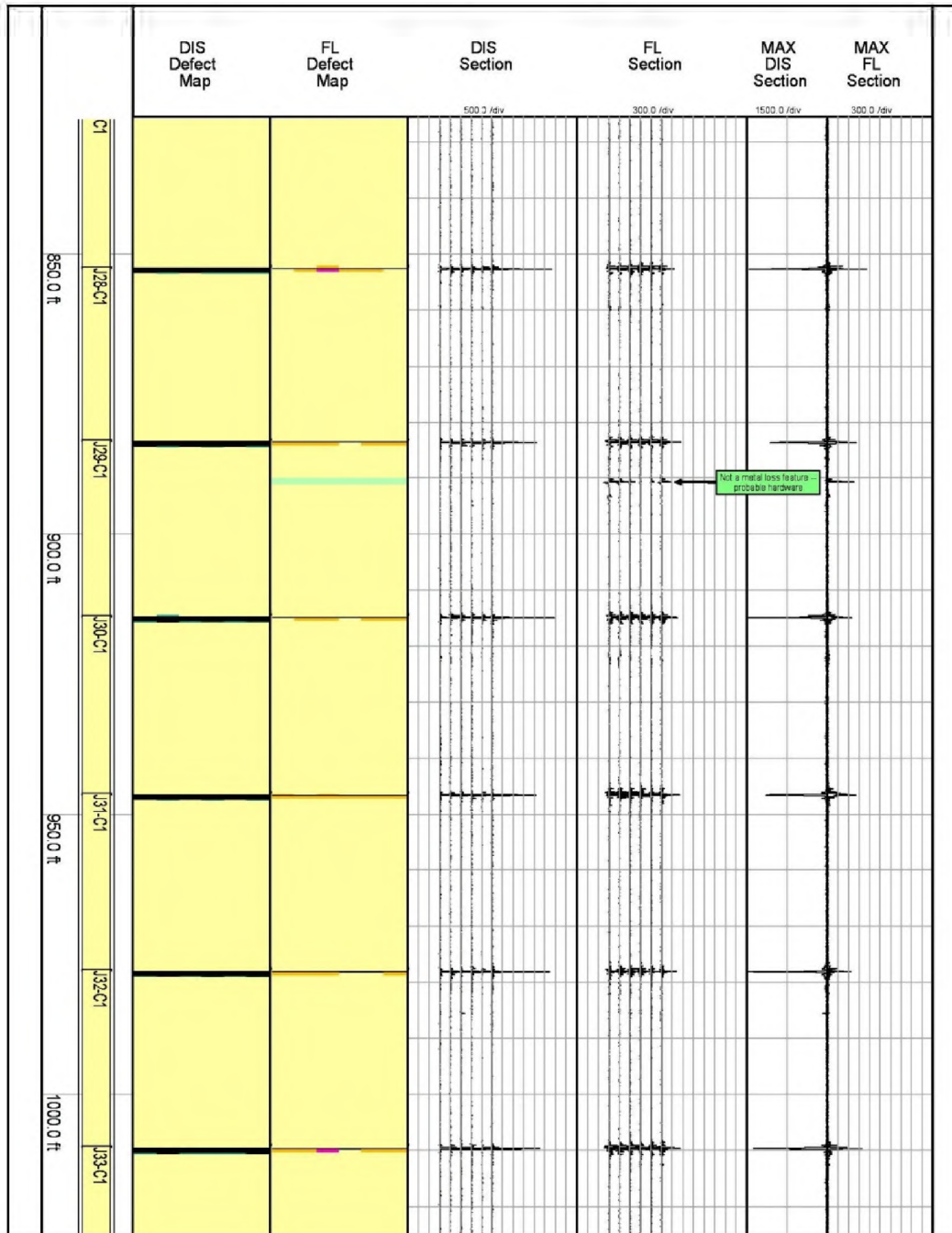


Figure 3: MicroVertilog Log of 2 7/8 in. Tubing, 830–1,020 ft [6]

### 2.1.3 Summary of April 18–20, 2016 MID-2 and MID-3 Logs

The main 7 in. casing logging program commenced November 27, 2017, and ran through December 10, 2017. Before this logging, we already had advanced knowledge of the 7 in. casing failure from the April 18, 2016, MID logs prior to extracting the 2 7/8 in. tubing because the MID-2 and MID-3 tools had the capability to inspect the 7 in. and 11 3/4 in. casing through the tubing. Figure 4 shows the MID Log for 800–950 ft with a 38% metal loss feature highlighted. Global New Petro Tech (GNPT) interpreted this to be a metal loss feature with the signature of through-wall metal loss or casing impairment. After the 7 in. casing was extracted, the depth of its failure was revised and did not match the log depths. The August 20, 2017, video imaging, discussed later, confirmed the findings from the MID logs.

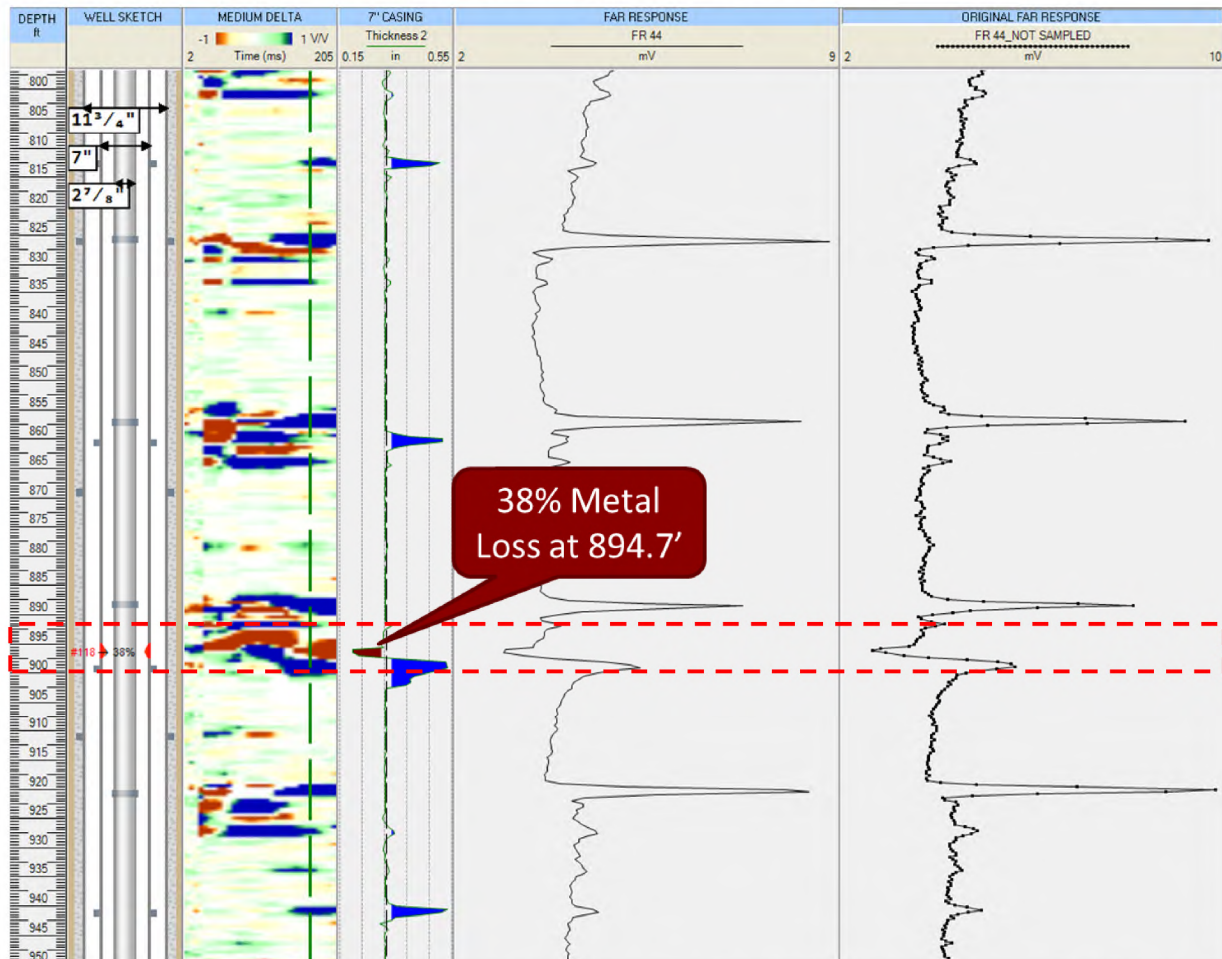


Figure 4: 7 in. Casing Defect Observed by the April 18, 2016, MID Logs at 894.7 ft (Later Revised to 892 ft)

Figure 5 shows the summary of the defects as found by the MID-3 log in the 11 3/4 in. casing on April 18, 2016. This log could not discern if the metal loss was internal or external. These defects were later confirmed to be through-wall holes and extensive external corrosion (Sections 2.4.2 and 2.4.3).

No	Interval of corrosion, ft	Metal Loss,%
134	150.9 – 152.5	34
135	191.4 – 193.8	36

Figure 5: Metal Loss Defects Found by the April 18, 2016, MID-3 Log in the 11 3/4 in. Casing

### 2.1.4 Visual Features

The EV Optis E-Line MK2 system consisted of two video cameras: a side view camera and a down view camera (Figure 6). The side view camera could rotate 360 degrees continuously; the down view camera was a fish eye lens to provide a wide viewing angle. Each camera had independent lights.

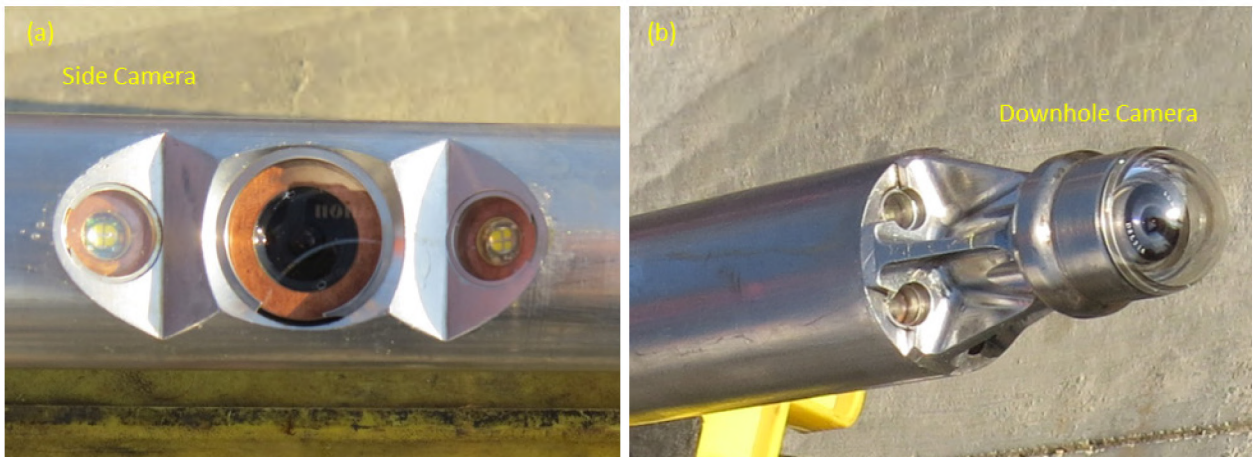


Figure 6: (a) Side View and (b) Down View Cameras

The cameras were run twice to look at the 7 in. casing failure concurrent with the extraction of the 2 7/8 in. tubing. Figure 7 shows some images of the tubing. The images agree with the observations of the previously discussed tubing inspection logs—no abnormalities were observed in the tubing. Note that the two images on the left hand side of the bottom row show the internal circumferential feature. The 7 in. casing failure is shown in Section 2.2.5.

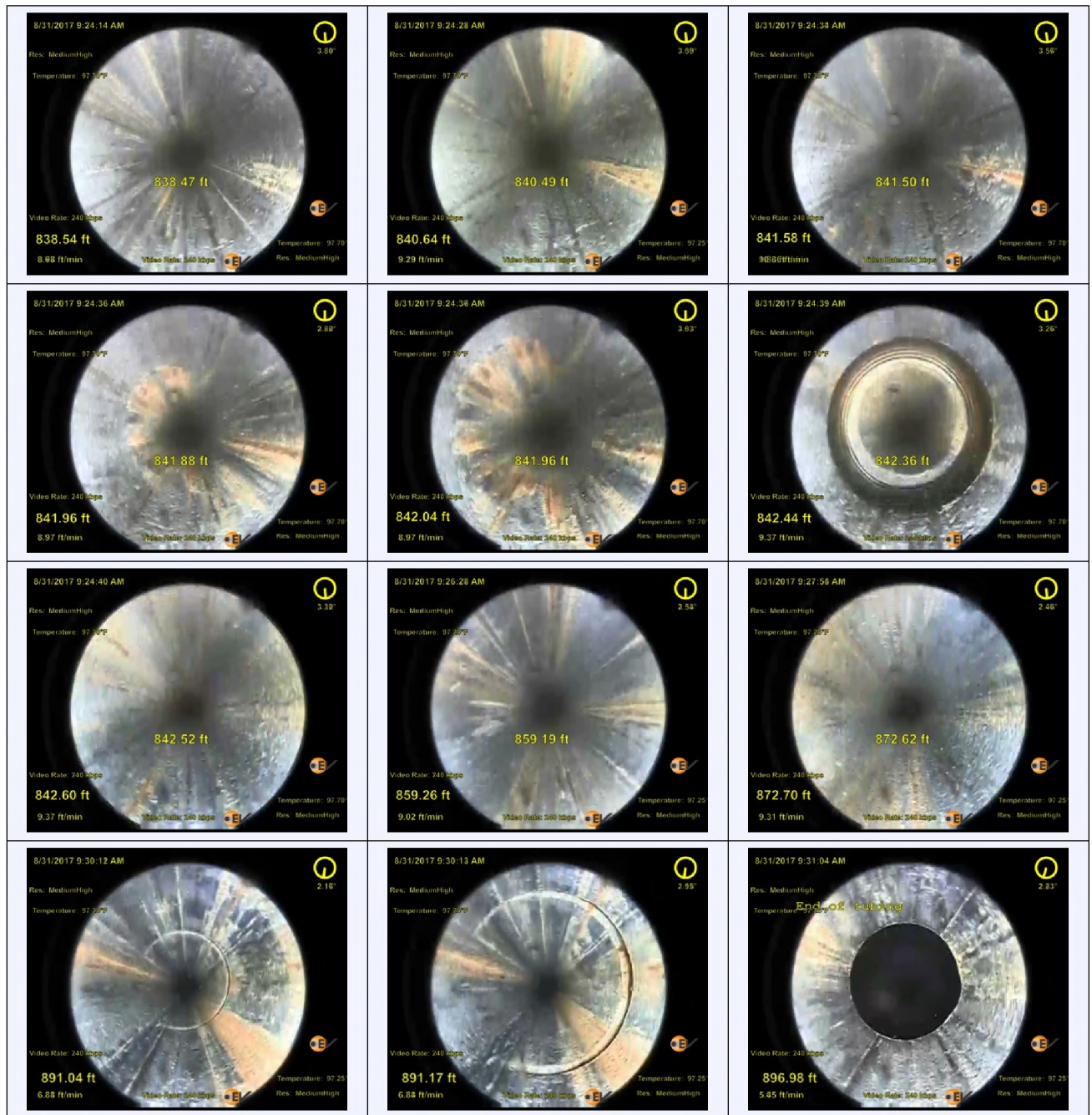


Figure 7: Camera Screenshots of Tubing ID

### 2.1.5 Pass-Through Issue at 3,608 ft

Baker Hughes was not able to run the MicroVertilog inspection logging tool through the tubing below 3,608 ft. A successful pass-through was achieved by using additional weight bars. We realized after the extraction of the tubing that this issue was related to deformation in the pipe body. Figure 8 shows the most severely bent tubing joint—joint 116 located at ~3,608 ft. There was a noticeable bend located in the upper third of this tubing joint (the uphole end is closest to the viewer, and the downhole end is into the page). Further evaluation of the extracted tubing is found in separate reports [1] [2].



Figure 8: 2 7/8 in. Tubing Joint 116 After Extraction

## 2.2 7 in. Summary

Table 4 shows a list of all the inspection logs requested and supervised by Blade. There were no historical 7 in. casing inspection logs run before the 7 in. casing failure. The logging program was comprehensive and intended to gather as much information about the 7 in. casing and annulus as possible; different technologies, multiple vendors, and state of the art inspection tools were employed. All the logs from and before October 10, 2017 were run through the original 7 in. casing; all the logs after November 15, 2017 were run through the 7 in. tieback casing, which was installed from surface to a depth of 939.5 ft.

Table 4: 7 in. Casing Inspection Logs

Date	Vendor	Log	Top (ft)	Bottom (ft)
April 18, 2016	TGT, Versa-line, GNPT	MID-2, MID-3	0	8,187
August 30, 2017	EV	Camera/Caliper	953	1,040
August 31, 2017	EV	Camera	887	892
October 10, 2017	EV	Camera	0	315
October 10, 2017	Baker Hughes GE	Caliper - 56 arm	0	866
November 8, 2017	EV	Camera	890	930
November 13, 2017	EV	Camera	890	930
November 27, 2017	Baker Hughes GE	Gauge/Junk Basket	939.5	7,397
November 27, 2017	Baker Hughes GE	Caliper - 56 arm	939.5	7,202

Date	Vendor	Log	Top (ft)	Bottom (ft)
December 1, 2017	Baker Hughes GE	Caliper - 56 arm	939.5	7,544
December 1, 2017	Baker Hughes GE	HRVRT	939.5	7,539
December 2, 2017	TGT, Versa-line, GNPT	MID-2, MID-3	939.5	7,537
December 3, 2017	Schlumberger	Ultrasonic Corrosion Imaging	939.5	7,553
December 4, 2017	Schlumberger	Isolation Scanner	939.5	7,546
December 4, 2017	Schlumberger	Sonic Scanner	939.5	7,546
December 7, 2017	Schlumberger	Corrosion Protection Evaluation Tool	939.5	7,535
December 10, 2017	EV	Camera	939.5	7,544

### 2.2.1 Metal Loss Summary

Figure 9 shows the metal loss features observed for the 7 in. casing for surface to 7,500 ft. The logs used were HRVRT, caliper, MID-2, MID-3, and the Isolation Scanner. The x axis is the percentage of penetration into the nominal casing wall thickness. For example, the nominal casing wall thickness for 7 in. 23 lb/ft is 0.317 in., and a 10% penetration would be a defect that extended into the wall thickness by 0.0317 in. The figure also shows the deepest defect for each joint. Most of the defects observed were less than 20%. The left graph shows 0–100% while the right graph shows 20-60%. The features annotated on the figure are discussed in detail in this section.

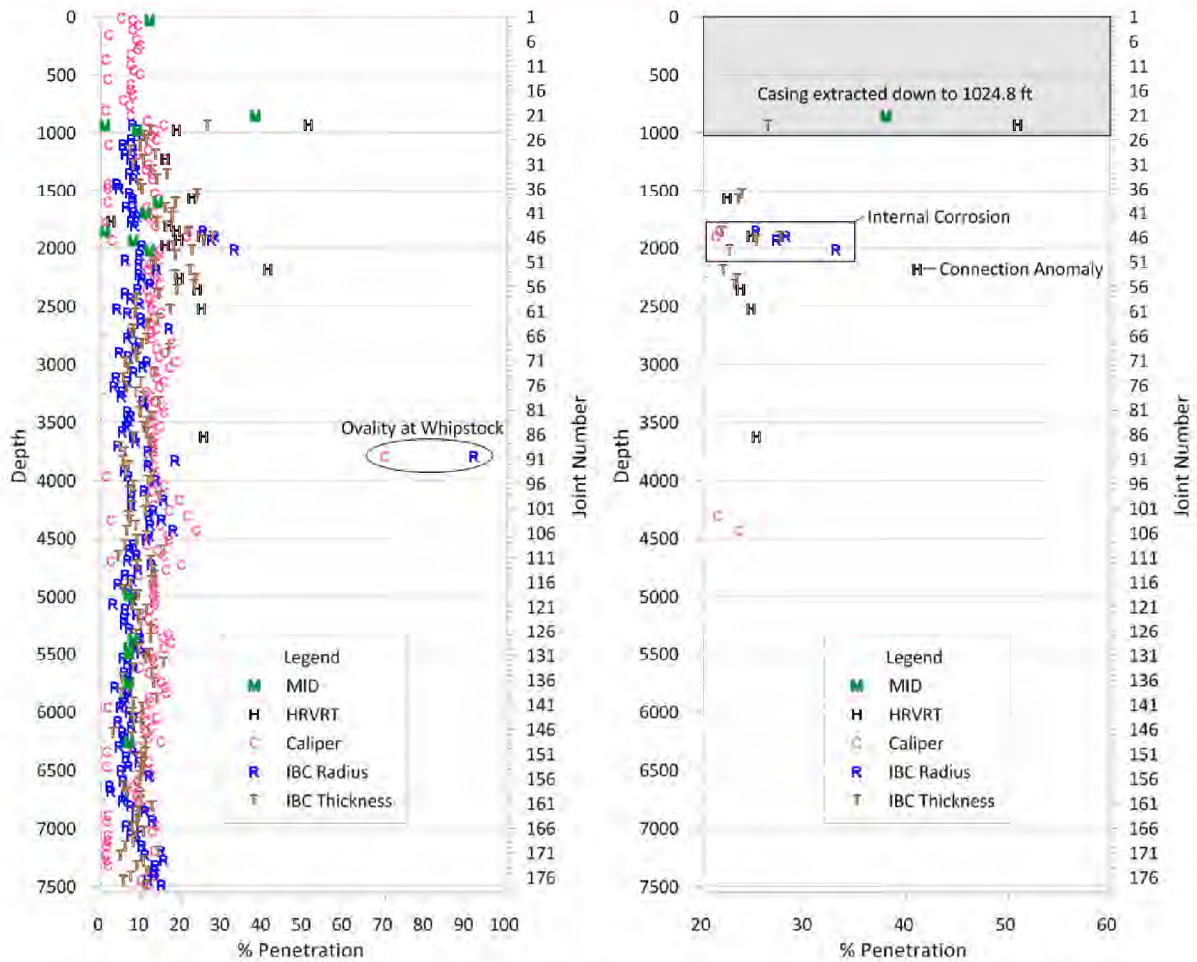


Figure 9: 7 in. Casing Defects by Depth, Joint Number, and Percent Penetration

### 2.2.2 Casing Deformation

Figure 10 shows the caliper data for the 7 in. casing from surface to 866 ft. The right track is ovalization (in black) displayed in inches and is the half of the maximum ID minus the minimum ID. The EV-Epidote software calculated ovalization using the caliper data for the 7 in. casing and, aside from the whipstock location at ~3,830 ft (Figure 11, Figure 12), found a range of ovality of 1–2%<sup>ii</sup>. The ovality in the area around the whipstock was 6%, which in our interpretation was expected.

<sup>ii</sup> To express ovalization as a percentage, take the ovalization in inches, divide it by the nominal ID, and multiply by 100 e.g. ovalization of 0.2 in. is 3.14% (0.2 in./nominal ID\*100).

### SS-25 Inspection Logs Analysis

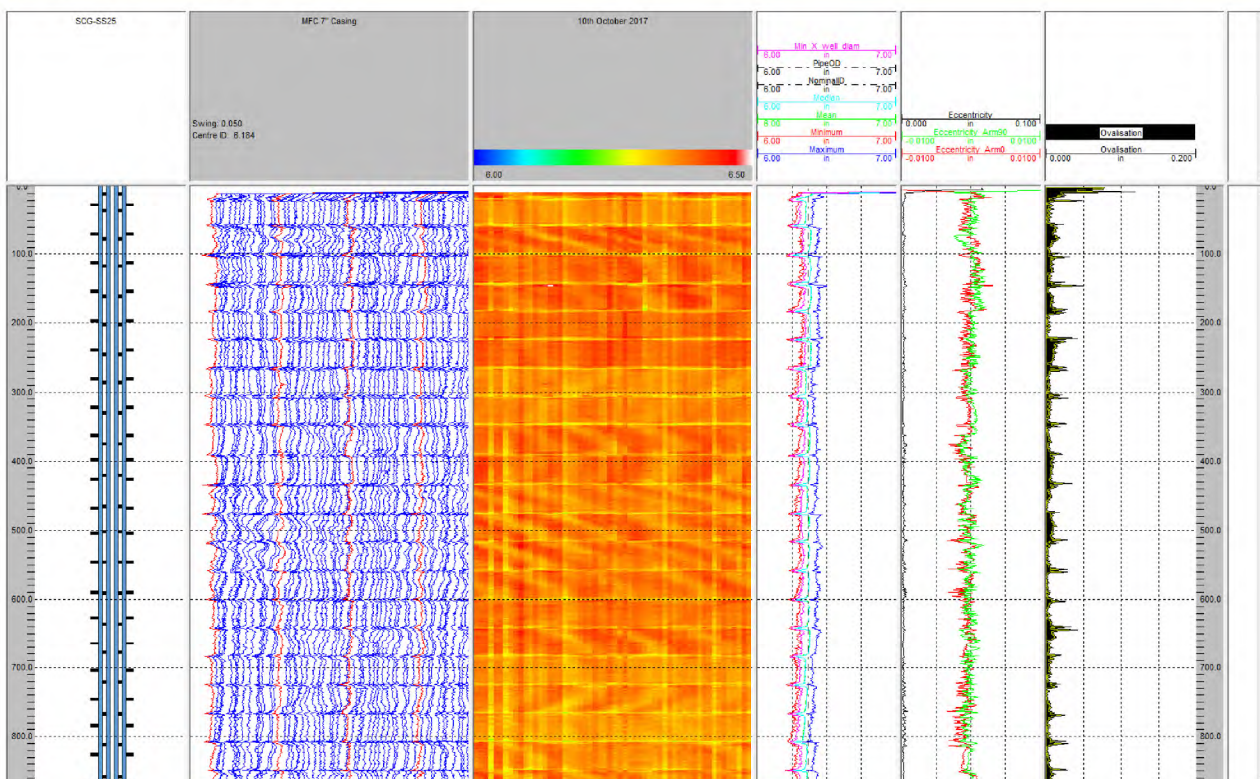


Figure 10: 7 in. Caliper Summary [7] to 866 ft

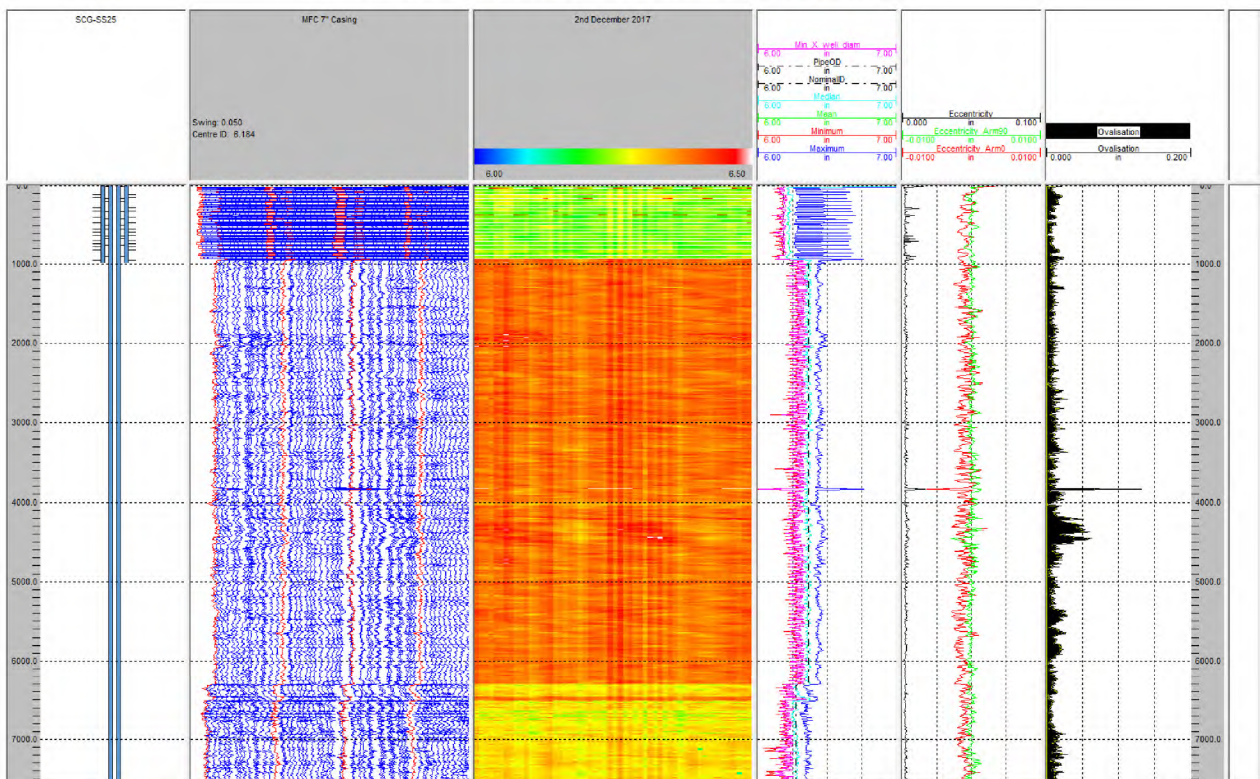


Figure 11: 7 in. Caliper Summary [7] with Tieback Installed



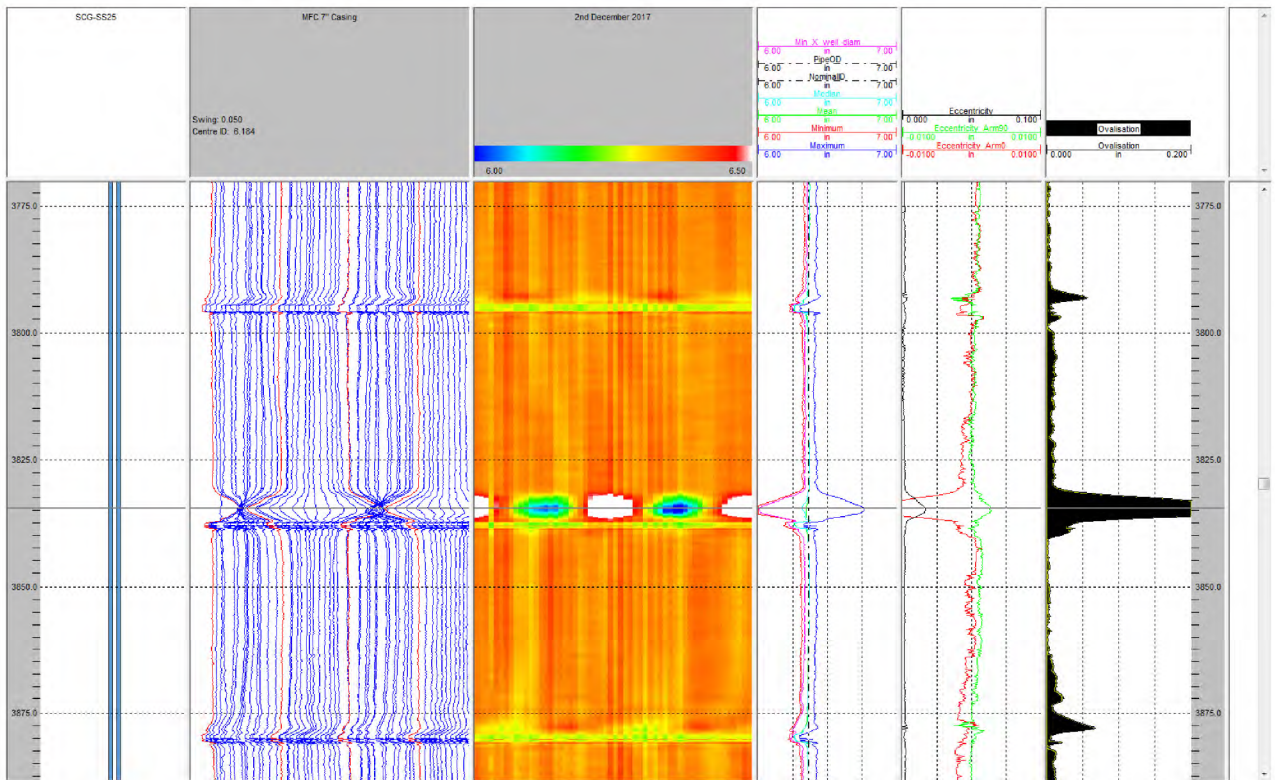


Figure 12: 7 in. Caliper Data [7] Showing Ovalization at 3,834 ft

Figure 13 shows the drilling record related to the placement of a whipstock. The bottom measurement of the whipstock was 3,860 ft. The top measurement was not reported; we assume it would have been ~3,840 ft.

OPERATOR: TIDE WATER ASSOCIATED OIL COMPANY  
 WELL NO.: Standard-Season 1-#25, Aliso Canyon Field

Page 2

1953

- 11/9 (cont.) well was producing gas at maximum rate of 1,591,000 CF/D. After 40 minutes, rate decreased to approximately 360,000 CF/D. After 55 minutes, well died. After 60 minutes, had medium to light heading blow for balance of 75 minute test. Recovered 1620' net rise of gas cut drilling mud. Pressure charts showed 1100# pressure.
- 11/10 Opened 8-1/2" hole to 10-5/8" to 4761', then drilled 8-1/2" hole from 4781' to 4796'.
- 11/11-13 Drilled 8-1/2" hole from 4796' to 4910'. Ran Schlumberger electric log to 4910'.
- 11/14 Ran Johnston formation tester on 4-1/2" drill pipe and set sidewall packers at 4787' and 4795' with perforated tailpipe to 4910'. Opened tester at 7:35 AM. Had fair, diminishing to light blow throughout one hour test. Recovered 2590' net rise; top 755' drilling mud, remainder salt water with average salinity of 373 g/g. Bottom hole pressure 1250#. Reran Schlumberger electric log to 4910'. Opened 8-1/2" hole to 10-5/8" from 4761' to 4788'.
- 11/15-16 Drilled 8-1/2" hole from 4910' to 4948'. Ran Lane-Wells Neutron Ray, Gamma Ray and sidewall sampler.
- 11/17 Hung 4-1/2" drill pipe and 97' of 2-7/8" tubing equipped with scratchers at 4948'. Pumped in 60 sacks Colton Slow cement preceded by 25 cu. ft. of water. Reciprocated and rotated pipe while displacing water and cement. Equalized cement at approximately 4830'. Time 11:30 AM. B.J. Service. Cleaned out to bottom and found no cement.
- 11/18 Hung 4-1/2" drill pipe and 97' of 2-7/8" tubing equipped with scratchers at 4948' and pumped in 60 sacks Colton Slow cement. Reciprocated and rotated pipe while displacing cement. Time 10:30 AM. B.J. Service. Found top of cement at 4830' and cleaned out to 4860'. Mud weight 74#, 33 viscosity, 3.3 c.c. water loss.
- 11/19 Ran Johnston tester on 4-1/2" drill pipe and set sidewall packers at 4715' and 4725' with perforated tailpipe to 4860'. Used 500' water cushion. Opened tester at 11:20 AM. Had light, steady blow for 5 minutes, decreasing to faint, intermittent blow throughout balance of 1 hour test. Could not pull tester loose. Jarred for 3 hours without results. Backed off left hand thread below packers and pipe rotated easily. Attempted to pull tester again but would not come loose. Rotated again and twisted off drill pipe, leaving a single, 7 doubles, drill collar and tools in hole (approximately 893' total fish). Backscuttled and recovered fresh water cushion. Ran in with fishing tool, jarred for 3 hours without results.
- 11/20 Jarred on fish for 4 hours with no results. Pulled out and laid down fishing tools. McAtear Drilling Contractor released at 10:00 AM. Moving out.
- 11/21-23 Standing idle.
- 11/24 Finished moving out rotary.
- 11/25-12/28 Idle.
- 12/29-31 Moved in and rigged up rotary.
- 1954
- 1/1 Replaced Series 600 casing flange with Series 900. Making up drill pipe.
- 1/2 Cleaned out to top of fish at 3967'. Hung 4-1/2" drill pipe at 3967' and pumped in 150 sacks Colton Slow cement, 20% sand. Time 12:00 Midnight. B.J. Service.
- 1/3 Found top of cement at 3770'. Cleaned out to solid cement at 3830'. Standing cemented. Mud weight 74#, 68 viscosity, 4.1 c.c. water loss.
- 1/4 Drilled out solid cement from 3830' to 3860'. Running Eastman "shoe horn type" whipstock. Mud weight 74#, 58 viscosity, 4.2 c.c. water loss.
- 1/5 Drilled off Eastman "shoe horn type" whipstock from 3860' to 3878' with 7-7/8" bit. Opened hole to 10-5/8" and drilled ahead to 3929'. Deviation at 3900' equals 3.5 degrees. Mud weight 73#, 65 viscosity, 4.2 c.c. water loss.

Figure 13: Drilling Record; Highlighted Section Shows the Placement of a Whipstock above 3,860 ft.

Figure 14 shows the well trajectory of SS-25. A large dogleg is located in the region of the whipstock and denoted with black boxes. We interpret the ovality observed in the 7 in. casing as being the result of the whipstock induced dogleg.

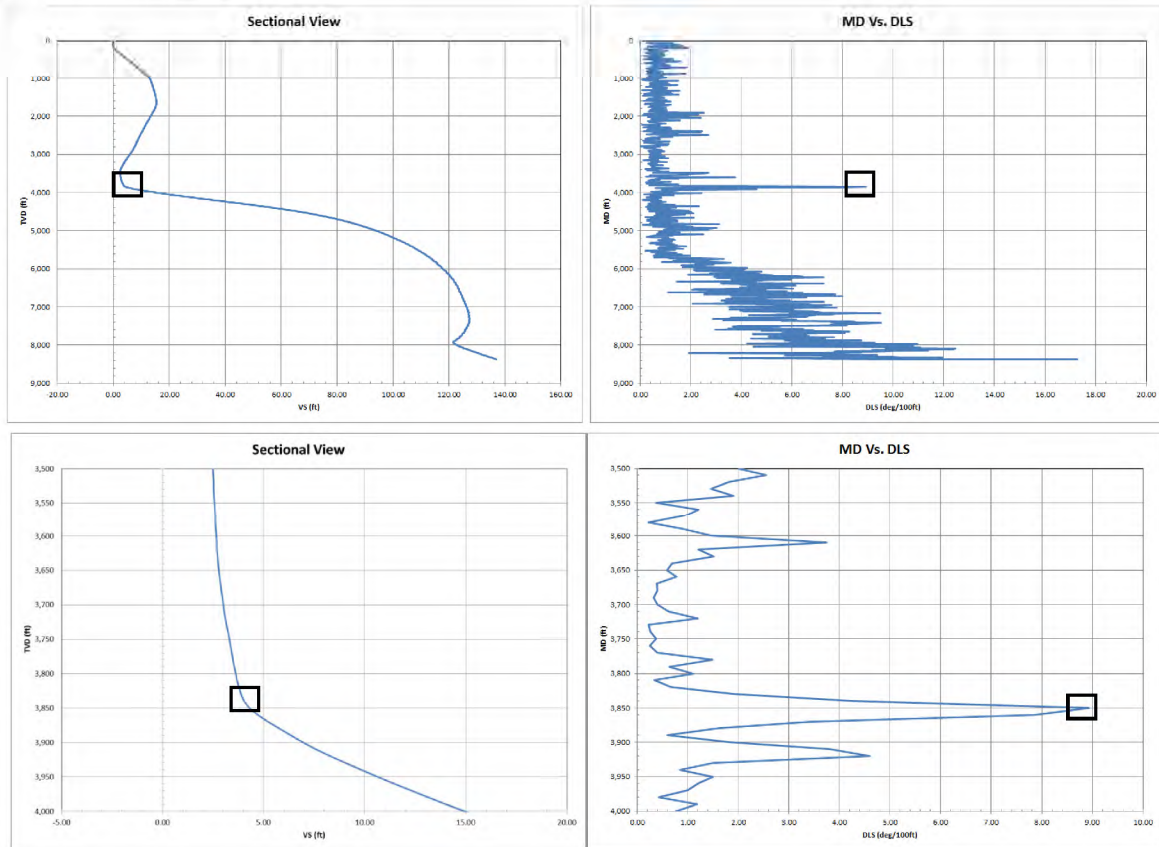
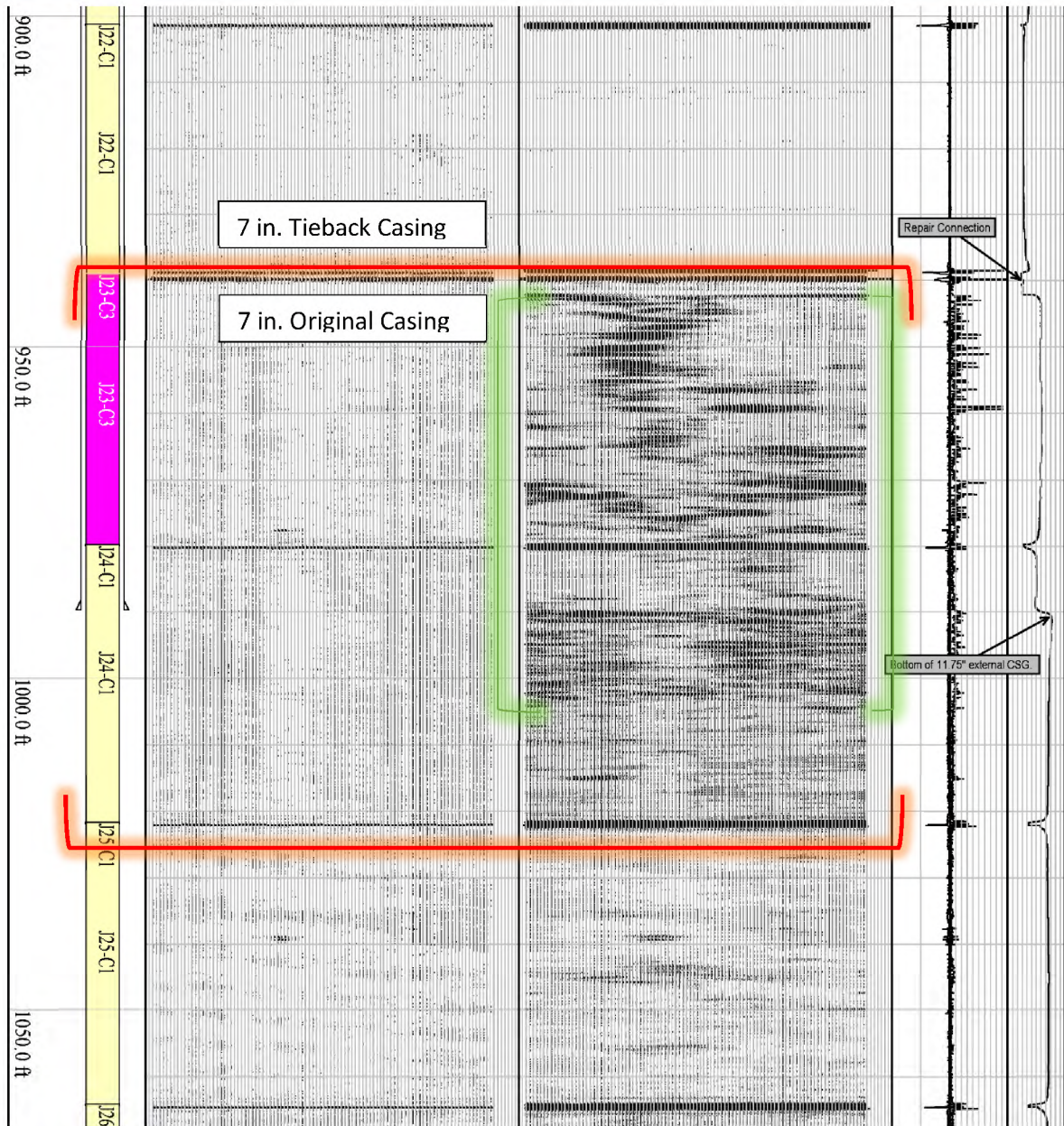


Figure 14: SS-25 Trajectory [8] (Whipstock Area in Black Box)

### 2.2.3 External Metal Loss

External metal loss was visually observed in the extracted 7 in. casing joints in November 2017. One of the key objectives of the logging operations (from late November to December 2017) was to ascertain the extent and severity of the external metal loss in the casing that remained in the well. Figure 15 shows the HRVRT log for the depths 900 ft–1,060 ft. The annotation “Repair Connection” is a reference to the casing patch (also known as overshot). Its location marks the bottom of the 7 in. 29 lb/ft tieback casing and the beginning of the original 7 in. 23 lb/ft casing. The 11 3/4 in. surface casing shoe was observed at 990 ft. The green brackets delimit a region of extensive external metal loss between 939 and 1,015 ft. The 7 in. external corrosion extends 25 ft below the 11 3/4 in. surface casing shoe.



**Figure 15: 7 in. HRVRT Log [9], December 2, 2017, External Corrosion at 939–1,015 ft - Green Bracket, Extracted August 8, 2018 – Red Bracket**

External corrosion in the 7 in. casing was also present in other locations. Figure 16 shows the location and dimensions of all the HRVRT external metal loss features that exceeded 15% penetration for the 7 in. casing between 939 and 7,500 ft. The depth vs. occurrence graphic and the inset table show an extensive external corrosion clustered above 1,000 ft.

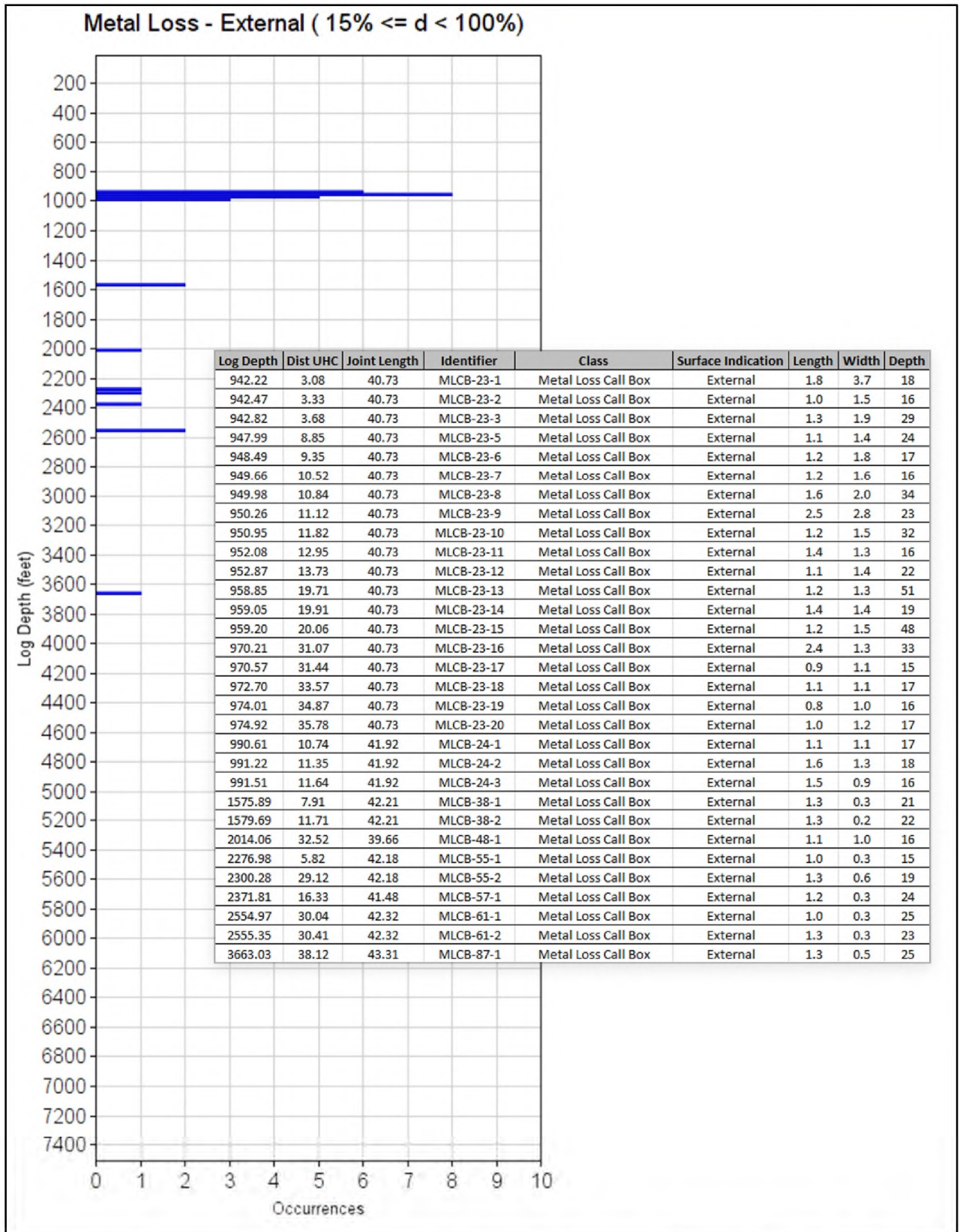
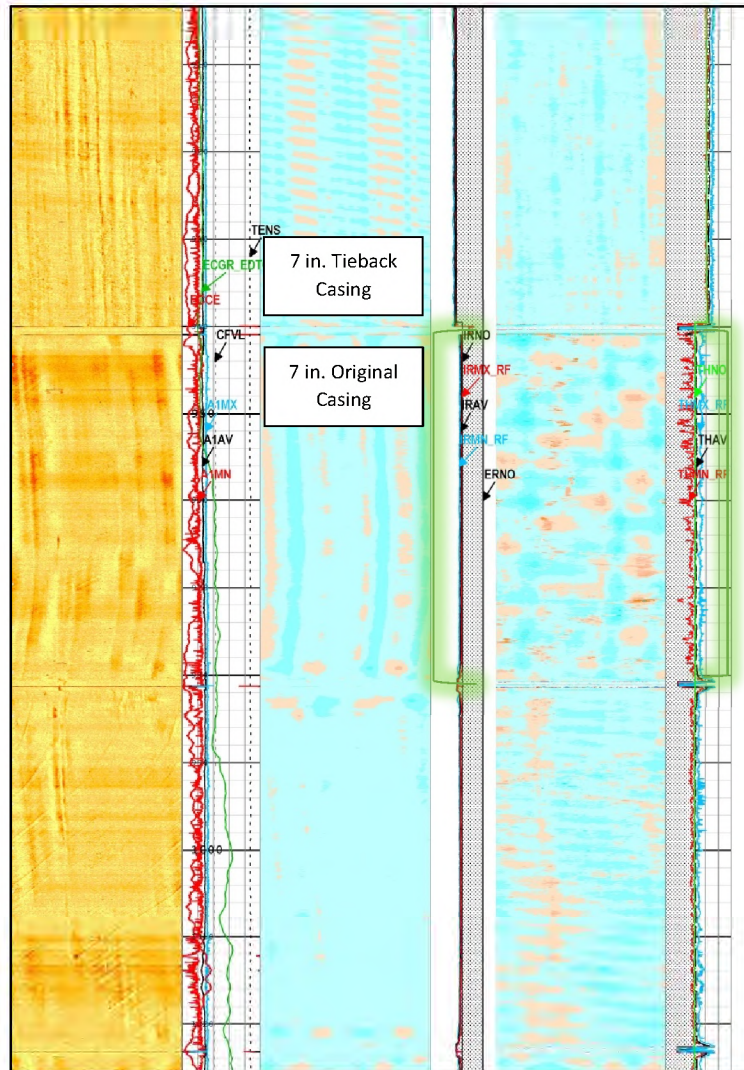


Figure 16: 7 in. Summary of External Metal Loss by HRVRT [9]; Extracted Top 1,024 ft

Figure 17 shows the UCI log at a depth range similar to Figure 15’s HRVRT log. The UCI log shows the same pattern of external corrosion on the joint beginning at 939 ft, like the HRVRT, but does not show the external corrosion on the joint beginning at 982 ft. In general, the ultrasonic logs (namely, UCI and IBC) agree very well with the HRVRT log in terms of position and severity of metal loss features.



**Figure 17: 7 in. UCI Log [10], December 2, 2017, External Corrosion at 939–980 ft - Green Bracket**

Two reports [1] [2] detail the severity, location, and type of corrosion observed in the extracted joints. Figure 18 shows just the 7 in. casing joint C026 observed by the HRVRT log (on the left) and Laser Scan (on the right). The HRVRT log was in situ; the Laser Scan data was acquired post-extraction. We observed a positive correlation in location and severity of features. One of the Laser Scan features at a depth of 1,006.5 ft approaches 40% penetration; this is a Cased Hole Dynamics Tester (CHDT) plug and was not present during the HRVRT logging.

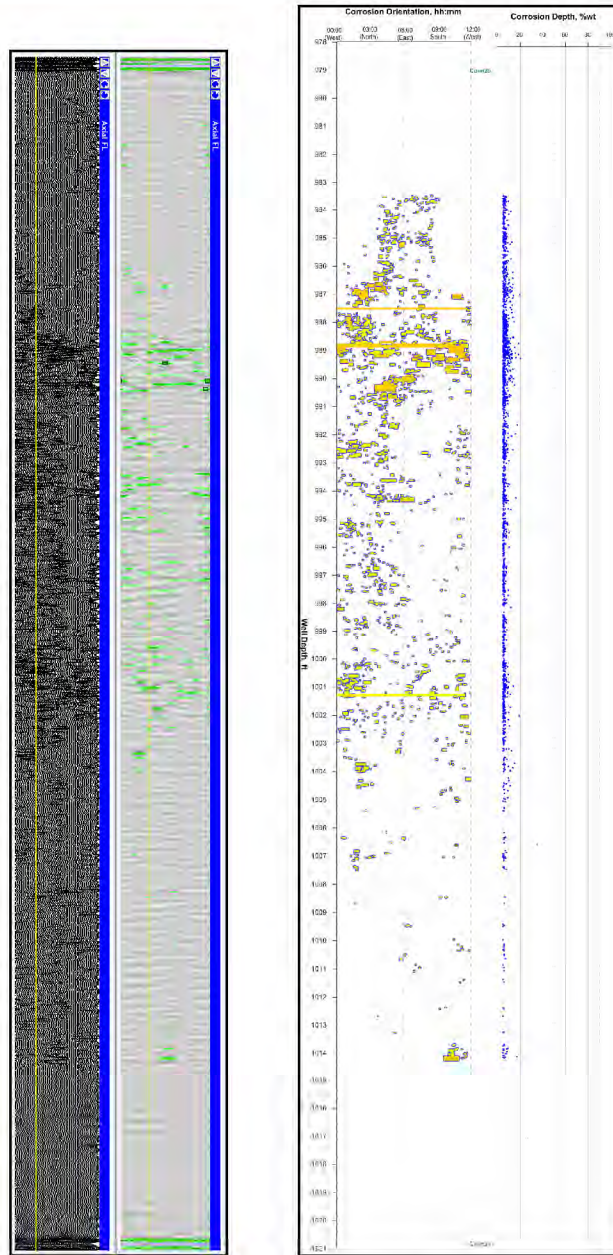


Figure 18: 7 in. Casing Joint 26, HRVRT [9] Flux Leakage Tracks (left), Laser Scan (right)

### 2.2.4 Internal Metal Loss

Figure 19 shows the location and listing of the 61 internal metal loss features observed in the HRVRT log. The range of penetration was 15–41%. Most of the defects (56 out of 61) were concentrated in a 200 ft zone centered at ~1,900 ft. For this zone, there is good agreement between the HRVRT, caliper, and Ultrasonic logs in regards to penetration; the range was 16–28%. Other areas of internal corrosion were present but isolated (not clustered), infrequent, and of low penetration. One notable exception was the internal defect at 2,228.5 ft—the HRVRT log found that it had a penetration of 41%. This defect was observed neither in the caliper, UCI, and IBC logs nor in the video imaging.

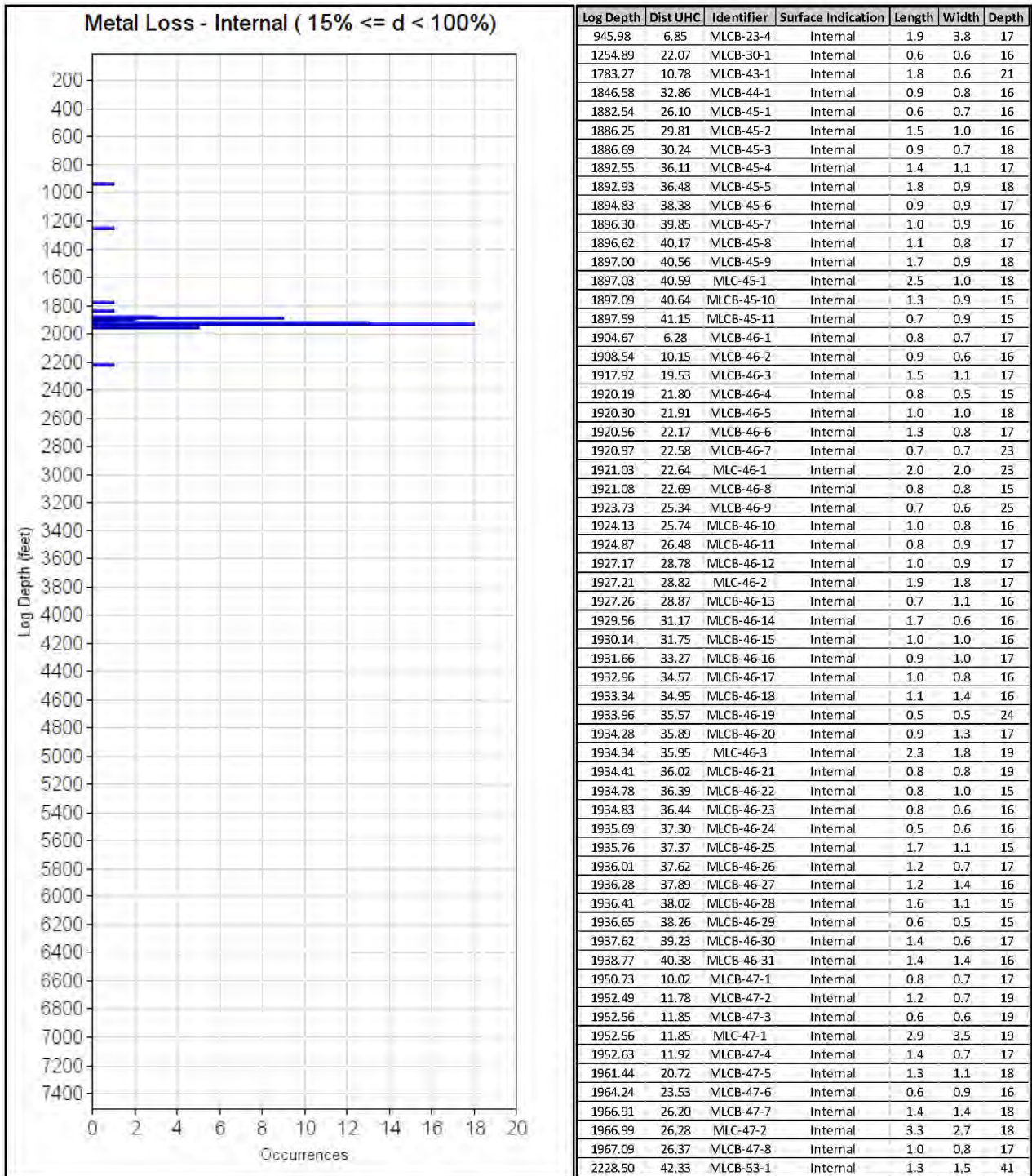


Figure 19: 7 in. HRVRT [9] Summary of Internal Corrosion

Figure 20 shows the 7 in. casing joints—the worst three joints with internal metal loss found by the caliper log at the depths of 1,840–2,010 ft. The graphic shows that the defects were clustered and vertically oriented on or about the same clock position. Figure 21 shows HRVRT log with the same depth range of Figure 20. The ultrasonic logs are not shown here, but the caliper, HRVRT, and ultrasonic logs all show the same pattern of internal metal loss.



### SS-25 Inspection Logs Analysis

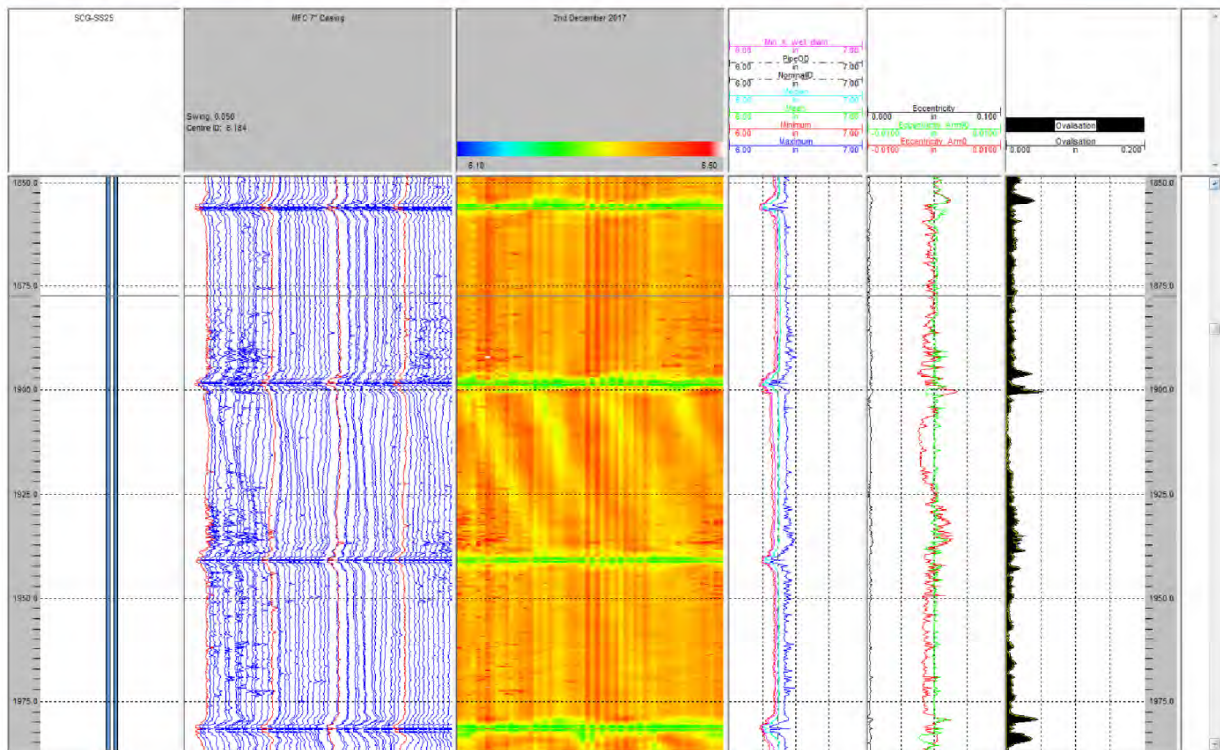


Figure 20: 7 in. Caliper Log [7] Showing Internal Corrosion at 1,850–1,985 ft

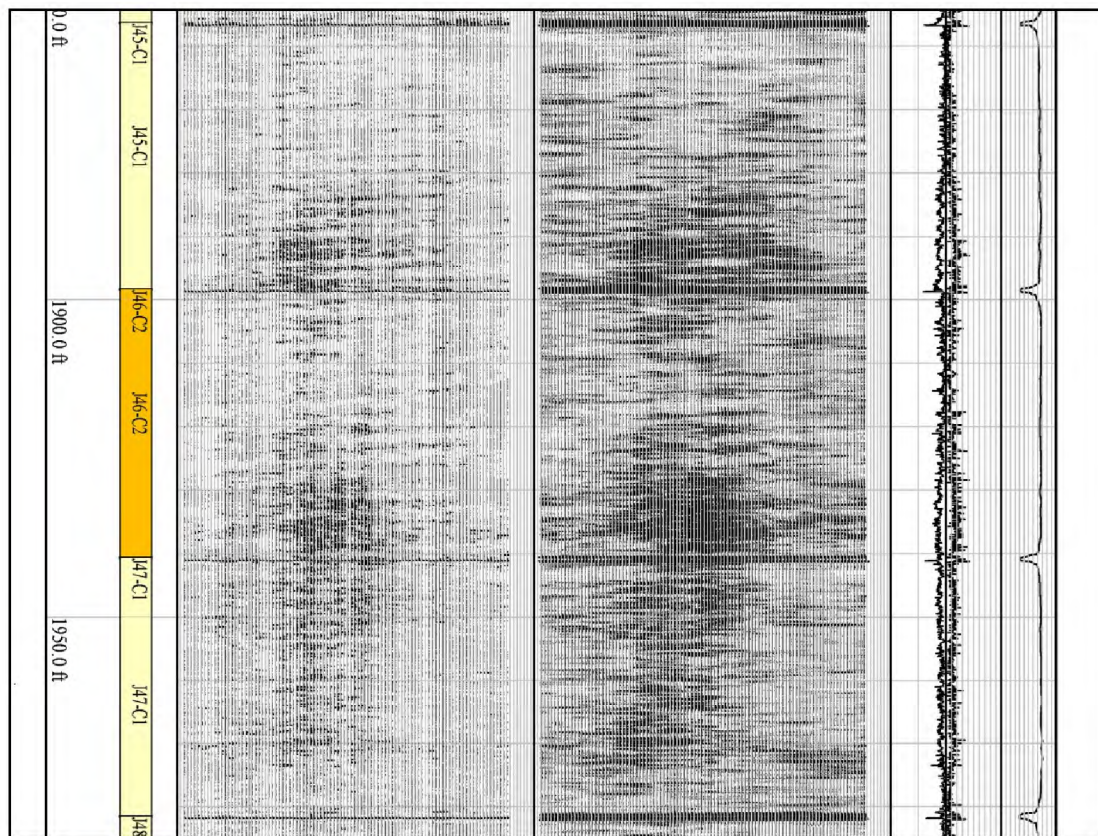


Figure 21: 7 in. HRVRT [9] Log Showing Internal Corrosion at 1,850–1,985 ft

Figure 22 shows the well record for SS-25 with the entry for March 18, 1954 highlighted in yellow. During its life as an oil and gas producer (prior to SoCalGas injection and withdrawal operations), SS-25 had a tubing and packer completion with five gas-lift mandrels. Gas lift is one form of artificial lift that uses an external source of gas to reduce the density of the produced fluids so as to encourage the well to flow. Compressed gas was injected down the annulus and exited through the gas-lift mandrels into the tubing. Each gas-lift mandrel was set to open and close at different pressures. Gas entered the uppermost valve first—in SS-25 it was at 1,965 ft. Typically, the gas that is injected is the same gas that is produced with the oil; we did not find data to confirm this. We presume that the 7 in. casing below the first gas-lift mandrel would have been liquid-filled and, along with the injection gas, the area would have been conducive to corrosion. We interpreted the internal corrosion shown in Figure 19, Figure 20, and Figure 21 to be related to the gas-lift mandrel at 1,965 ft when SS-25 was producing oil with gas lift.

OPERATOR: TIDE WATER ASSOCIATED OIL COMPANY

Page 6

WELL NO.: Standard-Session 1-#25, Aliso Canyon Field

1954

3/9

In 8 hours well flowed on gas lift 29 barrels gross fluid, 29 barrels approximate net oil, 0.1% cut, 21.2 gravity, 16/64" bean, 680# tubing pressure, 1250# casing pressure, 0 MCF gas.

3/10

Shut in. 1300# tubing pressure; 1300# casing pressure.

3/11

Shut in. Let off tubing pressure but well would not flow. 100# tubing pressure; 1400# casing pressure.

3/12

In 8 hours well flowed 76 barrels gross fluid, approximately 74 barrels net oil, 3.0% cut, 21.0 gravity, 16/64" bean, 200# tubing pressure, 1400# casing pressure. Bleeding off pressures. Preparing to install gas flow valves.

3/13

Bleeding off pressure. 200# tubing pressure; 1400# casing pressure.

3/14

Bleeding off pressure. 150# tubing pressure; 700# casing pressure.

3/15

Bleeding off pressure. 200# tubing pressure; 0# casing pressure.

3/16

Bled off pressure and filled hole with dead oil. Will move in mast if weather permits.

3/17

California Production Service moving in with mast.

3/18

Pulled tubing. Ran 7" Guiberson KV-30 wall packer and set at 8525' with 14,000#; included are five Guiberson gas lift flow valves as follows: 1000# valve - 1965'; 975# valve - 3835'; 950# valve - 5504'; 925# valve - 6973'; 900# valve - 8271' (no ball and check on this valve). Above depths are from tubing head.

3/19

Hooked up tree and began injecting gas. In 15 hours well flowed on gas lift as follows:

	Gross	Net	Cut	Gravity	Bean	Tubing Pressure	Casing Pressure	MCF Gas Inj	Net
	211 gross fluid, of which 171 barrels is formation oil, 166 barrels net oil, cut 3.0%, 50# tubing pressure, 300# casing pressure, 20.3 gravity, 153 MCF injected gas, 47 MCF net.								
3/20	238	232	2.6%	20.3	32/64	100#	700#	217	89
3/21	103	103	0.3%	20.7	32/64	200#	750#	49	88
	Off 13 hours - gas injection line froze.								
	Injection line frozen 3-1/2 hours.								
3/22	190	190	0.2%	21.0	32/64	360#	750#	220	79
3/23	146	143	2.0%	20.6	32/64	140#	750#	211	109
3/24	152	151	0.4%	20.5	32/64	100#	940#	207	109
3/25	130	130	0.2%	20.5	32/64	250#	900#	232	68
	Off 4-1/2 hours - gas injection line frozen.								
3/26	166	166	0.2%	20.5	32/64	250#	900#	232	68
3/27	130	130	0.2%	20.5	32/64	250#	900#	220	118
3/28	119	119	0.2%	20.5	32/64	250#	900#	187	56
	Off 4 hours - gas injection line frozen.								
3/29	70	70	0.3%	20.8	14/64	250#	900#	61	65
	Off 11 hours - gas injection line frozen.								
3/30	95	95	0.3%	20.8	14/64	250#	900#	92	78
3/31	74	74	0.3%	20.8	14/64	250#	900#	115	97
4/1	71	70	0.8%	20.8	14/64	250#	900#	87	53
4/2	97	97	0.8%	20.8	14/64	250#	900#	92	78
4/3	38	38	0.8%	20.8	14/64	250#	900#	150	73

12

AC\_CPUC\_000034

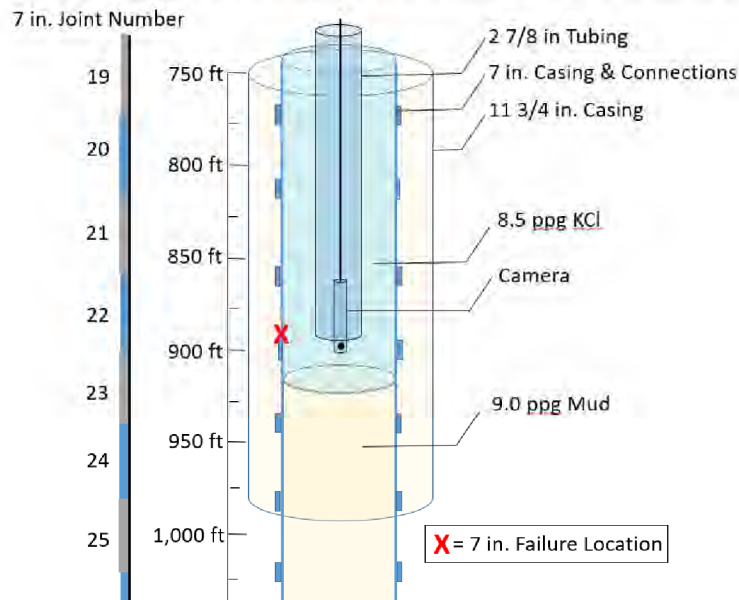
Figure 22: Gas-lift Mandrel at 1,965 ft Related to Internal Corrosion

### 2.2.5 Downhole Visual Observations

Appendix B shows the 7 in. casing pictures taken by EV Camera under Blade’s direction and supervision on August 31, October 10, and December 10–13, 2017. The operational details for each date are provided below.

#### August 31, 2017

Blade observed an occasional low-magnitude but a sharp increase in tension (i.e., overpull) on the string weight indicator during the extraction of the 2 7/8 in. tubing. The overpull was spaced roughly in 31 ft increments. Some of the tubing connections were observed to have a 1/2 to 1 in. area of shallow deformation at the bevel on the upper side of the connection. Blade interpreted this as a probable full circumferential parting of the 7 in. casing and that the tubing connections were momentarily hung up as they passed through the parted area. This needed to be confirmed because it had major implications on further operations, so the tubing extraction was stopped when the base of the tubing reached 953 ft. Baker Hughes wireline was rigged up and used to run the video camera through the tubing and out into the 7 in. casing. Figure 23 shows a schematic of the well configuration for the video imaging work. With the video camera positioned at the end of tubing, the tubing was slowly raised concurrent with pumping clear 8.5 ppg KCl fluid while the ID of the 7 in. casing was observed with the camera.



**Figure 23: Well Configuration for Through-Tubing Camera Run to View 7 in. Failure Area**

Table 5 shows the operations summary for August 31, 2017. Note that the depth of the 7 in. casing failure was revised after the extraction of the 7 in. casing and did not match the MID log or camera depths. There was only one 7 in. casing failure—at 892 ft—based on pipe length measurements.

**Table 5: Operations Summary for August 31, 2017**

Date	Report No.	Depth (ft)	Operations Summary
August 31, 2017	32	7,555	Pull and LD 1 jt 2-7/8" tubing and transfer to PS-20. RU Baker WL, Ran camera to EOT and investigate area from 892-888' while slowly pumping brine down tubing. Found 7" casing parted at ~887.5 ft (wireline measured depth).

Figure 24, Figure 25, and Figure 26 show the 7 in. casing failure as seen by the video imaging of August 31, 2017. The 7 in. casing was found to have completely parted at 892 ft near the base of joint number 22. The distance between the upper and lower parted sections was approximately 5 in. Additional images of the 7 in. casing failure can be found in Appendix B.

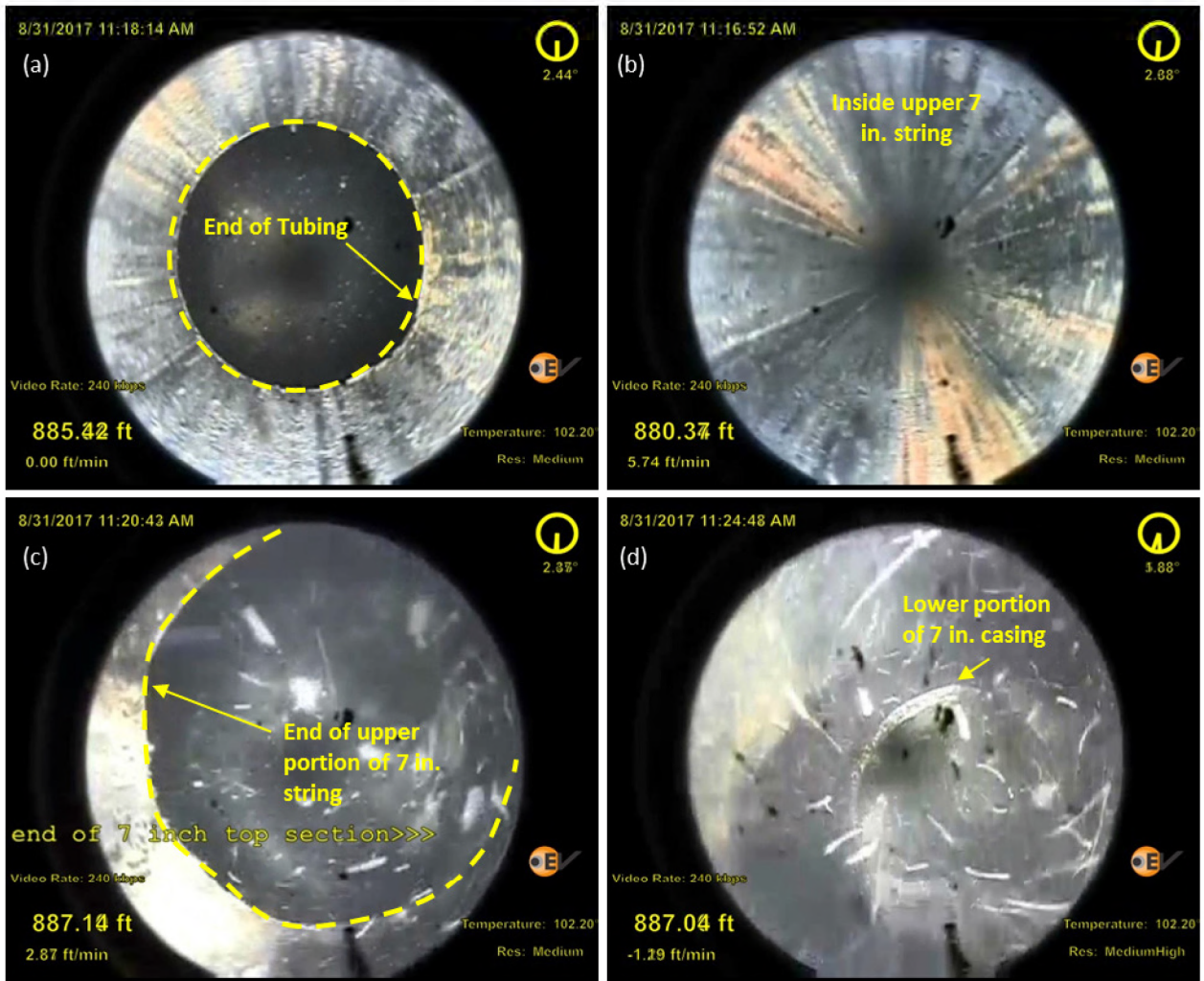


Figure 24: Video Imaging from August 31, 2017, Parted 7 in. Casing

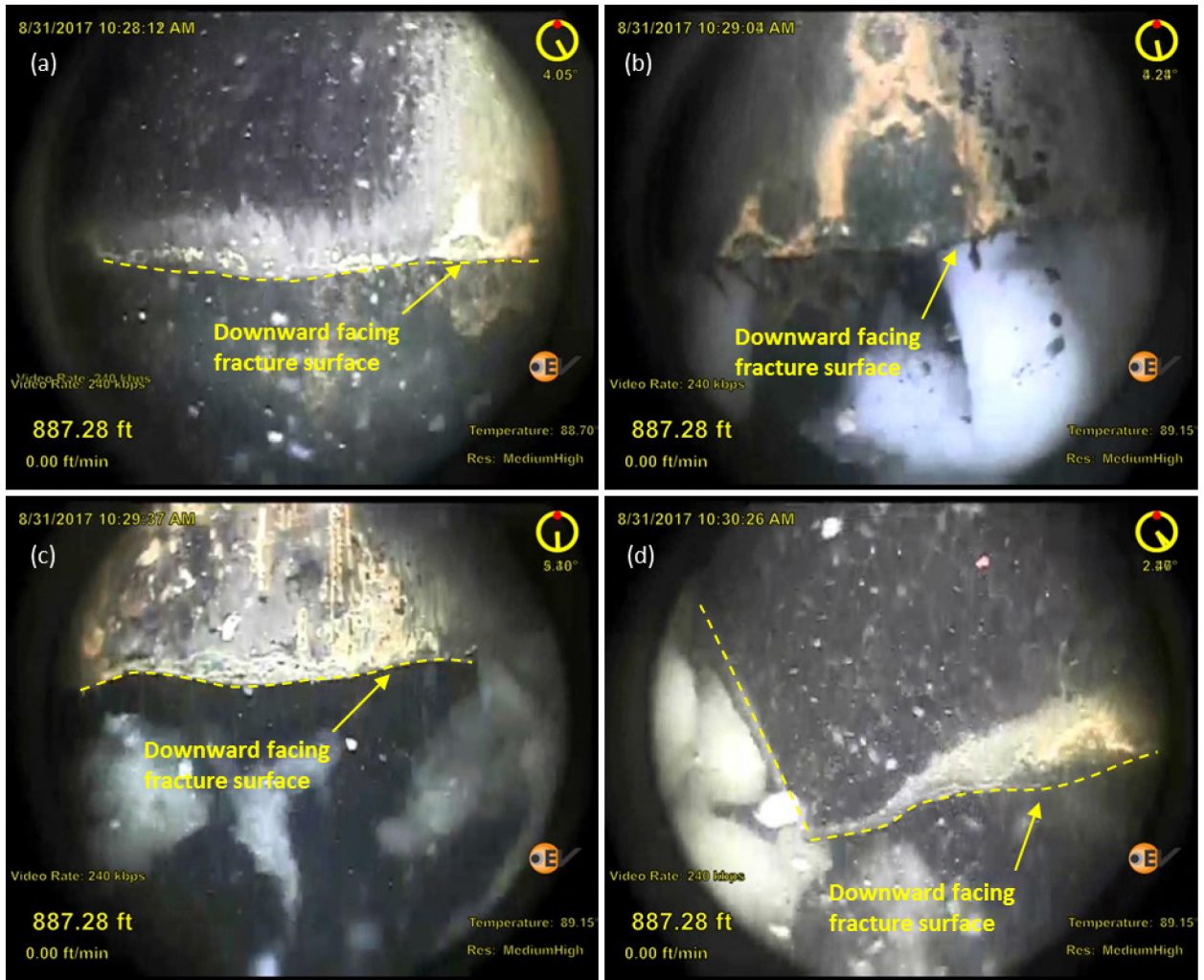


Figure 25: Video Imaging from August 31, 2017, Parted 7 in. Casing (Upper Portion)

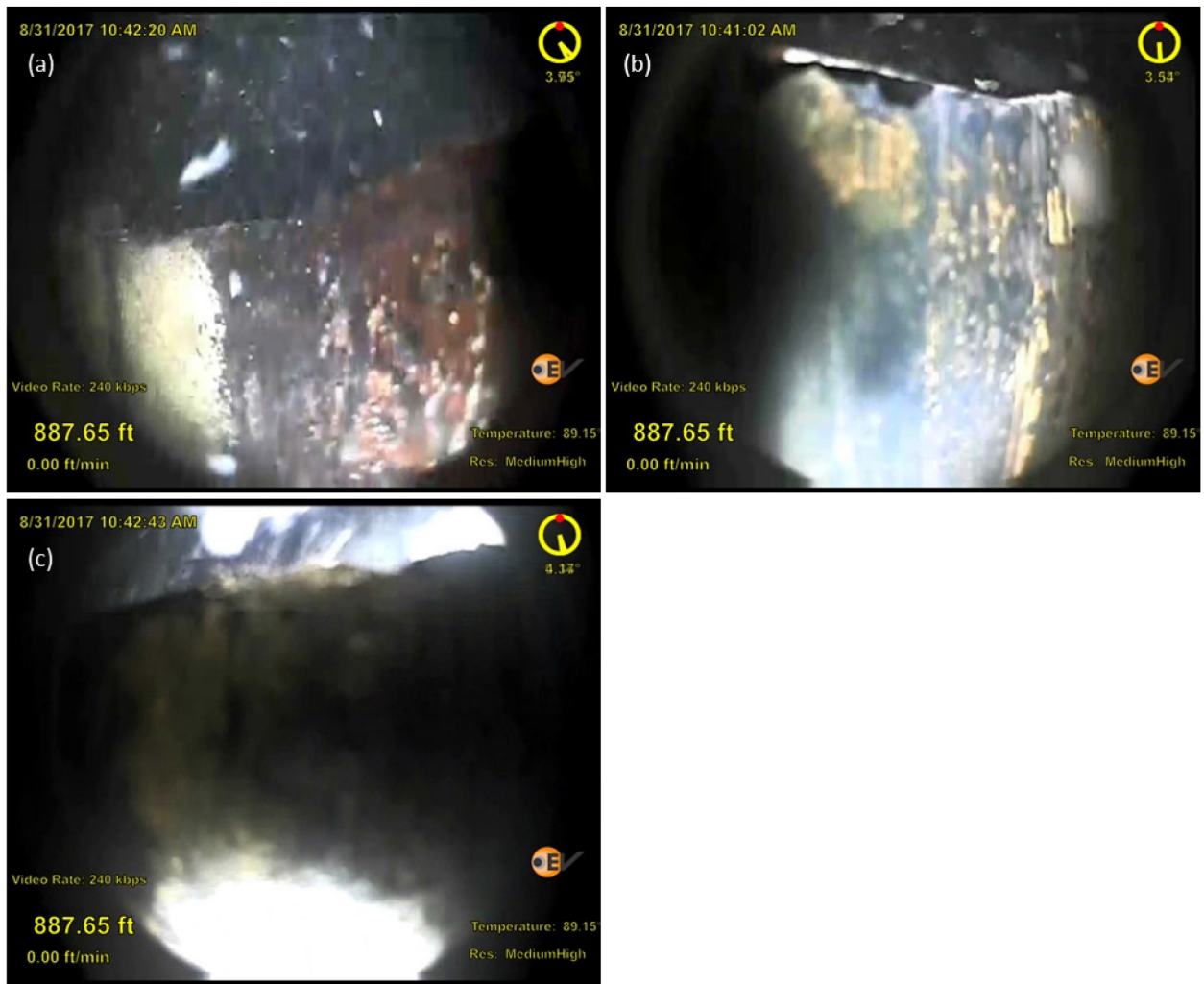


Figure 26: Video Imaging from August 31, 2017, Parted 7 in. Casing (Lower Portion)

### October 10, 2017

Following the 2 7/8 in. tubing extraction, a downhole video camera was run in the 7 in. casing from surface down to the fluid level, which was observed at 322 ft. The purpose of the inspection was to evaluate the condition of the ID of the 7 in. casing and select a depth for setting a retrievable bridge plug (RBP). The camera was run according to Phase 3A Contingency Work Plan [5].

Table 6 shows the operations summary for the October 10, 2017 camera work. In general, the internal surface was covered with a thin layer of oil and debris. No defects were observed. An area for the RBP was selected at ~200 ft.

**Table 6: Operations Summary for October 10, 2017**

Date	Report No.	Depth (ft)	Operations Summary
October 10, 2017	72	200	RU Baker WL. RIH inspecting 7" ID with EV camera to top of fluid at 322' WLM. Ran Baker caliper log from 865'. RIH with WFord RBP on 2-7/8" WS and set at 200'.

## December 10–13, 2017

The objective of our Dec 10–13, 2017 camera work was to add visual information to the previously acquired logging data. The original 7 in. casing (including the failed joint) had been recovered at a depth of 939 ft and replaced by a 7 in. new tieback casing. The depth coverage of the camera work was 939–7,530 ft. The Areas of Interest (AOI) were areas of internal metal loss, the 7 in. casing connections, and the general surface condition. The camera was run according to Phase 3A Contingency Work Plan [5]. Table 7 shows the operational summary for those days. The language is verbatim from the original table [11].

**Table 7: Operations Summary for December 10–13, 2017**

Date	Report No.	Depth (ft)	Operations Summary
December 10, 2017	133	7,555	Cont filtering fluid. Final NTU = 935. RD Baker and POOH to 3983 ft. RU Baker WL. RIH with EV Camera thru tubing to 4007' - lost communication. POOH
December 11, 2017	134	7,555	RIH with EV Camera thru tubing (tail at 3896 ft). Inspect each connection from 4008 to 4304 ft. Side view camera failed. POOH. Change out camera motor and RIH. Cont inspecting each connection from 4304 to 5027 ft. Inspect 7" to 7544 ft. POOH.
December 12, 2017	135	7,555	RU Baker DE filters. Reverse circ/filter fluid from 4011 ft. Final NTU = 2. POOH to 1739 ft. RIH with EV Camera. Inspect each connection from 1730 to 4006 ft. POOH
December 13, 2017	136	7,555	RU Baker DE filters. Reverse circ/filter fluid from 1770 ft. Final NTU = 1. POOH to surface. RIH with EV Camera. Inspect each connection from 1730 to surface. RD Baker and EV.

The fluid clarity was mostly good but at times poor, which may have obscured some features; even with poor clarity, we were able to observe over 60 connections. There were minor defects that appeared to be small pits or gouges near some connections; the most common location of the defects was where the pin nose met the box. No visible threads were observed. There were no indications of a connection leak (e.g., washout or erosion). The surface condition was generally good and agreed well with the logging data. Figure 27 shows an example of a 7 in. connection as captured by video imaging—connection 177 at 7,488.1 ft. This connection is a representative example because it shows small gouges, no visible threads, and no indication of a leak. The lower portion of the figure shows a portion the caliper log for the same connection. The connections were slightly smaller in diameter than the pipe body. The mean pipe ID for joint 177 was 6.282 in. while the mean ID at the connection was 6.208 in.—a difference of 0.074 in. We interpreted that the connections defects were, in most cases, gouges at the connections related to the passage of bits, mills, scrapers, packers, and other tools.



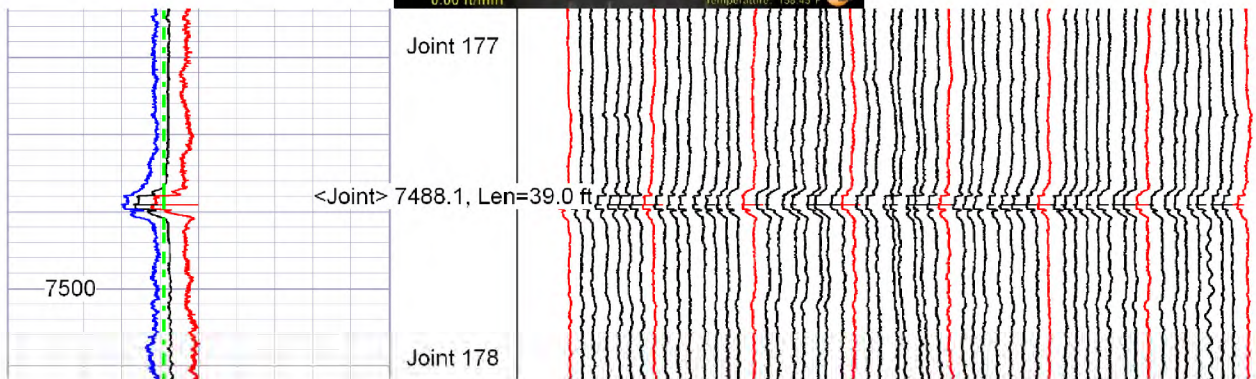
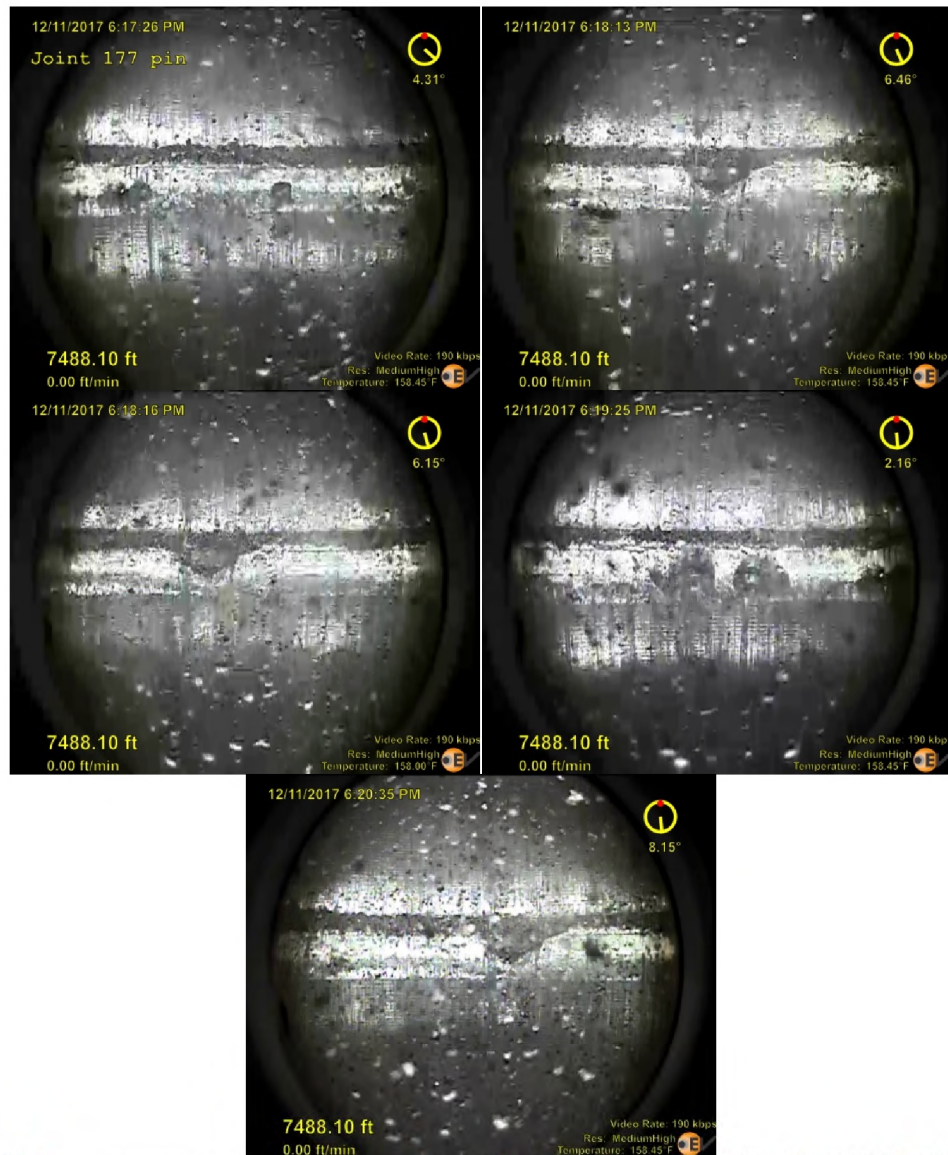


Figure 27: December 11, 2017 EV Camera (Images Above) and December 2 Caliper Log (Bottom), 7 in. Casing Connection 177 at 7,488.1 ft, Minor Gouges

Figure 28 shows our count of the trips through the 7 in. casing with drillpipe or tubing based on the well records provided by SoCalGas [12]. There were 19 trips, lending support to our interpretation that, in most cases, the connections defects were gouges related to the passage of bits, mills, scrapers, packers, and other tools.

SS-25 Summary of DP and tubing trips in the 7" OD production casing					
Date	Date	No. Trips	Trip Depth (ft)	Pipe OD (in.)	Trip Description
2/11/1954		0.5	8,584	3.5	Tag cement. CO cement to 8584'.
2/11/1954		0.5	8,584	3.5	POH.
2/12/1954		0.5	8,522	3.5	RIH WSO tester.
2/12/1954		0.5	8,522	3.5	POH WSO tester.
2/12/1954		0.5	8,534	3.5	RIH WSO tester.
2/12/1954		0.5	8,534	3.5	POH WSO tester.
2/12/1954		0.5	8,584	3.5	RIH with 6" bit.
2/13/1954		0.5	8,634	3.5	Drill to 8634'. POH.
2/15/1954		0.5	8,585	3.5	RIH and set 5-1/2" liner.
2/15/1954		0.5	8,585	3.5	POH.
2/16/1954		0.5	8,540	2.875	RIH with tubing.
3/18/1954		0.5	8,540	2.875	POH with tubing.
3/18/1954		0.5	8,525	2.875	RIH with tubing and packer.
5/25/1973		0.5	8,525	2.875	POH wth tubing and packer.
5/25/1973		0.5	8,748	2.875	RIH with 4-5/8" bit and scraper.
5/26/1973		0.5	8,748	2.875	POH with 4-5/8" bit and scraper.
5/29/1973		0.5	8,525	2.875	RIH with test packer.
5/29/1973		0.5	8,525	2.875	POH with test packer.
5/29/1973		0.5	8,550	2.875	RIH and set BP.
5/29/1973		0.5	8,550	2.875	POH.
5/30/1973		0.5	8,487	2.875	RIH with tester.
5/31/1973		0.5	8,487	2.875	POH with tester.
5/31/1973		0.5	8,550	2.875	RIH with retrieving tool.
5/31/1973		0.5	8,550	2.875	POH with BP and set at 4975'. POH.
6/4/1973		0.5	4,975	2.875	RIH with retrieving tool.
6/4/1973		0.5	4,975	2.875	POH with BP.
6/5/1973		0.5	8,492	2.875	RIH with packer and tubing.
7/1/1976		0.5	8,492	2.875	POH with packer and tubing.
7/1/1976		0.5	8,748	2.875	RIH with 4-5/8" bit and scraper.
7/1/1976		0.5	8,748	2.875	POH with 4-5/8" bit and scraper.
7/3/1976		0.5	8,559	2.875	RIH with 6" mill and scraper.
7/3/1976		0.5	8,559	2.875	POH with 6" mill and scraper.
7/7/1976		0.5	8,480	2.875	RIH with tubing.
2/17/1979		0.5	8,480	2.875	POH with tubing.
2/17/1979		0.5	8,480	2.875	RIH with seals.
2/19/1979		0.5	8,480	2.875	POH with seals.
2/19/1979		0.5	8,480	2.875	RIH with completion.
8/22/2017	9/1/2017	0.5	7,555	2.875	POH and LD tubing for RCA.
		19	317,021	Totals	

Figure 28: Historical Count [13] of the Number of Trips Through the 7 in. Casing, 19 Trips

As discussed in Section 2.2.4, most of the internal defects (56 out of 61) were concentrated in a 200 ft zone centered about 1,900 ft. Video imaging also observed these defects. Figure 29 shows 35 snapshots for 1,818–1,775 ft. We interpreted these defects as being corrosion pitting.

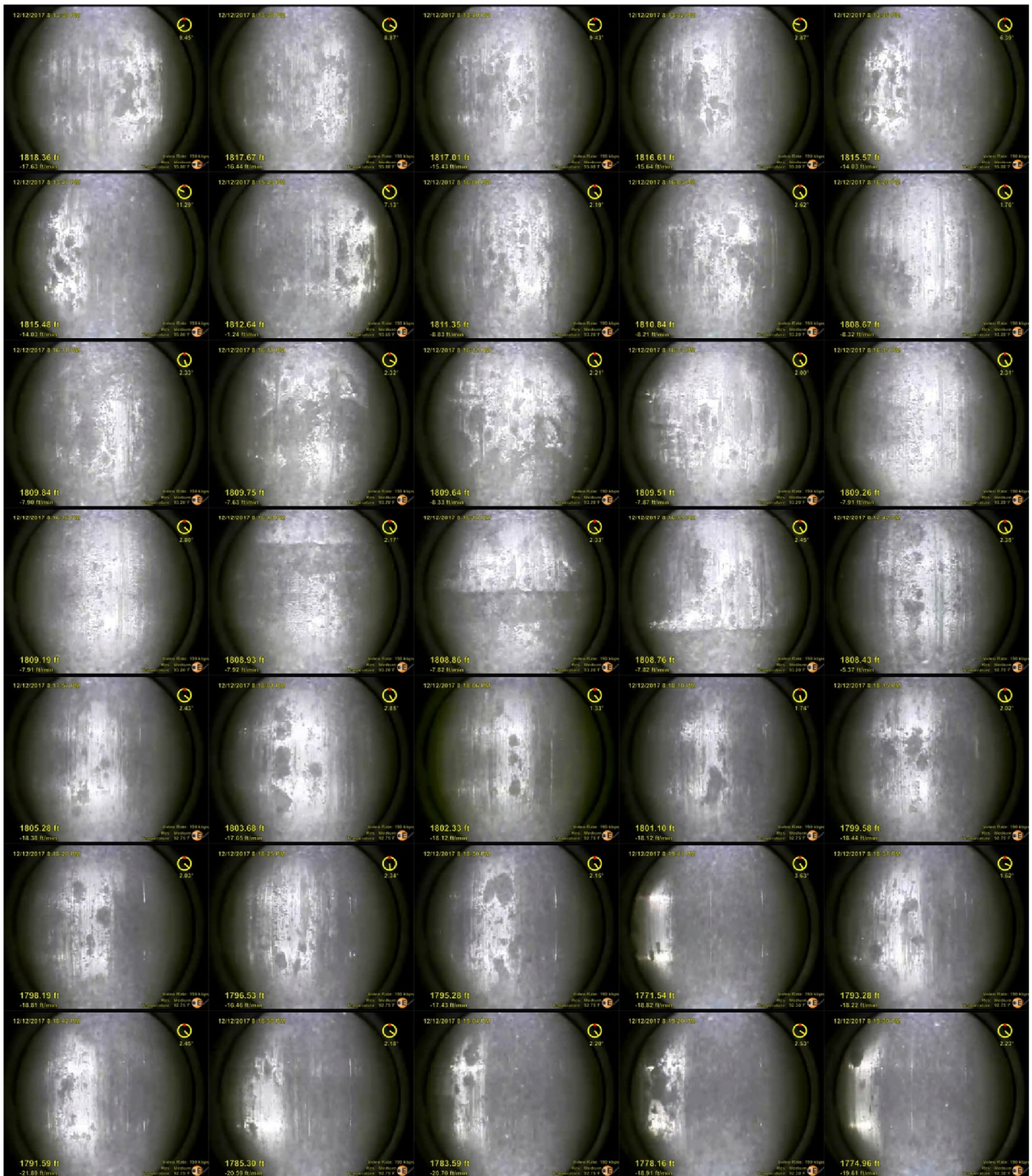


Figure 29: December 12, 2017, EV Camera, Example of Internal Corrosion on 7 in. Casing for 1,818–1,775

### 2.2.6 Annulus Condition

Figure 30 shows the Isolation Scanner log for 6,940–7,030 ft. Schlumberger interpreted that the cement top in the 7 in. annulus was at 6,980 ft, and we concurred. After the initial cementing of the 7 in. casing in

1954, our interpretation was that the 7 in. annulus above the top of cement area would have been filled with drilling mud and cement spacers only.

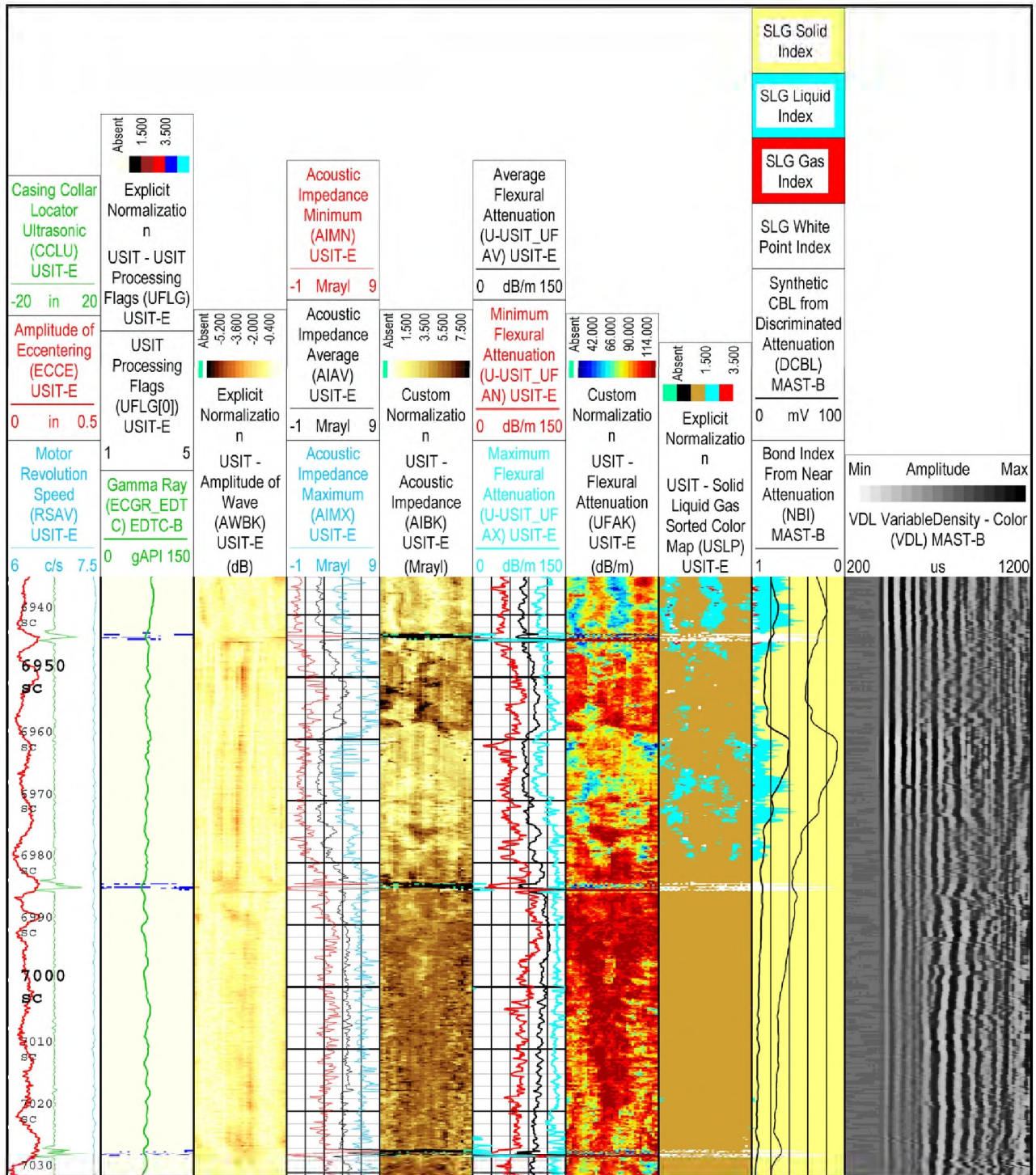


Figure 30: 7 in. IBC and CBL [10] Log Showing Top of Cement at 6,980 ft

Figure 31 shows that this annulus was logged as a combination of solids, liquids, and gases (second track from right to left: light blue, red, and yellow).

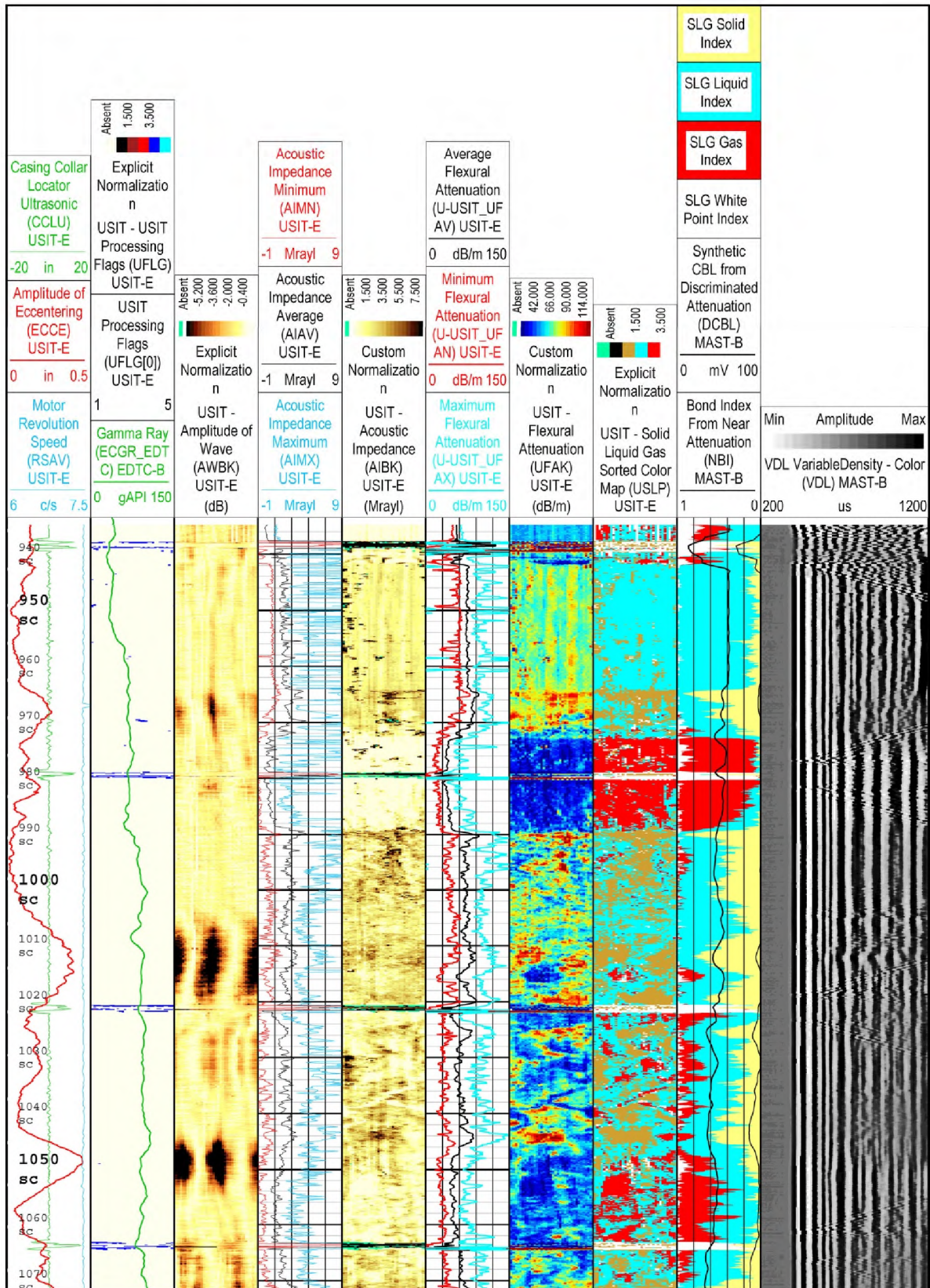


Figure 31: 7 in. IBC and CBL [10] Log Showing Annulus Condition 940–1,070 ft

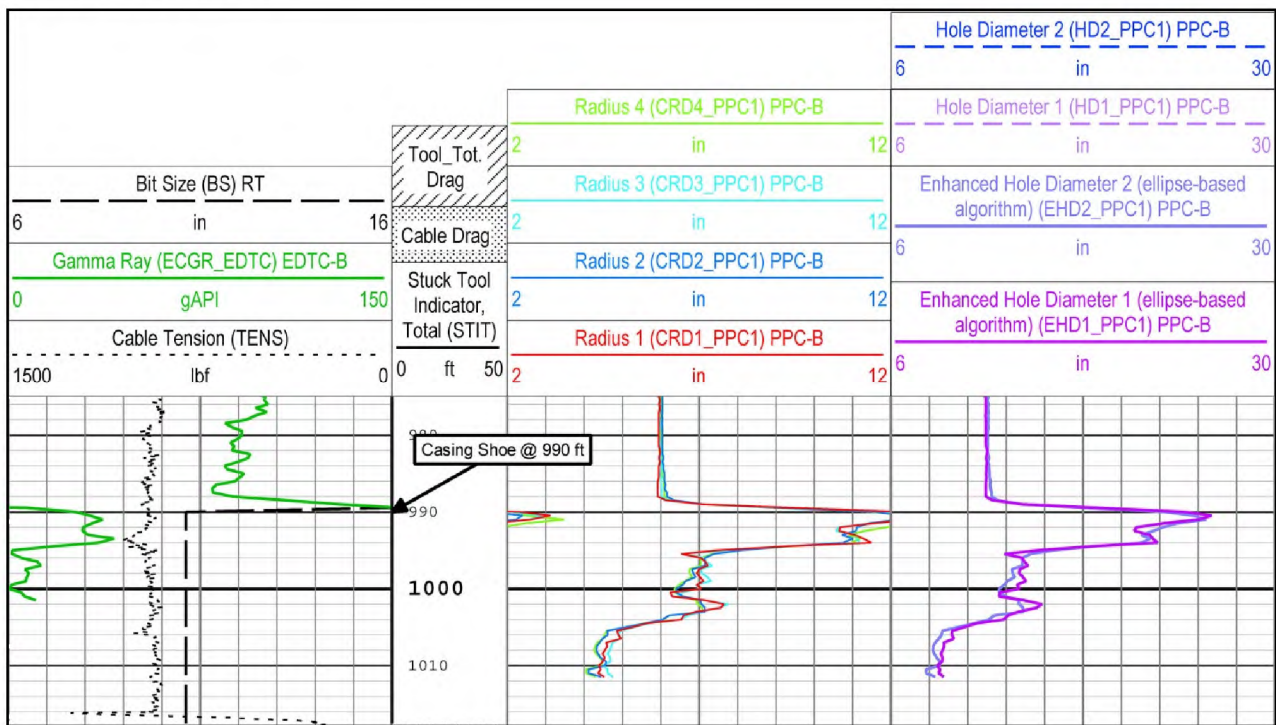
### 2.3 Openhole Summary

Table 8 shows the two logs that were run in the openhole below the 11 3/4 in. casing shoe.

**Table 8: Openhole Inspection Logs**

Date	Vendor	Log	Top (ft)	Bottom (ft)
August 10, 2018	Schlumberger	Caliper - 4 arm	870	1016
August 10, 2018	Schlumberger	Formation Microresistivity Imager	993	1016

Figure 32 shows the caliper log, which identified a 24–26 in. diameter area at 990–994 ft directly below the 11 3/4 in. surface casing shoe, which is denoted by the black arrow and annotation. The Formation Microresistivity Imager (FMI) also confirmed the diameter. In 1953, when the original openhole was drilled, the hole diameter was reported as 16 in. down to 990 ft and 10 5/8 in [12]. thereafter. The 24–26 in. observed was much greater than both the original openhole diameters; we could not ascertain if this hole enlargement was related to drilling and cementing operations from 1953, or related to the October 23, 2015 blowout. Additional observations on the FMI log regarding conductive fractures are found in the Hydrology report [14].



**Figure 32: 4-Arm Caliper [15] Log, 940–1,070 ft**

### 2.4 11-3/4 in. Summary

Table 9 shows the logs that provided information about the 11 3/4 in. casing. There were no historical 11 3/4 in. casing inspection logs that preceded the 7 in. casing failure. As with the 7 in., the 11 3/4 in. logging program was comprehensive and intended to gather as much information about the 11 3/4 in.

casing and annulus as possible; different technologies, multiple vendors, and state of the art inspection tools were employed. All of the logs listed were requested and supervised by Blade according to the Phase 3A Contingency Part 2 Work Plan [5]. Some of these logs were run through the 2 7/8 in. tubing and 7 in. casing (e.g., April 18, 2016, MID-2 and MID-3) and provided early information on the integrity issues that were confirmed with other logs.

**Table 9: 11 3/4 in. Casing Inspection Logs**

Date	Vendor	Log	Top (ft)	Bottom (ft)
April 18, 2016	TGT, Versa-line, GNPT	MID-2, MID-3	0	990
November 2, 2017	Baker Hughes GE	Caliper - 56 arm	0	875
November 7, 2017	EV	Camera	0	275
November 8, 2017	EV	Camera	890	930
November 15, 2017	Baker Hughes GE	Caliper - 56 arm	0	935
November 16, 2017	TGT	MID-2	0	929
December 2, 2017	TGT	MID-2, MID-3	0	990
May 20, 2018	Well Analysis Corporation	Noise	0	990
August 10, 2018	Schlumberger	Caliper - 4 arm	870	990
August 11, 2018	Well Analysis Corporation	Noise	0	990
August 12, 2018	Baker Hughes GE	Caliper - 56 arm	0	990
August 12, 2018	Baker Hughes GE	INTeX	0	970
August 13, 2018	Baker Hughes GE	HRVRT	0	950
August 14, 2018	Schlumberger	Isolation Scanner	196	990
August 15, 2018	Schlumberger	Ultrasonic Corrosion Imaging	195	990
August 15, 2018	Schlumberger	Sonic Scanner	196	970
August 18, 2018	EV	Camera	0	212
August 19, 2018	EV	Camera	700	995

Table 10 shows our interpretation of the 11 3/4 in. anomalies observed in the logs listed in Table 9. On a joint by joint basis, when anomalies are present, they are marked with a 'y'. If anomalies are not present, then the entry is blank. The anomalies observed were the following:

- Joints with a casing weight probably heavier than 42 lb/ft
- Joints with external metal loss
- Joints with holes
- Joints with internal metal loss
- Joints with ovality
- Joints with casing wear

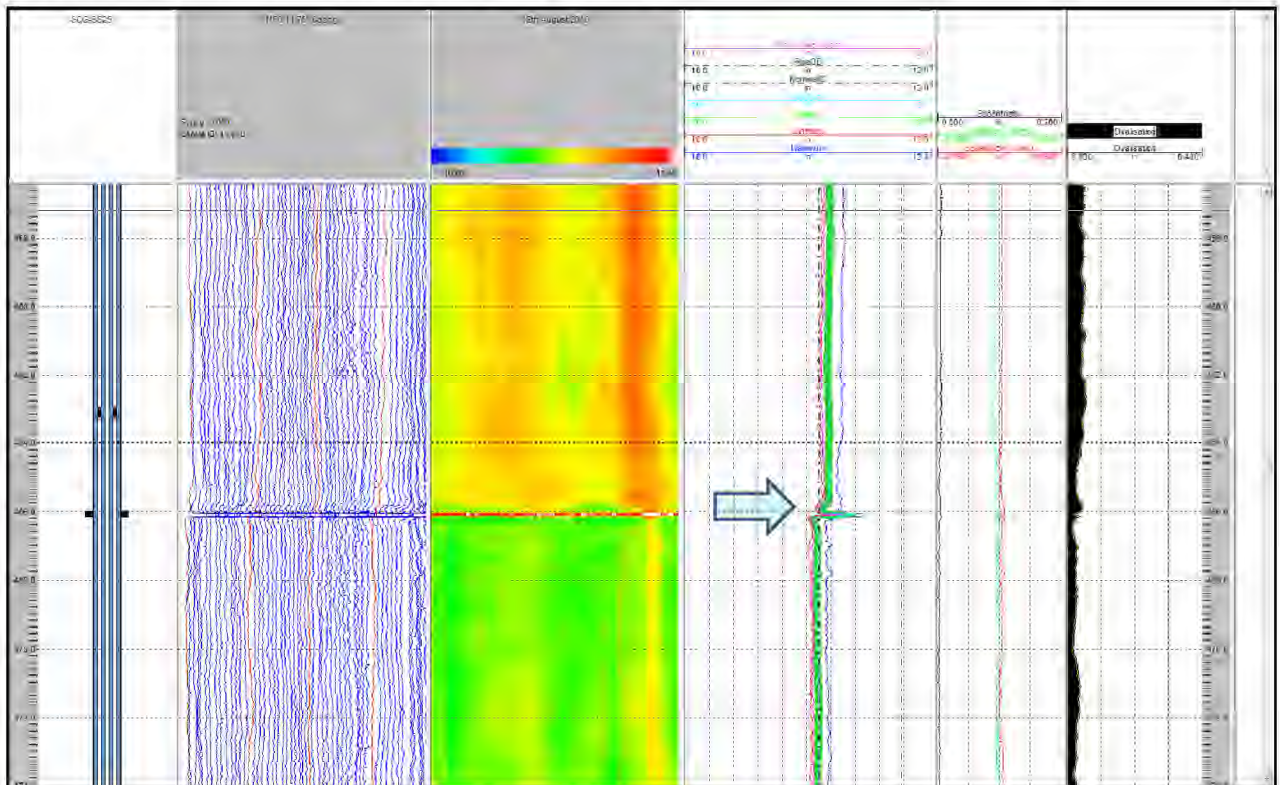
Table 10: 11 3/4 in. Defect Summary

Joint Number	Heavier than 42 lb/ft	External Metal Loss	Holes	Internal Metal Loss	Ovality	Casing Wear	Top Body (ft)	Body Length (ft)
1	y						12.6	13.7
2					y		26.5	42.5
3		y			y		69.1	42.4
4		y	y				111.6	40.2
5		y	y				152.1	43.1
6		y	y			y	195.4	41.3
7		y	y			y	237.0	42.5
8		y	y			y	279.7	40.4
9		y				y	320.3	41.2
10		y			y	y	361.7	34.7
11						y	396.6	27.5
12					y	y	424.3	41.7
13	y					y	466.2	36.4
14					y	y	502.8	41.3
15							544.3	43.6
16					y		588.1	36.8
17							625.1	36.8
18							662.1	40.0
19				y			702.3	41.6
20				y			744.1	37.8
21				y			782.1	42.0
22							824.3	41.8
23				y		y	866.4	40.5
24				y		y	907.1	41.9
25	y			y	y	y	949.2	38.3



### 2.4.1 Casing Weight Changes

The 11 3/4 in. caliper log shows three joints (namely 1, 13, 25) that may have been a heavier weight casing than the 42 lb/ft reported during the original drilling and completion records. Figure 33 shows what the heavier weight casing looked like on the 11 3/4 in. caliper log. At a depth of ~466 ft, the mean ID (green highlighted line) reduced from joint 12 (above) to joint 13 (below). Our interpretation was that this reduction in ID was indicative of a casing weight change.



**Figure 33: 11 3/4 in. Caliper Log, Mean Average ID Changes (Green Line) Joints 12–13 (Arrow)**

The ultrasonic logs observed changes in dimensions at the same joints as the caliper log, except for joint 1. The nominal wall thickness of 11 3/4 in. 42 lb/ft is 0.333 in. [4] The ultrasonic logs observed an average wall thickness of 0.356 in. and 0.369 in. for joints 13 and 25, respectively, whereas the range of wall thicknesses for all other joints was 0.311–0.336 in. The ultrasonic logs could not measure the wall thickness of joint 1 because it was above the fluid level in the well.

### 2.4.2 External Metal Loss

Figure 34 shows the 11 3/4 in. HRVRT and Isolation Scanner logs with the depth range of surface to 430 ft. Blade, Baker Hughes, and Schlumberger’s interpretation was that external corrosion is present. This area was highlighted with a green box on the HRVRT track and was logged at a depth of approximately 90–385 ft. The external corrosion was predominantly on joints 3–10. Joint 5 (from 152–195 ft) showed the greatest occurrence of external corrosion. The yellow boxes show the “Max FL Axial” track from HRVRT and the “Thickness” track from Isolation Scanner. There was close agreement in the shape of the curves. The isolation scanner shows that the joint maximum penetration by thickness ranged from 62.19 to 94.50% (orange box) for joints 6–10.

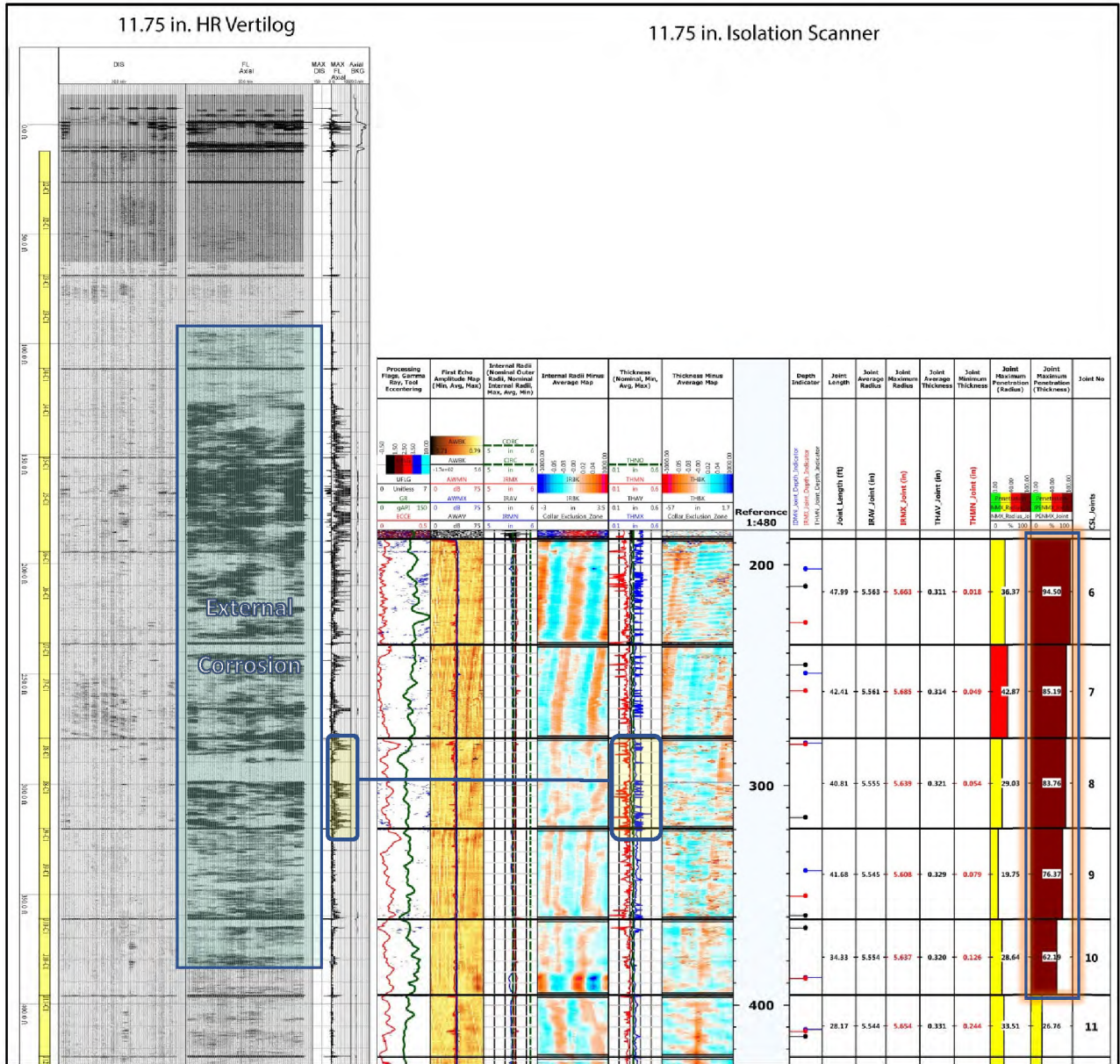


Figure 34: 11 3/4 in. HRVRT [16] and Isolation Scanner [17], External Corrosion Observed (Green Box)

Figure 35 shows the maximum penetration by wall thickness for the 11 3/4 in. joints 6–25. The deepest wall thickness penetration occurred in joints 6–10; the deeper joints did not show the same level of penetration. Figure 36 shows an example of a location of isolated external corrosion on joint 17. Schlumberger reported that the deepest penetration was approximately 26%; the magnitude was much lower than the one shown in joints 6–10 (Figure 34).

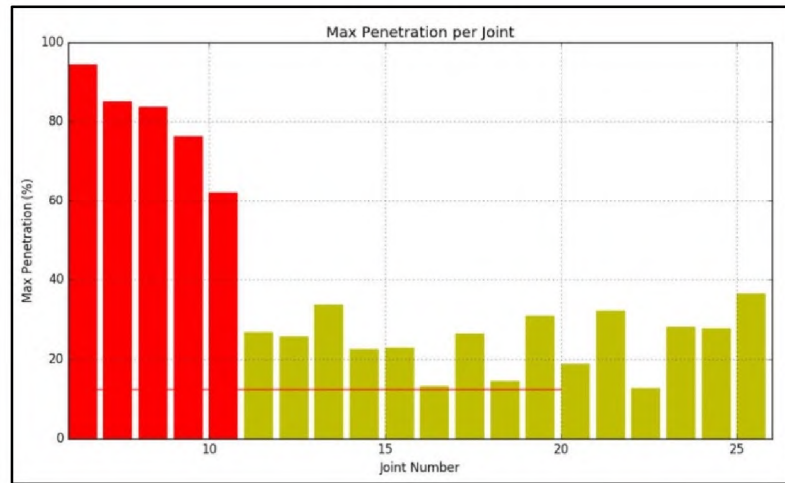


Figure 35: 11 3/4 in. IBC [17] Summary of Maximum Penetration by Wall Thickness for Joints 6–25

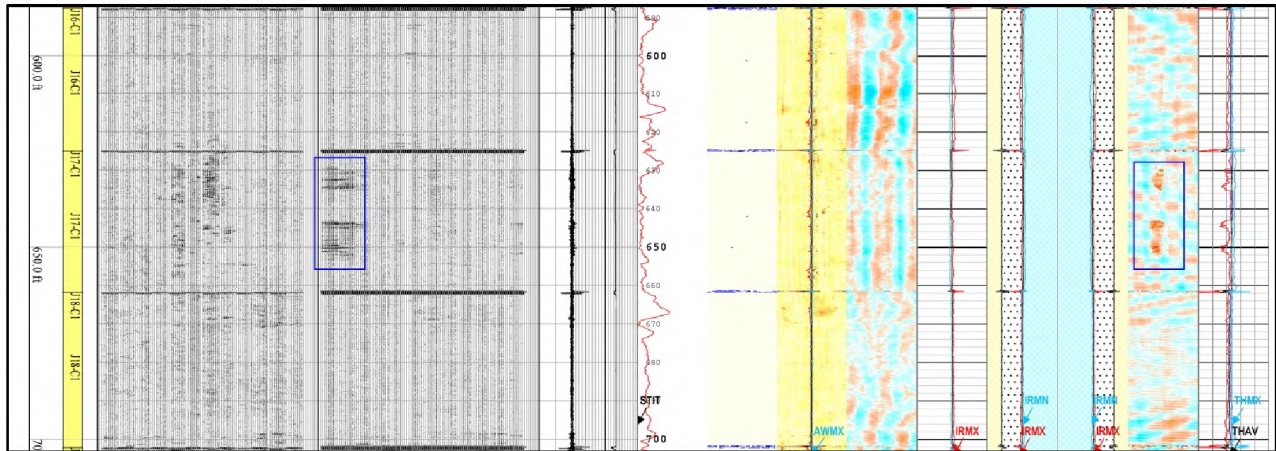


Figure 36: 11 3/4 in. HRVRT [16] and IBC [17] Log, Joints 16–18, Isolated External Corrosion at Joint 17 (Blue Box)

### 2.4.3 Holes

We observed the presence of holes in the 11 3/4 in. casing via the ultrasonic, MFL, caliper, and video imaging logs. The holes were observed from 134–300 ft in joints 4–8. Figure 37 shows the caliper log from 144–148 ft and video imaging at approximately 145 ft and 147 ft. The caliper log clearly shows the presence of holes in the second, third, and fourth tracks, further corroborated by the photographs from video imaging. We did not observe casing wear or pitting adjacent to the holes visually and using the caliper data. We used the caliper log to identify 58 holes; 50 holes were detected on joint 5 alone.

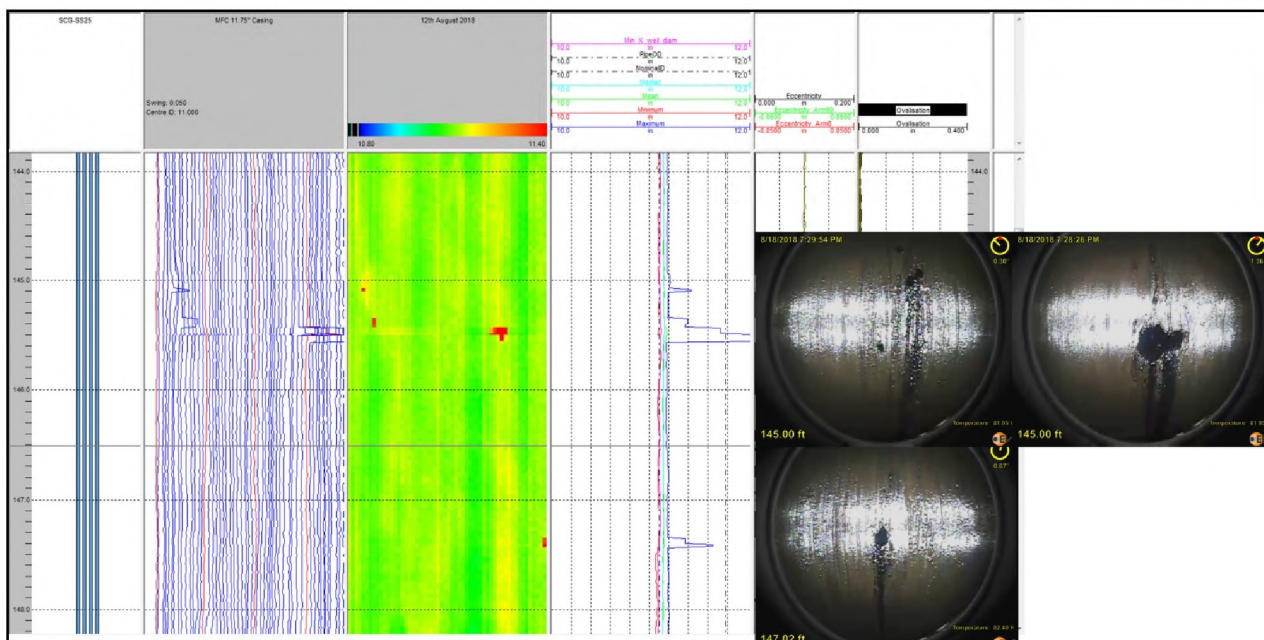


Figure 37: 11 3/4 in. Caliper Log [7] and Pictures from Video Imaging at 145 ft and 147 ft

Figure 38 shows an example of a hole at 145 ft dimensioned for length and width. EV Camera provided dimensions for 24 holes. Appendices C.1 and C.3 contain additional images. There were holes through the wall thickness of the casing and what appeared to be a void or cavity extending behind the hole. For many of the holes, this visual observation was confirmed by the caliper fingers reading diameters of 14 in., which was the maximum diameter capability of the tool.

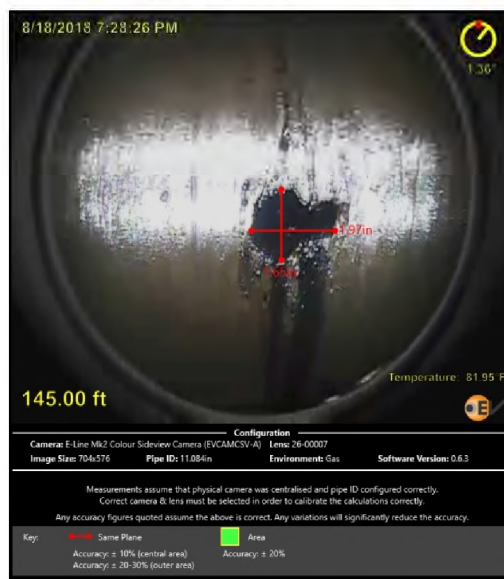


Figure 38: Picture of Hole in 11 3/4 in Casing with Dimensions from Video Imaging at 145 ft

### 2.4.4 Internal Metal Loss

We concur with Schlumberger and Baker’s interpretation that internal metal loss was observed in many joints. But not all of the internal metal loss observed should be interpreted as internal pitting. Figure 39

and Figure 40 shows joint 13 with the internal metal loss feature highlighted in blue rectangles. Each rectangle is comprised of two, three, or four metal loss features that have uniform dimensions, regular spacing and are stacked vertically.

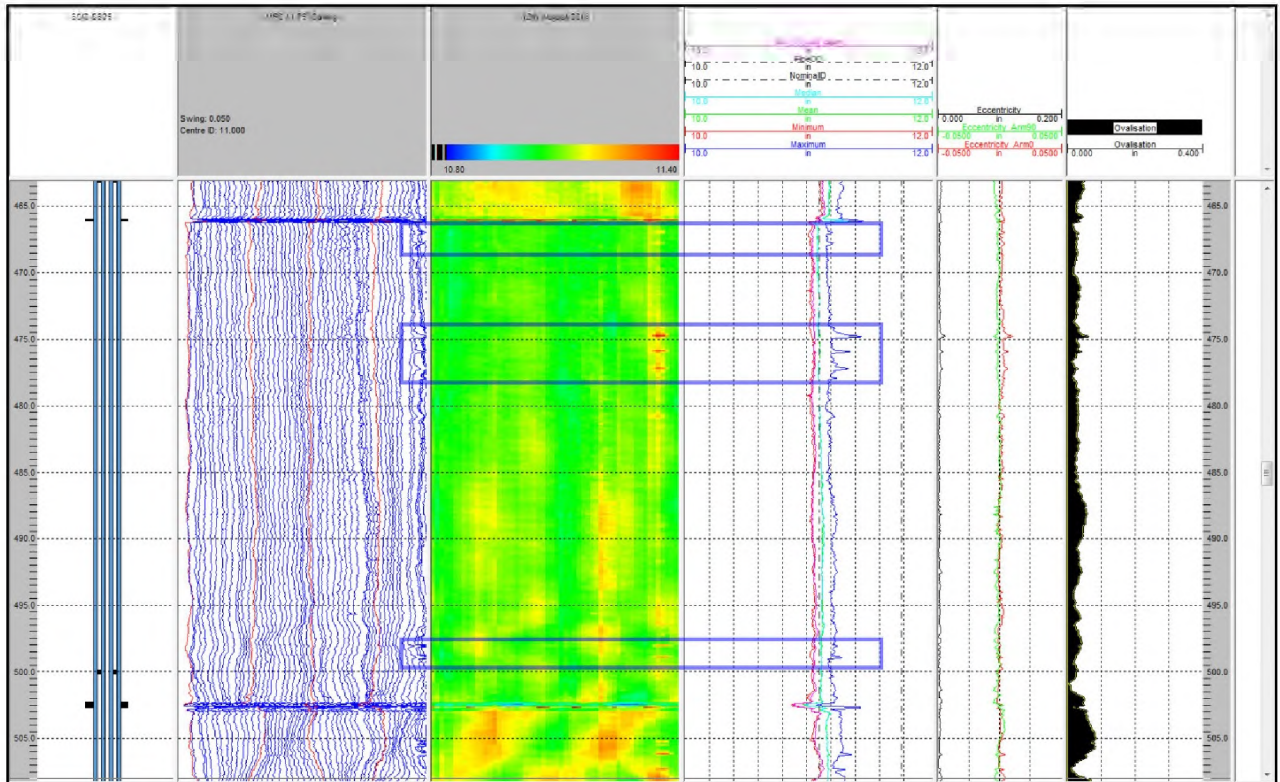


Figure 39: Caliper Log [7] Example of Internal Metal Features (Blue Rectangles) at 11 3/4 in. Joint 13

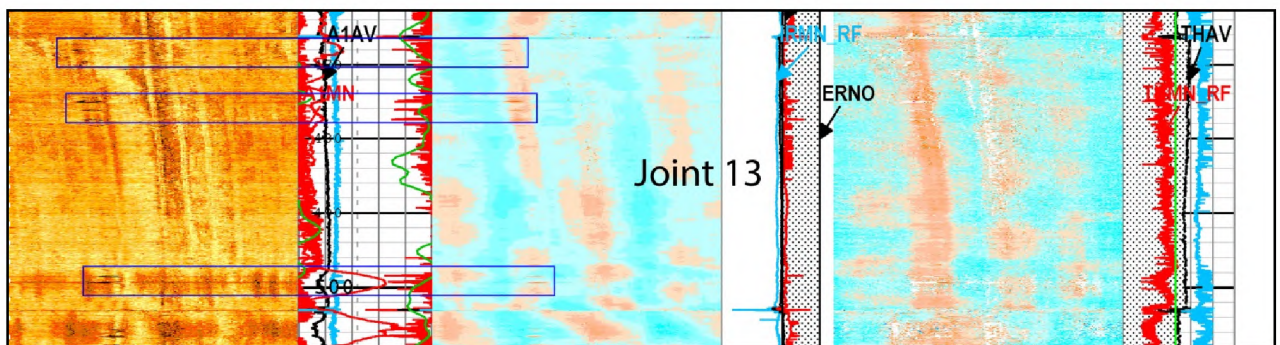


Figure 40: UCI Log [17] Example of Internal Metal Features (Blue Rectangles) at 11 3/4 in. Joint 13

Figure 41 shows the HRVRT log for joints 10–15. Within the blue shaded rectangles are the uniform internal metal loss features. They are present on multiple joints at the same orientation, i.e., at the same clock position. Our interpretation is that if they were manufacturing related, it would be unlikely to see these features line up in the well so consistently. The uniform internal metal loss features are found almost exclusively in joints that have casing wear. Casing wear was expected to some degree considering that fishing operations, an openhole sidetrack, and approximately 6,000 ft of drilling operations were performed through the 11 3/4 in. casing. The drillpipe tool joints may have been hardbanded and caused these uniform metal loss features. Another possible explanation is the use of hardened slips (in packers,

bridge plugs, or similar service tools) imprinting their shape on the ID as the tools were set. This was discounted because no operations records of running these tools were found; if they had been run, the imprints would have likely had more circumferential characteristics than those observed.

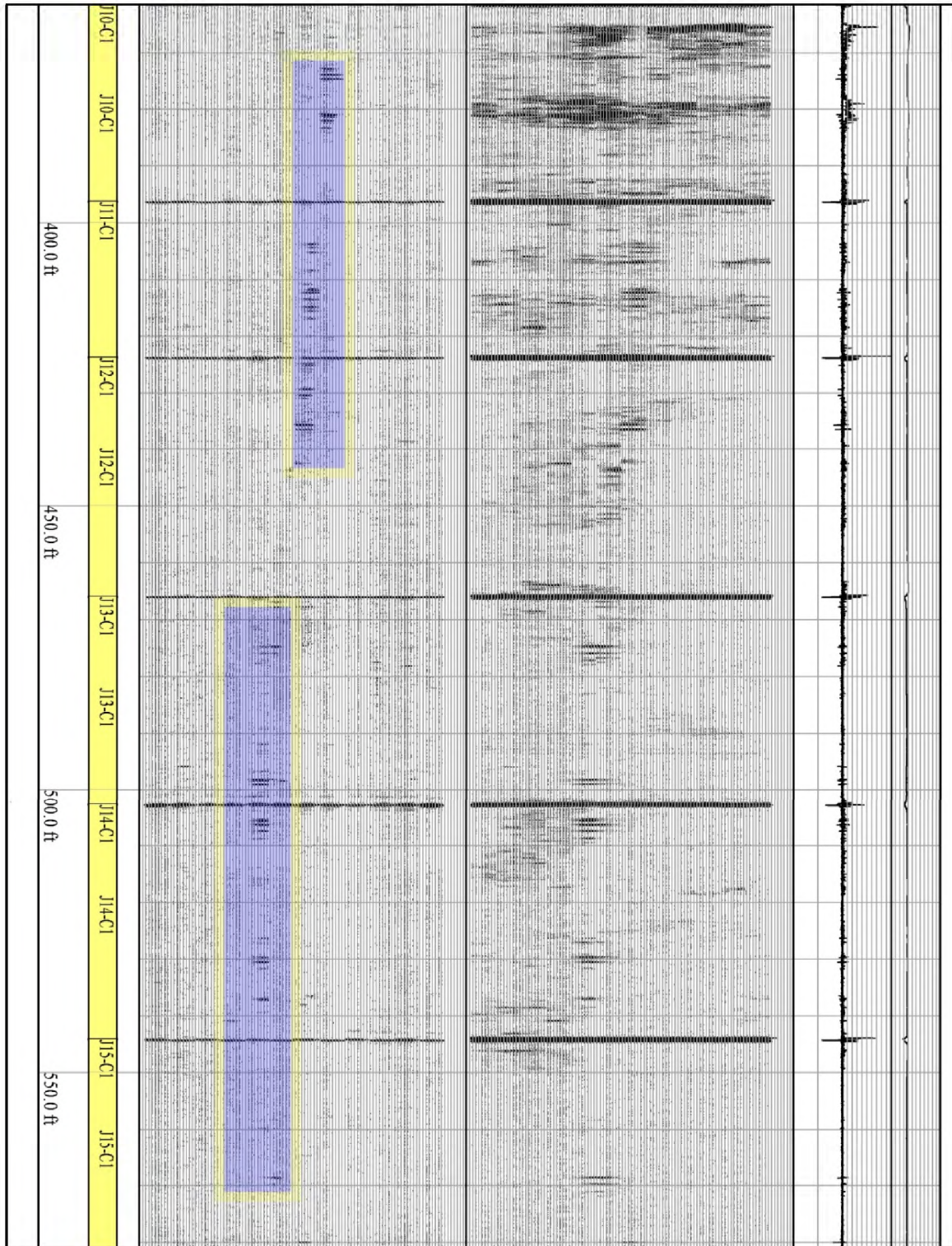


Figure 41: HRVRT Log [16], Examples of Internal Metal Loss Features (Highlighted Blue), Joints 10–15

Figure 42 shows the three caliper logs and one HRVRT log run in the 11 3/4 in. casing. The caliper logs were run first, after extraction of the 892 ft of 7 in. casing (down to the upper fish), second, after the fishing and extraction of 892–939 ft of 7 in. casing (the lower fish), and third, after three 11 3/4 in. casing scraper runs. Discussion of why redundant logging was performed and what its relationship to the protection of evidence was can be found in a separate report [4].

Our interpretation is that the caliper logs repeatedly found instances of metal loss beginning at approximately 700 ft and extending to the shoe. These metal loss features were in the same location, at the same or similar penetration, and further corroborated by the HRVRT and the ultrasonic logs. Based on the scattered distribution and non-uniform penetration, our interpretation is that this internal metal loss was pitting, which was observed between 700 and 990 ft in joints 18–25. Figure 43 shows video imaging from August 19, 2018, of an oval shaped feature at ~731 ft substantiating this interpretation. Appendix C contains additional video images.

# 11 3/4 in. Caliper Data

# 11 3/4 in. HRVRT

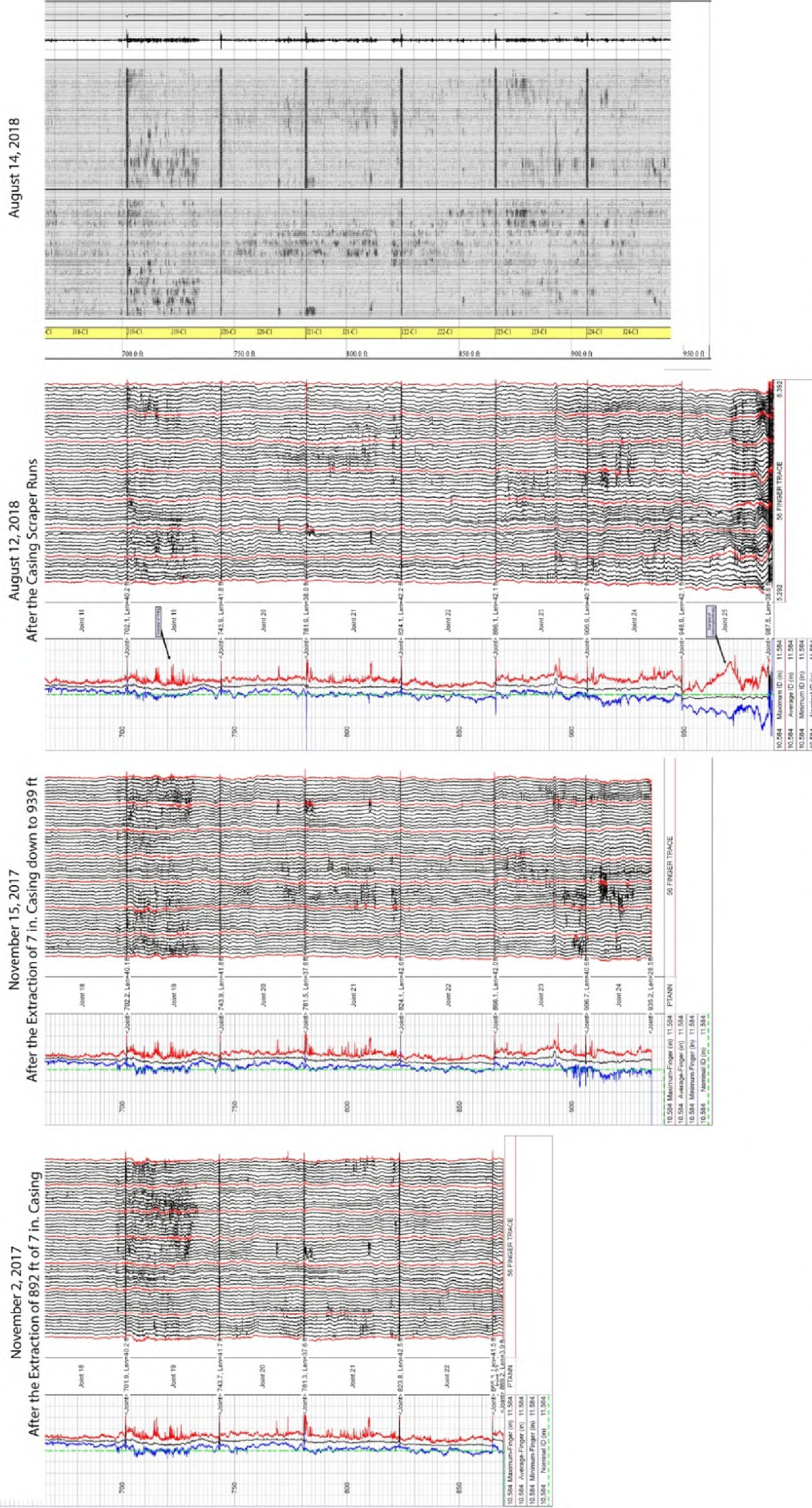


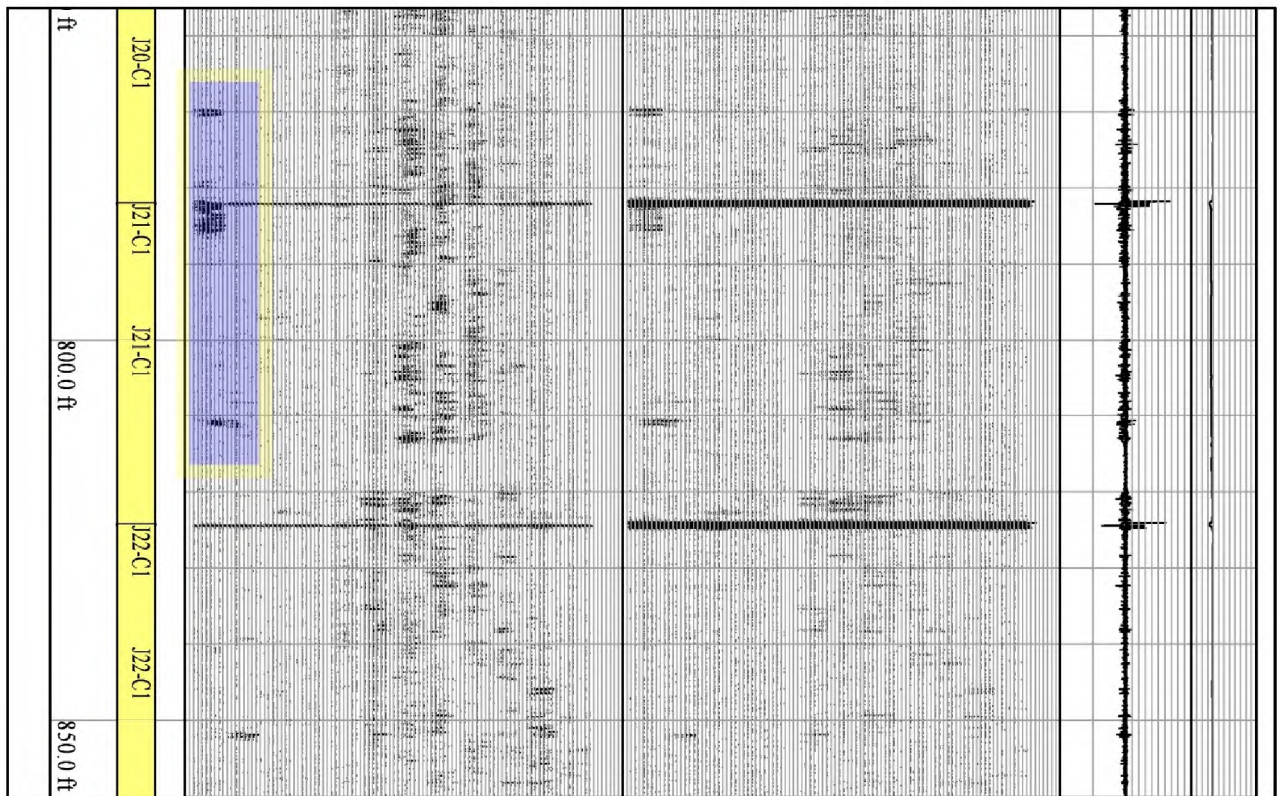
Figure 42: 11 3/4 in. Caliper Logs and HRVRT Log [16] (Right), Internal Metal Loss as Pitting from 700–990 ft





Figure 43: 11 3/4 in. Video Imaging at ~731 ft, Example of Pitting Observed

Figure 44 shows an area (blue rectangle) containing a nonrandom metal loss feature from 770–812 ft. We observed this feature in the caliper log (Figure 42) and ultrasonic logs (not shown) in the same likeness. Blade observed external corrosion on the OD of 7 in. casing and connections, classified internally as a type III corrosion feature [2]. Type III corrosion features were found on 7 in. casing connection 19, joint 20, and connection 20 at depths 769.7 ft, 782-787 ft, and 810.6 ft respectively—the same depths of the 11 3/4 in. features in the blue rectangle. The IBC log sized the penetration of these features as 0.095–0.103 in. (28.7–30.8%)



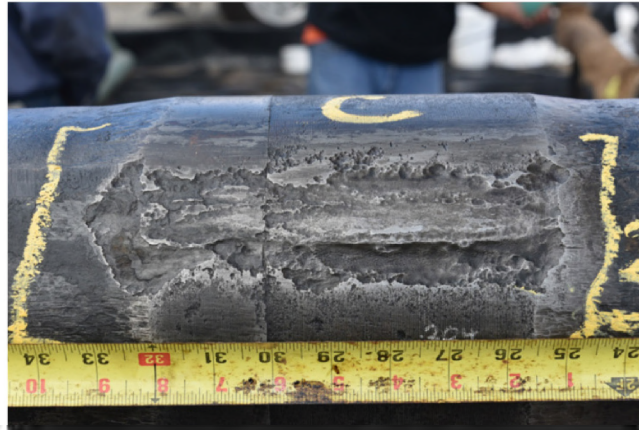
**Figure 44: 11 3/4 in. HRVRT Log [16], Nonrandom Internal Metal Loss (Blue Rectangle)**

Besides connection 19, joint 20, and connection 20, additional locations for type III corrosion feature are identified in the report *SS-25 Casing Failure Analyses* [2] ; these locations coincide with the metal loss features in the 11 3/4 in. logs. Figure 45 shows the description of the type III corrosion feature.

See Appendix D for an additional figure regarding the 7 in. casing type III corrosion feature and the related 11 3/4 in. casing internal corrosion.

## Type III Corrosion Feature

- Metal loss along the perimeter of the rectangular shape, but middle portion is usually not affected.
- Usually seen in the connection



**Figure 45: Type III Corrosion Feature, Photograph of 7 in. Casing Connection No. 19 [2]**

Figure 46 shows the trajectory of the well for the extents of the 11 3/4 in. casing, which is from surface to 990 ft. The average inclination is 0.94°, which may seem vertical. However, the well at 990 ft is ~13 ft to the east of the surface location; this is seen in the inset graphs entitled Vertical Section and Top View. The way we interpret the 13 ft is that contact between the 7 in. casing and the 11 3/4 in. casing was unavoidable. Denoted by green arrows are the estimated contact locations; they match the casing connections.

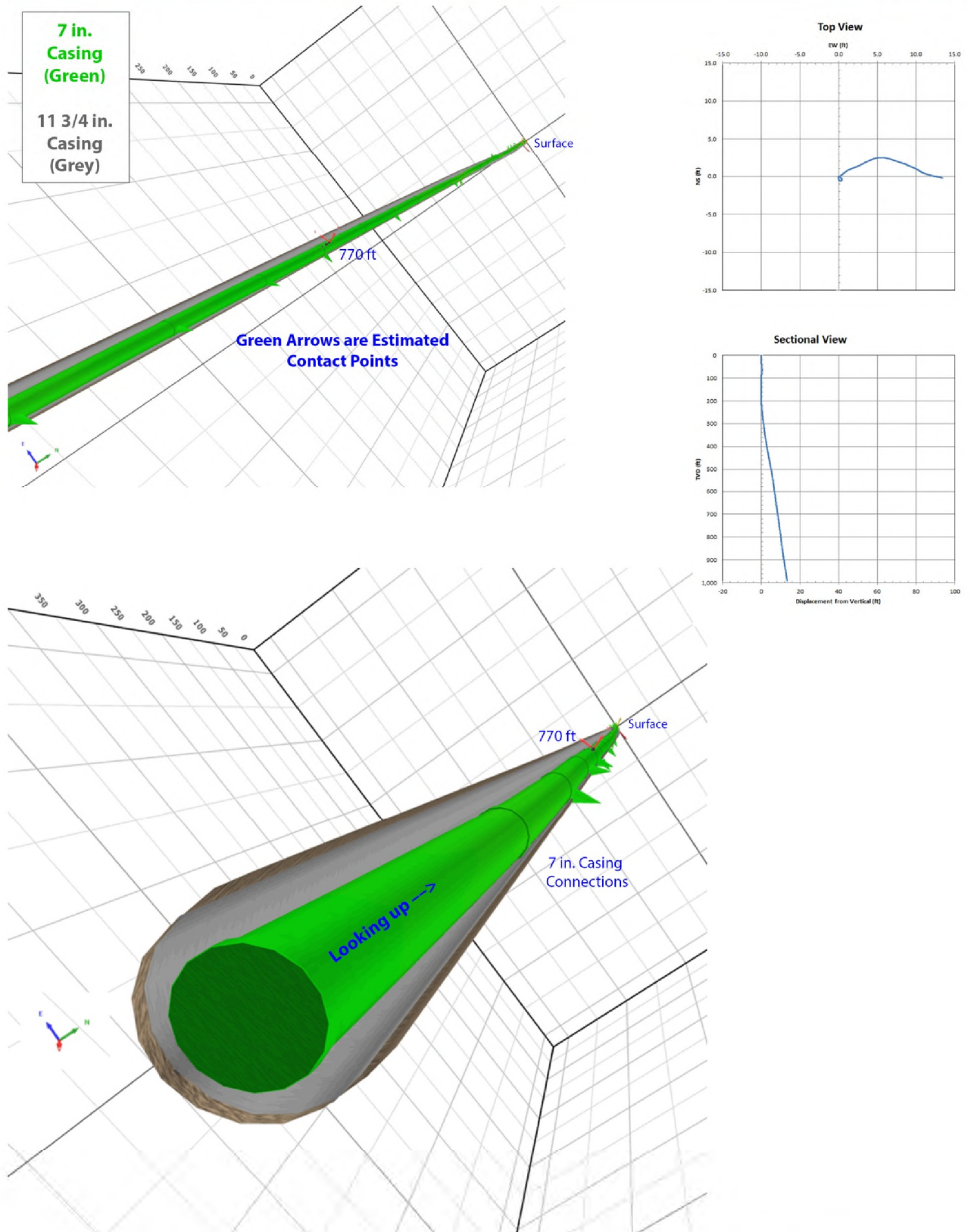


Figure 46: Trajectory [18] and Estimated 7 in. and 11 3/4 in. Casings Contact Locations